Journal of
Functional Biomaterials

Special Issue Reprint

Antibacterial Materials

Recent Advances in Methodologies and Regulations

Edited by
Claudia Vineis and Alessio Varesano

mdpi.com/journal/jfb

MDPI

Antibacterial Materials: Recent Advances in Methodologies and Regulations

Antibacterial Materials: Recent Advances in Methodologies and Regulations

Guest Editors

Claudia Vineis
Alessio Varesano

MDPI

Basel • Beijing • Wuhan • Barcelona • Belgrade • Novi Sad • Cluj • Manchester

Guest Editors

Claudia Vineis
Institute of Intelligent Industrial Technologies and Systems for Advanced Manufacturing (STIIMA)
Consiglio Nazionale delle Ricerche (CNR)
Biella
Italy

Alessio Varesano
Institute of Intelligent Industrial Technologies and Systems for Advanced Manufacturing (STIIMA)
Consiglio Nazionale delle Ricerche (CNR)
Biella
Italy

Editorial Office
MDPI AG
Grosspeteranlage 5
4052 Basel, Switzerland

This is a reprint of the Special Issue, published open access by the journal *Journal of Functional Biomaterials* (ISSN 2079-4983), freely accessible at: https://www.mdpi.com/journal/jfb/special_issues/59IN49NX52.

For citation purposes, cite each article independently as indicated on the article page online and as indicated below:

Lastname, A.A.; Lastname, B.B. Article Title. *Journal Name* **Year**, *Volume Number*, Page Range.

ISBN 978-3-7258-4177-6 (Hbk)
ISBN 978-3-7258-4178-3 (PDF)
https://doi.org/10.3390/books978-3-7258-4178-3

Contents

About the Editors

Claudia Vineis

Senior Researcher at CNR-STIIMA. Biologist. She manages the Biological laboratory at CNR-STIIMA in Biella (Italy). Responsible for CNR Relations with the "Textile for Future" Partnership in Europe. Scientific Director of the STIIMA Biella for the Joint Research Laboratory between CNR-STIIMA and the University of Bergamo. Representative's CNR of the Technical Committee Textiles and Clothing n. 046 UNI and ISO group WG22. Member of the "European Technology Platform for the Future of Textiles and Clothing" (Euratex, Brussels). Expert member of "Rete Nazionale Tessile, Innovazione e Salute". Member of the Scientific Committee of Associazione Tessile & Salute. "Guest Editor" for Polymers MDPI Journal and Journal of Functional Biomaterials MDPI. She was a member of the Institute Council of CNR-ISMAC (2009-2016). She won the third AWI/DWI Award for Excellence in Wool Science. She is the author of numerous papers in international peer-reviewed journals, book chapters, patents, and presentations at conferences, with an h-index of 31 (by Scopus). Her main activities are in the field of synthesis and analysis of new antimicrobial finishing for textiles; study and characterization of biopolymers, mainly structural proteins; extraction keratin from wool fibres; preparation and characterization of nanofibres by means of electrospinning process; development of analytical methods for distinguish fine animals hairs; fibre science and processing; fibre testing, structure and properties of textile materials. She led International and National Research Projects and Industrial Research Contracts.

Alessio Varesano

Senior Researcher at CNR-STIIMA. Chemical Engineer. He manages the Prototypes and Pilot Plants laboratory at CNR-STIIMA in Biella (Italy). His main research activities deal with the development of innovative textile materials and new finishing for textiles (electrically conducting polymers, antimicrobial finishing, nanoparticles) and electrospinning. He led and coordinated research activities of 8 National and Regional research projects and 3 industrial research contracts. He participated in European Projects in FP7 and H2020 as Participant Contact. He is a member of the Steering Committee "Innovative production processes" of the Italian Technology Cluster "Fabbrica Intelligente" (Italian Smart Industry Cluster) and a member of the "European Technology Platform for the Future of Textiles and Clothing" (Euratex, Brussels). He participated in the research activities of about 25 research projects. He is the author of over 150 presentations at national and international conferences, about 80 papers in international peer-reviewed journals, with an h-index of 31 (Scopus).

Preface

In recent years, the rise in antibiotic-resistant bacteria has driven extensive research into the development of antibacterial materials across various fields, aiming to curb the spread of resistant strains. These innovative materials encompass a wide range of substances, including nanoparticles, polymers, chemicals, proteins, and enzymes. Additionally, the final products incorporating these antibacterial agents come in diverse forms, such as textiles, plastics, ceramics, and metals.

This Special Issue illustrates advances of antibacterial biomaterials in biomedical fields for implants, wound healing, bone regeneration and medical textiles.

Claudia Vineis and Alessio Varesano
Guest Editors

Journal of
Functional
Biomaterials

MDPI

Article

Green Synthesis of Controlled Shape Silver Nanostructures and Their Peroxidase, Catalytic Degradation, and Antibacterial Activity

Ayesha Shafiq, Aarti R. Deshmukh, Khaled AbouAitah and Beom-Soo Kim *

Department of Chemical Engineering, Chungbuk National University, Cheongju 28644, Republic of Korea; engr.ayesha.shafiq@gmail.com (A.S.); aartideshmukh1@gmail.com (A.R.D.); ke.abouaitah@gmail.com (K.A.)
* Correspondence: bskim@chungbuk.ac.kr; Tel.: +82-43-261-2372; Fax: +82-43-269-2370

Abstract: Nanoparticles with unique shapes have garnered significant interest due to their enhanced surface area-to-volume ratio, leading to improved potential compared to their spherical counterparts. The present study focuses on a biological approach to producing different silver nanostructures employing *Moringa oleifera* leaf extract. Phytoextract provides metabolites, serving as reducing and stabilizing agents in the reaction. Two different silver nanostructures, dendritic (AgNDs) and spherical (AgNPs), were successfully formed by adjusting the phytoextract concentration with and without copper ions in the reaction system, resulting in particle sizes of ~300 ± 30 nm (AgNDs) and ~100 ± 30 nm (AgNPs). These nanostructures were characterized by several techniques to ascertain their physicochemical properties; the surface was distinguished by functional groups related to polyphenols due to plant extract that led to critical controlling of the shape of nanoparticles. Nanostructures performance was assessed in terms of peroxidase-like activity, catalytic behavior for dye degradation, and antibacterial activity. Spectroscopic analysis revealed that AgNDs demonstrated significantly higher peroxidase activity compared to AgNPs when evaluated using chromogenic reagent 3,3′,5,5′-tetramethylbenzidine. Furthermore, AgNDs exhibited enhanced catalytic degradation activities, achieving degradation percentages of 92.2% and 91.0% for methyl orange and methylene blue dyes, respectively, compared to 66.6% and 58.0% for AgNPs. Additionally, AgNDs exhibited superior antibacterial properties against Gram-negative *E. coli* compared to Gram-positive *S. aureus*, as evidenced by the calculated zone of inhibition. These findings highlight the potential of the green synthesis method in generating novel nanoparticle morphologies, such as dendritic shape, compared with the traditionally synthesized spherical shape of silver nanostructures. The synthesis of such unique nanostructures holds promise for various applications and further investigations in diverse sectors, including chemical and biomedical fields.

Keywords: green synthesis; silver nanodendrites; peroxidase activity; dye degradation; antibacterial activity

1. Introduction

Recently, there has been a notable surge for nanoparticles in multiple applications and products that support human life. High-quality metal nanoparticles (e.g., Au, Ag, Pt, and others) have gained extensive research in diverse biomedical domains, e.g., anticancer therapy, radiotherapy augmentation, drug delivery, antibacterial treatments, diagnostic assays, antifungal treatments, bioimaging, biosensing, gene delivery, and numerous others [1–3]. When concerning silver nanoparticles, they are utilized in composites [4,5], ceramics, polymers, agriculture, and energy [6]. Several methods have been employed to synthesize nanoparticles, including the chemical process, physical process, biological process, thermal decomposition [7], heat-induced evaporation, and laser ablation [8]. Chemical methods typically involve reduction using reducing agents (i.e., sodium borohydride, dimethylformamide, trisodium citrate, hydrazine, ascorbic acid, m-hydroxy benzaldehyde, oleyl amine, and polyvinylpyrrolidone). Nanoparticles produced by these techniques range in

particle size from 25 nm to 650 nm [9]. However, compared with the biological approach, the production cost and toxicity of hazardous chemicals are disadvantages. Biological methods typically utilize microorganisms such as algae, fungi, and bacteria that are safe as bio-reducing agents, but their synthesis rates are slower compared with green synthesis using plant-based materials. Therefore, among biological methods, green synthesis, which utilizes plant materials (biomass, juice, and extracts) to synthesize silver nanoparticles, is increasingly supported by researchers. This is due to simplicity, eco-friendliness, safety, cost-effectiveness, reproducibility, stability, and source availability [10].

In the current study, the *Moringa oleifera* plant, a member of the *Moringa* family commonly used as a vegetable in Asian countries, was employed as a bio-reducing agent. *Moringa oleifera* is a fast-growing, draft-resistant plant native to Asian countries such as Nepal, Pakistan, and India. It is also grown in tropical and subtropical regions of America and Africa [11] and is readily available in local markets for a variety of purposes. This plant exhibits a variety of benefits [12]. For example, from a nutritional perspective, *Moringa* leaves contain protein, zinc, potassium, magnesium, and copper [13]. It is rich in natural bioactive components with medicinal properties such as flavonoids, phenolic compounds, terpenoids, carotenoids, sterols, anthraquinones, alkaloids, and saponins [14–17]. Some flavonoids demonstrate anticancer activity against Hela cancer cells [18]. In the realm of nanoscience, *Moringa oleifera* has received huge attention over the past decades for its potential ability to synthesize various metal nanoplatforms, as reported in various studies related to iron oxide, nickel oxide, lanthanum oxide [19], magnesium oxide [20], tungsten [21], and palladium nanoparticles [22] and others [23].

Important requirements in the development of nanoparticles are size and shape, as crucial factors that determine the reactivity and use of nanoparticles. Thus, changes in these properties can have a significant impact on their applications [24]. It is acknowledged that nanoparticles with complex structures have received more attention than simple particles due to their intricate structure [25]. Particle morphology, such as silver nanoflowers, silver dendrites, silver nanostars, and silver nanowires, provides more surface area or reactive sites compared with spherical nanoparticles [26]. Several studies have been conducted using trisodium citrate [27], ammonium citrate dibasic [28], polyvinylpyrrolidone, and formamide [29] to achieve nanoflower-like morphology.

The current study provides a straightforward method for the green synthesis of silver nanostructures in a controlled shape using *Moringa oleifera* leaf extract. Interestingly, two distinct morphologies of silver nanostructures, dendritic shapes (AgNDs) and spherical shapes (AgNPs), were feasibly obtained for the first time by varying the concentration of plant extract as a critical factor when reacted with silver nitrate with and without copper ions in the reaction mixture. Our results showed that silver nanodendrites exhibit superior properties compared with spherical nanoparticles when evaluated for oxidation, catalytic degradation, and antibacterial activity. These findings could open many opportunities and possible applications in various fields.

2. Materials and Methods

2.1. Synthesis of Silver Nanoparticles

Chemicals in all studies were used as purchased. Distilled water used in the experiment was produced with a Green RO 350 water purification system (Seoul, Korea). *Moringa oleifera* dried leaves were purchased from the Hands Herb Company, Korea. Leaves were rinsed with plenty of distilled water before drying again at 80 °C using an oven. The dried leaves were then ground with a mortar and pestle and stored in a glass bottle until use. For plant extraction, 3 g of dried leaves were added to 100 mL distilled water and refluxed at 100 °C for 1 h. Next, the solution was filtered and stored at 4 °C. To synthesize silver nanostructures, 5 mM $AgNO_3$ (silver nitrate, Samchun Chemicals Company, Seoul, Korea) and 3 mM of Cu $(NO_3)_2 \cdot xH_2O$ (copper nitrate (II) hydrate 99.99%, Sigma-Aldrich, St. Louis, MO, USA) were added together to a 20 mL distilled water solution. Plant extracts of different volumes were added dropwise to this solution to form silver nanoparticles with

a controlled shape effectively. Two types of experiments were performed to determine the growth mechanism. The first type of experiment involved fixing precursor concentration (metal salt) and varying the volumetric concentration of the reducing agent (plant extract) as 10%, 20%, 30%, and 40% of the precursor, while the second type involved fixing the concentration of plant extract and varying the volumetric concentration of metal salt as 12.5%, 16.6%, and 25% of the precursor. These experiments were performed with and without copper nitrate hydrate. The mixture solution of each designed sample was incubated at room temperature for 24 h with a stirring speed of 200 rpm and then centrifuged (15,000 rpm for 10 min) using a Hanil Mega 17r high-speed refrigerated centrifuge, Korea. After removing the supernatant, the pellet precipitate was washed several times with distilled water. Finally, nanoparticles were obtained using a freeze dryer (Ilshin, Korea).

2.2. Peroxidase Activity

Peroxidase assay was performed according to Deshmukh and colleagues [30]. Briefly, 0.15 mL of concentrated AgNDs/AgNPs suspension (50 μg/mL) was mixed with 0.1 mL (10 mM) hydrogen peroxide (H_2O_2) (Samchun Chemicals Company, Seoul, Korea) in a test tube and allowed to stand at room temperature. Then, 0.25 mL acetate buffer solution (pH 4.2) was added, followed by rapid addition of 0.2 mL (12 mM) of 3,3′,5,5′-tetramethylbenzidine (TMB, 99%, Sigma-Aldrich, St. Louis, MO, USA) in ethanol. The colorless TMB was oxidized to a blue diimine. Absorbance was monitored over time, and comparisons were recorded at 655 nm at regular intervals [31].

2.3. Catalytic Activity

Two types of dyes were investigated to evaluate the catalytic behavior of silver nanoparticles in degradation. Methyl orange (MO, 85% dye content), methylene blue trihydrate (MB, 97% dye content), and sodium borohydride ($NaBH_4$, extra pure) were purchased from Samchun Chemicals Company, Seoul, Korea. A catalytic dye degradation experiment was performed by adding 5 mL of 15 mg/L dyes (MO, MB) to a 15 mL test tube, followed by adding 50 μL (0.06 M) $NaBH_4$ to each tube. The catalytic behavior was observed by adding 150 μL of 100 μg/mL AgNDs or AgNPs to this solution. The reaction started immediately, and the solids were removed after 5 min by centrifugation (13,000 rpm for 10 min). The degradation percentage was measured by recording the optical density using a UV–Vis spectrophotometer.

The % dye degradation was calculated from the equation:

$$\% \text{ Degradation} = \frac{(c_0 - c_t)}{c_0} \times 100 \quad (1)$$

where C_0 represents the initial dye concentration, and C_t represents the final dye concentration after degradation.

2.4. Antibacterial Activity

The antibacterial activity of AgNDs and AgNPs was evaluated using the disk-diffusion agar method [32] against representative microorganisms, *Staphylococcus aureus* (ATCC 6538) and *Escherichia coli* (ATCC 11775). Bacteria were cultivated on Luria-Bertani (LB) medium and incubated at 37 °C for 24 h. Antibacterial tests were performed using nanoparticle concentrations (100 μg/mL) [33,34] as effective concentrations against bacterial strains. After dropping 100 μL of silver nanostructures (100 μg/mL) on a sterile paper disc (Advantech, Japan) with a diameter of 10 mm, it was dried, placed on an LB agar plate, and incubated at 37 °C for 24 h. Then, the antibacterial activity was obtained by measuring the zone of inhibition diameter (mm). Antibacterial activity was assessed in triplicate, and data were plotted with error bars after calculating standard deviations.

2.5. Characterization of Silver Nanostructures

A UV–Vis absorbance spectrum of 200–800 nm wavelength was acquired using a UV–Vis spectrophotometer at a resolution of 10 nm (mini, Shimadzu, Japan). Fourier transform infrared spectroscopy (FTIR) analysis was used to identify functional groups. FTIR measurements were performed using an IR200 FTIR spectrometer (Thermo Scientific) with a wavenumber range of 500–4000 cm^{-1} and a resolution of 4 cm^{-1} after 32 scans. The crystallinity of the nanostructures was measured using an X-ray diffractometer (XRD, X'Pert-Pro, Analytical) under the following conditions: room temperature, voltage 40 kV, CuKα radiation at λ = 1.5406 Å, and scanning with 2θ range from 0° to 100° with 2°/min. The average crystallite size was determined by the Debye equation.

$$D = \frac{0.9\,\lambda}{\beta\ \cos\ \theta} \quad (2)$$

where D is the particle size, λ is the X-ray wavelength (0.154 nm), and β is the full width at half maximum (FWHM). The interplanar spacing (d) between atoms was calculated by Bragg's law.

$$2d\ \sin\ \theta = n\lambda \quad (3)$$

$$d = \frac{\lambda}{2\sin\theta}(n = 1) \quad (4)$$

The nanostructures morphology was characterized using transmission electron microscopy (TEM, Libra 120, Carl Zeiss, Jena, Germany). For TEM observation, drops of the colloidal nanostructure solution were placed on a carbon-coated copper grid and dried at room temperature. Particle morphology and elemental composition were analyzed using a scanning electron microscope (SEM, LEO-1530) coupled to energy-dispersive X-ray spectroscopy (EDS). X-ray photoelectron spectroscopy (PHI Quentera-II) analysis was performed to investigate the chemical oxidation state and surface composition, providing compositional information at the top of the monolayers, with a detection limit of 0.01–0.5 atomic%, an analysis depth of 0.5–7.5 nm, and a resolution of $\leq$10 μm probe size.

3. Results and Discussion

Silver nanostructures were synthesized utilizing *Moringa oleifera* extract from leaves due to its properties as a reducing and capping agent. A green synthesis approach to metal nanoparticles can incorporate carbohydrates, amino acids, proteins, phenolic compounds, and flavonoids that promote metal ions to reduce and stabilize nanostructures [35,36].

3.1. Microscopic Observation of Silver Nanostructures

The obtained results reveal different morphologies depending on the plant extract concentration in the presence and absence of Cu^{2+} ions. The nanostructures obtained at a low concentration of 10% of the precursor with Cu^{2+} ions in the reaction system are spherical with a size of about 100 ± 30 nm, as shown in Figure 1a–c. Increasing the plant extract concentration to 20% in the presence of Cu^{2+} ions results in a transition state that slightly changes the spherical shape to an unstable and undefine structure, as shown in Figure 1d–f. Afterward, the plant extract concentration was increased to 30% to investigate the possibility of changing the shape of the nanostructure. It is found that the shape of dendrites is clearly formed as the concentration of the plant extract increases (Figure 1g–i). The nanodendrites have an average size of ~300 ± 30 nm. Figure 1j shows the results obtained in the absence of copper nitrate hydrate when using a low concentration of 10% of precursor. The obtained nanoparticles are spherical at this concentration, and no dendritic morphology was observed even when the concentration was increased to 30% of the precursor (as shown in Figure 1k,l). Therefore, for the formulation of nanodendrites, the volumetric concentration of plant extract should be as high as 30% in the presence of Cu^{2+} ions. Additionally, Figure 1m shows the SEM observation results for AgNPs, and Figure 1n,o displays AgNDs.

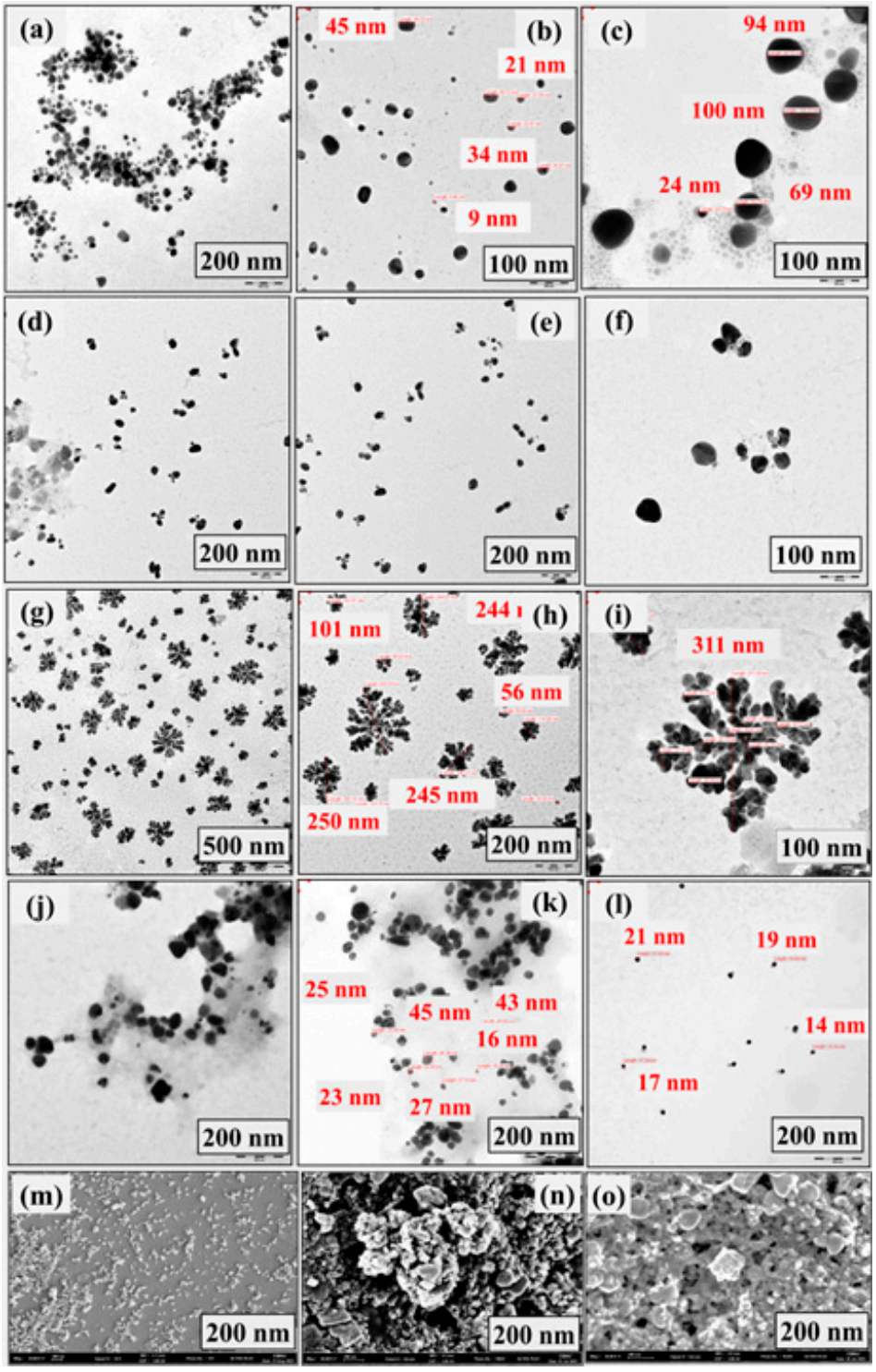

Figure 1. Morphologies of synthesized silver nanostructures by TEM and SEM observations. (**a**–**c**) TEM images of silver nanospheres of different sizes in the presence of Cu^{2+} ions. (**d**–**f**) Deformed TEM images of spheres for particle bud formation in the presence of Cu^{2+} ions. (**g**–**i**) Stabilized silver nanodendrites in the presence of Cu^{2+} ions. (**j**–**l**) AgNPs in the absence of Cu^{2+} ions. (**m**) SEM image of silver nanospheres. (**n**,**o**) SEM images of silver nanodendrites.

The phytochemicals in the extract act as a reducing agent for the silver ions. One possible mechanism for the reduction of silver nitrate by phytoextract can be hypothesized as the following: Initially, silver nitrate exists as Ag^{+} and NO^{3-} ions in solution. The bioactive molecules in the plant extract provide hydroxyl and carbonyl groups donating

electrons to silver ions, causing bio-reduction of Ag^{+} to Ag^{0}. These reduced silver ions start to aggregate and form clusters. These clusters further grow and eventually stabilize to form silver nanoparticles. Consistent with this hypothesis, many studies have disclosed that flavonoids from various plant extracts exhibit bio-reductive functions of metal ions through a mechanism of keto-enol tautomeric transformation [37,38].

The above results show that AgNPs and AgNDs can be successfully prepared using *Moringa oleifera* leaf extract in the presence of Cu^{2+} ions. Cu^{2+} ions are necessary for nanodendritic formulation. The addition of Cu^{2+} ions can slow down the reaction, forming thermodynamically unstable branched structures that provide high specific surface areas. These branches then aggregate to reduce the uncovered area and create a self-assembled, stabilized dendritic structure [39,40]. Importantly, the shape of the nanoparticles in the synthesis system changes from spherical to dendritic as the concentration of the plant extract increases with the addition of Cu^{2+} ions. Increasing the concentration of the metal salt was found to have no effect on the morphology. Without Cu^{2+} ions in the system, there was no change in morphology, even at high plant extract concentration (30%). Therefore, for the formulation of nanodendrites, the volumetric concentration of plant extract should be as high as 30% in the presence of Cu^{2+} ions. Xu et al. [41] reported similar observations for the chemically synthesized 3-dimensional silver nanostructures in the presence of Cu^{2+} ions.

3.2. UV–Vis Spectroscopy and Elemental Analysis

Figure 2 demonstrates possible differences in the optical properties of nanomaterials depending on the shape and size formed. According to the results, AgNDs show a broader spectrum with a maximum of 460 nm (Figure 2a), while AgNPs exhibit a narrower band with a maximum of 443 nm (Figure 2b). The obtained data is like previous data showing different morphologies for silver nanoparticles [42]. The elemental content of AgNDs was analyzed. Figure 2c clearly reveals that AgNDs have a strong absorption peak (3 keV), which is typical for silver nanocrystals [43]. Mass percentage analysis indicates that silver is predominantly present at 88.4%, along with the organic content on the surface of the silver nanodendrites, especially C (4.69%) and O (6.41%), while the Cu content is negligible at 0.72%. It has been reported that *Moringa oleifera* cannot induce copper nanoparticles under room temperature conditions and that high temperatures ($\geq$80 °C) are required for the formation of copper nanoparticles [44], but high temperatures were not used in our conditions. This indicates that copper nitrate does not act as a strong competitor but slows down the reaction rate for silver nanoparticles formation. Figure 2d also presents the EDS mapping demonstrating the Ag atoms in AgNDs and confirming the distribution of the major elements in the nanoparticles.

3.3. FTIR Analysis

FTIR investigations were employed to determine whether bioactive compounds are found on the surface of nanoparticles. Figure 3a demonstrates that AgNDs exhibit a peak at 3287 cm^{-1} related to O–H stretching vibrations of hydroxyl groups present mainly in plant phenols and alcohols. Two peaks are observed at 2917 cm^{-1} and 2850 cm^{-1}, which are associated with C–H stretching vibrations. The peak observed at 1635 cm^{-1} can be attributed to C=C stretching (in aromatic rings present in terpenoids) and C=O ketones (in flavonoids). C-N bending vibrations appear at 1216 cm^{-1} and 1024 cm^{-1} related to the amide group of plant extract [45]. Figure 3b illustrates the FTIR spectrum of AgNPs. The broader spectrum detected at 3454 cm^{-1} can be ascribed to the O–H stretching. The peak seen at 1625 cm^{-1} is due to C=C and/or C=O stretching vibrations. Figure 3c displays the functional groups of *Moringa oleifera* extract leaf powder. The peak at 3291.2 cm^{-1} can be represented by the O–H stretching vibration, and the other peaks (2919 cm^{-1} and 2858 cm^{-1}) can be confirmed by the C–H stretching of the alkane group. The peak at 1637 cm^{-1} can be assigned to C=C stretching and C=O. The peaks seen at 1230 cm^{-1} and 1033 cm^{-1} are associated with C–N bonds in the amine group [46]. From the FTIR results, it is predicted that the C=O group is dominantly involved in the reduction, while C–H and

C–N stretching are likely involved in the shaping of the nanoparticles because they are not observed in the silver nanosphere vibration analysis. These results for *Moringa oleifera* are like previously reported results [47]. The presence of identical peaks with a slight peak shift in nanoparticles and *Moringa oleifera* powder suggests that the synthesized nanoparticles are capped with bioactive functional groups present in this plant. Silver nitrate shows an intense peak at 1291.1 cm^{-1} [48], indicating an $Ag^{+}NO^{3-}$ ion pair, as shown in Figure 3d.

3.4. XRD Analysis

Figure 4 indicates that both AgNDs and AgNPs have cubic face-centered (FCC) structures. As shown in Figure 4a, significant peaks and crystal planes are observed at 37.91° (111), 44.08° (200), 64.3° (220), and 77.30° (311) corresponding to d-spacings of 0.237 nm, 0.220 nm, 0.144 nm, and 0.123 nm for AgNDs. XRD analysis shows that the synthesized silver nanostructures correspond to well-defined surfaces with an arrangement of atoms in a crystal lattice manner. The intense peak at 2θ = 37.91° corresponds to the (111) reflection as one of the most compressed packed planes, indicative of the FCC structure. These results are in accordance with the standard powder diffraction card of a joint committee on powder diffraction standards (JCPDS), silver file No. 04-0783 [49]. In Figure 4b, distinct peaks and crystal planes are detected at 37.88° (111), 44.18° (200), 64.258° (220), and 77.203° (311) for AgNPs, which are attributed to d-spacings of 0.237 nm, 0.204 nm, 0.144 nm, and 0.123 nm. The approximate crystal size corresponding to (111) is 26.82 nm and 32.48 nm for AgNPs and AgNDs, respectively. The XRD data also reveals peaks representing organic compounds from the plant extract (32.104°, 37.16°, and 44.18°) in addition to peaks representing silver nanocrystals. These results are consistent with previous studies as XRD contains similar 2θ patterns [50,51]. Furthermore, no remarkable peaks are observed for the copper crystal due to its low presence in the reaction system.

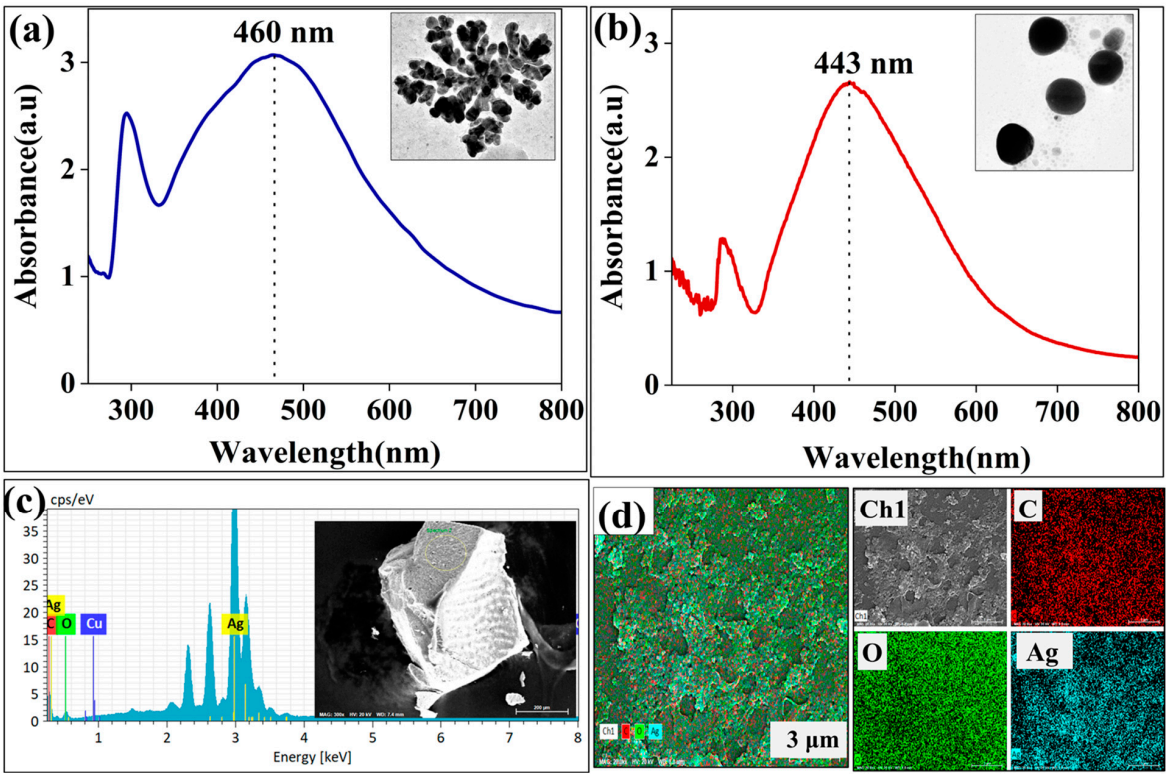

Figure 2. UV–Vis spectra and EDS elemental analysis of silver nanostructures. (**a**) UV–Vis spectra of silver nanodendrites. (**b**) UV–Vis spectra of silver nanospheres. (**c**) EDS spectrum of silver nanodendrites with the selected region. (**d**) EDS mapping of silver nanodendrites.

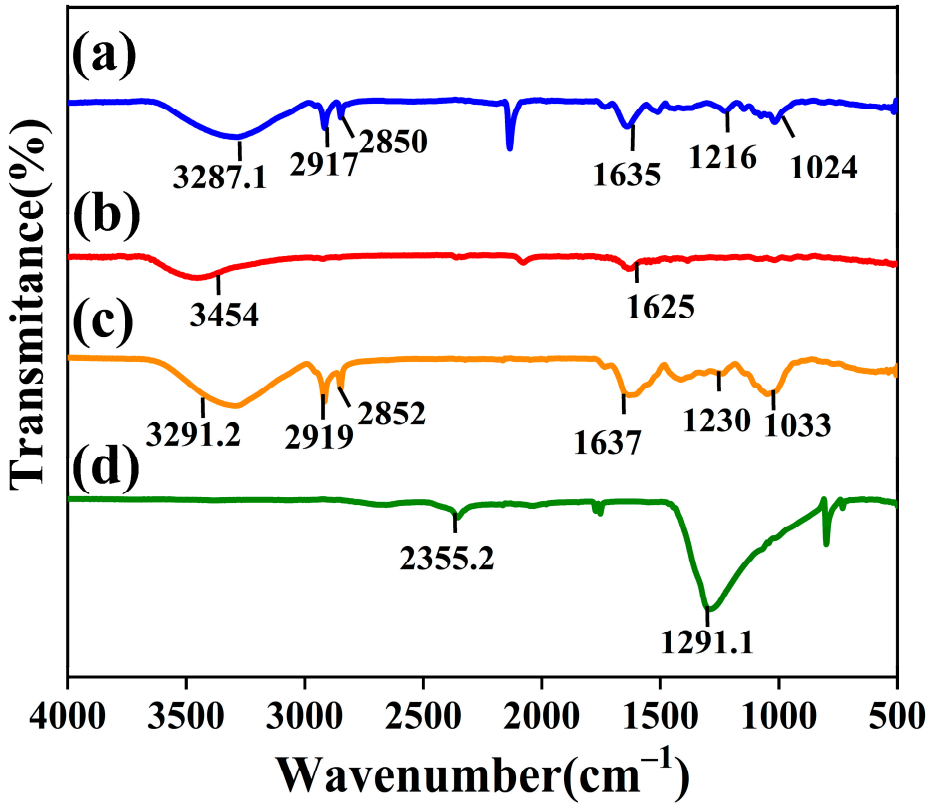

Figure 3. FTIR spectrum of (**a**) silver nanodendrites, (**b**) silver nanospheres, (**c**) *Moringa oleifera* leaf powder, and (**d**) silver nitrate.

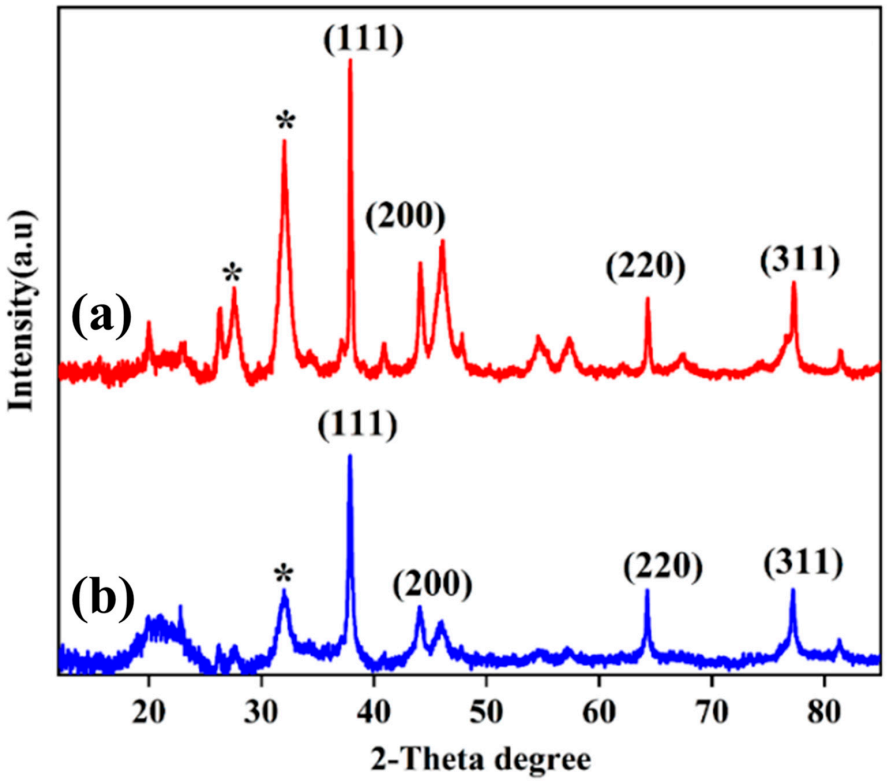

Figure 4. XRD analysis of (**a**) silver nanodendrites and (**b**) silver nanospheres. Extra peaks with (*) sign indicate the presence of organic compounds from *Moringa oleifera*.

3.5. XPS Analysis

The synthesized silver nanostructures are further analyzed using XPS, as manifested in Figure 5. Figure 5a,e shows the survey spectra for AgNDs and AgNPs, confirming the presence of Ag^0 as a major constituent. Ag peaks are detected at 365–376 eV (Figure 5b,f). As a spin-orbital splitting, the Ag3d peak is shown as a doublet with two states: 367.5 eV $Ag3d_{5/2}$ and 373.5 eV $Ag3d_{3/2}$ with splitting energy of 6 eV, confirming the state in Ag^0 [52,53]. Figure 5c describes the deconvolution of C1s spectra from AgNDs with four signals at 284.28, 285.5, 286.39, and 287.66 eV with respect to the C=C, C–O, C–N, and C=O relationships [54–56]. The O1s XPS spectrum exhibits three signals at 530.88, 532.23, and 533.35 eV (Figure 5d) due to AgO, O–H, and C–O, respectively [57,58]. For AgNPs, the pattern gives a C1s spectrum (Figure 5g) with deconvolution into three peaks at 284.2, 285.6, and 287.3 eV, indicating the presence of C=C, C–O, and C–C connections [59–61]. The O1s XPS (Figure 5h) represents four peaks at 531.24, 532.12, 532.7, and 533.35 eV corresponding to the O–H, C=O, C–O linkages [62,63]. These results confirm the successful synthesis of silver nanostructures with *Moringa oleifera* leaf extract. Results are in accordance with FTIR studies confirming the connection.

3.6. Peroxidase Activity

Several nanoparticles are known to exhibit peroxidase activity, including cobalt tertraoxide [64], copper [65], nickel [66], gold [67], and silver nanoparticles [68]. In this study, the peroxidase activity of silver nanostructures was investigated using a chromogenic reagent TMB as shown in Figure 6. Originally, TMB did not exhibit any peak and appeared colorless, but when oxidation begins, with the release of Ag^+ ions, colorless TMB undergoes oxidation and turns into a blue-colored diimine. The phenomena can be observed visually, and spectrometry analysis confirms the reaction as a band at 655 nm (Figure 6a). The absorbance of the samples was monitored over time, and comparisons were recorded specifically at 655 nm every 30 min with a spectral range of 400 to 800 nm, which gradually increases with rising TMB-oxide, as shown in Figure 6b. In contrast to AgNPs with a maximum OD of 0.8, AgNDs displayed higher oxidation, i.e., a maximum OD of 1.1. The plausible mechanism that could take place during this reaction and result in peroxidase activity is shown in Figure 6c. The process involves the following main steps: catalytic decomposition of H_2O_2 upon the addition of nanoparticles, and TMB oxidation via Ag^+ ions, which is confirmed by a color change from colorless to blue. Initially, with H_2O_2, Ag^0 undergoes Ag^+ ion formation, which leads to the decomposition of H_2O_2 into OH radicals [69]. The free radicals then oxidize the peroxide substrate TMB, which confirms the formation of silver cation (Ag^+) on the surface of silver nanostructures. In addition, the oxidized form of TMB can exist in equilibrium with the charge transfer complex and the diimine derivative for TMB.

3.7. Catalytic Degradation

Methylene blue (MB) is a heterocyclic aromatic cationic dye that poses a threat to aquatic life due to its non-degradability and potential to cause carcinogenesis and toxicity. This dye is water-soluble and shows a dark blue color when dissolved in water and generates a significant signal at 664 nm when analyzed by a UV–Vis spectrophotometer. MB degrades to leuco-methylene blue [70]. Methyl orange (MO) is an anionic azo dye that displays a strong peak at 464 nm and is also water-soluble. The color ranges from orange, red to yellow depending on the acidity and alkalinity of the medium. When degraded, it forms hydrazine-derivatives [71]. Our results demonstrate the positive impact of silver nanostructures on the catalytic degradation of the used dyes (MO and MB). This is clearly shown in Figure 7a,b. Degradation of the dyes was slow when sodium borohydride was introduced, as observed both visually and by absorbance measurements. However, with the addition of silver nanostructures in the solution, the reaction rate was accelerated, and the reaction was completed in 3 to 5 min. The color of each dye disappeared, but black pellets were formed along with the colorless supernatant. In addition, the absorbance spectrum

of the dyes was significantly reduced. These observations suggest that the degradation of dyes with sodium borohydride is thermodynamically favorable but not kinetically [72,73]. In this system, silver nanostructures act as a catalyst that increases the reduction/oxidation reaction of dyes with sodium borohydride [74,75].

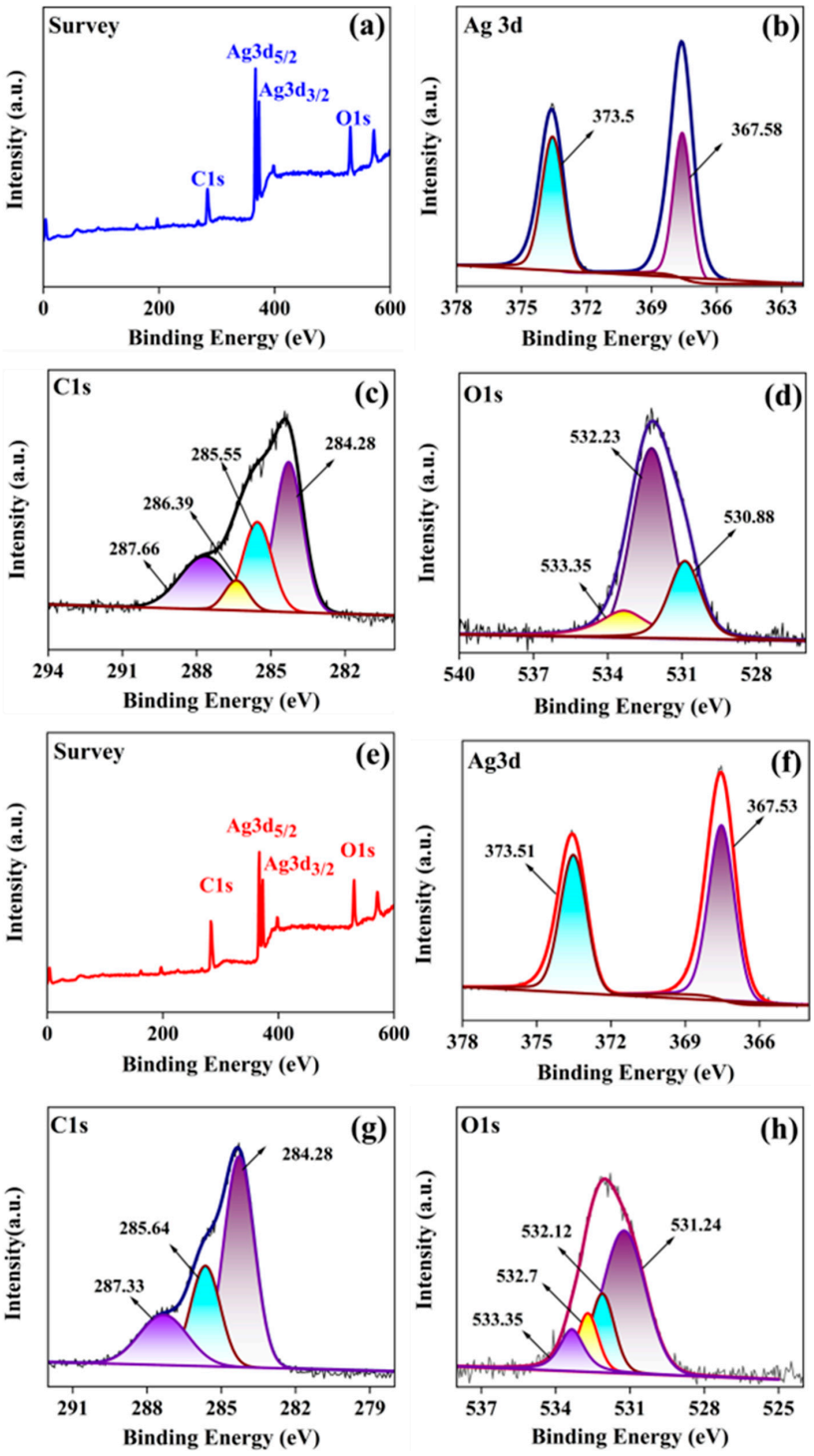

Figure 5. High-resolution XPS spectra of silver nanostructures. (**a**) Survey spectra of AgNDs. (**b**) Ag3d spectra of AgNDs. (**c**) Deconvoluted C1s spectra of AgNDs. (**d**) Deconvoluted O1s spectra of AgNDs. (**e**) Survey spectra of silver nanospheres. (**f**) Deconvoluted Ag3d spectra of AgNPs. (**g**) C1s spectra of AgNPs. (**h**) O1s spectra of AgNPs.

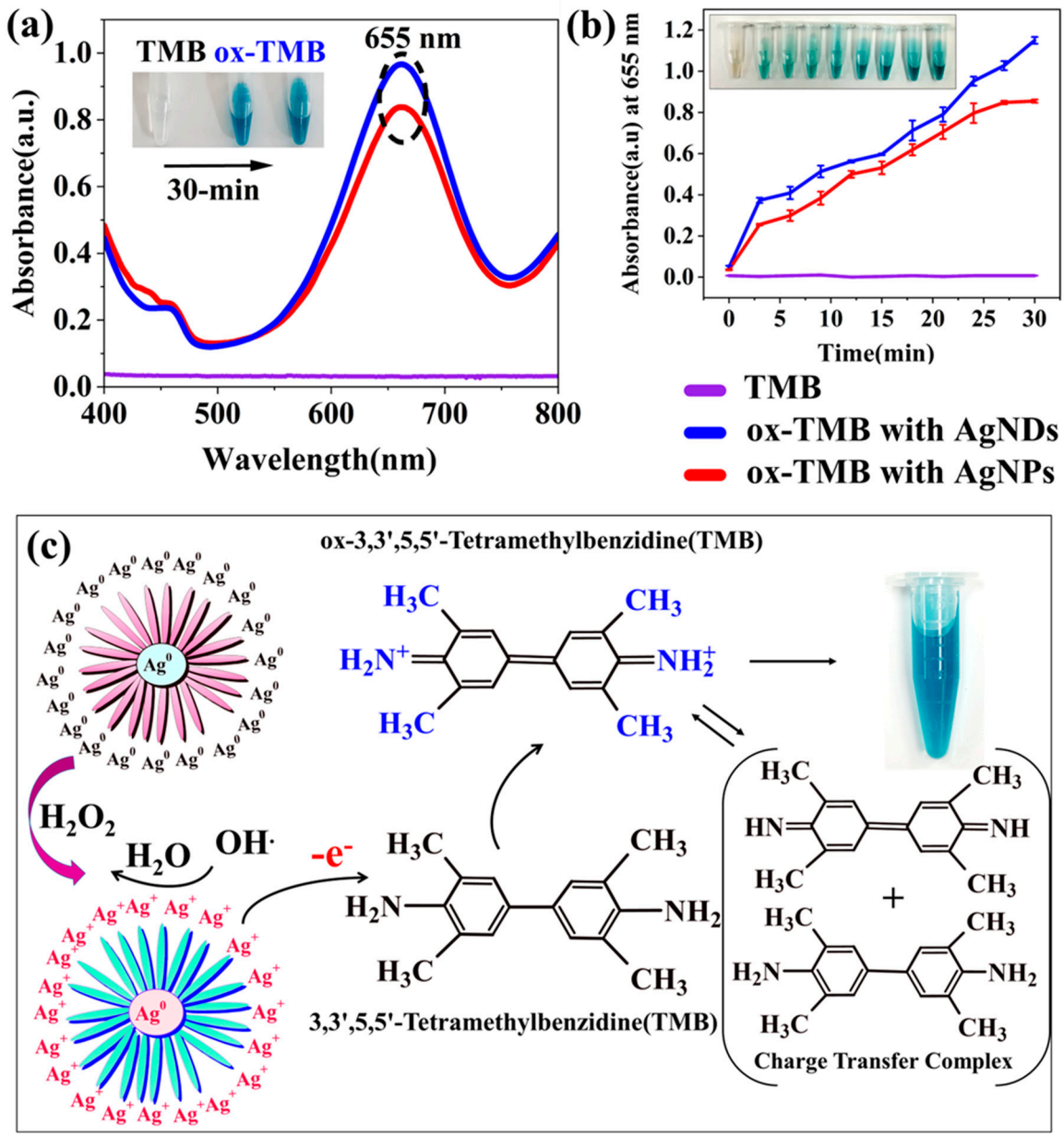

Figure 6. Oxidation of TMB in the presence of H_2O_2 on the surface of silver nanostructures. (**a**) Absorbance spectra of TMB, TMB + AgNPs, and TMB + AgNDs. (**b**) Changes in optical density at 652 nm at regular time intervals for TMB, TMB + AgNPs, and TMB +AgNDs. (**c**) Possible mechanisms related to the oxidation of TMB substrate in the presence of H_2O_2 facilitated by silver nanostructures.

The calculated degradation activity results show that AgNDs exhibit a higher degradation percentage compared to AgNPs (Figure 7c) as follows: 66.6% (AgNPs) and 92.2% (AgNDs) for MO dye degradation; 58.3% (AgNPs) and 91.0% (AgNDs) for MB dye degradation. The experiment was performed in triplicate, and the calculated standard deviation was less than 2%. It indicates that AgNDs have a superior catalytic effect required for the degradation of dyes.

A reasonable mechanism for this reaction to occur can be attributed to the rapid transfer of electrons available on the silver nanoparticles. Degradation activity relies on the doner $NaBH_4$ capability and acceptor dye. Initially, dye molecules and BH_4^- are adsorbed on the surface of nanoparticles [76]. Here, $NaBH_4$ acts as a nucleophile, the dye molecules act as an electrophile, and the silver nanoparticles act as an electron relay system mixture that supports both electron transfer and degradation rate acceleration. These observations

reflect the role of nanoparticles as substrates due to their high specific surface area [77,78]. For silver nanoparticles, several studies have demonstrated enhanced catalytic behavior for dye degradation with $NaBH_4$ [79–82].

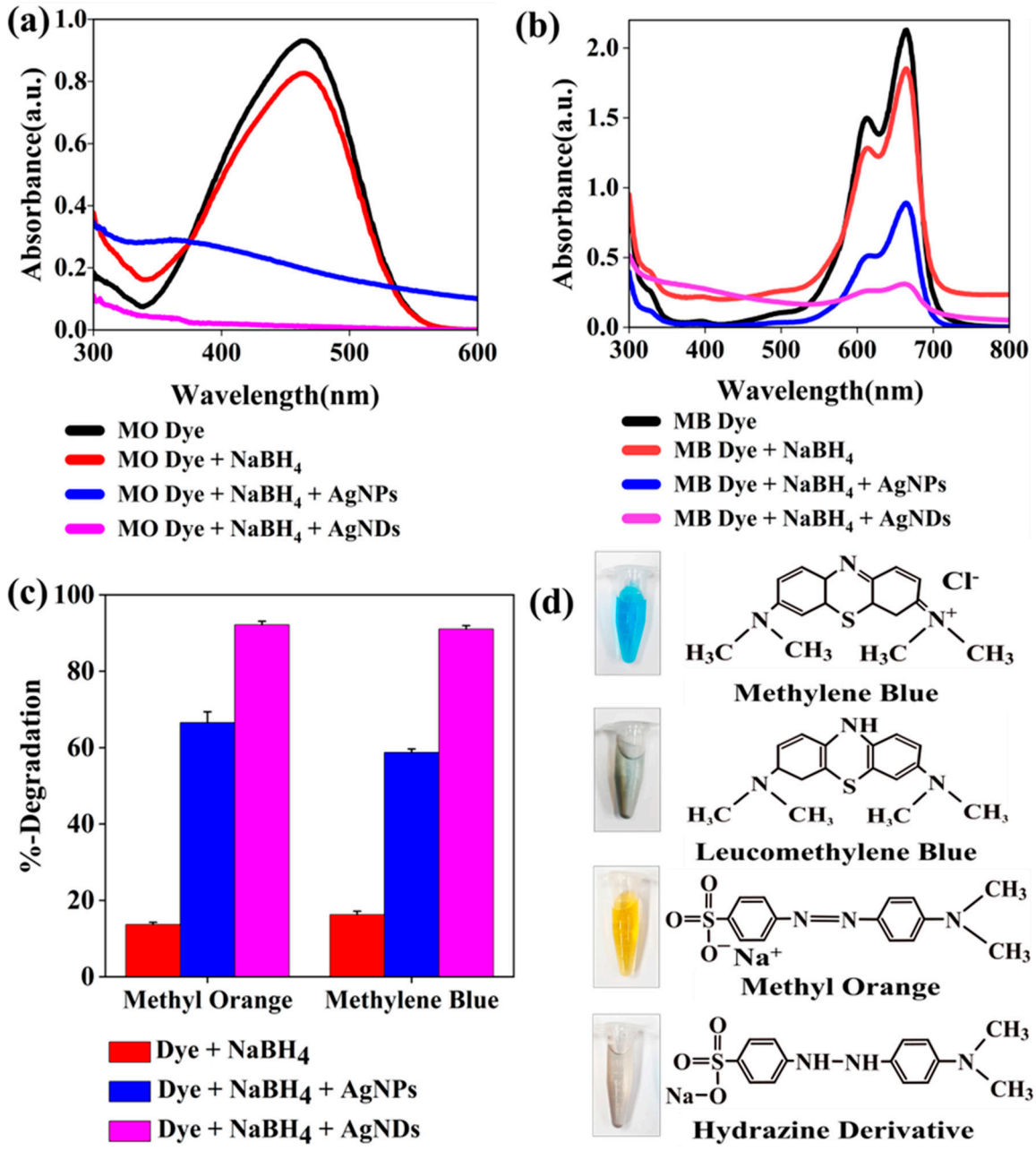

Figure 7. Catalytic degradation of dyes in the presence of $NaBH_4$ on the surface of silver nanostructures. (**a**) Absorbance spectra of methyl orange, methyl orange + $NaBH_4$, methyl orange + $NaBH_4$ + AgNPs, and methyl orange + $NaBH_4$ + AgNDs. (**b**) Absorbance spectra of methylene blue, methylene blue + $NaBH_4$, methylene blue + $NaBH_4$ + AgNPs, and methylene blue + $NaBH_4$ + AgNDs. (**c**) Degradation percentage of dye + $NaBH_4$, dye + $NaBH_4$ + AgNPs, and dye + $NaBH_4$ + AgNDs. Error bars show the standard deviation for three replicates of data. (**d**) Dye structures before and after reduction.

3.8. Antibacterial Activity

Silver nanostructures are primarily known for their potent antibacterial potential [83–85]. The antibacterial activity of the synthesized silver nanostructures was investigated against Gram-positive bacteria (*S. aureus*) and Gram-negative bacteria (*E. coli*). Figure 8a,b demon-

strates the efficient killing of bacteria by AgNDs compared with AgNPs, showing specific antibacterial action when tested by the zone of inhibition. AgNDs have a higher antibacterial effect against *E. coli*, reaching an inhibition of 40 ± 1.5 mm, when compared with *S. aureus*, which had an inhibition of 10 ± 0.6 mm. In contrast, AgNPs treatment for both strains resulted in insignificant inhibition of 12.6 ± 1.2 mm against *E. coli* and 5 ± 0.91 mm against *S. aureus*. These results illustrate that nanoparticle shape enables antibacterial effectiveness depending on the morphology change. The possible antibacterial action mechanism of silver nanoparticles is explained as follows. Bacterial cells are composed of various structures, such as cell membranes, proteins, and DNA, which contain sulfur and phosphorus. They act as Lewis bases, while silver is considered a Lewis acid, resulting in an electrostatic attraction between sulfur proteins and silver ions [86,87]. Therefore, AgNDs can bind to the wall and penetrate bacterial cells [88,89]. Internalization of silver nanostructures into cells interrupts respiratory function, resulting in the deactivation of respiratory enzymes with the generation of reactive oxygen species (ROS) [90,91]. As such, overproduction of ROS can destroy intercellular components such as DNA, lipids, and proteins. Cellular membrane destruction thus causes loss of cytoplasm from the cell, followed by cell death. Additionally, cell wall thickness can determine the antibacterial efficiency of different bacteria upon contact with silver nanoparticles. Gram-negative *E. coli* has a thinner cell wall, making it more susceptible to silver nanoparticle penetration than Gram-positive bacteria such as *S. aureus*, which are characterized by thicker cell walls [92]. The structural shape of silver nanoparticles is also important in determining antimicrobial efficacy, and the dendritic shape possesses a more reactive crystal surface than the spherical-shaped nanoparticles, leading to enhanced antibacterial performance [93–95].

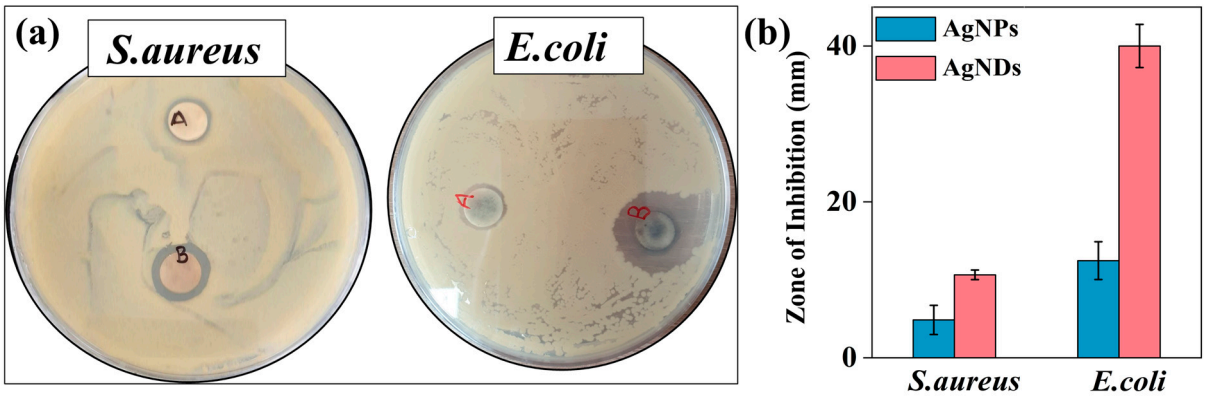

Figure 8. Antibacterial activity of nanostructures against Gram-positive and Gram-negative bacteria. (**a**) Antimicrobial activity of silver nanospheres (A) and silver nanodendrites (B) against *S. aureus* and *E. coli*. (**b**) Zone of inhibition (mm) of silver nanospheres (AgNPs) and silver nanodendrites (AgNDs) against representative bacteria. Error bars represent the standard deviation of triplicate experiments.

4. Conclusions

In search of an environmentally friendly method to produce nanostructures, a green synthetic route was introduced to obtain controlled silver nanostructures, dendrites (AgNDs), and spheres (AgNPs) using *Moringa oleifera* leaf extract at room temperature. These nanostructures were characterized by surfaces containing bioactive functional groups. Dendritic silver nanostructures were obtained with increasing plant extract concentration in the presence of Cu^{2+} ions in the solution supporting the formation of nanostructures. These nanoparticles were achieved with particle sizes of ~100 ± 30 nm (AgNPs) and ~300 ± 30 nm (AgNDs). Results demonstrated that AgNDs were more effective in terms of peroxidase, catalytic degradation, and antibacterial activity. AgNDs showed >90% catalytic degradation of methyl orange and methylene blue dyes. Additionally, AgNDs exhibited higher inhibition against *E. coli* than against *S. aureus*, suggesting added value in biomedical

applications. Certain nanostructured forms, such as dendritic silver nanoparticles, can be applied to various fields in the future through green synthesis strategies.

Author Contributions: A.S.: writing original draft, investigation, data curation, formal analysis, methodology, and conceptualization. A.R.D.: methodology. K.A.: writing—review and editing. B.-S.K.: supervision and writing—review and editing. All authors have read and agreed to the published version of the manuscript.

Funding: This research was supported by the National Research Foundation of Korea (NRF-2019R1I1 A3A02058523).

Data Availability Statement: Data will be available upon request.

Conflicts of Interest: There are no conflicts to declare.

References

1. Qin, L.; Zeng, G.; Lai, C.; Huang, D.; Xu, P.; Zhang, C.; Cheng, M.; Liu, X.; Liu, S.; Li, B.; et al. "Gold Rush" in Modern Science: Fabrication Strategies and Typical Advanced Applications of Gold Nanoparticles in Sensing. *Coord. Chem. Rev.* **2018**, *359*, 1–31. [CrossRef]
2. Dimapilis, E.A.S.; Hsu, C.S.; Mendoza, R.M.O.; Lu, M.C. Zinc Oxide Nanoparticles for Water Disinfection. *Sustain. Environ. Res.* **2018**, *28*, 47–56. [CrossRef]
3. AbouAitah, K.; Piotrowska, U.; Wojnarowicz, J.; Swiderska-Sroda, A.; El-Desoky, A.H.H.; Lojkowski, W. Enhanced Activity and Sustained Release of Protocatechuic Acid, a Natural Antibacterial Agent, from Hybrid Nanoformulations with Zinc Oxide Nanoparticles. *Int. J. Mol. Sci.* **2021**, *22*, 5287. [CrossRef]
4. Xu, M.; Luo, H.; Rong, H.; Wu, S.; Zheng, Z.; Chen, B. Calcium Alginate Gels-Functionalized Polyurethane Foam Decorated with Silver Nanoparticles as an Antibacterial Agent for Point-of-Use Water Disinfection. *Int. J. Biol. Macromol.* **2023**, *231*, 123289. [CrossRef] [PubMed]
5. Islam, M.A.; Jacob, M.V.; Antunes, E. A Critical Review on Silver Nanoparticles: From Synthesis and Applications to Its Mitigation through Low-Cost Adsorption by Biochar. *J. Environ. Manag.* **2021**, *281*, 111918. [CrossRef] [PubMed]
6. Calderón-Jiménez, B.; Johnson, M.E.; Montoro Bustos, A.R.; Murphy, K.E.; Winchester, M.R.; Baudrit, J.R.V. Silver Nanoparticles: Technological Advances, Societal Impacts, and Metrological Challenges. *Front. Chem.* **2017**, *5*, 6. [CrossRef]
7. Navaladian, S.; Viswanathan, B.; Viswanath, R.P.; Varadarajan, T.K. Thermal Decomposition as Route for Silver Nanoparticles. *Nanoscale Res. Lett.* **2007**, *2*, 44–48. [CrossRef]
8. Pathrose, B.; Nampoori, V.P.N.; Radhakrishnan, P.; Sahira, H.; Mujeeb, A. Effect of Femtosecond Laser Ablated Silver Nanoparticles in the Thermo-Optic Properties of Basic Fuchsin Dye. *Optik* **2016**, *127*, 3684–3687. [CrossRef]
9. Iravani, S.; Korbekandi, H.; Mirmohammadi, S.V.; Zolfaghari, B. Synthesis of Silver Nanoparticles: Chemical, Physical and Biological Methods. *Res. Pharm. Sci.* **2014**, *9*, 385–406.
10. Alabdallah, N.M.; Hasan, M.M. Plant-Based Green Synthesis of Silver Nanoparticles and Its Effective Role in Abiotic Stress Tolerance in Crop Plants. *Saudi J. Biol. Sci.* **2021**, *28*, 5631–5639. [CrossRef] [PubMed]
11. Islam, Z.; Islam, S.M.R.; Hossen, F.; Mahtab-Ul-Islam, K.; Hasan, M.R.; Karim, R. *Moringa oleifera* is a Prominent Source of Nutrients with Potential Health Benefits. *Int. J. Food Sci.* **2021**, *2021*, 6627265. [CrossRef]
12. Fahey, J.W.D. *Moringa oleifera*: A Review of the Medical Evidence for Its Nutritional, Therapeutic, and Prophylactic Properties. Part 1. *Trees Life J.* **2005**, *1*, 5.
13. Shousha, W.G.; Aboulthana, W.M.; Salama, A.H.; Saleh, M.H.; Essawy, E.A. Evaluation of the Biological Activity of *Moringa oleifera* Leaves Extract after Incorporating Silver Nanoparticles, in Vitro Study. *Bull. Natl. Res. Cent.* **2019**, *43*, 212. [CrossRef]
14. Saini, R.K.; Shetty, N.P.; Giridhar, P. GC-FID/MS Analysis of Fatty Acids in Indian Cultivars of *Moringa oleifera*: Potential Sources of PUFA. *J. Am. Oil Chem. Soc.* **2014**, *91*, 1029–1034. [CrossRef]
15. Abdulkadir, A.R.; Zawawi, D.D.; Jahan, M.S. Proximate and Phytochemical Screening of Different Parts of Moringa Oleifera. *Russ. Agric. Sci.* **2016**, *42*, 34–36. [CrossRef]
16. Cuellar-Nuñez, M.L.; Luzardo-Ocampo, I.; Campos-Vega, R.; Gallegos-Corona, M.A.; González de Mejía, E.; Loarca-Piña, G. Physicochemical and Nutraceutical Properties of Moringa (*Moringa Oleifera*) Leaves and Their Effects in an in Vivo AOM/DSS-Induced Colorectal Carcinogenesis Model. *Food Res. Int.* **2018**, *105*, 159–168. [CrossRef]
17. Leone, A.; Spada, A.; Battezzati, A.; Schiraldi, A.; Aristil, J.; Bertoli, S. *Moringa oleifera* Seeds and Oil: Characteristics and Uses for Human Health. *Int. J. Mol. Sci.* **2016**, *17*, 2141. [CrossRef] [PubMed]
18. Mumtaz, M.Z.; Kausar, F.; Hassan, M.; Javaid, S.; Malik, A. Anticancer Activities of Phenolic Compounds from *Moringa oleifera* Leaves: In Vitro and in Silico Mechanistic Study. *Beni. Suef. Univ. J. Basic Appl. Sci.* **2021**, *10*, 12. [CrossRef]
19. Maheshwaran, G.; Malai Selvi, M.; Selva Muneeswari, R.; Nivedhitha Bharathi, A.; Krishna Kumar, M.; Sudhahar, S. Green Synthesis of Lanthanum Oxide Nanoparticles Using *Moringa oleifera* Leaves Extract and Its Biological Activities. *Adv. Powder Technol.* **2021**, *32*, 1963–1971. [CrossRef]

20. Fatiqin, A.; Amrulloh, H.; Simanjuntak, W. Green Synthesis of MgO Nanoparticles Using *Moringa oleifera* Leaf Aqueous Extract for Antibacterial Activity. *Bull. Chem. Soc. Ethiop.* **2021**, *35*, 161–170. [CrossRef]
21. Sharma, A.K.; Swami, A.K.; Jangir, D.; Saran, M.; Upadhyay, T.K.; Prajapat, R.K.; Sharma, D.; Mathur, M. An Eco-Friendly Green Synthesis of Tungsten Nanoparticles from *Moringa oleifera* Lam. and Their Pharmacological Studies. *Gazi Med. J.* **2021**, *31*, 719–725. [CrossRef]
22. Anand, K.; Tiloke, C.; Phulukdaree, A.; Ranjan, B.; Chuturgoon, A.; Singh, S.; Gengan, R.M. Biosynthesis of Palladium Nanoparticles by Using *Moringa oleifera* Flower Extract and Their Catalytic and Biological Properties. *J. Photochem. Photobiol. B* **2016**, *165*, 87–95. [CrossRef]
23. Jadhav, V.; Bhagare, A.; Ali, I.H.; Dhayagude, A.; Lokhande, D.; Aher, J.; Jameel, M.; Dutta, M. Role of *Moringa oleifera* on Green Synthesis of Metal/Metal Oxide Nanomaterials. *J. Nanomater.* **2022**, *2022*, 2147393. [CrossRef]
24. Sharma, S.; Kumar, K.; Thakur, N.; Chauhan, S.; Chauhan, M.S. The Effect of Shape and Size of ZnO Nanoparticles on Their Antimicrobial and Photocatalytic Activities: A Green Approach. *Bull. Mater. Sci.* **2020**, *43*, 20. [CrossRef]
25. Khan, I.; Saeed, K.; Khan, I. Nanoparticles: Properties, Applications and Toxicities. *Arab. J. Chem.* **2019**, *12*, 908–931. [CrossRef]
26. Ashkarran, A.A.; Estakhri, S.; Nezhad, M.R.H.; Eshghi, S. Controlling the Geometry of Silver Nanostructures for Biological Applications. *Phys. Procedia* **2013**, *40*, 76–83. [CrossRef]
27. Wu, L.; Wu, W.; Jing, X.; Huang, J.; Sun, D.; Odoom-Wubah, T.; Liu, H.; Wang, H.; Li, Q. Trisodium Citrate-Assisted Biosynthesis of Silver Nanoflowers by *Canarium album* Foliar Broths as a Platform for SERS Detection. *Ind. Eng. Chem. Res.* **2013**, *52*, 5085–5094. [CrossRef]
28. Chathanchira, M.A.; Faseela K, P.F.; Singh, S.; Baik, S. Hierarchically-Structured Silver Nanoflowers for Highly Conductive Metallic Inks with Dramatically Reduced Filler Concentration. *Sci. Rep.* **2016**, *6*, 34894. [CrossRef]
29. Mdluli, P.S.; Revaprasadu, N. Time Dependant Evolution of Silver Nanodendrites. *Mater. Lett.* **2009**, *63*, 447–450. [CrossRef]
30. Deshmukh, A.R.; Aloui, H.; Kim, B.S. In Situ Growth of Gold and Silver Nanoparticles onto Phyto-Functionalized Boron Nitride Nanosheets: Catalytic, Peroxidase Mimicking, and Antimicrobial Activity. *J. Clean. Prod.* **2020**, *270*, 122339. [CrossRef]
31. Palladino, P.; Torrini, F.; Scarano, S.; Minunni, M. 3,3′,5,5′-Tetramethylbenzidine as Multi-Colorimetric Indicator of Chlorine in Water in Line with Health Guideline Values. *Anal. Bioanal. Chem.* **2020**, *412*, 7861–7869. [CrossRef] [PubMed]
32. Deshmukh, A.R.; Gupta, A.; Kim, B.S. Ultrasound Assisted Green Synthesis of Silver and Iron Oxide Nanoparticles Using Fenugreek Seed Extract and Their Enhanced Antibacterial and Antioxidant Activities. *Biomed. Res. Int.* **2019**, *2019*, 1714358. [CrossRef] [PubMed]
33. Mickymaray, S. One-Step Synthesis of Silver Nanoparticles Using Saudi Arabian Desert Seasonal Plant *Sisymbrium irio* and Antibacterial Activity Against Multidrug-Resistant Bacterial Strains. *Biomolecules* **2019**, *9*, 662. [CrossRef] [PubMed]
34. Lai, M.-J.; Huang, Y.-W.; Chen, H.-C.; Tsao, L.-I.; Chang Chien, C.-F.; Singh, B.; Liu, B.R. Effect of Size and Concentration of Copper Nanoparticles on the Antimicrobial Activity in *Escherichia coli* through Multiple Mechanisms. *Nanomaterials* **2022**, *12*, 3715. [CrossRef] [PubMed]
35. Makarov, V.V.; Love, A.J.; Sinitsyna, O.V.; Makarova, S.S.; Yaminsky, I.V.; Taliansky, M.E.; Kalinina, N.O. "Green" Nanotechnologies: Synthesis of Metal Nanoparticles Using Plants. *Acta Nat.* **2014**, *6*, 35–44. [CrossRef]
36. Shreyash, N.; Bajpai, S.; Khan, M.A.; Vijay, Y.; Tiwary, S.K.; Sonker, M. Green Synthesis of Nanoparticles and Their Biomedical Applications: A Review. *ACS Appl. Nano Mater.* **2021**, *4*, 11428–11457. [CrossRef]
37. Marslin, G.; Siram, K.; Maqbool, Q.; Selvakesavan, R.K.; Kruszka, D.; Kachlicki, P.; Franklin, G. Secondary Metabolites in the Green Synthesis of Metallic Nanoparticles. *Materials* **2018**, *11*, 940. [CrossRef]
38. Khandel, P.; Yadaw, R.K.; Soni, D.K.; Kanwar, L.; Shahi, S.K. Biogenesis of Metal Nanoparticles and Their Pharmacological Applications: Present Status and Application Prospects. *J. Nanostruct. Chem.* **2018**, *8*, 217–254. [CrossRef]
39. Wang, K.-Y.; Bu, S.-J.; Ju, C.-J.; Li, C.-T.; Li, Z.-Y.; Han, Y.; Ma, C.-Y.; Wang, C.-Y.; Hao, Z.; Liu, W.-S.; et al. Hemin-Incorporated Nanoflowers as Enzyme Mimics for Colorimetric Detection of Foodborne Pathogenic Bacteria. *Bioorg. Med. Chem. Lett.* **2018**, *28*, 3802–3807. [CrossRef]
40. Zhang, Y.X.; Jia, Y.; Jin, Z.; Yu, X.Y.; Xu, W.H.; Luo, T.; Zhu, B.J.; Liu, J.H.; Huang, X.J. Self-Assembled, Monodispersed, Flower-like γ-AlOOH Hierarchical Superstructures for Efficient and Fast Removal of Heavy Metal Ions from Water. *CrystEngComm* **2012**, *14*, 3005–3007. [CrossRef]
41. Xu, S.; Wang, L.; Li, H.; Yue, Q.; Li, R.; Liu, J.; Gu, X.; Zhang, S. Copper Ions Mediated Formation of Three-Dimensional Self-Assembled Ag Nanostructures via a Facile Solution Route. *CrystEngComm* **2013**, *15*, 6368–6373. [CrossRef]
42. Ren, W.; Guo, S.; Dong, S.; Wang, E. A Simple Route for the Synthesis of Morphology-Controlled and SERS-Active Ag Dendrites with near-Infrared Absorption. *J. Phys. Chem. C* **2011**, *115*, 10315–10320. [CrossRef]
43. Wang, C.; Kim, Y.J.; Singh, P.; Mathiyalagan, R.; Jin, Y.; Yang, D.C. Green Synthesis of Silver Nanoparticles by *Bacillus methylotrophicus*, and Their Antimicrobial Activity. *Artif. Cells Nanomed. Biotechnol.* **2016**, *44*, 1127–1132. [CrossRef]
44. Kalaiyan, G.; Suresh, S.; Prabu, K.M.; Thambidurai, S.; Kandasamy, M.; Pugazhenthiran, N.; Kumar, S.K.; Muneeswaran, T. Bactericidal Activity of *Moringa oleifera* Leaf Extract Assisted Green Synthesis of Hierarchical Copper Oxide Microspheres against Pathogenic Bacterial Strains. *J. Environ. Chem. Eng.* **2021**, *9*, 104847. [CrossRef]
45. Pandian, A.M.K.; Karthikeyan, C.; Rajasimman, M.; Dinesh, M.G. Synthesis of Silver Nanoparticle and Its Application. *Ecotoxicol. Environ. Saf.* **2015**, *121*, 211–217. [CrossRef]
46. Cornelius, W. Phytochemical Analysis of *Moringa oleifera* (leaves and flowers) and the Funtional Group. *Glob. Sci. J.* **2019**, *7*, 41–51.

47. Bello, O.S.; Adegoke, K.A.; Akinyunni, O.O. Preparation and Characterization of a Novel Adsorbent from *Moringa oleifera* Leaf. *Appl. Water Sci.* **2017**, *7*, 1295–1305. [CrossRef]
48. Ansari, M.J.; Rehman, N.U.; Ibnouf, E.; Alalaiwe, A.; Ganaie, M.A.; Zafar, A. Gum Acacia- and Gum Tragacanth-Coated Silver Nanoparticles: Synthesis, Physiological Stability, In-Vitro, Ex-Vivo and In-Vivo Activity Evaluations. *Coatings* **2022**, *12*, 1579. [CrossRef]
49. El-Naggar, N.E.-A.; Hussein, M.H.; El-Sawah, A.A. Bio-Fabrication of Silver Nanoparticles by Phycocyanin, Characterization, in Vitro Anticancer Activity against Breast Cancer Cell Line and in Vivo Cytotxicity. *Sci. Rep.* **2017**, *7*, 10844. [CrossRef]
50. Thiruvengadam, V.; Bansod, A.V. Characterization of Silver Nanoparticles Synthesized Using Chemical Method and Its Antibacterial Property. *Biointerface Res. Appl. Chem.* **2020**, *10*, 7257–7264. [CrossRef]
51. Halawani, E.M. Rapid Biosynthesis Method and Characterization of Silver Nanoparticles Using *Zizyphus spina christi* Leaf Extract and Their Antibacterial Efficacy in Therapeutic Application. *J. Biomater. Nanobiotechnol.* **2017**, *8*, 22–35. [CrossRef]
52. Bu, Y.; Kushwaha, A.; Goswami, L.; Kim, B.S. Green Production of Functionalized Few-Layer Graphene–Silver Nanocomposites Using Gallnut Extract for Antibacterial Application. *Micromachines* **2022**, *13*, 1232. [CrossRef] [PubMed]
53. Paul Das, M.; Rebecca Livingstone, J.; Veluswamy, P.; Das, J. Exploration of *Wedelia chinensis* Leaf-Assisted Silver Nanoparticles for Antioxidant, Antibacterial and in Vitro Cytotoxic Applications. *J. Food Drug Anal.* **2018**, *26*, 917–925. [CrossRef] [PubMed]
54. D'Anna, E.; De Giorgi, M.L.; Luches, A.; Martino, M.; Perrone, A.; Zocco, A. Study of C N Binding States in Carbon Nitride Films Deposited by Reactive XeCl Laser Ablation. *Thin Solid Film.* **1999**, *347*, 72–77. [CrossRef]
55. Diel, J.C.; Franco, D.S.P.; Igansi, A.V.; Cadaval, T.R.S.; Pereira, H.A.; Nunes, I.D.S.; Basso, C.W.; Maria do Carmo, M.A.; Morais, J.; Pinto, D.; et al. Green Synthesis of Carbon Nanotubes Impregnated with Metallic Nanoparticles: Characterization and Application in Glyphosate Adsorption. *Chemosphere* **2021**, *283*, 131193. [CrossRef]
56. Gómez-Vilchis, J.C.; García-Rosales, G.; Longoria-Gándara, L.C.; Pérez-Gómez, E.O.; Castilleros, D.T. Obtention of Biochar-Fe/Ce Using *Punica granatum* with High Adsorption of Ampicillin Capacity. *Heliyon* **2022**, *8*, e08841. [CrossRef]
57. Firet, N.J.; Blommaert, M.A.; Burdyny, T.; Venugopal, A.; Bohra, D.; Longo, A.; Smith, W.A. Operando EXAFS Study Reveals Presence of Oxygen in Oxide-Derived Silver Catalysts for Electrochemical CO_2 Reduction. *J. Mater. Chem. A Mater.* **2019**, *7*, 2597–2607. [CrossRef]
58. Yoon, M.; Seo, M.; Jeong, C.; Jang, J.H.; Jeon, K.S. Synthesis of Liposome-Templated Titania Nanodisks: Optical Properties and Photocatalytic Activities. *Chem. Mater.* **2005**, *17*, 6069–6079. [CrossRef]
59. El-Reash, Y.G.A.; Ghaith, E.A.; El-Awady, O.; Algethami, F.K.; Lin, H.; Abdelrahman, E.A.; Awad, F.S. Highly Fluorescent Hydroxyl Groups Functionalized Graphitic Carbon Nitride for Ultrasensitive and Selective Determination of Mercury Ions in Water and Fish Samples. *J. Anal. Sci. Technol.* **2023**, *14*, 16. [CrossRef]
60. Alhokbany, N.; Ahama, T.; Ruksana; Naushad, M.; Alshehri, S.M. AgNPs Embedded N- Doped Highly Porous Carbon Derived from Chitosan Based Hydrogel as Catalysts for the Reduction of 4-Nitrophenol. *Compos. B Eng.* **2019**, *173*, 106950. [CrossRef]
61. Ghosh, S.; Khan, T.S.; Ghosh, A.; Chowdhury, A.H.; Haider, M.A.; Khan, A.; Islam, S.M. Utility of Silver Nanoparticles Embedded Covalent Organic Frameworks as Recyclable Catalysts for the Sustainable Synthesis of Cyclic Carbamates and 2-Oxazolidinones via Atmospheric Cyclizative CO_2 Capture. *ACS Sustain. Chem. Eng.* **2020**, *8*, 5495–5513. [CrossRef]
62. Zhao, T.; Sun, R.; Yu, S.; Zhang, Z.; Zhou, L.; Huang, H.; Du, R. Size-Controlled Preparation of Silver Nanoparticles by a Modified Polyol Method. *Colloids Surf. A Physicochem. Eng. Asp.* **2010**, *366*, 197–202. [CrossRef]
63. Boronin, A.I.; Koscheev, S.V.; Zhidomirov, G.M. XPS and UPS Study of Oxygen States on Silver. *J. Electron Spectrosc. Relat. Phenom.* **1998**, *96*, 43–51. [CrossRef]
64. Mu, J.; Zhang, L.; Zhao, M.; Wang, Y. Co_3O_4 Nanoparticles as an Efficient Catalase Mimic: Properties, Mechanism and Its Electrocatalytic Sensing Application for Hydrogen Peroxide. *J. Mol. Catal. A Chem.* **2013**, *378*, 30–37. [CrossRef]
65. Bu, Y.; Kim, B.S. Eco-Friendly Production of Functionalized Few-Layer Graphene Using Coffee Waste Extract and in-Situ Growth of Copper Oxide Nanoparticles. *J. Environ. Chem. Eng.* **2023**, *11*, 109350. [CrossRef]
66. Zarif, F.; Rauf, S.; Khurshid, S.; Muhammad, N.; Hayat, A.; Rahim, A.; Shah, N.S.; Yang, C.P. Effect of Pyridinium Based Ionic Liquid on the Sensing Property of NiO Nanoparticle for the Colorimetric Detection of Hydrogen Peroxide. *J. Mol. Struct.* **2020**, *1219*, 128620. [CrossRef]
67. Naya, S.I.; Teranishi, M.; Kimura, K.; Tada, H. A Strong Support-Effect on the Catalytic Activity of Gold Nanoparticles for Hydrogen Peroxide Decomposition. *Chem. Commun.* **2011**, *47*, 3230–3232. [CrossRef] [PubMed]
68. Liu, S.; Tian, J.; Wang, L.; Sun, X. Highly Sensitive and Selective Colorimetric Detection of Ag(I) Ion Using 3,3′,5,5′,-Tetramethylbenzidine (TMB) as an Indicator. *Sens. Actuators B Chem.* **2012**, *165*, 44–47. [CrossRef]
69. Üzer, A.; Durmazel, S.; Erçağ, E.; Apak, R. Determination of Hydrogen Peroxide and Triacetone Triperoxide (TATP) with a Silver Nanoparticles—Based Turn-on Colorimetric Sensor. *Sens. Actuators B Chem.* **2017**, *247*, 98–107. [CrossRef]
70. Mills, A. An Overview of the Methylene Blue ISO Test for Assessing the Activities of Photocatalytic Films. *Appl. Catal. B* **2012**, *128*, 144–149. [CrossRef]
71. Ismail, M.; Khan, M.I.; Khan, S.A.; Qayum, M.; Khan, M.A.; Anwar, Y.; Akhtar, K.; Asiri, A.M.; Khan, S.B. Green Synthesis of Antibacterial Bimetallic Ag–Cu Nanoparticles for Catalytic Reduction of Persistent Organic Pollutants. *J. Mater. Sci. Mater. Electron.* **2018**, *29*, 20840–20855. [CrossRef]
72. Asli, B.; Abdelkrim, S.; Zahraoui, M.; Mokhtar, A.; Hachemaoui, M.; Bennabi, F.; Ahmed, A.B.; Sardi, A.; Boukoussa, B. Catalytic Reduction and Antibacterial Activity of MCM-41 Modified by Silver Nanoparticles. *Silicon* **2022**, *14*, 12587–12598. [CrossRef]

73. Ismail, M.; Gul, S.; Khan, M.I.; Khan, M.A.; Asiri, A.M.; Khan, S.B. Medicago Polymorpha-Mediated Antibacterial Silver Nanoparticles in the Reduction of Methyl Orange. *Green Process. Synth.* **2019**, *8*, 118–127. [CrossRef]
74. Chandra Paul, S.; Bhowmik, S.; Rani Nath, M.; Islam, M.S.; Kanti Paul, S.; Neazi, J.; Sabnam Binta Monir, T.; Dewanjee, S.; Abdus Salam, M. Silver Nanoparticles Synthesis in a Green Approach: Size Dependent Catalytic Degradation of Cationic and Anionic Dyes. *Orient. J. Chem.* **2020**, *36*, 353–360. [CrossRef]
75. Zahid, M.; Al-Majmaie, S.; Shather, A.H.; Khan, M.F.; Alguno, A.C.; Capangpangan, R.Y.; Ismail, A. Elettaria Cardamomum Seed Extract Synthesized Silver Nanoparticles for Efficient Catalytic Reduction of Toxic Dyes. *Environ. Nanotechnol. Monit. Manag.* **2023**, *20*, 100809. [CrossRef]
76. Padre, S.M.; Kiruthika, S.; Mundinamani, S.; Ravikirana; Surabhi, S.; Jeong, J.R.; Eshwarappa, K.M.; Murari, M.S.; Shetty, V.; Ballal, M.; et al. Mono- and Bimetallic Nanoparticles for Catalytic Degradation of Hazardous Organic Dyes and Antibacterial Applications. *ACS Omega* **2022**, *7*, 35023–35034. [CrossRef] [PubMed]
77. Ghosh, S.K.; Kundu, S.; Mandal, M.; Pal, T. Silver and Gold Nanocluster Catalyzed Reduction of Methylene Blue by Arsine in a Micellar Medium. *Langmuir* **2002**, *18*, 8756–8760. [CrossRef]
78. Somasundaram, C.K.; Atchudan, R.; Edison, T.N.J.I.; Perumal, S.; Vinodh, R.; Sundramoorthy, A.K.; Babu, R.S.; Alagan, M.; Lee, Y.R. Sustainable Synthesis of Silver Nanoparticles Using Marine Algae for Catalytic Degradation of Methylene Blue. *Catalysts* **2021**, *11*, 1377. [CrossRef]
79. Hao, Y.; Zhang, N.; Luo, J.; Liu, X. Green Synthesis of Silver Nanoparticles by Tannic Acid with Improved Catalytic Performance Towards the Reduction of Methylene Blue. *Nano* **2018**, *13*, 1850003. [CrossRef]
80. Kumar, P.; Dixit, J.; Singh, A.K.; Rajput, V.D.; Verma, P.; Tiwari, K.N.; Mishra, S.K.; Minkina, T.; Mandzhieva, S. Efficient Catalytic Degradation of Selected Toxic Dyes by Green Biosynthesized Silver Nanoparticles Using Aqueous Leaf Extract of *Cestrum nocturnum* L. *Nanomaterials* **2022**, *12*, 3851. [CrossRef] [PubMed]
81. Al-Shehri, A.S.; Zaheer, Z.; Alsudairi, A.M.; Kosa, S.A. Photo-Oxidative Decolorization of Brilliant Blue with AgNPs as an Activator in the Presence of $K_2S_2O_8$ and $NaBH_4$. *ACS Omega* **2021**, *6*, 27510–27526. [CrossRef] [PubMed]
82. Barman, K.; Chowdhury, D.; Baruah, P.K. Bio-Synthesized Silver Nanoparticles Using *Zingiber officinale* Rhizome Extract as Efficient Catalyst for the Degradation of Environmental Pollutants. *Inorg. Nano-Met. Chem.* **2020**, *50*, 57–65. [CrossRef]
83. Maiti, S.; Krishnan, D.; Barman, G.; Ghosh, S.K.; Laha, J.K. Antimicrobial Activities of Silver Nanoparticles Synthesized from *Lycopersicon esculentum* Extract. *J. Anal. Sci. Technol.* **2014**, *5*, 40. [CrossRef]
84. Hamad, A.; Khashan, K.S.; Hadi, A. Silver Nanoparticles and Silver Ions as Potential Antibacterial Agents. *J. Inorg. Organomet. Polym. Mater.* **2020**, *30*, 4811–4828. [CrossRef]
85. Urnukhsaikhan, E.; Bold, B.-E.; Gunbileg, A.; Sukhbaatar, N.; Mishig-Ochir, T. Antibacterial Activity and Characteristics of Silver Nanoparticles Biosynthesized from *Carduus crispus*. *Sci. Rep.* **2021**, *11*, 21047. [CrossRef] [PubMed]
86. Ansari, M.A.; Khan, H.M.; Khan, A.A.; Ahmad, M.K.; Mahdi, A.A.; Pal, R.; Cameotra, S.S. Interaction of Silver Nanoparticles with *Escherichia coli* and Their Cell Envelope Biomolecules. *J. Basic Microbiol.* **2014**, *54*, 905–915. [CrossRef] [PubMed]
87. Sondi, I.; Salopek-Sondi, B. Silver Nanoparticles as Antimicrobial Agent: A Case Study on E. Coli as a Model for Gram-Negative Bacteria. *J. Colloid Interface Sci.* **2004**, *275*, 177–182. [CrossRef]
88. Thill, A.; Zeyons, O.; Spalla, O.; Chauvat, F.; Rose, J.; Auffan, M.; Flank, A.M. Cytotoxicity of CeO_2 Nanoparticles for *Escherichia coli*. Physico-Chemical Insight of the Cytotoxicity Mechanism. *Environ. Sci. Technol.* **2006**, *40*, 6151–6156. [CrossRef] [PubMed]
89. Morales-Avila, E.; Ferro-Flores, G.; Ocampo-Garciá, B.E.; López-Téllez, G.; López-Ortega, J.; Rogel-Ayala, D.G.; Sánchez-Padilla, D. Antibacterial Efficacy of Gold and Silver Nanoparticles Functionalized with the Ubiquicidin (29-41) Antimicrobial Peptide. *J. Nanomater.* **2017**, *2017*, 5831959. [CrossRef]
90. Ramalingam, B.; Parandhaman, T.; Das, S.K. Antibacterial Effects of Biosynthesized Silver Nanoparticles on Surface Ultrastructure and Nanomechanical Properties of Gram-Negative Bacteria Viz. *Escherichia coli and Pseudomonas aeruginosa*. *ACS Appl. Mater. Interfaces* **2016**, *8*, 4963–4976. [CrossRef]
91. Javani, S.; Lorca, R.; Latorre, A.; Flors, C.; Cortajarena, A.L.; Somoza, Á. Antibacterial Activity of DNA-Stabilized Silver Nanoclusters Tuned by Oligonucleotide Sequence. *ACS Appl. Mater. Interfaces* **2016**, *8*, 10147–10154. [CrossRef] [PubMed]
92. Meikle, T.G.; Dyett, B.P.; Strachan, J.B.; White, J.; Drummond, C.J.; Conn, C.E. Preparation, Characterization, and Antimicrobial Activity of Cubosome Encapsulated Metal Nanocrystals. *ACS Appl. Mater. Interfaces* **2020**, *12*, 6944–6954. [CrossRef] [PubMed]
93. Cheon, J.Y.; Kim, S.J.; Rhee, Y.H.; Kwon, O.H.; Park, W.H. Shape-Dependent Antimicrobial Activities of Silver Nanoparticles. *Int. J. Nanomed.* **2019**, *14*, 2773–2780. [CrossRef] [PubMed]
94. Alshareef, A.; Laird, K.; Cross, R.B.M. Shape-Dependent Antibacterial Activity of Silver Nanoparticles on *Escherichia coli* and *Enterococcus faecium* Bacterium. *Appl. Surf. Sci.* **2017**, *424*, 310–315. [CrossRef]
95. dos Santos, V.E.; Junior; Targino, A.G.R.; Flores, M.A.P.; Rodríguez-Díaz, J.M.; Teixeira, J.A.; Heimer, M.V.; Pessoa, H.D.L.F.; Galembeck, A.; Rosenblatt, A. Antimicrobial Activity of Silver Nanoparticle Colloids of Different Sizes and Shapes against *Streptococcus* Mutans. *Res. Chem. Intermed.* **2017**, *43*, 5889–5899. [CrossRef]

Journal of
Functional
Biomaterials

MDPI

Review

Engineering Antioxidant Surfaces for Titanium-Based Metallic Biomaterials

Jithin Vishnu [1], Praveenkumar Kesavan [2], Balakrishnan Shankar [1], Katarzyna Dembińska [3], Maria Swiontek Brzezinska [3] and Beata Kaczmarek-Szczepańska [4,*]

[1] Department of Mechanical Engineering, Amrita Vishwa Vidyapeetham, Amritapuri Campus, Clappana 690525, India; jithinv@am.amrita.edu (J.V.); bala@am.amrita.edu (B.S.)
[2] Department of Materials Engineering, Indian Institute of Science, Bangalore 560012, India; praveenkk@iisc.ac.in
[3] Department of Environmental Microbiology and Biotechnology, Faculty of Biological and Veterinary Sciences, Nicolaus Copernicus University in Toruń, 87-100 Toruń, Poland; 311943@stud.umk.pl (K.D.); swiontek@umk.pl (M.S.B.)
[4] Department of Biomaterials and Cosmetic Chemistry, Faculty of Chemistry, Nicolaus Copernicus University in Toruń, 87-100 Toruń, Poland
* Correspondence: beata.kaczmarek@umk.pl; Tel.: +48-56-611-48-33

Abstract: Prolonged inflammation induced by orthopedic metallic implants can critically affect the success rates, which can even lead to aseptic loosening and consequent implant failure. In the case of adverse clinical conditions involving osteoporosis, orthopedic trauma and implant corrosion-wear in peri-implant region, the reactive oxygen species (ROS) activity is enhanced which leads to increased oxidative stress. Metallic implant materials (such as titanium and its alloys) can induce increased amount of ROS, thereby critically influencing the healing process. This will consequently affect the bone remodeling process and increase healing time. The current review explores the ROS generation aspects associated with Ti-based metallic biomaterials and the various surface modification strategies developed specifically to improve antioxidant aspects of Ti surfaces. The initial part of this review explores the ROS generation associated with Ti implant materials and the associated ROS metabolism resulting in the formation of superoxide anion, hydroxyl radical and hydrogen peroxide radicals. This is followed by a comprehensive overview of various organic and inorganic coatings/materials for effective antioxidant surfaces and outlook in this research direction. Overall, this review highlights the critical need to consider the aspects of ROS generation as well as oxidative stress while designing an implant material and its effective surface engineering.

Keywords: antioxidant; surfaces; titanium; reactive oxygen species (ROS); biomaterials

1. Introduction

One of the key factors associated with inflammatory response is the oxidative stress, which is characterized by the imbalance/disparity between the generation of reactive oxygen species (ROS) and antioxidant defense system [1]. Osteoporosis, the most common bone disorder globally, is a systemic skeletal disorder associated with diminishing bone mass and micro-architectural bone tissue degradation with concomitant bone fragility and osteoporotic fracture [2–4]. Considered as one of the major global pandemics of the 21st century, osteoporosis induces more than 8.9 million bone fractures per annum, affecting about 200 million people, and in addition, poses a high risk specifically to post-menopausal women, with 40–50% prevalence in women older than 60 years [5–7]. Other leading causes for bone fracture includes road accidents, falls and sports injuries. Following the bone fracture, secondary healing ensues involving various stages such as hematoma formation, acute inflammation, callus formation and bone remodeling [8]. The fracture trauma results in blood vessel rupture in the region of fracture leading to hematoma [9]. The hematoma

micro-environment in the fracture site is structurally unstable, hypoxic and acidic, which requires a cross-talk between inflammatory cells and cells related to bone healing in order to re-establish normal homeostatic state [9,10]. The bone remodeling involves a collective involvement of various bone cells such as osteoclasts (removal of damaged and old bones), osteoblasts (synthesis and secretion of osteoid matrix during mineralization) and osteocytes (regulating new bone formation and old bone resorption) [11–13]. Oxidative stress is a predominant factor which negatively affects the bone remodeling process resulting in a deteriorated bone mineral density, contributing in the etiology of osteoporosis [14–16].

Clinical intervention of bone fractures and defects considers the usage of orthopedic implants for the treatment of orthopedic trauma with minimal harm to the patients. Metallic, ceramic and polymeric biomaterials have been explored and researched for orthopedic implant applications, with each class of materials possessing its own advantages and disadvantages [17–19]. Thanks to their superior mechanical properties, metallic materials are the most widely used material for internal fracture fixation components. The three dominant material classes in this aspect are 316L stainless steel, Co-Cr alloys and Ti and its alloys [20–23]. However, metallic materials are prone to degradation due to corrosion-wear synergy (tribocorrosion) in complex physiological environments capable of eliciting the release of ions and debris in the peri-implant region [24,25]. Such wear-debris release from articulating components can result in the activation and senescence of resident cells including macrophages, fibroblasts, osteoclasts and osteoblasts, eventually leading to the production and release of pro-inflammatory cytokines, chemokines, ROS and reactive nitrogen species (RNS) [26,27]. This elicits chronic inflammatory cascades and oxidative stress reactions eventually resulting in bone resorption and osteolysis induced implant failure [26,28].

During normal healing process, osteoblasts express antioxidant enzymes such as superoxide dismutase (SOD) for inducing the conversion of ROS into O and H_2O to induce osteoblast differentiation [29,30]. However, during adverse conditions as mentioned above, enhanced ROS activity results in oxidative stress reducing the bone mineralization density by affecting the remodeling process [31,32]. In spite of the presence of endogenous antioxidants, excessive generation of free radicals and inflammatory processes result in oxidative stress [33]. The occurrence of oxidative stress can be ascribed to abnormal activation of enzymes which generates ROS. ROS are highly reactive, short-lived molecules formed as by-products during molecular oxygen reduction which are capable of oxidative damage to macromolecules in biological cells [34–38]. ROS include radical and non-radical oxygen species such as superoxide anion (O^{2-}), hydroxyl radical (OH^{-}) and hydrogen peroxide (H_2O_2) [39–42]. The mechanism of ROS formation via electrochemical corrosion reaction, radical transformation via Fenton and Haber–Weiss Reactions, light induction and surface catalytic reactions is elaborately reviewed by Kessier et al. [43].

Antioxidants are naturally occurring reducing agents which can hinder the generation of ROS via the phenomenon of scavenging free radicals and eradicating ROS derivatives. Hence, the origin of oxidative stress can be linked to the imbalance between ROS and antioxidants which encompass enzymatic antioxidants (e.g., polyphenols, carotenoids, glutathione, tocopherols) and antioxidant enzymes (SOD, catalase, glutathione peroxidase) [44]. An increment in antioxidant levels can be potentially harmful as it could induce molecular damages, apoptosis or necrosis, and oxidative stress is found to be associated with several diseases including cardiovascular, neurodegenerative, carcinoma, diabetes, ischemia/reperfusion injury, rheumatoid arthritis and aging [45]. Endogenous enzymatic antioxidants include SOD, catalase, glutathione peroxidase and glutathione reductase, whereas non-enzymatic endogenous antioxidants include glutathione and lipoic acid [46].

Metallic implant materials are widely used for bone-anchored therapy for orthopedic and dental treatments. Apart from the wear-induced oxidative stress as discussed above, metallic material insertion during surgical procedure induces large amount of ROS generation and is incapable of generating antioxidants, thereby critically influencing the healing process which elevates the healing time.

Implant surface plays a pivotal role in dictating the host response of the implanted material. In most cases, surface modification of implants alters the surface morphology, topography, chemistry and surface energy, particularly aimed at improving matrix protein adhesion, cellular adhesion and proliferation, to attain better osseointegration [47,48]. A variety of surface modification strategies involving surface texturing and surface coatings have been developed to improve the interfacial mechanical strength, wear resistance, tribo-corrosion resistance and biocompatibility in order to enhance the longevity of orthopedic implants [49,50]. Recently, surface modification of Ti implants has been gaining research attention to repair the impaired osseointegration by developing surfaces with antioxidant activity [51–53]. In summary, it is imperative to gain more insights into the advancements in this field to further improve the antioxidant activities of Ti implant surface by proper surface modification to improve its clinical efficiency. In view of these aspects, the present review is focused towards the various surface engineering techniques to combat the undesirable ROS generation associated with Ti-based metallic implants. Several review articles have been published reporting the underlying mechanism of ROS formation and antioxidative mechanisms [30,54,55]. In addition, review articles comprehensively describing surface modification techniques for Ti surface are published [56,57]. The novelty aspect of the present review lies in collating the available reported works in improving the antioxidant properties of Ti-based metallic implant surfaces via various organic and inorganic coatings. Even though several research articles have explored the antioxidant activity of surfaces developed for antibacterial and biocompatible applications, this review exempts these articles and is focused on research associated with surfaces/materials specifically developed for antioxidant purpose. This review initially presents an outline of ROS generation associated with the insertion of Ti implants. This is followed by sections describing organic- and inorganic-based coatings on Ti surfaces to ameliorate the antioxidant aspects along with prospective future perspectives. The major objective of the present review is to provide an overall idea about how surface modification can assist in improving the ROS scavenging activity and reduce oxidative damage to improve the clinical efficiency of Ti-based implants.

2. Titanium Alloys and Reactive Oxygen Species Metabolism

Titanium (Ti) and its alloys are the widely used material for a variety of load-bearing orthopedic implant applications thanks to the excellent mechanical aspects, lower modulus values, corrosion resistance and excellent biocompatibility [58]. Ti is a transition metal which exists in a hexagonal closed pack (hcp) crystal structure (α-Ti), which transforms into its allotropic form with a body-centered cubic (bcc) structure (β-Ti) above a temperature of 882 °C, which is retained up to its melting point (1688 °C). Several Ti-based alloys such as commercially pure Ti (cp-Ti, ASTM-F67), Ti-6Al-4V (ASTM-F136), Ti-6Al-7Nb (ASTM-F1472, F1295) and Ti-13Nb-13Zr (ASTM-F1713-08) have been explored for dental implants, bone fixation plates, screws and hip joint stems [59,60]. Current research focus is more shifted towards β-Ti alloys as they possess comparatively lower elastic modulus (as low as 46–55 GPa), high strength, good cold workability and, most importantly, the beneficial biocompatibility aspects due to β-phase stabilizing alloying additions (Nb, Ta, Mo, Mn, Fe etc.) [61–63]. In addition, Ti-based shape memory alloys are prospective materials for various biomedical applications owing to the shape memory and super-elasticity effects [64]. Despite these beneficial aspects, wear-induced aseptic loosening is a limiting factor hampering the efficiency of Ti-based orthopedic implants [65]. Wear-particle phagocytosis by macrophages can induce cytokine and free radical release, resulting in an aseptic inflammatory response, capable of promoting osteoclast resorption [66]. The role of high oxidative stress as one of the main causative factors in various inflammatory and degenerative disorders points towards the contribution of ROS towards aseptic loosening. As a response to the released metallic particles in a physiological condition, the immune system elicits an inflammation process, which involves generation of ROS through a series of enzyme-assisted biochemical reactions (schematic figure as shown in Figure 1) [67].

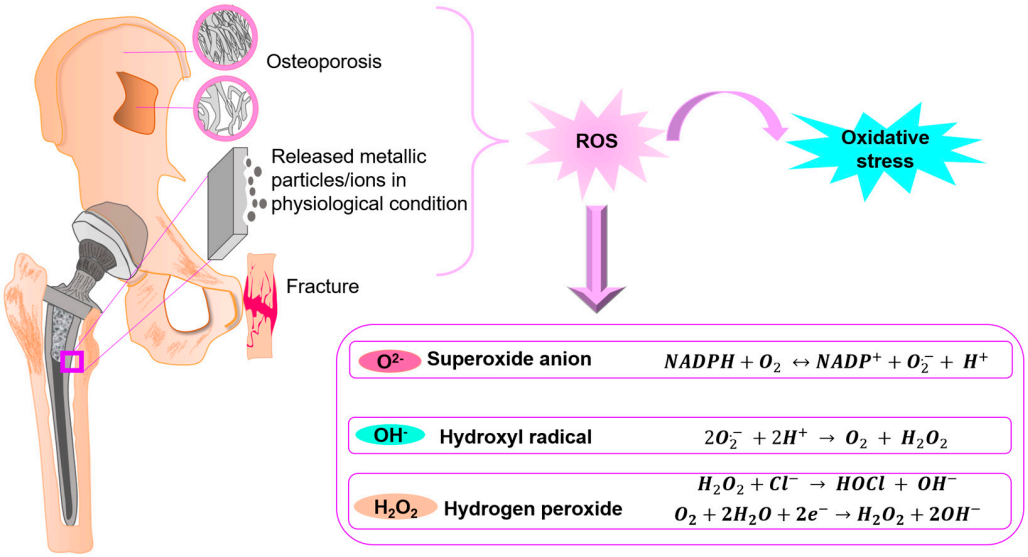

Figure 1. Schematic depicting the ROS generation associated with Ti implants with associated biochemical reactions.

Superoxide radical generation is catalyzed by NADPH (nicotinamide adenine dinucleotide phosphate) oxidase (Equation (1)). Electrons from NADPH is accepted by the cytosolic domain of $gp91^{phox}$ (electron transferase of NADPH oxidase) and is transferred across membrane to O_2 to generate superoxide radical (O_2^-) as the primary product [68]. $Gp91^{phox}$ contains all the required co-factors to effectuate electron transfer reaction, in which electrons transfer from NADPH onto flavin adenine dinucleotide (FAD) and to the haem group in the following step, inducing reduction of O_2 to O_2^- [69].

$$NADPH + O_2 \leftrightarrow NADP^+ + O_2^- + H^+ \quad (1)$$

In response to this, antioxidant scavenging enzymes such as SOD promote dismutation to convert superoxide to hydrogen peroxide and an oxygen molecule (Equation (2)), which occurs spontaneously (rate constant = 5×10^5 $M^{-1}s^{-1}$ at neutral pH) [70]. This reaction is greatly accelerated by SOD, and the corresponding catalytic activity is attributed partly to the electrostatic interactions in active center of SOD protein [71].

$$2O_2^- + 2H^+ \rightarrow O_2 + H_2O_2 \quad (2)$$

Stimulation of neutrophils results in oxygen consumption in a respiratory burst that produces O_2^- and H_2O_2. Simultaneous discharge of abundant myeloperoxidase enzyme occurs, which utilizes H_2O_2 to oxidize halides (chlorides, bromides) and thiocyanates to corresponding hypohalous acids and hypothiocyanite [72]. Myeloperoxidase, also called verdoperoxidase, is a heme-containing peroxidase generated mostly from polymorphonuclear neutrophils and found in primary granules of granulocytic cells [73]. The reaction between hydrogen peroxide with halides (such as Cl^- in physiological environment) is catalyzed by granule-localized myeloperoxidase to form hypochlorous acid (bleach) (Equation (3)).

$$H_2O_2 + Cl^- \rightarrow HOCl + OH^- \quad (3)$$

In addition, hydrogen peroxide can generate hydroxide and hydroperoxyl radicals by reacting with ferrous and ferric cations (Fenton reactions). Fenton chemistry can significantly enhance the degradation of many transition metals (including Ti alloys, Co-Cr alloys) [74]. Fenton reaction involves an initial electron transfer with neither bond formation nor breaking and the generation of hydroxyl radicals [75]. Haber Weiss reaction which makes use of Fenton chemistry involves vital mechanism in which highly reactive hydroxyl radical generation occurs [76]. Another possible cathodic reaction taking place at

implant/bone interface is oxygen reduction to generate hydrogen peroxide (Equation (4)). The cathodic oxygen reduction can be sub-divided into several reactions, resulting in the generation of hydroxyl radicals and hydrogen peroxide.

$$O_2 + 2H_2O + 2e^- \rightarrow H_2O_2 + 2OH^- \quad (4)$$

Hence, ROS are additional products of overall electrochemical reactions occurring in the implant interface other than the metallic ions and/or particles. The presence of ROS (hydroxyl radicals and hydrogen peroxide) can further promote degradation of Ti implants [77]. Among the various ROS molecules, hydrogen peroxide can mix with water and diffuse through membranes of peri-implant tissues, critically affecting intracellular redox status, thereby increasing the chances of implant failure [78].

3. Surface Modification for Antioxidant Ti Surfaces

Surface modification of Ti alloys offers an effective strategy to combat the limitations associated with ROS activity. To develop such surfaces/coatings, several surface modification techniques such as layer-by-layer technique, immersion/dip coating, spin coating, plasma immersion ion implantation and radiofrequency plasma-enhanced chemical vapor deposition (enlisted in Table 1) are being researched. A limited number of coating surfaces/materials have been explored to improve the antioxidant activity of Ti surfaces which can be conveniently categorized as organic and inorganic materials for surface modification.

Table 1. Various reported techniques used for developing antioxidant surfaces on Ti/Ti alloy surfaces.

Technique	Description	Ref.
Layer-by-layer technique	Bottom-up adsorption technique which involves the development of multi-layered (layers of oppositely charged species) thin films bound together through electrostatic interactions.	[79,80]
Immersion/dip coating	Solution-based deposition method which involves the immersion of substrate into a solution of material to be coated which depends on parameters such as dwelling time, substrate-withdrawal speed, number of dip-coating cycles and coating evaporation factor.	[81,82]
Spin coating	A technique which uses centrifugal force for deposition, in which a suspension is dropped from top into the rotating substrate, and the resulting centrifugal force will assist in spreading out the coating on the substrate, thereby coating it. The process is dependent on parameters such as dispense volume, spin speed, solution viscosity, solution concentration, spin time, etc.	[83–85]
Plasma immersion ion implantation (PIII)	Method to improve biocompatibility aspects of material surfaces by immersing in a plasma environment and applying negative-high-voltage pulsed bias. Compared to traditional plasma techniques, PIII can extend to some tens of nanometers beneath sample surface and can treat complex geometries.	[86–88]
Plasma enhanced chemical vapor deposition	Low temperature chemical vapor deposition in which plasma is used to drive chemical reactions between plasma-generated-reactive species and substrate instead of high temperatures.	[89–91]

3.1. Organic Materials for Surface Modification

3.1.1. Tannic Acid

Tannic acid is a water-soluble natural polyphenol compound, which is often present in tea, wine and fruits and possesses excellent antioxidant and antibacterial activity owing to the presence of pyrogallol and catechol groups [92]. The antioxidant activity of tannic acid is dependent on its capability to chelate metal ions such as Fe(II) and interfering one of the reaction steps in Fenton reaction, thereby retarding oxidation [93]. There are several

published review articles pertaining to the surface modification aspects of tannic acid-based coatings for various applications [94,95]. Several techniques such as layer-by-layer deposition [96,97], electrodeposition, UV-assisted deposition [98] and immersion [53] have been used to deposit tannic acid coatings. The presence of catechol groups renders tannic acid substrate-independent adhesive properties. Polyphenol group interactions can occur via several catechol–surface interactions ranging from noncovalent interactions (hydrogen bonding, pi–pi interactions) to chemical bonding (coordination, covalent) [99]. In addition, polyphenol tannic acid is capable of forming functional coatings on various materials by means of an intrinsic auto-oxidative surface polymerization. Sebastian et al. investigated the deposition kinetics of tannic acid on Ti surfaces which revealed a multiphase layer generation [100]. An initial growth phase revealed build-up of layer which is compact as well as rigid (approx. 2 h), followed by adsorption of an increasingly dissipative layer (approx. 5 h). Following this, a coating discontinuation was observed which was corroborated with large particle precipitation in coating solutions.

In order to develop multifunctional coatings on Ti surface, tannic acid is often co-deposited along with other functional biomaterial coatings for prospective implant applications. Hydroxyapatite ($Ca_{10}(PO_4)_6(OH)_2$) is a bioactive material, the main inorganic bone component which possesses excellent osteoinduction and osteoconduction properties. In view of rendering Ti surfaces (which are bioinert) with bioactive and antioxidant properties, hydroxyapatite and tannic acid based composite coatings have been explored. A consistent and strong antioxidant activity was displayed by hydroxyapatite/tannic acid coatings deposited on Ti substrates modified by titania (TiO_2) nanotubes (Figure 2a–c) [101]. Gelatin added to hydroxyapatite can improve the osteogenic aspects to enhance bone formation. However, gelatin-hydroxyapatite coatings failed in bone conduction function due to weak bonding between them. Tannic acid has been found to strongly adsorb to hydroxyapatite surface and firmly glued gelatin and hydroxyapatite [96]. The resultant tannic acid-hydroxyapatite-gelatin complex coating demonstrated significantly higher antioxidant activity and reduced cell damage/changes in the presence of H_2O_2. There are limitations reported with the adherence of tannic acid onto hydroxyapatite and salivary acquired pellicle peptide modified tannic acid exhibited better adsorption performance on hydroxyapatite surface [102]. Tightly adsorbed coating exhibited smooth, superhydrophilic surface with excellent antibacterial and antibiofouling performance.

In order to develop multifunctional antioxidant and antibacterial coatings, tannic acid is coated along with antibacterial elements which can be contact killing, release killing or anti-adhesive. Despite being widely explored for a wide spectrum of antibacterial applications, silver (Ag) usage for bio-surfaces is limited by dose dependent cytotoxicity. Hydroxyapatite-tannic acid coating developed by immersion technique on a Ag-loaded TiO_2 nanotubular Ti surface demonstrated high antibacterial activity, improved cytocompatibility and revealed slow release of tannic acid from surface, which contributed towards persistent antioxidant activity as shown in Figure 2d–f [53]. Polyethylene glycol is a promising antifouling polymeric interface, an appropriate proton acceptor and can generate hydrogen bonds with tannic acid [103]. Simultaneous deposition of polyethylene glycol resulted in increased coating thickness and improved surface coverage [104]. A novel pH-bacteria triggered antibiotic release mechanism has been developed by layer-by layer deposition of tannic acid with cationic antibiotics such as tobramycin, gentamicin and polymyxin B [105]. Unlike linear polymer molecules which are incapable of retaining antibiotics, tannic acid through its hydrogen bonding and electrostatic interactions interacted well with the antibiotics. The interesting aspect is the non-eluting characteristic of the tannic acid/antibiotic coating which is capable of triggering antibiotic release created by pH reduction induced by bacterial pathogens. Hizal et al. reported an ultrathin tannic acid/gentamicin layer-by-layer film on 3D nano-pillared structures, which exhibited a 10-fold decrease in bacterial attachment due to larger surface area of nanostructured surface and lower bacterial adhesion forces on nanopillar tips [106]. Apart from these, strontium

(Sr^{2+}) incorporated tannic acid functionalized on Ti surface revealed enhanced osteoblast differentiation and reduced osteoclast activity [107].

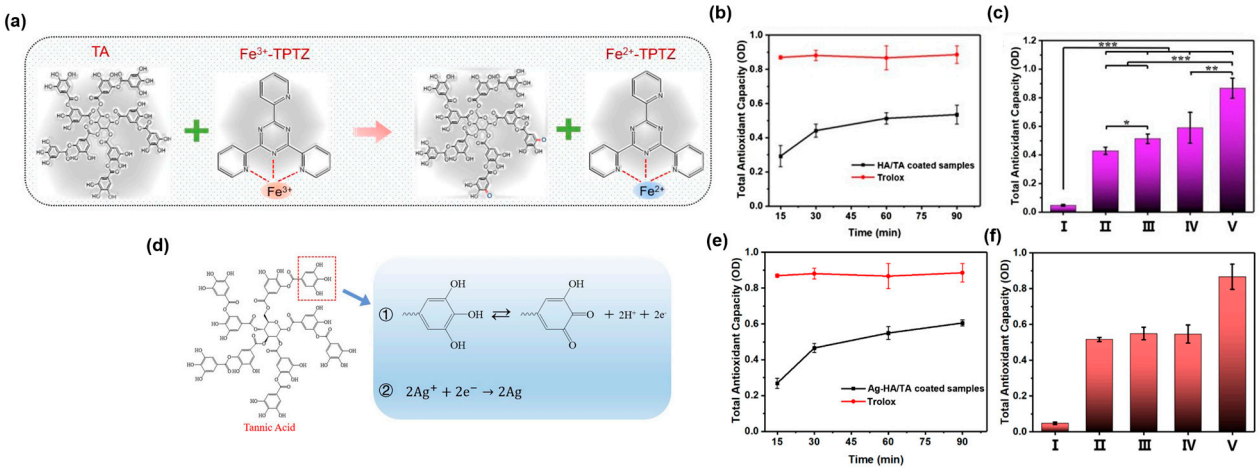

Figure 2. Antioxidant activity of HAP/tannic acid composite coating. (**a**) Mechanism illustrating antioxidant activity; (**b**,**c**) antioxidant activity as a function of incubation time of HAP/tannic acid coating compared to Trolox; (**c**) antioxidant activity of (I) negative control (deionized water), (II–IV) 10, 30 and 50 g/L of tannic acid, (V) positive control (Trolox). Data reported as means ± standard deviations, n = 3 (* $p < 0.05$, ** $p < 0.01$, *** $p < 0.001$). Reprinted from [101] with permission from Elsevier. (**d**) Formation mechanism depiction of Ag nanoparticles; (**e**) antioxidant activity with respect to incubation time of Ag/HAP/tannic acid coating compared to Trolox; and (**f**) antioxidant activity of (I) negative control (deionized water), (II–IV) 0.05, 0.1 and 0.2 M $AgNO_3$, (V) positive control (Trolox). Reprinted from [53] with permission from Elsevier.

3.1.2. Chitosan

Chitosan is a polycationic natural macromolecule (with a molecular structure of (1,4)-linked 2-amino-2-deoxy-β-d-glucan), which is capable of reacting with many physiologically relevant ROS [108–111]. Owing to its various beneficial aspects such as improvement of osseointegration and cellular interactions, minimal foreign body response, favorable degradation rate and, most importantly, due to antioxidant and free radical scavenging activities, this partly deacetylated form of chitin is a prospective material for surface modification [112,113]. Chitosan can form functional coatings on Ti surface owing to the existence of amine groups in chitosan polymer chains, which are capable of developing covalent bonds with Ti via silanization [114]. Reasonable mechanisms for antioxidative action of chitosan include presence of intra-molecular hydrogen bonding [115], residual-free amino groups in water-soluble chitosan which may induce metal chelation [116] and the ability of NH_2 amino groups to react with hydroxyl groups (OH^-) to generate stable macromolecule radicals [117].

Lieder et al. studied the effect of degree of deacetylation of chitosan membranes coated on Ti surfaces which resulted in an improved fibronectin adsorption, cellular attachment and proliferation, but with no instigation of spontaneous osteogenic differentiation [114]. Chitosan coating (85–90% deacetylated) on porous Ti surface evidenced excellent antioxidant effect and favored osteoblast activity under diabetic conditions through reactivation of P13K/AKT pathway [118]. The study elucidated that chitosan can play a role in the reactivation of P13K/AKT pathway which mediates diabetes-induced ROS overproduction at bone-implant interface (Figure 3c,d). A multi-step layer-by-layer self-assembly was employed to deposit biofunctional composite coatings of chitosan and alginate enriched with caffeic acid on Ti-6Al-7Nb surface [119].

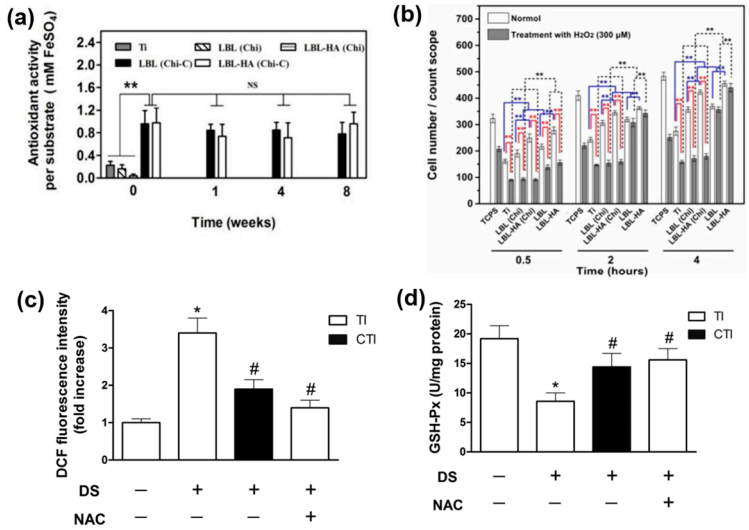

Figure 3. Antioxidant activity of chitosan based surfaces on Ti. (**a**) Antioxidant activity measured over a period of 8 weeks; (**b**) osteoblast interaction with and without treatment of hydrogen peroxide. Reprinted from [51] with permission from Elsevier. (**c**) intracellular ROS activity measured by DCF fluorescence intensity and (**d**) intracellular GSH-Px activity to quantify the rate of oxidation of the reduced glutathione to the oxidized glutathione by H_2O_2 (* $p < 0.05$ vs. TI + NS; # $p < 0.05$ vs. TI + DS; ** $p < 0.01$). Reprinted from [118] with permission from Elsevier.

Multiple steps consisted of piranha solution treatment of Ti alloy surface, plasma chemical activation and dip coating. Antioxidant activity measured in terms of DPPH-scavenging activity was higher for chitosan coating due to its potent reducing activity by hydrogen-donating ability. Conjugation of caffeic acid on chitosan resulted in the generation of amide linkages, increasing the amount of electron-donating groups. Another chitosan-based composite coating consisting of chitosan-catechol, gelatin and hydroxyapatite nanofibres deposited on Ti substrates exhibited high level of ROS scavenging activity and decreased oxidative damage on cellular level as displayed in Figure 3a,b [51]. This coating was able to retain increased level of p-FAK (assists in cell spreading and migration) and p-Akt (control cell survival and apoptosis) compared to pure Ti. The developed multilayer coating improved cell matrix adhesion and intercellular adhesion, while attenuating ROS-induced damage by interfering expressions of integrin αv and β3, cadherin genes, anti-apoptotic and pro-apoptotic gene amounts. Electrophoretic deposition technique is also explored recently to coat chitosan-based composite coatings with hydroxyapatite, graphene and gentamycin [120].

3.1.3. Proanthocyanidin

Proanthocyanidin is condensed tannins (comprising of flavan-3-ol monomeric units), which belongs to the class of naturally occurring polyphenol flavonoid (non-thiol natural antioxidant), is found abundantly in berries and fruits [121,122]. Proanthocyanidin possesses excellent ROS scavenging activity, can regulate macrophage behavior and is capable of stimulating bone formation under oxidative stress conditions [123–126]. Tang et al. reported layer-by-layer self-assembly method to deposit hyaluronic acid/chitosan multilayers with proanthocyanidins [127]. The three-dimensional multilayered network of hyaluronic acid/chitosan on Ti surface facilitated proanthocyanidin incorporation into the micro interspaces between hyaluronic acid and chitosan, eventually leading to its controlled release. Proanthocyanidin incorporation is based on the electrostatic interaction between reactive OH^- radical in proanthocyanidin and positive amine groups in chitosan. Layer-by-layer assembly is a self-assembly technique based on the electrostatic attractions (polyanions and polycations) between the assembled components to generate polyelectrolyte multilayers. Layer-by-layer technique involves charging Ti substrates by

conjugating polyethylenimine for the purpose of obtaining higher binding forces. A sustained release of proanthocyanidin for a prolonged period of 14 days and mitigation of ROS-mediated inflammatory response were inferred. In other work, layer-by-layer technique was employed to integrate collagen type-II with proanthocyanidin which assisted in accelerating proliferation and osteogenic differentiation via Wnt/b-catenin signaling pathway and improved bone generation in vivo [128]. A novel covalent-conjugation strategy is reported to immobilize chitosan-encapsulated proanthocyanidin on Ti surface based on coupling agents (3-aminopropyl) triethoxysilane and glutaraldehyde [129]. Effective attenuation of the inhibitory effect of oxidative stress was induced by proanthocyanidin by the decrease of p53 gene expression. This study also indicated the improved stability of covalently immobilized coatings with improved wear and compression resistances attributed to strong chemical bonding and possessed the advantage of using nanoparticles as roller bearings.

4. Inorganic Materials for Surface Engineering Antioxidative Properties

4.1. Ceria Based Coatings

Cerium is a rare earth metallic element in lanthanide series and can exist in either free metal or metallic oxide form. Cerium possesses dual oxidation states: trivalent cerium sesquioxide (cerous Ce^{3+}) and tetravalent cerium dioxide (ceric Ce^{4+}) forms. Cerium oxide nanoparticles have received widespread attention for biocompatibility improvement, ophthalmic applications [130], cardiovascular pathology, treating neurodegenerative disorders and spinal cord injury owing to its ROS-scavenging ability [131,132]. The role of cerium oxide nanoparticles to effectuate ROS-scavenging activity and antioxidant mimicking role has been extensively reviewed by Nelson et al. [133]. Cerium oxide nanoparticles exhibit rapid and expedient switches in oxidation state between Ce^{3+} and Ce^{4+} during redox reactions. Owing to its lower reduction potential, cerium oxide exhibits redox-cycling property.

Cerium oxide is one of the most interesting oxides due to the presence of oxygen vacancy defects (which can be quickly generated and eliminated), and it can act as an oxygen buffer. The presence of oxygen vacancy sites on nanoceria lattice is responsible for the unusual catalytic activity of this class of material which is dependent on the efficient supply of lattice oxygen at reaction sites governed by the formation of oxygen vacancy sites [134]. Catalytic reaction of cerium oxide nanoparticles with super oxide anion (O^{2-}) and hydrogen peroxide (H_2O_2) mimics biological action of SOD-mimetic and catalase thereby protecting cells against ROS induced damage [135]. Multi-enzymatic antioxidant activity is based on the ability of cerium oxide to rapidly switch between the multiple valence states. SOD mimic activity is elicited by a shift from Ce^{3+} to Ce^{4+} (scavenging of O^{2-}), and catalase mimic activity is induced by a shift from Ce^{4+} to Ce^{3+} (deactivating hydrogen peroxide) [135–137]. SOD and catalase mimic activity of cerium oxide nanoparticles is particularly relevant under physiological pH condition (pH-7.5), rendering ROS-scavenging properties and inhibiting inflammatory mediator production.

Plasma-sprayed cerium oxide coating with a hierarchical topography was developed for antioxidant surfaces to preserve the intracellular antioxidant defense system [138]. Ceria oxide coating was found to be successful in decreasing SOD activity, reducing ROS generation and suppressing malondialdehyde development in hydrogen peroxide-treated osteoblasts. Li et al. reported magnetron sputtering (2, 3 and 5 min, $\approx 10^{-4}$ Pa) and vacuum annealing (450 °C) to deposit tiny homogenously distributed cerium oxide nanoparticle coatings with varying surface Ce^{4+}/Ce^{3+} ratios by tuning of deposition time [131]. Quite interestingly, the Ce^{4+}/Ce^{3+} ratio in this work reported the opposite trend for SOD and catalase mimetic activity. This work also highlighted the effective antioxidative mechanism of cerium oxide only when SOD and catalase mimetic activities are coordinated (H_2O_2 decomposition rate $\geq$ generation rate). The observed Ce^{4+}/Ce^{3+} ratio resulted in improved cytocompatibility, new bone formation, bone integration and upregulation of osteogenic genes and protein expressions (Figure 4a). Apart from the surface chemistry, the shape of ceria-based nanoparticles has also been reported to influence its ROS scav-

enging activity. Nanowire-shaped ceria is reported to occupy the extracellular space as its cellular internalization rate is slow [139]. Hence, nanowire-shaped ceria present on the cell surface can level down the hydrogen peroxide molecules and induce ROS consumption as schematically shown in Figure 4b. Spin coating represents a quick and facile surface modification technique to obtain coatings of thickness ranging from a few nanometers to few micrometers. Spin coating technique was used to deposit hydrothermally synthesized nano-CeO_2 with varying morphologies (nanorod, nano-cube and nano-octahedra) which yielded uniform coatings in Ti surfaces [140]. Total antioxidant capacity was in the order of nano-octahedron > nano-cube > nanorod. The anti-inflammation ability was correlated to the relative Ce^{3+} or Ce^{4+} content (XPS results displayed in Figure 4c) which, in turn, was influenced by the particle size and exposed crystalline lattice planes. With decreased particles size, Ce^{3+} content increased and rendered nano-octahedron improved SOD mimetic activity.

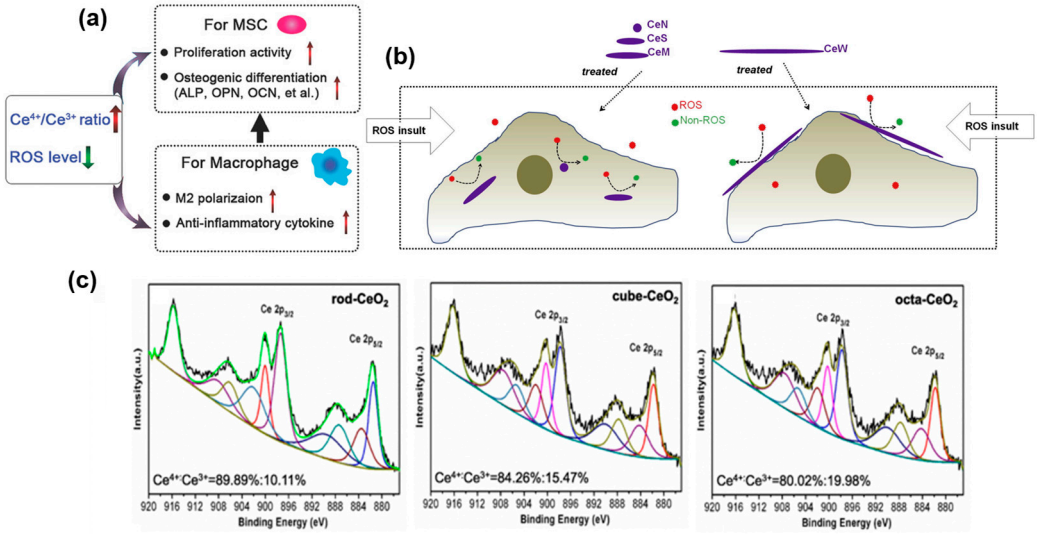

Figure 4. Influence of ceria surface chemistry and shape on the ROS scavenging activity. (**a**) Influence of Ce^{4+}/Ce^{3+} ratio on MSC and macrophage. Reprinted from [131] with permission from John Wiley & Sons. (**b**) X-ray-photoelectron spectroscopy analysis of nanorod, nano-cube and nano-octahedron-shaped ceria with varying Ce^{4+}/Ce^{3+} ratio. Reprinted from [139] with permission from Elsevier. (**c**) Schematic depicting the scavenging of extracellular matrix ROS by nanowire-shaped ceria present at the cell surface. Reprinted from [140] with permission from Elsevier.

High energy Ce plasma was used to develop cerium-modified Ti surface by using plasma immersion ion implantation technology [141]. A shift in the appearance of surface from nano-grains to nano-pits was noted, with treatment time increased from 30 to 60 and 90 min. Cerium implantation on Ti surface resulted in reducing the hydroxyl radical generation on Ti surface with increase in plasma immersion time. Reduction in fluorescence intensities and enhanced protection of E.coli model from oxidative stress are attributed to the improved corrosion resistance of the modified surface and the capability of the CeO_x on Ti surface to consume hydroxyl radical and hydrogen peroxide. In a similar work, atmospheric plasma was used to deposit cerium oxide-incorporated calcium silicate coating on Ti-6Al-4V substrates [142]. The developed surfaces demonstrated good biochemical stability, cellular viability and antibacterial activity against *E. faecalis*. Recently metal organic framework (MOF) coating was developed in situ on Ti surface to develop bio-responsive Ce/Sr incorporated bio-MOF coating based on hydrothermal technique [143]. Hydrothermally treated Ce-MOF and Ce/Sr-MOF revealed a Ce^{4+}/Ce^{3+} ratio of 1.186 and 2.76, respectively. Both of these Ce-containing surfaces revealed excellent H_2O_2 decomposition, superoxide anion disintegrating capacity, 80% of radical clearance during DPPH assay and persistence of antioxidant activity with TMB assay.

4.2. Silica

Various silicon based coatings have been explored for biocompatibility applications such as amorphous silicon oxygen thin films (a-SiOx) [144,145], calcium silicate [146], sol-gel-based silica bioglasses [147], silicon nitride [148], etc. Silicon is an important element which possesses an influential role in the activity of SOD to improve the ROS scavenging ability. Ilias et al. studied the plasma-enhanced chemical vapor deposition of amorphous silicon oxynitride in view of attaining rapid bone regeneration and fracture healing [149]. This study is the first of its kind to reveal the dependence of Si^{4+} on SOD1 to improve osteogenesis. For an effective bone healing, a sustained released of Si^{4+} should be ensured from the implant surface. Nitrogen incorporation into amorphous silica effectuated a continual Si^{4+} release which can be fine-tuned based on the surface chemistry (O/N ratio), and thickness of deposited film dictates the total release period. Plasma-enhanced chemical vapor deposition was similarly utilized by the same research group to develop coatings in the form of silicon oxynitrophosphide [150]. Up-regulation of SOD1 and cat-1 was observed in cells exposed to silicon oxynitrophosphide with varying oxygen and nitrogen contents. In other work, a radio frequency plasma-enhanced chemical vapor deposition (RF-PECVD) method which makes use of silane as Si source was used to deposit hydrogenated amorphous silicon coatings on Ti-6Al-4V substrate [151]. Hydrogen incorporation into the coating resulted in lower surface oxidation and amorphous silicon coating influenced fibroblasts with no significant effect on keratinocytes. A table enlisting the summary of advantages and limitations of different organic and inorganic coatings/materials described is provided in Table 2.

Table 2. Summary of various coatings used for antioxidant properties.

Type of Coating/Surface	Antioxidant Mechanism	Advantages	Limitations	Ref.
Tannic acid	Ability to chelate metal ions such as Fe(II), thereby interfering with one of the reaction steps in the Fenton reaction and thereby slowing oxidation	Antibacterial, antioxidant, high hemostatic efficiency, anticancer property, regenerative potential	Weak lipid solubility, low bioavailability, and short half-life, release rate should be controlled to exclude potential cytotoxicity, unstable adhesion	[152–155]
Chitosan	Reasonable mechanisms include presence of intra-molecular hydrogen bonding, metal chelation, ability of NH_2 amino groups to react with hydroxyl groups	Biological activity, antimicrobial activity, hydrophilicity, and biodegradability	Delamination, unstable adhesion	[156–158]
Proanthocyanidin	By scavenging free radicals and by modifying signaling pathways, including those involving nuclear factor erythroid 2-related factor 2 (Nrf2), mitogen-activated protein kinase (MAPK), nuclear factor-kappaB (NF-κB), and phosphoinositide 3-kinase (PI3K)/Akt	Antioxidant, anticancer, antidiabetic, neuroprotective, and antimicrobial	High cost, low chemical stability and limited binding sites, difficulties in resolving the chemical labeling pattern of PAs with their proposed biosynthetic pathway, and defining the subcellular sites of biosynthesis	[121,124,159]

Table 2. *Cont.*

Type of Coating/Surface	Antioxidant Mechanism	Advantages	Limitations	Ref.
Ceria	Ability to rapidly switch between multiple valence states. SOD mimic activity is elicited by a shift from Ce^{3+} to Ce^{4+} (scavenging of O^{2-}) and catalase mimic activity is induced by a shift from Ce^{4+} to Ce^{3+} (deactivating hydrogen peroxide)	Antioxidant, anticancer and anti-inflammatory properties, biosensors	Toxicity associated with small-sized nano-ceria	[160,161]
Silica	Hydroxylation degree, By regulation of antioxidants enzyme activity	Accelerated bone fracture healing, biomineral synthesis	Lipid peroxidation induced toxicity	[149,162]

5. Conclusions and Future Perspectives

There are several titanium-surface modification techniques being used which can be classified as mechanical (polishing, blasting, peening), chemical (chemical treatment, sol-gel, anodic oxidation, chemical vapor deposition) and physical (thermal spraying, plasma spraying, physical vapor deposition, evaporation, ion plating, sputtering, glow discharge plasma, ion implantation and deposition) techniques [57,163]. In spite of the fact that several surface modification strategies are being researched with focus on antibacterial and cytocompatible surfaces, Ti surfaces with improved antioxidant properties require further research focus. The most common techniques explored on depositing functional molecules on the Ti surfaces are based on physical adsorption, based on weak hydrogen bonding and van der Waals forces. This is a limiting factor as it restricts the bond strength and coating life, which will potentially affect the efficacy of the implant. This can be tackled based on chemical immobilization via covalent bonding, in which case a more sustained release of functional molecules can be achieved as compared to physical adsorption techniques.

A critical limitation hampering the potentiality of Ti and its alloys is the inferior wear resistance to be used in articulating surfaces. In spite of the fact that various organic coatings on Ti are bioactive and can develop antioxidant activity, these coatings are mechanically instable, which is a particularly relevant aspect to be considered in terms of wear resistance. During surgical procedures, these implants often encounter mechanical forces of up to 15 N, which will critically affect the life of the coatings and sometimes can lead to coating spalling [129]. One way to tackle this will be the immobilization of such molecules on an already-modified surface layer [163]. Hence, a prospective idea is the development of bi-layer coating consisting of (a) an inner wear/corrosion resistant layer and (b) an outer bioactive layer with antioxidant activity. More research should be focused towards the extraction of exogenous antioxidants (mainly derived from food and medicinal plants, such as fruits, vegetables, cereals, mushrooms, beverages, flowers, spices and traditional medicinal herbs [164]) and its immobilization on Ti surface. Increasing the complexity of a surface modification process will render the process difficult and expensive for rapid commercialization.

One of the critical factors to be assessed while developing such surface is the effect of surface oxide layer on Ti surface. Ti and its alloys, when exposed to air, form a spontaneous native titanium dioxide (TiO_2) layer with thickness in the range of 2–20 nm. This possesses a profound influence on the binding of molecules on the Ti surface and coating adhesion. Antioxidant release kinetics should also be given prior focus, as burst release in physiological environment can induce harmful enzymatic imbalances. More computational studies focused towards the stimulatory effect of various prospective coating materials on inducing oxidative stress and ROS need emphasis. Apart from these aspects, various factors to stimulate physiological conditions to assess the antioxidant activity of the developed

surfaces shall be incorporated in studies, as synergetic influence of factors can alter the ROS scavenging activity.

Despite the beneficial aspects possessed by Ti and its alloy for load-bearing implant applications, there is a plenty of room for investigating the complex biological phenomena associated with ROS activity in the physiological environment. Most of the published works intended to improve the antioxidant properties of Ti surface are based on organic materials such as tannic acid, chitosan and proanthocyanidin and inorganic coatings based on ceria and silica. Future relevant research trends can be foreseen in improving the mechanical stability and controlled drug elution associated with organic coatings. It is also highly desirable that multifactorial aspects in a real physiological environment shall be considered while assessing the ROS scavenging activity of the developed surfaces. Overall, it is suggested to consider the ROS generation and antioxidant aspects with more research in this direction to develop an efficient implant surface of metallic biomaterials for improving the clinical efficiency. Most importantly, complex challenges associated with translation of lab research to clinical practice demands effective collaboration between material scientists, engineers, biologists and clinicians.

Author Contributions: Conceptualization, J.V. and B.K.-S.; writing—original draft preparation, J.V. and B.K.-S.; writing—review and editing, P.K., K.D., M.S.B. and B.S.; supervision, B.S. and B.K.-S.; funding acquisition, B.K.-S. All authors have read and agreed to the published version of the manuscript.

Funding: This research received no external funding.

Data Availability Statement: The data presented in this study are available on request from the corresponding author.

Acknowledgments: J.V. and B.S. would like to gratefully acknowledge the support and encouragement received from Amrita University, Amritapuri Campus.

Conflicts of Interest: The authors declare no conflict of interest.

References

1. Mohamad, N.-V.; Ima-Nirwana, S.; Chin, K.-Y. Are Oxidative Stress and Inflammation Mediators of Bone Loss due to Estrogen Deficiency? A Review of Current Evidence. *Endocr. Metab. Immune Disord.-Drug Targets* **2020**, *20*, 1478–1487. [CrossRef] [PubMed]
2. Consensus development conference: Diagnosis, prophylaxis, and treatment of osteoporosis. *Am. J. Med.* **1993**, *94*, 646–650. [CrossRef] [PubMed]
3. Harvey, N.; Dennison, E.; Cooper, C. Osteoporosis: Impact on health and economics. *Nat. Rev. Rheumatol.* **2010**, *6*, 99–105. [CrossRef] [PubMed]
4. Salari, N.; Ghasemi, H.; Mohammadi, L.; Behzadi, M.H.; Rabieenia, E.; Shohaimi, S.; Mohammadi, M. The global prevalence of osteoporosis in the world: A comprehensive systematic review and meta-analysis. *J. Orthop. Surg. Res.* **2021**, *16*, 609. [CrossRef]
5. Al Anouti, F.; Taha, Z.; Shamim, S.; Khalaf, K.; Al Kaabi, L.; Alsafar, H. An insight into the paradigms of osteoporosis: From genetics to biomechanics. *Bone Rep.* **2019**, *11*, 100216. [CrossRef]
6. Johnell, O.; Kanis, J.A. An estimate of the worldwide prevalence and disability associated with osteoporotic fractures. *Osteoporos. Int.* **2006**, *17*, 1726–1733. [CrossRef]
7. Ji, M.X.; Yu, Q. Primary osteoporosis in postmenopausal women. *Chronic Dis. Transl. Med.* **2015**, *1*, 9–13. [CrossRef]
8. Loi, F.; Córdova, L.A.; Pajarinen, J.; Lin, T.-H.; Yao, Z.; Goodman, S.B. Inflammation, fracture and bone repair. *Bone* **2016**, *86*, 119–130. [CrossRef]
9. Schell, H.; Duda, G.N.; Peters, A.; Tsitsilonis, S.; Johnson, K.A.; Schmidt-Bleek, K. The haematoma and its role in bone healing. *J. Exp. Orthop.* **2017**, *4*, 5. [CrossRef]
10. Walters, G.; Pountos, I.; Giannoudis, P.V. The cytokines and micro-environment of fracture haematoma: Current evidence. *J. Tissue Eng. Regen. Med.* **2018**, *12*, e1662–e1677. [CrossRef]
11. Raggatt, L.J.; Partridge, N.C. Cellular and Molecular Mechanisms of Bone Remodeling. *J. Biol. Chem.* **2010**, *285*, 25103–25108. [CrossRef]
12. Bellido, T. Osteocyte-Driven Bone Remodeling. *Calcif. Tissue Int.* **2014**, *94*, 25–34. [CrossRef] [PubMed]
13. Xiong, J.; O'Brien, C.A. Osteocyte RANKL: New insights into the control of bone remodeling. *J. Bone Miner. Res.* **2012**, *27*, 499–505. [CrossRef] [PubMed]
14. Marcucci, G.; Domazetovic, V.; Nediani, C.; Ruzzolini, J.; Favre, C.; Brandi, M.L. Oxidative Stress and Natural Antioxidants in Osteoporosis: Novel Preventive and Therapeutic Approaches. *Antioxidants* **2023**, *12*, 373. [CrossRef] [PubMed]

15. Bădilă, A.E.; Rădulescu, D.M.; Ilie, A.; Niculescu, A.-G.; Grumezescu, A.M.; Rădulescu, A.R. Bone Regeneration and Oxidative Stress: An Updated Overview. *Antioxidants* **2022**, *11*, 318. [CrossRef] [PubMed]
16. León-Reyes, G.; Argoty-Pantoja, A.D.; Becerra-Cervera, A.; López-Montoya, P.; Rivera-Paredez, B.; Velázquez-Cruz, R. Oxidative-Stress-Related Genes in Osteoporosis: A Systematic Review. *Antioxidants* **2023**, *12*, 915. [CrossRef]
17. Hallab, N.J.; Jacobs, J.J. 2.5.4—Orthopedic Applications. In *Biomaterials Science*, 4th ed.; Wagner, W.R., Sakiyama-Elbert, S.E., Zhang, G., Yaszemski, M.J., Eds.; Academic Press: Cambridge, MA, USA, 2020; pp. 1079–1118. [CrossRef]
18. Ratner, B.D.; Zhang, G. 1.1.2—A History of Biomaterials. In *Biomaterials Science*, 4th ed.; Wagner, W.R., Sakiyama-Elbert, S.E., Zhang, G., Yaszemski, M.J., Eds.; Academic Press: Cambridge, MA, USA, 2020; pp. 21–34. [CrossRef]
19. Wagner, W.R. 1.3.1—The Materials Side of the Biomaterials Relationship. In *Biomaterials Science*, 4th ed.; Wagner, W.R., Sakiyama-Elbert, S.E., Zhang, G., Yaszemski, M.J., Eds.; Academic Press: Cambridge, MA, USA, 2020; pp. 83–84. [CrossRef]
20. Bai, L.; Gong, C.; Chen, X.; Sun, Y.; Zhang, J.; Cai, L.; Zhu, S.; Xie, S.Q. Additive Manufacturing of Customized Metallic Orthopedic Implants: Materials, Structures, and Surface Modifications. *Metals* **2019**, *9*, 1004. [CrossRef]
21. Pilliar, R.M. Metallic Biomaterials. In *Biomedical Materials*; Narayan, R., Ed.; Springer International Publishing: Cham, Germany, 2021; pp. 1–47. [CrossRef]
22. Prasad, K.; Bazaka, O.; Chua, M.; Rochford, M.; Fedrick, L.; Spoor, J.; Symes, R.; Tieppo, M.; Collins, C.; Cao, A.; et al. Metallic Biomaterials: Current Challenges and Opportunities. *Materials* **2017**, *10*, 884. [CrossRef]
23. Chen, Q.; Thouas, G.A. Metallic implant biomaterials. *Mater. Sci. Eng. R Rep.* **2015**, *87*, 1–57. [CrossRef]
24. Villanueva, J.; Trino, L.; Thomas, J.; Bijukumar, D.; Royhman, D.; Stack, M.M.; Mathew, M.T. Corrosion, Tribology, and Tribocorrosion Research in Biomedical Implants: Progressive Trend in the Published Literature. *J. Bio-Tribo-Corros.* **2016**, *3*, 1. [CrossRef]
25. Eliaz, N. Corrosion of Metallic Biomaterials: A Review. *Materials* **2019**, *12*, 407. [CrossRef]
26. Steinbeck, M.J.; Jablonowski, L.J.; Parvizi, J.; Freeman, T.A. The Role of Oxidative Stress in Aseptic Loosening of Total Hip Arthroplasties. *J. Arthroplast.* **2014**, *29*, 843–849. [CrossRef]
27. Primožič, J.; Poljšak, B.; Jamnik, P.; Kovač, V.; Čanadi Jurešić, G.; Spalj, S. Risk Assessment of Oxidative Stress Induced by Metal Ions Released from Fixed Orthodontic Appliances during Treatment and Indications for Supportive Antioxidant Therapy: A Narrative Review. *Antioxidants* **2021**, *10*, 1359. [CrossRef]
28. Goodman, S.B.; Gallo, J. Periprosthetic Osteolysis: Mechanisms, Prevention and Treatment. *J. Clin.Med.* **2019**, *8*, 2091. [CrossRef]
29. Wang, Y.; Branicky, R.; Noë, A.; Hekimi, S. Superoxide dismutases: Dual roles in controlling ROS damage and regulating ROS signaling. *J. Cell Biol.* **2018**, *217*, 1915–1928. [CrossRef]
30. Atashi, F.; Modarressi, A.; Pepper, M.S. The role of reactive oxygen species in mesenchymal stem cell adipogenic and osteogenic differentiation: A review. *Stem Cells Dev.* **2015**, *24*, 1150–1163. [CrossRef]
31. Cerqueni, G.; Scalzone, A.; Licini, C.; Gentile, P.; Mattioli-Belmonte, M. Insights into oxidative stress in bone tissue and novel challenges for biomaterials. *Mater. Sci. Eng. C* **2021**, *130*, 112433. [CrossRef] [PubMed]
32. Domazetovic, V.; Marcucci, G.; Iantomasi, T.; Brandi, M.L.; Vincenzini, M.T. Oxidative stress in bone remodeling: Role of antioxidants. *Clin. Cases Miner. Bone Metab. Off. J. Ital. Soc. Osteoporos. Miner. Metab. Skelet. Dis.* **2017**, *14*, 209–216. [CrossRef] [PubMed]
33. Pizzino, G.; Irrera, N.; Cucinotta, M.; Pallio, G.; Mannino, F.; Arcoraci, V.; Squadrito, F.; Altavilla, D.; Bitto, A. Oxidative Stress: Harms and Benefits for Human Health. *Oxidative Med. Cell. Longev.* **2017**, *2017*, 8416763. [CrossRef]
34. Sies, H.; Belousov, V.V.; Chandel, N.S.; Davies, M.J.; Jones, D.P.; Mann, G.E.; Murphy, M.P.; Yamamoto, M.; Winterbourn, C. Defining roles of specific reactive oxygen species (ROS) in cell biology and physiology. *Nat. Rev. Mol. Cell Biol.* **2022**, *23*, 499–515. [CrossRef] [PubMed]
35. Thannickal, V.J.; Fanburg, B.L. Reactive oxygen species in cell signaling. *Am. J. Physiol.-Lung Cell. Mol. Physiol.* **2000**, *279*, L1005–L1028. [CrossRef] [PubMed]
36. Brieger, K.; Schiavone, S.; Miller, F.J., Jr.; Krause, K.-H. Reactive oxygen species: From health to disease. *Swiss Med. Wkly.* **2012**, *142*, w13659. [CrossRef] [PubMed]
37. Nosaka, Y.; Nosaka, A.Y. Generation and Detection of Reactive Oxygen Species in Photocatalysis. *Chem. Rev.* **2017**, *117*, 11302–11336. [CrossRef] [PubMed]
38. Parham, S.; Kharazi, A.Z.; Bakhsheshi-Rad, H.R.; Nur, H.; Ismail, A.F.; Sharif, S.; RamaKrishna, S.; Berto, F. Antioxidant, Antimicrobial and Antiviral Properties of Herbal Materials. *Antioxidants* **2020**, *9*, 1309. [CrossRef] [PubMed]
39. Collin, F. Chemical Basis of Reactive Oxygen Species Reactivity and Involvement in Neurodegenerative Diseases. *Int. J. Mol.Sci.* **2019**, *20*, 2407. [CrossRef]
40. Murphy, M.P.; Bayir, H.; Belousov, V.; Chang, C.J.; Davies, K.J.A.; Davies, M.J.; Dick, T.P.; Finkel, T.; Forman, H.J.; Janssen-Heininger, Y.; et al. Guidelines for measuring reactive oxygen species and oxidative damage in cells and in vivo. *Nat. Metab.* **2022**, *4*, 651–662. [CrossRef]
41. Andrés, C.M.; Pérez de la Lastra, J.M.; Andrés Juan, C.; Plou, F.J.; Pérez-Lebeña, E. Superoxide Anion Chemistry—Its Role at the Core of the Innate Immunity. *Int. J. Mol.Sci.* **2023**, *24*, 1841.
42. Pervaiz, S.; Clement, M.-V. Superoxide anion: Oncogenic reactive oxygen species? *Int. J. Biochem. Cell Biol.* **2007**, *39*, 1297–1304. [CrossRef]

43. Kessler, A.; Hedberg, J.; Blomberg, E.; Odnevall, I. Reactive Oxygen Species Formed by Metal and Metal Oxide Nanoparticles in Physiological Media&Mdash;A Review of Reactions of Importance to Nanotoxicity and Proposal for Categorization. *Nanomaterials* **2022**, *12*, 1922.
44. Bešlo, D.; Golubić, N.; Rastija, V.; Agić, D.; Karnaš, M.; Šubarić, D.; Lučić, B. Antioxidant Activity, Metabolism, and Bioavailability of Polyphenols in the Diet of Animals. *Antioxidants* **2023**, *12*, 1141. [CrossRef]
45. Valko, M.; Leibfritz, D.; Moncol, J.; Cronin, M.T.D.; Mazur, M.; Telser, J. Free radicals and antioxidants in normal physiological functions and human disease. *Int. J. Biochem. Cell Biol.* **2007**, *39*, 44–84. [CrossRef] [PubMed]
46. Kotha, R.R.; Tareq, F.S.; Yildiz, E.; Luthria, D.L. Oxidative Stress and Antioxidants&Mdash; A Critical Review on In Vitro Antioxidant Assays. *Antioxidants* **2022**, *11*, 2388.
47. Smeets, R.; Stadlinger, B.; Schwarz, F.; Beck-Broichsitter, B.; Jung, O.; Precht, C.; Kloss, F.; Gröbe, A.; Heiland, M.; Ebker, T. Impact of Dental Implant Surface Modifications on Osseointegration. *BioMed Res. Int.* **2016**, *2016*, 6285620. [CrossRef]
48. Zhu, G.; Wang, G.; Li, J.J. Advances in implant surface modifications to improve osseointegration. *Mater. Adv.* **2021**, *2*, 6901–6927. [CrossRef]
49. Ghosh, S.; Abanteriba, S. Status of surface modification techniques for artificial hip implants. *Sci. Technol. Adv. Mater.* **2016**, *17*, 715–735. [CrossRef] [PubMed]
50. Liu, Y.; Rath, B.; Tingart, M.; Eschweiler, J. Role of implants surface modification in osseointegration: A systematic review. *J. Biomed. Mater. Res. Part A* **2020**, *108*, 470–484. [CrossRef]
51. Chen, W.; Shen, X.; Hu, Y.; Xu, K.; Ran, Q.; Yu, Y.; Dai, L.; Yuan, Z.; Huang, L.; Shen, T.; et al. Surface functionalization of titanium implants with chitosan-catechol conjugate for suppression of ROS-induced cells damage and improvement of osteogenesis. *Biomaterials* **2017**, *114*, 82–96. [CrossRef]
52. Dumitriu, C.; Ungureanu, C.; Popescu, S.; Tofan, V.; Popescu, M.; Pirvu, C. Ti surface modification with a natural antioxidant and antimicrobial agent. *Surf. Coat. Technol.* **2015**, *276*, 175–185. [CrossRef]
53. Di, H.; Qiaoxia, L.; Yujie, Z.; Jingxuan, L.; Yan, W.; Yinchun, H.; Xiaojie, L.; Song, C.; Weiyi, C. Ag nanoparticles incorporated tannic acid/nanoapatite composite coating on Ti implant surfaces for enhancement of antibacterial and antioxidant properties. *Surf. Coat. Technol.* **2020**, *399*, 126169. [CrossRef]
54. Clanton, T.L. Hypoxia-induced reactive oxygen species formation in skeletal muscle. *J. Appl. Physiol.* **2007**, *102*, 2379–2388. [CrossRef]
55. Chapple, I.L.C. Reactive oxygen species and antioxidants in inflammatory diseases. *J. Clin. Periodontol.* **1997**, *24*, 287–296. [CrossRef]
56. Han, X.; Ma, J.; Tian, A.; Wang, Y.; Li, Y.; Dong, B.; Tong, X.; Ma, X. Surface modification techniques of titanium and titanium alloys for biomedical orthopaedics applications: A review. *Colloids Surf. B Biointerfaces* **2023**, *227*, 113339. [CrossRef]
57. Liu, X.; Chu, P.K.; Ding, C. Surface modification of titanium, titanium alloys, and related materials for biomedical applications. *Mater. Sci. Eng. R Rep.* **2004**, *47*, 49–121. [CrossRef]
58. Geetha, M.; Singh, A.K.; Asokamani, R.; Gogia, A.K. Ti based biomaterials, the ultimate choice for orthopaedic implants—A review. *Prog. Mater. Sci.* **2009**, *54*, 397–425. [CrossRef]
59. Kaur, M.; Singh, K. Review on titanium and titanium based alloys as biomaterials for orthopaedic applications. *Mater. Sci. Eng. C* **2019**, *102*, 844–862. [CrossRef] [PubMed]
60. Quinn, J.; McFadden, R.; Chan, C.-W.; Carson, L. Titanium for Orthopedic Applications: An Overview of Surface Modification to Improve Biocompatibility and Prevent Bacterial Biofilm Formation. *iScience* **2020**, *23*, 101745. [CrossRef] [PubMed]
61. Chen, L.-Y.; Cui, Y.-W.; Zhang, L.-C. Recent Development in Beta Titanium Alloys for Biomedical Applications. *Metals* **2020**, *10*, 1139. [CrossRef]
62. Kolli, R.P.; Devaraj, A. A Review of Metastable Beta Titanium Alloys. *Metals* **2018**, *8*, 506. [CrossRef]
63. Abdel-Hady Gepreel, M.; Niinomi, M. Biocompatibility of Ti-alloys for long-term implantation. *J. Mech. Behav. Biomed. Mater.* **2013**, *20*, 407–415. [CrossRef]
64. Biesiekierski, A.; Wang, J.; Abdel-Hady Gepreel, M.; Wen, C. A new look at biomedical Ti-based shape memory alloys. *Acta Biomater.* **2012**, *8*, 1661–1669. [CrossRef]
65. Vishnu, J.; Manivasagam, G. Surface Modification and Biological Approaches for Tackling Titanium Wear-Induced Aseptic Loosening. *J. Bio-Tribo-Corros.* **2021**, *7*, 32. [CrossRef]
66. Peng, K.T.; Hsu, W.H.; Shih, H.N.; Hsieh, C.W.; Huang, T.W.; Hsu, R.W.W.; Chang, P.J. The role of reactive oxygen species scavenging enzymes in the development of septic loosening after total hip replacement. *J. Bone Jt. Surg. Br. Vol.* **2011**, *93-B*, 1201–1209. [CrossRef] [PubMed]
67. Prestat, M.; Thierry, D. Corrosion of titanium under simulated inflammation conditions: Clinical context and in vitro investigations. *Acta Biomater.* **2021**, *136*, 72–87. [CrossRef] [PubMed]
68. Nguyen, G.T.; Green, E.R.; Mecsas, J. Neutrophils to the ROScue: Mechanisms of NADPH Oxidase Activation and Bacterial Resistance. *Front. Cell. Infect. Microbiol.* **2017**, *7*, 373. [CrossRef] [PubMed]
69. Groemping, Y.; Rittinger, K. Activation and assembly of the NADPH oxidase: A structural perspective. *Biochem. J.* **2005**, *386*, 401–416. [CrossRef]
70. Fujii, J.; Homma, T.; Osaki, T. Superoxide Radicals in the Execution of Cell Death. *Antioxidants* **2022**, *11*, 501. [CrossRef]

71. Getzoff, E.D.; Tainer, J.A.; Weiner, P.K.; Kollman, P.A.; Richardson, J.S.; Richardson, D.C. Electrostatic recognition between superoxide and copper, zinc superoxide dismutase. *Nature* **1983**, *306*, 287–290. [CrossRef]
72. Paumann-Page, M.; Furtmüller, P.G.; Hofbauer, S.; Paton, L.N.; Obinger, C.; Kettle, A.J. Inactivation of human myeloperoxidase by hydrogen peroxide. *Arch. Biochem. Biophys.* **2013**, *539*, 51–62. [CrossRef]
73. Khan, A.A.; Alsahli, M.A.; Rahmani, A.H. Myeloperoxidase as an Active Disease Biomarker: Recent Biochemical and Pathological Perspectives. *Med. Sci.* **2018**, *6*, 33. [CrossRef]
74. Prousek, J. Fenton chemistry in biology and medicine. *Pure Appl. Chem.* **2007**, *79*, 2325–2338. [CrossRef]
75. Winterbourn, C.C. Toxicity of iron and hydrogen peroxide: The Fenton reaction. *Toxicol. Lett.* **1995**, *82–83*, 969–974. [CrossRef]
76. Kehrer, J.P. The Haber—Weiss reaction and mechanisms of toxicity. *Toxicology* **2000**, *149*, 43–50. [CrossRef] [PubMed]
77. Peñarrieta-Juanito, G.; Sordi, M.B.; Henriques, B.; Dotto, M.E.R.; Teughels, W.; Silva, F.S.; Magini, R.S.; Souza, J.C.M. Surface damage of dental implant systems and ions release after exposure to fluoride and hydrogen peroxide. *J. Periodontal Res.* **2019**, *54*, 46–52. [CrossRef] [PubMed]
78. Kalbacova, M.; Roessler, S.; Hempel, U.; Tsaryk, R.; Peters, K.; Scharnweber, D.; Kirkpatrick, J.C.; Dieter, P. The effect of electrochemically simulated titanium cathodic corrosion products on ROS production and metabolic activity of osteoblasts and monocytes/macrophages. *Biomaterials* **2007**, *28*, 3263–3272. [CrossRef] [PubMed]
79. Brown, P.S.; Bhushan, B. Mechanically durable, superomniphobic coatings prepared by layer-by-layer technique for self-cleaning and anti-smudge. *J. Colloid Interface Sci.* **2015**, *456*, 210–218. [CrossRef]
80. Ariga, K.; Hill, J.P.; Ji, Q. Layer-by-layer assembly as a versatile bottom-up nanofabrication technique for exploratory research and realistic application. *Phys. Chem. Chem. Phys.* **2007**, *9*, 2319–2340. [CrossRef]
81. Neacşu, I.A.; Nicoară, A.I.; Vasile, O.R.; Vasile, B.Ş. Chapter 9—Inorganic micro- and nanostructured implants for tissue engineering. In *Nanobiomaterials in Hard Tissue Engineering*; Grumezescu, A.M., Ed.; William Andrew Publishing: Norwich, NY, USA, 2016; pp. 271–295. [CrossRef]
82. Alfieri, M.L.; Riccucci, G.; Ferraris, S.; Cochis, A.; Scalia, A.C.; Rimondini, L.; Panzella, L.; Spriano, S.; Napolitano, A. Deposition of Antioxidant and Cytocompatible Caffeic Acid-Based Thin Films onto Ti6Al4V Alloys through Hexamethylenediamine-Mediated Crosslinking. *ACS Appl. Mater. Interfaces* **2023**, *15*, 29618–29635. [CrossRef]
83. Rased, N.H.; Vengadaesvaran, B.; Raihan, S.R.S.; Rahim, N.A. Chapter 6—Introduction to solar energy and its conversion into electrical energy by using dye-sensitized solar cells. In *Energy Materials*; Dhoble, S.J., Kalyani, N.T., Vengadaesvaran, B., Kariem Arof, A., Eds.; Elsevier: Amsterdam, The Netherlands, 2021; pp. 139–178. [CrossRef]
84. Sahu, N.; Parija, B.; Panigrahi, S. Fundamental understanding and modeling of spin coating process: A review. *Indian J. Phys.* **2009**, *83*, 493–502. [CrossRef]
85. Hashizume, M.; Kunitake, T. Preparation of Self-Supporting Ultrathin Films of Titania by Spin Coating. *Langmuir* **2003**, *19*, 10172–10178. [CrossRef]
86. Chen, Y.; Xu, C.; Wang, C.-H.; Bilek, M.M.M.; Cheng, X. An effective method to optimise plasma immersion ion implantation: Sensitivity analysis and design based on low-density polyethylene. *Plasma Process. Polym.* **2022**, *19*, 2100199. [CrossRef]
87. Sotoudeh Bagha, P.; Paternoster, C.; Khakbiz, M.; Sheibani, S.; Gholami, N.; Mantovani, D. Surface Modification of an Absorbable Bimodal Fe-Mn-Ag Alloy by Nitrogen Plasma Immersion Ion Implantation. *Materials* **2023**, *16*, 1048. [CrossRef]
88. Walschus, U.; Hoene, A.; Patrzyk, M.; Lucke, S.; Finke, B.; Polak, M.; Lukowski, G.; Bader, R.; Zietz, C.; Podbielski, A.; et al. A Cell-Adhesive Plasma Polymerized Allylamine Coating Reduces the In Vivo Inflammatory Response Induced by Ti6Al4V Modified with Plasma Immersion Ion Implantation of Copper. *J. Funct. Biomater.* **2017**, *8*, 30. [CrossRef]
89. Terasawa, T.-O.; Saiki, K. Growth of graphene on Cu by plasma enhanced chemical vapor deposition. *Carbon* **2012**, *50*, 869–874. [CrossRef]
90. Gan, Z.; Wang, C.; Chen, Z. Material Structure and Mechanical Properties of Silicon Nitride and Silicon Oxynitride Thin Films Deposited by Plasma Enhanced Chemical Vapor Deposition. *Surfaces* **2018**, *1*, 59–72. [CrossRef]
91. Vasudev, M.C.; Anderson, K.D.; Bunning, T.J.; Tsukruk, V.V.; Naik, R.R. Exploration of Plasma-Enhanced Chemical Vapor Deposition as a Method for Thin-Film Fabrication with Biological Applications. *ACS Appl. Mater. Interfaces* **2013**, *5*, 3983–3994. [CrossRef]
92. Kaczmarek, B. Tannic Acid with Antiviral and Antibacterial Activity as A Promising Component of Biomaterials—A Minireview. *Materials* **2020**, *13*, 3224. [CrossRef]
93. Lopes, G.K.B.; Schulman, H.M.; Hermes-Lima, M. Polyphenol tannic acid inhibits hydroxyl radical formation from Fenton reaction by complexing ferrous ions1This study is dedicated to the memory of Botany Professor Luiz F.G. Labouriau (1921–1996).1. *Biochim. Et Biophys. Acta BBA-Gen. Subj.* **1999**, *1472*, 142–152. [CrossRef]
94. Sathishkumar, G.; Gopinath, K.; Zhang, K.; Kang, E.-T.; Xu, L.; Yu, Y. Recent progress in tannic acid-driven antibacterial/antifouling surface coating strategies. *J. Mater. Chem. B* **2022**, *10*, 2296–2315. [CrossRef]
95. Wang, Z.; Gao, J.; Zhu, L.; Meng, J.; He, F. Tannic acid-based functional coating: Surface engineering of membranes for oil-in-water emulsion separation. *Chem. Commun.* **2022**, *58*, 12629–12641. [CrossRef]
96. Zhu, Y.; Zhou, D.; Zan, X.; Ye, Q.; Sheng, S. Engineering the surfaces of orthopedic implants with osteogenesis and antioxidants to enhance bone formation in vitro and in vivo. *Colloids Surf. B Biointerfaces* **2022**, *212*, 112319. [CrossRef]

97. Iqbal, M.H.; Schroder, A.; Kerdjoudj, H.; Njel, C.; Senger, B.; Ball, V.; Meyer, F.; Boulmedais, F. Effect of the Buffer on the Buildup and Stability of Tannic Acid/Collagen Multilayer Films Applied as Antibacterial Coatings. *ACS Appl. Mater. Interfaces* **2020**, *12*, 22601–22612. [CrossRef]
98. He, X.; Gopinath, K.; Sathishkumar, G.; Guo, L.; Zhang, K.; Lu, Z.; Li, C.; Kang, E.-T.; Xu, L. UV-Assisted Deposition of Antibacterial Ag–Tannic Acid Nanocomposite Coating. *ACS Appl. Mater. Interfaces* **2021**, *13*, 20708–20717. [CrossRef]
99. Saiz-Poseu, J.; Mancebo-Aracil, J.; Nador, F.; Busqué, F.; Ruiz-Molina, D. The Chemistry behind Catechol-Based Adhesion. *Angew. Chem. Int. Ed.* **2019**, *58*, 696–714. [CrossRef] [PubMed]
100. Geißler, S.; Barrantes, A.; Tengvall, P.; Messersmith, P.B.; Tiainen, H. Deposition Kinetics of Bioinspired Phenolic Coatings on Titanium Surfaces. *Langmuir* **2016**, *32*, 8050–8060. [CrossRef] [PubMed]
101. Qiaoxia, L.; Yujie, Z.; Meng, Y.; Yizhu, C.; Yan, W.; Yinchun, H.; Xiaojie, L.; Weiyi, C.; Di, H. Hydroxyapatite/tannic acid composite coating formation based on Ti modified by TiO_2 nanotubes. *Colloids Surf. B Biointerfaces* **2020**, *196*, 111304. [CrossRef] [PubMed]
102. Yang, X.; Huang, P.; Wang, H.; Cai, S.; Liao, Y.; Mo, Z.; Xu, X.; Ding, C.; Zhao, C.; Li, J. Antibacterial and anti-biofouling coating on hydroxyapatite surface based on peptide-modified tannic acid. *Colloids Surf. B Biointerfaces* **2017**, *160*, 136–143. [CrossRef] [PubMed]
103. Camós Noguer, A.; Olsen, S.M.; Hvilsted, S.; Kiil, S. Long-term stability of PEG-based antifouling surfaces in seawater. *J. Coat. Technol. Res.* **2016**, *13*, 567–575. [CrossRef]
104. Guo, L.L.; Cheng, Y.F.; Ren, X.; Gopinath, K.; Lu, Z.S.; Li, C.M.; Xu, L.Q. Simultaneous deposition of tannic acid and poly(ethylene glycol) to construct the antifouling polymeric coating on Titanium surface. *Colloids Surf. B Biointerfaces* **2021**, *200*, 111592. [CrossRef]
105. Zhuk, I.; Jariwala, F.; Attygalle, A.B.; Wu, Y.; Libera, M.R.; Sukhishvili, S.A. Self-Defensive Layer-by-Layer Films with Bacteria-Triggered Antibiotic Release. *ACS Nano* **2014**, *8*, 7733–7745. [CrossRef]
106. Hizal, F.; Zhuk, I.; Sukhishvili, S.; Busscher, H.J.; van der Mei, H.C.; Choi, C.-H. Impact of 3D Hierarchical Nanostructures on the Antibacterial Efficacy of a Bacteria-Triggered Self-Defensive Antibiotic Coating. *ACS Appl. Mater. Interfaces* **2015**, *7*, 20304–20313. [CrossRef] [PubMed]
107. Steffi, C.; Shi, Z.; Kong, C.H.; Chong, S.W.; Wang, D.; Wang, W. Use of Polyphenol Tannic Acid to Functionalize Titanium with Strontium for Enhancement of Osteoblast Differentiation and Reduction of Osteoclast Activity. *Polymers* **2019**, *11*, 1256. [CrossRef] [PubMed]
108. Lin, W.; Qi, X.; Guo, W.; Liang, D.; Chen, H.; Lin, B.; Deng, X. A barrier against reactive oxygen species: Chitosan/acellular dermal matrix scaffold enhances stem cell retention and improves cutaneous wound healing. *Stem Cell Res. Ther.* **2020**, *11*, 383. [CrossRef]
109. Khokon, M.A.R.; Uraji, M.; Munemasa, S.; Okuma, E.; Nakamura, Y.; Mori, I.C.; Murata, Y. Chitosan-Induced Stomatal Closure Accompanied by Peroxidase-Mediated Reactive Oxygen Species Production in Arabidopsis. *Biosci. Biotechnol. Biochem.* **2010**, *74*, 2313–2315. [CrossRef]
110. Banerjee, M.; Mallick, S.; Paul, A.; Chattopadhyay, A.; Ghosh, S.S. Heightened Reactive Oxygen Species Generation in the Antimicrobial Activity of a Three Component Iodinated Chitosan−Silver Nanoparticle Composite. *Langmuir* **2010**, *26*, 5901–5908. [CrossRef] [PubMed]
111. Parham, S.; Kharazi, A.Z.; Bakhsheshi-Rad, H.R.; Kharaziha, M.; Ismail, A.F.; Sharif, S.; Razzaghi, M.; RamaKrishna, S.; Berto, F. Antimicrobial Synthetic and Natural Polymeric Nanofibers as Wound Dressing: A Review. *Adv. Eng. Mater.* **2022**, *24*, 2101460. [CrossRef]
112. Kumari, S.; Tiyyagura, H.R.; Pottathara, Y.B.; Sadasivuni, K.K.; Ponnamma, D.; Douglas, T.E.L.; Skirtach, A.G.; Mohan, M.K. Surface functionalization of chitosan as a coating material for orthopaedic applications: A comprehensive review. *Carbohydr. Polym.* **2021**, *255*, 117487. [CrossRef]
113. Abinaya, B.; Prasith, T.P.; Ashwin, B.; Viji Chandran, S.; Selvamurugan, N. Chitosan in Surface Modification for Bone Tissue Engineering Applications. *Biotechnol. J.* **2019**, *14*, 1900171. [CrossRef]
114. Lieder, R.; Darai, M.; Thor, M.B.; Ng, C.H.; Einarsson, J.M.; Gudmundsson, S.; Helgason, B.; Gaware, V.S.; Másson, M.; Gíslason, J.; et al. In vitro bioactivity of different degree of deacetylation chitosan, a potential coating material for titanium implants. *J. Biomed. Mater. Res. Part A* **2012**, *100A*, 3392–3399. [CrossRef]
115. Tomida, H.; Fujii, T.; Furutani, N.; Michihara, A.; Yasufuku, T.; Akasaki, K.; Maruyama, T.; Otagiri, M.; Gebicki, J.M.; Anraku, M. Antioxidant properties of some different molecular weight chitosans. *Carbohydr. Res.* **2009**, *344*, 1690–1696. [CrossRef]
116. Xue, C.; Yu, G.; Hirata, T.; Terao, J.; Lin, H. Antioxidative Activities of Several Marine Polysaccharides Evaluated in a Phosphatidylcholine-liposomal Suspension and Organic Solvents. *Biosci. Biotechnol. Biochem.* **1998**, *62*, 206–209. [CrossRef]
117. Xie, W.; Xu, P.; Liu, Q. Antioxidant activity of water-soluble chitosan derivatives. *Bioorganic Med. Chem. Lett.* **2001**, *11*, 1699–1701. [CrossRef] [PubMed]
118. Li, X.; Ma, X.-Y.; Feng, Y.-F.; Ma, Z.-S.; Wang, J.; Ma, T.-C.; Qi, W.; Lei, W.; Wang, L. Osseointegration of chitosan coated porous titanium alloy implant by reactive oxygen species-mediated activation of the PI3K/AKT pathway under diabetic conditions. *Biomaterials* **2015**, *36*, 44–54. [CrossRef] [PubMed]
119. Jabłoński, P.; Kyzioł, A.; Pawcenis, D.; Pucelik, B.; Hebda, M.; Migdalska, M.; Krawiec, H.; Arruebo, M.; Kyzioł, K. Electrostatic self-assembly approach in the deposition of bio-functional chitosan-based layers enriched with caffeic acid on Ti-6Al-7Nb alloys by alternate immersion. *Biomater. Adv.* **2022**, *136*, 212791. [CrossRef] [PubMed]

120. Stevanović, M.; Djošić, M.; Janković, A.; Kojić, V.; Stojanović, J.; Grujić, S.; Bujagić, I.M.; Rhee, K.Y.; Mišković-Stanković, V. The chitosan-based bioactive composite coating on titanium. *J. Mater. Res. Technol.* **2021**, *15*, 4461–4474. [CrossRef]
121. Rauf, A.; Imran, M.; Abu-Izneid, T.; Iahtisham Ul, H.; Patel, S.; Pan, X.; Naz, S.; Sanches Silva, A.; Saeed, F.; Rasul Suleria, H.A. Proanthocyanidins: A comprehensive review. *Biomed. Pharmacother.* **2019**, *116*, 108999. [CrossRef]
122. de la Iglesia, R.; Milagro, F.I.; Campión, J.; Boqué, N.; Martínez, J.A. Healthy properties of proanthocyanidins. *BioFactors* **2010**, *36*, 159–168. [CrossRef] [PubMed]
123. Park, Y.S.; Jeon, M.H.; Hwang, H.J.; Park, M.R.; Lee, S.H.; Kim, S.G.; Kim, M. Antioxidant activity and analysis of proanthocyanidins from pine (*Pinus densiflora*) needles. *Nutr. Res. Pract.* **2011**, *5*, 281–287. [CrossRef]
124. Yang, L.; Xian, D.; Xiong, X.; Lai, R.; Song, J.; Zhong, J. Proanthocyanidins against Oxidative Stress: From Molecular Mechanisms to Clinical Applications. *BioMed Res. Int.* **2018**, *2018*, 8584136. [CrossRef]
125. Andersen-Civil, A.I.S.; Leppä, M.M.; Thamsborg, S.M.; Salminen, J.-P.; Williams, A.R. Structure-function analysis of purified proanthocyanidins reveals a role for polymer size in suppressing inflammatory responses. *Commun. Biol.* **2021**, *4*, 896. [CrossRef]
126. Tenkumo, T.; Aobulikasimu, A.; Asou, Y.; Shirato, M.; Shishido, S.; Kanno, T.; Niwano, Y.; Sasaki, K.; Nakamura, K. Proanthocyanidin-rich grape seed extract improves bone loss, bone healing, and implant osseointegration in ovariectomized animals. *Sci. Rep.* **2020**, *10*, 8812. [CrossRef]
127. Tang, J.; Chen, L.; Yan, D.; Shen, Z.; Wang, B.; Weng, S.; Wu, Z.; Xie, Z.; Shao, J.; Yang, L.; et al. Surface Functionalization with Proanthocyanidins Provides an Anti-Oxidant Defense Mechanism That Improves the Long-Term Stability and Osteogenesis of Titanium Implants. *Int. J. Nanomed.* **2020**, *15*, 1643–1659. [CrossRef]
128. Bai, Z.; Hu, K.; Shou, Z.; Yu, J.; Meng, H.; Zhou, H.; Chen, L.; Yu, T.; Lu, R.; Li, N.; et al. Layer-by-layer assembly of procyanidin and collagen promotes mesenchymal stem cell proliferation and osteogenic differentiation in vitro and in vivo. *Regen. Biomater.* **2023**, *10*, rbac107. [CrossRef] [PubMed]
129. Zhou, Q.; Wu, T.; Bai, Z.; Hong, G.; Bian, J.; Xie, H.; Chen, C. A silane-based coupling strategy for enhancing the mechanical properties of proanthocyanidin nanocoatings on Ti dental implants. *Appl. Surf. Sci.* **2022**, *602*, 154400. [CrossRef]
130. Maccarone, R.; Tisi, A.; Passacantando, M.; Ciancaglini, M. Ophthalmic Applications of Cerium Oxide Nanoparticles. *J. Ocul. Pharmacol. Ther.* **2019**, *36*, 376–383. [CrossRef]
131. Li, J.; Wen, J.; Li, B.; Li, W.; Qiao, W.; Shen, J.; Jin, W.; Jiang, X.; Yeung, K.W.K.; Chu, P.K. Valence State Manipulation of Cerium Oxide Nanoparticles on a Titanium Surface for Modulating Cell Fate and Bone Formation. *Adv. Sci.* **2018**, *5*, 1700678. [CrossRef] [PubMed]
132. Dhall, A.; Self, W. Cerium Oxide Nanoparticles: A Brief Review of Their Synthesis Methods and Biomedical Applications. *Antioxidants* **2018**, *7*, 97. [CrossRef]
133. Nelson, B.C.; Johnson, M.E.; Walker, M.L.; Riley, K.R.; Sims, C.M. Antioxidant Cerium Oxide Nanoparticles in Biology and Medicine. *Antioxidants* **2016**, *5*, 15. [CrossRef]
134. Esch, F.; Fabris, S.; Zhou, L.; Montini, T.; Africh, C.; Fornasiero, P.; Comelli, G.; Rosei, R. Electron Localization Determines Defect Formation on Ceria Substrates. *Science* **2005**, *309*, 752–755. [CrossRef]
135. Heckert, E.G.; Karakoti, A.S.; Seal, S.; Self, W.T. The role of cerium redox state in the SOD mimetic activity of nanoceria. *Biomaterials* **2008**, *29*, 2705–2709. [CrossRef]
136. Korsvik, C.; Patil, S.; Seal, S.; Self, W.T. Superoxide dismutase mimetic properties exhibited by vacancy engineered ceria nanoparticles. *Chem. Commun.* **2007**, 1056–1058. [CrossRef]
137. Pirmohamed, T.; Dowding, J.M.; Singh, S.; Wasserman, B.; Heckert, E.; Karakoti, A.S.; King, J.E.S.; Seal, S.; Self, W.T. Nanoceria exhibit redox state-dependent catalase mimetic activity. *Chem. Commun.* **2010**, *46*, 2736–2738. [CrossRef] [PubMed]
138. Li, K.; Xie, Y.; You, M.; Huang, L.; Zheng, X. Plasma sprayed cerium oxide coating inhibits H2O2-induced oxidative stress and supports cell viability. *J. Mater. Sci. Mater. Med.* **2016**, *27*, 100. [CrossRef] [PubMed]
139. Mahapatra, C.; Singh, R.K.; Lee, J.-H.; Jung, J.; Hyun, J.K.; Kim, H.-W. Nano-shape varied cerium oxide nanomaterials rescue human dental stem cells from oxidative insult through intracellular or extracellular actions. *Acta Biomater.* **2017**, *50*, 142–153. [CrossRef] [PubMed]
140. Li, X.; Qi, M.; Sun, X.; Weir, M.D.; Tay, F.R.; Oates, T.W.; Dong, B.; Zhou, Y.; Wang, L.; Xu, H.H.K. Surface treatments on titanium implants via nanostructured ceria for antibacterial and anti-inflammatory capabilities. *Acta Biomater.* **2019**, *94*, 627–643. [CrossRef] [PubMed]
141. Zhang, H.; Qiu, J.; Liu, X. Enhanced antioxidant capability and osteogenic property of medical titanium by cerium plasma immersion ion implantation. *Surf. Interfaces* **2021**, *26*, 101402. [CrossRef]
142. Qi, S.; Wu, J.; Xu, Y.; Zhang, Y.; Wang, R.; Li, K.; Xu, Y. Chemical Stability and Antimicrobial Activity of Plasma-Sprayed Cerium Oxide–Incorporated Calcium Silicate Coating in Dental Implants. *Implant Dent.* **2019**, *28*, 564–570. [CrossRef] [PubMed]
143. Chen, M.; Wang, D.; Li, M.; He, Y.; He, T.; Chen, M.; Hu, Y.; Luo, Z.; Cai, K. Nanocatalytic Biofunctional MOF Coating on Titanium Implants Promotes Osteoporotic Bone Regeneration through Cooperative Pro-osteoblastogenesis MSC Reprogramming. *ACS Nano* **2022**, *16*, 15397–15412. [CrossRef]
144. Mandracci, P.; Mussano, F.; Ceruti, P.; Pirri, C.F.; Carossa, S. Reduction of bacterial adhesion on dental composite resins by silicon–oxygen thin film coatings. *Biomed. Mater.* **2015**, *10*, 015017. [CrossRef]

145. Mandracci, P.; Ceruti, P.; Ricciardi, C.; Mussano, F.; Carossa, S. a-SiOx Coatings Grown on Dental Materials by PECVD: Compositional Analysis and Preliminary Investigation of Biocompatibility Improvements. *Chem. Vap. Depos.* **2010**, *16*, 29–34. [CrossRef]
146. Alves Silva, E.C.; Tanomaru-Filho, M.; da Silva, G.F.; Delfino, M.M.; Cerri, P.S.; Guerreiro-Tanomaru, J.M. Biocompatibility and Bioactive Potential of New Calcium Silicate–based Endodontic Sealers: Bio-C Sealer and Sealer Plus BC. *J. Endod.* **2020**, *46*, 1470–1477. [CrossRef]
147. Arcos, D.; Vallet-Regí, M. Sol–gel silica-based biomaterials and bone tissue regeneration. *Acta Biomater.* **2010**, *6*, 2874–2888. [CrossRef]
148. Heimann, R.B. Silicon Nitride, a Close to Ideal Ceramic Material for Medical Application. *Ceramics* **2021**, *4*, 208–223. [CrossRef]
149. Ilyas, A.; Odatsu, T.; Shah, A.; Monte, F.; Kim, H.K.W.; Kramer, P.; Aswath, P.B.; Varanasi, V.G. Amorphous Silica: A New Antioxidant Role for Rapid Critical-Sized Bone Defect Healing. *Adv. Healthc. Mater.* **2016**, *5*, 2199–2213. [CrossRef]
150. Monte, F.A.D.; Awad, K.R.; Ahuja, N.; Kim, H.K.W.; Aswath, P.; Brotto, M.; Varanasi, V.G. Amorphous Silicon Oxynitrophosphide-Coated Implants Boost Angiogenic Activity of Endothelial Cells. *Tissue Eng. Part A* **2019**, *26*, 15–27. [CrossRef] [PubMed]
151. Mussano, F.; Genova, T.; Laurenti, M.; Munaron, L.; Pirri, C.F.; Rivolo, P.; Carossa, S.; Mandracci, P. Hydrogenated amorphous silicon coatings may modulate gingival cell response. *Appl. Surf. Sci.* **2018**, *436*, 603–612. [CrossRef]
152. Bigham, A.; Rahimkhoei, V.; Abasian, P.; Delfi, M.; Naderi, J.; Ghomi, M.; Dabbagh Moghaddam, F.; Waqar, T.; Nuri Ertas, Y.; Sharifi, S.; et al. Advances in tannic acid-incorporated biomaterials: Infection treatment, regenerative medicine, cancer therapy, and biosensing. *Chem. Eng. J.* **2022**, *432*, 134146. [CrossRef]
153. Kaczmarek-Szczepańska, B.; Polkowska, I.; Paździor-Czapula, K.; Nowicka, B.; Gierszewska, M.; Michalska-Sionkowska, M.; Otrocka-Domagała, I. Chitosan/Phenolic Compounds Scaffolds for Connective Tissue Regeneration. *J. Funct. Biomater.* **2023**, *14*, 69. [CrossRef] [PubMed]
154. Widsten, P.; Salo, S.; Niemelä, K.; Helin, H.; Salonen, M.; Alakomi, H.-L. Tannin-Based Microbicidal Coatings for Hospital Privacy Curtains. *J. Funct. Biomater.* **2023**, *14*, 187. [CrossRef]
155. Amarowicz, R. Tannins: The new natural antioxidants? *Eur. J. Lipid Sci. Technol.* **2007**, *109*, 549–551. [CrossRef]
156. Sanguedolce, M.; Saffioti, M.R.; Rotella, G.; Curcio, F.; Cassano, R.; Umbrello, D.; Filice, L. The Effects of Substrate Material on Chitosan Coating Performance for Biomedical Application. *Procedia CIRP* **2022**, *108*, 817–820. [CrossRef]
157. Ganesh, S.S.; Anushikaa, R.; Swetha Victoria, V.S.; Lavanya, K.; Shanmugavadivu, A.; Selvamurugan, N. Recent Advancements in Electrospun Chitin and Chitosan Nanofibers for Bone Tissue Engineering Applications. *J. Funct. Biomater.* **2023**, *14*, 288. [CrossRef]
158. Oe, T.; Dechojarassri, D.; Kakinoki, S.; Kawasaki, H.; Furuike, T.; Tamura, H. Microwave-Assisted Incorporation of AgNP into Chitosan–Alginate Hydrogels for Antimicrobial Applications. *J. Funct. Biomater.* **2023**, *14*, 199. [PubMed]
159. Yu, K.; Song, Y.; Lin, J.; Dixon, R.A. The complexities of proanthocyanidin biosynthesis and its regulation in plants. *Plant Commun.* **2023**, *4*, 100498. [CrossRef] [PubMed]
160. Banavar, S.; Deshpande, A.; Sur, S.; Andreescu, S. Ceria nanoparticle theranostics: Harnessing antioxidant properties in biomedicine and beyond. *J. Phys. Mater.* **2021**, *4*, 042003. [CrossRef]
161. Yokel, R.A.; Hussain, S.; Garantziotis, S.; Demokritou, P.; Castranova, V.; Cassee, F.R. The yin: An adverse health perspective of nanoceria: Uptake, distribution, accumulation, and mechanisms of its toxicity. *Environ. Sci. Nano* **2014**, *1*, 406–428. [CrossRef] [PubMed]
162. Huang, Y.; Li, P.; Zhao, R.; Zhao, L.; Liu, J.; Peng, S.; Fu, X.; Wang, X.; Luo, R.; Wang, R.; et al. Silica nanoparticles: Biomedical applications and toxicity. *Biomed. Pharmacother.* **2022**, *151*, 113053. [CrossRef] [PubMed]
163. Zhang, L.-C.; Chen, L.-Y.; Wang, L. Surface Modification of Titanium and Titanium Alloys: Technologies, Developments, and Future Interests. *Adv. Eng. Mater.* **2020**, *22*, 1901258. [CrossRef]
164. Xu, D.-P.; Li, Y.; Meng, X.; Zhou, T.; Zhou, Y.; Zheng, J.; Zhang, J.-J.; Li, H.-B. Natural Antioxidants in Foods and Medicinal Plants: Extraction, Assessment and Resources. *Int. J. Mol. Sci.* **2017**, *18*, 96. [CrossRef]

Journal of
Functional
Biomaterials

MDPI

Article

Antibacterial Biomaterial Based on Bioglass Modified with Copper for Implants Coating

Imen Hammami [1], Sílvia Rodrigues Gavinho [1], Suresh Kumar Jakka [1], Manuel Almeida Valente [1], Manuel Pedro Fernandes Graça [1], Ana Sofia Pádua [2], Jorge Carvalho Silva [2], Isabel Sá-Nogueira [3,4] and João Paulo Borges [5,*]

[1] I3N and Physics Department, Aveiro University, 3810-193 Aveiro, Portugal; imenhammami@ua.pt (I.H.); silviagavinho@ua.pt (S.R.G.); suresh@ua.pt (S.K.J.); mav@ua.pt (M.A.V.); mpfg@ua.pt (M.P.F.G.)
[2] I3N-CENIMAT and Physics Department, NOVA School of Science and Technology, Campus de Caparica, 2829-516 Caparica, Portugal; as.padua@campus.fct.unl.pt (A.S.P.); jcs@fct.unl.pt (J.C.S.)
[3] Associate Laboratory i4HB—Institute for Health and Bioeconomy, NOVA School of Science and Technology, NOVA University Lisbon, 2819-516 Caparica, Portugal; isn@fct.unl.pt
[4] UCIBIO—Applied Molecular Biosciences Unit, Department of Life Sciences, NOVA School of Science and Technology, NOVA University Lisbon, 2819-516 Caparica, Portugal
[5] I3N-CENIMAT and Materials Science Department, NOVA School of Science and Technology, Campus de Caparica, 2829-516 Caparica, Portugal
* Correspondence: jpb@fct.unl.pt

Abstract: Biofilm-related implant infections pose a substantial threat to patients, leading to inflammation in the surrounding tissue, and often resulting in implant loss and the necessity for additional surgeries. Overcoming this implantology challenge is crucial to ensure the success and durability of implants. This study shows the development of antibacterial materials for implant coatings by incorporating copper into 45S5 Bioglass®. By combining the regenerative properties of Bioglass® with the antimicrobial effects of copper, this material has the potential to prevent infections, enhance osseointegration and improve the long-term success of implants. Bioglasses modified with various concentrations of CuO (from 0 to 8 mol%) were prepared with the melt-quenching technique. Structural analysis using Raman and FTIR spectroscopies did not reveal significant alterations in the bioglasses structure with the addition of Cu. The antibacterial activity of the samples was assessed against *Gram-positive* and *Gram-negative* bacteria, and the results demonstrated significant inhibition of bacterial growth for the bioglass with 0.5 mol% of CuO. Cell viability studies indicated that the samples modified with up to 4 mol% of CuO maintained good cytocompatibility with the Saos-2 cell line at extract concentrations up to 25 mg/mL. Furthermore, the bioactivity assessment demonstrated the formation of a calcium phosphate (CaP)-rich layer on the surfaces of all bioglasses within 24 h. Our findings show that the inclusion of copper in the bioglass offers a significant enhancement in its potential as a coating material for implants, resulting in notable advancements in both antibacterial efficacy and osteointegration properties.

Keywords: Bioglass®; copper; antibacterial activity; bioactivity; osseointegration; implant coating

1. Introduction

The use of implantable medical devices, such as orthopedic or dental implants, has become common practice in almost all fields of medicine. However, foreign bodies are associated with a significant risk of bacterial infections. These infections are a significant concern in healthcare settings, and can lead to serious complications. The biofilms, which are communities of bacteria encased in a protective matrix, can form on the surface of the implants, and trigger an inflammatory response in the surrounding tissue, leading to further complications. In the case of dental implants, biofilm formation plays a significant role in the development of peri-implantitis, which is a chronic inflammatory disease caused

by anaerobic *Gram-positive* and *Gram-negative* bacteria that gradually leads to bone loss and implant failure [1–4]. Despite taking all necessary precautions, such as maintaining patient asepsis and ensuring sterilization of instruments, infections can still occur after surgery. The treatment of implant-related infections typically involves a combination of approaches, with antibiotics being commonly employed. However, their effectiveness against biofilm-associated infections is limited [5,6]. The protective matrix of biofilms can prevent antibiotics from reaching the bacteria, making them less effective. Consequently, addressing biofilm-associated infections may necessitate surgical intervention to remove the infected device, which places an additional burden on the patient and increases the associated surgical risks. Prioritizing preventive solutions to prevent bacterial colonization during surgery is crucial for minimizing the risk of implant-related infections. One effective approach is the development of antibacterial materials for implant coatings that are capable of directly combating bacteria at the infection source [7–9]. Moreover, the surface modification of the implant enhances material–bone interaction and, therefore, stability [10,11]. Several studies have demonstrated the impact of implant surface roughness on cell integration and its association with increased osteointegration at the clinical level [12–14]. Increased surface roughness has been found to significantly affect cell behavior, leading to a higher expression of integrin for osteoblastic cells. This promotes osteoblast differentiation and cell proliferation [15].

The 45S5 bioglass® (46.1% SiO_2, 24.4% Na_2O, 26.9% CaO and 2.6% P_2O_5 (mol%)), developed by Hench et al., has emerged as a highly successful material for implant coating due to its distinctive properties [16,17]. The release of antimicrobial ions, notably sodium and calcium, from the bioglass coating disrupts the cell membranes of bacteria and fungi, impeding their proliferation. Furthermore, the bioactive nature of bioglass facilitates the formation of a hydroxyapatite layer upon contact with bodily fluids, promoting osseointegration and stimulating new bone growth. By enhancing stability and integration with surrounding tissues, the bioglass coating effectively deters bacterial colonization on implant surfaces [17–20].

In recent years, efforts have been undertaken to enhance the biological performance of bioactive glasses by integrating metallic ions into the glass network [4,21–26]. Copper (Cu), in particular, has garnered significant attention due to its potential antibacterial effects when released in the physiological environment upon the dissolution of the bioglass matrix. The presence of Cu ions leads to the generation of reactive oxygen species (ROS), which can cause oxidative stress and damage cellular components in bacteria [27–29]. Additionally, Cu can induce lipid peroxidation, disrupting the integrity of bacterial cell membranes. The oxidation of proteins and DNA by Cu ions further impairs bacterial functions and viability [27–29]. In the case of human cells, they have sophisticated antioxidant defense systems that neutralize excess ROS to maintain cellular homeostasis. These defense mechanisms include enzymes such as superoxide dismutase, catalase and glutathione peroxidase, which detoxify ROS and protect the cells from oxidative damage [30,31]. The combined action of these processes contributes to the antimicrobial activity exhibited by copper ions, making them effective agents for incorporation into the bioglass matrix. Additionally, copper plays a significant role in the regulation of angiogenesis by promoting endothelial cell proliferation and migration [32,33]. Moreover, studies have demonstrated that Cu can induce an increase in the differentiation of mesenchymal stem cells (MSCs) into osteoblasts, promoting bone formation and mineralization [34,35]. Although copper is recognized for its pivotal role in hemostasis and bone formation, an excess amount of this element can be cytotoxic [36]. Studies have reported that the body tolerates low doses of copper, typically up to 8.66 mg kg^{-1}, while doses ranging from 50 to 54.4 mg kg^{-1} can be lethal due to the generation of free radicals, resulting in toxicity and inflammatory effects [36–38].

The present study focused on the synthesis of copper-modified 45S5 bioactive glass through the melt-quenching method, to explore its potential as a coating material for dental implants. The synthesized bioglasses with varying percentages of copper oxide (from 0 to 8 mol%) were subjected to comprehensive morphological, structural and biological

investigations. This research encompasses a combination of these specific analyses that collectively contribute to a comprehensive understanding of the biological properties of the copper-modified bioglass. By examining the physicochemical properties, we have gained insights into the material's composition and structural characteristics, which can impact its biocompatibility and bioactivity. Additionally, we have assessed the antibacterial activity, demonstrating the potential of the copper modification to confer enhanced antimicrobial properties to the bioglass. The cytotoxicity assessment has provided valuable information on the material's compatibility with the human osteosarcoma cell line (Saos-2 cells), while the bioactivity analysis aimed to determine its ability to promote bone integration and regeneration. The findings of this study provide valuable insights into the development of advanced biomaterials for dental implant applications.

2. Materials and Methods

2.1. Synthesis Method

A series of 45S5 bioglass® samples (46.1 SiO_2, 24.4 Na_2O, 26.9 CaO, 2.6 P_2O_5, mol%) incorporating varying percentages of copper oxide (CuO), from 0 to 8 mol% (named Cu0, Cu0.25, ... Cu8), were successfully synthesized using the melt-quenching technique. The chemical precursors, including SiO_2, P_2O_5, $CaCO_3$, Na_2CO_3 and CuO, with a high purity grade (>99.99%), were initially thoroughly mixed using a planetary ball milling process for 1 h at 300 rpm. The resulting mixed powder was calcined at 800 °C for 8 h. The calcined powder was then carefully melted, using a platinum crucible, at 1300 °C for 1 h, ensuring regular hand mixing to improve the melt homogeneity. After the quench, the resulting bulk glass samples were then finely ground and milled into powder form using the same planetary ball milling process, for 1 h at 500 rpm.

2.2. Structural and Physicochemical Characterization

FTIR spectra in the range of 400–1200 cm^{-1} were collected using the FT Perkin-Elmer Spectrum BX Spectrometer (Waltham, MA, USA) in the ATR crystal (Golden Gate Diamond ATR accessory). The measurements were performed using powder samples. Throughout the acquisition, the room temperature and humidity were maintained at approximately 23 °C and 35%, respectively, to ensure consistent conditions.

Raman spectroscopy was performed at room temperature utilizing a Horiba Jobin Yvon HR 800 spectrometer (Longjumeau, France) equipped with an Ar + laser (λ = 532 nm). The measurements were conducted employing a back-scattering geometry across the spectral range of 200 to 1500 cm^{-1}. A 50× lens was employed to precisely focus on the sample during data collection.

Photoluminescence (PL) emission spectra were obtained on a Horiba Jobin Yvon Fluorolog-3 instrument equipped with a continuous Xe lamp of 450 W and photomultiplier (PMT) detector, in the range of 400–700 nm with a step width of 0.5 nm with the source, sample and the detector placed in orthogonal geometry.

2.3. Morphological Characterization

The surface morphology of the glass samples pellets produced from the synthesized powders using a uniaxial pressure system and cylindrical steel mold, was assessed using a TESCAN Vega 3 scanning electron microscope (SEM), Brno, Czech Republic. The chemical composition of the samples was semi-quantitatively analyzed using the Bruker QUANTAX EDS (energy dispersive spectroscopy) system coupled to the Vega 3 SEM. A 5 μm diameter electron beam spot was utilized to examine specific surface sites on each sample.

2.4. Cytotoxicity Assay

The cytotoxicity assessment of the samples followed the extract method, and utilized the human osteosarcoma cell line (Saos-2 cells, ATCC® HTB-85™) in compliance with the International Standard ISO 10993-5. Prior to the evaluation, the bioglass powders underwent sterilization at 120 °C for 2 h. Two types of extract, non-passivated and passivated,

were generated by exposing the samples to culture medium (McCoy 5A medium, from Merck KGaA, Darmstadt, Germany, supplemented with 10% fetal bovine serum, from Biowest, France, and 1% penicillin, 100 U/mL, and streptomycin, 100 µg/mL, Gibco, ThermoFisher, Waltham, MA, USA) at a concentration of 100 mg/mL. For the non-passivated extract, the powder in contact with the medium was incubated for 24 h at 37 °C, filtered through a 0.22 µm cellulose acetate filter, and stored at 37 °C. In the case of the passivated extract, fresh McCoy 5A medium was added to the same bioglass powder and incubated for 24 h at 37 °C.

Saos-2 cells were seeded onto 96-well plates at a density of 30 k cells per cm^2 and incubated for 24 h at 37 °C with a 5% CO_2 atmosphere. Subsequently, the culture medium was replaced by the non-passivated and passivated extracts. In addition to the initial concentration of 100 mg/mL, four serial dilutions were prepared (50 mg/mL, 25 mg/mL, 12.5 mg/mL and 6.25 mg/mL). A positive control (cells in a cytotoxic environment, caused by the supplementation of the culture medium with 10% dimethyl sulfoxide) and a negative control (cells cultured with normal medium) were set up. After 48 h of incubation, the cell viability was assessed using the resazurin cell viability indicator. The optical absorbances of each well were measured at 570 nm and 600 nm using a Biotek ELX800 microplate reader. To ensure the reproducibility of the results, the study was performed in triplicate with six replicates in each experiment.

2.5. Antibacterial Activity

The antibacterial potential of bioactive glasses with varying copper concentrations was investigated against the reference strains *Escherichia coli* K12 DSM498 (DSMZ, Braunschweig, Germany), *Staphylococcus aureus* COL MRSA (methicillin-resistant strain, obtained from Rockefeller University) and *Streptococcus mutans* DSM20523 (DSMZ, Braunschweig, Germany). All of the microorganisms were cultured at 37 °C in tryptic soy broth (TSB) medium and *S. mutans* in a 5% CO_2 incubator. Before conducting the experiments, bioglass powder pellets measuring 6 mm in diameter and approximately 2 mm in thickness were subjected to sterilization at 180 °C for 2 h.

The agar diffusion assay using the two-layer bioassay method was employed, involving the use of TSB medium solidified with agar 1.5% w/v for the base layer, and with agar 0.8% w/v for the top layer. Preparation of the assay plates entailed pouring 18–20 mL of the base layer, followed by the addition of 4 mL of molten seeded overlay containing approximately 10^7–10^8 CFU/mL of the respective indicator bacteria grown overnight, as described above. The pellets were positioned in the center of the plate, left at room temperature for 4 h and subsequently, the plates were incubated at 37 °C for 24 h.

Images of the pellets were taken, and the diameter of the resulting inhibition zone was determined using ImageJ software. To ensure accuracy, each pellet underwent meticulous measurement from multiple orientations, with a total of 30 measurements per pellet. Statistical analysis of the data was performed using GraphPad Prism 8.0 software, employing an unpaired *t*-test, to compare the antibacterial effects of the bioactive glass base composition with each of the different samples.

2.6. In Vitro Bioactivity Assay

Following the ISO 23317:2017 standard, the evaluation of bioactivity for the bi-oglasses samples was conducted by transforming the powders in disk form (pellets) with a diameter of 7 mm, and then immersing them in a simulated bodily fluid (SBF). The pellets, placed in various flasks and immersed in SBF, were then incubated at a constant temperature of 37 °C for different times (12, 24, 48, 96 h, 14 and 28 d). Throughout the incubation period, the samples were placed on continuous oscillating support to mimic the continuous flow of biological fluids. The SBF solutions were refreshed every 48 h to simulate the biological environment.

The calculation of the SBF volume required for each sample followed a specific formula:

$$V_s = 100\ mm \times S_a, \quad (1)$$

where V_s is the volume of SBF in mm^3, and S_a is the surface area of the pellet in mm^2.

Once the immersion period concluded, the pellets were taken out from the SBF medium, gently cleansed using deionized water, and allowed to dry at room temperature. Subsequently, the samples were subjected to SEM/EDS analysis. This analysis aimed to determine the change in ion concentration and the development of an apatite-like layer on the surface over 28 d.

3. Results and Discussion

3.1. Structural and Physicochemical Characterization

The FTIR spectra of the glasses revealed the following features, as shown in Figure 1a. The bands observed at around 1010 cm^{-1} and 721 cm^{-1} were assigned to Si–O–Si stretching modes [22,35,39–43]. The appearance of a band at 912 cm^{-1}, assigned to Si–O_{NBO} stretching mode [22,35,39–43], demonstrates the existence of the non-bridging oxygen ions. The band located at 596 cm^{-1} is related to a P-O-P bending mode [22,35,40–44]. The presence of a band at 497 cm^{-1} is associated with an Si-O-Si bending mode [22,35,39–43]. The observed shift of this band towards lower wavenumbers with the increase in copper content is caused by the presence of copper, which leads to a change in the degree of polymerization of the glass structure. The FTIR measurements do not show any type of modification with the insertion of copper ions in the glass matrix.

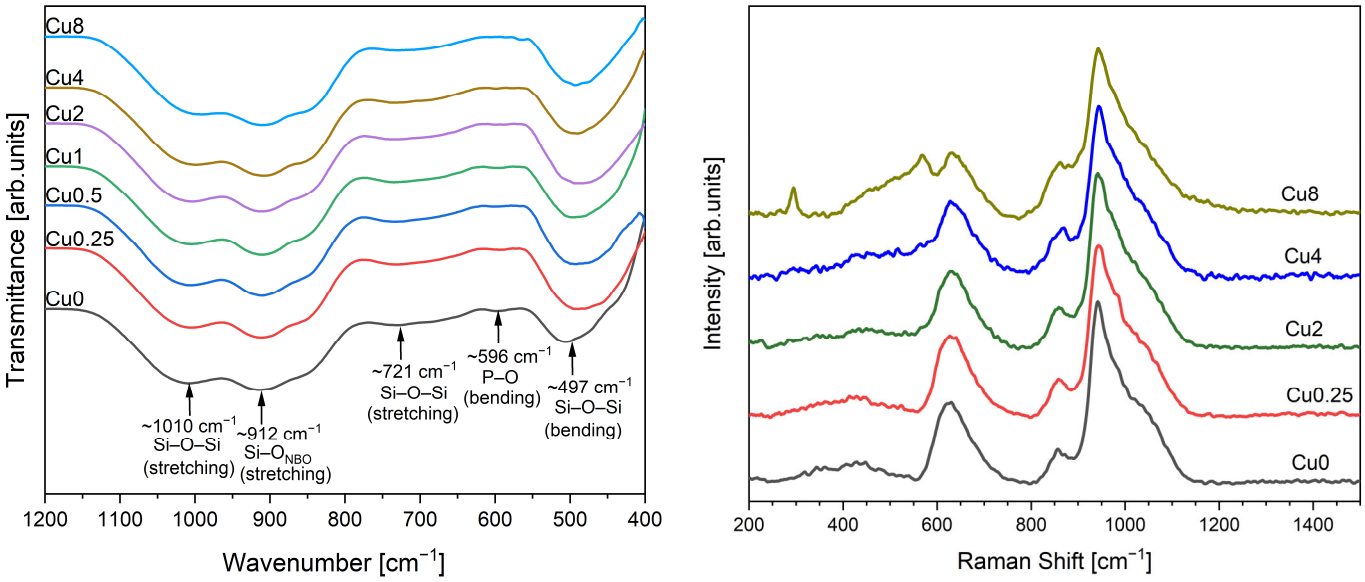

Figure 1. (**a**) FTIR spectra and (**b**) Raman spectra of bioactive glasses modified with CuO.

The Raman spectra for the modified bioglasses by CuO are displayed in Figure 1b, revealing a comparable trend among them. Nevertheless, with increasing the Cu concentration to 8 mol%, two distinct bands corresponding to the Ag and Bg modes of CuO become evident at 293 and 569 cm^{-1}, respectively [45,46]. The vibrational modes of asymmetric and symmetric stretching in the high-frequency region (800 and 1200 cm^{-1}) are considered particularly significant for silicate glasses. Figure 2 depicts the deconvolution of Raman spectra in this region for the Cu0.25, Cu2 and Cu8 samples. Six discernible vibrational modes can be identified at 855–859 cm^{-1}, 899–904 cm^{-1}, 938cm^{-1}, 961–968 cm^{-1},

1016–1019 cm^{-1} and 1050–1063 cm^{-1}, which are associated with Q_0 Si units Q_1 Si, Q_2 Si, Q_0 P, and Q_1 P units and Q_3 Si units, respectively [22,44,47,48].

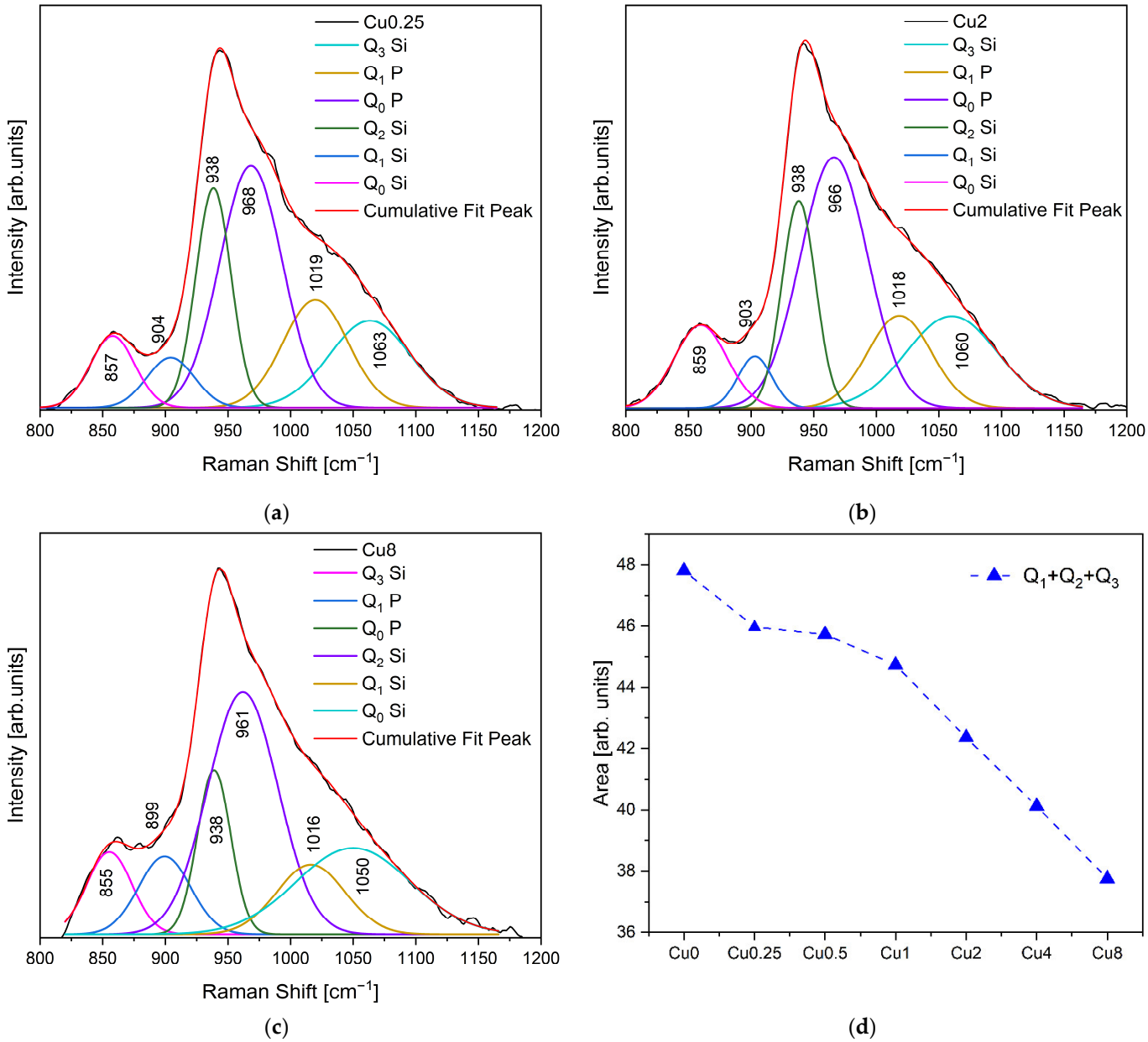

Figure 2. Deconvolution of Raman spectra for the (**a**) Cu0.25, (**b**) Cu2 and (**c**) Cu8 samples ($R^2 > 0.999$); and (**d**) sum of areas of Q_0 and Q_1 + Q_2 + Q_3 (NBOs) units of the different bioglass samples.

Figure 2d illustrates the variation in the sum of the area of Raman vibration bands Q_1, Q_2 and Q_3 units associated with non-bridging oxygen ions (NBOs) as a function of Cu concentration. The results show that the NBO amount decreases with the rise in copper concentration, suggesting an increase in the connectivity of the glass network. The samples Cu0.25 and Cu0.5 exhibited a similar concentration of NBOs.

Figure 3 displays the photoluminescence (PL) spectra of the glass samples modified with copper upon excitation at 280 nm. Ultraviolet excitation induces significant and wide emission peaks in the visible range in copper-containing glasses, and it is worth noting that copper can be introduced into the glass network in two different oxidation states, Cu^{2+} and Cu^{+} [49,50]. The excitation bands of these ions are located in the UV region [51,52]. The spectral analysis revealed the presence of one main peak at around

475 nm, accompanied by a shoulder at 523 nm. The luminescence peak at 475 nm is associated with the $3d^9 4s^1 – 4s^2 3d^{10}$ transition of Cu^{2+} ions [51,53]. The shoulder peak at 523 nm is a consequence of the transition from the degraded T_{1g} and T_{2g} levels to the ^1A_g energy level of the Cu^+ copper ions [51,54]. This transition arises from the interaction between NBOs with the Cu^{2+}. Therefore, the PL spectra indicate the existence of both Cu^+ and Cu^{2+} ions, contributing to the observed emission peaks. It was also observed that with the increase in CuO concentration, the PL intensity decreased; this is attributed to the loss of excited energy from copper ions to the host lattice [51]. The decrease in the PL intensity with higher concentration made the PL signal of the Cu8 sample indistinguishable from the noise.

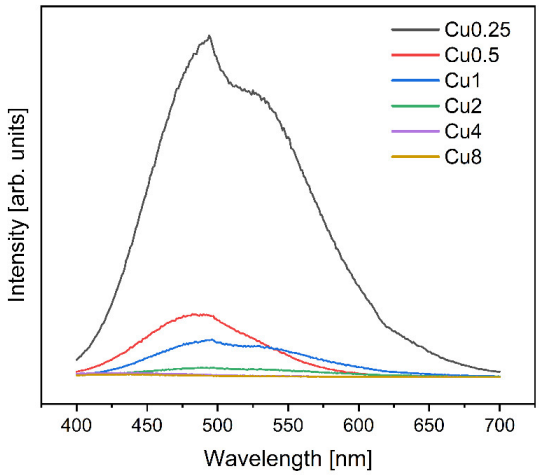

Figure 3. PL emission spectra excited at 280 nm of the bioglasses modified with copper.

Figure 4 depicts the deconvolution of the PL spectrum for bioglasses with different CuO content. When the spectra were normalized, the relative intensities of both peaks were changing in such a way that the intensity of the peak at 475 nm due to Cu^{2+} ions increased with respect to the Cu^+ peak at 523 nm with the rise in Cu concentration inserted into the bioglass. This observation is correlated with the results obtained with the Raman analysis, which shows the decrease in NBOs with the increase in copper concentration inserted into the bioglass (Figure 2d) due to the increase in Cu^{2+} ions at the expense of Cu^+, thus forming stronger bonds with oxygen and leading to a decrease in the number of available NBOs.

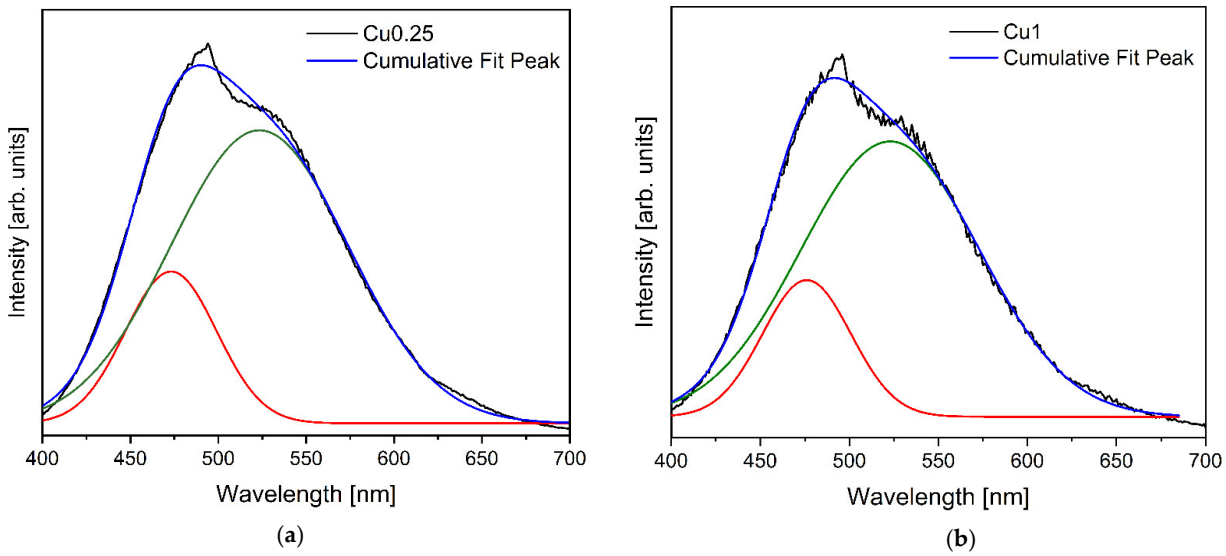

Figure 4. *Cont.*

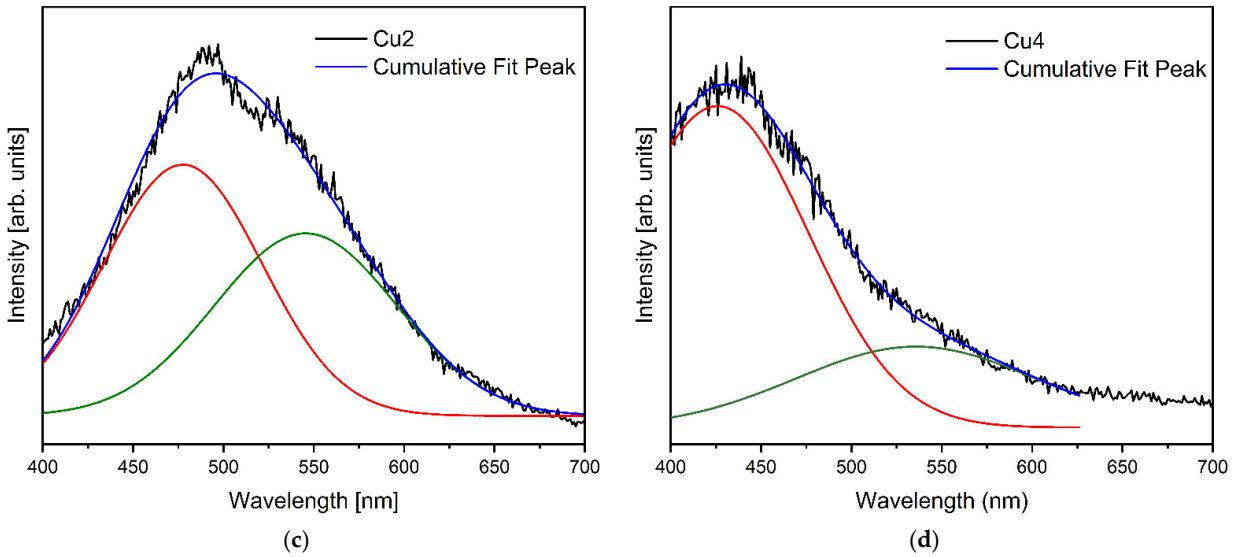

Figure 4. Deconvolution of the PL spectrum of the (**a**) Cu0.25, (**b**) Cu1, (**c**) Cu2 and (**d**) Cu4 bioglass samples.

3.2. Morphological Characterization

SEM–EDS elemental mapping of the Cu0.5 and Cu8 samples are reported in Figures 5 and 6, respectively. The results obtained show the homogenous distribution of the Si, Ca, Na, P and Cu elements.

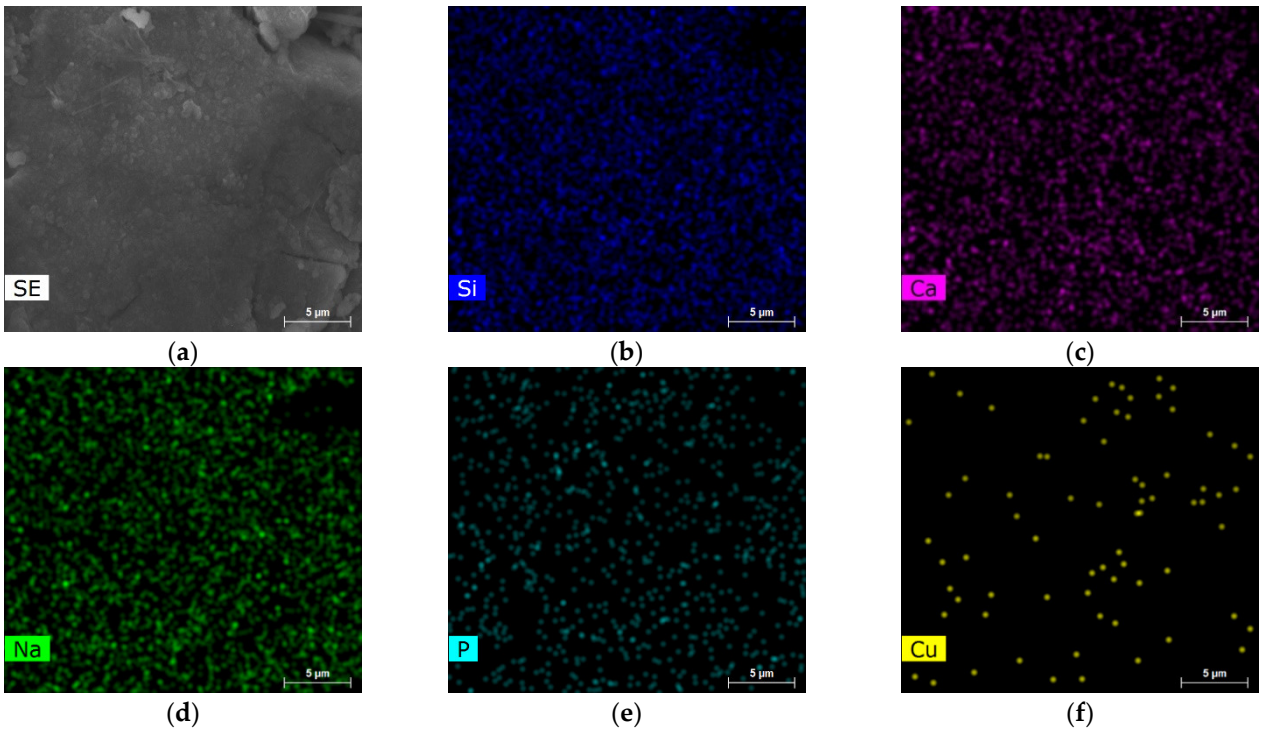

Figure 5. SEM/EDX analyses of Cu0.25 sample (**a**) SEM image, EDS elemental mapping of (**b**) Si, (**c**) Ca, (**d**) Na, (**e**) P and (**f**) Cu.

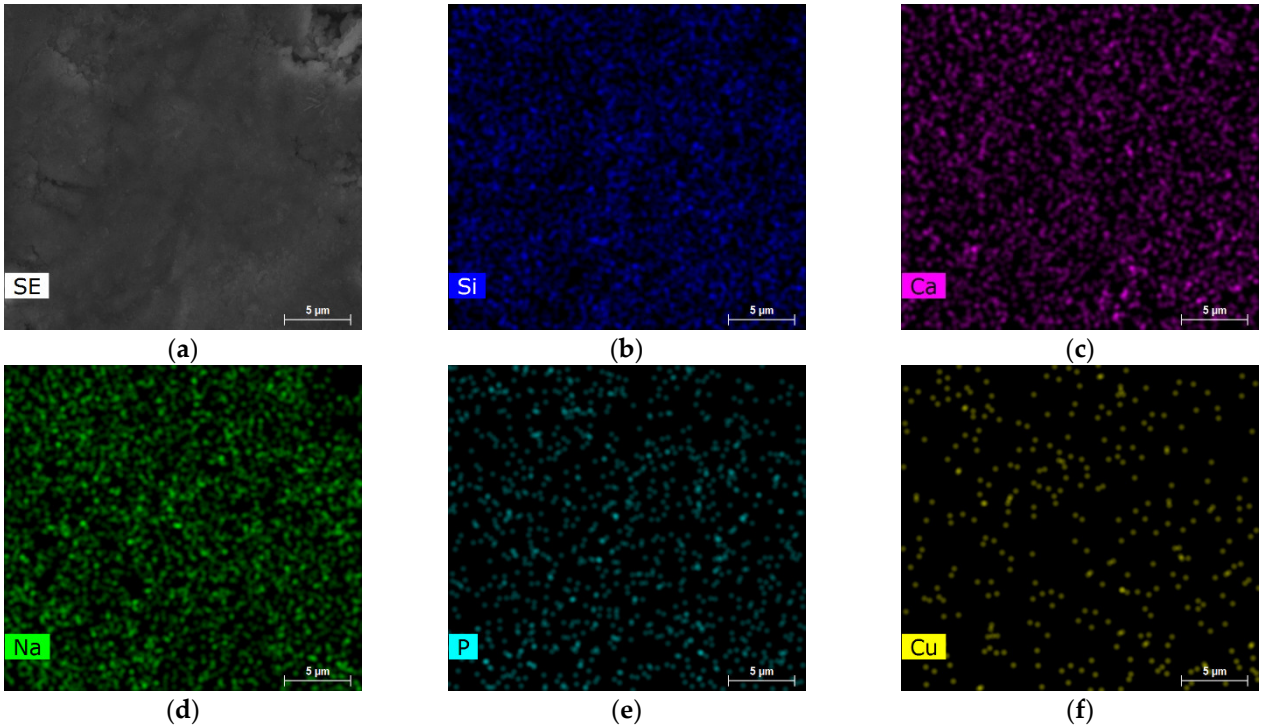

Figure 6. SEM/EDX analyses of Cu8 sample (**a**) SEM image, EDS elemental mapping of (**b**) Si, (**c**) Ca, (**d**) Na, (**e**) P and (**f**) Cu.

3.3. Cytotoxicity Assay

In order to explore the biocompatibility of various bioglass compositions for their potential in bone regeneration, Saos-2 cell line viability was evaluated upon exposure to bioglass extracts. Employing a resazurin assay as an indicator of cell viability, the impact of extract–cell line interactions was examined. The results demonstrate that non-passivated extracts, i.e., those not preconditioned with McCoy's culture medium, induced a drastic decline in cell viability at concentrations of 100 mg/mL and 50 mg/mL, thus exhibiting a potent cytotoxic effect. When the extract concentration was reduced to 25 mg/mL, the samples with a Cu content lower than 2 mol% demonstrated enhanced cell viability, despite the discernible presence of their cytotoxic attributes. However, when the extract was diluted to 12.5 mg/mL, a noticeable reduction in cytotoxicity was observed for the samples modified with low concentrations of copper, exhibiting a significantly improved cell viability compared to the sample containing copper concentrations of 2 mol% and above. These findings strongly indicate that the introduction of CuO into the bioactive glass confers diminished biocompatibility to the materials, which aligns with the findings of prior research studies [55,56]. By subjecting the materials to a passivation process, as depicted in Figure 7b, the cytotoxicity of the extracts can be alleviated. It is important to note that cytotoxicity is linked to a rise in local pH caused by ion-exchange reactions upon contact of the sample with the cell culture medium within the initial 24 h [42]. Upon interaction with the cellular medium, bioactive glass experiences the breakdown of its Si-O-Si bonds, leading to the release of soluble silica in the form of $Si(OH)_4$ into the solution. Consequently, the dissolution rate and pH of the surrounding environment are elevated, thereby influencing cellular metabolism and function. However, when the samples are passivated, the influence of pH alkalinization caused by bioactive glasses diminishes. The passivated extracts derived from the bioglasses modified with copper from 0 to 2 mol% demonstrated a remarkable lack of cytotoxicity at a concentration of 25 mg/mL, whereas the samples Cu4 and Cu8 exhibited no cytotoxic effects at extract concentrations of 12.5 mg/mL and 6.75 mg/mL, respectively. These findings indicate that at these particular

concentrations, the samples no longer present a risk to the organism since they can be effectively regulated through natural in vivo pH regulatory mechanisms [57,58].

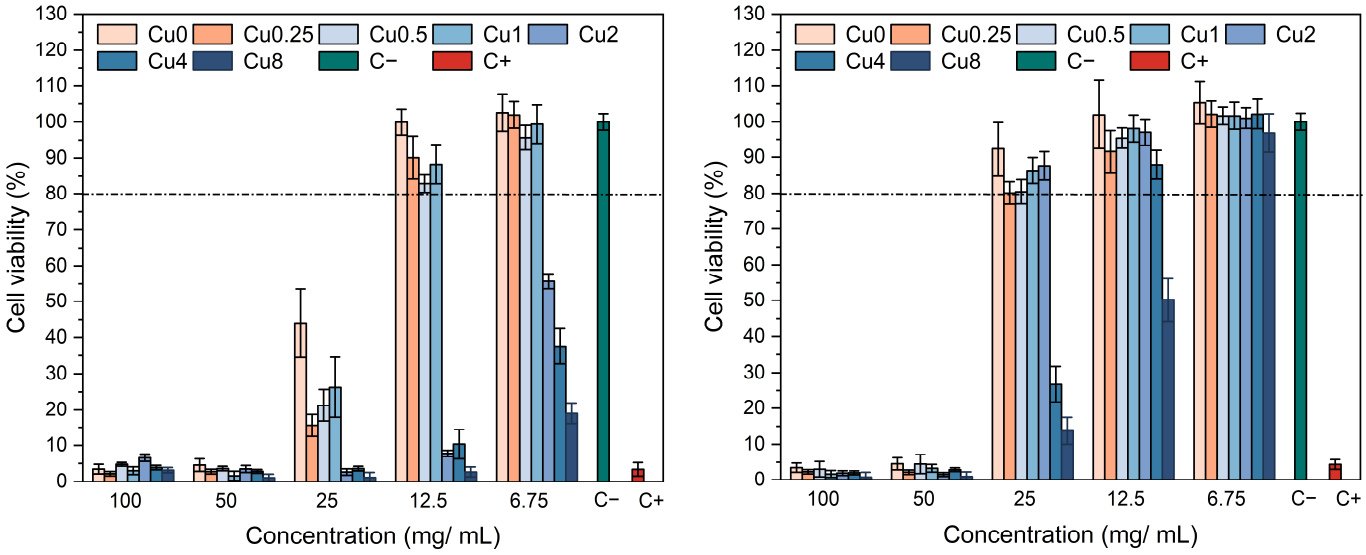

Figure 7. Relative viabilities of (**a**) non-passivated and (**b**) passivated bioglass extracts modified by CuO in culture with Saos-2 cells.

3.4. Antibacterial Activity

In the realm of implantation therapy, tackling bacterial infections has become a crucial aspect. While 45S5 bioactive glass has shown exceptional properties in promoting bone regeneration and inhibiting bacterial growth [59–61], it is crucial to explore the potential of bioglass modified with copper in exerting antibacterial effects.

The results presented in Figure 8 illustrate the outcomes of the antibacterial properties assessment conducted on the bioglasses using the agar disc diffusion method. The findings substantiate the antibacterial activity exhibited by all the samples, as evidenced by the presence of inhibition zones surrounding the bioglass pellets. These zones exhibited mean values exceeding 6 mm, corresponding to the diameter of the pellets. The antibacterial effect of 45S5 bioglass against specific bacteria can be attributed to two principle mechanisms: the pH changes towards alkalinity, and the osmotic pressure resulting from the release of bioglass ions, notably Na^+ and Ca^{2+}, into the surrounding medium [59,62]. The alkaline pH range is detrimental to bacterial growth and metabolic activities, resulting in the disruption of proteins and enzymes, and the inhibition of their normal functions. Furthermore, the release of ions and subsequent variations in their concentrations within the bacterial environment impact the integrity of the bacterial cell membrane and intramembrane pressure. Consequently, these alterations evoke modifications in cellular dimensions, morphology, as well as membrane tension levels, ultimately leading to bacterial death. Moreover, several studies showed the potential antibacterial effect of copper due to its capacity to stimulate the production of ROS, which induces oxidative stress and damage to cellular components [63–66]. Additionally, copper ions directly interact with bacterial DNA, causing DNA damage and genetic instability. According to the results, the Cu0.5 sample exhibited the most potent antimicrobial activity among all the Cu-modified bioglass samples. It demonstrated mean inhibition halo sizes of 11.19 mm, 11.05 mm and 10.98 mm against *E. coli*, *S. aureus* and *S. mutans* bacteria, respectively. However, when the Cu concentration surpassed 0.5 mol%, a noticeable reduction in the inhibition halo size was observed. This reduction indicates a simultaneous decline in the antibacterial effectiveness of the bioglass. In fact, the insertion of Cu into the glass network led to the decrease in NBOs concentration, as shown in Figure 2d. The samples containing the highest percentages of

copper showed a reduction in NBOs compared to the bioglass base. The decrease in NBO numbers suggests a reduction in ions released, such as Na^+ and Ca^{2+}, which can impact the antibacterial activity with increasing copper concentration. Moreover, the presence of different oxidation states of copper can affect the antibacterial properties of the bioglass. Previous studies showed that Cu^+ ions exhibited significantly more antibacterial effects than Cu^{2+} ions [67–69]. Therefore, the decrease in the antibacterial effect for the glass with a high concentration of Cu may be associated with increased concentrations of Cu^{2+} compared to Cu^+, as shown in Figure 4.

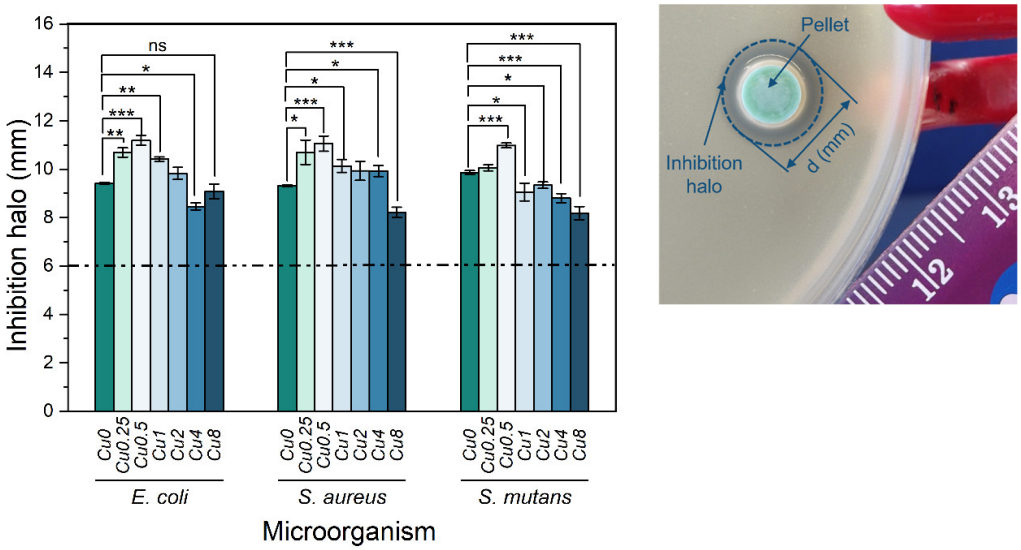

Figure 8. Measurements of inhibition halo diameters of the bioglasses modified with Cu against *E. coli*, *S. aureus* and *S. mutans* bacteria after incubation for 24 h. Results are reported as mean ± SD. The asterisks indicate significance in an unpaired *t*-test; * $p \leq 0.05$; ** $p \leq 0.01$; *** $p \leq 0.001$; ns: non-significant. The image on the right side is an example of an essay plate illustrating the inhibition halo of a Cu0.5 pellet on *E. coli*.

3.5. In Vitro Bioactivity Assay

For a comprehensive evaluation of the in vitro bioactivity of synthesized bioglasses within a biological environment, we employed the SBF immersion test as a reliable methodology. This test enables a thorough exploration of the physicochemical interactions between bioactive glass and physiological fluids. Surface chemistry modifications, particularly the development of an apatitic layer, play a vital role in assessing bioglass in vitro, as it profoundly influences the proliferation and adhesion of osteoblast cells [70]. Micrographs acquired via SEM at the surface of bioglass samples after 0, 1, 4 and 14 days in SBF are shown in Figure 9. The development of an apatitic layer on the surface of the samples was confirmed by SEM examination, which showed the presence of spherical particles with cauliflower morphologies, indicating the bioactivity of the bioglasses. The apatite particles agglomerated and became denser with prolonged immersion in SBF, leading to a completely covered surface by 14 d of immersion. These findings serve as compelling evidence of the potential osteoconductive properties of the prepared samples, highlighting their capacities to promote bone growth and regeneration. Furthermore, upon comparing bioglass samples containing varying Cu content, it was observed that the inclusion of high concentrations of Cu reduced the bioactivity of the material within the first day of immersion in SBF. This occurrence can be attributed to the conversion of bridging-oxygen ions (BOs) to NBOs, as presented in Figure 2d, leading to an increase in the glass connectivity, and therefore a drop in the dissolution rate and ions released.

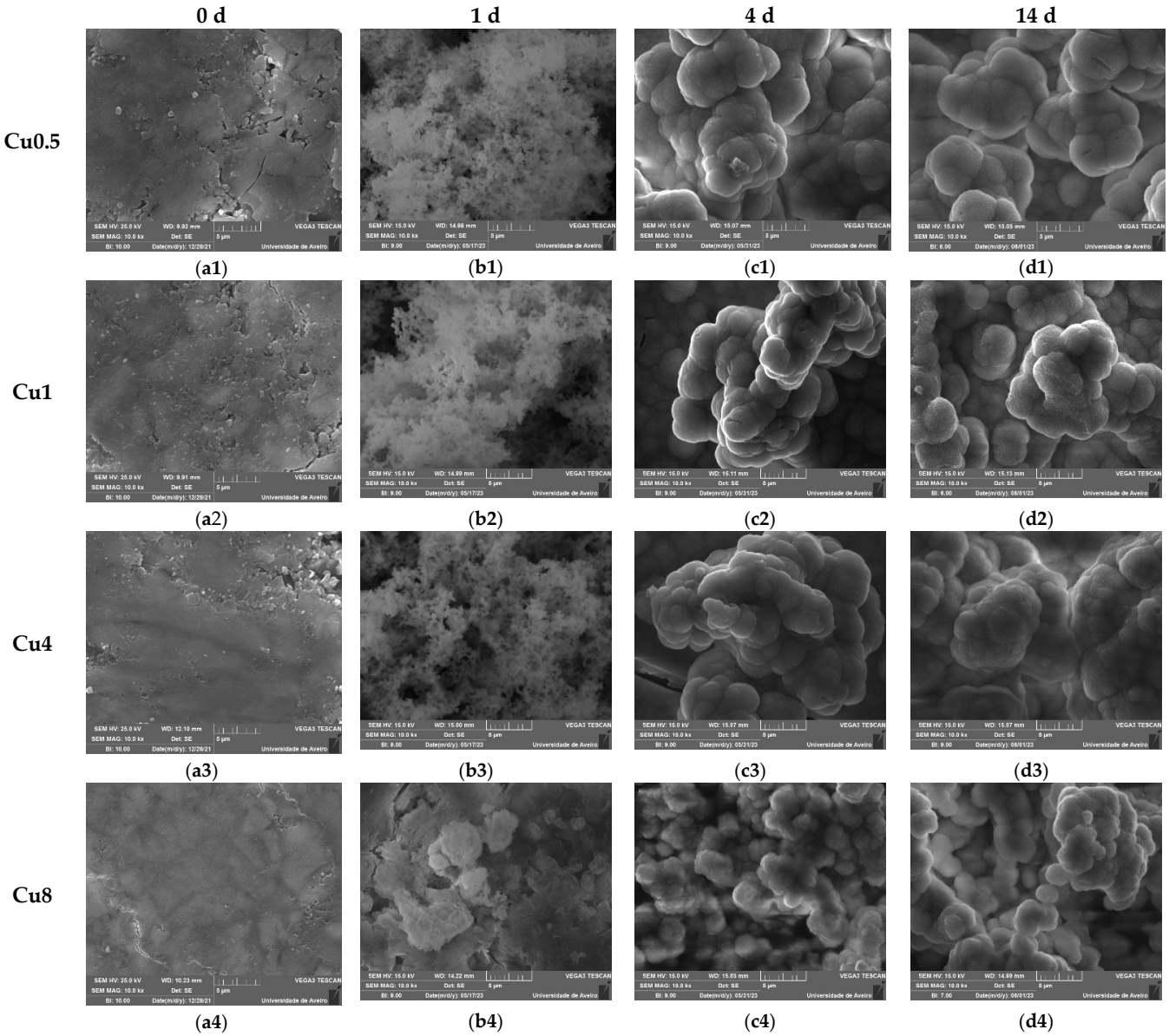

Figure 9. SEM micrographs of bioglass pellets modified with various concentrations of Cu after immersion in SBF for (**a1**–**a4**) 0 d; (**b1**–**b4**) 1 d; (**c1**–**c4**) 4 d; (**d1**–**d4**) 14 d. (The magnification of the SEM images is 10 kX).

The reaction mechanism and ionic exchange between the bioglass and the SBF medium were also observed through SEM–EDS analysis. This analysis revealed the changes in atomic percentages of chemical elements on the sample surfaces as the immersion time in SBF increased. Figure 10 presents the variations in the atomic percentages of Si, Na and the Ca/P ratio with the immersion time on the surfaces of different bioglass samples. Upon immersion in SBF, the bioactive glass engages in an ionic exchange with the surrounding medium, leading to a fast release of soluble ionic species. Within the first 24 h, the soaking triggers the development of a surface layer of Si–OH, resulting in a rise in pH and subsequent formation of soluble $Si(OH)_4$. This process leads to the creation of a silica gel layer, enabling the absorption of ions from the surrounding environment. Concurrently, Ca^{2+} and phosphate ($PO_4{}^{3-}$) diffuse through this layer towards the sample surface, promoting the formation of an amorphous calcium phosphate film. Over time, this amorphous CaP-rich layer undergoes crystallization [7,71]. Figure 10a,b illustrate a notable reduction in Si and Na concentrations on the sample surfaces during the initial days, followed by a subsequent

stabilization in the succeeding days. This phenomenon is attributed to the dissolution of these elements into the surrounding medium, and the formation of a layer rich in Ca and P. In addition, the Ca/P confirms the formation of an apatite layer, revealing a value that is close to the Ca/P ratio of hydroxyapatite in natural bone (Ca/P ≈ 1.67) [72,73]. The Ca/P ratio for the Cu0.5 sample reached a value of 1.79 within the first day of immersion in SBF, compared to 2.07 for the Cu0 sample. This indicates a positive effect of copper on the bioactivity of the glass, promoting bioactivity within the initial 24 h, as evidenced by the faster approach of the Ca/P value towards those of hydroxyapatite.

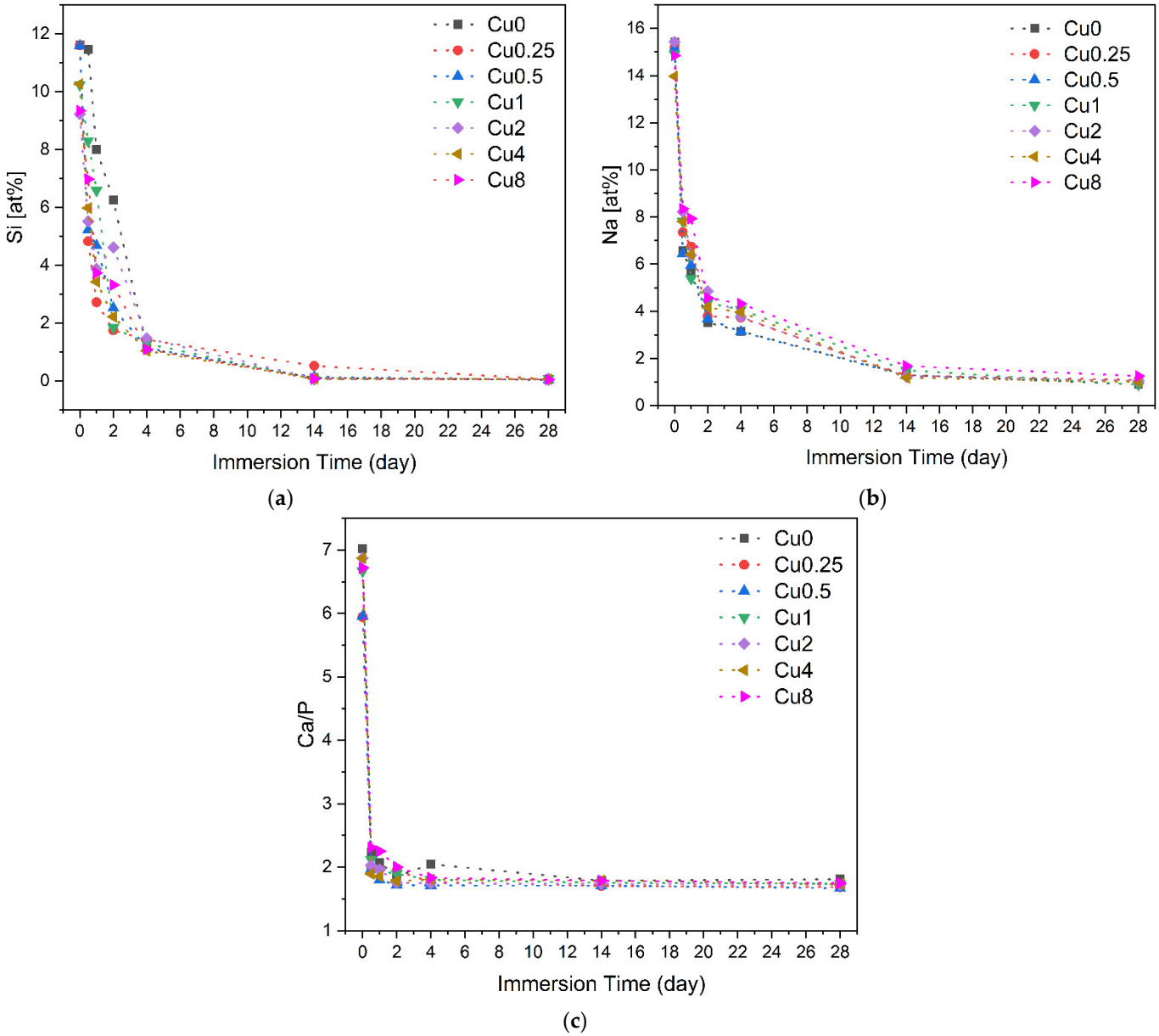

Figure 10. Variations in the concentrations of (**a**) Si; (**b**) Na; (**c**) Ca/P ratio on the bioglass pellets surfaces after immersion in SBF.

The pH levels of the SBF were monitored at different intervals of time for all glasses, regardless of whether the medium was changed every two days or not. The obtained results are depicted in Figure 11.

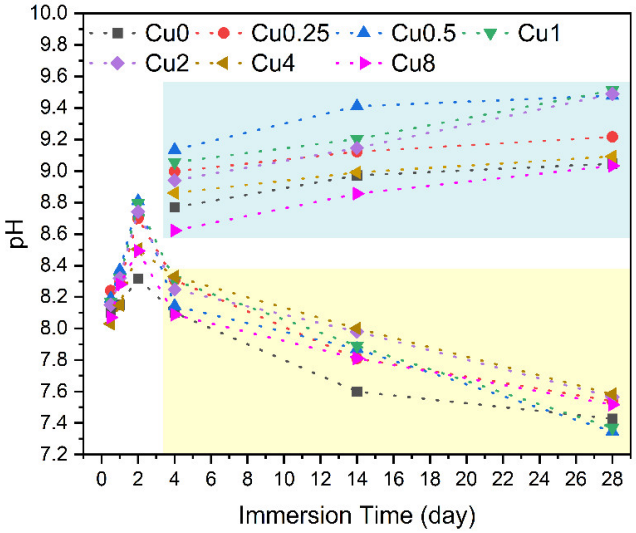

Figure 11. Variation in pH values of the SBF solution with the immersion times of all bioglass samples, with the medium changed every two days (yellow rectangle) and without medium change (blue rectangle).

As mentioned earlier, the pH of the SBF solution surrounding the bioglass exhibited a gradual increase throughout the immersion time due to the dissolution of alkaline metal ions (Na^+ and Ca^{2+}) from the samples. During the initial two days, this rise was particularly pronounced, and the increment became more gradual during the remaining period, as indicated by the values enclosed within the blue rectangle (corresponding to samples where the medium was not changed). Nevertheless, upon simulating the conditions resembling the in vivo environment by changing the medium every two days, the pH decrease was observed that is attributed to the formation of the apatite layer on the surface of the bioglass.

4. Conclusions

The synthesis of bioactive 45S5 glass samples was successfully achieved using the melt-quenching technique, incorporating varying amounts of copper oxide (CuO). Analysis using FTIR and Raman revealed no changes in the glass matrix upon CuO addition. The deconvolution of the Raman spectra demonstrated a decrease in the amount of Q1, Q2 and Q3 units with copper insertion, suggesting a decrease in NBOs concentration, and thus a reduction in the glass dissolution rate. Moreover, the PL spectra showed the presence of copper in the glass network in two oxidation states, Cu^+ and Cu^{2+}, which have an effect on the antibacterial properties of the bioglass. It was observed that the antibacterial properties decreased for the samples with a high content of CuO, where Cu^{2+} ions predominate over Cu^+ ions. The antibacterial evaluation against *E. coli*, *S. aureus* and *S. mutans* indicated that the 0.5 mol% CuO-loaded glass demonstrated the most substantial antibacterial effect. The assessment of cytotoxicity for these glasses demonstrated that the incorporation of copper up to 4 mol% into the 45S5 bioglass did not induce adverse effects on a Saos-2 cell line at extract concentrations below 25 mg/mL. The in vitro immersion tests in SBF showed that the addition of low copper content enhances the bioactivity characteristic of 45S5 glass. This study offers valuable insights for the future advancement of antibacterial coatings for implants using copper-containing bioglass.

Author Contributions: Conceptualization, I.H., S.R.G., I.S.-N. and M.P.F.G.; methodology, I.H., S.R.G., S.K.J., A.S.P., I.S.-N. and M.P.F.G.; software, I.H. and M.P.F.G.; validation, I.H., J.C.S., J.P.B., I.S.-N. and M.P.F.G.; formal analysis, I.H.; investigation, I.H., S.R.G., S.K.J., A.S.P., I.S.-N. and M.P.F.G.; resources, J.C.S., J.P.B., I.S.-N. and M.P.F.G.; data curation, I.H.; writing—original draft preparation, I.H.; writing—review and editing, S.K.J., M.A.V., M.P.F.G., I.S.-N., J.C.S. and J.P.B.; visualization, I.H.; supervision, M.P.F.G., J.C.S. and J.P.B. All authors have read and agreed to the published version of the manuscript.

Funding: This research was funded by FEDER funds through the COMPETE 2020 Program and National Funds through FCT—Portuguese Foundation for Science and Technology under the projects LISBOA-01-0247-FEDER-039985/POCI-01-0247-FEDER-039985, LA/P/0037/2020, UIDP/50025/2020 and UIDB/50025/2020 of the Associate Laboratory Institute of Nanostructures, Nanomodeling and Nanofabrication—i3N, UIDP/04378/2020 and UIDB/04378/2020 of the Research Unit on Applied Molecular Biosciences—UCIBIO, and LA/P/0140/2020 of the Associate Laboratory Institute for Health and Bioeconomy—i4HB. S.R.G. and A.S.P. acknowledge FCT—Portuguese Foundation for Science and Technology—for the PhD grants (SFRH/BD/148233/2019 and UI/DB/151287/2021, respectively). S.K.J. acknowledges FCT—Fundaçao para a Ciência e Tecnologia, Portugal, I.P.—in the scope of the framework contract foreseen in the numbers 4, 5 and 6 of article 23 of the Decree Law 57/2016 of 29 August, changed by Law 57/2017 of 19 July.

Data Availability Statement: The data presented in this study are available on request from the corresponding author.

Conflicts of Interest: The authors declare no conflict of interest.

References

1. Allan, I.; Wilson, M.; Newman, H. Particulate Bioglass®Reduces the Viability of Bacterial Biofilms Formed on Its Surface in an in Vitro Model. *Clin. Oral Implant. Res.* **2002**, *13*, 53–58. [CrossRef]
2. Gavinho, S.R.; Prezas, P.R.; Ramos, D.J.; Sá-Nogueira, I.; Borges, J.P.; Lança, M.C.; Silva, J.C.; Henriques, C.M.R.; Pires, E.; Kumar, J.S.; et al. Nontoxic Glasses: Preparation, Structural, Electrical and Biological Properties. *Int. J. Appl. Ceram. Technol.* **2019**, *16*, 1885–1894. [CrossRef]
3. Gavinho, S.R.; Pádua, A.S.; Sá-Nogueira, I.; Silva, J.C.; Borges, J.P.; Costa, L.C.; Graça, M.P.F. Fabrication, Structural and Biological Characterization of Zinc-Containing Bioactive Glasses and Their Use in Membranes for Guided Bone Regeneration. *Materials* **2023**, *16*, 956. [CrossRef]
4. Hammami, I.; Gavinho, S.R.; Pádua, A.S.; Sá-Nogueira, I.; Silva, J.C.; Borges, J.P.; Valente, M.A.; Graça, M.P.F. Bioactive Glass Modified with Zirconium Incorporation for Dental Implant Applications: Fabrication, Structural, Electrical, and Biological Analysis. *Int. J. Mol. Sci.* **2023**, *24*, 10571. [CrossRef]
5. Gbejuade, H.O.; Lovering, A.M.; Webb, J.C. The Role of Microbial Biofilms in Prosthetic Joint Infections. *Acta Orthop.* **2015**, *86*, 147–158. [CrossRef]
6. Davidson, D.J.; Spratt, D.; Liddle, A.D. Implant Materials and Prosthetic Joint Infection: The Battle with the Biofilm. *EFORT Open Rev.* **2019**, *4*, 633–639. [CrossRef]
7. Maximov, M.; Maximov, O.-C.; Craciun, L.; Ficai, D.; Ficai, A.; Andronescu, E. Bioactive Glass—An Extensive Study of the Preparation and Coating Methods. *Coatings* **2021**, *11*, 1386. [CrossRef]
8. Damiati, L.; Eales, M.G.; Nobbs, A.H.; Su, B.; Tsimbouri, P.M.; Salmeron-Sanchez, M.; Dalby, M.J. Impact of Surface Topography and Coating on Osteogenesis and Bacterial Attachment on Titanium Implants. *J. Tissue Eng.* **2018**, *9*, 2041731418790694. [CrossRef] [PubMed]
9. Zhang, B.G.; Myers, D.E.; Wallace, G.G.; Brandt, M.; Choong, P.F. Bioactive Coatings for Orthopaedic Implants—Recent Trends in Development of Implant Coatings. *Int. J. Mol. Sci.* **2014**, *15*, 11878–11921. [CrossRef] [PubMed]
10. Aboushelib, M.N.; Osman, E.; Jansen, I.; Everts, V.; Feilzer, A.J. Influence of a Nanoporous Zirconia Implant Surface of on Cell Viability of Human Osteoblasts. *J. Prosthodont.* **2013**, *22*, 190–195. [CrossRef]
11. Delgado-Ruíz, R.A.; Calvo-Guirado, J.L.; Moreno, P.; Guardia, J.; Gomez-Moreno, G.; Mate-Sánchez, J.E.; Ramirez-Fernández, P.; Chiva, F. Femtosecond Laser Microstructuring of Zirconia Dental Implants. *J. Biomed. Mater. Res. Part B Appl. Biomater.* **2011**, *96B*, 91–100. [CrossRef] [PubMed]
12. Bornstein, M.M.; Lussi, A.; Schmid, B.; Belser, U.C.; Buser, D. Early Loading of Nonsubmerged Titanium Implants with a Sandblasted and Acid-Etched (SLA) Surface: 3-Year Results of a Prospective Study in Partially Edentulous Patients. *Int. J. Oral Maxillofac. Implant.* **2003**, *18*, 659–666.
13. Thalji, G.; Cooper, L.F. Molecular Assessment of Osseointegration in Vivo: A Review of the Current Literature. *Int. J. Oral Maxillofac. Implant.* **2013**, *28*, e521–e534. [CrossRef]
14. Trisi, P.; Marcato, C.; Todisco, M. Bone-to-Implant Apposition with Machined and MTX Microtextured Implant Surfaces in Human Sinus Grafts. *Int. J. Periodontics Restor. Dent.* **2003**, *23*, 427–437.
15. Lange, R.; Lüthen, F.; Beck, U.; Rychly, J.; Baumann, A.; Nebe, B. Cell-Extracellular Matrix Interaction and Physico-Chemical Characteristics of Titanium Surfaces Depend on the Roughness of the Material. *Biomol. Eng.* **2002**, *19*, 255–261. [CrossRef] [PubMed]
16. Hench, L.L. The Story of Bioglass®. *J. Mater. Sci. Mater. Med.* **2006**, *17*, 967–978. [CrossRef]
17. Hench, L.L. (Ed.) *An Introduction to Bioceramics*, 2nd ed.; Imperial College Press: London, UK, 2013; ISBN 978-1-908977-15-1.
18. Bano, S.; Romero, A.R.; Grant, D.M.; Nommeots-Nomm, A.; Scotchford, C.; Ahmed, I.; Hussain, T. In-Vitro Cell Interaction and Apatite Forming Ability in Simulated Body Fluid of ICIE16 and 13–93 Bioactive Glass Coatings Deposited by an Emerging Suspension High Velocity Oxy Fuel (SHVOF) Thermal Spray. *Surf. Coat. Technol.* **2021**, *407*, 126764. [CrossRef]

19. Al Mugeiren, O.M.; Baseer, M.A. Dental Implant Bioactive Surface Modifiers: An Update. *J. Int. Soc. Prev. Community Dent.* **2019**, *9*, 1. [CrossRef]
20. Hench, L.L.; Greenspan, D. Interactions between Bioactive Glass and Collagen: A Review and New Perspectives. *J. Aust. Ceram. Soc.* **2013**, *49*, 1–40.
21. Hammami, I.; Gavinho, S.R.; Pádua, A.S.; Graça, M.P.F.; Silva, J.C. Synthesis and Characterization of Iron Containing Bioactive Glass for Implants. In Proceedings of the 2022 E-Health and Bioengineering Conference (EHB), Iasi, Romania, 17–18 November 2022; IEEE: Piscataway, NJ, USA, 2022; pp. 1–4.
22. Hammami, I.; Gavinho, S.R.; Pádua, A.S.; Lança, M.d.C.; Borges, J.P.; Silva, J.C.; Sá-Nogueira, I.; Jakka, S.K.; Graça, M.P.F. Extensive Investigation on the Effect of Niobium Insertion on the Physical and Biological Properties of 45S5 Bioactive Glass for Dental Implant. *Int. J. Mol. Sci.* **2023**, *24*, 5244. [CrossRef]
23. Gavinho, S.R.; Pádua, A.S.; Sá-Nogueira, I.; Silva, J.C.; Borges, J.P.; Costa, L.C.; Graça, M.P.F. Biocompatibility, Bioactivity, and Antibacterial Behaviour of Cerium-Containing Bioglass®. *Nanomaterials* **2022**, *12*, 4479. [CrossRef] [PubMed]
24. Leung, Y.H.; Ng, A.M.; Xu, X.; Shen, Z.; Gethings, L.A.; Wong, M.T.; Chan, C.M.; Guo, M.Y.; Ng, Y.H.; Djurišić, A.B. Mechanisms of Antibacterial Activity of MgO: Non-ROS Mediated Toxicity of MgO Nanoparticles towards Escherichia Coli. *Small* **2014**, *10*, 1171–1183. [CrossRef] [PubMed]
25. Oliveira, R.L.; Barbosa, L.; Hurtado, C.R.; Ramos, L.d.P.; Montanheiro, T.L.; Oliveira, L.D.; Tada, D.B.; de Sousa Triches, E. Bioglass-Based Scaffolds Coated with Silver Nanoparticles: Synthesis, Processing and Antimicrobial Activity. *J. Biomed. Mater. Res. Part A* **2020**, *108*, 2447–2459. [CrossRef] [PubMed]
26. Mokhtari, S.; Wren, A.W.; Kazuo, S.M. Copper Containing Glass-Based Bone Adhesives for Orthopaedic Applications: Glass Characterization and Advanced Mechanical Evaluation. *bioRxiv* **2020**, bioRxiv:2020.11.19.390138. [CrossRef]
27. Applerot, G.; Lellouche, J.; Lipovsky, A.; Nitzan, Y.; Lubart, R.; Gedanken, A.; Banin, E. Understanding the Antibacterial Mechanism of CuO Nanoparticles: Revealing the Route of Induced Oxidative Stress. *Small* **2012**, *8*, 3326–3337. [CrossRef]
28. Baino, F. Copper-Doped Ordered Mesoporous Bioactive Glass: A Promising Multifunctional Platform for Bone Tissue Engineering. *Bioengineering* **2020**, *7*, 45. [CrossRef]
29. Chatterjee, A.K.; Chakraborty, R.; Basu, T. Mechanism of Antibacterial Activity of Copper Nanoparticles. *Nanotechnology* **2014**, *25*, 135101. [CrossRef]
30. Pizzino, G.; Irrera, N.; Cucinotta, M.; Pallio, G.; Mannino, F.; Arcoraci, V.; Squadrito, F.; Altavilla, D.; Bitto, A. Oxidative Stress: Harms and Benefits for Human Health. *Oxidative Med. Cell. Longev.* **2017**, *2017*, e8416763. [CrossRef]
31. Tavassolifar, M.J.; Vodjgani, M.; Salehi, Z.; Izad, M. The Influence of Reactive Oxygen Species in the Immune System and Pathogenesis of Multiple Sclerosis. *Autoimmune Dis.* **2020**, *2020*, e5793817. [CrossRef]
32. Hu, G. Copper Stimulates Proliferation of Human Endothelial Cells under Culture. *J. Cell. Biochem.* **1998**, *69*, 326–335. [CrossRef]
33. Gérard, C.; Bordeleau, L.-J.; Barralet, J.; Doillon, C.J. The Stimulation of Angiogenesis and Collagen Deposition by Copper. *Biomaterials* **2010**, *31*, 824–831. [CrossRef] [PubMed]
34. Rodríguez, J.P.; Ríos, S.; González, M. Modulation of the Proliferation and Differentiation of Human Mesenchymal Stem Cells by Copper. *J. Cell. Biochem.* **2002**, *85*, 92–100. [CrossRef] [PubMed]
35. Hoppe, A.; Meszaros, R.; Stähli, C.; Romeis, S.; Schmidt, J.; Peukert, W.; Marelli, B.; Nazhat, S.N.; Wondraczek, L.; Lao, J.; et al. In Vitro Reactivity of Cu Doped 45S5 Bioglass®Derived Scaffolds for Bone Tissue Engineering. *J. Mater. Chem. B* **2013**, *1*, 5659–5674. [CrossRef]
36. Ingle, A.P.; Duran, N.; Rai, M. Bioactivity, Mechanism of Action, and Cytotoxicity of Copper-Based Nanoparticles: A Review. *Appl. Microbiol. Biotechnol.* **2014**, *98*, 1001–1009. [CrossRef] [PubMed]
37. Soorani, M.; Mele, E.; Christie, J.K. Structural Effects of Incorporating Cu^{+} and Cu^{2+} Ions into Silicate Bioactive Glasses Using Molecular Dynamics Simulations. *Mater. Adv.* **2023**, *4*, 2078–2087. [CrossRef]
38. Kargozar, S.; Mozafari, M.; Ghodrat, S.; Fiume, E.; Baino, F. Copper-Containing Bioactive Glasses and Glass-Ceramics: From Tissue Regeneration to Cancer Therapeutic Strategies. *Mater. Sci. Eng. C* **2021**, *121*, 111741. [CrossRef]
39. Gupta, N.; Santhiya, D.; Murugavel, S.; Kumar, A.; Aditya, A.; Ganguli, M.; Gupta, S. Effects of Transition Metal Ion Dopants (Ag, Cu and Fe) on the Structural, Mechanical and Antibacterial Properties of Bioactive Glass. *Colloids Surf. A Physicochem. Eng. Asp.* **2018**, *538*, 393–403. [CrossRef]
40. Ibrahim, N.F.; Mohamad, H.; Noor, S.N.F.M. Characterization on Melt-Derived Bioactive Glass Powder from SiO2-CaO-Na2O-P2O5 System. *J. Non-Cryst. Solids* **2017**, *462*, 23–31. [CrossRef]
41. Ibrahim, N.F.; Mohamad, H.; Noor, S.N.F.M.; Ahmad, N. Melt-Derived Bioactive Glass Based on SiO2-CaO-Na2O-P2O5 System Fabricated at Lower Melting Temperature. *J. Alloys Compd.* **2018**, *732*, 603–612. [CrossRef]
42. El-Rashidy, A.A.; Roether, J.A.; Harhaus, L.; Kneser, U.; Boccaccini, A.R. Regenerating Bone with Bioactive Glass Scaffolds: A Review of in Vivo Studies in Bone Defect Models. *Acta Biomater.* **2017**, *62*, 1–28. [CrossRef]
43. Boccaccini, A.R.; Chen, Q.; Lefebvre, L.; Gremillard, L.; Chevalier, J. Sintering, Crystallisation and Biodegradation Behaviour of Bioglass®-Derived Glass–Ceramics. *Faraday Discuss.* **2007**, *136*, 27–44. [CrossRef]
44. Dziadek, M.; Zagrajczuk, B.; Jelen, P.; Olejniczak, Z.; Cholewa-Kowalska, K. Structural Variations of Bioactive Glasses Obtained by Different Synthesis Routes. *Ceram. Int.* **2016**, *42*, 14700–14709. [CrossRef]
45. Saleem, M.F.; Haleem, Y.A.; Sun, W.; Ma, L.; Wang, D. Surface-Enhanced Resonance Raman Scattering in Partially Oxidized Thin Copper Film. *J. Raman Spectrosc.* **2020**, *51*, 1286–1294. [CrossRef]

46. Sriyutha Murthy, P.; Venugopalan, V.P.; Arunya, D.D.; Dhara, S.; Pandiyan, R.; Tyagi, A.K. Antibiofilm Activity of Nano Sized CuO. In Proceedings of the International Conference on Nanoscience, Engineering and Technology, ICONSET 2011, Chennai, India, 28–30 November 2011; pp. 580–583. [CrossRef]
47. Araujo, M.S.; Silva, A.C.; Bartolomé, J.F.; Mello-Castanho, S. Structural and Thermal Behavior of 45S5 Bioglass®-Based Compositions Containing Alumina and Strontium. *J. Am. Ceram. Soc.* **2020**, *103*, 3620–3630. [CrossRef]
48. Gavinho, S.R.; Melo, B.M.G.; Borges, J.P.; Silva, J.C.; Graça, M.P.F. Thermal, Structural, Morphological and Electrical Characterization of Cerium-Containing 45S5 for Metal Implant Coatings. *Coatings* **2023**, *13*, 294. [CrossRef]
49. Jiménez, J.A. Efficient Stabilization of Cu^{+} Ions in Phosphate Glasses via Reduction of Cu^{2+} by Sn^{2+} during Ambient Atmosphere Melting. *J. Mater. Sci.* **2014**, *49*, 4387–4393. [CrossRef]
50. Yasumori, A.; Tada, F.; Yanagida, S.; Kishi, T. Yellow Photoluminescence Properties of Copper Ion Doped Phase–Separated Glasses in Alkali Borosilicate System. *J. Electrochem. Soc.* **2012**, *159*, J143. [CrossRef]
51. Ibrahim, S.; Hamdy, Y.M.; Darwish, H.; Ali, A.A. Effect of CuO Doping on Structural Features, Optical Absorption and Photoluminescence Behavior of ZnO-Based Glasses. *J. Mater. Sci. Mater. Electron.* **2023**, *34*, 899. [CrossRef]
52. Figgis, B.N. *Introduction to Ligand Fields*; Interscience Publishers: Geneva, Switzerland, 1966.
53. Rajyasree, C.h.; Vinaya Teja, P.M.; Murthy, K.V.R.; Krishna Rao, D. Optical and Other Spectroscopic Studies of Lead, Zinc Bismuth Borate Glasses Doped with CuO. *Phys. B Condens. Matter* **2011**, *406*, 4366–4372. [CrossRef]
54. Kashif, I.; Ratep, A. Blue, Red, and Green Emission from Chromium and Copper Metal Doped Lithium Borate Glass. *IOP Conf. Ser. Mater. Sci. Eng.* **2020**, *956*, 012013. [CrossRef]
55. Kaur, G.; Sriranganathan, N.; Waldrop, S.G.; Sharma, P.; Chudasama, B.N. Effect of Copper on the Up-Regulation/down-Regulation of Genes, Cytotoxicity and Ion Dissolution for Mesoporous Bioactive Glasses. *Biomed. Mater.* **2017**, *12*, 045020. [CrossRef]
56. Milkovic, L.; Hoppe, A.; Detsch, R.; Boccaccini, A.R.; Zarkovic, N. Effects of Cu-Doped 45S5 Bioactive Glass on the Lipid Peroxidation-Associated Growth of Human Osteoblast-like Cells in Vitro. *J. Biomed. Mater. Res. Part A* **2014**, *102*, 3556–3561. [CrossRef]
57. Hohenbild, F.; Arango-Ospina, M.; Moghaddam, A.; Boccaccini, A.R.; Westhauser, F. Preconditioning of Bioactive Glasses before Introduction to Static Cell Culture: What Is Really Necessary? *Methods Protoc.* **2020**, *3*, 38. [CrossRef] [PubMed]
58. Ciraldo, F.E.; Boccardi, E.; Melli, V.; Westhauser, F.; Boccaccini, A.R. Tackling Bioactive Glass Excessive in Vitro Bioreactivity: Preconditioning Approaches for Cell Culture Tests. *Acta Biomater.* **2018**, *75*, 3–10. [CrossRef] [PubMed]
59. Hu, S.; Chang, J.; Liu, M.; Ning, C. Study on Antibacterial Effect of 45S5 Bioglass®. *J. Mater. Sci. Mater. Med.* **2009**, *20*, 281–286. [CrossRef]
60. Mashitah, M.D.; San Chan, Y.; Jason, J. Antimicrobial Properties of Nanobiomaterials and the Mechanism. In *Nanobiomaterials in Antimicrobial Therapy*; Elsevier: Amsterdam, The Netherlands, 2016; pp. 261–312.
61. Allan, I.; Newman, H.; Wilson, M. Antibacterial Activity of Particulate Bioglass®against Supra-and Subgingival Bacteria. *Biomaterials* **2001**, *22*, 1683–1687. [CrossRef] [PubMed]
62. Drago, L.; Toscano, M.; Bottagisio, M. Recent Evidence on Bioactive Glass Antimicrobial and Antibiofilm Activity: A Mini-Review. *Materials* **2018**, *11*, 326. [CrossRef]
63. Vincent, M.; Duval, R.E.; Hartemann, P.; Engels-Deutsch, M. Contact Killing and Antimicrobial Properties of Copper. *J. Appl. Microbiol.* **2018**, *124*, 1032–1046. [CrossRef]
64. Bari, A.; Bloise, N.; Fiorilli, S.; Novajra, G.; Vallet-Regí, M.; Bruni, G.; Torres-Pardo, A.; González-Calbet, J.M.; Visai, L.; Vitale-Brovarone, C. Copper-Containing Mesoporous Bioactive Glass Nanoparticles as Multifunctional Agent for Bone Regeneration. *Acta Biomater.* **2017**, *55*, 493–504. [CrossRef]
65. Raffi, M.; Mehrwan, S.; Bhatti, T.M.; Akhter, J.I.; Hameed, A.; Yawar, W. Investigations into the Antibacterial Behavior of Copper Nanoparticles against Escherichia Coli. *Ann. Microbiol.* **2010**, *60*, 75–80. [CrossRef]
66. Akhtach, S.; Tabia, Z.; El Mabrouk, K.; Bricha, M.; Belkhou, R. A Comprehensive Study on Copper Incorporated Bio-Glass Matrix for Its Potential Antimicrobial Applications. *Ceram. Int.* **2021**, *47*, 424–433. [CrossRef]
67. Solioz, M. Copper Oxidation State and Mycobacterial Infection. *Mycobact. Dis.* **2016**, *6*, 1000210. [CrossRef]
68. Mathews, S.; Kumar, R.; Solioz, M. Copper Reduction and Contact Killing of Bacteria by Iron Surfaces. *Appl. Environ. Microbiol.* **2015**, *81*, 6399–6403. [CrossRef] [PubMed]
69. Hans, M.; Erbe, A.; Mathews, S.; Chen, Y.; Solioz, M.; Mücklich, F. Role of Copper Oxides in Contact Killing of Bacteria. *Langmuir* **2013**, *29*, 16160–16166. [CrossRef] [PubMed]
70. Dorozhkin, S.V.; Epple, M. Biological and Medical Significance of Calcium Phosphates. *Angew. Chem. Int. Ed.* **2002**, *41*, 3130–3146. [CrossRef]
71. Plewinski, M.; Schickle, K.; Lindner, M.; Kirsten, A.; Weber, M.; Fischer, H. The Effect of Crystallization of Bioactive Bioglass 45S5 on Apatite Formation and Degradation. *Dent. Mater.* **2013**, *29*, 1256–1264. [CrossRef]
72. Boukha, Z.; Yeste, M.P.; Cauqui, M.Á.; González-Velasco, J.R. Influence of Ca/P Ratio on the Catalytic Performance of Ni/Hydroxyapatite Samples in Dry Reforming of Methane. *Appl. Catal. A Gen.* **2019**, *580*, 34–45. [CrossRef]
73. Beaufils, S.; Rouillon, T.; Millet, P.; Le Bideau, J.; Weiss, P.; Chopart, J.-P.; Daltin, A.-L. Synthesis of Calcium-Deficient Hydroxyapatite Nanowires and Nanotubes Performed by Template-Assisted Electrodeposition. *Mater. Sci. Eng. C* **2019**, *98*, 333–346. [CrossRef]

Journal of
Functional
Biomaterials

MDPI

Article

Microwave-Assisted Hydrothermal Treatment of Multifunctional Substituted Hydroxyapatite with Prospective Applications in Bone Regeneration

Alexandra-Cristina Burdusel [1,2], Ionela Andreea Neacsu [1,2,*], Alexandra Catalina Birca [1,2], Cristina Chircov [1,2], Alexandru-Mihai Grumezescu [1,2,3], Alina Maria Holban [3,4], Carmen Curutiu [3,4], Lia Mara Ditu [3,4], Miruna Stan [3,5] and Ecaterina Andronescu [1,2]

[1] Department of Science and Engineering of Oxide Materials and Nanomaterials, Faculty of Chemical Engineering and Biotechnologies, University Politehnica of Bucharest, 1–7 Gheorghe Polizu Street, 011061 Bucharest, Romania
[2] Academy of Romanian Scientists, Splaiul Independentei 54, 050044 Bucharest, Romania
[3] Research Institute of the University of Bucharest—ICUB, University of Bucharest, 050657 Bucharest, Romania
[4] Department of Microbiology and Immunology, Faculty of Biology, University of Bucharest, 077206 Bucharest, Romania
[5] Department of Biochemistry and Molecular Biology, Faculty of Biology, University of Bucharest, 050095 Bucharest, Romania
* Correspondence: ionela.neacsu@upb.ro

Abstract: Orthopedic bone graft infections are major complications in today's medicine, and the demand for antibacterial treatments is expanding because of the spread of antibiotic resistance. Various compositions of hydroxyapatite (HAp) in which Calcium (Ca^{2+}) ions are substituted with Cerium (Ce^{3+}) and Magnesium (Mg^{2+}) are herein proposed as biomaterials for hard tissue implants. This approach gained popularity in recent years and, in the pursuit of mimicking the natural bone mineral's composition, over 70 elements of the Periodic Table were already reported as substituents into HAp structure. The current study aimed to create materials based on HAp, Hap-Ce, and Hap-Mg using hydrothermal maturation in the microwave field. This route has been considered a novel, promising, and effective way to obtain monodisperse, fine nanoparticles while easily controlling the synthesis parameters. The synthesized HAp powders were characterized morphologically and structurally by XRD diffraction, Dynamic light scattering, zeta potential, FTIR spectrometry, and SEM analysis. Proliferation and morphological analysis on osteoblast cell cultures were used to demonstrate the cytocompatibility of the produced biomaterials. The antimicrobial effect was highlighted in the synthesized samples, especially for hydroxyapatite substituted with cerium. Therefore, the samples of HAp substituted with cerium or magnesium are proposed as biomaterials with enhanced osseointegration, also having the capacity to reduce device-associated infections.

Keywords: hydroxyapatite; magnesium; cerium; bone regeneration

1. Introduction

The main components of a mineralized bone matrix include a calcium phosphate crystal, hydroxyapatite, and various organic materials [1]. Hydroxyapatite (HAp, $Ca_{10}(PO_4)_6(OH)_2$) is among the most promising crystalline calcium phosphate considered to be biomaterial due to its chemical resemblance to the inorganic part of human hard tissues such as bone and teeth [2–4]. Stoichiometric and pure HAp crystallizes in the monoclinic system, and it most often crystallizes in the hexagonal system at over 250 °C and thermally decomposes at temperatures between 800 and 1200 °C [5,6]. Bone hydroxyapatite has a small dimensional structure, about 25 nm wide, 50 nm long, and 10 nm high [7]. Due to their quicker growth and development, small microcrystals are favorable for bone regeneration and repair when rapid mineralization is needed, as well as for postnatal and embryonic

bone development. In addition, these tiny nanoscale crystals have a high surface area-to-volume ratio and are quickly dispersed by the fluid around them in response to particular circumstances. In the course of homeostatic bone remodeling, the particular crystalline shape of bone hydroxyapatite may promote effective bone demineralization and resorption by osteoclasts [8–10].

Hap and other calcium phosphates have long been investigated as biological agents for the treatment and diagnosis of bone diseases due to their qualities such as biocompatibility, osteoconductivity, similarity to the bone mineral phase, and osteogenic activity that ensure a high affinity of these materials for bone tissues [11–13]. This affinity is being studied intensively to develop specific delivery systems of biologically active molecules for bone metastases, osteosarcoma, and other bone diseases [14], enabling theranostic applications. In addition, by functionalizing the hydroxyapatite surface with some specific molecules, more accurate delivery to bone tissues is possible [15–18].

The use of metal ions can be an appropriate alternative for improving HAp because they have high stability and broad antibacterial spectra [19,20]. Magnesium represents a very innovative option for the development of antibacterial bone grafts, as it shows powerful antibacterial activity in certain doses and is highly biocompatible [21–23]. The introduction of magnesium into the synthesis reduced bacterial development and biofilm formation in hydroxyapatite-based bone substitutes [13,14]. Moreover, the materials in their composition, magnesium ions, are beneficial for bone regeneration mechanisms, as this compound hastens the healing of bone defects by improving the differentiation and proliferation of osteoblasts [24]. Due to its mechanical and osteopromoting qualities, magnesium (Mg)-based biomaterials have been employed as orthopedic implants for a very long time [25–27]. Additionally, their benefits over comparable standard products have been thoroughly studied, with Mg-based alloys, bioceramics [28], bioglass [29], and polymer composites [30], all demonstrating unique superiority in hastening bone formation and fracture healing [31]. Mg-based bioceramics may provide various advantages as biodegradable bone graft alternatives since they can progressively break down and be replaced by fresh bone [32]. Magnesium incorporation for Mg-based polymeric materials not only overcomes acid degradation products but also enhances osteopromoting activity [33]. According to earlier research, magnesium ions (Mg^{2+}) have an impact on the pace at which calcium phosphate crystallizes off the surface of bones and the subsequent development of hydroxyapatite [34–36]. Additionally, the usage of degradable magnesium metals and alloys produces osteogenic differentiation and osteoblast development, which is induced by Mg^{2+} and promotes bone regeneration [37]. On the other hand, Mg^{2+} shortage (about 0.04–10%) inhibits bone formation by reducing osteoblasts and bone volume and increasing osteoclastic bone resorption as a result of increased proinflammatory cytokine release [38,39].

Cerium, a different metal ion with antibacterial properties, can reduce cytokine levels, decrease inflammation, and give cellular protection in vitro and in vivo, which implies that it may have anti-inflammatory effects on designed tissues. Among the various calcium cationic substitution ions in the hydroxyapatite structure, the Ce ion substitution has been actively investigated [40,41], with HAp-Ce(III) being reported to exhibit silver-like bacteriostatic properties [42–44]. Recently, cerium has also been found to have multi-enzymatic properties that make it attractive for biological applications. The biological effects of cerium oxide have been studied, and it has been demonstrated that by directly altering the levels of oxygen in intracellular settings, it is capable of inducing angiogenesis. But it can induce local inflammatory reactions when using a high concentration (over 3.5% CeO_2) [45,46]. Since the electronegativity and radius of Ce^{3+} are 1.06 and 0.107 nm, respectively, close to those of Ca^{2+} ion (1.01 and 0.100 nm), it can displace Ca^{2+} and penetrate the HAp network to form Ce^{3+} substituted HAp (Ce-HAp), that may result in increased solubility, which may, enhance the antibacterial effect and biodegradability [47]. Compared to other metal ions, Ce^{3+} ions have shown great results as antibacterial agents used in medicine for a long time due to their wide range of antibacterial activity (*Escherichia*

coli, *Salmonella typhimurium*, *Bacillus subtilis*, and *Enterococcus faecalis*) [48]. Cerium-based biomaterials represent a new element in research due to the low level of Ce^{3+} ions that do not harm human cells, as well as due to a long-lasting biocide and excellent thermal stability [49].

To increase and improve the range of possible uses for functional nanomaterials, it is crucial to create quick, easy, and environmentally friendly synthetic methodologies [50]. In the present work, hydroxyapatite substituted with cerium and magnesium was obtained through an unconventional, microwave-assisted hydrothermal method. This route has been recently considered a novel, promising, and effective way to obtain monodisperse, fine nanoparticles while easily controlling the synthesis parameters (e.g., initial pressure in the autoclave, the maximum temperature, and heating rate, time). In comparison with the traditional hydrothermal method, the microwave-assisted improved version has several advantages, with great impact on the final material's properties: (i) homogenous heating in the entire volume of the reaction mixture, without temperature gradients leading to non-homogeneity in particle size and morphology; (ii) rapid heating, due to the microwave irradiation of the polar molecules normally used in the chemical reactions (water, alcohol); (iii) reduced reaction time and energy consumption. As a result, the obtained HA powders have reduced particle size, increased purity, and a narrower size distribution compared with other methods [51,52].

2. Materials and Methods

2.1. Reagents and Chemicals

The chemicals used to accomplish the experiments are as follows: $(NH_4)_2HPO_4$ (98%) from Sigma–Aldrich, $Ca(NO_3)_2{*}4H_2O$ (99%), NH_4OH (25% solution), $Ce(NO_3)_3{*}6H_2O$ (99%), $Mg(NO_3)_2{*}6H_2O$ (99%) from Fluka—Honeywell Research Chemicals, and ultrapure water.

2.2. Pristine Hydroxyapatite Synthesis

The synthesis of hydroxyapatite was carried out by co-precipitation followed by hydrothermal maturation in a microwave field using the synthWAVE equipment (Milestone Srl, Sorisole, Bergamo, Italy). The operating principle of the equipment is as follows: the reagents are poured into the vials on a rotating support, which will be closed tightly using Teflon caps. The second step is the automatic lowering of the mechanical stirrer. The vials are positioned in a liquid capable of absorbing microwaves (usually water), thus allowing the transfer of energy and heat to the samples. The chamber containing the samples is automatically clamped and pressurized using nitrogen to prevent the boiling of the solvents. At the end of the reaction, an integrated cooling device rapidly lowers the temperature in the chamber where the vials are located. The benefits of the method are the ease of the method and the short synthesis time, the reproduction of the conditions developed in the small-scale reactions, and the modification of the parameters easily.

Calcium nitrate tetrahydrate and diammonium phosphate acid powders, corresponding to a Ca/P ratio of 1.67 (specific to HAp), were solubilized in distilled water under magnetic stirring. The phosphate precursor was added dropwise over the $Ca(NO_3)_2{*}4H_2O$, maintaining magnetic stirring. Since the conditions for obtaining hydroxyapatite involve an alkaline medium, the pH of the reaction mixture was monitored and adapted to the range of 10–10.5 by dropping ammonium hydroxide solution 25 wt.%. After reaching this value, the mixture was poured into the containers of microwave-assisted equipment and subjected to hydrothermal maturation. To study the effect of this treatment on the obtained materials, the temperature was varied as a reaction parameter. Thus, a previously obtained mixture was subjected to treatment at 150 °C, respectively another at 250 °C, at an initial pressure of 2 bars for 30 min in both cases.

After this step, the hydroxyapatite was separated by filtration and washed with distilled water until a neutral pH was fulfilled. Finally, the resulting precipitates were dried

in an oven at 60 °C for 24 h, and the resulting materials were further referenced according to the varied synthesis parameter (temperature), as follows: HAp_150, respectively HAp_250.

2.3. Substituted Hydroxyapatite Synthesis

In the case of the synthesis of hydroxyapatite substituted with cerium (Ce^{3+}) or magnesium (Mg^{2+}) ions, the process is similar to the one mentioned above for obtaining HAp. The new factor involved in this process is represented by the addition of the substituents precursors—$Ce(NO_3)_3$*$6H_2O$ or $Mg(NO_3)_2$*$6H_2O$, corresponding to different Ca^{2+} substitution molar ratio (1, 3, and 5%) in the initial mixture of reaction, along with $Ca(NO_3)_2$*$4H_2O$.

Each time, two solutions were prepared, the first resulting from the mixture of $Ca(NO_3)_2$*$4H_2O$ with 200 mL of distilled water and the stoichiometric amount of Ce/Mg precursor, and the second solution from the mixture of diammonium acid phosphate $(NH_4)_2HPO_4$ with 200 mL of distilled water. The next step consisted in dropping the second solution over the first solution under magnetic stirring, and the mixture thus obtained was subjected to hydrothermal maturation in the microwave field. In this case, the temperature of 150 °C was chosen based on the characterization results of pristine HAp (although HAp_150 presented a considerably reduced crystallinity, the average crystallite size proved to be lower, an advantage in the case of bone regeneration materials).

The obtained precipitate was filtered, washed with distilled water to reduce the pH of 10 to a physiological one of 7–7.5, and then was left to dry in an oven at 60 °C for 24 h. The resulting materials are further referenced according to the varied synthesis parameters (substituent and concentration), as follows: HAp_Ce_1%, HAp_Ce_3%, HAp_Ce_5%, HAp_Mg_1%, HAp_Mg_3%, HAp_Mg_5%.

2.4. Morphological and Structural Characterization

2.4.1. X-ray Diffraction

In order to determine the individual crystalline phases that made up the produced powders, the X-ray diffraction technique was used for analysis. In order to complete this, a PANalytical Empyrean diffractometer from Malvern PANalytical in Bruno, The Netherlands, was employed. It was outfitted with a hybrid monochromator (2xGe 220) on the incident side and a parallel plate collimator set on a PIXcel 3D detector on the diffracted side. At room temperature, with an incidence angle of 0.5° for Bragg angle values of 2 between 10° and 80°, an acquisition period of 255 s, a step of 0.01414°, and Cu K radiation with an angle of incidence of 1.5406° (40 mA and 45 kV), X-ray diffraction measurements analysis were accomplished. In order to ascertain the average crystallite size, unit cell parameters, and crystallinity of the examined powders, the diffractograms were further submitted to Rietveld refinement using the HighScore Plus program (version 3.0e, PANalytical B.V. Almelo, The Netherlands). The diffractogram fits were deemed acceptable if the goodness of fit was lower than 4.

2.4.2. Dynamic Light Scattering (DLS) and Zeta Potential

Each series of hydroxyapatite nanoparticles synthesized using different parameters of microwave-assisted hydrothermal treatment and/or substituted with cerium and magnesium ions at different concentrations was characterized by dynamic light scattering (DLS) technique and zeta potential in order to establish the hydrodynamic diameter and surface charges. The measurements were made using the DelsaMax Pro light scattering analyzer (Backman Coulter, Brea, CA, USA), having as a component a laser with a wavelength of 532 nm. The powders were distributed in ultrapure water at a concentration of 0.33 mg/mL at room temperature. To achieve a homogeneous dispersion, all samples were subjected to ultrasound for 10 min using an ultrasound bath.

2.4.3. Scanning Electron Microscopy (SEM)

The QUANTA INSPECT F50 scanning electron microscope (Thermo Fisher, Eindhoven, The Netherlands) was used for the scanning electron microscopy (SEM). It is equipped

with an energy-dispersive X-ray spectrometer (EDS) with a resolution at MnK of 133 eV and a field emission electron gun (FEG) with a resolution of 1.2 nm. The powdery samples were set on slide supports with the use of carbon tape in order to analyze the shape and size; they were then placed into the microscope analysis chamber, where the images were captured by recording the ensuing secondary electrons.

2.4.4. Fourier-Transform Infrared Spectroscopy (FT-IR)

Thermo Nicolet's Nicolet 6700 (Thermo Fisher Scientific, Waltham, MA, USA) FT-IR spectrometer's ZnSe crystal was used to evaluate a small sample of powder in order to look into the functional groups that are typical of the produced nanoparticles. The analysis was completed at room temperature using 32 scans of the material at a resolution of 4 cm^{-1} between 4000 and 1000 cm^{-1}. It was able to record the data obtained by connecting the spectrometer to a data collection and processing device using the Omnic work program. (Thermo Nicolet, Version 8.2).

2.5. In Vitro Interactions with Osteoblast Cells

In full Dulbecco's Modified Eagle's Medium supplemented with 10% fetal bovine serum, mouse osteoblasts MC3T3-E1 were cultured at 37 °C in a humidified environment with 5% CO_2. At a cell density of 5 × 104 cells per cm^2, the cells were planted in 96-well plates and allowed to adhere for the night. These were then sterilized under UV irradiation and incubated with 25, 100, and 250 g/mL HAap samples over the following 24 or 72 h. All in vitro tests were conducted using untreated cells as a control.

2.5.1. Cell Viability Assay

The cellular proliferation was measured using the 3-(4,5-dimethylthiazol-2-yl)-2,5-diphenyltetrazolium bromide (MTT; Sigma-Aldrich, Saint Louis, MO, USA) assay based on the succinate dehydrogenase mitochondrial activity in the viable cells. After 24 and 72 h of incubation, the culture medium was removed, and the cells were incubated with 1 mg/mL MTT for 2 h in the incubator at 37 °C. The purple formazan crystals formed in the viable cells were dissolved with 2-propanol (Sigma-Aldrich, Saint Louis, MO, USA), and the absorbance was measured at 595 nm using FlexStation 3 multi-mode microplate reader from Molecular Devices (San Jose, CA, USA).

2.5.2. Griess Assay

Nitric oxide (NO) content in the culture medium that had been previously collected after 24 and 72 h of incubation was measured using the Griess reagent, a stoichiometric solution (*v/v*) of 0.1% naphthyl ethylenediamine dihydrochloride and 1% sulphanilamide in 5% H_3PO_4. Enhanced NO levels are associated with cytotoxic effects because they are directly linked to inflammatory and apoptotic processes. The FlexStation 3 multi-mode microplate reader was used to quantify the absorbance of the solutions as they were acquired at 550 nm. The $NaNO_2$ standard curve was used to compute the NO concentration.

2.5.3. Fluorescence Microscopy

Following each incubation period, the osteoblasts were permeabilized for an hour using 0.1% Triton X-100/2% bovine serum albumin (BSA) and fixed with 4% paraformaldehyde for 20 min. The nuclei were counterstained with 2 g/mL DAPI (4′,6-diamino-2-phenylindole) after the actin filaments had been stained with 10 g/mL phalloidin-FITC (fluorescein isothiocyanate). The Olympus IX71 inverted fluorescent microscope (Olympus, Tokyo, Japan) was used to study the cells.

2.6. Microbiological Evaluation

The ATCC strains used for this study are *Staphylococcus aureus*, *Enterococcus faecalis* (Gram-positive), *Escherichia coli*, *and Pseudomonas aeruginosa*) (Gram-negative), and yeast

(*Candida albicans*) were obtained from the strain collection of the Microbiology laboratory, Faculty of Biology, University of Bucharest.

2.6.1. MIC (Minimum Inhibitory Concentration) Method

A quantitative approach based on serial binary microdilutions in a liquid medium (simple broth), uniformly distributed in 96-well plates, was utilized to calculate the MIC. An amount of the bioactive chemical or nanosystem equal to a concentration of 5 mg/mL was applied to the first well of each row. A micropipette was then used to make 10 binary dilutions, starting with well 1 (concentration of 5 mg/mL) and ending with well 10 (where the ultimate concentration will be 0.009765625 mg/L). Wells 11 and 12 were then used as positive control (medium containing bacteria) and negative control (medium devoid of bacteria), respectively. A total of 15 L of 0.5 McFarland density microbial suspension were then added to each well following the microdilutions. The seeded plates were incubated for 24 h at 37° Celsius, and following incubation, the MIC value for each compound or nanosystem was determined macroscopically as the point at which microbial growth or the emergence of turbidity in the environment was no longer visible [53].

2.6.2. Development of Monospecific Biofilms

A quantitative approach based on the execution of binary serial microdilutions in a liquid medium (simple broth) dispersed sterile in 96-well plates was used to determine the impact of the acquired biomaterials on the development of biofilms. An amount of the bioactive chemical or nanosystem equal to a concentration of 5 mg/mL was applied to the first well of each row. Later, 12 binary dilutions were performed using a micropipette, commencing with well 1 (concentration 5 mg/mL) and ending with well 10 (final concentration 0.009765625 mg/mL). A total of 15 L of 0.5 McFarland density microbial suspension were then added to each well following the microdilutions. The seeded plates were incubated for 24 h at 37 degrees Celsius. Following incubation, the biofilms were thoroughly washed three times with sterile physiological water (AFS) and fixed for 5 min with cold methanol.

The dry plates were dyed with 1% crystal violet solution for 20 min after the methanol had been removed. With a 100× magnification, an inverted microscope was used to examine the dyed biofilms. Instead, after staining, the excess dye was removed with tap water, and the dye present in the cells of the biofilm that had grown on the well's walls was then soluble in a solution of 33% acetic acid. In order to understand the data based on the spectrophotometric reading of the colored suspension's absorbance at 490 nm, suspensions were prepared in this manner.

3. Results

3.1. X-ray Diffraction

Figure 1a shows the X-ray diffractograms for the hydroxyapatite powders synthesized using different microwave-assisted hydrothermal treatment parameters. As can be seen, the only crystalline phase identified is hydroxyapatite in the hexagonal crystallization system P63/m, according to ICSD file 01-073-8419. However, increasing the temperature leads to an increase in the crystallinity of the samples, shown by the high intensity of the corresponding diffraction peaks. Figure 1b shows the X-ray diffractograms for cerium ion-substituted hydroxyapatite powders at 1, 3, and 5% concentrations. As can be seen, boosting the concentration of the substituent leads to a decrease in the intensity of the diffraction peaks and, implicitly, in the crystallinity of the sample. However, the only crystalline phase identified is hydroxyapatite, which confirms the success of the substitution reaction by the absence of the formation of other phases, such as cerium oxide or cerium phosphate. In the case of substitution with magnesium ions at concentrations of 1, 3, and 5%, the diffractograms show different behavior compared to the case of substitution with cerium (Figure 1c, Table 1). On the one hand, 1 and 3% concentrations do not produce considerable differences in the powders' crystallinity but reduce the crystallite's average size. However, in the case of the 5% substituted hydroxyapatite sample, the appearance

of new diffraction maxima attributed to the magnesium whitlockite crystalline phase, a mixed calcium and magnesium phosphate with the chemical formula $Ca_9Mg(HPO_4)(PO_4)_6$ (ICSD 04-008)-8604). In this case, the average crystallite size attributed to hydroxyapatite decreases insignificantly; the expansion in the degree of crystallinity is associated with the large crystallite size related to whitlockite. Despite the development of a new phase, the applicability of magnesium ion-substituted hydroxyapatite powder at a concentration of 5% in the medical field is justified by the abundance of this phase in natural bone [54,55].

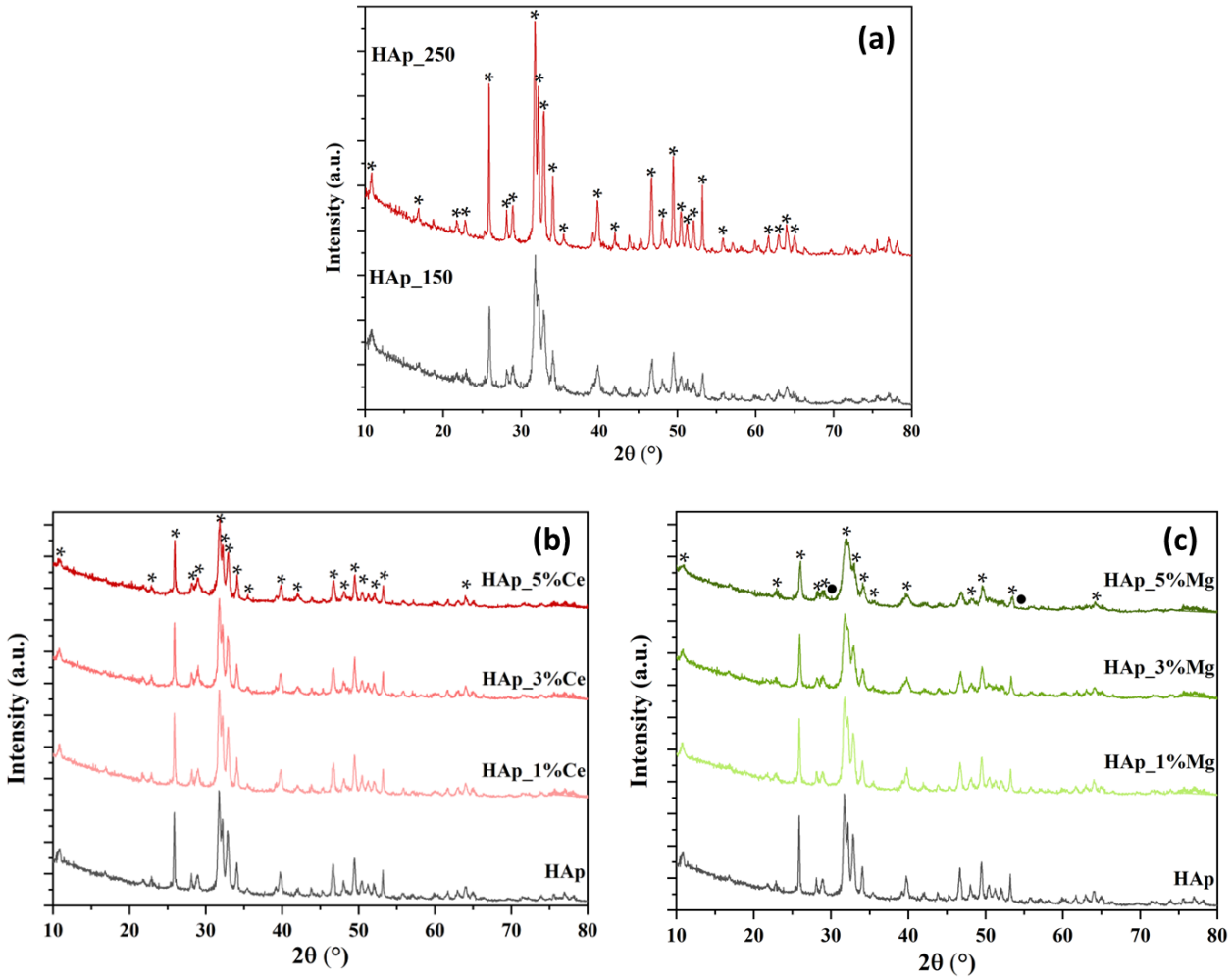

Figure 1. X-ray diffractogram for hydroxyapatite powders synthesized at different parameters of microwave-assisted hydrothermal treatment (**a**) and hydroxyapatite powders substituted with cerium (**b**) and magnesium (**c**) ions at concentrations of 1, 3, and 5% (*—HAp, •—Whitlockite).

The results obtained from Rietveld refinement (Table 1) confirm the increase in crystallinity of the sample with increasing temperature. Moreover, the high crystallinity of the sample treated at the temperature of 250 °C is due to the increase in crystallite size, a natural process encountered in this type of synthesis. Specifically, with the increase in pressure, temperature, or reaction time, the size of the crystallites and, implicitly, of the nanoparticles increases proportionally. The results of the Rietveld refinement confirm the previous observations, namely the reduction of the crystallinity of the powders concomitant with the decrease of the crystallite size, are presented in Table 1.

Table 1. Unit cell parameters, average crystallite size, and crystallinity of hydroxyapatite powders substituted with cerium and magnesium ions at concentrations of 1, 3, and 5% according to Rietveld refinement.

Sample	Unit Cell Parameters						Average Crystallite Size [nm]	Crystallinity [%]
	a [Å]	b [Å]	c [Å]	α [°]	β [°]	γ [°]		
HAp_150	9.431	9.431	6.880	90	90	120	18.65	27.45
HAp_250	9.425	9.425	6.880	90	90	120	46.13	40.49
HAp_Ce_1%	9.444	9.444	6.877	90	90	120	16.15	22.99
HAp_Ce_3%	9.449	9.449	6.873	90	90	120	12.16	21.13
HAp_Ce_5%	9.455	9.455	6.865	90	90	120	10.42	18.31
HAp_Mg_1%	9.446	9.446	6.878	90	90	120	12.81	25.50
HAp_Mg_3%	9.446	9.446	6.876	90	90	120	12.79	26.54
HAp_Mg_5%								
* HAp 50.1%	9.450	9.450	6.878	90	90	120	12.23	30.99
• Whitlockit 49.9%	10.419	10.419	37.292	90	90	120	49.54	

3.2. Dynamic Light Scattering (DLS) and Zeta Potential

Figure 2 shows the hydrodynamic diameter values of hydroxyapatite nanoparticles treated at two distinct temperatures (150 °C and 250 °C). In this context, the hydrodynamic diameter is lower for the sample treated at 250 °C, which may be due to larger particle size and, consequently, a reduced surface reactivity that would lead to particle agglomeration. The results are confirmed by the zeta potential values (Figure 2), where more negative values are recorded for this sample, so increased stability prevents particle aggregation. Additionally, the results follow the hypothesis behind the hydrothermal treatment of the nanoparticles, as higher temperatures are expected to generate particle growth. However, the differences between the two samples in terms of stability are not significant.

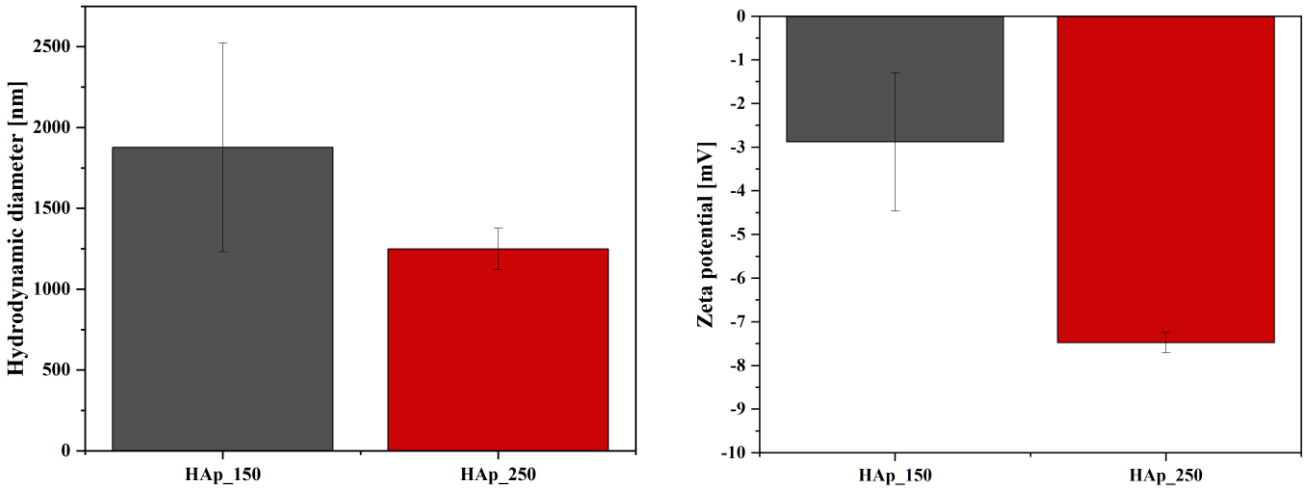

Figure 2. Hydrodynamic diameter and zeta potential values for hydroxyapatite treated at 150 and 250 °C.

Figure 3 shows the hydrodynamic diameter values of hydroxyapatite nanoparticles substituted with cerium and magnesium ions at concentrations of 1, 3, and 5%. Thus, the high degree of agglomeration can be observed in the case of all the samples, a fact also

confirmed by the low values of the zeta potential (Figure 3). Furthermore, in both types of substitutions, increasing concentrations lead to the increase of the zeta potential values, i.e., from negative values to positive values. However, the substitution with cerium ions at the concentration of 1% seems to increase the stability of the hydroxyapatite nanoparticles, also shown by the hydrodynamic diameter values. Further increasing the substitution concentration leads to a decrease in nanoparticle stability, as the zeta potential values are close to 0 mV with no significant differences between the 3% and 5% concentrations, and in nanoparticle size, as compared to the HAp_150 sample. However, the presence of whitlockite at the level of the hydroxyapatite sample substituted with 5% magnesium leads to a considerable decrease in the hydrodynamic diameter compared to the samples substituted with 1 and 3%, which also denotes a growth in particle size, therefore a decrease in surface reactivity, with the formation of this phase. This could be explained by the defects occurring in the unit cell of hydroxyapatite due to the introduction of magnesium ions.

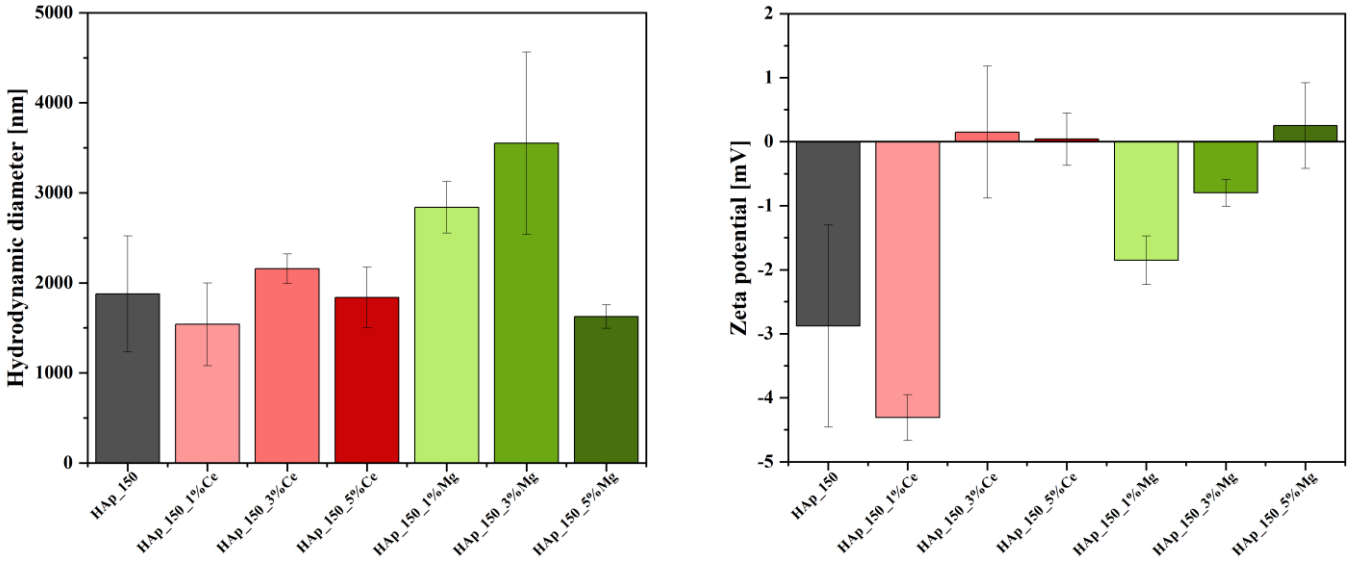

Figure 3. Hydrodynamic diameter and zeta potential values for hydroxyapatite treated at 150 °C and substituted with cerium and magnesium ions at concentrations of 1, 3, and 5%.

3.3. Scanning Electron Microscopy (SEM)

Figure 4A shows the SEM micrographs obtained for the unsubstituted HAp powder obtained at 150 °C and the dimensional distribution of the particles (Figure 5A,B). In this case, the micrographs obtained show the rod-like morphology characteristic of hydroxyapatite, similar to the physiological one found in the structure of hard tissue. From a dimensional point of view, this falls into the field of nanomaterials, the rods having a diameter between 15 and 45 nm, the average size being 28.23 nm. The morphology of the hydroxyapatite powder is preserved with the increase of the heat treatment temperature; thus, in Figure 4B, better-contoured rods can be observed than in the previous case, with slightly increased dimensions for the HAp_250 sample. Thus, an increase in the average diameter to 37.29 nm (Figure 5D) is observed for the hydroxyapatite treated at 250 °C, with the increase in temperature. Regarding the length distribution, in this case, values between 80 and 320 nm can be observed, with an average size of 190 nm (Figure 5C). This dimensional increase is in good correlation with the X-ray diffraction results regarding the crystallite size.

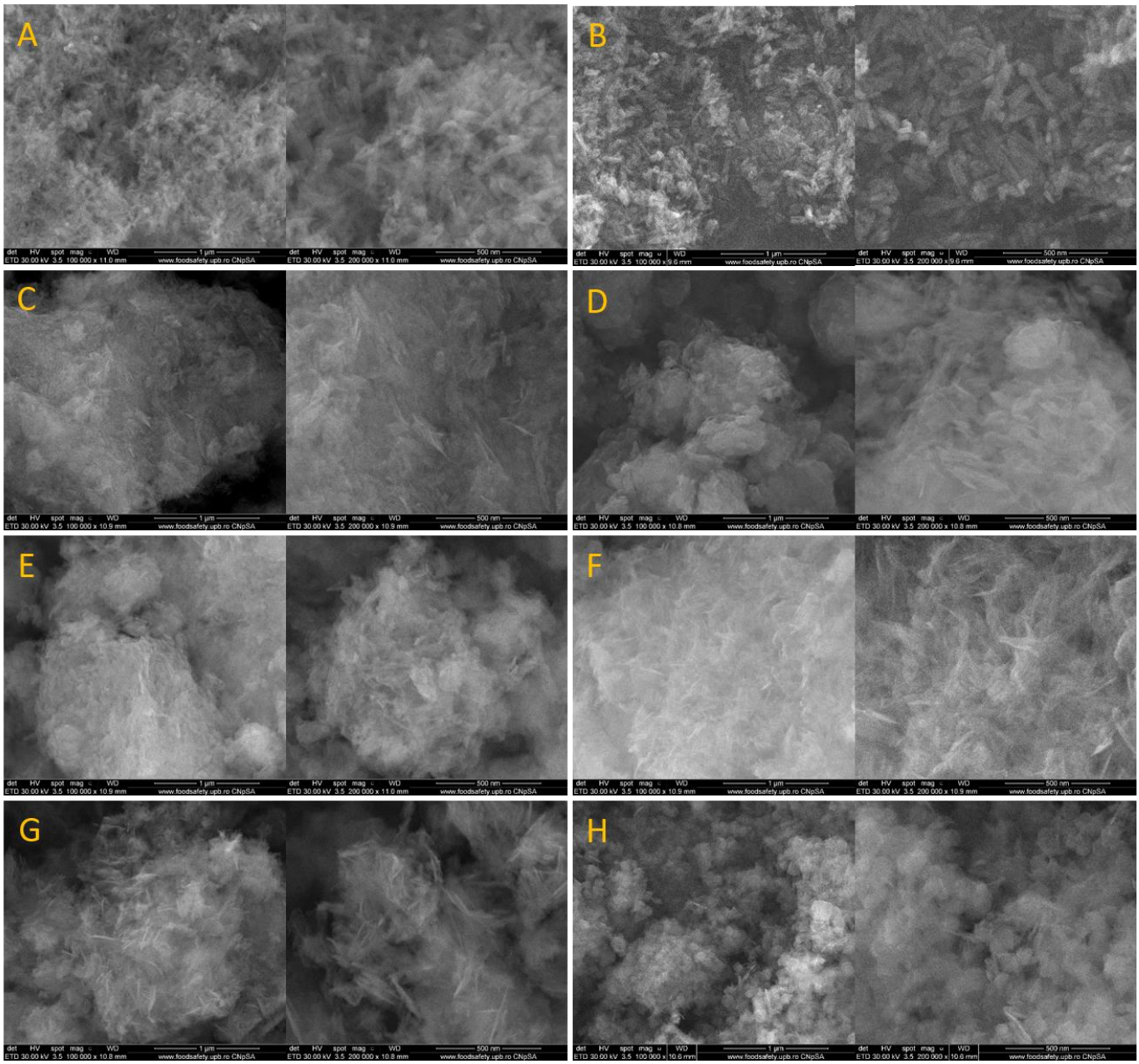

Figure 4. SEM micrographs recorded for HAp_150 (**A**), HAp_250 (**B**), HAp_Ce_1% (**C**), HAp_Ce_3% (**D**), HAp_Ce_5% (**E**), HAp_Mg_1% (**F**), HAp_Mg_3% (**G**), HAp_Mg_5% (**H**).

Following the morphological evaluation, it is observed that the cerium substitution does not substantially change the appearance of the hydroxyapatite. Thus, all three concentrations (1%, 3%, 5%) maintain the rod-like structure with nanometric dimensions found in the case of unsubstituted powders. In this sense, their large specific surface area may conduct the formation of agglomerates that can be observed, especially in the case of the three samples of hydroxyapatite substituted with cerium (Figure 4C–E). Analyzing the histograms made for the three cerium-doped hydroxyapatite samples (Figure 5E–J), it can be seen that the diameter of the rods is between 10 and 80 nm and increases with increasing cerium concentration. Considering the distribution by length, a dimensional inhomogeneity can be observed, with values between 50 and 450 nm.

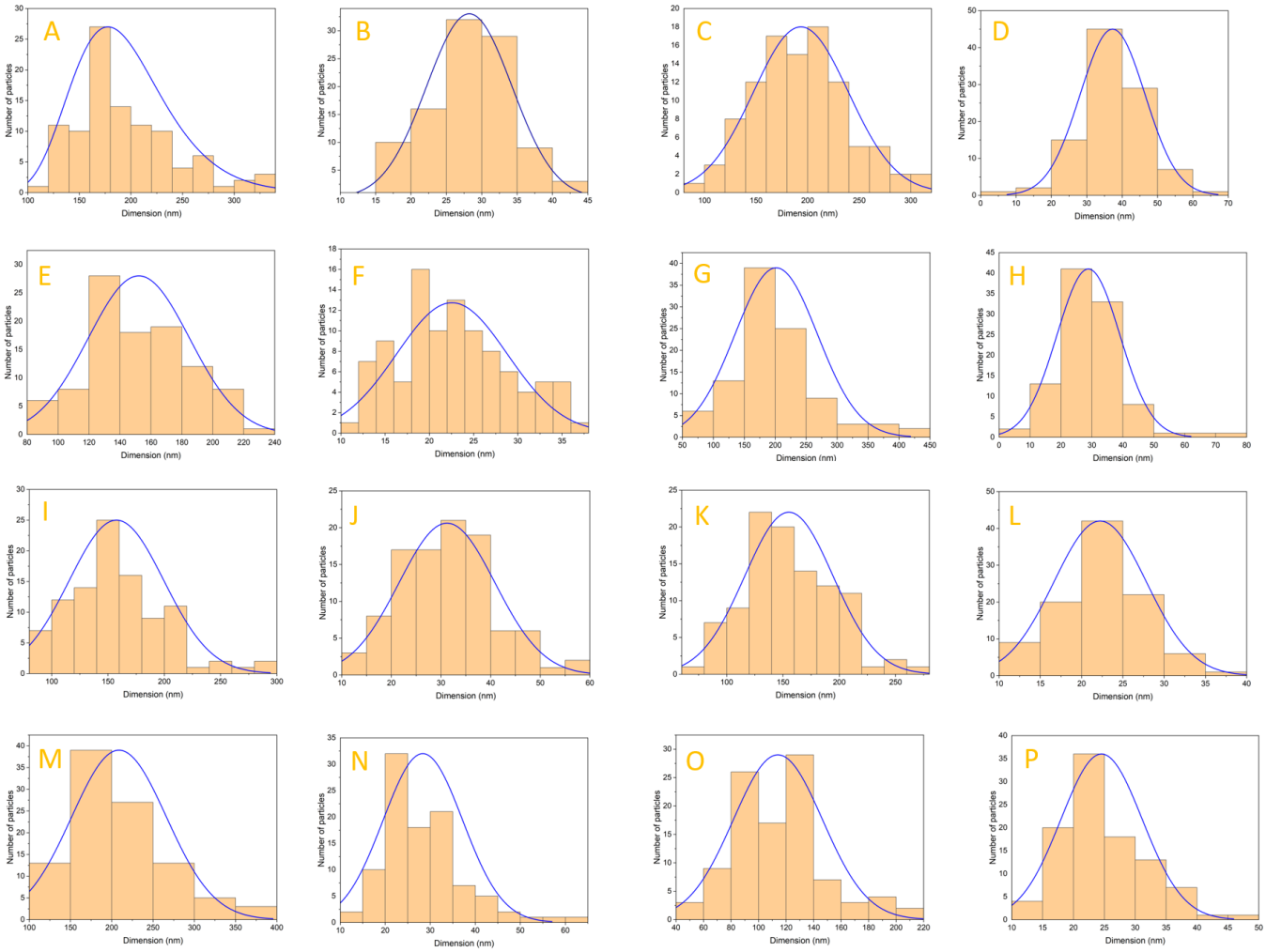

Figure 5. Dimensional distribution for HAp_150, HAp_250, HAp_Ce_1%, HAp_Ce_3%, HAp_Ce_5%, HAp_Mg_1%, HAp_Mg_3%, HAp_Mg_5% by length (**A**,**C**,**E**,**G**,**I**,**K**,**M**,**O**) and by diameter (**B**,**D**,**F**,**H**,**J**,**L**,**N**,**P**).

The magnesium-substituted hydroxyapatite samples were also subjected to SEM analysis, the results being shown in Figure 4F–H. The three magnesium concentrations (1%, 3%, 5%) influence the hydroxyapatite morphology compared to the cerium-substituted samples. In the case of the HAp_Mg_1% sample, the rod-type architecture is preserved, but with the increase in magnesium concentration, small irregular platelets begin to appear (average diameter of 114.07 nm and average thickness of 24.54 nm), interconnected with the characteristic rods of hydroxyapatite. The sample with the highest concentration of magnesium (5%) shows the highest proportion of such platelets and a very low presence of rods.

Also, all three samples present dimensional characteristics within the nanometric range, with a high tendency to agglomerate. It can be seen for the samples with magnesium concentrations of 1% and 3% that both the diameter and the length increased with increasing concentration.

Analyzing the hydroxyapatite powder with the highest proportion of cerium, the presence of the substituent element is observed, uniformly distributed alongside the element's characteristic of hydroxyapatite (Figure 6).

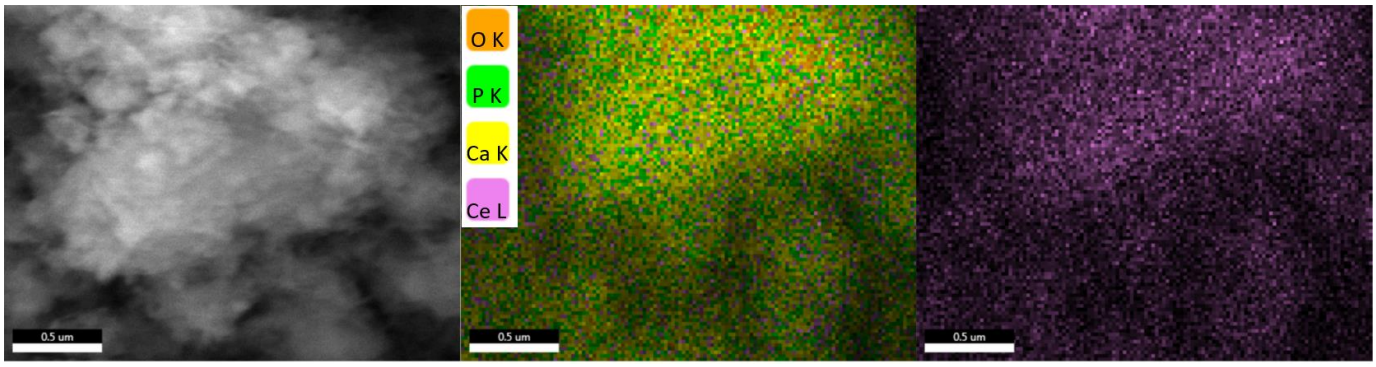

Figure 6. Elemental mapping recorded for HAp_Ce_5%.

A similar behavior is also observed analyzing the hydroxyapatite powder with the highest proportion of magnesium, where the presence of the substituent element uniformly distributed alongside the elements characteristic of hydroxyapatite is observed (Figure 7).

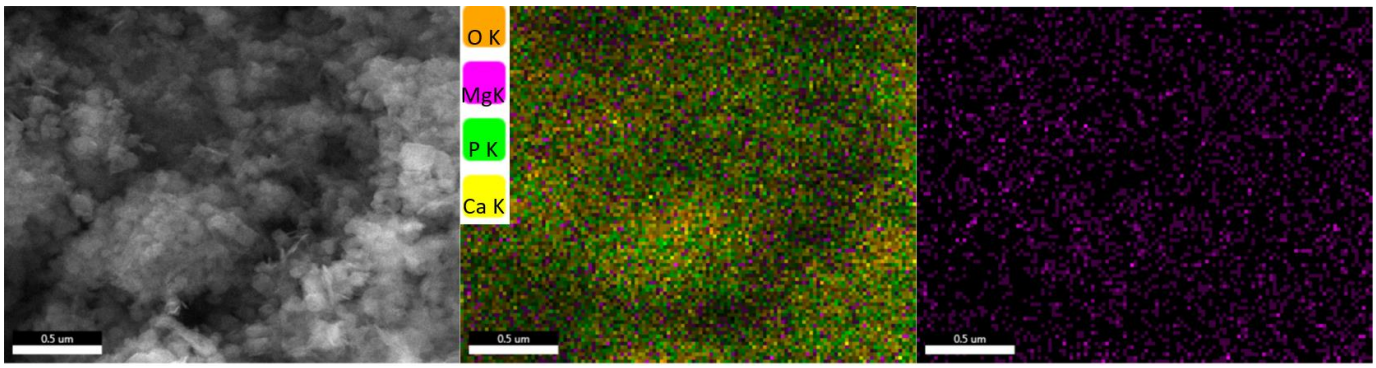

Figure 7. Elemental mapping recorded for HAp_Mg_5%.

3.4. Fourier-Transform Infrared Spectroscopy (FT-IR)

The FT-IR spectra of HAp_Ce (1%, 3%, 5%) and HAp_150 powders show bands corresponding to the vibrational modes of the different functional groups that were found in the sample. Thus, the cerium-substituted hydroxyapatite samples are similar in terms of molecular structure to the plain hydroxyapatite sample. However, a difference is observed by the presence of the O–H group at the wave number of about 3380 cm^{-1} found in the cerium samples, attributed to water molecules adsorbed on the surface. The vibrational band at wave number 1022 cm^{-1} is characteristic of the PO_4^{3-} group, characteristic of hydroxyapatite. Also, in the case of samples substituted with cerium, the debut of the band at approximately 1638 cm^{-1} confirms the carbonation of the samples, being attributed to the CO_3^{2-} group, a process that occurs when the powders come into contact with the atmosphere (Figure 8a).

Also, the FT-IR results obtained for the HAp_150, and HAp_Mg (1%, 3%, 5%) samples, show the similarity between the spectra for magnesium-substituted hydroxyapatite and simple hydroxyapatite can be observed. Its carbonated nature is also observed compared to the other samples. At the wave number from approximately 1022 cm^{-1}, the imprint of hydroxyapatite is observed through the PO_4^{3-} group (Figure 8b).

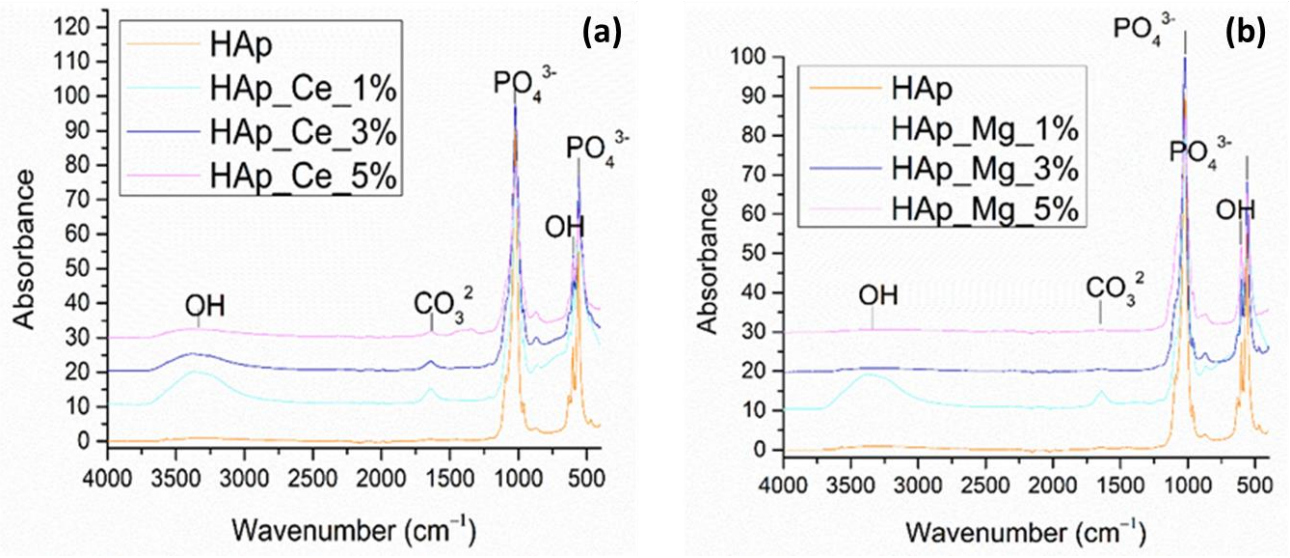

Figure 8. FT-IR spectra recorded for HAp_150, HAp_Ce_1%, HAp_Ce_3%, HAp_Ce_5% (**a**) and Hap_150, HAp_Mg_1%, HAp_Mg_3%, HAp_Mg_5% (**b**).

3.5. Biological Evaluation of HAp Samples

MC3T3-E1 osteoblast cells were used to analyze the biological behavior of hydroxyapatite samples with cerium and magnesium ions by both quantitative (MTT viability and NO cytotoxicity assays) and qualitative (fluorescence microscopy) evaluation. The metabolic activity of osteoblasts incubated with HAp samples was evaluated and was comparable with the levels obtained for control as revealed by MTT assay (Figure 9a,b), proving that all types of tested samples can represent biocompatible substrates for normal osteoblastic cell proliferation. Also, no statistically significant changes were observed compared to the control for both time intervals (24 h and 72 h), confirming the absence of cytotoxicity of HAp-based suspensions after three days of incubation. Furthermore, the levels of NO release after the HAp exposure were not significantly different compared to the control (Figure 9c,d), confirming the good biocompatibility in the presence of these samples. However, a slight increase of 15% above the control level was noticed in the case of HAp_150 after 72 h. This change could be explained by its higher crystallite size (46.13 nm) compared to the other samples, which have a size lower than 20 nm. This characteristic could influence the release of different intracellular molecules, including the NO, to the culture medium, by affecting cell permeability.

Fluorescence microscopy experiments, which allowed the cytoskeleton and nuclei visualization, have offered additional details on the biological effects of HAp-based samples. The fluorescent micrographs in Figures 10–12 demonstrate that MC3T3 cells had uniform spreading and good adherence after being cultured for 24 and 72 h with the investigated substances. The cells also had a typical osteoblast-like phenotype and normal cell shape. (flattened structure, multiple cytoskeleton extensions, elongated actin filaments, and prominent central nuclei).

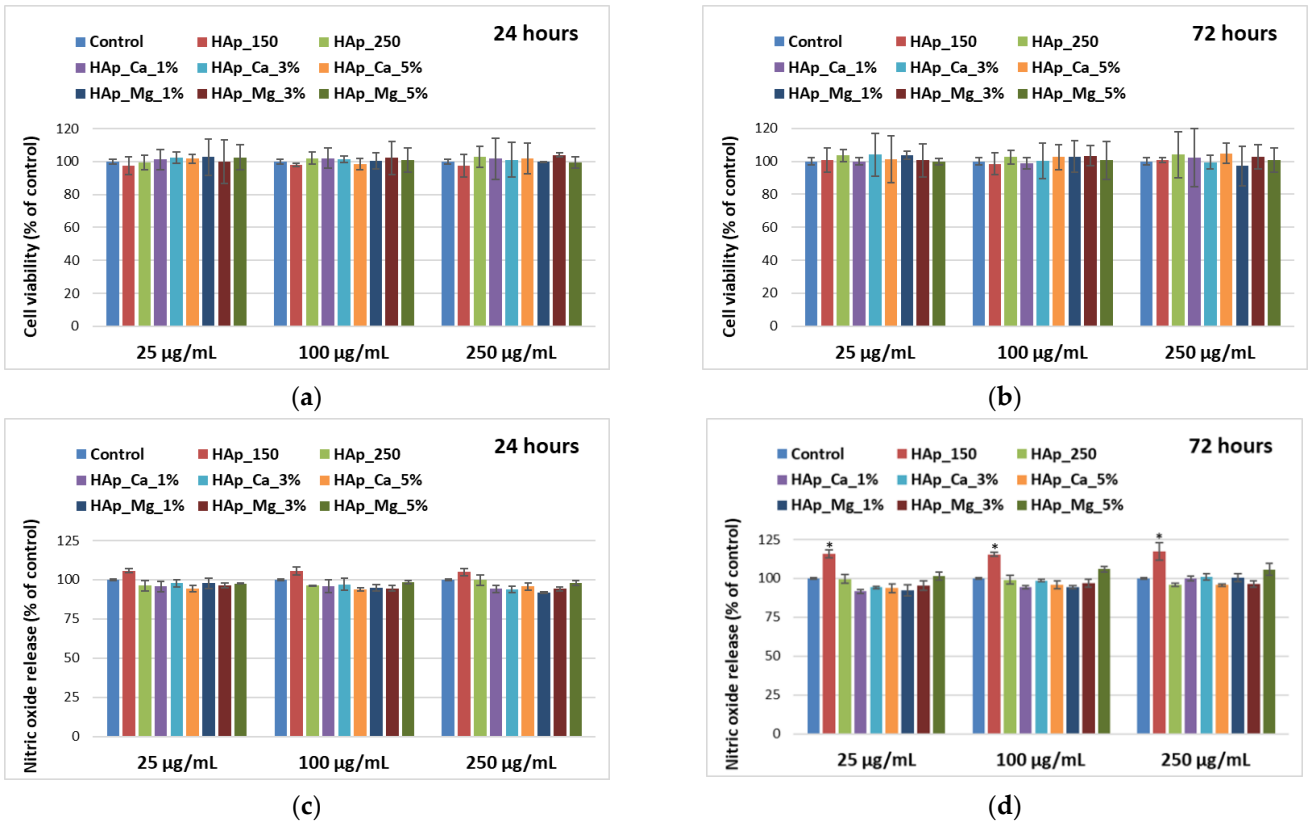

Figure 9. Viability level (**a**,**b**) and nitric oxide release (**c**,**d**) of MC3T3-E1 osteoblasts cultured in the presence of different concentrations (25, 100, and 250 µg/mL) of HAp samples for 24 h and 72 h. Results are calculated as means ± SD (n = 3) and represented relative to control (cells that were not incubated with HAp samples); the statistical analysis: two-tailed Student's test * $p \leq 0.05$ were considered as statistically significant.

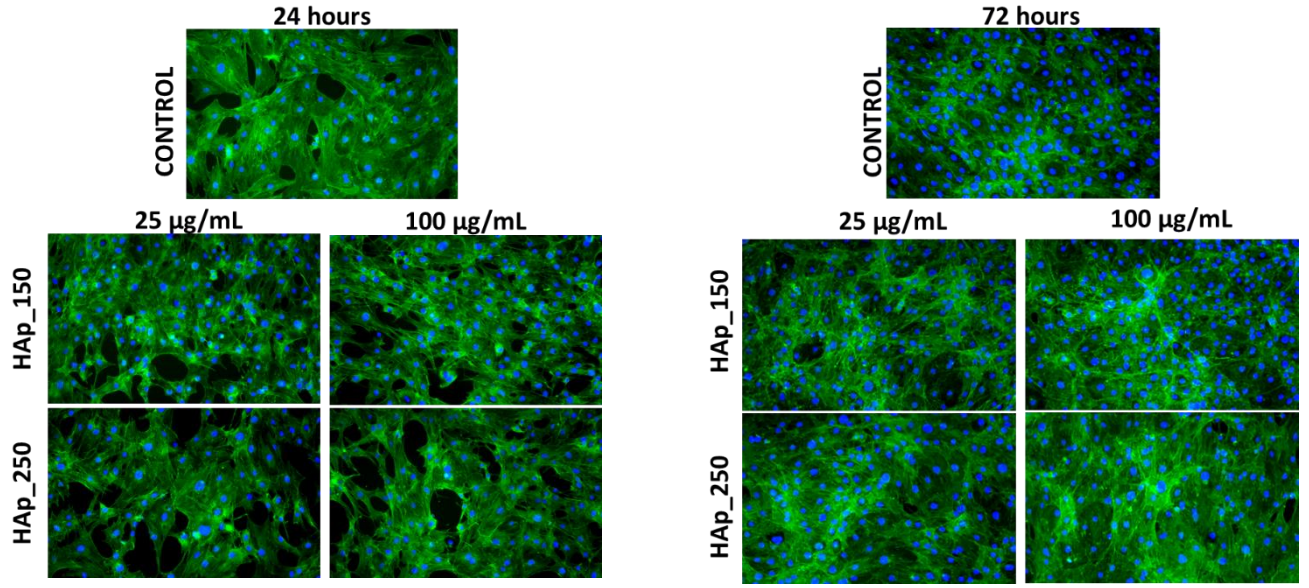

Figure 10. Fluorescence micrographs of MC3T3-E1 osteoblasts cultured for 24 h and 72 h in the presence of different concentrations (25 and 100 µg/mL) of HAp_150 and HAp_250 samples. The actin cytoskeleton is stained with phalloidin-FITC (green) and nuclei with DAPI (blue). All images were captured with a 10× objective.

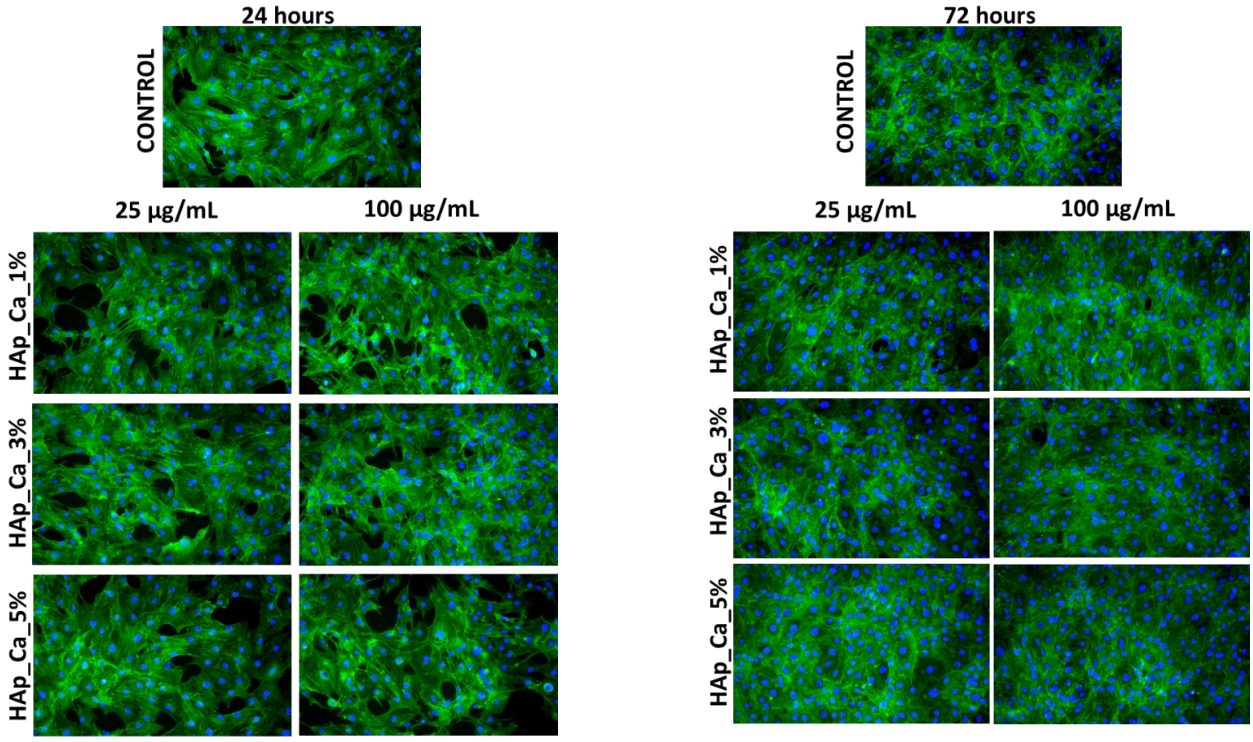

Figure 11. Fluorescence micrographs of MC3T3-E1 osteoblasts cultured for 24 h and 72 h in the presence of different concentrations (25 and 100 µg/mL) of HAp_Ce_1%, HAp_Ce_3%, HAp_Ce_5% samples. The actin cytoskeleton is stained with phalloidin-FITC (green) and nuclei with DAPI (blue). All images were captured with a 10× objective.

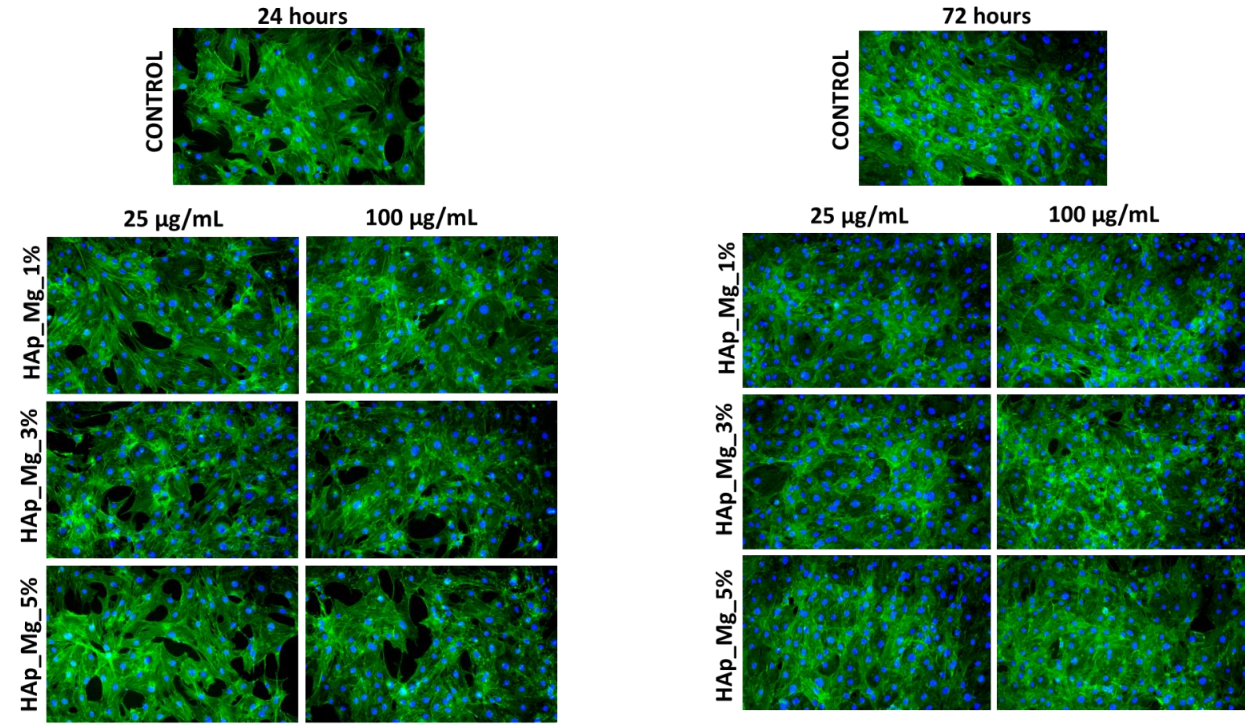

Figure 12. Fluorescence micrographs of MC3T3-E1 osteoblasts cultured for 24 h and 72 h in the presence of different concentrations (25 and 100 µg/mL) of HAp_Mg_1%, HAp_Mg_3%, HAp_Mg_5% samples. The Actin cytoskeleton is stained with phalloidin-FITC (green) and nuclei with DAPI (blue). All images were captured with a 10× objective.

3.6. Microbiological Evaluation

3.6.1. MIC (Minimum Inhibitory Concentration) Method

The minimum inhibitory concentration was evaluated after 24h. The concentration where the MIC was observed is presented in Figure 13. As observed, the MIC values range from 0.1–2.5 mg/mL for bacteria strains and 5 mg/mL for *C. albicans*.

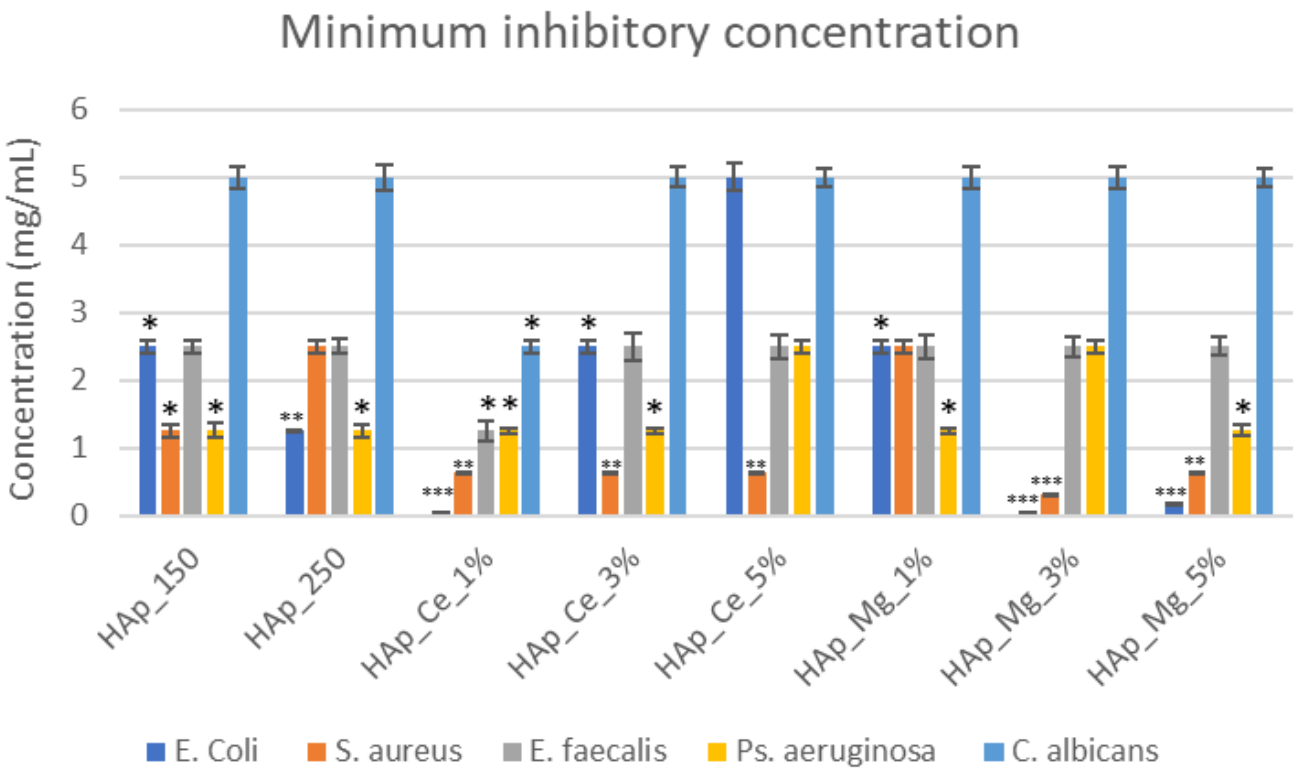

Figure 13. Minimum Inhibitory Concentration for hydroxyapatite samples. Results are calculated as means ± SD (n = 3); the statistical analysis: two-tailed Student's test * $p \leq 0.05$, ** $p \leq 0.01$, *** $p \leq 0.001$ were considered as statistically significant (for each strain).

3.6.2. Development of Monospecific Biofilms

After 24 h, the developed monospecific biofilms were evaluated by optic microscopy (Figure 14); it was observed that the hydroxyapatite substituted with cerium inhibited bacteria better than samples unsubstituted and hydroxyapatite substituted with magnesium. Figure 14 below reveals that the biofilms develop differently in the presence of HAp powders, depending on their concentrations; usually, concentrations above 2.5 mg/mL reveal a significant inhibition, as shown in the microscopy images.

OD 492nm (Abs) results confirmed that hydroxyapatite samples could interfere with *E. faecalis*, *E. coli.*, *S. aureus*, *P. aeruginosa*, and *C. albicans* biofilm formation. (Figure 15a–c). The hydroxyapatite substituted with cerium showed improved bacteria inhibition, as compared with hydroxyapatite substituted with magnesium. For the Gram-negative bacteria such as *E. coli* and *P. aeruginosa*, the samples showed a limited effect (Figure 15d,e).

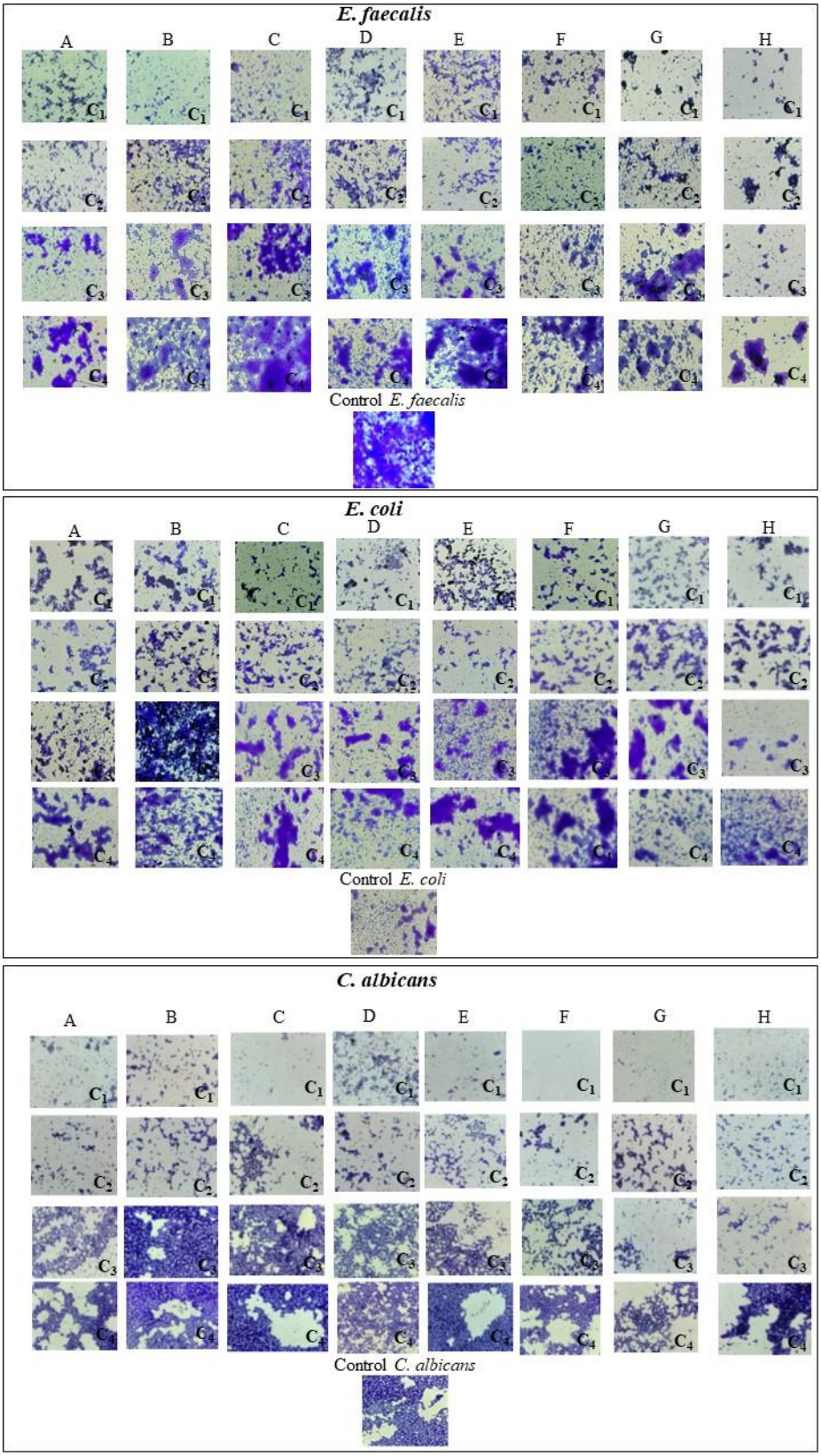

Figure 14. Optical microscopy for hydroxyapatite samples for *E. faecalis*, *E. coli*, *C. albicans*. A-HAp_150, B-HAp_250, C-HAp_Mg_1%, D-HAp_Mg_3%, E-HAp_Mg_5%, F-HAp_Ce_1%, G-HAp_Ce_3%, H-HAp_Ce_5%, C1-Concentration 1 (5 mg/mL), C2-Concentration 2 (2.5 mg/mL), C3-Concentration 3 (0.62 mg/mL), C4-Concentration 4 (0.15 mg/mL).

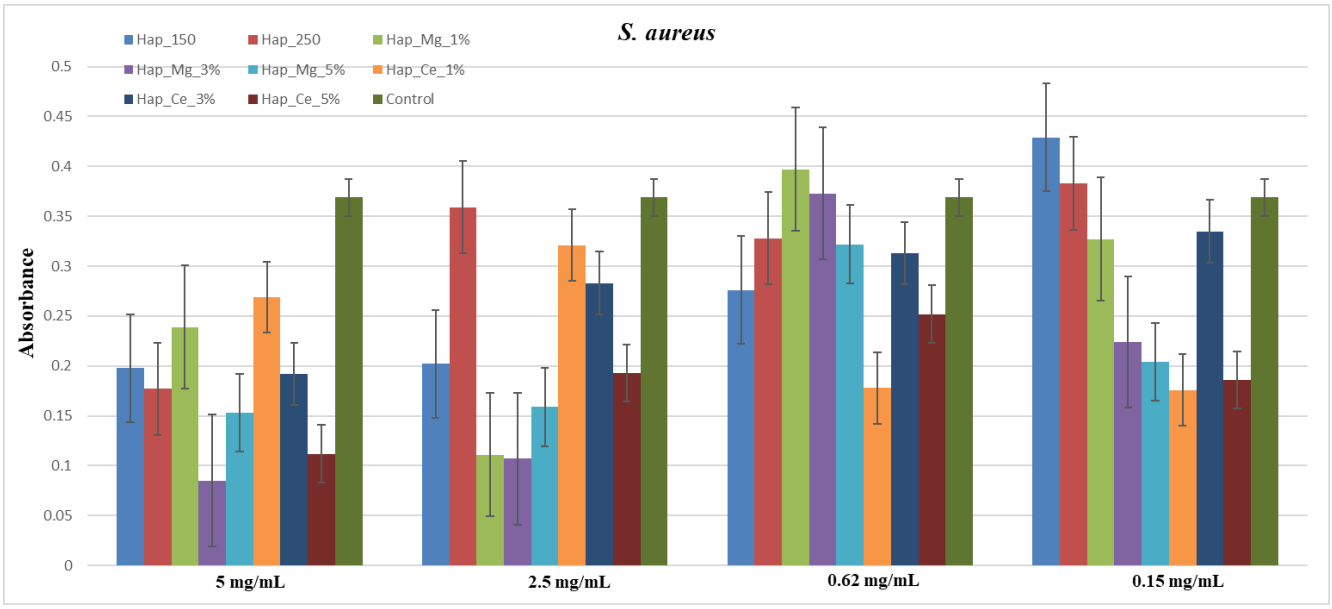

(**a**)

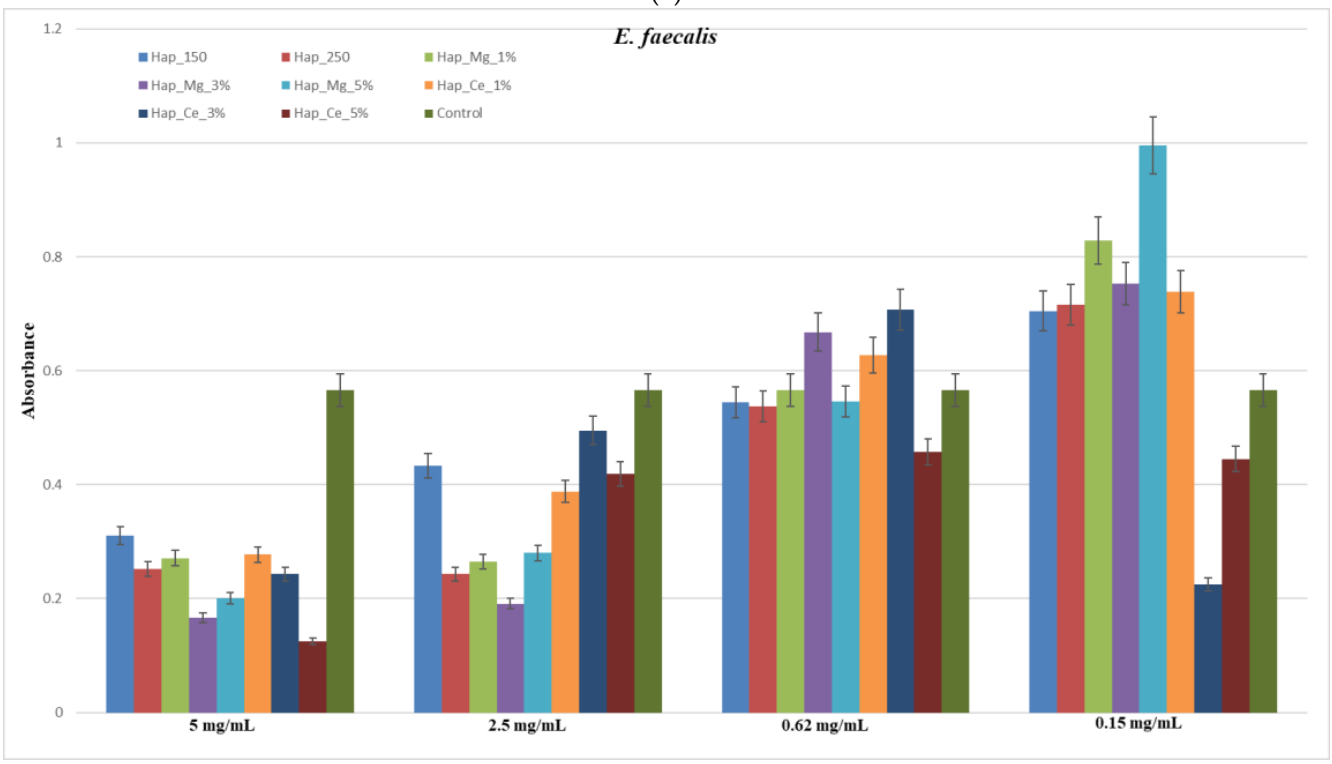

(**b**)

Figure 15. *Cont.*

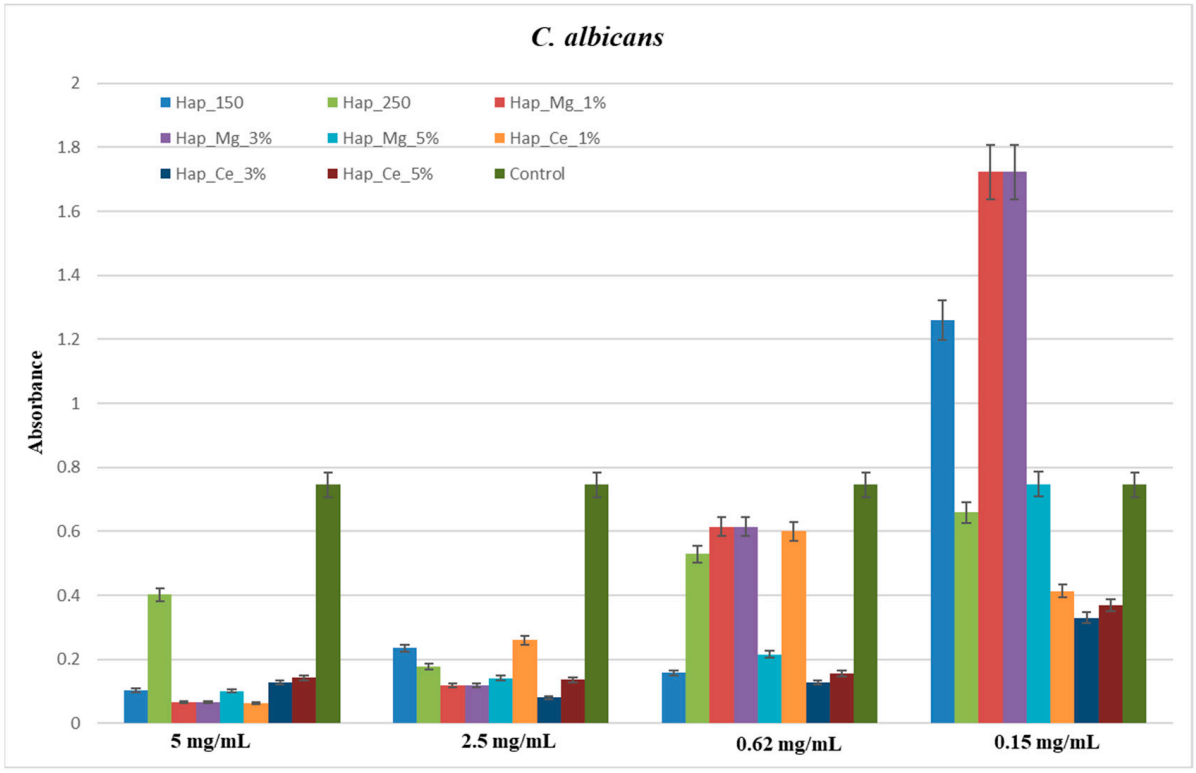

(c)

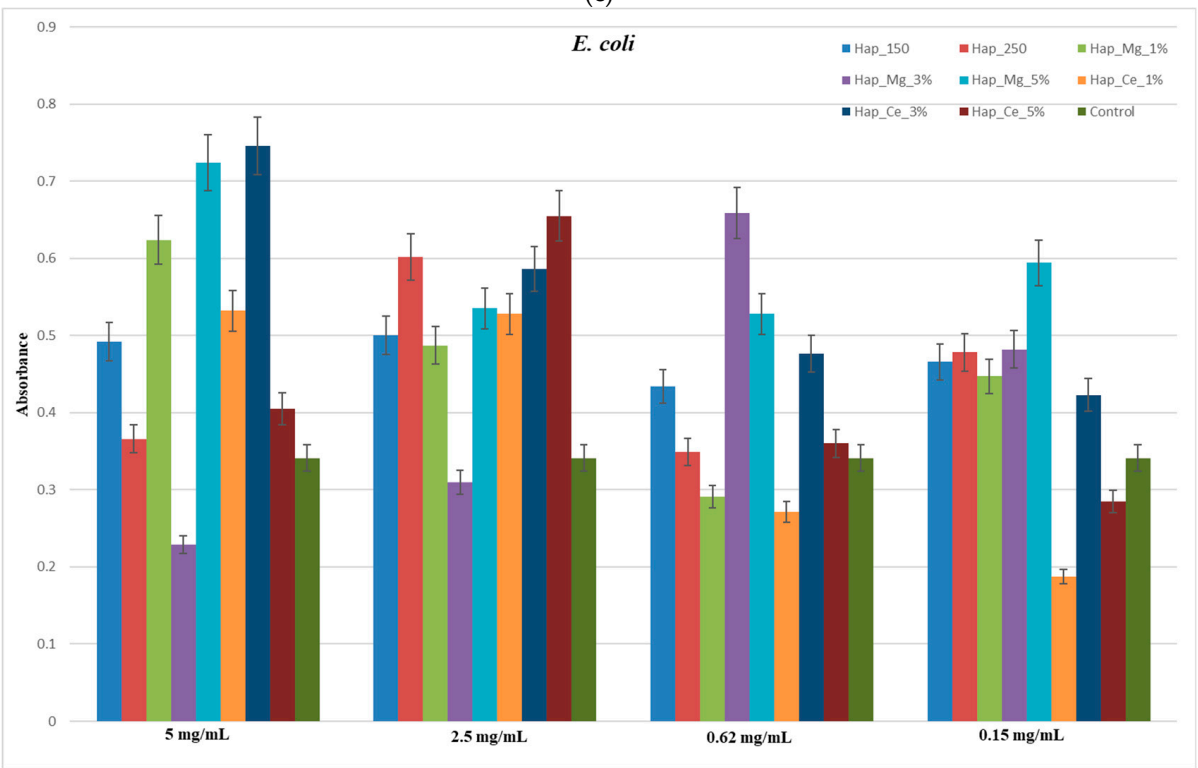

(d)

Figure 15. *Cont.*

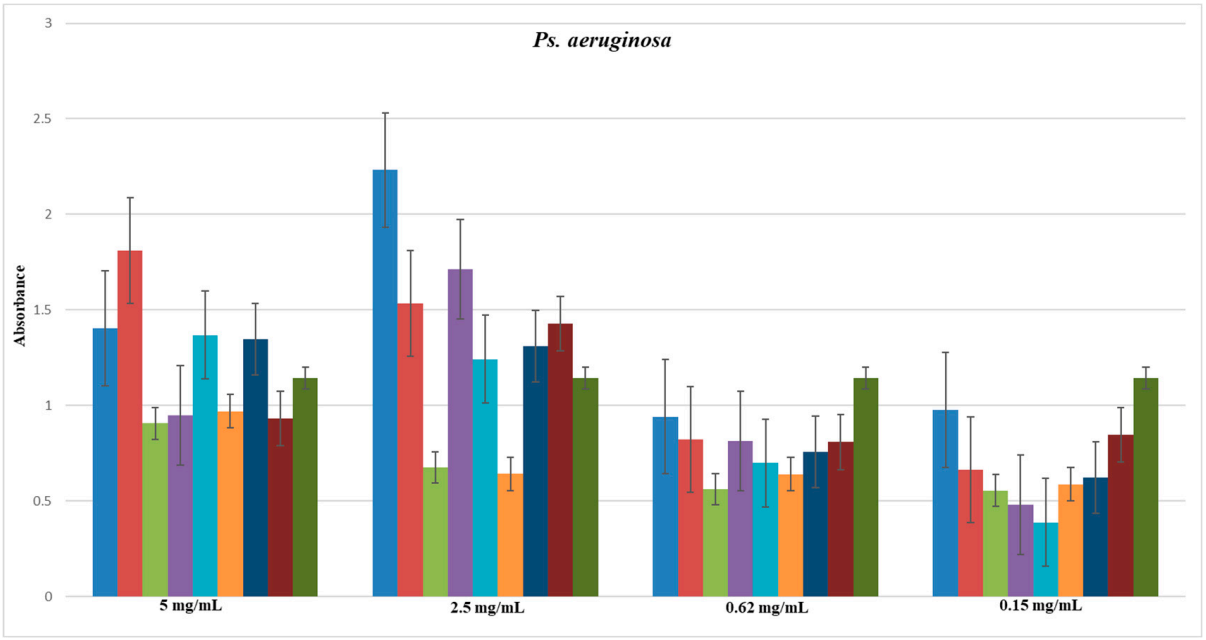

(**e**)

Figure 15. Development of monospecific biofilm of (**a**) *S. aureus*, (**b**) *E. faecalis*, (**c**) *C. albicans*, (**d**) *E. coli*, (**e**) *Ps. aeruginosa*.

4. Discussion

4.1. X-ray Diffraction

HAp-based biomaterials can be easily designed using the microwave-assisted hydrothermal process since modifying different nanoparticle features, such as dimension, is simple. Additionally, this adaptable method can increase the bioactivity and biofunctionality of HAp by substituting it with different inorganic ions [56]. Figure 1 depicts the phases of pure hydroxyapatite (HAp), Ce(III)-substituted hydroxyapatite, and Mg-substituted hydroxyapatite formed by microwave-assisted hydrothermal, respectively. The calcium phosphate in Figure 1's XRD image can be seen as a single phase with all relevant diffraction peaks. For cerium-substituted samples, a recent study showed that compared to pure hydroxyapatite, all Ce(III)-substituted hydroxyapatite samples may exhibit a drop in X-ray peak intensities with increasing ion doping concentration levels [57]. In our situation, a similar decrease in diffraction peak strength was seen when the cerium concentration increased. However, the sole crystalline phase found is hydroxyapatite, indicating that the substitution reaction was successful because no additional phases, such as cerium oxide or cerium phosphate, were formed. In the case of substitution with magnesium ions at concentrations of 1, 3, and 5%, the diffractograms show different behavior compared to substituting with cerium (Figure 1c, Table 1). On the one hand, 1 and 3% concentrations decrease the average size of the crystallites while making little to no effect on the powders' crystallinity. The occurrence of new diffraction maxima in the 5% magnesium substituted hydroxyapatite sample was attributed to the mixed calcium and magnesium phosphate crystal phase known as magnesium whitlockite. Additionally, Table 1 shows that for both cerium and magnesium, the crystallite size decreases as concentration increases. The main difference appears for the sample with 5% magnesium; the crystallite size has been increased due to the formation of whitlockite. Additionally, it can be seen that the crystallite size increases due to the higher temperature for the HAp produced at 250 °C. Whitlockite, or magnesium whitlockite, is a calcium orthophosphate crystal in which calcium and magnesium are partially substituted under biological conditions. The difference is observed in X-ray or electron diffraction patterns and occurs in extra- or intra-tissular places under normal or pathological settings, primarily in tissues of non-epithelial origin [58,59]. By

using X-ray diffraction, a recent study examined a variety of pathological calcifications and found that whitlockite and apatite appeared to be present often [60].

4.2. Dynamic Light Scattering (DLS) and Zeta Potential

Through measurements of the hydrodynamic diameter and zeta potential, the stability of pure HAp, Ce(III)-substituted hydroxyapatite, and Mg-substituted HAp was evaluated. The Rayleigh scattering from suspended nanoparticles moving with Brownian motion is the foundation of the dynamic light scattering (DLS) method. By shining a laser source on the sample, we can observe the particle diffusion velocity and calculate the hydrodynamic diameter of the nanoparticles [61].

From the DLS analysis, it was concluded that the hydrodynamic diameter is lower for the sample synthesized at 250 °C temperature because of larger particle size and reduced surface reactivity; the zeta potential also confirmed the increased stability for this sample.

For the samples of hydroxyapatite substituted with cerium and magnesium, it can be observed a high degree of agglomeration, while also having a low zeta potential. The most important difference is observed in the hydroxyapatite sample substituted with 5% magnesium which has a decrease in the hydrodynamic diameter, showing an increase in particle size.

4.3. Scanning Electron Microscopy (SEM)

From the SEM micrographs in Figure 4, it can be seen that the HAp powder sample has a rod-shaped form with width and length comparable to those of hard tissue (tens and hundreds of nanometers, respectively). It can be shown that the nanoparticles, in the case of HAp_250, have larger diameters, with the dimension expanding as the heat temperature rises. The X-ray diffraction results regarding the crystallite size are well correlated with this dimensional increase. Figure 5A,B depicts the dimensions distribution of the particles, while Figure 4A displays the SEM micrographs for the unsubstituted HAp powder obtained at 150 °C. The acquired micrographs, in this instance, exhibit the rod-like morphology that characterizes hydroxyapatite and is comparable to the physiological one observed in the composition of hard tissue. This is a type of nanomaterial from a dimensional perspective, with rods that range in diameter from 15 to 45 nm and have an average size of 28.23 nm. Because the morphology of the hydroxyapatite powder is conserved while the heat treatment temperature is raised, better-contoured rods with slightly larger diameters for the HAp_250 sample can be seen in Figure 4B. As a result, for the hydroxyapatite treated at 250 °C, an increase in the temperature causes the average diameter to grow to 37.29 nm (Figure 5D). In this instance, values between 80 and 320 nm with an average size of 190 nm can be seen in the length distribution (Figure 5C). The results of the X-ray diffraction regarding the crystallite size are well correlated with this dimensional increase. Following morphological analysis, it is found that the cerium substitution has little effect on the hydroxyapatite's appearance. As a result, the rod-like structure with nanometric dimensions present in the case of unsubstituted powders is maintained at all three concentrations (1%, 3%, and 5%). In this way, their huge specific surface area causes the development of observable agglomerates. Similar findings were recently published in a study using hydroxyapatite doped with Ce(III) and Ce(IV), where it was revealed that the dimension varies depending on the concentration [57,62]. The findings of the SEM examination performed on the magnesium-substituted hydroxyapatite samples are depicted in Figure 4F–H). Comparatively to the cerium-substituted samples, the three magnesium concentrations (1%, 3%, and 5%) impacted the hydroxyapatite morphology. The rod-type architecture is still present in the HAp_Mg_1% sample, but as the magnesium concentration rises, little irregular platelets with an average diameter of 114.07 nm and an average thickness of 24.54 nm start to emerge being interconnected with the characteristic rods of hydroxyapatite. The sample with the highest magnesium content (5%) exhibits the largest percentage of these platelets and the least number of rods. Whitlockite synthesis was explained by Macha et al. [63], and the addition of magnesium to hydroxyapatite was observed to alter particle size in a study

presented by Nigar et al., intriguingly, at a higher temperature (i.e., 350 °C) in this system, a tubular morphology of HA and rhombohedral-shaped Mg-WH particles were seen [64].

4.4. Fourier-Transform Infrared Spectroscopy (FT-IR)

When the hydroxyapatite powders with the largest amounts of cerium and magnesium are analyzed, the substituent elements are present and consistently distributed with the hydroxyapatite-specific elements.

Unsubstituted hydroxyapatite (HAp_150 and HAp_250) IR spectra exhibit absorption maxima that are unique to hydroxyapatite, including stretching vibrations from structural hydroxyl groups (~3530 cm^{-1}), ν3 asymmetric stretching of the PO_4^{3-} (~1110, ~1080, and ~1050 cm^{-1}) and PO_4^{3-} ν1 stretching (~990 and ~880 cm^{-1}) [65,66]. The overlapping stretch of OH (hydroxyl groups) bound in HAp may be the cause of the weaker peak at ~3500 cm^{-1}. The presence of the O-H group at about 3380 cm^{-1} in the cerium samples is attributed to water molecules adsorbed on the surface, distinguishing the hydroxyapatite substituted with cerium. The emergence of the band at roughly 1638 cm^{-1}, which is attributed to the CO_3^{2-} group and indicates the carbonation of the samples in both the cerium-substituted samples as well, is a process that takes place when the powders come into contact with the atmosphere. The decrease in HAp crystallinity is related to the increase of Ce^{3+} ion concentration, which reduced band intensity [67]. The XRD study provided additional support for these conclusions. In comparison to the other samples, its carbonated character is also observed. The imprint of hydroxyapatite is visible through the PO_4^{3-} group at a wave number of about 1022 cm^{-1} [68]. In an investigation based on the investigation of magnesium incorporated in hydroxyapatite, a peak at 3698 cm^{-1} was found to match the stretching mode of hydroxyl groups that manifests when associated with magnesium, showing the existence of Mg^{2+} in the apatite structure [69].

4.5. Biological Behavior Evaluation on Osteoblast Cells

Due to its osteoconductivity and osteoinductivity, hydroxyapatite (HA), which has a composition and structure highly very much alike to those of natural bone minerals, has been regarded as the best material to construct bone tissue engineering scaffolds [70]. According to research by Vieria et al. on the effects of hydroxyapatite-containing cerium on fibroblast, none of the tested samples had viability levels consistent with a cytotoxic effect [40]. A study using MG-63 osteoblast cell lines obtained from human osteosarcoma provided similar results as well [71]. MC3T3 cells were used to perform the MTT assay on the samples obtained in our study. The samples were evaluated at 24 and 72 h, and it was found that at neither time point did they have any harmful effects on the cells supporting the normal development and proliferation of osteoblastic cells, the metabolic activity being comparable with control. Also, the samples did not produce NO release; their level was kept close to the control values for all tested samples. In the instance of the magnesium-substituted hydroxyapatite and cerium-substituted hydroxyapatite, the metabolic activity of each HAp powder was compared with the control, and the MTT assay (Figure 9a,b) demonstrated that all recommended samples are appropriate substrates for normal osteoblastic cell growth and proliferation. MC3T3-E1 cells showed good adherence and homogeneous spreading onto the substrate when treated with HAp-based coatings for 24 h. The cells also had a typical osteoblast-like phenotype and normal cell shape according to fluorescence micrographs (Figures 10–12).

A recent study observed that, according to the hypothesized osteoprotective action of Mg, certain proteins involved in osteogenesis were much more regulated in the presence of Mg discs than in Ti-disc. Due to its propensity for biodegradation and outstanding biocompatibility, magnesium is a promising metal for biodegradable implant applications. Compared to Ti metal discs, the overall effect of decomposing Mg on osteoblast is noticeably bigger and more complex [72–74]. In the case of cerium, recent research has shown that hydroxyapatite substituted with cerium and Fe_3O_4 may become toxic due to Ce and Fe release at higher concentrations [75]. In our study, the samples with all three cerium

concentrations (1%, 3%, 5%) did not show any toxic effect on the cells. In a recent study based on hydroxyapatite substituted with cerium, cellular viability was also maintained for a concentration of 10% cerium [57].

4.6. Microbiological Evaluation

In order to create implants that are more resistant to bacterial colonization, advances have been made in the field of implant surface engineering, with implant-associated bone and joint infection (BJI) being a rare but devastating side effect of arthroplasty and orthopedic trauma. The number of implant-associated infections is rising due to the expanding number of implant devices, despite technical and medical efforts to prevent such illnesses [76].

The development of antimicrobial protection against the adhesion and growth of microbial biofilms was one of the anticipated uses of the created bioactive coatings. After forming on the surface of a prosthetic device or implant, biofilms are exceedingly difficult, if not impossible, to treat due to their strong resistance to antibiotics and host immunity; the damaged implant is typically removed as a result [77]. As a result, it is still difficult for materials science and many medical disciplines to prevent biofilm growth on the implant surface.

The development of new materials with enhanced resistance to microbial colonization or bioactive implant coatings capable of delivering an antimicrobial effect close to the implanted material by first encapsulating and then locally releasing conventional antibiotics or other antimicrobial agents are two research directions that are currently being pursued [78–81]. Along with their inherent bioactivity, HAp-based coatings have a remarkable ability for immobilizing or encasing antimicrobial agents. Inorganic structures, including bismuth, cerium, copper, magnesium ions, silver ions, and nanoparticles, and zinc ions and nanoparticles have been found to have enhanced anti-pathogenic properties [82].

In the case of hydroxyapatite substituted with cerium, recently, it was reported in a study that after a 24 h incubation period, the cerium substituted hydroxyapatite's antibacterial activity against the pathogens *E. coli* 714 and *S. aureus* ATCC 6538 was investigated. The antibacterial activity of pure hydroxyapatite (xCe = 0), which served as the standard, is compared to the antimicrobial activity of cerium-substituted hydroxyapatite. A prior study found that pure HAp had no bactericidal activity against *E. coli* 714 and *S. aureus* ATCC 6538 [83]. According to the study results, *E. coli* 714 bacterial strain survival rates decline as Ce concentrations in hydroxyapatite rise. When the amount of Ce in the hydroxyapatite increases, the S. aureus ATCC 6538 bacterial strain's survival rate declines [84]. Recently, it has been proposed that *E. faecalis*' capacity to develop biofilms plays a significant role in the pathophysiology of enterococci infections [85]. *E. faecalis* forms a multilayer, antibiotic-resistant biofilm by secreting a protective extracellular matrix that adheres to both biotic and abiotic surfaces. This intrinsic antibiotic resistance represents an important challenge to treating enterococci infections [86]. In accordance with a recent study based on hydroxyapatite substituted with rare earth elements, both HAp and Nd-Ce/HAp exhibited an inhibitory zone against all of the bacteria test species. The synthesized hydroxyapatite without substitution and HAp with neodymium and cerium displayed antibacterial and antifungal activities. Regarding *S. aureus*, *S. mutans*, and *S. epidermidis*, the inhibitory zone was nearly within reach for both HAp and Nd-Ce/HAp. Nd-Ce/HAp has a larger inhibition zone for *E. coli* than HAp, which showed a larger inhibition zone for fungi. Commercial HAp did not affect Gram-positive or Gram-negative bacteria. Surprisingly, the method used to synthesize hydroxyapatite has a significant influence on how effective it is against bacteria. For example, HAp samples made using the microwave-assisted combustion method demonstrated superior resistance to both Gram-positive and Gram-negative bacteria [73].

The antibacterial qualities of magnesium have been connected to several mechanisms that are related to those shown in the case of other metallic ions. According to the literature, nanoparticles harm human organisms through indirect DNA damage, oxidative stress,

and inflammation. Additionally, the generation of reactive oxygen species (ROS), which may conduct oxidative DNA damage, protein denaturation, and lipid peroxidation, has been linked to the toxicity of metal oxide nanoparticles. Reactive oxygen species (ROS) generation has also been linked to the toxicity of magnesium oxide nanoparticles, as it has been for other metal oxide nanoparticles. It has also been demonstrated that MgO nanoparticles produce large quantities of magnesium ions; however, these ions do not exhibit appreciable toxicity. The harmful effects of MgONPs have been studied by many researchers utilizing fish as model organisms [86–90].

Studies on the effects of magnesium addition to hydroxyapatite highlighted that MgHAp suspensions, compared to both the control and HAp suspensions, demonstrated good antibacterial activities even after 24 h in the case of Gram-negative *P. aeruginosa* and Gram-positive *S. aureus* bacterial strains. The results of the antimicrobial assays showed that HAp suspensions tended to make it easier for all of the microbial cells under investigation to form biofilms at all of the examined concentrations and time intervals. These findings show that when magnesium is combined with hydroxyapatite, it gives the MgHAp solutions their antibacterial properties. A recent study showed that *P. aeruginosa's* ability to produce biofilms was also decreased by the MgHAp solution at all concentrations tested, covering from 5 to 0.009 mg/mL; however, for the *S. aureus* bacterial strain, the inhibition was first noted at 2.5 mg/mL. In contrast, *P. aeruginosa* and *S. aureus* bacterial strains were more likely to produce biofilms when exposed to the HAp solutions than when not exposed, even after 24 h of incubation. For doses ranging from 5 to 1.25 mg/mL of the MgHAp suspensions, a mild suppression of biofilm development was also seen after 24 h in the instance of the fungus *C. albicans*. More than that, HAp suspensions had a stimulating effect on the *E. faecalis* and *E. coli* biofilm development [89].

In a further study, the antibacterial effectiveness of the HAp/MgO spherical granules was assessed in terms of planktonic development and early bacterial adherence against three of the most significant bacteria reported in orthopedic illnesses. It was demonstrated that HAp/MgO composites sintered at 900 and 1100 °C were able to significantly limit bacterial growth for all strains tested in contrast to pure HAp spherical granules. The outcomes are consistent with earlier research showing that MgO can inhibit Gram-positive and Gram-negative bacteria [91,92] and that the antibacterial impact relies on MgO concentration. Furthermore, it was clear that *S. aureus* growth was more positively impacted by the HAp/MgO composite's antibacterial action than *E. coli* growth was. This outcome is consistent with other research that found MgO to have stronger antibacterial activity against *S. aureus* than *E. coli*. Other research, however, demonstrates the reverse result [93]. Their different cell walls, in terms of chemical composition, structure, and thickness, can be associated with differences in antibacterial action toward *S. aureus* and *E. coli.* Gram-positive *S. aureus* bacteria have thick peptidoglycan coatings on their cell walls. Gram-negative bacteria, like *E. coli*, have more complex cell walls with a lipopolysaccharide outer membrane and a weaker peptidoglycan layer, which may give them some resistance to outside dangers [42,94].

In our study, hydroxyapatite samples' ability to interact with monospecific bacterial biofilm formation was evaluated against *E. faecalis*, *E. coli. S. aureus*, *Ps. aeruginosa* and *C. albicans*. For the samples with cerium, it can be observed that they exhibited an excellent antibacterial effect for *S. aureus* for the concentration of 5 mg/mL, 2.5 mg/mL, 0.62 mg/mL, and 0.15 mg/mL, the hydroxyapatite sample substituted with 5% cerium having the most intense effect, the similar effect is also observed for *E. faecalis* and *C. albicans*. However, in the case of *E. coli,* the hydroxyapatite samples substituted with cerium showed a less antibacterial effect, with little modification that appeared for the sample with 5% cerium. In the case of *P. aeruginosa*, the samples of hydroxyapatite substituted with cerium (1%, 3%, 5%) inhibited the biofilm formation for all concentrations.

In the case of samples of hydroxyapatite substituted with magnesium for *S. aureus*, they inhibited the biofilm formation for the concentration of 5 mg/mL and 2.5 mg/mL for 1%, 3%, 5% magnesium concentration and for the 0.62 mg/mL and 0.15 mg/mL suspension

only the sample with 5% magnesium showed an inhibitory effect. In the case of *E. faecalis*, samples substituted with magnesium (1%, 3%, 5%) inhibited the antibacterial activity only for 5 mg/mL and 2.5 mg/mL suspension. For *C. albicans* fungal strain, all three samples of hydroxyapatite substituted with magnesium showed an inhibitory effect for the suspension of 5 mg/mL, 2.5 mg/mL, and 0.62 mg/mL. In the case of *E. coli*, the only inhibition of bacteria can be observed for the sample of hydroxyapatite substituted with magnesium 3% for the suspension of 5 mg/mL and 2.5 mg/mL. As for *Ps. aeruginosa*, the inhibitory effect of bacteria was shown for the suspension of 5 mg/mL for the samples with 1%, 3%, and 5% magnesium concentration, 2.5 mg/mL for the sample with 1% magnesium concentration and for the suspension of 0.62 mg/mL and 0.15 mg/mL all the three samples (1%, 3%, 5% magnesium) shown bacteria inhibitory effect. It can be concluded that the samples of hydroxyapatite substituted with magnesium have a better inhibitory effect for Gram-positive bacteria and *C. albicans* fungal strain.

5. Conclusions

The present research pursued the synthesis through the microwave-assisted hydrothermal method and complex characterization of hydroxyapatite substituted with Ce^{3+} or Mg^{2+} powders. Following the analysis results, in all cases, hydroxyapatite was observed as the only crystalline phase, except hydroxyapatite with 5% Mg, for which were also observed the diffraction maxima attributed to the magnesium whitlockite crystalline phase. The size of cerium-substituted hydroxyapatite nanoparticles increased with the Ce^{3+} concentration, while in the case of samples substituted with magnesium, a change in the morphology was observed as the Mg^{2+} concentration increased, acquiring a platelet shape at 5% substitution. Based on the elemental mapping from the EDS analysis, the homogenous presence of the two substituents was confirmed. The FT-IR analysis confirmed the presence of specific groups for the carbonated hydroxyapatite without substantial changes following the addition of the two substituents. At the same time, the values of the hydrodynamic diameter of the hydroxyapatite nanoparticles substituted with cerium and magnesium ions obtained from the DLS analysis showed a high degree of agglomeration that can be observed in the case of all the samples. However, for hydroxyapatite substituted with 5% magnesium, a decrease in hydrodynamic diameter was observed due to the presence of whitlockite. From the biological evaluation, it was confirmed that the obtained hydroxyapatite samples do not produce cytotoxicity, and from the antimicrobial analysis, it was confirmed that the samples inhibit bacteria on *S. aureus*, *E. faecalis*, and *C. albicans* strains. According to microbiological assays, it was highlighted that the obtained samples had an increased antimicrobial effect for Gram-positive bacteria and *C. albicans* and that the cerium-substituted samples may inhibit the biofilm formation better.

Author Contributions: Conceptualization, I.A.N.; Formal analysis, A.M.H., C.C. (Carmen Curutiu), L.M.D. and M.S.; Funding acquisition, A.-M.G., and E.A.; Investigation, A.C.B., C.C. (Cristina Chircov), A.M.H., C.C. (Carmen Curutiu), L.M.D. and M.S.; Methodology, A.-C.B., and I.A.N.; Supervision, A.-M.G., and E.A.; Visualization, A.C.B. and C.C. (Cristina Chircov); Writing—original draft, A.-C.B.; Writing—review and editing, I.A.N. All authors have read and agreed to the published version of the manuscript.

Funding: This research received no external funding.

Acknowledgments: A.C.B. acknowledges the support offered by the grant POCU/993/6/13-153178, co-financed by the European Social Fund within the Sectorial Operational Program Human Capital 2014–2020. M.S.S. acknowledges the support of the UEFISCDI within project no. 81TE/2022 (PN-III-P1-1_1-TE-2021-1375-TRANS-NANO-BIO). I.A.N. acknowledges the help of the European Social Fund from the Sectoral Operational Program Human Capital 2014–2020 through the Financial Agreement with the title "Training of students and postdoctoral researchers in order to acquire applied research skills—SMART," Contract no. 13530/16.06.2022—SMIS code: 153734.

Conflicts of Interest: The authors declare no conflict of interest.

References

1. Florencio-Silva, R.; Sasso, G.R.; Sasso-Cerri, E.; Simões, M.J.; Cerri, P.S. Biology of Bone Tissue: Structure, Function, and Factors That Influence Bone Cells. *BioMed Res. Int.* **2015**, *2015*, 421746. [CrossRef] [PubMed]
2. DileepKumar, V.G.; Sridhar, M.S.; Aramwit, P.; Krut'ko, V.K.; Musskaya, O.N.; Glazov, I.E.; Reddy, N. A review on the synthesis and properties of hydroxyapatite for biomedical applications. *J. Biomater. Sci. Polym. Ed.* **2022**, *33*, 229–261. [CrossRef] [PubMed]
3. Tălpeanu, D.; Lungu, M.V.; PĂTroi, D.; Marinescu, V.E.; Cojocaru, A. Study on porous hydroxyapatite based ceramic materials as bone substitutes for cranioplasty. *Rev. Română De Mater./Rom. J. Mater.* **2021**, *51*, 178–185.
4. Ullah, I.; Hussain, Z.; Zhang, Y.; Liu, X.; Ullah, S.; Zhang, Y.; Zheng, P.; Gao, T.; Liu, Y.; Zhang, Z.; et al. Inorganic nanomaterial-reinforced hydrogel membrane as an artificial periosteum. *Appl. Mater. Today* **2022**, *28*, 101532. [CrossRef]
5. Razak, A.; Isa, N.M.; Adzila, S. Synthesis of calcium phosphate extracted from eggshell waste through precipitation method. *Biointerface Res. Appl. Chem* **2021**, *11*, 15058–15067.
6. Forero-Sossa, P.A.; Salazar-Martínez, J.D.; Giraldo-Betancur, A.L.; Segura-Giraldo, B.; Restrepo-Parra, E. Temperature effect in physicochemical and bioactive behavior of biogenic hydroxyapatite obtained from porcine bones. *Sci. Rep.* **2021**, *11*, 11069. [CrossRef]
7. Zaman, S.U.; Irfan, M.; Irfan, M.; Zaman, M.K.U.; Muhammad, N. Overview of hydroxyapatite; composition, structure, synthesis methods and its biomedical uses. *Biomed. Lett.* **2020**, *6*, 84–99.
8. Palmer, L.C.; Newcomb, C.J.; Kaltz, S.R.; Spoerke, E.D.; Stupp, S.I. Biomimetic Systems for Hydroxyapatite Mineralization Inspired By Bone and Enamel. *Chem. Rev.* **2008**, *108*, 4754–4783. [CrossRef]
9. Von Euw, S.; Wang, Y.; Laurent, G.; Drouet, C.; Babonneau, F.; Nassif, N.; Azaïs, T. Bone mineral: New insights into its chemical composition. *Sci. Rep.* **2019**, *9*, 8456. [CrossRef]
10. Neacsu, I.A.; Matei, L.; Birca, A.C.; Nicoara, A.I.; Ene, V.L.; Dragu, L.D.; Ficai, A.; Bleotu, C.; Andronescu, E. Curcumin-hydroxyapatite systems used for bone cancer treatment. *Rev. Romana De Mater. Rom. J. Mater.* **2021**, *51*, 505–513.
11. Ojo, O.A.; Olayide, I.I.; Akalabu, M.C.; Ajiboye, B.O.; Ojo, A.B.; Oyinloye, B.E.; Ramalingam, M. Nanoparticles and their biomedical applications. *Biointerface Res. Appl. Chem.* **2021**, *11*, 8431–8445.
12. Ucar, S.; Bjørnøy, S.H.; Bassett, D.C.; Strand, B.L.; Sikorski, P.; Andreassen, J.-P. Formation of Hydroxyapatite via Transformation of Amorphous Calcium Phosphate in the Presence of Alginate Additives. *Cryst. Growth Des.* **2019**, *19*, 7077–7087. [CrossRef]
13. Oni, O.P.; Hu, Y.; Tang, S.; Yan, H.; Zeng, H.; Wang, H.; Ma, L.; Yang, C.; Ran, J. Syntheses and applications of mesoporous hydroxyapatite: A review. *Mater. Chem. Front.* **2023**, *7*, 9–43. [CrossRef]
14. Zhang, Q.; Qiang, L.; Liu, Y.; Fan, M.; Si, X.; Zheng, P. Biomaterial-assisted tumor therapy: A brief review of hydroxyapatite nanoparticles and its composites used in bone tumors therapy. *Front. Bioeng. Biotechnol.* **2023**, *11*, 1167474. [CrossRef]
15. Kelly, R.R.; Sidles, S.J.; LaRue, A.C. Effects of Neurological Disorders on Bone Health. *Front. Psychol.* **2020**, *11*, 612366. [CrossRef]
16. Bhat, S.; Uthappa, U.T.; Altalhi, T.; Jung, H.Y.; Kurkuri, M.D. Functionalized Porous Hydroxyapatite Scaffolds for Tissue Engineering Applications: A Focused Review. *ACS Biomater. Sci. Eng.* **2022**, *8*, 4039–4076. [CrossRef] [PubMed]
17. Boyapati, P.C.S.; Srinivas, K.; Akhil, S.; Bollikolla, H.B.; Chandu, B. A Comprehensive Review on Novel Graphene-Hydroxyapatite Nanocomposites For Potential Bioimplant Applications. *ChemistrySelect* **2023**, *8*, e202204585. [CrossRef]
18. Kumar Yadav, M.; Hiren Shukla, R.; Prashanth, K.G. A comprehensive review on development of waste derived hydroxyapatite (HAp) for tissue engineering application. *Mater. Today Proc.* **2023**. [CrossRef]
19. Lertcumfu, N.; Jarupoom, P.; Pengpat, K.; Tunkasiri, T.; Rujijanagul, G. Effect of Metal Oxide Nanoparticles Addition on Physical Properties of Hydroxyapatite. *Adv. Mater. Res.* **2012**, *506*, 234–237. [CrossRef]
20. He, M.; Chen, L.; Yin, M.; Xu, S.; Liang, Z. Review on magnesium and magnesium-based alloys as biomaterials for bone immobilization. *J. Mater. Res. Technol.* **2023**, *23*, 4396–4419. [CrossRef]
21. Melinescu, A.; Ionita, G.; Trusca, R.; Preda, M. Ceramic porous materials obtained by the geopolymer route. *Rev. Romana De Mater.-Rom. J. Mater.* **2020**, *50*, 146–150.
22. Venkatraman, S.K.; Swamiappan, S. Review on calcium- and magnesium-based silicates for bone tissue engineering applications. *J. Biomed. Mater. Res. Part A* **2020**, *108*, 1545–1562. [CrossRef] [PubMed]
23. Ballouze, R.; Marahat, M.H.; Mohamad, S.; Saidin, N.A.; Kasim, S.R.; Ooi, J.P. Biocompatible magnesium-doped biphasic calcium phosphate for bone regeneration. *J. Biomed. Mater. Res. Part B Appl. Biomater.* **2021**, *109*, 1426–1435. [CrossRef] [PubMed]
24. Hung, C.C.; Chaya, A.; Liu, K.; Verdelis, K.; Sfeir, C. The role of magnesium ions in bone regeneration involves the canonical Wnt signaling pathway. *Acta Biomater.* **2019**, *98*, 246–255. [CrossRef] [PubMed]
25. Sezer, N.; Evis, Z.; Kayhan, S.M.; Tahmasebifar, A.; Koç, M. Review of magnesium-based biomaterials and their applications. *J. Magnes. Alloys* **2018**, *6*, 23–43. [CrossRef]
26. Antoniac, I.; Miculescu, M.; Mănescu Păltânea, V.; Stere, A.; Quan, P.H.; Păltânea, G.; Robu, A.; Earar, K. Magnesium-Based Alloys Used in Orthopedic Surgery. *Materials* **2022**, *15*, 1148. [CrossRef]
27. Blašković, M.; Butorac Prpić, I.; Blašković, D.; Rider, P.; Tomas, M.; Čandrlić, S.; Botond Hangyasi, D.; Čandrlić, M.; Perić Kačarević, Ž. Guided Bone Regeneration Using a Novel Magnesium Membrane: A Literature Review and a Report of Two Cases in Humans. *J. Funct. Biomater.* **2023**, *14*, 307. [CrossRef]
28. Nabiyouni, M.; Brückner, T.; Zhou, H.; Gbureck, U.; Bhaduri, S.B. Magnesium-based bioceramics in orthopedic applications. *Acta Biomater.* **2018**, *66*, 23–43. [CrossRef]

29. Esfahanizadeh, N.; Montazeri, M.; Nourani, M.R.; Harandi, M. Use of bioactive glass doped with magnesium or strontium for bone regeneration: A rabbit critical-size calvarial defects study. *Dent. Res. J.* **2022**, *19*, 18. [CrossRef]
30. Fu, Z.; Cui, J.; Zhao, B.; Shen, S.G.F.; Lin, K. An overview of polyester/hydroxyapatite composites for bone tissue repairing. *J. Orthop. Transl.* **2021**, *28*, 118–130. [CrossRef]
31. Zhu, Y.; Liu, W.; Ngai, T. Polymer coatings on magnesium-based implants for orthopedic applications. *J. Polym. Sci.* **2022**, *60*, 32–51. [CrossRef]
32. Zhou, H.; Liang, B.; Jiang, H.; Deng, Z.; Yu, K. Magnesium-based biomaterials as emerging agents for bone repair and regeneration: From mechanism to application. *J. Magnes. Alloys* **2021**, *9*, 779–804. [CrossRef]
33. Tiomno, O.; Coelho, F.; Pellizaro, T.; Chanfrau, R.; Capote, T.; Basmaji, P.; Veranes Pantoja, Y.; Carlos, G. Preparation of Scaffolds of Amorphous Calcium Phosphate and Bacterial Cellulose for Use in Tissue Regeneration by Freeze-Drying Process. *Biointerface Res. Appl. Chem.* **2021**, *11*, 7357–7367. [CrossRef]
34. Mammoli, F.; Castiglioni, S.; Parenti, S.; Cappadone, C.; Farruggia, G.; Iotti, S.; Davalli, P.; Maier, J.A.M.; Grande, A.; Frassineti, C. Magnesium Is a Key Regulator of the Balance between Osteoclast and Osteoblast Differentiation in the Presence of Vitamin D_3. *Int. J. Mol. Sci.* **2019**, *20*, 385. [CrossRef] [PubMed]
35. Francisco, E.M.; Zoccolotti, J.D.; Tiomnova, O.T.; Tolaba, A.G.; Chanfrau, J.E.R.; Jorge, J.H.; Basmaji, P.; Guastaldi, A.C. Sterilization of scaffolds of calcium phosphates and bacterial cellulose for their use in tissue regeneration. *Biointerface Res. Appl. Chem.* **2021**, *11*, 10089–10098.
36. Hernández-Montes, V.; Buitrago-Sierra, R.; Echeverry-Rendón, M.; Santa-Marín, J.F. Ceria-based coatings on magnesium alloys for biomedical applications: A literature review. *RSC Adv.* **2023**, *13*, 1422–1433. [CrossRef]
37. Zhang, X.; Chen, Q.; Mao, X. Magnesium Enhances Osteogenesis of BMSCs by Tuning Osteoimmunomodulation. *BioMed Res. Int.* **2019**, *2019*, 7908205. [CrossRef]
38. Groenendijk, I.; van Delft, M.; Versloot, P.; van Loon, L.J.C.; de Groot, L.C.P.G.M. Impact of magnesium on bone health in older adults: A systematic review and meta-analysis. *Bone* **2022**, *154*, 116233. [CrossRef]
39. Uppal, G.; Thakur, A.; Chauhan, A.; Bala, S. Magnesium based implants for functional bone tissue regeneration—A review. *J. Magnes. Alloys* **2022**, *10*, 356–386. [CrossRef]
40. Vieira, E.; Silva, M.; Maia-Filho, A.; Ferreira, D.; Figuerêdo-Silva, J.; Rovaris, K.; Fialho, A.C.; Leite-Oliveira, A.; Menezes de Oliveira, A.L.; da Fonseca, M.G.; et al. Effect of Cerium-Containing Hydroxyapatite in Bone Repair in Female Rats with Osteoporosis Induced by Ovariectomy. *Minerals* **2021**, *11*, 377. [CrossRef]
41. Allu, I.; Kumar Sahi, A.; Kumari, P.; Sakhile, K.; Sionkowska, A.; Gundu, S. A Brief Review on Cerium Oxide (CeO2NPs)-Based Scaffolds: Recent Advances in Wound Healing Applications. *Micromachines* **2023**, *14*, 865. [CrossRef] [PubMed]
42. Barker, E.; Shepherd, J.; Asencio, I.O. The Use of Cerium Compounds as Antimicrobials for Biomedical Applications. *Molecules* **2022**, *27*, 2678. [CrossRef] [PubMed]
43. Lamkhao, S.; Phaya, M.; Jansakun, C.; Chandet, N.; Thongkorn, K.; Rujijanagul, G.; Bangrak, P.; Randorn, C. Synthesis of Hydroxyapatite with Antibacterial Properties Using a Microwave-Assisted Combustion Method. *Sci. Rep.* **2019**, *9*, 4015. [CrossRef] [PubMed]
44. Zhang, M.; Zhai, X.; Ma, T.; Huang, Y.; Jin, M.; Yang, H.; Fu, H.; Zhang, S.; Sun, T.; Jin, X.; et al. Sequential Therapy for Bone Regeneration by Cerium Oxide-Reinforced 3D-Printed Bioactive Glass Scaffolds. *ACS Nano* **2023**, *17*, 4433–4444. [CrossRef] [PubMed]
45. Stephen Inbaraj, B.; Chen, B.-H. An overview on recent in vivo biological application of cerium oxide nanoparticles. *Asian J. Pharm. Sci.* **2020**, *15*, 558–575. [CrossRef] [PubMed]
46. Rajeshkumar, S.; Naik, P. Synthesis and biomedical applications of Cerium oxide nanoparticles—A Review. *Biotechnol. Rep.* **2018**, *17*, 1–5. [CrossRef]
47. Qi, M.; Li, W.; Zheng, X.; Li, X.; Sun, Y.; Wang, Y.; Li, C.; Wang, L. Cerium and Its Oxidant-Based Nanomaterials for Antibacterial Applications: A State-of-the-Art Review. *Front. Mater.* **2020**, *7*, 213. [CrossRef]
48. Pop, O.L.; Mesaros, A.; Vodnar, D.C.; Suharoschi, R.; Tăbăran, F.; Mageruşan, L.; Tódor, I.S.; Diaconeasa, Z.; Balint, A.; Ciontea, L.; et al. Cerium Oxide Nanoparticles and Their Efficient Antibacterial Application In Vitro against Gram-Positive and Gram-Negative Pathogens. *Nanomaterials* **2020**, *10*, 1614. [CrossRef]
49. Hosseini, M.; Mozafari, M. Cerium Oxide Nanoparticles: Recent Advances in Tissue Engineering. *Materials* **2020**, *13*, 3072. [CrossRef]
50. Arokiasamy, P.; Al Bakri Abdullah, M.M.; Abd Rahim, S.Z.; Luhar, S.; Sandu, A.V.; Jamil, N.H.; Nabiałek, M. Synthesis methods of hydroxyapatite from natural sources: A review. *Ceram. Int.* **2022**, *48*, 14959–14979. [CrossRef]
51. Schmidt, R.; Prado-Gonjal, J.; Morán, E. *Microwaves: Microwave Assisted Hydrothermal Synthesis of Nanoparticles*; CRC Press: Boca Raton, FL, USA, 2015; pp. 561–572.
52. Ebrahimi, S.; Stephen Sipaut@ Mohd Nasri, C.; Bin Arshad, S.E. Hydrothermal synthesis of hydroxyapatite powders using Response Surface Methodology (RSM). *PLoS ONE* **2021**, *16*, e0251009. [CrossRef] [PubMed]
53. Jorgensen, J.H.; Ferraro, M.J. Antimicrobial susceptibility testing: A review of general principles and contemporary practices. *Clin. Infect. Dis. Off. Publ. Infect. Dis. Soc. Am.* **2009**, *49*, 1749–1755. [CrossRef] [PubMed]
54. Batool, S.; Liaqat, U.; Hussain, Z.; Sohail, M. Synthesis, Characterization and Process Optimization of Bone Whitlockite. *Nanomaterials* **2020**, *10*, 1856. [CrossRef] [PubMed]

55. Shah, F.A. Magnesium whitlockite—Omnipresent in pathological mineralisation of soft tissues but not a significant inorganic constituent of bone. *Acta Biomater.* **2021**, *125*, 72–82. [CrossRef] [PubMed]
56. Castro, M.A.M.; Portela, T.O.; Correa, G.S.; Oliveira, M.M.; Rangel, J.H.G.; Rodrigues, S.F.; Mercury, J.M.R. Synthesis of hydroxyapatite by hydrothermal and microwave irradiation methods from biogenic calcium source varying pH and synthesis time. *Boletín Soc. Española Cerámica Y Vidr.* **2022**, *61*, 35–41. [CrossRef]
57. Paduraru, A.V.; Musuc, A.M.; Oprea, O.C.; Trusca, R.; Iordache, F.; Vasile, B.S.; Andronescu, E. Synthesis and Characterization of Photoluminescent Ce(III) and Ce(IV) Substituted Hydroxyapatite Nanomaterials by Co-Precipitation Method: Cytotoxicity and Biocompatibility Evaluation. *Nanomaterials* **2021**, *11*, 1911. [CrossRef]
58. Jang, H.L.; Lee, H.K.; Jin, K.; Ahn, H.-Y.; Lee, H.-E.; Nam, K.T. Phase transformation from hydroxyapatite to the secondary bone mineral, whitlockite. *J. Mater. Chem. B* **2015**, *3*, 1342–1349. [CrossRef]
59. Cheng, H.; Chabok, R.; Guan, X.; Chawla, A.; Li, Y.; Khademhosseini, A.; Jang, H.L. Synergistic interplay between the two major bone minerals, hydroxyapatite and whitlockite nanoparticles, for osteogenic differentiation of mesenchymal stem cells. *Acta Biomater.* **2018**, *69*, 342–351. [CrossRef]
60. Lagier, R.; Baud, C.A. Magnesium Whitlockite, a Calcium Phosphate Crystal of Special Interest in Pathology. *Pathol. Res. Pract.* **2003**, *199*, 329–335. [CrossRef]
61. McComiskey, K.P.M.; Tajber, L. Comparison of particle size methodology and assessment of nanoparticle tracking analysis (NTA) as a tool for live monitoring of crystallisation pathways. *Eur. J. Pharm. Biopharm.* **2018**, *130*, 314–326. [CrossRef]
62. Singh, G.; Jolly, S.S.; Singh, R.P. Cerium substituted hydroxyapatite mesoporous nanorods: Synthesis and characterization for drug delivery applications. *Mater. Today: Proc.* **2020**, *28*, 1460–1466. [CrossRef]
63. Cegla, R.-N.; Macha, I.; Ben-Nissan, B.; Grossin, D.; Heness, G.; Chung, R.-J. Comparative Study of Conversion of Coral with Ammonium Dihydrogen Phosphate and Orthophosphoric Acid to Produce Calcium Phosphates. *J. Aust. Ceram. Soc.* **2014**, *50*, 154–161.
64. Nigar, F.; Johnston, A.-L.; Smith, J.; Oakley, W.; Islam, T.; Felfel, R.; Grant, D.; Lester, E.; Ahmed, I. Production of Nano Hydroxyapatite and Mg-Whitlockite from Biowaste-Derived Products via Continuous Flow Hydrothermal Synthesis: A Step towards Circular Economy. *Materials* **2023**, *16*, 2138. [CrossRef] [PubMed]
65. Chanfrau, R. Evaluation of the influence of microwaves radiation on a biomaterial composed of three phases of calcium phosphates. *Biointerface Res. Appl. Chem.* **2020**, *10*, 5141–5144. [CrossRef]
66. Gherasim, O.; Grumezescu, A.M.; Grumezescu, V.; Negut, I.; Dumitrescu, M.F.; Stan, M.S.; Nica, I.C.; Holban, A.M.; Socol, G.; Andronescu, E. Bioactive Coatings Based on Hydroxyapatite, Kanamycin, and Growth Factor for Biofilm Modulation. *Antibiotics* **2021**, *10*, 160. [CrossRef] [PubMed]
67. Ciobanu, G.; Harja, M. Cerium-doped hydroxyapatite/collagen coatings on titanium for bone implants. *Ceram. Int.* **2019**, *45*, 2852–2857. [CrossRef]
68. El Makhloufy, S.; Oubouaza, R.; Ouasri, A.; Belaaouad, S. X-Ray diffraction and infrared spectroscopy data review analyses of the Calcium phosphates. *Biointerface Res. Appl. Chem.* **2022**, *12*, 732–755.
69. Farzadi, A.; Bakhshi, F.; Solati-Hashjin, M.; Asadi, M.; Abu Osman, N.A. Magnesium incorporated hydroxyapatite: Synthesis and structural properties characterization. *Ceram. Int.* **2014**, *40*, 6021–6029. [CrossRef]
70. Bal, Z.; Kaito, T.; Korkusuz, F.; Yoshikawa, H. Bone regeneration with hydroxyapatite-based biomaterials. *Emergent Mater.* **2020**, *3*, 521–544. [CrossRef]
71. Koski, C.; Vu, A.A.; Bose, S. Effects of chitosan-loaded hydroxyapatite on osteoblasts and osteosarcoma for chemopreventative applications. *Mater. Sci. Eng. C Mater. Biol. Appl.* **2020**, *115*, 111041. [CrossRef]
72. Omidi, M.; Ahmad Agha, N.; Müller, A.; Feyerabend, F.; Helmholz, H.; Willumeit-Römer, R.; Schlüter, H.; Luthringer-Feyerabend, B.J.C. Investigation of the impact of magnesium versus titanium implants on protein composition in osteoblast by label free quantification†. *Metallomics* **2020**, *12*, 916–934. [CrossRef] [PubMed]
73. Al-Shahrabalee, S.Q.; Jaber, H.A. Bioinorganic Preparation of Hydroxyapatite and Rare Earth Substituted Hydroxyapatite for Biomaterials Applications. *Bioinorg. Chem. Appl.* **2023**, *2023*, 7856300. [CrossRef] [PubMed]
74. Farazin, A.; Aghadavoudi, F.; Motififard, M.; Saber-Samandari, S.; Khandan, A. Nanostructure, Molecular Dynamics Simulation and Mechanical Performance of PCL Membranes Reinforced with Antibacterial Nanoparticles. *J. Appl. Comput. Mech.* **2021**, *7*, 1907–1915. [CrossRef]
75. Baskaran, P.; Udduttula, A.; Uthirapathy, V. Development and characterisation of novel Ce-doped hydroxyapatite–Fe3 O4 nanocomposites and their in vitro biological evaluations for biomedical applications. *IET Nanobiotechnol.* **2018**, *12*, 138–146. [CrossRef]
76. Gonzalez-Moreno, M.; Morovic, P.; Tkhilaishvili, T.; Trampuz, A. Bacteriophages for Treatment of Biofilm Infections. In *Bone and Joint Infections*; Wiley: Hoboken, NJ, USA, 2021; pp. 65–80.
77. Wang, H.; Xiong, C.; Yu, Z.; Zhang, J.; Huang, Y.; Zhou, X. Research Progress on Antibacterial Coatings for Preventing Implant-Related Infection in Fractures: A Literature Review. *Coatings* **2022**, *12*, 1921. [CrossRef]
78. Silva-Holguín, P.N.; Reyes-López, S.Y. Synthesis of Hydroxyapatite-Ag Composite as Antimicrobial Agent. *Dose-Response A Publ. Int. Hormesis Soc.* **2020**, *18*, 1559325820951342. [CrossRef]
79. Oshima, S.; Sato, T.; Honda, M.; Suetsugu, Y.; Ozeki, K.; Kikuchi, M. Fabrication of Gentamicin-Loaded Hydroxyapatite/Collagen Bone-Like Nanocomposite for Anti-Infection Bone Void Fillers. *Int. J. Mol. Sci.* **2020**, *21*, 551. [CrossRef]

80. Bee, S.L.; Bustami, Y.; Ul-Hamid, A.; Lim, K.; Abdul Hamid, Z.A. Synthesis of silver nanoparticle-decorated hydroxyapatite nanocomposite with combined bioactivity and antibacterial properties. *J. Mater. Sci. Mater. Med.* **2021**, *32*, 106. [CrossRef]
81. Coulon, A.; Laurencin, D.; Grandjean, A.; Cau Dit Coumes, C.; Rossignol, S.; Campayo, L. Immobilization of iodine into a hydroxyapatite structure prepared by cementation. *J. Mater. Chem. A* **2014**, *2*, 20923–20932. [CrossRef]
82. Surmeneva, M.; Sharonova, A.; Chernousova, S.; Prymak, O.; Loza, K.; Tkachev, M.; Shulepov, I.; Epple, M.; Surmenev, R. Incorporation of silver nanoparticles into magnetron-sputtered calcium phosphate layers on titanium as an antibacterial coating. *Colloids Surf. B Biointerfaces* **2017**, *156*, 104–113. [CrossRef]
83. Guangjian, D.A.I.; Aili, Y.U.; Xiang, C.A.I.; Qingshan, S.H.I.; Ouyang, Y.; Shaozao, T.A.N. Synthesis, characterization and antimicrobial activity of zinc and cerium co-doped α-zirconium phosphate. *J. Rare Earths* **2012**, *30*, 820–825.
84. Carmen, C.; Popa, C.; Predoi, D. Cerium doped hydroxyapatite nanoparticles synthesized by coprecipitation method. *J. Serbian Chem. Soc.* **2016**, *81*, 433–446. [CrossRef]
85. Zheng, J.X.; Li, H.; Pu, Z.Y.; Wang, H.Y.; Deng, X.B.; Liu, X.J.; Deng, Q.W.; Yu, Z.J. Bloodstream infections caused by *Enterococcus* spp: A 10-year retrospective analysis at a tertiary hospital in China. *J. Huazhong Univ. Sci. Technol. Med. Sci.* **2017**, *37*, 257–263. [CrossRef] [PubMed]
86. Uruén, C.; Chopo-Escuin, G.; Tommassen, J.; Mainar-Jaime, R.C.; Arenas, J. Biofilms as Promoters of Bacterial Antibiotic Resistance and Tolerance. *Antibiotics* **2020**, *10*, 3. [CrossRef]
87. Pokharel, P.; Dhakal, S.; Dozois, C.M. The Diversity of Escherichia coli Pathotypes and Vaccination Strategies against This Versatile Bacterial Pathogen. *Microorganisms* **2023**, *11*, 344. [CrossRef] [PubMed]
88. Braz, V.S.; Melchior, K.; Moreira, C.G. Escherichia coli as a Multifaceted Pathogenic and Versatile Bacterium. *Front. Cell. Infect. Microbiol.* **2020**, *10*, 548492. [CrossRef] [PubMed]
89. Predoi, D.; Iconaru, S.L.; Predoi, M.V.; Stan, G.E.; Buton, N. Synthesis, Characterization, and Antimicrobial Activity of Magnesium-Doped Hydroxyapatite Suspensions. *Nanomaterials* **2019**, *9*, 1295. [CrossRef]
90. Coelho, C.C.; Araújo, R.; Quadros, P.A.; Sousa, S.R.; Monteiro, F.J. Antibacterial bone substitute of hydroxyapatite and magnesium oxide to prevent dental and orthopaedic infections. *Mater. Sci. Eng. C* **2019**, *97*, 529–538. [CrossRef]
91. Sawai, J. Quantitative evaluation of antibacterial activities of metallic oxide powders (ZnO, MgO and CaO) by conductimetric assay. *J. Microbiol. Methods* **2003**, *54*, 177–182. [CrossRef]
92. Yamamoto, O.; Ohira, T.; Alvarez, K.; Fukuda, M. Antibacterial characteristics of CaCO3–MgO composites. *Mater. Sci. Eng. B* **2010**, *173*, 208–212. [CrossRef]
93. Chou, Y.-F.; Chiou, W.-A.; Xu, Y.; Dunn, J.C.Y.; Wu, B.M. The effect of pH on the structural evolution of accelerated biomimetic apatite. *Biomaterials* **2004**, *25*, 5323–5331. [CrossRef] [PubMed]
94. Coelho, C.C.; Padrão, T.; Costa, L.; Pinto, M.T.; Costa, P.C.; Domingues, V.F.; Quadros, P.A.; Monteiro, F.J.; Sousa, S.R. The antibacterial and angiogenic effect of magnesium oxide in a hydroxyapatite bone substitute. *Sci. Rep.* **2020**, *10*, 19098. [CrossRef] [PubMed]

Journal of
Functional
Biomaterials

MDPI

Article

Combined System for the Simultaneous Delivery of Levofloxacin and Rifampicin: Structural and Functional Properties and Antibacterial Activity

Irina M. Le-Deygen *, Polina V. Mamaeva, Anna A. Skuredina, Anastasia S. Safronova, Natalia G. Belogurova and Elena V. Kudryashova

Chemical Enzymology Department, Lomonosov Moscow State University, 119991 Moscow, Russia; mamaevapolina@yahoo.com (P.V.M.); skuredinanna@gmail.com (A.A.S.); milarika09@mail.ru (A.S.S.); nbelog@mail.ru (N.G.B.); helena_koudriachova@hotmail.com (E.V.K.)
* Correspondence: i.m.deygen@gmail.com

Abstract: The therapy of resistant forms of tuberculosis requires the simultaneous use of several drugs, in particular, a combination of rifampicin and levofloxacin. In this paper, we aimed to design a combined system for the simultaneous delivery of these drugs for potential inhalation administration. A feature of this system is the incorporation of rifampicin into optimized liposomal vesicles capable of forming a multipoint non-covalent complex with chitosan-β-cyclodextrin conjugates. Levofloxacin is incorporated into cyclodextrin tori by forming a host–guest complex. Here, a comprehensive study of the physicochemical properties of the obtained systems was carried out and special attention was paid to the kinetics of cargo release for individual drugs and in the combined system. The release of levofloxacin in combined system is slow and is described by the Higuchi model in all cases. The release of rifampicin from liposomes during the formation of complexes with polymeric conjugates is characterized by the change of the Higuchi model to the Korsmeyer–Peppas model with the main type of diffusion against Fick′s law. Microbiological studies in solid and liquid growth media a consistently high antibacterial activity of the obtained systems was shown against *B. subtilis* and *E. coli*.

Keywords: antibiotics; levofloxacin; rifampicin; liposomes; chitosan; cyclodextrin

1. Introduction

The spread of tuberculosis continues to be one of the greatest threats to public health on a global scale. The WHO reports that tuberculosis is remains one of the top ten leading causes of death worldwide. In addition, it tops the list of causes of death with rising mortality, and it is the leading killer of HIV-positive individuals [1]. Moreover, the COVID-19 pandemic of recent years has significantly impacted the overall state of public health and the spread of diseases of the respiratory system (including tuberculosis, pneumonia, etc.), in addition to making other problems more prevalent [2].

The typical anti-tuberculosis treatment protocol requires the administration of antibacterial drugs for an extended period of time at high doses, which is accompanied by serious side effects, decreased patient compliance, and the emergence of drug resistance in the pathogen [3].

Rifampicin (Rif) is one of the main first-line anti-tuberculosis drugs, which is usually included in the standard treatment regimen. Its mechanism of action is to inhibit the transcription of *M. tuberculosis* by acting on DNA-dependent RNA polymerase; however, to achieve such an effect, an antibacterial drug must penetrate into the bacterial cytoplasm [4]. That is why one of the most common mechanisms for the emergence of resistance to rifampicin is the modification of cell permeability due to changes in the nature of the lipid

bilayer of the cell and the use of special energy efflux pumps [5]. The minimal inhibition concentration (MIC) of rifampicin for *M. tuberculosis* is 0.05–0.5 mg/L [6].

Rif-based therapy may be accompanied by side effects such as nausea, vomiting, headache, increased levels of liver enzymes, thrombocytopenia, renal failure, etc. [4].

The therapy of resistant forms of tuberculosis is carried out most often with the help of second- or third-line drugs, e.g., levofloxacin (Lev). Lev belongs to third-generation fluoroquinolones, which are broad-spectrum antibacterial drugs. Thus, the use of levofloxacin as an independent drug is less effective than its combination with others [7]. The MIC of levofloxacin for *M. tuberculosis* is 0.25–4 mg/L [8].

Lev's mechanism of action is the selective inhibition of bacterial DNA gyrase, which leads to the disruption of DNA supercoiling and the suppression of bacterial DNA replication and transcription. The result is a reduction in the growth and reproduction of bacteria, and, as a consequence, their death. Lev may also have an immunomodulatory effect by increasing phagocytosis and neutrophil activity [9].

To increase the effectiveness of the treatment and to reduce the side effects, drugs are included in various delivery systems, including liposomes, β-cyclodextrin derivatives, polymers, etc. One of the most promising ways to administer such systems for antituberculosis therapy is inhalation, since, in this case, the drug formulation effectively reaches infected cells [10].

Such systems for the inhalation delivery of antibacterial drugs must provide a sustained release of cargo to maintain therapeutic concentrations, as well as have an affinity for pulmonary surfactant. At the same time, various delivery systems have limited applicability in relation to drugs. For hydrophobic Rif, one of the most suitable delivery systems is liposomal forms. The high potential of liposomes as carriers for Rif was demonstrated in [11]. Recently, we found that for Rif liposomes based on dipalmitoylphosphatidylcholine (DPPC) and cardiolipin (CL) at a weight ratio of 80:20 provides high loading efficacy, effective binding at the room temperature, and a suitable phase transition profile at physiological temperatures [12].

Moreover, the high therapeutic potential of the liposomal forms of Rif decorated with chitosan or ε-poly-L-lysine was demonstrated in [13], including outstanding mucoadhesive properties and stability upon nebulization. Combined rifampicin formulations delivered by the pulmonary route have been proven to be effective for tuberculosis treatment in the guinea pigs [14].

For Lev, one could choose β-cyclodextrin derivatives, with which it is able to form stable guest–host complexes. According to the European Medicines Agency (2014) ("Background review for cyclodextrins used as excipient" (EMA/CHMP/333892/2013)) beta-cyclodextrins with maximum applicable volume of 10% provide excellent tolerance via nasal mucosa, which was demonstrated in irritation studies with rabbits that did not show any local or systemic toxic effects from nasal administration for 3 months. However, such small complexes are not suitable for inhaled delivery, and thus, we synthetized a polymer-based carrier of low-molecular-based chitosan conjugated with β-cyclodextrin tori [15]. This carrier provides high encapsulation efficacy and a suitable release profile. Moreover, mucoadhesive chitosan provides several benefits because of affinity to the mucus of airways and its own antibacterial activity. Chitosan–cyclodextrin conjugates are the focus of research, as they could be promising carriers [16] suitable both for slow and fast release. Variable substituents in the cyclodextrin structure provides higher loading efficacy and stability [17]. Different conjugates based on chitosan and cyclodextrins are suitable for oral [18], pulmonary [19], and ocular administration [20].

The combination of these delivery systems is possible due to the creation of liposome surface complexes with the functionalized chitosan described above. Thus, the use of a combination of liposomal delivery forms of anti-tuberculosis drugs and complexes of antibacterial agents with β-cyclodextrin derivatives, united by a mucoadhesive polymer, can significantly increase the effectiveness of therapy and reduce its duration.

Combined systems used in the inhalation delivery of anti-tuberculosis drugs are diverse. For example, in [21] a synergistic effect of the double capture of moxifloxacin and amikacin was shown in comparison with alginate-modified PLGA nanoparticles containing one drug. The development of such systems leads to the necessity of creating methods for the simultaneous registration of several drug molecules in pharmaceutical preparations, which was demonstrated in the determination of moxifloxacin and prednisolone by reverse-phase high-performance liquid chromatography in [22].

Despite the variability of such combined drug delivery systems, there is a lack of understanding of the fundamental patterns of its formation and physico-chemical and biological properties. Here, we aimed to study a combined system, where Rif is loaded into liposomes and the vesicles are covered with a polymer shell. The polymer is chitosan with a molecular weight of 5 kDa, covalently linked to beta-cyclodextrin tori. When beta-cyclodextrin is 2-hydroxypropyl-beta-cyclodextrin, the polymer is named HP-CD-Chit, and when the cyclodextrin moiety is presented with an amino-cyclodextrin, the polymer is named NH_2-CD-Chit. Although liposome-based delivery systems for rifampicin and cyclodextrin-based delivery systems for levofloxacin are described for the first time in this work, we aim to create a combined simultaneous delivery system and uncover whether new properties will appear in the system or whether the properties will be the sum of existing ones.

To discover this, we are focusing on structural studies and in-depth studies with drug release kinetics as the key parameter of each drug delivery system. Moreover, we aimed to study the antibacterial activity of the developed systems on several Gram-positive and Gram-negative strains.

Thus, to create a system for the simultaneous delivery of rifampicin and levofloxacin, it is necessary to study the structural and functional properties of the combination of liposomal forms of rifampicin with complexes of levofloxacin and conjugates based on chitosan and β-cyclodextrin.

2. Materials and Methods

2.1. Materials

Mono-(6-(hexamethylenediamine)-6-deoxy)-β-cyclodextrin (NH_2-CD), 2-hydroxy propyl-β-cyclodextrin (HP-CD), 5 kDa Chitosan oligosaccharide lactate with deacetylation degree 98% (Chit), levofloxacin and rifampicin were obtained from Sigma Aldrich (St. Louis, MO, USA); tablets of phosphate-buffered saline and HCl were obtained from "PanEco" (Moscow, Russia); dipalmitoylphosphatidylcholine, sodium salt and 16:0 cardiolipin 1′,3′-bis-[1,2-dipalmitoyl-sn -glycero-3-phospho]-glycerol were obtained from "Avanti Polar Lipids" (Alabaster, AL, USA); dialysis bags with a cut-off molecular weight of 12–14 kDa were obtained from "Orange Scientific" (Braine-l'Alleud, Belgium); and dialysis bags with a cut-off molecular weight of 3,5 kDa were obtained from "Serva" (Heidelberg, Germany). NH_2-CD-Chit and HP-CD-Chit were synthetized and purified according to the methodic [15] and used in this research without additional treatment.

2.2. Liposomal form of Rif Preparation

Liposomes were obtained through lipid film hydration followed by sonication. Solutions of DPPC and CL in chloroform (25 mg/mL) in the required mass ratio (DPPC 100 w. % and DPPC:CL w. % 80:20) and were placed in a round bottom flask, then the solvent was removed on a rotary evaporator at a temperature below 55 °C. The resulting thin film was dispersed in 0.01 M sodium phosphate-buffered solution (pH = 7.4) to a lipid concentration of 5 mg/mL, then the flask was exposed to an ultrasonic bath (37 Hz) for 5 min. The opaque suspension was transferred into a plastic tube and sonicated (22 kHz) for 10 min continuously with constant cooling on a 4710 Cole-Parmer Instrument disperser.

Liposomal forms of rifampicin were obtained in a similar way with some changes: a thin lipid film was dispersed in 0.01 M sodium phosphate-buffered solution (pH = 7.4) containing rifampicin at a concentration of 2 mg/mL. The unloaded drug was separated

by dialysis against 0.01 M sodium phosphate-buffered solution (pH = 7.4) in Serva dialysis bags with a cut-off molecular weight of 3500 Da for 120 min at 4 °C.

The encapsulation efficiency (*EE*) of rifampicin in liposomes was calculated according to Equation (1):

$$EE = \frac{\nu(\text{Rif})_{total} - \nu(\text{Rif})_{dialysis}}{\nu(\text{Rif})_{total}} \times 100\% \quad (1)$$

where $\nu(\text{Rif})_{total}$ is the total amount of Rif in the initial system before dialysis and $\nu(\text{Rif})_{dialysis}$ is the amount of Rif determined in the external solution after dialysis against sodium phosphate-buffered solution 0.01 M for 120 min at a temperature of 4 °C.

Complexes of liposomes with conjugates of chitosan and β-cyclodextrin were obtained by adding a solution of NH_2-CD-Chit or HP-CD-Chit (5 mg/mL) (loaded with Lev or empty) to a solution of liposomes (5 mg/mL) in a sodium phosphate-buffered solution (pH = 7.4) at a base-molar ratio of 7:1. The complexes were incubated at room temperature for 15 min.

2.3. Complexes of Levofloxacin with the Conjugate of Chitosan and B-Cyclodextrin Preparation

The solution of levofloxacin in hydrochloric acid (pH 4.0, 3 mg/mL) was combined with a solution of NH_2-CD-Chit (5 mg/mL) with the same pH at the same ratio to achieve 2× excess of CD-tori in relation to Lev molecules. The complexes were incubated at 37 °C for 60 min.

The encapsulation efficiency (*EE*) of Lev in carrier was calculated according to Equation (2):

$$EE = \frac{\nu(\text{Lev})_{total} - \nu(\text{Lev})_{dialysis}}{\nu(\text{Lev})_{total}} \times 100\% \quad (2)$$

where $\nu(\text{Lev})_{total}$ is the total amount of Lev in the initial system before dialysis and $\nu(\text{Lev})_{dialysis}$ is the amount of Lev determined in the external solution after dialysis against a $1 \cdot 10^{-4}$ M HCl solution in Serva dialysis bags with a cut-off molecular weight of 3500 Da for 15 min at a temperature of 4 °C.

2.4. Drug Release Kinetics Studies

Experiments on the kinetics of Lev release from β-cyclodextrin derivatives were carried out in an HCl solution (pH = 4.0) at a temperature of 37 °C and at a rotation speed of 120 rpm. For this, samples of 1 mL of complex solution were placed in an Orange Scientific dialysis bag with a cut-off molecular weight of 12–14 kDa against 10 mL of an external HCl solution (pH = 4.0). Sampling with a volume of 100 µL was carried out during the day, maintaining a constant volume of the external solution. Samples were analyzed via UV spectroscopy to determine the amount of drug released.

Experiments on the kinetics of Rif release from liposomes were carried out in almost the same way. Experiments were conducted in 0.01 M sodium phosphate-buffered solution (pH = 7.4) at a temperature of 37 °C and a rotation speed of 120 rpm. Liposomal forms of rifampicin (LRif) with a sample volume of 1 mL were placed in Orange Scientific dialysis bags with cut-off molecular weights of 12–14 kDa against 10 mL of an external 0.01 M sodium phosphate-buffered solution (pH = 7.4). Sampling with a volume of 100 µL was carried out during the day, maintaining a constant volume of the external solution. Samples were analyzed via UV spectroscopy to determine the proportion of the drug released.

Experiments on the kinetics of the simultaneous release of rifampicin and levofloxacin from the combined system were carried out in 0.01 M sodium phosphate-buffered solution (pH = 7.4) at a temperature of 37 °C and a rotation speed of 120 rpm. For this, complexes of liposomes (5 mg/mL) loaded with rifampicin (2 mg/mL) were obtained through the NH_2-CD-Chit-Lev complex at a base-molar ratio of 1:7. The resulting complexes, 1 mL in volume, were placed in 10 mL of an external 0.01 M sodium phosphate-buffered solution (pH = 7.4). Sampling with a volume of 100 µL was carried out during the day, maintaining a constant volume of the external solution. We obtained points of 5, 10, 15, 30, 45, 60, 75,

90, 120, 150, 180, 210, 240, 270, 300, 960 and 1440 min. Samples were analyzed through UV spectroscopy to determine the proportion of the drug released.

The study of drug release was carried out by describing the kinetic curves with zero- and first-order models, Higuchi, Korsmeyer–Peppas and Hickson–Crowell models according to Equations (3)–(7):

Zero-order:

$$Q_t = Q_0 + K_0 \cdot t \quad (3)$$

First-order:

$$\ln Q_t = \ln Q_0 \cdot K_1 \cdot t \quad (4)$$

Higuchi model:

$$Q_t = K_H \cdot \sqrt{t} \quad (5)$$

Korsmeyer–Peppas model:

$$\frac{Q_t}{Q_\infty} = K_{KP} \cdot t^n \quad (6)$$

Hickson–Crowell model:

$$Q_0^{1/3} - Q_t^{1/3} = K_{HC} \cdot t \quad (7)$$

where t—time, minutes; Q_t—amount of the drug released during t minutes, %; Q_0—initial amount of the drug, %; Q_∞—maximal release of the drug, %; K_0—release constant for the zero-order model, min^{-1}; K_1—release constant for the first-order model, min^{-1}; K_H—release constant for the Higuchi model, $min^{-0.5}$; K_{KP}—release constant for the Korsmeyer–Peppas model; n—release coefficient; and K_{HC}—release constant for the Hickson–Crowell model, min^{-1}.

2.5. Antibacterial Activity Tests

The study of the antibacterial activity of dosage forms *in vitro* was carried out via the agar diffusion method [23] in the Luria–Bertani nutrient medium (pH 7.4). An overnight culture of *Escherichia coli* ATCC 25922 or *Bacillus subtilis* ATCC 6633 (All-Russian Collection of Industrial Microorganisms, Kurchatov Institute, Moscow, Russia) was diluted to 0.5 McFarland turbidity standard. Next, 500 µL of the bacterial suspension was spread over the surface of the solid nutrient medium. After 20 min, agar discs (diameter of ~9 mm) were removed from the agar by sterile plastic tip, and the samples (50 µL each) were placed in the agar wells. Petri dishes were incubated at 37 °C for 24 h. Then, the diameters of the emerged zones of bacterial growth inhibition were analyzed. The minimum inhibitory concentration (MIC) was defined as the sample concentration (µg/mL) at which the diameter of the inhibition zone corresponds to 9 mm, according to a method published previously [24].

For experiments in liquid media, the overnight culture was diluted twice with fresh media. Then, the 0.2 mL of the sample was added (buffer 7.4 as a control and Lev 0.15 µg/mL or Rif 0.1 µg/mL). The tubes were shaken at 160 rpm 37 °C for 6 h and the aliquots were measured at 600 nm each hour. The experiments were carried out independently three times, the obtained values are averaged and presented with a standard deviation.

2.6. ATR–FTIR Spectroscopy

The ATR–FTIR spectra were recorded on a Bruker Tensor 27 Fourier IR spectrometer (Bruker, Ettlingen, Germany) equipped with an MCT detector cooled with liquid nitrogen and a Huber thermostat (Raleigh, NC, USA). The measurements were carried out in a thermostated cell of attenuated total internal reflection (FTIR, BioATR-II, Bruker, Germany), using a ZnSe single reflection crystal at 22 °C, and a constant speed of dry air blowing through the system, using a Jun-Air apparatus (Redditch, UK). An aliquot (50 µL) of the sample was applied to the ATR cell crystal, and the spectrum was recorded three times in the range from 3000 to 950 cm^{-1}, with a resolution of 1 cm^{-1}. Then, scanning and averaging

were performed 70-fold. The background was recorded in a similar way. The spectra were analyzed using the Opus 7.0 program. Typical spectrum is presented on Supplementary Materials Figure S1.

2.7. DLS Measurements

ζ-potentials and particle hydrodynamic diameters Dh were measured using a Malvern Zetasizer Nano ZS machine (Malvern, UK) equipped with a helium–neon laser (5 mW, 633 nm) as a light source. The experiment was carried out in a thermostated cell at 22 °C.

2.8. UV Spectroscopy

The UV spectra were recorded with an Ultrospec 2100 pro (Amersham Biosciences, Amersharm, UK) within a wavelength range of 200–600 nm in a 1 mL quartz cell (Hellma Analytics, Muellheim, Germany). For Lev, the intensity of the band of 295 nm was studied and for Rif the intensity of 470 nm was examined. Typical spectra of Lev and Rif are presented on Figure S2.

All measurements were triplicated.

2.9. Statistical Analysis

All experiments performed in triplicate, and the results were expressed as the mean value ± standard deviation, SD (n = 3). AtteStat 3.04 for Microsoft Excel was used for statistical analysis. Significance was analyzed via the Mann–Whitney test, with $p \leq 0.05$ considered statistically significant.

3. Results and Discussion

Previously, we considered the mechanism of the interaction of rifampicin with liposomes of various lipid compositions [12], as well as the interaction of levofloxacin with the chitosan–cyclodextrin polymer [15]. Here, we aimed to investigate the properties and antibacterial activity of combined system, where the liposomal form of Rif is covered with chitosan–cyclodextrin shell, loaded with levofloxacin. Figure 1 represents formulae of substances under consideration.

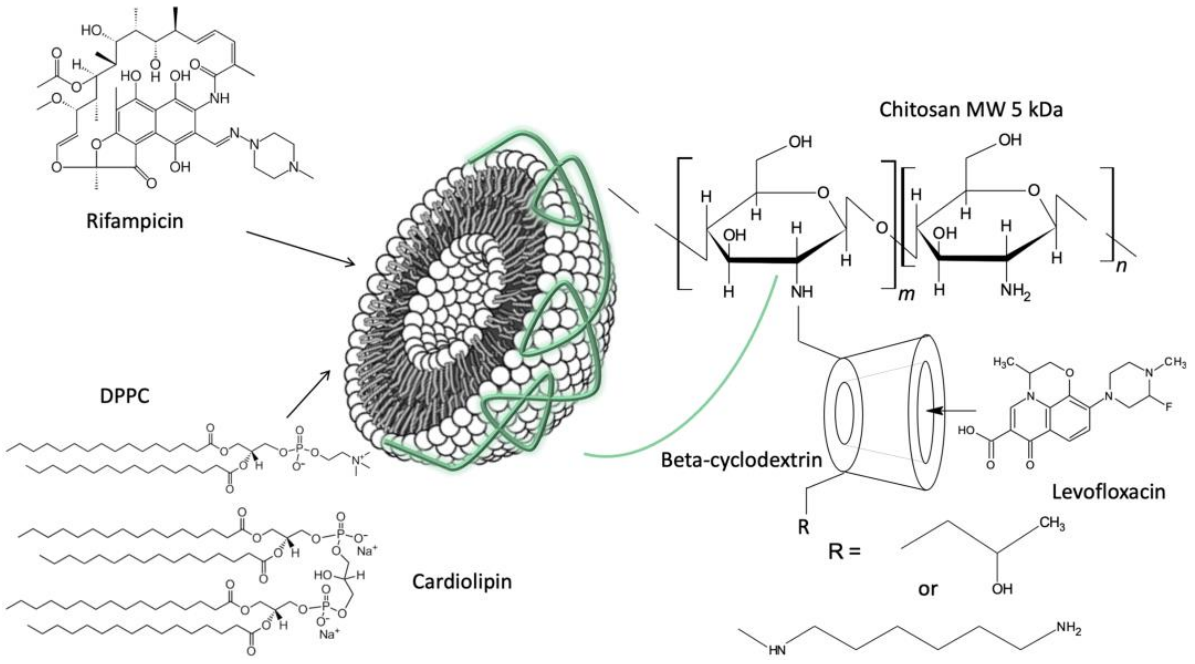

Figure 1. Structures of substances under consideration and the schematic cartoon representing the structure of combined system.

3.1. LRif Pysico-Chemical Studies

As we demonstrated previously for Rif [12], anionic DPPC:CL 80:20 weight % liposomes proved to be a better lipid matrix in comparison with DPPC vesicles, with an incorporation efficiency of about 35 percent. The main sites of drug binding in the bilayer are the polar groups of phospholipids, which form hydrogen bonds with the heterocycle and the secondary amine of rifampicin. The main characteristics of the resulting liposomes are presented in Table 1. The obtained data are in the good agreement with previously published studies. The Rif-loading into liposomes does not lead to the significant changes in particle size or zeta potential, which is predominantly determined through lipid composition. The loading efficiency for the passive method is satisfactory: the lipid composition does not significantly affect this parameter.

Table 1. Main characteristics of control and LRif-loaded liposomes DPPC and DPPC:CL 80:20 and its complexes with various ligands. A total of 0.01 M sodium phosphate-buffered solution, pH = 7.4, T = 22 °C. SD (n = 3).

Lipid Composition	Encapsulation Efficacy, %	D_h, nm (Z-Average)	PDI	ζ-Potential, mV
DPPC control	–	100 ± 3	0.096	−10.1 ± 2.2
LRif DPPC	32 ± 3	102 ± 6	0.123	−10.4 ± 4.1
DPPC:CL control	–	99 ± 4	0.104	−20.1 ± 4.2
LRif DPPC:CL	35 ± 5	101 ± 6	0.117	−20.0 ± 5.0
LRif DPPC + HP-CD-Chit	32 ± 3	180 ± 16	0.178	+8.0 ± 4.0
LRif DPPC + NH_2-CD-Chit	32 ± 3	170 ± 20	0.154	+12.2 ± 3.6
LRif DPPC:CL + HP-CD-Chit	35 ± 5	168 ± 20	0.169	+11.9 ± 4.5
LRif DPPC:CL + NH_2-CD-Chit	35 ± 5	175 ± 20	0.170	+12.9 ± 2.9
LRif DPPC + HP-CD-Chit + Lev	32 ± 3	171 ± 24	0.198	+11.1 ± 2.6
LRif DPPC + NH_2-CD-Chit + Lev	32 ± 3	166 ± 22	0.163	+13.2 ± 2.9
LRif DPPC:CL + HP-CD-Chit + Lev	35 ± 5	162 ± 21	0.180	+13.0 ± 2.8
LRif DPPC:CL + NH_2-CD-Chit + Lev	35 ± 5	173 ± 25	0.172	+14.9 ± 3.1

The complex formation of liposomes with polymers, namely HP-CD-Chit and NH_2-CD-Chit, is accompanied by a change in the particle charge towards positive values and an increase in particle size. For anionic DPPC:CL 80:20 liposomes, a more significant change in charge is observed, which presumably indicates a more efficient electrostatic interaction of polymer chains with the surface of liposomes [25]. The results obtained concerning the change in the ζ-potential [26] and particle size [27] are in good agreement with the literature data.

Complex formation is proven through ATR–FTIR spectroscopy. Usually, this method is suitable for studies on colloidal systems like liposomal suspensions. One could judge the state of hydrophobic area of bilayer through the analysis of the spectral region 3000–2800 cm^{-1}, where the most intensive bands $\nu_{as}(CH_2)$ at 2917–2925 cm^{-1} and $\nu_s(CH_2)$ at 2850–2852 cm^{-1} are shown. When these bands undergo a low-frequent shift, this indicates a more ordered bilayer, and in contrast, when a high-frequent shift occurs, this indicates disordering and even phase transition of the vesicle [28,29]. A typical shift for the phase transition gel-like bilayer is a liquid crystal bilayer reflected in the spectrum as a high-frequency shift of 4–5 cm^{-1} [30].

When it comes to the interactions of several ligands, including polyelectrolytes, with the bilayer, the most pronounced changes are usually observed in the area of the bands of carbonyl groups ν(CO) at 1720–1750 cm^{-1} and phosphate groups $\nu_{as}(PO_2^-)$ at 1220–1260 cm^{-1}. The high-frequent shifts of these bands indicate the decrease in the hydration and breaking of hydrogen bonds most often due to the formation of new non-covalent interactions with polar ligands [29,31].

When LRif vesicles interact with polymers (HP-CD-Chit or NH_2-CD-Chit), we observed that the ATR–FTIR spectra changes are typical for complex formations between liposomes and chitosan derivatives (Table 2).

Table 2. Position of the main absorption bands (cm^{-1}) in the ATR–FTIR spectra of LRif and complexes with HP-CD-Chit or NH_2-CD-Chit at a base–molar ratio of 7:1; 0.01 M sodium phosphate-buffered solution; pH 7.4, 22 °C. SD (n = 3).

Sample	$\nu_{as}(CH_2)$	$\nu_s(CH_2)$	$\nu(CO)$	$\nu_{as}(PO_2^-)$
LRif DPPC	2917.9 ± 0.5	2850.0 ± 0.5	1735.5 ± 0.5 1730.5 shoulder	1223.3 ± 0.5 1242.2 shoulder
LRif DPPC:CL	2919.0 ± 0.5	2850.0 ± 0.5	1730.0 ± 0.5 1742.0 shoulder 1715.0 shoulder	1226.5 ± 0.5 1240.2 shoulder
LRif DPPC + HP-CD-Chit	2917.9 ± 0.5	2850.0 ± 0.5	1742.5 ± 0.5 1730.5 shoulder	1225.2 ± 0.5 1242.2 shoulder
LRif DPPC + NH_2-CD-Chit	2917.9 ± 0.5	2850.0 ± 0.5	1742.0 ± 0.5 1730.5 shoulder	1225.7 ± 0.5 1242.2 shoulder
LRif DPPC:CL + HP-CD-Chit	2919.1 ± 0.5	2850.0 ± 0.5	1737.0 ± 0.5 1742.0 shoulder	1226.5 ± 0.5 1240.2 shoulder 1260.0 shoulder
LRif DPPC:CL + NH_2-CD-Chit	2919.1 ± 0.5	2850.0 ± 0.5	1737.2 ± 0.5 1742.0 shoulder	1226.5 ± 0.5 1240.2 shoulder 1260.0 shoulder

Complex formation occurs in a typical chitosan-based liposome polymer way. The hydrophobic area of bilayer does not interact with polymer according to the stable $\nu_{as}(CH_2)$ and $\nu_s(CH_2)$ band positions. Regarding the most pronounced changes that we observed for the $\nu(CO)$ and $\nu_{as}(PO_2^-)$ bands: interactions with polymers lead to the either a high-frequency shift, such as the $\nu_{as}(PO_2^-)$ bands for all samples, or the disappearance of some shoulders, such as the 1715.0 shoulder on the spectrum of LRif DPPC:CL, corresponding to the highly hydrated carbonyl groups. We have not observed any significant differences between HP-CD-Chit and NH_2-CD-Chit, as the main role in their interactions with chitosan belong to the amino groups of the polysaccharide chain.

On the other hand, complex formation could significantly change the drug release profile. Since Rif at physiological temperatures can disturb the membrane [12] and lead to significant changes in the phase transition of liposomes, it is especially important to study the kinetics of drug release from vesicles.

3.2. LRif Release Studies

According to the data on the kinetics of Rif release from neutral and anionic liposomes, the role of cardiolipin in this process is insignificant: the curves (Figure 2a,b, blue lines) run symbatically and the DPPC:CL 80:20 ratio liposomes retain the drug slightly better, which indicates that a plateau on the kinetic curve and an almost complete release of the drug within 5 h is achieved.

Complex formation with chitosan-based ligands is accompanied by a significant slowing down in the release of Rif into the external solution (Figure 2a,b, green and red lines). So, within 3 h, in the presence of a polymeric conjugate, a two-fold smaller amount of the drug is released compared to liposomes without a polymer. In [32], a similar effect was demonstrated: in the presence of maltoheptose, an oligomeric carbohydrate ligand similar to β-CD, the release of liposomes based on DPPC Rif was slowed down by 1.5 times in 5 h. The results obtained are in good agreement with the previously obtained results on the kinetics of moxifloxacin release from DPPC:CL (80:20) liposomes in the presence of mannosylated Chit (90–120 kDa), and a similar course of the curve is observed [33]. The release of gentamicin from liposomes based on DPPC and cholesterol was shown in [34], which is significantly slowed down in the presence of Chit nanofibers (416 kDa).

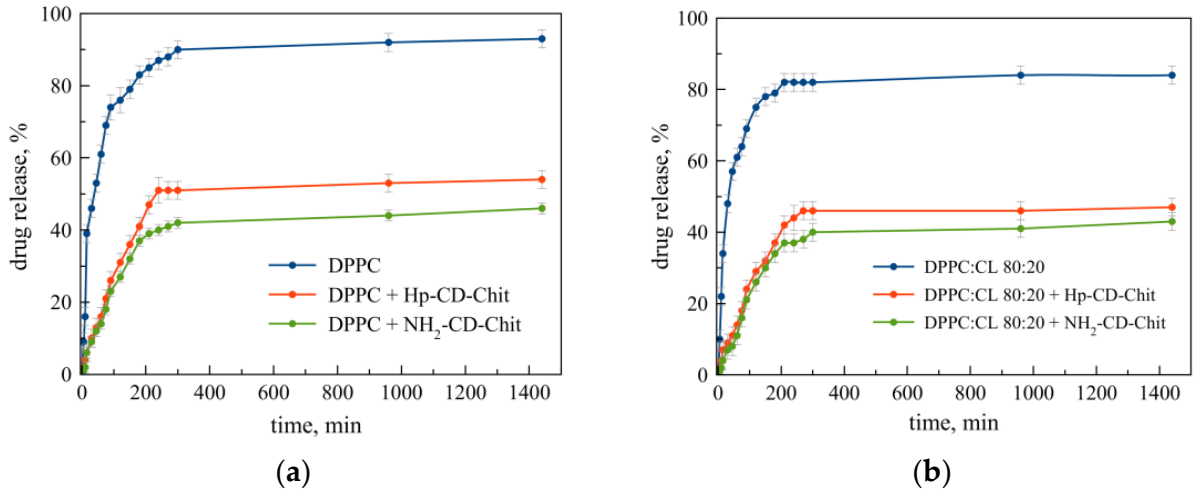

Figure 2. Rifampicin release from liposomal forms with and without a polymer shell. (**a**) LRif DPPC (blue line) and its complex with HP-CD-Chit (red) and NH_2-CD-Chit (green). (**b**) LRif DPPC:CL 80:20 (blue line) and its complex with HP-CD-Chit (red) and NH_2-CD-Chit (green). For all complexes, the liposome : polymer base–molar ratio was 1:7. Total lipid concentration 3 mg/mL in 0.01 M Na phosphate-buffered solution, pH 7.4. 37 °C. SD (n = 3).

The most noticeable effect of the prolongation of the release of rifampicin is observed during the formation of an anionic complex with an amino derivative of the polymer carrier. It is known that chitosan-based polymers usually cover the surface of anionic charged liposomes due to electrostatic interactions between negatively charged phospholipids and the positive charges of the primary amino groups of chitosan [31], although hydrogen bonds could also be involved in the process of complex formation [35]. Thus, with an increase in the proportion of positively charged amino groups, the stability of the complex of liposomes with the polymeric ligand increases, as a result of which, the release of Rif can be limited. In addition, during the release of Rif from liposomes, electrostatic interactions with an increasingly charged polymeric conjugate may occur, and the release of the drug into the external solution was slowed down.

In order to more accurately describe the observed patterns of drug release, we analyzed the data within the frameworks of the main kinetic models (zero- and first-order, Korsmeyer–Peppas, Hickson–Crowell and Higuchi models). The zero-order model describes the release of a drug independent of its concentration. This model is typically used to characterize the release from slowly dissolving matrices or transdermal systems. The first-order model describes the release of drugs from porous matrices—it considers the change in drug concentration when leaving the matrix. The Hickson–Crowell model is applicable to drug release from monodisperse drug formulations. The Higuchi model is commonly used to describe the release of a drug via diffusion from an insoluble or partially soluble matrix. The Korsmeyer–Peppas model considers the many parameters of the system (the dissolution of the polymer matrix, the diffusion of water into the matrix, etc.), and also allows researchers to determine the type of diffusion during the release of the drug.

We analyzed all results in all models, and the values of R^2 are presented in Table S1. Here, we discuss the most probable models and how they change when the composition of system changes, i.e., from LRif to the LRif complexed with polymer.

Rif release from neutral and anionic liposomes in the absence of a polymer is described by the Higuchi model, implying that the diffusion from the lipid bilayer into the external solution is the rate-limiting step in the process. Following the Higuchi model, the release of the drug from liposomes can be identified by the presence of an initial accelerated (so-called burst) release, followed subsequently by zero-order kinetics. The results obtained are in

good agreement with the literature data for similar systems based on the liposomal form of Rif [36].

The formation of multipoint non-covalent complexes of liposomes with the polymeric substituent, for example, NH_2-CD-Chit, leads to a change in the kinetic model of Rif release: the Higuchi model passes to the Korsmeyer–Peppas model with a predominant anomalous diffusion type (Figure 3a,b). The change in the model of Rif release from neutral and anionic liposomes during the formation of the complex may be due to the interaction of Rif with chitosan polymer chains; the change of the model occurs in the vast majority of the described cases. In addition, the Korsmeyer–Peppas model allows, among other factors, the consideration of the swelling of the matrix and the penetration of water into the polymer, and it is these factors that can become decisive in the formation of the complex. Diffusion against Fick's law can be explained as follows: complexation leads to a decrease in the mobility of polymer chains, as a result of which the determining factor for the release of Rif is not so much diffusion from the lipid matrix as interaction with the polymer chains surrounding the lipid bilayer.

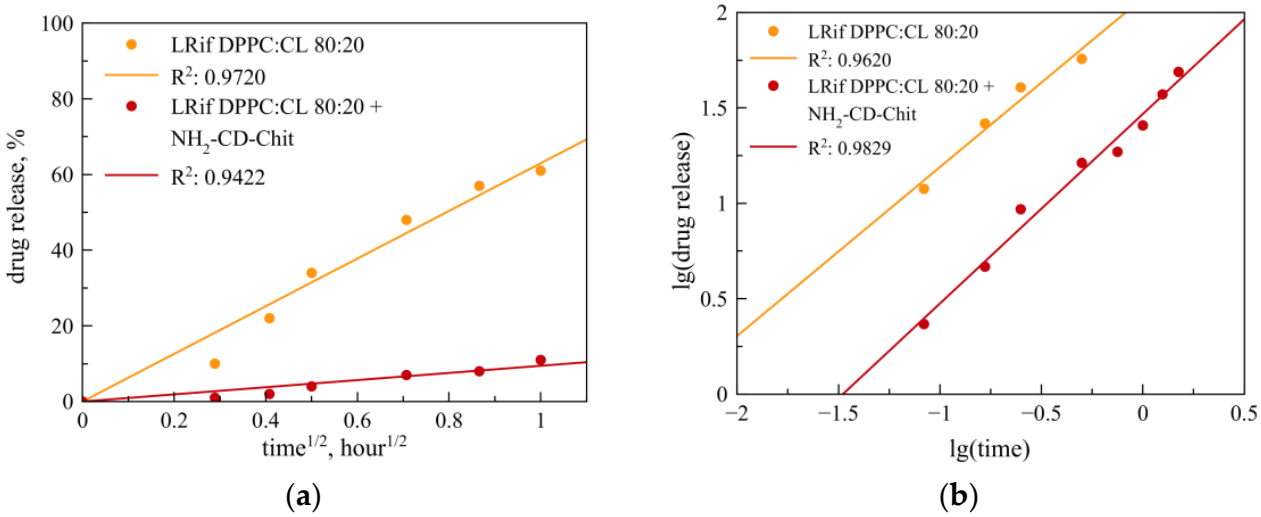

Figure 3. Mathematical processing of Rif release curves from DPPC:CL (80:20) liposomes without polymers (orange line) and in a complex with NH_2-CD-Chit (red line) through the Higuchi (**a**) and Korsmeyer–Peppas (**b**) models. For all complexes, the liposome : polymer base–molar ratio was 1:7. Total lipid concentration 3 mg/mL in 0.01 M Na phosphate-buffered solution, pH 7.4. 37 °C.

Thus, the complex formation of LRif with polymeric ligands based on chitosan and β-cyclodextrin derivatives provides not only a simple "wall", slowing the release down, but in contrast, the chitosan-based polymer acts as a significant player, changing the physico-chemical basis of drug release. Based on the most pronounced effect obtained for the system LRif DPPC:CL + NH_2-CD-Chit for experiments on the study of the kinetics of the simultaneous release of rifampicin and levofloxacin, a combined system containing NH_2-CD-Chit as a polymeric conjugate was used.

3.3. Levofloxacin Release from Complexes with NH_2-CD and NH_2-CD-Chit

Recently, we reported on the prolonged release of Lev from the complexes with NH_2-CD-Chit polymer carrier in comparison with initial NH_2-CD. It was found that the release of Lev was significantly slowed in the presence of a polymeric carrier: in two hours, the release of the drug reached 100% for unmodified NH_2-CD and 60% for the NH_2-CD-Chit conjugate. In order to compare all results from all systems accurately, we analyzed these data in all the kinetic models described above.

The processing of the experimental results showed that the release of levofloxacin from the complex with NH_2-CD-Chit is described in the best way by the Higuchi kinetic model (Figure 4), which characterizes the release of the drug from an insoluble or partially

soluble matrix that is not prone to swelling, according to the diffusion mechanism. These results are expected and are in good agreement with the literature data [37,38]. For the host–guest control system, i.e., of the Lev complex with NH_2-CD, the best approximation parameters were calculated for the Korsmeyer–Peppas model; however, this kinetic curve cannot be described by this model due to the limitation $\frac{Q_t}{Q_\infty} < 0.6$.

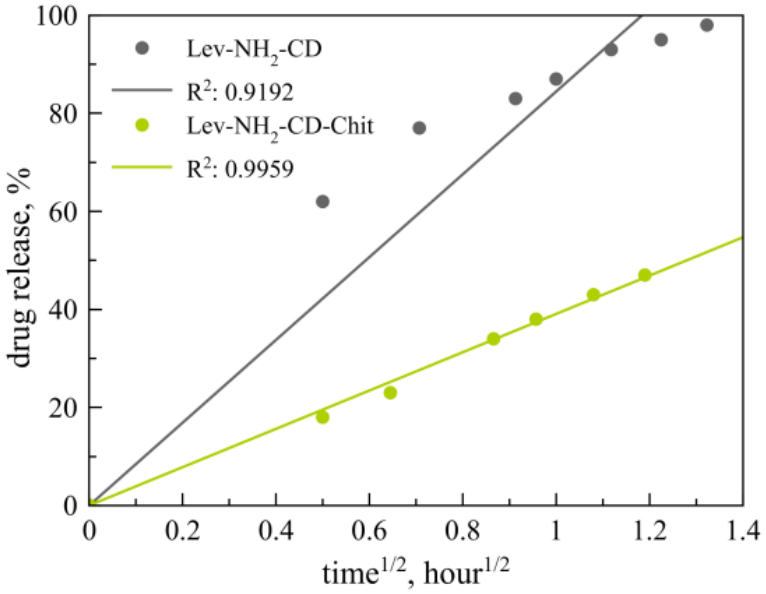

Figure 4. Mathematical processing of Lev release curves from the guest–host complex with NH_2-CD (grey line) and NH_2-CD-Chit (green line) by the Higuchi models. A total of 0.01 M Na phosphate-buffered solution, pH 7.4. 37 °C.

Thus, for the Lev complex formation with polymeric ligands does not leads to the change of kinetic model. Will it change when complex is united with LRif? Let us consider further results concerning the combined drug delivery system.

3.4. Combined System Design

To design a combined system for the simultaneous delivery of levofloxacin and rifampicin, we have chosen the components that demonstrated the best properties in the separate studies described above.

We obtained the combined systems of both lipid composition (DPPC and DPPC:CL 80:20) and both HP-CD-Chit and NH_2-CD-Chit. The hydrodynamic diameters and ζ-potentials of the obtained complexes are presented on Table 1. Generally, the loading of Lev does not significantly influence the properties of the system. For the further studies, we have chosen the following. For Rif the most suitable carrier is LRif DPPC:CL (80:20) with optimal drug release profile and physic-chemical proprieties. As the polymeric ligand is the carrier for Lev, we chose NH_2-CD-Chit, as it is able to form stable complexes with Lev and provide prolonged Rif release. So, let us consider a system consisting of a liposomal form of Rif functionalized with NH_2-CD-Chit and where the β-CD tori are loaded with Lev.

The release of drugs from the combined system based on the liposomal form of Rif and Lev, loaded into NH_2-CD-Chit, differs from the release from independent carriers discussed above (Figure 5).

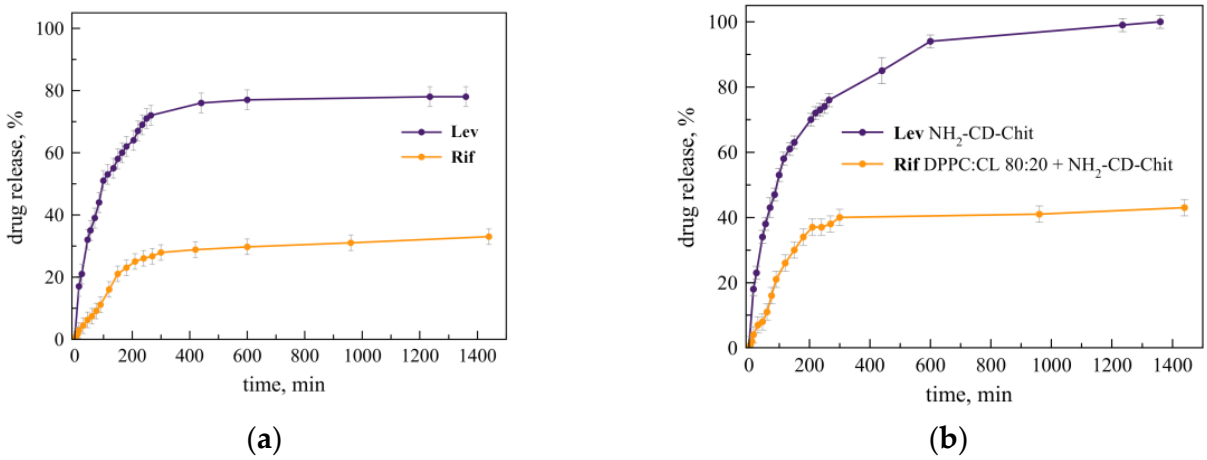

Figure 5. (**a**) Lev release profile from the NH_2-CD-Chit and Lev (purple) complex and the Rif (orange) from the LRif NH_2-CD-Chit complex. Independent experiments. (**b**) The simultaneous release of Lev (purple) and Rif (orange) from the combined system LRif DPPC:CL + NH_2-CD-Chit, loaded with Lev. A total of 0.01 M Na phosphate-buffered solution, pH 7.4. 37 °C. SD (n = 3).

Let us consider what happens to the Lev release profile in a combined system. In experiments on the release of drugs from such a system at 37 °C in a sodium phosphate-buffered solution (Figure 5a,b), it was found that the release of levofloxacin (purple line on the both plots) slows down relative to the control system—the Lev complex with NH_2-CD-Chit. In detail, 10 h after the start of the experiment, the share of Lev output exceeds 90%, while in the combined system, it is 77%, reaching a maximum value, and the slope becomes 20% smaller (Table 3).

Table 3. Parameters characterizing the release of Lev from NH_2-CD-Chit and a combined system containing LRif DPPC:CL 80:20 + Lev-NH_2-CD-Chit.

Parameter/System	Lev-NH_2-CD-Chit	LRif DPPC:CL + Lev-NH_2-CD-Chit
Percentage of drug release in 10 h, %	90	77
The tangent of the slope of the initial section of the release curve	0.40	0.32

This is a somewhat unexpected result, since, assuming that the β-CD tori are exposed to the solution, the rate of Lev release should not be significantly reduced. In the experiment, on the contrary, it was possible to reliably demonstrate a slowdown in the release of Lev, which may indicate the participation of β-CD tori in the interaction with the surface of liposomes.

The ability of liposomes to interact with cyclodextrins is known from the literature: cyclodextrins and polymeric ligands based on these are adsorbed on the liposomal bilayer and cause defects. This effect is also characteristic of the interactions of cyclodextrins loaded with Lev with the cell membrane: the outer membrane absorbs the Lev complex with cyclodextrin much better than the Lev-based control solution [24]. Thus, there is reason to believe that not all cyclodextrin tori in this system are exposed to the solution and some of them interact with the liposomal bilayer, but this hypothesis requires further confirmation.

Let us consider the results of the release of Rif from the combined system. An unusual effect was also found here: loading into the polymer conjugate Lev leads to a slowdown in the release of Rif relative to a similar system without Lev: within 5 h, 40% and 28% of the drug are released into the external solution, respectively (Table 4). The slope of the initial section of the curve differs by ca. 1/3, which gives grounds to assume an increase in the density of the polymer shell.

Table 4. Parameters characterizing the release of Rif from NH_2-CD-Chit and a combined system containing LRif DPPC:CL 80:20 + Lev-NH_2-CD-Chit.

Parameter/System	LRif DPPC:CL + NH_2-CD-Chit	LRif DPPC:CL + Lev-NH_2-CD-Chit
Percentage of drug release in 5 h, %	40	28
The tangent of the slope of the initial section of the release curve	0.11	0.07

The formation of guest–host complexes of the drug with CD is accompanied by organization into strictly ordered and rigid structures as a result of the appearance of numerous non-covalent interactions that can change the CD structure with the formation of hierarchical structures [39]. Due to hydrophobic interactions with ordered CD structures that change the geometry of the conjugate, polymer molecules in the solution can form a three-dimensional network structure, which can increase the viscosity of the solution and thus resist diffusion [40]. A similar effect was demonstrated in [41]: when CD was conjugated with polyacrylamide, side CD substituents prevented chain rotation inside the copolymer and increased its rigidity.

Thus, the formation of the Lev-NH_2-CD-Chit guest–host complex leads to the formation of an ordered structure of β-CD tori, which affects the steric accessibility of amino groups not conjugated with NH_2-CD. The free amino groups of NH_2-CD-Chit probably form a stable complex with the surface of liposomes, which, in turn, slows down the release of Rif from the combined system.

When it comes to the suitable kinetic model, we observed that for Rif, the Korsmeyer–Peppas is still the best one, while for Lev, the Higuchi model provides the most reliable results (Table S1). The Korsmeyer–Peppas model makes it possible to determine the type of diffusion during the release of the drug from the matrix. Thus, for Rif, the determining type of release from the combined system turned out to be anomalous diffusion ($0.5 < n < 1$, $n = 0.85$), through which the rates of diffusion and relaxation of the polymer are comparable. The results obtained are consistent with the literature data: the release of Rif from polymer nanoparticles based on alginate and chitosan is also characterized through diffusion that does not agree with Fick′s law ($n = 0.77$) [42]. A similar effect was demonstrated in [43] on another system: the release of the bronchodilator drug, salbutamol, from niosomes based on sorbitan monostearate and cholesterol can be described as having the same type of diffusion.

Thus, the formation of a complex of the liposomal form of Rif with the NH_2-CD-Chit polymeric conjugate loaded with Lev leads to a significant slowing of the release of Lev and Rif into the external solution. The release of Lev is described by the Higuchi model for each system, and for Rif, the release into the external solution upon the formation of a complex with the NH_2-CD-Chit (by itself or loaded with Lev) polymer is accompanied by a change from the Higuchi model to the Korsmeyer–Peppas model.

In order to uncover how such features of cargo release will affect the antibacterial activity of the systems, we conducted classical microbiological experiments.

3.5. Antibacterial Activity Studies

The study of the antibacterial activity of the systems was carried out via the agar diffusion method on two strains: Gram-negative bacteria *Escherichia coli* ATCC 25922 (Figure 6) and Gram-positive bacteria *Bacillus subtilis* ATCC 6633, since they are model systems for studying the antibacterial activity of drugs.

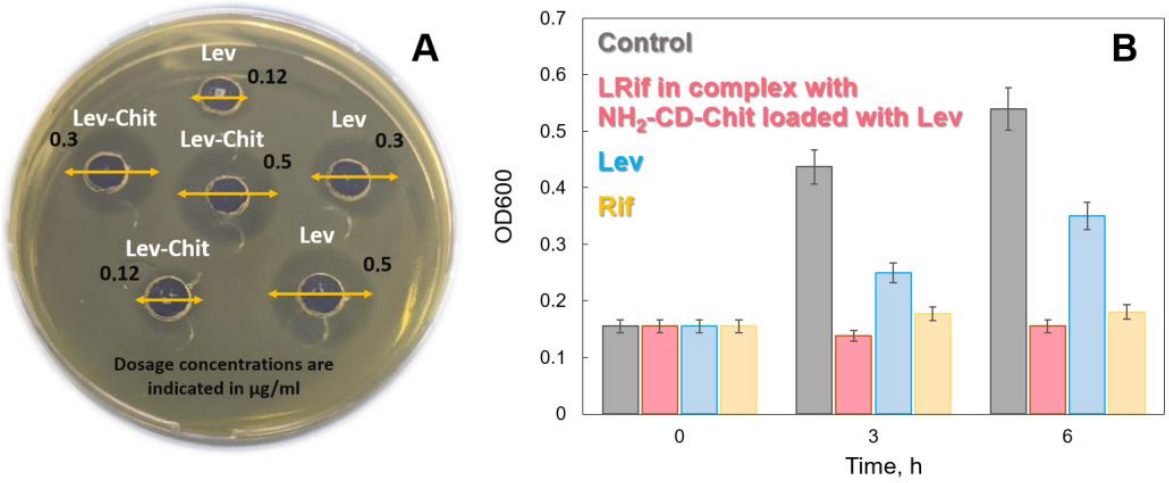

Figure 6. In vitro experiments in solid media (**A**) on *E. coli ATCC* 25922 and in liquid media (**B**) on *B. subtilis* 6633, 37 °C.

MICs were determined for Lev and Rif, as well as their formulations (Table 5). For Rif MIC *E. coli* >> MIC *B. subtilis*, which indicates a more pronounced antibacterial properties of Rif against Gram-positive bacteria. Lev shows comparable activity on both strains. It is important to note that the inclusion of drug molecules in the delivery systems (Lev-NH_2-CD-Chit and LRif DPPC:CL 80:20) did not lead to a decrease in the antibacterial activity of the drugs, which may be due to the almost complete release of the components in 24 h.

Table 5. MIC determined for samples under consideration (μg/mL). SD, n = 3.

Sample	*Escherichia coli* ATCC 25922	*Bacillus subtilis* ATCC 6633
Lev	0.1 ± 0.02	0.3 ± 0.03
Lev-NH_2-CD-Chit	0.1 ± 0.02	0.28 ± 0.03
Rif	12 ± 1	0.2 ± 0.02
LRif DPPC:CL	12 ± 1	0.2 ± 0.03
Lev:Rif = 4:1 (molar ratio.)	-	0.25 ± 0.03
Lev-NH_2-CD-Chit + LRif DPPC:CL (Lev:Rif = 4:1 molar ratio)	-	0.24 ± 0.02

The combined system containing Lev-NH_2-CD-Chit + LRif DPPC:CL (80:20) has a molar ratio for the drugs Lev:Rif of 4:1, corresponding to the therapeutic ratio. An in vitro study of the properties of this system was carried out only on *B. subtilis*, since the high MIC values of Rif for *E. coli* do not allow the use of Lev concentrations required for the method used.

Thus, it was found that Lev-NH_2-CD-Chit + LRif DPPC:CL (80:20) exhibits antibacterial activity against Gram-positive bacteria, and MIC is 0.24 ± 0.02 μg/mL. A combination of free drug molecules in a given ratio was used as a control. Since the limited diffusion might be the reason for the insignificant difference between the combination of Lev and Rif and the combined system, we also conducted the experiments in liquid growth media on B. subtilis (Figure 5). The control demonstrated the OD600 increase, whereas both antibacterial forms (Lev in complex with NH_2-CD-Chit) and LRif inhibit bacterial growth in accordance with their impact on solid media (Lev < Rif). The combined system demonstrated pronounced antibacterial action comparable to the combination of Lev + Rif. Thus, it is shown that the combined system has a comparable effect with the control, which indicates the absence of a negative effect of the delivery system on the in vitro properties of the drug composition.

4. Conclusions

Combined systems that deliver inhaled antibiotics simultaneously are a promising approach to improving the efficacy of tuberculosis treatment. In this work, we investigated the physicochemical and antibacterial properties of a system based on levofloxacin complexes with conjugates based on β-cyclodextrin and chitosan derivatives and liposomal forms of rifampicin. Although there are already liposomal delivery systems for rifampicin and delivery systems based on chitosan–cyclodextrin conjugates for levofloxacin, the combination of identified carriers in one system that is a reliable assessment of active particles and a comprehensive study of the properties of such a combined delivery system is presented here for the first time. The effect of the complex formation of liposomes with conjugates based on chitosan and β-cyclodextrin derivatives was revealed: a slowdown in the release of rifampicin and a change in the model of drug release from the system were demonstrated.

For a combined system consisting of liposomal forms of rifampicin coated with a conjugate of chitosan with β-cyclodextrin derivatives, the sizes and ζ-potentials of the particles were determined and the simultaneous release of rifampicin and levofloxacin was studied. A change in the release pattern of rifampicin compared to the liposomal form in the absence of a polymer was established, while the release pattern of levofloxacin from polymeric conjugates was preserved. For a combined system based on liposomal forms of rifampicin and complexes of levofloxacin with the polymeric conjugates of β-cyclodextrin derivatives with chitosan, it was found that the release of levofloxacin slowed down but was described by the Higuchi model in both cases. The release of rifampicin from liposomes during the formation of complexes with polymeric conjugates was characterized by the change in the Higuchi model to the Korsmeyer–Peppas model with the governing type of diffusion against Fick's law. This can probably be explained by the effect of the modified release of rifampicin from liposomes upon the interaction with chitosan polymer chains.

Moreover, for the combined system, the antibacterial activity against Gram-positive bacteria was demonstrated using the example of *B. subtilis*, as well as the absence of a negative effect of the delivery system on the in vitro properties of the drug formulation. For the combined system, the preservation of antibacterial activity was shown compared to control drugs, and the MIC for *B. subtilis* ATCC 6633 was 0.24 ± 0.02 μg/mL.

The results obtained open up new prospects for the further study of combined delivery systems for various drugs and for increasing the effectiveness of anti-tuberculosis therapy.

Supplementary Materials: The following supporting information can be downloaded at: https://www.mdpi.com/article/10.3390/jfb14070381/s1, Table S1: The values of the coefficient of determination R^2 obtained by processing using various models of the release curves of liposomal preparations of Rif without a polymer shell and coated with a polymer, Lev, in an unmodified β-cyclodextrin derivative and in the complex with NH_2-CD-Chit. Figure S1. ATR-FTIR spectra of unloaded DPPC liposomes (red line) and DPPC liposomes containing Rif (blue line). Sodium phosphate-buffered solution, pH = 7.4, T = 22 °C, lipid concentration 5 mg/mL. Figure S2. UV–VIS spectra of (a) levofloxacin 0.03 mM in 0.1 mM HCl solution (b) Rif 0.03 mM in sodium phosphate-buffered solution, pH = 7.4, T = 22 °C.

Author Contributions: Conceptualization, I.M.L.-D.; data curation, I.M.L.-D., P.V.M., A.A.S. and A.S.S.; investigation, P.V.M. and A.S.S.; methodology, I.M.L.-D., A.A.S. and N.G.B.; project administration, I.M.L.-D.; writing—original draft, I.M.L.-D.; writing—review and editing, P.V.M., A.A.S., N.G.B. and E.V.K. All authors have read and agreed to the published version of the manuscript.

Funding: This research was funded by the President of Russia grant for young PhDs 075-15-2022-397.

Data Availability Statement: The data presented in this study are available on request from the corresponding author. The data are not publicly available due to privacy reasons.

Acknowledgments: The work was performed using the equipment (FTIR spectrometer Bruker Tensor 27) of the program for the development of Moscow State University and equipment purchased by the Developmental Program of Lomonosov Moscow State University (PNR 5.13).

Conflicts of Interest: The authors declare no conflict of interest.

References

1. Zumla, A.; Malon, P.; Henderson, J.; Grange, J.M. Impact of HIV infection on tuberculosis. *Postgrad. Med. J.* **2000**, *76*, 259–268. [CrossRef]
2. Luke, E.; Swafford, K.; Shirazi, G.; Venketaraman, V. TB and COVID-19: An Exploration of the characteristics and resulting complications of co-infection. *Front. Biosci.* **2022**, *14*, 6. [CrossRef]
3. Zumla, A.; Hafner, R.; Lienhardt, C.; Hoelscher, M.; Nunn, A. Advancing the development of tuberculosis therapy. *Nat. Rev. Drug Discov.* **2012**, *11*, 171–172. [CrossRef]
4. Grobbelaar, M.; Louw, G.E.; Sampson, S.L.; van Helden, P.D.; Donald, P.R.; Warren, R.M. Evolution of rifampicin treatment for tuberculosis. *Infect. Genet. Evol.* **2019**, *74*, 103937. [CrossRef]
5. Tupin, A.; Gualtieri, M.; Roquet-Banères, F.; Morichaud, Z.; Brodolin, K.; Leonetti, J.-P. Resistance to rifampicin: At the crossroads between ecological, genomic and medical concerns. *Int. J. Antimicrob. Agents* **2010**, *35*, 519. [CrossRef]
6. Unissa, A.N.; Hanna, L.E.; Swaminathan, S. A Note on Derivatives of isoniazid, rifampicin, and pyrazinamide showing activity against resistant *Mycobacterium tuberculosis*. *Chem. Biol. Drug Des.* **2016**, *87*, 537–550. [CrossRef]
7. Berning, S.E. The role of fluoroquinolones in tuberculosis today. *Drugs* **2001**, *61*, 9–18. [CrossRef]
8. Jacobs, M.R. Activity of quinolones against mycobacteria. *Drugs* **1999**, *58*, 19–22. [CrossRef]
9. Davis, R.; Bryson, H.M.; Maddix, D.; Pascual, A.; Pfaller, M.A. Levofloxacin review of its antibacterial activity, pharmacokinetics and therapeutic efficacy. *Drugs* **1994**, *47*, 677–700. [CrossRef]
10. Pham, D.D.; Fattal, E.; Tsapis, N. Pulmonary drug delivery systems for tuberculosis treatment. *Int. J. Pharm.* **2015**, *478*, 517–529. [CrossRef]
11. Manca, M.L.; Sinico, C.; Maccioni, A.M.; Diez, O.; Fadda, A.M.; Manconi, M. Composition influence on pulmonary delivery of rifampicin liposomes. *Pharmaceutics* **2012**, *4*, 590–606. [CrossRef]
12. Le-Deygen, I.M.; Safronova, A.S.; Mamaeva, P.V.; Kolmogorov, I.M.; Skuredina, A.A.; Kudryashova, E.V. Drug–membrane interaction as revealed by spectroscopic methods: The role of drug structure in the example of rifampicin, levofloxacin and rapamycin. *Biophysica* **2022**, *2*, 353–365. [CrossRef]
13. Forte, J.; Hanieh, P.N.; Poerio, N.; Olimpieri, T.; Ammendolia, M.G.; Fraziano, M.; Fabiano, M.G.; Marianecci, C.; Carafa, M.; Bordi, F.; et al. Mucoadhesive rifampicin-liposomes for the treatment of pulmonary infection by *Mycobacterium abscessus*: Chitosan or ε-Poly-L-Lysine decoration. *Biomolecules* **2023**, *13*, 924. [CrossRef]
14. Garcia-Contreras, L.; Sethuraman, V.; Kazantseva, M.; Hickey, A. Efficacy of combined rifampicin formulations delivered by the pulmonary route to treat tuberculosis in the guinea pig model. *Pharmaceutics* **2021**, *13*, 1309. [CrossRef]
15. Le-Deygen, I.M.; Skuredina, A.A.; Mamaeva, P.V.; Kolmogorov, I.M.; Kudryashova, E.V. Conjugates of chitosan with β-Cyclodextrins as promising carriers for the delivery of levofloxacin: Spectral and microbiological studies. *Life* **2023**, *13*, 272. [CrossRef]
16. Krauland, A.H.; Alonso, M.J. Chitosan/cyclodextrin nanoparticles as macromolecular drug delivery system. *Int. J. Pharm.* **2007**, *340*, 134–142. [CrossRef]
17. Ammar, H.O.; El-Nahhas, S.A.; Ghorab, M.M.; Salama, A.H. Chitosan/cyclodextrin nanoparticles as drug delivery system. *J. Incl. Phenom. Macrocycl. Chem.* **2012**, *72*, 127–136. [CrossRef]
18. He, M.; Zhong, C.; Hu, H.; Jin, Y.; Chen, Y.; Lou, K.; Gao, F. Cyclodextrin/chitosan nanoparticles for oral ovalbumin delivery: Preparation, characterization and intestinal mucosal immunity in mice. *Asian J. Pharm. Sci.* **2019**, *14*, 193–203. [CrossRef]
19. Zhang, W.F.; Zhou, H.Y.; Chen, X.G.; Tang, S.H.; Zhang, J.J. Biocompatibility study of theophylline/chitosan/β-cyclodextrin microspheres as pulmonary delivery carriers. *J. Mater. Sci. Mater. Med.* **2009**, *20*, 1321–1330. [CrossRef]
20. De Gaetano, F.; Marino, A.; Marchetta, A.; Bongiorno, C.; Zagami, R.; Cristiano, M.C.; Paolino, D.; Pistarà, V.; Ventura, C.A. Development of chitosan/cyclodextrin nanospheres for levofloxacin ocular delivery. *Pharmaceutics* **2021**, *13*, 1293. [CrossRef]
21. Chopra, H.; Mohanta, Y.K.; Rauta, P.R.; Ahmed, R.; Mahanta, S.; Mishra, P.K.; Panda, P.; Rabaan, A.A.; Alshehri, A.A.; Othman, B.; et al. An insight into advances in developing nanotechnology based therapeutics, drug delivery, diagnostics and vaccines: Multidimensional applications in tuberculosis disease management. *Pharmaceuticals* **2023**, *16*, 581. [CrossRef]
22. Razzaq, S.N.; Khan, I.U.; Mariam, I.; Razzaq, S.S. Stability indicating HPLC method for the simultaneous determination of moxifloxacin and prednisolone in pharmaceutical formulations. *Chem. Cent. J.* **2012**, *6*, 94. [CrossRef]
23. Balouiri, M.; Sadiki, M.; Ibnsouda, S.K. Methods for in vitro evaluating antimicrobial activity: A review. *J. Pharm. Anal.* **2016**, *6*, 71–79. [CrossRef]
24. Skuredina, A.A.; Tychinina, A.S.; Le-Deygen, I.M.; Golyshev, S.A.; Kopnova, T.Y.; Le, N.T.; Belogurova, N.G.; Kudryashova, E.V. Cyclodextrins and their polymers affect the lipid membrane permeability and increase levofloxacin's antibacterial activity in vitro. *Polymers* **2022**, *14*, 4476. [CrossRef]

25. Hamedinasab, H.; Rezayan, A.H.; Mellat, M.; Mashreghi, M.; Jaafari, M.R. Development of chitosan-coated liposome for pulmonary delivery of N-acetylcysteine. *Int. J. Biol. Macromol.* **2020**, *156*, 1455–1463. [CrossRef]
26. Quemeneur, F.; Rinaudo, M.; Pépin-Donat, B. Influence of polyelectrolyte chemical structure on their interaction with lipid menbrane of Zwitterionic liposomes. *Biomacromolecules* **2008**, *9*, 2237–2243. [CrossRef]
27. Yaroslavov, A.A.; Efimova, A.A.; Krasnikov, E.A.; Trosheva, K.S.; Popov, A.S.; Melik-Nubarov, N.S.; Krivtsov, G.G. Chitosan-based multi-liposomal complexes: Synthesis, biodegradability and cytotoxicity. *Int. J. Biol. Macromol.* **2021**, *177*, 455–462. [CrossRef]
28. Manrique-Moreno, M.; Moreno, M.M.; Garidel, P.; Suwalsky, M.; Howe, J.; Brandenburg, K. The membrane-activity of ibuprofen, diclofenac, and naproxen: A physico-chemical study with lecithin phospholipids. *Biochim. Biophys. Acta* **2009**, *1788*, 1296–1303. [CrossRef]
29. Manrique-Moreno, M.; Howe, J.; Suwalsky, M.; Garidel, P.; Brandenburg, K. Physicochemical interaction study of non-steroidal anti-inflammatory drugs with dimyristoylphosphatidylethanolamine liposomes. *Lett. Drug Des. Discov.* **2009**, *7*, 50–56. [CrossRef]
30. Le-Deygen, I.M.; Vlasova, K.Y.; Kutsenok, E.O.; Usvaliev, A.D.; Efremova, M.V.; Zhigachev, A.O.; Rudakovskaya, P.G.; Golovin, D.Y.; Gribanovsky, S.L.; Kudryashova, E.V.; et al. Magnetic nanorods for remote disruption of lipid membranes by non-heating low frequency magnetic field. *Nanomedicine* **2019**, *21*, 102065. [CrossRef]
31. Deygen, I.M.; Kudryashova, E.V. Structure and stability of anionic liposomes complexes with PEG-chitosan branched copolymer. *Russ. J. Bioorg. Chem.* **2014**, *40*, 547–557. [CrossRef]
32. Wu, B.; Ndugire, W.; Chen, X.; Yan, M. Maltoheptaose-presenting nanoscale glycoliposomes for the delivery of rifampicin to *E. coli*. *ACS Appl. Nano Mater.* **2021**, *4*, 7343–7357. [CrossRef]
33. Le-Deygen, I.M.; Rokosovina, V.V.; Skuredina, A.A.; Yakimov, I.D.; Kudryashova, E.V. The charge and phase state of liposomes dramatically affects the binding of Mannosylated chitosan. *Future Pharmacol.* **2022**, *2*, 330–346. [CrossRef]
34. Monteiro, N.; Martins, M.; Martins, A.; Fonseca, N.A.; Moreira, J.N.; Reis, R.L.; Neves, N.M. Antibacterial activity of chitosan nanofiber meshes with liposomes immobilized releasing gentamicin. *Acta Biomater.* **2015**, *18*, 196–205. [CrossRef]
35. Efimova, A.A.; Abramova, T.A.; Popov, A.S. Complexes of negatively charged liposomes with chitosan: Effect of phase state of the lipid bilayer. *Russ. J. Gen. Chem.* **2021**, *91*, 2079–2085. [CrossRef]
36. Hussain, A.; Altamimi, M.A.; Alshehri, S.; Imam, S.S.; Singh, S.K. Vesicular elastic liposomes for transdermal delivery of rifampicin: In-vitro, in-vivo and in silico GastroPlus^{TM} prediction studies. *Eur. J. Pharm. Sci.* **2020**, *151*, 105411. [CrossRef] [PubMed]
37. Saher, O.; Ghorab, D.M.; Mursi, N.M. Preparation and in vitro/in vivo evaluation of antimicrobial ocular in situ gels containing a disappearing preservative for topical treatment of bacterial conjunctivitis. *Pharm. Dev. Technol.* **2016**, *21*, 600–610. [CrossRef]
38. MacHín, R.; Isasi, J.R.; Vélaz, I. β-Cyclodextrin hydrogels as potential drug delivery systems. *Carbohydr. Polym.* **2012**, *87*, 2024–2030. [CrossRef]
39. Wu, C.; Xie, Q.; Xu, W.; Tu, M.; Jiang, L. Lattice self-assembly of cyclodextrin complexes and beyond. *Curr. Opin. Colloid Interface Sci.* **2019**, *39*, 76–85. [CrossRef]
40. Tang, W.; Zou, C.; Da, C.; Cao, Y.; Peng, H. A review on the recent development of cyclodextrin-based materials used in oilfield applications. *Carbohydr. Polym.* **2020**, *240*, 116321. [CrossRef]
41. Zou, C.; Zhao, P.; Hu, X.; Yan, X.; Zhang, Y.; Wang, X.; Song, R.; Luo, P. β-Cyclodextrin-functionalized hydrophobically associating acrylamide copolymer for enhanced oil recovery. *Energy Fuels* **2013**, *27*, 2827–2834. [CrossRef]
42. Thomas, D.; Latha, M.S.; Thomas, K.K. Alginate/chitosan nanoparticles for improved oral delivery of rifampicin: Optimization, characterization and in vitro evaluation. *Asian J. Chem.* **2018**, *30*, 736–740. [CrossRef]
43. Arafa, M.G.; Ayoub, B.M. Nano-vesicles of salbutamol sulphate in metered dose inhalers: Formulation, characterization and in vitro evaluation. *Int. J. Appl. Pharm.* **2017**, *9*, 100–105. [CrossRef]

Journal of
Functional
Biomaterials

MDPI

Opinion

Electrospun Scaffolds as Antimicrobial Herbal Extract Delivery Vehicles for Wound Healing

Caglar Ersanli [1,2,3], Chrysoula (Chrysa) Voidarou [2], Athina Tzora [2], Konstantina Fotou [2], Dimitrios I. Zeugolis [3] and Ioannis Skoufos [1,*]

[1] Laboratory of Animal Science, Nutrition and Biotechnology, Department of Agriculture, University of Ioannina, 47100 Arta, Greece; c.ersanli@uoi.gr
[2] Laboratory of Animal Health, Food Hygiene and Quality, Department of Agriculture, University of Ioannina, 47100 Arta, Greece; xvoidarou@uoi.gr (C.V.); tzora@uoi.gr (A.T.); kfotou@uoi.gr (K.F.)
[3] Regenerative, Modular & Developmental Engineering Laboratory (REMODEL), Charles Institute of Dermatology, Conway Institute of Biomolecular and Biomedical Research, School of Mechanical and Materials Engineering, University College Dublin, D04 V1W8 Dublin, Ireland; dimitrios.zevgolis@ucd.ie
* Correspondence: jskoufos@uoi.gr

Abstract: Herbal extracts have been used in traditional remedies since the earliest myths. They have excellent antimicrobial, anti-inflammatory, and antioxidant activities owing to various bioactive components in their structure. However, due to their inability to reach a target and low biostability, their use with a delivery vehicle has come into prominence. For this purpose, electrospun nanofibrous scaffolds have been widely preferred for the delivery and release of antimicrobial herbal extracts due to the flexibility and operational versatility of the electrospinning technique. Herein, we briefly reviewed the electrospun nanofibrous scaffolds as delivery systems for herbal extracts with a particular focus on the preclinical studies for wound-healing applications that have been published in the last five years. We also discussed the indirect effects of herbal extracts on wound healing by altering the characteristics of electrospun mats.

Keywords: herbal extract; antibacterial; electrospinning; nanofibrous scaffold; delivery vehicle; wound healing

1. Introduction

A wound is the damage of a living tissue [1] which is caused intentionally (e.g., gunshots [2]) or unintentionally (e.g., skin cut, animal bite, traumas [3]) [4]. Although the human body has an excellent capability for healing wounds through a cascade of simultaneous phases, imperfect repair of damaged skin may cause vital damage, in particular the emergence of an infection, commonly in chronic wounds [5,6]. In contravention of the existence of various types of bacteria in the skin microbiota, biofilm formation or threshold value of substantial bacteria may block the wound-healing process [7]. The most common pathogenic strains that infect the wound site were revealed to be the *Staphylococcus aureus* (*S. aureus*), *Pseudomonas aeruginosa* (*P. aeruginosa*), and methicillin-resistant *S. aureus* [8]. Antibiotics are generally the first option for the treatment of infections, especially local ones [9]. However, overuse and maladministration of antibiotics [10–12] give rise to systemic toxicity and generation of antibiotic-resistant microorganisms. Therefore, due to the stated crucial concerns, alternative, unconventional, and non-antibiotic natural-based therapeutics (e.g., herbal extracts and essential oils) have come into prominence among most scientists as well as companies.

Herbal extracts have been used for traditional treatment purposes, e.g., burn wounds, bone fractures, and intestinal problems, since the earliest myths [13]. They demonstrate an excellent antimicrobial, antioxidant, anti-inflammatory, and anticarcinogenic activity owing to the bioactive compounds (e.g., polyphenols, vitamins) in their structure [14,15].

Almost 70% of people worldwide believe the primary health benefit of herbal compounds, according to the report by the World Health Organization [16]. Herbs present limitless sources to develop alternative, safe, and renewable therapeutics. For instance, among over two hundred and fifty thousand vascular plants, only around 17% of them have been researched for medicinal purposes [13]. Even though herbal extracts have been known for their excellent biological activities, some shortfalls still appear, such as poor biostability and the inability to reach the target [17]. Hence, there has been a need to develop engineered carrier and delivery vehicle systems (e.g., electrospun nanofibers, hydrogels) to increase the treatment and targeting efficacy.

Electrospinning is a simple and effective technique to fabricate various size ranges of nanofibers using electric force to pull charged threads of polymer solutions either with or without including any herbal extract [18]. Moreover, electrospinning can provide the sustained and targeted release of therapeutics [19]. One of the promising advantages of this technique is its operational versatility and flexibility to achieve desirable surface characteristics like large surface-to-volume ratio, and desired porosity [20,21]. It is a favorable method for the spinning of several kinds of materials such as natural, synthetic, or blended polymers. Nevertheless, several health concerns related to the usage of synthetic materials started to appear [18]. Consequently, the perspective shifted from a preference for synthetic to one for natural materials. In this manner, herbal extracts have become rising stars as attractive sources of electrospun biomaterials for many applications [22]. Herein, we briefly describe the role of antimicrobial herbal extracts incorporated in electrospun scaffold delivery systems (Figure 1), with a particular focus on preclinical studies for wound-healing applications that have been published in the last five years.

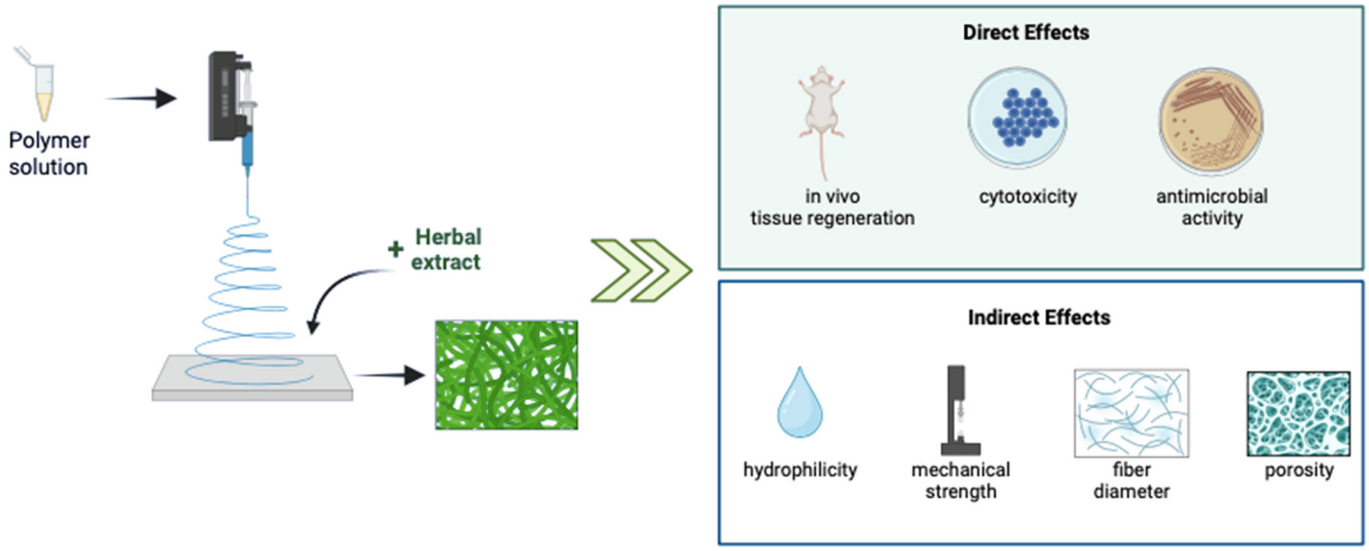

Figure 1. Direct and indirect effects of the incorporation of herbal extracts into electrospun biomaterials. This figure was created using BioRender.com.

2. Direct Effect of Herbal Extracts on Wound Healing

Herbal extracts are outstanding and alternative antimicrobial compounds, as opposed to common, traditional therapeutic agents (e.g., antibiotics), owing to their excellent biological properties, such as antimicrobial, antioxidant, anticarcinogenic, and anti-inflammatory activities, arising from various bioactive phytochemicals in their structure. Herbal extracts can regenerate damaged tissue in the wound area and fasten the healing process thanks to these bioactive components [23,24]. Furthermore, these phytochemicals can exert their antimicrobial action by damaging the bacterial cell wall and membrane, blocking or disrupting the synthesis of crucial bacterial proteins, as well as inhibiting the action of significant bacterial metabolic pathways (e.g., DNA replication) [15,25,26]. The incorporation of herbal

extracts into electrospun nanofibrous mats has been extensively studied to enhance their biostability, despite their effective bioactivity.

The preclinical studies revealed that the treatment of wounds with herbal extract including nanofibers enhances the in vivo wound-healing rate (Table 1). The 20% (*w/w*) of *Malva sylvestris* extract incorporated in a polyurethane/carboxymethyl cellulose (PU/CMC) mats yielded a complete wound closure on the 14th post-treatment day, whilst its lower concentrations (5–10% *w/w*) were not sufficient. Due to the presence of various polysaccharides (e.g., flavonoids, naphthoquinones, and anthocyanins), *M. sylvestris* displayed good biological activity in a full-thickness diabetic wound model [27]. The addition of *Calendula officinalis* increased the closure rate of a wound treated with a pristine chitosan/polyethylene oxide (Chi/PEO) nanofibrous mat for 14 days from 80% to 90% [28]. In a study, peppermint extract and gelatin nanoparticles (NPs) were embedded into a PU/Pluronic F127 nanofibrous membrane to enhance wound healing. While both extract- and gelatin NPs-loaded membranes showed a 97% wound recovery rate, the scaffolds that contained only peppermint extract presented an almost 75% wound-closure rate within 21 days [29]. The treatment of wounds on a BALB/c mice model with henna extract-loaded gelatin/oxidized starch nanofibers presented a reduction in the number of macrophages, an inflammatory response with a thinner inflammation zone, and enhanced collagen deposition, which might have been due to the existence of various aromatic hydrocarbons in the henna structure [30]. The addition of palmatine accelerated the wound-healing ability of the PCL/gelatin nanofibers on the rabbit ear model by decreasing the healing time from 14 to 12 days, as well as inhibited hypertrophic scar formation. However, the highest concentration of palmatine (8 *w*%) showed cytotoxicity on the L929 fibroblasts [31]. In addition, almost 97% of the wound on the Wistar rat recovered due to the synergetic effect of the *Achyranthes aspera* and *Datura metel* extracts, which were incorporated into the PCL nanofibrous mats within 9 days post-treatment [32].

According to Table 1, when compared to extracts which were applied in the same concentration units (%, *w/w*), the addition of 2% of *Lawsonia inermis* extract [33] led to the almost complete wound closure at day 14, whilst the 15% of *Malva sylvestris* [27], 1% of curcumin [34], and 15% of peppermint [29] extracts displayed around 95%, 75%, and 65% in vivo wound-closure rates, respectively. Moreover, 2–8% of palmatine addition into the PCL/gelatin nanofibers [31] yielded an almost complete wound closure in 12 days. Additionally, none of the extracts showed any cytotoxic effect. Hence, it may be concluded that palmatine is the most effective extract with its lower concentrations for wound healing, followed by the *Lawsonia inermis*, *Malva sylvestris*, curcumin, and peppermint extracts.

Table 1. Indicative examples of electrospun scaffolds as antimicrobial herbal extract delivery vehicles for wound-healing applications published in the last five years. Abbreviations: antimicrobial susceptibility test: AST; Chitosan: Chi; Polycaprolactone: PCL; Poly (lactic acid): PLA; Poly(vinyl alcohol): PVA; Carboxymethyl cellulose: CMC; Polyurethane: PU; Poly(ethylene glycol): PEG; Nanoparticle: NP; Poly(lactic-co-glycolic acid): PLGA; Collagen: Col; Carboxyethyl chitosan: CE-Chi; Poly(ethylene oxide): PEO; Sodium tripolyphosphate: TPP; Microparticle: MP; Poly(hydroxy butyrate): PHB; Graphene oxide: GO; Poly-L-lactic acid: PLLA; PCL-PEG–block copolymer: PCL-b-PEG; Poly(3-hydroxybutyrate-co-3-hydroxyvalerate): PHBV; Polyvinyl pyrrolidone: PVP; (2,2,6,6-Tetramethylpiperidin-1-yl)oxyl: TEMPO; TEMPO oxidized cellulose nanofiber: TOCN; Polyethylene glycol methyl ether methacrylate: PEGMA; Gulmohar seed polysaccharide: GSP; Glutaraldehyde: GTA; human mesenchymal stem cell: hMSC; human dermal fibroblast: HDF; human keratinocytes cell line: HaCaT; human umbilical cord matrix: hUCM; normal human foreskin: NHF; human umbilical vein endothelial cell: HUVEC; *Propionibacterium acnes*: *P. acnes*; *Corynebacterium diphtheriae*: *C. diphtheriae*; *Staphylococcus epidermidis*: *S. epidermidis*; *Lactobacillus acidophilus*: *L. acidophilus*; *Bacillus subtilis*: *B. subtilis*; *Escherichia coli*: *E. coli*; *Vibrio parahaemolyticus*: *V. parahaemolyticus*; *Pseudomonas otitidis*: *P. otitidis*; *Klebsiella pneumoniae*: *K. pneumoniae*; *Staphylococcus aureus*: *S. aureus*; Methicillin-resistant *Staphylococcus aureus*: MRSA; *Pseudomonas aeruginosa*: *P. aeruginosa*.

Scaffold Conformation	Herbal Additive	AST	Antibacterial Activity Against	Cell Line	In Vivo Model	Important Biological Activity Outcome	Refs.
• cellulose acetate (5 g) nanofibrous mat • No crosslink	annatto extract (20 mL)	-	-	mouse fibroblasts	Wistar rat wound model	Annatto extract modulated the inflammation process.	[35]
• PVA (10% *w/v*)/Chi (3% *w/v*) nanofibrous mat • No crosslink	spray-dried *Centella asiatica*, *Portulaca oleracea*, and *Houttuynia cordata* extracts (3, 6, and 9% *w/w* of each)	disc diffusion	*P. acnes*	Chick chorioallantoic membrane (CAM) in vitro model	10 patients with mild-to-moderate facial *Acne vulgaris* aged between 20 and 30	Developed patches presented good bacterial inhibition for *P. acnes*, while they were not effective for pathogenic *E. coli* and *S. aureus*.	[36]
• PCL (14% *w/v*) nanofibrous mat • No crosslink	*Achyranthes aspera* and *Datura metel* leaf extracts (10, 20, and 30% *w/v*)	well diffusion	*C. diphtheriae*, *Enterococcus* spp., *S. epidermidis*, *L. acidophilus*, *B. subtilis*, *E. coli*, *Shigella* spp., *V. parahaemolyticu*, *Pseudomonas* spp., *P. otitidis*, *K. pneumoniae*, and *Vibrio* spp.	the vero kidney cells	male Wistar rat wound model	Hybrid scaffolds recovered the wound in vivo within 9 days.	[32]
• PU/CMC (20% *w/w*) nanofibrous mat (various PU:CMC *w* ratio) • No crosslink	*Malva sylvestris* dried leaf extract (5–20% *w/w*)	agar dilution	*S. aureus*, and *E. coli*	hMSCs	male Wistar rat full-thickness diabetic wound model	Developed dressings containing 15% *w/w* extract showed about 95% of wound-healing rate within day 14.	[27]

Table 1. *Cont.*

Scaffold Conformation	Herbal Additive	AST	Antibacterial Activity Against	Cell Line	In Vivo Model	Important Biological Activity Outcome	Refs.
• Chi (2% *w/v*)/PEO (3% *w/v*) nanofibrous mat crosslinked with 25% *v/v* GTA vapor	*Calendula officinalis* (1, 2, and 3% *w/v*)	agar well diffusion, viable cell count method	*S. aureus*, and *E. coli*	HDFs	male Wistar rat full-thickness wound model	Developed hybrid scaffold led to 87.5% of wound closure after 14 days.	[28]
• PVA (10 *w*%)/guar gum (1 *w*%) nanofibrous mat crosslinked with 5 *w*% citric acid	*Acalypha indica*, *Aristolochia bracteolate*, *Thespesia populnea*, and *Lawsonia inermis* (henna) extracts (20 *w*% of total polymer weight)	-	-	MSCs	female Wistar rat splint excisional model	In vivo efficacy of the hybrid scaffold with/without MSCs showed complete wound restoration with minimal scarring.	[37]
• PU (7% *w/v*)/pluronic F127 (0.7% *w/v*) nanofibrous mat crosslinked with 5–20% *w/w* gelatin NPs	peppermint ethanolic leaf extract (15% *w/w*)	agar dilution	*S. aureus*, and *E. coli*	hUCM cells	male Wistar rat diabetic wound model	The addition of 15% extract and 10% NPs as a crosslinker enhanced the wound-closure rate from 75% to 95% within 21 days.	[29]
• Gelatin (13 *w*%)/oxidized starch (5% *w/v*) nanofibrous mat crosslinked with 2% *w/v* oxidized starch	*Lawsonia inermis* (henna) aqueous leaf extract (10–40 *v*%)	disc diffusion, liquid medium microdilution	*S. aureus*, and *E. coli*	L929 fibroblasts	BALB/c mice second-degree burn wound model	The implantation of wounds treated with 30% henna-loaded mats exhibited clear epithelialization, angiogenesis, well-organized collagen molecules, and hair follicles on the fourth post-treatment day.	[30]
• PVA (10–30% *w/v*) nanofibrous mat • No crosslink	propolis dried alcoholic extract (1.25 mg/mL)	-	-	NIH 3T3 fibroblasts	male Swiss mice diabetic wound model	Propolis-loaded dressings showed partial wound closure (68%) within 7 days.	[38]
• PCL (20% *w/v*)/gelatin (8% *w/v*) nanofibrous mat • No crosslink	palmatine (2, 5, and 8 *w*%)	disc diffusion	*S. aureus*, and *E. coli*	L929 fibroblasts	rabbit ear model of hypertrophic scar (HS)	Sustained release of palmatine led to inhibition of HS formation, as well as accelerated wound healing.	[31]

Table 1. *Cont.*

Scaffold Conformation	Herbal Additive	AST	Antibacterial Activity Against	Cell Line	In Vivo Model	Important Biological Activity Outcome	Refs.
• PCL (10% *w/v*)/Mesoporous silica (5 *w*%) nanofibrous mat • No crosslink	curcumin (1 *w*%)	well diffusion	*S. aureus*, and *E. coli*	3T6 Swiss cells	female Wistar albino rat full-thickness excision skin wound model	The incorporation of both curcumin and silica contributed to 99% of scarless wound healing in vivo within 21 days.	[34]
• Gelatin (17 *w*%)/PVA (10 *w*%)/Chi (2 *w*%) bilayer nanofibrous mat crosslinked with 50 *w*% GTA vapors for 45 min.	curcumin (400 µg/mL), and *Lithospermi radix* extract (625 µg/mL)	-	-	L929 fibroblasts	male SD rat streptozotocin-induced diabetic wound model	While single incorporation of curcumin and LR extract increased the TGF-ß secretion level and collagen synthesis, respectively, their synergetic effect demonstrated curative activity.	[39]
• Chi (3 *w*%)/PEO (4 *w*%) nanofibrous mat • No crosslink	*Lawsonia inermis* (henna) and ethanolic leaf extract (1, and 2 *w*%)	disc diffusion	*S. aureus*, and *E. coli*	NHF fibroblasts	male Wistar rat wound model	The synergetic effect of henna extract and Chi polymer promoted antibacterial activity, biocompatibility, and wound-healing rate.	[33]
• Chi (3 *w*%)/PEO (3 *w*%) nanofibrous mat • No crosslink	*Aloe vera*	agar well diffusion	*S. aureus*, and *E. coli*	NIH 3T3 fibroblasts	Swiss albino mice wound model	*Aloe vera*-incorporated mats gave better in vitro and in vivo results when compared to pristine mats.	[40]
• PCL (8 *w*%)/Gelatin (4, 8 *w*%) core/shell nanofibrous mat • No crosslink	*Gymnema sylvestre* ultrasound-assisted and cold-macerated leaf extracts (10 *w*%) with minocycline hydrochloride (2 *w*%)	disc diffusion, bacterial cell viability assay	*S. aureus*, MRSA, *S. epidermidis*, *P. aeruginosa*, and *E. coli*	HDFs, and HaCaTs	female porcine second-degree burn wound model	Developed composite mats showed a potent bactericidal effect against biofilm-forming pathogenic bacterial strains which can prolong wound healing.	[41]
• PCL (4% *w/v*)/Gelatin (10% *w/v*) nanofibrous mat • No crosslink	Lawsone (0.5, 1, and 1.5%)	disc diffusion	*S. aureus*	human normal gingival fibroblasts	male Wistar rat excision wound model	The expression of healing-related genes TGF-B1 and COL1 significantly increased on extract-loaded mats.	[42]

Table 1. *Cont.*

Scaffold Conformation	Herbal Additive	AST	Antibacterial Activity Against	Cell Line	In Vivo Model	Important Biological Activity Outcome	Refs.
• PCL (10% *w/v*) nanofibrous mat • No crosslink	*Areca catechu* petroleum ether phytoextracts (5% *w/w*)	disc diffusion	*S. aureus*, and *P. aeruginosa*	L929 fibroblasts	female SD rat skin wound model	Phytoextracts showed slightly higher antibacterial activity on gram-positive *S. aureus* when compared to gram-negative *P. aeruginosa*.	[43]
• PVA (6% *w/v*) nanofibrous mat crosslinked with 10% *v/v* GTA vapor for 10 h at ambient temperature	*Cordia myxa* ethanolic fruit extract (2.5, and 5% *w/v*)	-	-	human foreskin fibroblasts	male albino mice skin wound model	The 5% *w/v* extract addition to mats supported fibroblast proliferation and attachment while being non-cytotoxic to the cells.	[44]
• Col (10, 11 *w*%)/PCL (10, 11 *w*%) three-layered nanofibrous mat • No crosslink	*Melilotus officinalis* (2, 4, and 8% *w/w* based on collagen weight)	-	-	L929 fibroblasts	male Wistar rat diabetic wound model	The 8% *w/w* extract-added mats demonstrated favorable reepithelization of in vivo diabetic wounds as well collagen production and deposition.	[45]
• Gelatin (10% *w/v*)/PCL (10% *w/v*)/PU (10% *w/v*) membrane/nanofiber bilayer scaffold • No crosslink	propolis ethanolic extract (0.5% *w/w*)	disc diffusion	*S. aureus*, *S. epidermidis*, and *E. coli*	L929 fibroblasts	female Wistar rat skin wound model	Approximately 40% of the loaded extract was released within 50 h, which showed significant antibacterial activity against *S. aureus*.	[46]
• PLGA (12% *w/v*)/PVA (0.5% *w/v*) nanofibrous mat • No crosslink	*Aloe vera* (250 mg/mL) caged into lipid NPs (25 mg/mL)	-	-	HaCaTs, and BalbC/3T3 A31 fibroblasts	male *db/db* mice full-thickness wound model	The extract-caged lipid NPs directly loaded into mats did not show a difference in wound closure and reepithelization rates, as well as cell adhesion percentage.	[47]
• PU (10% *w/v*) nanofibrous mat • No crosslink	*Nigella sativa* oil (10% *v/v*)	ASTM E2149, and shake flask test	*S. aureus*, and *E. coli*	HUVECs	female SD rat	The synergetic effect of the nanofibers' advantage and bioactive oil presented the fastest wound closure in vivo.	[48]

3. Indirect Effect of Herbal Extracts on Wound Healing

In addition to their direct effect on wound healing due to their bioactive compounds, herbal extracts may enhance the wound healing ability of electrospun nanofibers by altering their physicochemical, mechanical, and morphological characteristics. At this point, we will review how herbal extracts affected the hydrophilicity, mechanical strength, average fiber diameter, and porosity of electrospun nanofibrous wound dressings that provide benefits such as improved wound-healing.

3.1. Effect of Herbal Extracts on the Hydrophilicity of Electrospun Mats

The water uptake capacity of electrospun mats plays a crucial role in wound healing. The fabricated mats can conserve the moisture and nutrients in the wound area, as well as promote cell adhesion and proliferation with a higher swelling ratio [42,49]. The water uptake percentage of the Chi/PEO nanofibers increased from 93% to 119% through the incorporation of 2 w% of hydro-alcoholic henna extract, which was attributed to the hydrophilic functional groups of henna, while wound-closure rates were evaluated to be approximately 85% and 90% for pristine and 2 w% henna-including mats, respectively [33]. Similarly, the addition of lawsone raised the water content of the PCL/gelatin nanofibers by almost three-fold in the PBS (pH:7) media. This composite mat displayed a lower number of inflammatory cells and more organized fibroblasts with accelerated wound-healing within 14 days [42]. Additionally, enhanced wettability of nanofibrous mats may benefit the diffusion of nutrients to the wound area, absorption of exudate, as well enhance cell binding. For example, the presence of several polar phytochemicals in the *Gymnema sylvestre* extract achieved a decrease in the water contact angle of the PCL/gelatin nanofibers and a slight increase in the wound recovery percentage on the 32nd day post-injury [42].

3.2. Effect of Herbal Extracts on the Mechanical Strength of Electrospun Mats

The adequate mechanical properties of engineered electrospun mats are another important parameter to promote the formation of new dermal tissue and resist biodegradation during the wound-healing process [50]. An ideal nanofibrous wound dressing should provide a balance between flexibility and hardness [51] and display a tensile strength in the range of 0.8 to 18 MPa, which is proper for dermal cell culture and skin tissue engineering applications [52,53]. Herbal extracts may act as a reinforcement agent [37,41] and increase the tensile strength of nanofibers, which leads to the enhancement of wound recovery. To exemplify, the incorporation of *Acalypha indica*, *Aristolochia bracteolate*, *Thespesia populnea*, and henna extracts together increased the tensile strength of the PVA/Guar gum nanofibers because of the crosslinking impact of *A. bracteolate* and *A. indica* extracts resulting from their increased nonpolar functional ratio. Although the improved mechanical properties of mats are not the only effective parameter, polyherbal extract-including mats showed a slightly higher wound-closure rate (97%) than pristine mats (93%) within 14 days [37]. A similar effect was observed with the addition of the *Gymnema sylvestre* extract, which improved the ultimate tensile stress of the PCL/gelatin mats from about 1.4 to 4.3 MPa, an effect which may be attributed to the high number of hydrogen-bonding donor molecules in the structure of the extract. In parallel, the presence of an extract in the core/shell nanofibers, which are one of the most common nanofiber structures, significantly improved wound-closure percentage with enhanced epidermal cell proliferation [41]. However, in some studies, herbal extracts showed a plasticizing effect [20,28,33,42], resulting in the reduction of the tensile strength. Nevertheless, despite the decreased mechanical strength, the wound-healing ability of mats was not negatively affected.

3.3. Effect of Herbal Extracts on the Average Fiber Diameter of Electrospun Mats

The morphology of nanofibrous dressings plays a significant role in wound-healing applications, since the random orientation of nanofibers can mimic the nature of the extracellular matrix (ECM) [54]. As a general trend, the incorporation of herbal extract reduced the viscosity of the polymeric spinning solution with the increase in the conductivity,

which induces the formation of smaller fibers since it acts as a plasticizer when added to a polymer blend [28,35,36,39,44,48]. Smaller-diameter nanofibers have a supportive effect on the wound-healing process due to their greater protein-absorption capacity. In other words, cell adhesion on smaller-diameter fibers is promoted due to their larger specific surface areas [55]. To illustrate, while the average diameter of the gelatin/PVA/Chi nanofibers was reduced almost two-fold by the incorporation of 400 μg/mL of curcumin, the curcumin-including composite dressings displayed greater wound recovery on the 14th day of treatment when compared to gauze control [39]. In contrast, it was reported that the addition of the palmatine [31] and *Melilotus officinalis* [45] extracts raised the average nanofiber diameters, which might be explained by the decreased electrical conductivity of the polymeric spinning solution. Nonetheless, the higher nanofiber diameters did not show an inhibitory effect on wound healing; even the acceleration of wound-healing rates [31] and more collagen deposition [45] were revealed. In summary, it can be concluded that, even though the general view is that of decreasing the nanofiber diameter by adding an herbal extract into the formulation, some studies showed opposite outcomes.

3.4. Effect of Herbal Extracts on the Porosity of Electrospun Mats

Besides the nanofiber dimension, porosity is accepted as another outstanding parameter for fibrous scaffolds [56]. Since the proper porosity allows the permeation of oxygen through the wound bed, it can benefit the acceleration of wound healing [57] by improving the proliferation of fibroblasts and keratinocytes. The resulting proliferating environment can lead to the reepithelization and formation of granulation tissue, advancing the secretion of wound-healing mediators (e.g., angiogenic factors, growth factors, and collagen) [47,54]. Case in point, the addition of 5% (*w/v*) of *Cordia myxa* ethanolic fruit extract increased the porosity of the PVA nanofibers by 11.8%, as well as provided the proper reepithelization, more collagen deposition, and a 33.6% smaller wound within 14 days [44]. Similarly, the incorporation of *Aloe vera* [56] and *Nigella sativa* oil [48] enhanced the porosity of the PLGA/PVA and PU nanofibrous scaffolds, respectively, with improved proliferation and wound-healing activity. The increased porosity might be explained by the thinner nanofibers produced through the addition of herbal extracts. Instead, the presence of various concentrations of *Calendula officinalis* did not affect the porosity of the Chi/PEO nanofibers [28].

4. Future Aspects

Electrospinning is one of the biomaterial fabrication processes that use the high-voltage-electric field to draw charged polymer melts/solutions through the collector to obtain nano-sized structures. Electrospinning has come into prominence when compared to traditional fabrication methods since it is a simple and user-friendly process that leads to control over the porosity and/or morphology of nanofibers by altering the fabrication parameters (e.g., flowrate, voltage of electric fields, and nozzle diameter). Moreover, electrospun nanofibers display various advantages for tissue engineering applications thanks to the possibility of adjusting the hydrophilicity and stimuli-responsive capacity of the fabricated materials. In particular, electrospun nanofibers are an excellent candidate for a wound dressing due to their high surface area to volume ratio, adjustable and high porosity, good biocompatibility, and mechanical properties. All these outstanding features favor cell attachment, growth, and proliferation, as well as wound moisturizing. In addition, due to growing health concerns regarding the use of synthetic molecules, nature-inspired molecules such as herbal extracts are constantly attracting attention for advancing greener and non-toxic products for wound-healing treatment. Therefore, we believe that electrospinning is a promising technology for developing wound dressings that incorporate natural therapeutics in the formulation of the nanofibers.

5. Conclusions

Wound care is a problem that has always concerned human health, from the beginning of humanity. In the quest for the treatment of infected wounds, herbal extracts have been slighted when compared to antibiotics, despite the fact that they have been a primary source of traditional remedies since ancient times. However, in the perspective of the development of alternative wound dressings, the study of herbal extract-incorporated delivery systems has recently begun to gain an important place in the literature to overcome the drawbacks of antibiotic usage, e.g., antimicrobial resistance and biofilm formation. Furthermore, electrospun scaffolds are one of the most prominent biomaterial forms owing to their highly porous, nano-sized structures. Through the incorporation of herbal extracts instead of synthetics, the reduction of several health concerns caused by the use of synthetics has been achieved. This review clearly exemplifies both the direct and indirect effects of herbal extracts on wound healing and gives countenance to the advancing of natural, herbal-based nanofibrous delivery systems for effective wound care and infectious treatment.

Author Contributions: Conceptualization: C.E.; Resources: C.E., K.F. and C.V.; Literature review and writing—original draft preparation: C.E.; Writing—review and editing: C.E., K.F., C.V., A.T., I.S. and D.I.Z.; Supervision: A.T., I.S. and D.I.Z. All authors have read and agreed to the published version of the manuscript.

Funding: This research received no external funding.

Data Availability Statement: Data are contained within the article.

Acknowledgments: The authors acknowledge the European Union, EuroNanoMed III, project nAngioDerm, through the Greek General Secretariat for Research and Innovation ERA-NETS (code number T9EPA3-00022).

Conflicts of Interest: The authors declare no conflict of interest.

References

1. Lima, T.D.; Passos, M.F. Skin wounds, the healing process, and hydrogel-based wound dressings: A short review. *J. Biomater. Sci. Polym. Ed.* **2021**, *32*, 1910–1925. [CrossRef] [PubMed]
2. Feinglass, J.; Patel, T.R.; Rydland, K.; Sheehan, K. Trends in hospital care for intentional assault gunshot wounds among residents of Cook County, Illinois, 2018–2020. *Am. J. Public Health* **2022**, *12*, 795–802. [CrossRef] [PubMed]
3. Mendes, J.J.; Leandro, C.I.; Bonaparte, D.P.; Pinto, A.L. A rat model of diabetic wound infection for the evaluation of topical antimicrobial therapies. *Comp. Med.* **2012**, *62*, 37–48. [PubMed]
4. Rahim, K.; Saleha, S.; Zhu, X.; Huo, L.; Basit, A.; Franco, O.L. Bacterial contribution in chronicity of wounds. *Microb. Ecol.* **2017**, *73*, 710–721. [CrossRef]
5. Sorg, H.; Tilkorn, D.J.; Hager, S.; Hauser, J.; Mirastschijski, U. Skin wound healing: An update on the current knowledge and concepts. *Eur. Surg. Res.* **2017**, *58*, 81–94. [CrossRef]
6. Fragkou, I.A.; Gougoulis, D.A.; Billinis, C.; Mavrogianni, V.S.; Bushnell, M.J.; Cripps, P.J.; Tzora, A.; Fthenakis, G.C. Transmission of Mannheimia haemolytica from the tonsils of lambs to the teat of ewes during sucking. *Vet. Microbiol.* **2011**, *148*, 66–74. [CrossRef]
7. Bowler, P.; Duerden, B.; Armstrong, D.G. Wound microbiology and associated approaches to wound management. *Clin. Microbiol. Rev.* **2001**, *14*, 244–269. [CrossRef] [PubMed]
8. Cardona, A.F.; Wilson, S.E. Skin and soft-tissue infections: A critical review and the role of telavancin in their treatment. *Clin. Infect. Dis.* **2015**, *61*, 69–78. [CrossRef]
9. Everts, R. How to Treat Wound Infection. Prevention and Treatment. 2016. Available online: https://www.acc.co.nz/assets/provider/treating-wound-infections.pdf (accessed on 20 June 2023).
10. Das, P.; Horton, R. Antibiotics: Achieving the balance between access and excess. *Lancet* **2016**, *387*, 102–104. [CrossRef]
11. Ersanli, C.; Tzora, A.; Skoufos, I.; Fotou, K.; Maloupa, E.; Gridoriadou, K.; Voidarou, C.; Zeugolis, D.I. The Assessment of Antimicrobial and Anti-Biofilm Activity of Essential Oils against *Staphylococcus aureus* Strains. *Antibiotics* **2023**, *12*, 384. [CrossRef]
12. Vaou, N.; Stavropoulou, E.; Voidarou, C.; Tsigalou, C.; Bezirtzoglou, E. Towards advances in medicinal plant antimicrobial activity: A review study on challenges and future perspectives. *Microorganisms* **2021**, *10*, 2041. [CrossRef] [PubMed]
13. Mamedov, N. Medicinal plants studies: History, challenges and prospective. *Med. Aromat. Plants* **2012**, *1*, 133. [CrossRef]
14. Fathi, M.; Ahmadi, N.; Forouhar, A.; Hamzeh Atani, S. Natural Hydrogels, the Interesting Carriers for Herbal Extracts. *Food Rev. Int.* **2021**, *38*, 1–25. [CrossRef]

15. Agarwal, T.; Tan, S.-A.; Onesto, V.; Law, J.X.; Agrawal, G.; Pal, S.; Lim, W.L.; Sharifi, E.; Moghaddam, F.D.; Maiti, T.K. Engineered herbal scaffolds for tissue repair and regeneration: Recent trends and technologies. *Biomed. Eng. Adv.* **2021**, *2*, 100015. [CrossRef]
16. Padulosi, S.; Leaman, D.; Quek, P. Challenges and opportunities in enhancing the conservation and use of medicinal and aromatic plants. *J. Herbs Spices Med.* **2002**, *9*, 243–267. [CrossRef]
17. Lai, W.-F.; Rogach, A.L. Hydrogel-based materials for delivery of herbal medicines. *ACS Appl. Mater. Interfaces* **2017**, *9*, 11309–11320. [CrossRef]
18. Khan, R.; Xiangyang, S.; Ahmad, A.; Mo, X. Electrospinning of crude plant extracts for antibacterial and wound healing applications: A review. *SM J. Biomed. Eng.* **2018**, *4*, 1024.
19. Fuller, K.; Pandit, A.; Zeugolis, D.I. The multifaceted potential of electro-spinning in regenerative medicine. *Pharm. Nanotechnol.* **2014**, *2*, 23–34. [CrossRef]
20. Teo, W.E.; Ramakrishna, S. A review on electrospinning design and nanofibre assemblies. *J. Nanotechnol.* **2006**, *17*, R89. [CrossRef]
21. Khajavi, R.; Abbasipour, M.J. Electrospinning as a versatile method for fabricating coreshell, hollow and porous nanofibers. *Sci.Iran.* **2012**, *19*, 2029–2034. [CrossRef]
22. Das, U.; Behera, S.S.; Singh, S.; Rizvi, S.I.; Singh, A.K. Progress in the development and applicability of potential medicinal plant extract-conjugated polymeric constructs for wound healing and tissue regeneration. *Phytother. Res.* **2016**, *30*, 1895–1904. [CrossRef] [PubMed]
23. Sharma, A.; Khanna, S.; Kaur, G.; Singh, I. Medicinal plants and their components for wound healing applications. *Future J. Pharm. Sci.* **2021**, *7*, 1–13. [CrossRef]
24. Giannenas, I.; Tzora, A.; Sarakatsianos, I.; Karamoutsios, A.; Skoufos, S.; Papaioannou, N.; Anastasiou, I.; Skoufos, I. The effectiveness of the use of oregano and laurel essential oils in chicken feeding. *Ann. Anim. Sci.* **2016**, *16*, 779–796. [CrossRef]
25. Yu, M.; Gouvinhas, I.; Rocha, J.; Barros, A.I. Phytochemical and antioxidant analysis of medicinal and food plants towards bioactive food and pharmaceutical resources. *Sci. Rep.* **2021**, *11*, 10041. [CrossRef]
26. Khameneh, B.; Iranshahy, M.; Soheili, V.; Bazzaz, B.S. Review on plant antimicrobials: A mechanistic viewpoint. *Antimicrob. Resist. Infect. Control* **2019**, *8*, 118. [CrossRef]
27. Almasian, A.; Najafi, F.; Eftekhari, M.; Ardekani, M.R.S.; Sharifzadeh, M.; Khanavi, M. Polyurethane/carboxymethylcellulose nanofibers containing *Malva sylvestris* extract for healing diabetic wounds: Preparation, characterization, in vitro and in vivo studies. *Mater. Sci. Eng. C* **2020**, *114*, 111039. [CrossRef]
28. Kharat, Z.; Goushki, M.A.; Sarvian, N.; Asad, S.; Dehghan, M.M.; Kabiri, M. Chitosan/PEO nanofibers containing *Calendula officinalis* extract: Preparation, characterization, in vitro and in vivo evaluation for wound healing applications. *Int. J. Pharm.* **2021**, *609*, 121132. [CrossRef]
29. Almasian, A.; Najafi, F.; Eftekhari, M.; Shams Ardekani, M.R.; Sharifzadeh, M.; Khanavi, M. Preparation of Polyurethane/Pluronic F127 Nanofibers Containing Peppermint Extract Loaded Gelatin Nanoparticles for Diabetic Wounds Healing: Characterization, In Vitro, and In Vivo Studies. *Evid.-Based Complement. Altern. Med.* **2021**, *2021*, e6646702. [CrossRef]
30. Hadisi, Z.; Nourmohammadi, J.; Nassiri, S.M. The antibacterial and anti-inflammatory investigation of Lawsonia Inermis-gelatin-starch nano-fibrous dressing in burn wound. *Int. J. Biol. Macromol.* **2018**, *107*, 2008–2019. [CrossRef]
31. Jiang, Z.; Zhao, L.; He, F.; Tan, H.; Li, Y.; Tang, Y.; Duan, X.; Li, Y. Palmatine-loaded electrospun poly (ε-caprolactone)/gelatin nanofibrous scaffolds accelerate wound healing and inhibit hypertrophic scar formation in a rabbit ear model. *J. Biomater. Appl.* **2021**, *35*, 869–886. [CrossRef]
32. Suryamathi, M.; Viswanathamurthi, P.; Seedevi, P. Herbal Plant Leaf Extracts Immobilized PCL Nanofibrous Mats as Skin Inspired Anti-infection Wound Healing Material. *Regen. Eng. Transl. Med.* **2022**, *8*, 94–105. [CrossRef]
33. Yousefi, I.; Pakravan, M.; Rahimi, H.; Bahador, A.; Farshadzadeh, Z.; Haririan, I. An investigation of electrospun Henna leaves extract-loaded chitosan based nanofibrous mats for skin tissue engineering. *Mater. Sci. Eng. C* **2017**, *75*, 433–444. [CrossRef] [PubMed]
34. Rathinavel, S.; Korrapati, P.S.; Kalaiselvi, P.; Dharmalingam, S. Mesoporous silica incorporated PCL/Curcumin nanofiber for wound healing application. *Eur. J. Pharm. Sci.* **2021**, *167*, 106021. [CrossRef] [PubMed]
35. Dos Santos, A.E.A.; Dos Santos, F.V.; Freitas, K.M.; Pimenta, L.P.S.; de Oliveira Andrade, L.; Marinho, T.A.; de Avelar, G.F.; da Silva, A.B.; Ferreira, R.V. Cellulose acetate nanofibers loaded with crude annatto extract: Preparation, characterization, and in vivo evaluation for potential wound healing applications. *Mater. Sci. Eng. C* **2021**, *118*, 111322. [CrossRef]
36. Tang, Y.; Liu, L.; Han, J.; Zhang, Z.; Yang, S.; Li, S.; Fan, Z.; Zhao, H. Fabrication and characterization of multiple herbal extractsloaded nanofibrous patches for topical treatment of acne vulgaris. *Fibers Polym.* **2021**, *22*, 323–333. [CrossRef]
37. Kalachaveedu, M.; Jenifer, P.; Pandian, R.; Arumugam, G. Fabrication and characterization of herbal drug enriched guar galactomannan based nanofibrous mats seeded with GMSC's for wound healing applications. *Int. J. Biol. Macromol.* **2020**, *148*, 737–749. [CrossRef]
38. Alberti, T.B.; Coelho, D.S.; de Prá, M.; Maraschin, M.; Veleirinho, B. Electrospun PVA nanoscaffolds associated with propolis nanoparticles with wound healing activity. *J. Mater. Sci.* **2020**, *55*, 9712–9727. [CrossRef]
39. Yang, B.Y.; Hu, C.H.; Huang, W.C.; Ho, C.Y.; Yao, C.H.; Huang, C.H. Effects of bilayer nanofibrous scaffolds containing curcumin/lithospermi radix extract on wound healing in streptozotocin-induced diabetic rats. *Polymers* **2019**, *11*, 1745. [CrossRef]

40. Pathalamuthu, P.; Siddharthan, A.; Giridev, V.; Victoria, V.; Thangam, R.; Sivasubramanian, S.; Savariar, V.; Hemamalini, T.J. Enhanced performance of Aloe vera incorporated chitosan-polyethylene oxide electrospun wound scaffold produced using novel Spirograph based collector assembly. *Int. J. Biol. Macromol.* **2019**, *140*, 808–824. [CrossRef]
41. Ramalingam, R.; Dhand, C.; Mayandi, V.; Leung, C.M.; Ezhilarasu, H.; Karuppannan, S.K.; Prasannan, P.; Ong, S.T.; Sunderasan, N.; Kaliappan, I.; et al. Core–shell structured antimicrobial nanofiber dressings containing herbal extract and antibiotics combination for the prevention of biofilms and promotion of cutaneous wound healing. *ACS Appl. Mater. Interfaces* **2021**, *13*, 24356–24369. [CrossRef]
42. Adeli-Sardou, M.; Yaghoobi, M.M.; Torkzadeh-Mahani, M.; Dodel, M. Controlled release of lawsone from polycaprolactone/gelatin electrospun nano fibers for skin tissue regeneration. *Int. J. Biol. Macromol.* **2019**, *124*, 478–491. [CrossRef] [PubMed]
43. Letha, N.; Joseph, J.; Sundar, G.; Pillai, A.U.; John, A.; Abraham, A. Incorporation of phytochemicals into electrospun scaffolds for wound-healing applications in vitro and in vivo. *J. Bioact. Compat. Polym.* **2020**, *35*, 451–466. [CrossRef]
44. Seyedian, R.; Isavi, F.; Najafiasl, M.; Zaeri, S. Electrospun fibers loaded with Cordia myxa L. fruit extract: Fabrication, characterization, biocompatibility and efficacy in wound healing. *J. Drug Deliv. Sci. Technol.* **2021**, *63*, 102528. [CrossRef]
45. Derakhshan, M.A.; Nazeri, N.; Khoshnevisan, K.; Heshmat, R.; Omidfar, K. Three-layered PCL-collagen nanofibers containing melilotus officinalis extract for diabetic ulcer healing in a rat model. *J. Diabetes Metab. Disord.* **2022**, *21*, 1–9. [CrossRef]
46. Eskandarinia, A.; Kefayat, A.; Agheb, M.; Rafienia, M.; Amini Baghbadorani, M.; Navid, S.; Ebrahimpour, K.; Khodabakhshi, D.; Ghahremani, F. A novel bilayer wound dressing composed of a dense polyurethane/propolis membrane and a biodegradable polycaprolactone/gelatin nanofibrous scaffold. *Sci. Rep.* **2020**, *10*, 3063. [CrossRef]
47. Garcia-Orue, I.; Gainza, G.; Garcia-Garcia, P.; Gutierrez, F.B.; Aguirre, J.J.; Hernandez, R.M.; Delgado, A.; Igartua, M. Composite nanofibrous membranes of PLGA/Aloe vera containing lipid nanoparticles for wound dressing applications. *Int. J. Pharm.* **2019**, *556*, 320–329. [CrossRef]
48. Aras, C.; Tümay Özer, E.; Göktalay, G.; Saat, G.; Karaca, E. Evaluation of Nigella sativa oil loaded electrospun polyurethane nanofibrous mat as wound dressing. *J. Biomater. Sci. Polym. Ed.* **2021**, *32*, 1718–1735. [CrossRef]
49. Razavi, S.; Karbasi, S.; Morshed, M.; Esfahani, H.Z.; Golozar, M.; Vaezifar, S.J.C.J. Cell attachment and proliferation of human adipose-derived stem cells on PLGA/chitosan electrospun nano-biocomposite. *Cell J.* **2015**, *17*, 429–437.
50. Joshi, M.K.; Tiwari, A.P.; Pant, H.R.; Shrestha, B.K.; Kim, H.J.; Park, C.H.; Kim, C.S. In situ generation of cellulose nanocrystals in polycaprolactone nanofibers: Effects on crystallinity, mechanical strength, biocompatibility, and biomimetic mineralization. *ACS Appl. Mater. Interfaces* **2015**, *7*, 19672–19683. [CrossRef]
51. Pedram Rad, Z.; Mokhtari, J.; Abbasi, M. Preparation and characterization of *Calendula officinalis*-loaded PCL/gum Arabic nanocomposite scaffolds for wound healing applications. *Iran. Polym. J.* **2019**, *28*, 51–63. [CrossRef]
52. Barnes, C.P.; Sell, S.A.; Boland, E.D.; Simpson, D.G.; Bowlin, G.L. Nanofiber technology: Designing the next generation of tissue engineering scaffolds. *Adv. Drug Deliv. Rev.* **2007**, *59*, 1413–1433. [CrossRef]
53. Gomes, S.R.; Rodrigues, G.; Martins, G.G.; Roberto, M.A.; Mafra, M.; Henriques, C.; Silva, J.C. In vitro and in vivo evaluation of electrospun nanofibers of PCL, chitosan and gelatin: A comparative study. *Mater. Sci. Eng. C* **2015**, *46*, 348–358. [CrossRef]
54. Abrigo, M.; McArthur, S.L.; Kingshott, P. Electrospun nanofibers as dressings for chronic wound care: Advances, challenges, and future prospects. *Macromol. Biosci.* **2014**, *14*, 772–792. [CrossRef] [PubMed]
55. Mani, M.P.; Jaganathan, S.K. Physicochemical and blood compatibility characteristics of garlic incorporated polyurethane nanofibrous scaffold for wound dressing applications. *J. Text. Inst.* **2019**, *110*, 1615–1623. [CrossRef]
56. Yang, Y.; Zhu, X.; Cui, W.; Li, X.; Jin, Y. Electrospun composite mats of poly [(D, L-lactide)-co-glycolide] and collagen with high porosity as potential scaffolds for skin tissue engineering. *Macromol. Mater. Eng.* **2009**, *294*, 611–619. [CrossRef]
57. Liu, X.; Lin, T.; Fang, J.; Yao, G.; Zhao, H.; Dodson, M.; Wang, X. In vivo wound healing and antibacterial performances of electrospun nanofibre membranes. *J. Biomed. Mater. Res. A* **2010**, *94*, 499–508. [PubMed]

Journal of
Functional
Biomaterials

MDPI

Article

Dyeing Improvement and Stability of Antibacterial Properties in Chitosan-Modified Cotton and Polyamide 6,6 Fabrics

Marta Piccioni, Roberta Peila *, Alessio Varesano and Claudia Vineis

CNR-STIIMA (National Research Council—Institute of Intelligent Industrial Technologies and Systems for Advanced Manufacturing), Corso Giuseppe Pella 16, 13900 Biella, Italy; marta.piccioni@stiima.cnr.it (M.P.); alessio.varesano@stiima.cnr.it (A.V.); claudia.vineis@stiima.cnr.it (C.V.)
* Correspondence: roberta.peila@stiima.cnr.it

Abstract: Cotton and polyamide 6,6 fabrics coated with chitosan, a natural biopolymer, have been tested against two different bacteria strains: *Staphylococcus aureus* as Gram-positive bacterium and *Escherichia coli* as Gram-negative bacterium. Using the ASTM standard method (Standard Test Method for Determining the Antimicrobial Activity of Antimicrobial Agents Under Dynamic Contact Conditions) for antibacterial testing, the treated fabrics is contacted for 1 h with the bacterial inoculum, the present study aims to investigate the possibility to reach interesting results considering shorter contact times. Moreover, the antibacterial activity of chitosan-treated fibers dyed with a natural dye, *Carmine Red*, was evaluated since chitosan has an interesting property that favors the attachment of the dye to the fiber (cross-linking ability). Finally, fabric samples were tested after washing cycles to verify the resistance of the dye and if the antibacterial property was maintained.

Keywords: textiles; cotton; polyamide 6,6; chitosan; antibacterial; dyeing

1. Introduction

Fabrics and protective clothes used in schools, hotels, hospitals, nursing homes, and crowded public areas can benefit from antimicrobial finishing. Antimicrobial finishes are an important market need to prevent a reduction in mechanical strength and the formation of unpleasant odors in athletic wear, intimate apparel, underwear, socks, upholstery, and hospital linen [1].

Other effects due to the biodeterioration of fabrics are the formation of stains and discoloration, which is of interest for almost all types of fibers.

Natural fibers, like cotton, are generally more susceptible to biodeterioration than synthetic fibers because their porous hydrophilic structure retains water, oxygen, and nutrients, providing an ideal environment for microbial growth [2].

Generally, the antibacterial finishes should be non-toxic to the textile user, and allergy, cytotoxicity, irritation or sensitization must be avoided.

The treatment should maintain the textiles' quality, handle or appearance, and it must have excellent fastness for use, mainly for repeated laundering. Also, the application method should be simple, easily implementable in the finishing process, and environmentally friendly [2].

Often, antimicrobial agents for textiles are synthetic, including metals (e.g., silver), metal oxides (e.g., zinc oxide) or salts, polymers (e.g., polypyrrole), and chemicals (e.g., quaternary ammonium compounds, synthetic azo dyes, triclosan). Most of these agents are toxic to humans and are not environmentally friendly.

Polypyrrole is an example of a synthetic antimicrobial agent that is safe for human skin with precaution for respiratory tissue [3], but the monomer (before synthesis) is toxic.

Quaternary ammonium compounds (QACs) are another example of antimicrobial agents of synthetic origin. These are widely used in industrial applications because they are effective against Gram-positive and Gram-negative bacteria, fungi, and certain viruses [4].

Despite the effectiveness of QACs, they present a disadvantage, namely, the poor fastness of the treatment due to the fast leaching from the textile for the lack of chemical or physical bonding [2].

Silver is an antimicrobial metal widely used in textiles. However, there are some concerns about its toxicity, particularly when used as nanoparticles [5,6].

The possible toxic effects of some of these agents on human beings are reported in Table 1 [7].

Table 1. Possible toxic effects of some synthetic antimicrobial agents on human beings.

Synthetic Agent	Toxic Effects
QACs	respiratory irritation, nausea, skin, and eye irritation [8]
silver	argyria, contact dermatitis, mucous membrane irritation [9]
zinc pyrithione	developmental and neurotoxicity [10]
azo dyes	carcinogenic [11]
triclosan	endocrine disrupter, skin and eye irritation [12]
zinc oxide	cytotoxicity, apoptosis induction, ROS generation [13]

In view of these environmental and ecological concerns, there has been a focus on the research and development of new antimicrobial compounds of natural origin in the last decades.

Plants have gained interest as a source of natural antimicrobials. In 2016, Katewaraphorn et al. [14] investigated the antibacterial activity of cotton fabrics treated with a leaf extract of *Psidium Guajava* containing phenolic compounds.

Strong antimicrobial properties have been found in flavonoids, quinonoids, terpenoids, and tannins extracted from different parts of plants such as roots, bark, leaves, and flowers [15].

However, chitosan and its derivatives appear to be the most effective natural antimicrobial agent on the market [2].

In fact, the natural polysaccharides used for the functional finishing of textiles are abundantly available as waste products and are of an eco-friendly nature [7].

Chitosan, 2-amino-2-deoxy-(1→4)-d-glucopyranan, is undoubtedly one of the more promising multifunctional polymers among textile finishing agents.

It is chemically composed of glucosamine and N-acetylglucosamine units linked by 1–4 glucosidic bonds [16] and has unique properties, such as biodegradability, non-toxicity, and antimicrobial activity [17].

Chitosan is derived from the deacetylation process by chitin, which is the second most abundant biopolymer in the world after cellulose. Chitin is a component of the shells of crustaceans and constitutes the exoskeleton of insects as well as the wall of fungi [18,19].

Chitosan shows antibacterial activity against both Gram-positive and Gram-negative bacteria, thanks to its combined bactericidal and bacteriostatic action. Its property mainly includes four mechanisms [17]: it causes damage to microbial DNA, as a blocking agent of oxygen and nutrients in the bacteria cell, it can bind to cationic metals (calcium, magnesium) and nutrients essential for the microorganism, and it causes the loss of cytoplasmic intracellular components necessary for cell survival.

The first two mechanisms are associated with the chitosan antibacterial activity against Gram-negative bacteria, while the third and fourth dominate the antibacterial activity against Gram-positive bacteria.

All antibacterial mechanisms described are due to the fact that chitosan molecules carry positively charged amine groups and thus, in turn, have an electrostatic interaction with negatively charged cell membranes of microorganisms [20]. This electrostatic interaction leads to bacterial death.

Moreover, chitosan has the intrinsic property of acting as a cross linker, favoring the attachment of natural dyes to the fibers [21]. This is due to the chemical structure of chitin that is similar to cellulose, with a hydroxyl group on each monomer replaced with an acetylamine group [19,22]. The different structures are reported in Figure 1. It is an important property because most natural dyes generally lack substantivity for fibers, especially fibers such as cotton [23].

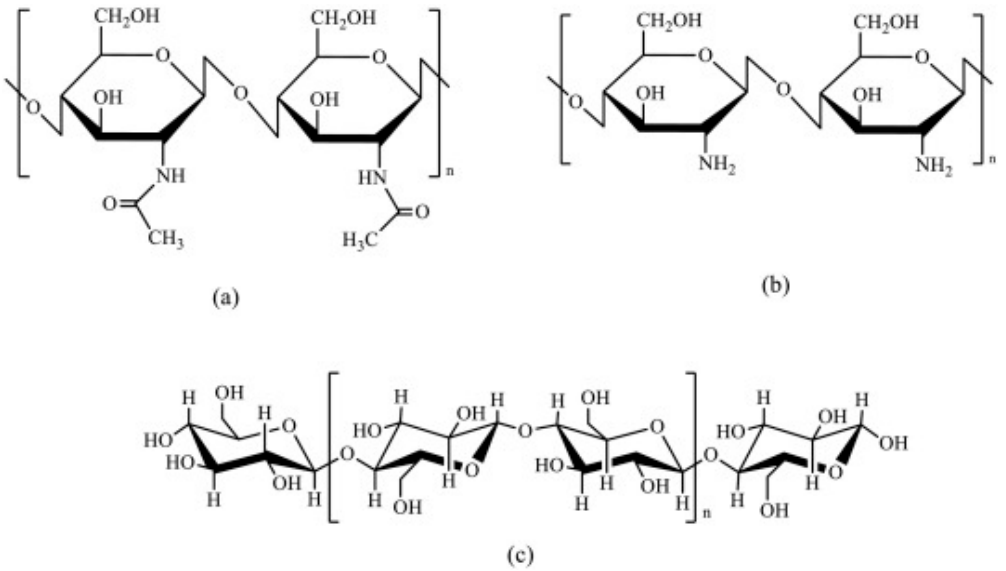

Figure 1. Structure of chitin, (**a**) chitosan, (**b**) and cellulose (**c**).

In a recent study [24], a double-layered chitosan coating was cured on cotton fabric to serve as a biomordant and form a protective layer on it. Through a second chitosan layer cured on the dyed fabric via the cross-linking method, the washing fastness of the cotton fabric dyed with sodium copper chlorophyllin can be improved from 3 to 5 (according to the standard method EN ISO 105-C06).

In 2021, Verma et al. [25] investigated the effect of biopolymer and dyeing treatment with natural dye on the functional properties (i.e., antibacterial and UV protection) of cotton fabric. It was found that the chitosan-treated onion skin-dyed cotton fabric showed 97.20% and 98.03% reduction in the growth of *Escherichia coli* and *Staphylococcus aureus* bacteria, respectively, and provided high UV protection.

In the present work, cotton and polyamide 6,6 fabrics were coated with a solution of chitosan to be tested as antibacterial fabrics against Gram-negative and Gram-positive bacteria.

The novelty of the present research work is related to the study of the contact time between the bacterial inoculum and the treated fabrics in order to evaluate how the antibacterial action of the chitosan-coated fibers changes, particularly after dyeing and washing.

The existing standard test methods [26] suggest using 1 h of contact time between the bacterial inoculum and antibacterial specimen. The aim of this work is to evaluate if shorter contact times can be more selective in evaluating the antibacterial performances of fabrics.

Chitosan has been selected because it quickly exerts a high antibacterial action in filtration [27], it is stable in water [22], and is widely proposed as a dyeing enhancer in textile finishing due to its cross-linking properties [23].

Since durability to repeated washing is the major challenge for the practical use of antimicrobial textiles [28], fabrics coated with chitosan have been subjected to several washing cycles to evaluate the resistance of the dye and if the antibacterial property is maintained.

2. Materials and Methods

2.1. Bacteria Strains and Fabrics

In this study, the antibacterial activity of fabrics coated with a chitosan solution was evaluated using model strains obtained from the American Type Culture Collection (ATCC): Gram-positive bacteria, *Staphylococcus aureus* ATCC 6538 and Gram-negative bacteria, *Escherichia coli* ATCC 11229 (supplied by Biogenetics Diagnostics Srl, Ponte San Nicolò, Italy). The media used in the ASTM E 2149-13 (Standard Test Method for Determining the Antimicrobial Activity of Antimicrobial Agents Under Dynamic Contact Conditions) was yeast extract agar (nutrient broth agar).

The adjacent cotton fabric (plain weave fabric suitable for ISO 105-F02, mass per unit area 110.75 g/m^2 determined in accordance with ISO 3801, supplied by Testfabrics Inc., West Pittston, PA, USA) and adjacent polyamide 6,6 fabric (plain weave fabric suitable for ISO 105-F03, mass per unit area 130.0 g/m^2 determined in accordance with ISO 3801, supplied by Testfabrics Inc., USA) were chosen to be used as textile substrates coated with chitosan for evaluating the antibacterial activity of the biopolymer. Fabrics were used as received from the supplier.

2.2. Preparation of the Chitosan Solution

A 2% *w*/*w* low molecular weight chitosan (50–190 kDa supplied by Sigma-Aldrich, Milan, Italy) in a 2% *w*/*v* glacial acetic acid solution was prepared. The solution was shaken for 7 h at room temperature.

Ten grams of cotton and polyamide 6,6 fabrics were dipped into the solution overnight to promote the adsorption of chitosan on the fabrics.

The impregnated fabrics were manually padded to reach a 90% wet pick up.

The fabrics were eventually placed in an oven at 95 °C for 3 min and at 150 °C for another 3 min to allow for the reaction between the chitosan and fabrics.

Finally, cotton and polyamide 6,6 materials were stored at 20 °C and 65% relative humidity at least 24 h before testing and further treatments.

2.3. Dyeing of Treated Fabrics

The chitosan-treated fabrics were dyed with the natural colorant *Carmine Red* (E120, C.I. Natural Red 4, C.I. 75470, supplied by Aromata Group srl, Bresso, Italy) which is largely soluble in water. Due to its high chemical and biological stability, it is used in textiles, pharmaceuticals, cosmetics, food, and beverages [29].

In the dyeing process, a 4% dye concentration was employed. The bath ratio was set at 1:20 (i.e., 10 g of fabric in 200 mL bath). For comparison, both the chitosan-treated and the untreated fabrics were dyed.

An Ahiba Nuance Top Speed II (Datacolor Italia srl, Giussano, Italy) dyeing machine was used. The working temperature was set at 100 °C with a 1 °C/min heating rate and left for 1 h. No additive was used during the dyeing.

At the end of the process, the chitosan-treated cotton fabric was homogeneously dyed, while the untreated cotton fabric maintained its natural white color (Figure 2).

The same experiment was realized on the synthetic fabric and in this case, as shown in Figure 3, only the chitosan-treated polyamide 6,6 fabric was dyed.

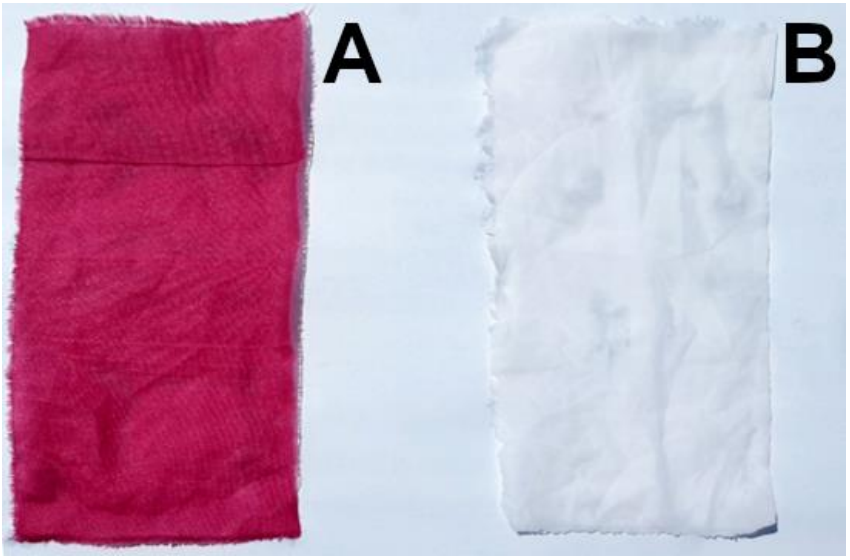

Figure 2. Dyed chitosan-treated cotton fabric (**A**), dyed untreated cotton fabric (**B**).

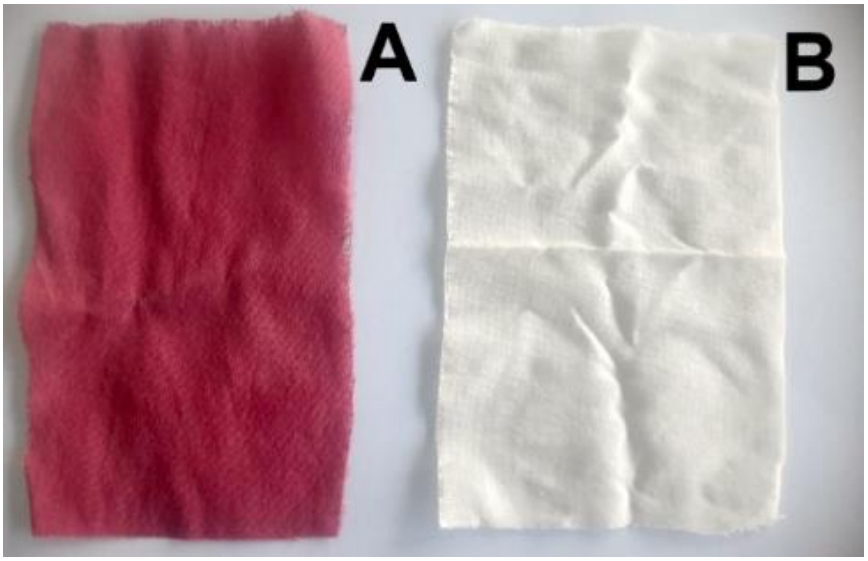

Figure 3. Dyed chitosan-treated polyamide 6,6 fabric (**A**), dyed untreated polyamide 6,6 fabric (**B**).

2.4. Washing Fastness

The washing fastness of the dyed samples was evaluated according to the standard method EN ISO 105-CO6 (2010) [30].

A water solution with a non-ionic detergent, Triton, was prepared at a concentration of 4 g/L. Dyed samples (10 cm by 5 cm) were cut and sewn with a sample of multifiber fabric (supplied by Testfabrics Inc., West Pittston, PA, USA) of the same size to verify if, during washing, the dye was released and absorbed by another type of fiber.

The samples were placed into a 150 mL bath together with ten stainless steel balls.

The temperature was raised to 40 °C and left for 30 min. The fabrics were then rinsed under tap water and dried in an oven at 37 °C.

It was observed that in both types of fibers, natural and synthetic, the color remained absorbed on the fabric even after washing. This was due to the property of chitosan which acts as a "bridge" between the dye and the fabric, ensuring washing fastness.

2.5. Characterizations

The natural and synthetic fabrics coated with dyed and washed chitosan were characterized by scanning electron microscopy (SEM), colorimetric analysis, water contact angle, and FT-IR analysis.

Characterizations were carried out on chitosan-treated fibers and dyed chitosan-treated fibers, and subjected to washing cycles.

The surface morphology of these fabrics was examined by SEM with a Zeiss EVO 10 (by Carl Zeiss AG, Oberkochen, Germany) scanning electron microscope at an acceleration voltage of 15 KV, a current probe of 400 pA, and a working distance of about 30 mm. The fabric samples were mounted on aluminum specimen stubs and sputter coated with a 20 nm thick gold layer in rarefied argon (20 Pa) using an Emitech K550 Sputter Coater with a current of 20 mA for 180 s before SEM observations.

Colorimetric analysis was performed with a Datacolor SF 600 X Spectralflash (Datacolor Italia srl, Italy) with CIE standard illuminant D65, 10°. Color coordinates and ΔE CIELab values were registered on the specimen of the dyed cotton and polyamide 6,6 fabrics with a size of about 5.0 × 5.0 cm. The reference samples for ΔE values were the untreated cotton and polyamide 6,6 fibers. The CIELab ΔE values were calculated according to Equation (1):

$$\Delta E = \sqrt{(L - L_0)^2 + (a - a_0)^2 + (b - b_0)^2} \quad (1)$$

where L_0, a_0, b_0 are the colorimetric parameters of the reference sample according to the CIELab color space (L, a, and b are the parameters of the samples after immersion in the buffered solutions).

Contact angle and drop absorption time evaluations were conducted with EasyDrop (Krüss Scientific GmbH, Hamburg, Germany) using deionized water in order to evaluate the hydrophilic/hydrophobic behavior of the fabrics and further discuss the improved dyeing performances, antibacterial properties, and overall stability to washing of chitosan coating and dyeing.

Fourier transformed infrared (FT-IR) analysis was carried out using the attenuated total feflection (ATR) technique in the range from 4000 to 650 cm^{-1} with 50 scansions and 4 cm^{-1} of band resolution by means of a Thermo Scientific Nicolet iZ10 spectrometer (Thermo Fisher Scientific, Waltham, MA, USA) equipped with a Smart Endurance™ apparatus. The FT-IR spectra were recorded using OMNIC 9 software.

2.6. Antibacterial Experiments

The antibacterial activity was evaluated on chitosan-treated samples, according to ASTM E 2149-2013 "Standard test method for determining the antimicrobial activity of antimicrobial agents under dynamic contact conditions". This method employed Gram-negative *E. coli* and Gram-positive *S. aureus*. Antibacterial tests were performed by diluting the test culture incubated in a nutrient broth (the bacterial inoculum) in a buffer (pH 7.0) to yield a concentration of 1.5–3.0 × 10^5 CFU/ mL (working dilution).

For each test, a sample of 0.5 g of fabric was immersed into a flask containing 25 mL of the working dilution. All flasks were shaken for different contact times (12 min, 30 min, and 1 h) at 190 rpm at room temperature.

After a series of dilutions with a buffer until a concentration of 150–300 CFU/mL, 1 mL of the liquid was plated in 15 mL of yeast extract agar. The inoculated plates were incubated at 37 °C for 24 h and surviving cells were counted by the plate count method. The tests were conducted in duplicate.

The antibacterial activity was expressed as a percent reduction in the organisms after contact with the test specimen compared to the number of bacterial cells surviving after contact with the control, according to Equation (2):

$$\%\ \text{reduction}\left(\text{CFUmL}^{-1}\right) = \frac{\text{B} - \text{A}}{\text{B}} \times 100 \quad (2)$$

where A is CFU/mL after contact (end test) and B is CFU/mL at zero contact time (reference).

3. Results and Discussion

First, it was necessary to verify whether untreated fabrics have negligible antibacterial effects. Using the ASTM method with both Gram-positive and Gram-negative bacteria, untreated cotton and polyamide 6,6 resulted in a bacterial reduction of 0%.

3.1. Chitosan Antibacterial Activity

The mechanism of the antibacterial activity of chitosan is related to its cationic-charged chemical structure, which is influenced by many factors, including the concentration of chitosan, pH value, temperature, degree of deacetylation, cell growth phase, and types of microorganisms [31].

It is well known that Gram-positive and Gram-negative bacteria have different cell wall compositions. In fact, the outer membrane of Gram-negative bacteria comprises essentially lipopolysaccharides containing phosphate and pyrophosphate groups, which renders the bacterial surface a density of negative charges superior to the Gram-positive ones [7].

Chung et al. [32] found a higher inhibitory effect on the Gram-negative bacteria because more chitosan adsorption was observed on their cell surface than on the tested Gram-positive bacteria. More negatively charged cell surfaces had a greater interaction with chitosan due to its cationic nature.

According to the literature, cotton fabrics coated with chitosan have shown interesting results. After 12 min of contact between treated fibers and inoculum bacterium, *E. coli* (Gram-negative bacterium) is immediately more sensitive to the antibacterial action of the biopolymer. There is a bacterial reduction of 99.8% compared to 96.6% of *S. aureus*.

Another essential aspect to consider is the contact time. It was observed that for both bacteria species, a more significant bacterial reduction increases as the contact time between the diluted bacterial inoculum and the cotton fabric treated with chitosan increases, as reported in Table 2.

The same experiment was carried out on the synthetic fiber, polyamide 6,6 treated with chitosan. The results, reported in Table 2, showed that 12 min of contact time between the treated polyamide 6,6 and the bacterial inoculum were enough to achieve a 100% bacterial reduction in both microorganisms studied. Hence, the antibacterial action of the biopolymer on the synthetic fiber was almost immediate. The test results highlighted an excellent antibacterial activity of the synthetic fabric treated with chitosan.

Table 2. Bacterial reduction rate of chitosan-treated cotton and polyamide 6,6 fabrics.

Fabric	Contact Time	Bacterial Reduction (%)	
		E. coli	***S. aureus***
Cotton	12 min	99.8	96.6
	30 min	99.8	100
	1 h	100	100
Polyamide 6,6	12 min	100	100
	30 min	100	100
	1 h	100	100

In the specific case of Gram-negative bacterium (i.e., *E. coli*), considering the antibacterial properties of the two different types of fibers, the results showed that the greater antibacterial action was obtained by the synthetic fiber treated with chitosan compared to the natural fiber, considering 12 and 30 min of contact. In both reduced contact times, the antibacterial effect obtained was 100% and the bacterial reduction was 99.8%, considering the natural fiber treated with chitosan, which was in any case an excellent result.

3.2. Cross-Linking Properties of Chitosan in Dyeing

Another very interesting property of chitosan is to bind the molecules of some natural dyes and allow for the dyeing of the textile substrate, especially cellulosic ones to which it links very well.

The molecular structure of chitosan can act as a "bridge" between the textile substrate and the dye molecule due to the protonation of nitrogen groups in an acid environment. Generally, synthetic dyes are preferred for dyeing fabrics, and are synthesized ad hoc to be applied to the various types of fibers. Synthetic dyes, however, are a major source of wastewater pollution. Natural dyes are, on the other hand, less toxic and less allergenic thanks to the existence of a large number of structurally different active compounds [25].

The natural polymer is distributed homogeneously on the fabric, as confirmed by dyeing tests using Carmine Red, an acid dye, and by the colorimetric analysis.

3.3. Antibacterial Test after Dyeing

Since chitosan is an excellent cross linker to improve the adhesion of natural dyes to fabrics, the antibacterial effect was also tested on fabrics treated with chitosan and dyed with Carmine Red. In this way, it was possible to understand if only the dye had a minimal influence on the antibacterial property conferred by chitosan.

In the following table (Table 3), the results obtained considering the bacterial reduction after the dyeing are reported.

Table 3. Bacterial reduction after dyeing of chitosan-treated cotton and polyamide 6,6 fabrics.

Fabric	Contact Time	Bacterial Reduction (%)	
		E. coli	*S. aureus*
Cotton	12 min	94.2	97.1
	30 min	97.8	94.2
	1 h	98.5	98.9
Polyamide 6,6	12 min	90.9	70.6
	30 min	99.1	83.2
	1 h	99.7	95.2

Fabrics (both natural and synthetic) functionalized with chitosan and subsequently dyed with Carmine Red showed good antibacterial properties, especially considering the polyamide 6,6 against Gram-negative bacteria. The dyeing influenced the chitosan antibacterial activity only at a shorter contact time with polyamide 6,6, observing a bacterial reduction of 70.6% at 12 min and 83.2% at 30 min of *S. aureus*.

In general, the bacterial reduction obtained is nearly 100% for both types of fibers with a contact time of 30 min or more. Therefore, the dye had a limited effect on the antibacterial activity of chitosan.

In view of a further exploitation, it is interesting to highlight that the fabrics treated with chitosan, whether they have undergone a dyeing process or not, maintain their antibacterial activity over time.

3.4. Durability to Washing

The various finished textile fabrics must have the characteristic of being resistant to washing. Therefore, the fabrics treated with chitosan and dyed were washed [30] and subsequently their antibacterial properties were evaluated to verify the resistance of the treatment.

Almost the same antibacterial behavior was found for both microbial species tested: the antibacterial action of chitosan was maintained at higher contact time. The results reported in Table 4 note that the antibacterial action of chitosan is stronger against Gram-negative bacteria.

Table 4. Bacterial reduction after dyeing and washing of chitosan-treated cotton and polyamide 6,6 fabrics.

Fabric	Contact Time	Bacterial Reduction (%)	
		E. coli	*S. aureus*
Cotton	12 min	59.0	64.4
	30 min	92.8	84.5
	1 h	98.5	97.7
Polyamide 6,6	12 min	61.4	36.5
	30 min	96.0	47.9
	1 h	95.5	90.4

Furthermore, the antibacterial activity was reduced only for short contact times (12 and 30 min), while at 1 h, the percentage bacterial reduction remained higher than 90%, and in most cases higher than 95%.

3.5. Analysis of Surface Morphology

SEM images in Figure 4 show the morphological aspect of natural and synthetic fibers. Cotton fibers presented a ribbon-like appearance (Figure 4A,B) with a rough surface, while the synthetic polyamide 6,6 fibers have a circular section with a more smooth surface (Figure 4C,D).

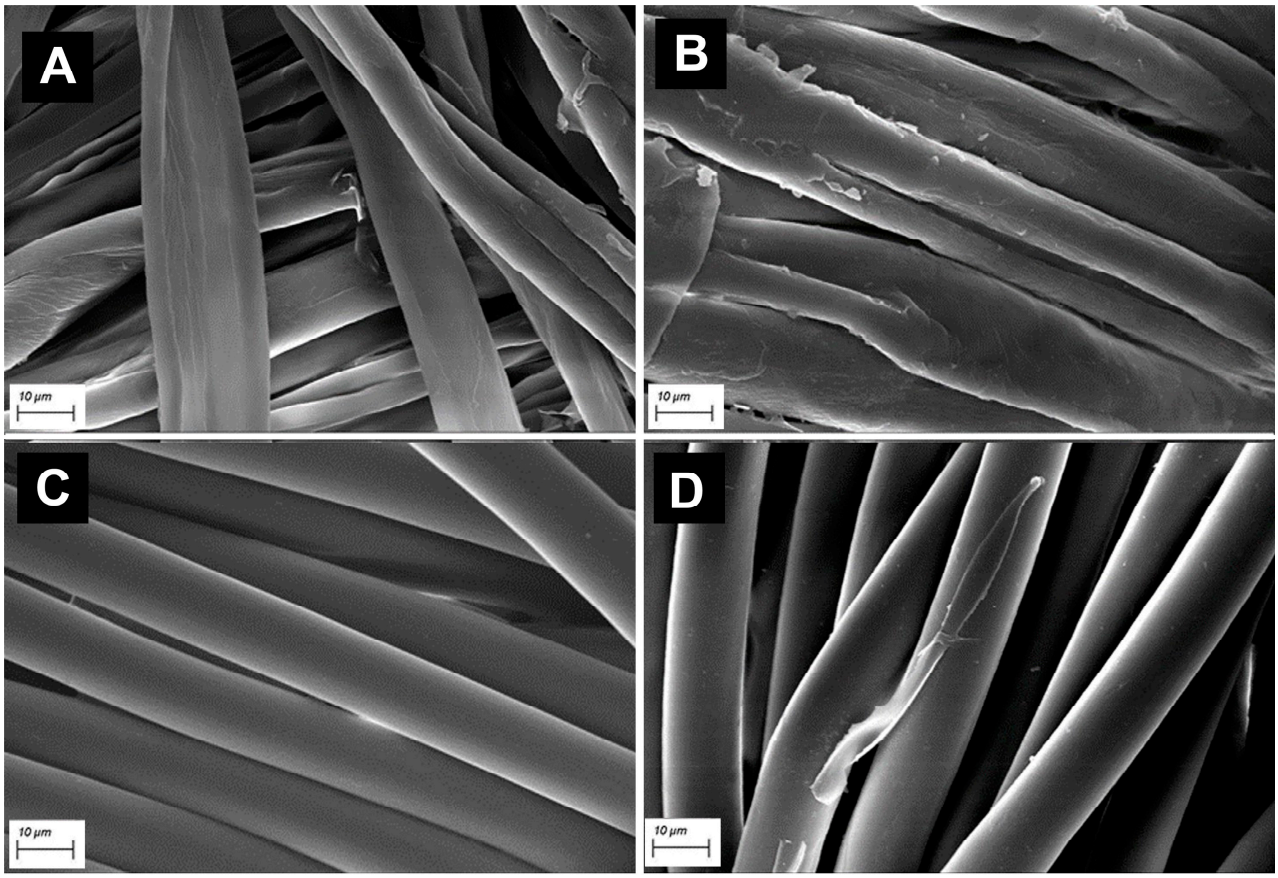

Figure 4. SEM images of cotton fibers treated with chitosan (**A**). Chitosan resistance on Carmine Red dyed and washed cotton fibers (**B**). SEM images of polyamide 6,6 fibers treated with chitosan (**C**). Chitosan resistance on Carmine Red dyed and washed polyamide 6,6 fibers (**D**). Scale bars: 10 µm.

Figure 4A,C showed a homogeneous distribution of chitosan on both cotton and polyamide 6,6 fibers.

An important aspect to consider was that washing does not remove the chitosan; the biopolymer was resistant to repeated laundering both on cotton (B) and polyamide 6,6 (D) fabrics. In fact, good antibacterial results were obtained on dyed and washed chitosan-treated samples.

3.6. Colorimetric Analysis

Colorimetric analysis was performed on cotton and polyamide 6,6 fabrics. For each sample, the average CIELab ΔE values were calculated on three different measurements and the results are reported in Table 5.

Table 5. ΔE values on cotton and polyamide 6,6 fabrics.

Fabric	Chitosan-Treated Cotton		Chitosan-Treated Polyamide 6,6	
	Dyed	Dyed and Washed	Dyed	Dyed and Washed
ΔE	43.8	41.8	50.5	48.9

As shown in Table 5, both the natural and synthetic chitosan-treated fabrics had an intense coloration (while the untreated fabrics cannot be dyed, as shown in Figures 2 and 3). The dyed and washed samples had a ΔE value slightly lower than the freshly dyed fabrics. This result was due to the washing effect because the washing removed weakly linked dye molecules, and therefore reduced the dyeing intensity. However, the dyed and washed samples were brighter than the freshly dyed fabrics because they were more similar to the reference sample (untreated cotton and polyamide 6,6 fabrics).

On the other hand, dyed chitosan-treated fabrics showed a higher ΔE value compared to the "white" because they had not been subjected to washing, maintaining a high degree of dyeing intensity.

Therefore, colorimetric analysis demonstrated the resistance of dyeing natural and synthetic fibers due to the presence of chitosan that was being distributed homogeneously on the fabric, ensuring dyeing and strong cross-linking properties.

3.7. Contact Angle

Contact angle measurements were performed using water in order to evaluate the hydrophilic/hydrophobic behavior of the fabrics. Since some samples absorbed the water drop quickly, a robust measure of the contact angle was impossible. In this case, only the absorption time was measured. The results are reported in Tables 6 and 7.

Untreated cotton fabric showed extremely high hydrophilicity since it could absorb a drop of water in about 100 ms; therefore, the contact angle was impossible to measure. The same situation was found on cotton treated with chitosan. In this case, the presence of the biopolymer onto the fabric increased the absorption time to 1 s. A contact angle of $121.3 \pm 4.1^{\circ}$ was measured on the dyed chitosan-coated cotton fabrics (Figure 5A) and the water drops were not absorbed, whereas a decrease in the contact angle to about 95° was observed on the fabrics after washing (Figure 5B) and the fabric was able to absorb water again in about 4 s.

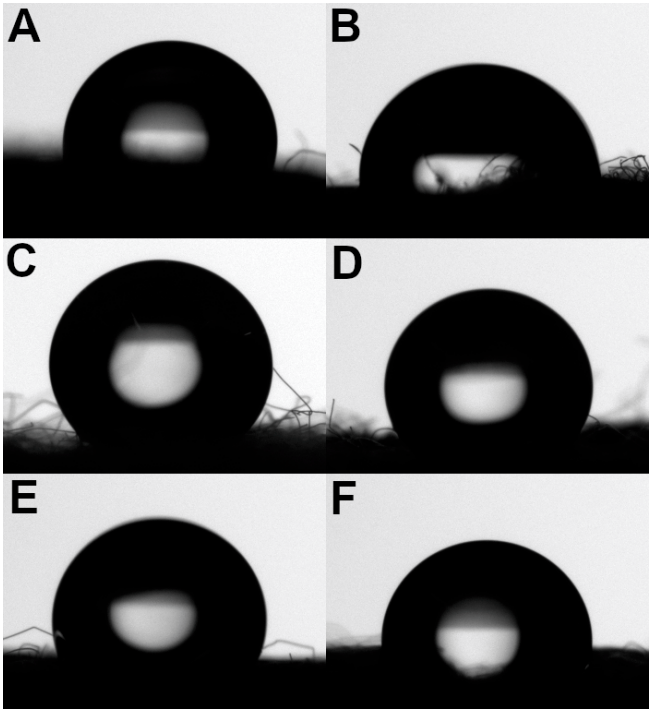

Figure 5. Pictures of the water drops during the contact angle measurements: dyed chitosan-coated cotton (**A**); dyed and washed chitosan-treated cotton (**B**); polyamide 6,6 (**C**); chitosan-coated polyamide 6,6 (**D**); dyed chitosan-coated polyamide 6,6 (**E**); dyed and washed chitosan-treated polyamide 6,6 (**F**).

The synthetic fiber showed an important hydrophobicity that made it possible to measure the contact angle. In all the polyamide 6,6 fabrics, the drop of water remained on the fabric surface for a long time without being absorbed. The measurements of contact angle decreased from $137.6 \pm 4.3^{\circ}$ for untreated polyamide 6,6 (Figure 5C) to $106.7 \pm 7.9^{\circ}$ for dyed and washed chitosan-treated polyamide 6,6 (Figure 5F).

It is worth noting that the chitosan treatment and dyeing have different effects on the hydrophilicity of the fibers depending on their hydrophilic/hydrophobic nature. Hydrophilic fibers such as cotton become progressively more hydrophobic when treated with chitosan and then dyed. This behavior is likely due to the fact that both the chitosan and dye led to the inaccessibility of water to the hydrophilic groups of cotton as well as inside the fibers.

On the other hand, in a hydrophobic fiber such as polyamide 6,6, the chitosan treatment and the following dyeing added hydrophilic groups to the fibers, making them progressively more hydrophilic. However, the chitosan treatment and dyeing involved just the surface of the fibers and, for that reason, the fabrics were not able to absorb the water drops at any stage.

Table 6. Measurements of contact angle and absorption time on different treated cotton fabrics.

Fabric	Contact Angle (°)	Absorption Time (s)
Cotton	–	0.1
Chitosan-treated cotton	–	1.0
Dyed chitosan-treated cotton	121.3 ± 4.1	∞
Dyed and washed chitosan-treated cotton	95.1 ± 16.4	3.95

Table 7. Measurements of contact angle on the different treated polyamide 6,6 fabrics.

Fabric	Contact Angle (°)	Absorption Time (s)
Polyamide 6,6	137.6 ± 4.3	∞
Chitosan-treated polyamide 6,6	122.5 ± 18.2	∞
Dyed chitosan-treated polyamide 6,6	118.8 ± 5.7	∞
Dyed and washed chitosan-treated polyamide 6,6	106.7 ± 7.9	∞

3.8. Infrared Spectroscopy

FT-IR analysis was carried out on the fabrics with the ATR technique. The spectra are shown in Figure 6 compared to the spectrum of pure chitosan powder. The spectrum of chitosan is characterized by a broad absorption band in the range of 3000–3600 cm^{-1} attributed to O–H stretching, a band at 2870 cm^{-1} attributed to C–H stretching, and several overlapping peaks at about 1000 cm^{-1} attributed to C–O stretching and C–O–C bridge [33].

The spectral features of chitosan are similar to those of cotton as shown in Figure 6. A small difference can be found in the range of 1500–1700 cm^{-1}, where chitosan has two partially overlapping weak adsorption bands attributed to the C=O stretching (Amide I) at 1655 cm^{-1} and N–H bending at 1560 cm^{-1} (Amide II), while cotton has a single peak attributed to Amide I and H–O–H bending of absorbed water at 1650 cm^{-1} [34,35].

No significant differences are noticeable in the spectra related to chitosan-treated cotton fabrics compared to the untreated cotton, except for the peak reduction at 1650 cm^{-1}, which is probably due to the desorption of water substituted by the linking of the chitosan. In fact, dyeing and washing did not alter the spectra.

Polyamide 6,6 has a typical peak at 3300 cm^{-1} attributed to N–H stretching. Moreover, the two peaks at 2960 cm^{-1} and 2850 cm^{-1} correspond to CH_2 bonds, while 1630 cm^{-1} and 1560 cm^{-1} indicate the C=O stretching (Amide I) and N–H bending (Amide II) vibrations [36].

Spectral features of chitosan-treated polyamide 6,6 fabric do not differ from the untreated polyamide 6,6 fabric (Figure 6B). Moreover, the spectra of chitosan-treated polyamide 6,6 fabrics after dyeing and washing do not show significant differences with the untreated fabrics, except for a slight increase in the absorption intensity of around 1000 cm^{-1}, where chitosan has the most intense absorption peak (see the box in Figure 6A).

FT-IR analysis revealed that the amount of chitosan linked to both cotton and polyamide 6,6 is little, but enough to exert excellent antibacterial effects and to change the hydrophilic/hydrophobic behavior of both fabrics. This finding is in agreement with SEM observations that have shown a thin coating of the fibers.

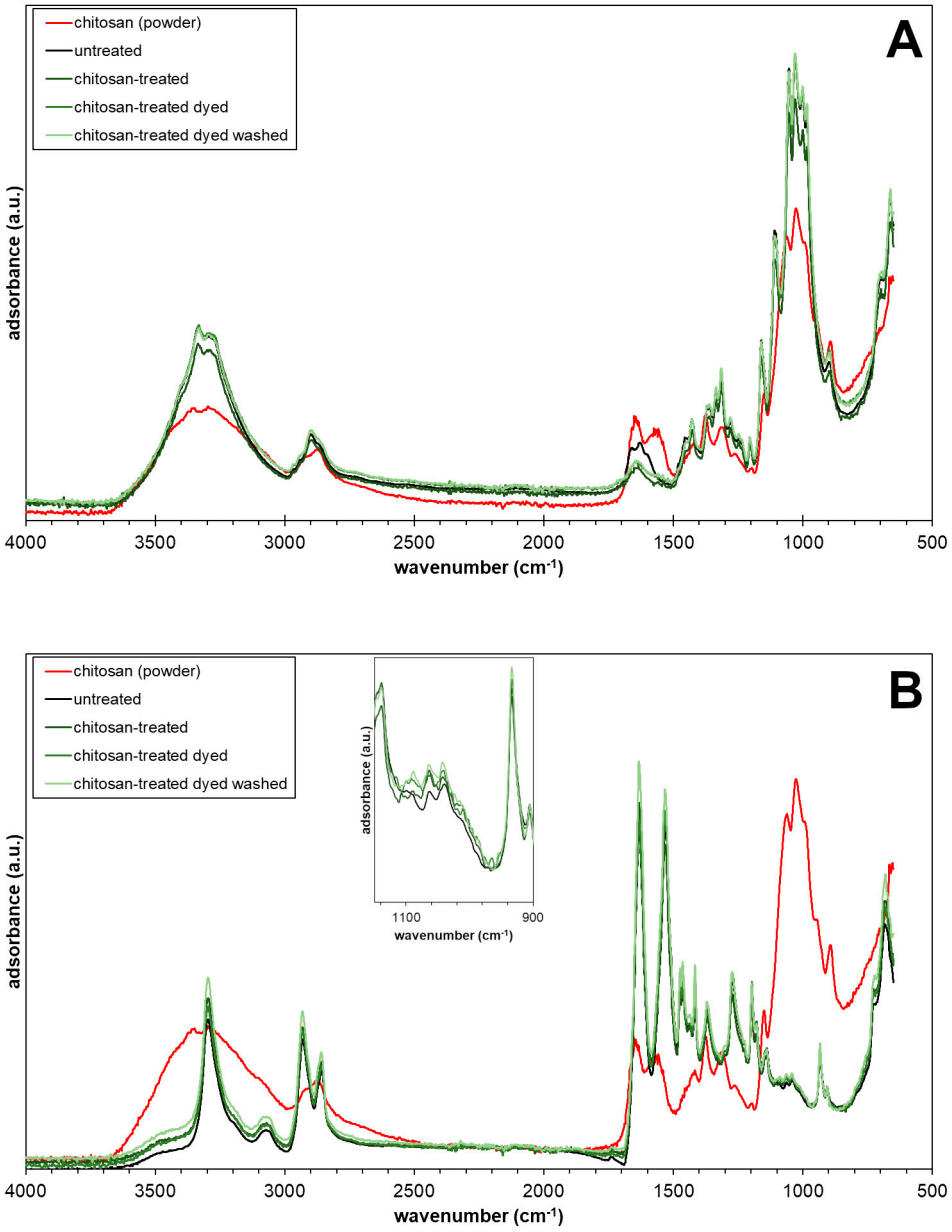

Figure 6. FT-IR spectra of (**A**) cotton and (**B**) polyamide 6,6 fabrics (untreated: black line; fresh chitosan-treated: dark green line; dyed chitosan-treated: green line; dyed chitosan-treated after washing: light green line) compared with chitosan powder (red line).

4. Conclusions

In the present work, cotton and polyamide 6,6 fibers were coated with chitosan, a natural biopolymer to be tested against Gram-positive (*S. aureus*) and Gram-negative (*E. coli*) bacteria using the ASTM standard method that requires 1 h of contact between the bacterial inoculum and the treated fabrics.

Chitosan, a useful non-toxic biopolymer, can be used as an effective antibacterial textile finish and an excellent premordant for dyeing. The innovative part of the work was to quantify the antibacterial efficacy of fabrics functionalized with chitosan at shorter contact times (12 min, 30 min, and 1 h) between the treated fabrics and the bacterial inoculum. In this way, it was possible to evaluate the trend of bacterial reduction over time on this type of material. A chitosan solution was prepared and fabrics were dipped into the solution overnight to promote the adsorption of chitosan on the fabrics.

Both cotton and polyamide 6,6 fibers treated with chitosan proved to be highly antibacterial after only 12 min of contact with the bacterial inoculum. Furthermore, the bactericidal action of the chitosan-treated fabrics is excellent up to 1 h of contact, as expected.

Since chitosan has the property of cross-linking natural dyes to provide fabrics with better dyeing and nonfading, a natural dye known as Carmine Red was used to evaluate the premordant property of chitosan, as well as the antibacterial properties of treated fabrics after dyeing. The results were very satisfactory in both aspects since the dyeing is improved by the treatment with chitosan and the bacterial reductions were nearly 100% after 30 min of contact time on both fibers under study.

The results showed that washing reduced the antibacterial effect, especially for evaluations at short contact times.

It can be concluded that chitosan is a biopolymer with a very strong and fast antibacterial efficacy that does not decrease significantly after dyeing. A decreased antibacterial activity was observed after washing only when short contact times were used in testing.

Finally, from a testing point of view, implementing procedures with different contact times were useful to highlight differences that can allow for discriminating among pairs of material/bacterium, even when excellent biocidal actions were found at a fixed contact time for a specific bacterium.

Author Contributions: Conceptualization, C.V. and A.V.; methodology, R.P. and M.P.; investigation, M.P., R.P., C.V. and A.V.; writing—original draft preparation, M.P.; writing—review and editing, R.P., C.V. and A.V. All authors have read and agreed to the published version of the manuscript.

Funding: This study was carried out within the MICS (Made in Italy—Circular and Sustainable) Extended Partnership and received funding from the European Union Next-GenerationEU (Piano Nazionale di Ripresa e Resilienza (PNRR)—Missione 4, Componente 2, Investimento 1.3—D.D. 1551.11-10-2022, PE00000004). This manuscript reflects only the authors' views and opinions, neither the European Union nor the European Commission can be considered responsible for them.

Data Availability Statement: Data sharing not applicable.

Conflicts of Interest: The authors declare no conflict of interest.

References

1. Periolatto, M.; Ferrero, F.; Vineis, C. Antimicrobial Chitosan Finish of Cotton and Silk Fabrics by UV-Curing with 2-Hydroxy-2-Methylphenylpropane-1-One. *Carbohydr. Polym.* **2012**, *88*, 201–205. [CrossRef]
2. Periolatto, M.; Ferrero, F.; Vineis, C.; Varesano, A.; Gozzelino, G. *Novel Antimicrobial Agents and Processes for Textile Applications*; Ferrero, F., Ed.; IntechOpen: Rijeka, Croatia, 2017; Chapter 2; ISBN 978-953-51-3200-4.
3. Bengalli, R.; Fiandra, L.; Vineis, C.; Sanchez-Ramirez, D.O.; Azoia, N.G.; Varesano, A.; Mantecca, P. Safety Assessment of Polypyrrole Nanoparticles and Spray-Coated Textiles. *Nanomaterials* **2021**, *11*, 1991. [CrossRef]
4. Yao, C.; Li, X.; Neoh, K.G.; Shi, Z.; Kang, E.T. Surface modification and antibacterial activity of electrospun polyurethane fibrous membranes with quaternary ammonium moieties. *J. Memb. Sci.* **2008**, *320*, 259–267. [CrossRef]
5. Kose, O.; Mantecca, P.; Costa, A.; Carrière, M. Putative adverse outcome pathways for silver nanoparticle toxicity on mammalian male reproductive system: A literature review. *Part. Fibre Toxicol.* **2023**, *20*, 1. [CrossRef]
6. Choudhary, A.; Singh, S.; Ravichandiran, V. Toxicity, preparation methods and applications of silver nanoparticles: An update. *Toxicol. Mech. Methods* **2022**, *32*, 650–661. [CrossRef] [PubMed]
7. Shahid-ul-Islam; Shahid, M.; Mohammad, F. Green Chemistry Approaches to Develop Antimicrobial Textiles Based on Sustainable Biopolymers—A Review. *Ind. Eng. Chem. Res.* **2013**, *52*, 5245–5260. [CrossRef]
8. Lin, G.H.Y.; Hemming, M. Ocular and dermal irritation studies of some quaternary ammonium compounds. *Food Chem. Toxicol.* **1996**, *34*, 177. [CrossRef]
9. Myerson Fisher, N.; Marsh, E.; Lazova, R. Scar-localized argyria secondary to silver sulfadiazine cream. *J. Am. Acad. Dermatol.* **2003**, *49*, 730–732. [CrossRef]
10. Windler, L.; Height, M.; Nowack, B. Comparative evaluation of antimicrobials for textile applications. *Environ. Int.* **2013**, *53*, 62. [CrossRef]
11. Oh, S.W.; Kang, M.N.; Cho, C.W.; Lee, M.W. Detection of carcinogenic amines from dyestuffs or dyed substrates. *Dyes Pigment.* **1997**, *33*, 119. [CrossRef]
12. Fang, J.L.; Stingley, R.L.; Beland, F.A.; Harrouk, W.; Lumpkins, D.L.; Howard, P. Occurrence, efficacy, metabolism, and toxicity of triclosan. *J. Environ. Sci. Health C Environ. Carcinog. Ecotoxicol. Rev.* **2010**, *28*, 147–171. [CrossRef] [PubMed]

13. Olejnik, M.; Kersting, M.; Rosenkranz, N.; Loza, K.; Breisch, M.; Rostek, A.; Prymak, O.; Schürmeyer, L.; Westphal, G.; Köller, M.; et al. Cell-biological effects of zinc oxide spheres and rods from the nano- to the microscale at sub-toxic levels. *Cell Biol. Toxicol.* **2021**, *37*, 573–593. [CrossRef] [PubMed]
14. Katewaraphorn, J.; Aldred, A. A Study of Microcapsules Containing Psidium Guajava Leaf Extract for Antibacterial Agent on Cotton Fabric. *Int. J. Chem. Eng. Appl.* **2016**, *7*, 27–31. [CrossRef]
15. Álvarez-Martínez, F.J.; Barrajón-Catalán, E.; Herranz-López, M.; Micol, V. Antibacterial plant compounds, extracts and essential oils: An updated review on their effects and putative mechanisms of action. *Phytomedicine* **2021**, *90*, 153626. [CrossRef] [PubMed]
16. Shahid-ul-Islam; Butola, B.S. Recent advances in chitosan polysaccharide and its derivatives in antimicrobial modification of textile materials. *Int. J. Biol. Macromol.* **2019**, *121*, 905–912. [CrossRef]
17. Periolatto, M.; Ferrero, F.; Vineis, C.; Rombaldoni, F. Multifunctional finishing of wool fabrics by chitosan UV-grafting: An approach. *Carbohydr. Polym.* **2013**, *98*, 624–629. [CrossRef]
18. Kvasnička, F.; Kouřimská, L.; Bleha, R.; Škvorová, P.; Kulma, M.; Rajchl, A. Electrophoretic determination of chitin in insects. *J. Chromatogr. A* **2023**, *1695*, 463952. [CrossRef]
19. Ahmed, S.; Annu; Ali, A.; Sheikh, J. A review on chitosan centred scaffolds and their applications in tissue engineering. *Int. J. Biol. Macromol.* **2018**, *116*, 849–862. [CrossRef]
20. Becenen, N.; Erdoğan, S.; Fındık, E. Chapter 4-Investigation into the functional properties of cotton, wool, and denim textile materials finished with chitosan and the use of chitosan in textile-reinforced composites and medical textiles. In *Handbook of Chitin and Chitosan*; Gopi, S., Thomas, S., Pius, A., Eds.; Elsevier: Amsterdam, The Netherlands, 2020; pp. 89–134. ISBN 978-0-12-817966-6.
21. Dev, V.; Venugopal, J.; Sudha, S.; Deepika, G.; Ramakrishna, S. Dyeing and antimicrobial characteristics of chitosan treated wool fabrics with henna dye. *Carbohydr. Polym.* **2009**, *75*, 646. [CrossRef]
22. Truffa Giachet, F.; Periolatto, M.; Sanchez Ramirez, D.O.; Carletto, R.A.; Varesano, A.; Vineis, C.; Bongiovanni, R. Stability of ultraviolet-cured chitosan coating on cotton gauze for water filtration. *J. Ind. Text.* **2019**, *48*, 1384–1396. [CrossRef]
23. Rahman, M.; Kim, M.; Youm, K.; Kumar, S.; Koh, J.; Hong, K. Sustainable one-bath natural dyeing of cotton fabric using turmeric root extract and chitosan biomordant. *J. Clean. Prod.* **2023**, *382*, 135303. [CrossRef]
24. Zhao, Z.; Hurren, C.; Zhang, M.; Zhou, L.; Wu, J.; Sun, L. In Situ Synthesis of a Double-Layer Chitosan Coating on Cotton Fabric to Improve the Color Fastness of Sodium Copper Chlorophyllin. *Materials* **2020**, *13*, 5365. [CrossRef]
25. Verma, M.; Gahlot, N.; Singh, S.; Rose, N. UV protection and antibacterial treatment of cellulosic fibre (cotton) using chitosan and onion skin dye. *Carbohydr. Polym.* **2021**, *257*, 117612. [CrossRef] [PubMed]
26. *ASTM E2149*; ASTM International Standard Test Method for Determining the Antimicrobial Activity of Antimicrobial Agents Under Dynamic Contact Conditions. ASTM International: West Conshohocken, PA, USA, 2013.
27. Ferrero, F.; Periolatto, M.; Vineis, C.; Varesano, A. Chitosan coated cotton gauze for antibacterial water filtration. *Carbohydr. Polym.* **2014**, *103*, 207–212. [CrossRef]
28. Zhao, Y.; Xu, Z.; Lin, T. 12-Barrier textiles for protection against microbes. In *Woodhead Publishing Series in Textiles*; Sun, G., Ed.; Woodhead Publishing: Sawston, UK, 2016; pp. 225–245, ISBN 978-0-08-100576-7.
29. Alizadeh, M.; Demir, E.; Aydogdu, N.; Zare, N.; Karimi, F.; Kandomal, S.M.; Rokni, H.; Ghasemi, Y. Recent advantages in electrochemical monitoring for the analysis of amaranth and carminic acid as food color. *Food Chem. Toxicol.* **2022**, *163*, 112929. [CrossRef]
30. *EN ISO 105-C06*; Textiles-Color Fastness Tests-Part C06: Color Fastness to Domestic and Commercial Washing. ISO International Organization for Standardization: Geneva, Switzerland, 2010.
31. Li, J.; Zhuang, S. Antibacterial activity of chitosan and its derivatives and their interaction mechanism with bacteria: Current state and perspectives. *Eur. Polym. J.* **2020**, *138*, 109984. [CrossRef]
32. Chung, Y.C.; Su, Y.P.; Chen, C.C.; Jia, G.; Wang, H.L.; Wu, J.C.; Lin, J.G. Relationship between antibacterial activity of chitosan and surface characteristics of cell wall. *Acta Pharmacol. Sin.* **2004**, *25*, 932–936. [PubMed]
33. Kasaai, M.R. A review of several reported procedures to determine the degree of N-acetylation for chitin and chitosan using infrared spectroscopy. *Carbohydr. Polym.* **2008**, *71*, 497–508. [CrossRef]
34. Liu, Y.; Kim, H.J. Fourier transform infrared spectroscopy (FT-IR) and simple algorithm analysis for rapid and non-destructive assessment of developmental cotton fibers. *Sensors* **2017**, *17*, 1469. [CrossRef]
35. Chung, C.; Lee, M.; Choe, E.K. Characterization of cotton fabric scouring by FT-IR ATR spectroscopy. *Carbohydr. Polym.* **2004**, *58*, 417–420. [CrossRef]
36. Shrestha, B.K.; Mousa, H.M.; Tiwari, A.P.; Ko, S.W.; Park, C.H.; Kim, C.S. Development of polyamide-6,6/chitosan electrospun hybrid nanofibrous scaffolds for tissue engineering application. *Carbohydr. Polym.* **2016**, *148*, 107–114. [CrossRef] [PubMed]

Journal of
Functional
Biomaterials

MDPI

Article

Antibacterial Size Effect of ZnO Nanoparticles and Their Role as Additives in Emulsion Waterborne Paint

Imroi El-Habib [1,2], Hassan Maatouk [2], Alex Lemarchand [1], Sarah Dine [1], Anne Roynette [2], Christine Mielcarek [2], Mamadou Traoré [1] and Rabah Azouani [2,*]

[1] Laboratoire des Sciences des Procédés et des Matériaux (LSPM-CNRS UPR 3407), Institut Galilée, Université Sorbonne Paris Nord, 99 Avenue Jean-Baptiste Clément, 93430 Villetaneuse, France; e.imroi@hubebi.com (I.E.-H.); alex.lemarchand@lspm.cnrs.fr (A.L.); sarah.dine@lspm.cnrs.fr (S.D.); mamadou.traore@lspm.cnrs.fr (M.T.)

[2] Ecole de Biologie Industrielle (EBI), EBInnov®, 49 Avenue des Genottes-CS 90009, 95895 Cergy Cedex, France; h.maatouk@hubebi.com (H.M.); a.roynette@hubebi.com (A.R.); c.mielcarek@hubebi.com (C.M.)

* Correspondence: r.azouani@hubebi.com

Abstract: Nosocomial infections, a prevalent issue in intensive care units due to antibiotic overuse, could potentially be addressed by metal oxide nanoparticles (NPs). However, there is still no comprehensive understanding of the impact of NPs' size on their antibacterial efficacy. Therefore, this study provides a novel investigation into the impact of ZnO NPs' size on bacterial growth kinetics. NPs were synthesized using a sol–gel process with monoethanolamine (MEA) and water. X-ray diffraction (XRD), transmission electron microscopy (TEM), and Raman spectroscopy confirmed their crystallization and size variations. ZnO NPs of 22, 35, and 66 nm were tested against the most common nosocomial bacteria: *Escherichia coli*, *Pseudomonas aeruginosa* (Gram-negative), and *Staphylococcus aureus* (Gram-positive). Evaluation of minimum inhibitory and bactericidal concentrations (MIC and MBC) revealed superior antibacterial activity in small NPs. Bacterial growth kinetics were monitored using optical absorbance, showing a reduced specific growth rate, a prolonged latency period, and an increased inhibition percentage with small NPs, indicating a slowdown in bacterial growth. *Pseudomonas aeruginosa* showed the lowest sensitivity to ZnO NPs, attributed to its resistance to environmental stress. Moreover, the antibacterial efficacy of paint containing 1 wt% of 22 nm ZnO NPs was evaluated, and showed activity against *E. coli* and *S. aureus*.

Keywords: ZnO nanoparticle; antibacterial activity; nanoparticle size effect; bacterial growth; antibacterial paint

1. Introduction

Nosocomial infections (Nis) represent common complications among patients admitted to intensive care units (ICUs), with an incidence ranging from 5% to 10% in Europe and America [1]. These infections result from antibiotic overuse, leading to microbial resistance. Antimicrobial resistance (ARM) occurs when microorganisms, including bacteria, viruses, fungi, and parasites, become able to adapt and grow in the presence of medications that once impacted them [2]. For example, the 2022 Global Antimicrobial Resistance and Use Surveillance System (GLASS) reported that in 2020, one in five cases of urinary tract infections caused by *E. coli* showed reduced susceptibility to standard antibiotics such as ampicillin, co-trimoxazole, and fluoroquinolones [3]. Antibiotic resistance increases the risk of incurable infections. The mechanisms of antimicrobial resistance include decreased drug inactivation or modification through enzyme production that destroys or alters antibiotics, alters target or binding sites such as penicillin-binding or ribosomal-binding proteins, and alters metabolic pathways, like the ability of enterococci to absorb folic acid from the environment, allowing them to bypass the effects of trimethoprim-sulfamethoxazole [4].

According to the OECD, the rate of antibiotic resistance is set to double by 2035 compared with 2005 [5]. Antibiotic-compromised efficacy leads to the exploration of alternative approaches, such as using metal oxide nanoparticles, notably ZnO nanoparticles, to combat antimicrobial resistance and prevent the emergence of resistant pathogens.

Metal oxide nanoparticles (NPs) have emerged as promising candidates for addressing ARM due to their unique physicochemical properties and high surface-to-volume ratio, which enable them to exert diverse modes of action (MOAs) against microorganisms. The mechanism of action of NPs encompasses chemical, physical, and combined interactions with bacterial cells. The chemical mechanism involves a series of steps, beginning with the release of ions and the subsequent generation of reactive oxygen species by NPs [6–8]. Metal ions are adsorbed on the cell membrane and later interact with the functional groups (-COOH, -NH_2, and -SH) of nucleic acids to deactivate the enzyme, causing a change in cell structure [9]. Elevated ROS have many effects on bacteria, and lipid peroxidation is one of them [8]. The physical interaction involves direct interactions between NPs and microorganisms. NPs can physically interact with bacterial cell walls, causing structural damage that leads to cell lysis. The combined mechanism involves electrostatic interactions between NPs and the cell membrane. This electrostatic interaction can cause the depolarization of the bacterial cell membrane, leading to potential membrane loss and cell disruption. In addition, NPs can also be internalized via endocytosis, nonspecific uptake, membrane diffusion, and adsorption [10,11]. Consequently, metal oxide nanoparticles show promise as potent antimicrobial agents [9,12] due to their ability to use multiple mechanisms of action to combat bacterial resistance.

Zinc oxide is attracting attention as a compelling metal oxide material due to its biocompatibility, easy synthesis, chemical stability, high abundance, and affordability [13–15]. These characteristics make it an ideal candidate for various biomedical applications, including its potential use in combatting bacterial infections. Previous studies have demonstrated the effectiveness of ZnO nanoparticles against a broad spectrum of pathogenic microorganisms, including Gram-positive and Gram-negative bacteria [16–18]. Their mode of action relies, in part, on the production of reactive oxygen species [19–23], which initiate the oxidation of cellular components, the disruption of bacterial membranes [11,23–27], direct contact [28–31], and internalization [16,22], ultimately resulting in cell death.

Enhancing the antibacterial potential of ZnO NPs is crucial for effectively preventing infections. The existing literature provides insights into how ZnO nanoparticle characteristics, such as shape [22,32–38], size [21,39–42], concentration [43,44], and surface modification [43–46], impact their antimicrobial activity. The effects are studied using techniques like disk and well diffusion assays, optical density measurements at short timescales ($\leq$6 h), and the determination of minimum inhibitory concentration (MIC) and minimum bactericidal concentration (MBC). However, our study focuses on the effect of nanoparticle size on bacterial growth kinetics. Smaller sizes mean a high surface area for the materials. This increase in specific surface area makes them more reactive, resulting in a high concentration of surface particles capable of interacting with electrons and holes. This unique characteristic offers more sites where electrical charges can accumulate, resulting in an increased surface electric charge, which leads to strong electrostatic interactions between ZnO NPs and bacterial membranes. The particle's charge can influence its biocompatibility and ability to traverse biological barriers [46]. The small dimension of these materials also makes them more abrasive [47]. Additionally, the sizes of NPs (ranging from 1 to 100 nm) are comparable to the size of protein globules (2 to 10 nm), the diameter of the DNA helix (2 nm), and the thickness of cell membranes (10 nm) [10]. Thus, the decrease in their size allows them to enter cells and cell organelles.

Previous studies have demonstrated that reducing nanoparticle size enhances their antibacterial activity [20,38,48]. Babayevska et al. [20] found that ZnO nanoparticles were more effective than microparticles against *Escherichia coli* and *Staphylococcus aureus*. They explained this difference by examining the mechanism through ROS measurements, and found that NPs produced more ROS than microparticles. Raghupathi et al. [49] found a

superior antibacterial activity of ZnO NPs at reduced sizes. They compared the growth curves of bacteria in the presence of ZnO NPs of various sizes (30 nm, 88 nm, 142 nm, and 212 nm) at a concentration of 6 mM during 6-h cultures. Despite these efforts, little research has been carried out to compare the bacterial growth kinetic across different sizes to understand the size-dependent mode of action.

The originality of this work lies in studying the influence of NPs' size on bacterial growth kinetics, focusing on the latency period and specific growth rate of bacteria. Determining these parameters sheds more light on the effect of NPs on the growth mechanisms of bacterial strains. Additionally, this study evaluates the antibacterial activity of paint formulated with synthesized NPs. The bacteria kinetic study was conducted on Gram-negative and Gram-positive bacteria by monitoring changes in bacterial optical density over a 24-h culture period with different NP sizes and concentrations. The specific growth rate and the latency period of bacteria were calculated using optical density data. Before this, the impact of the size of synthesized ZnO NPs on their antibacterial activity was preliminarily examined by determining their minimal inhibitory concentration (MIC) and bactericidal concentration (MBC). Finally, the conservation of the antibacterial activity of synthesized ZnO NPs in a paint formulation as a biocidal agent was evaluated.

2. Material and Methods

2.1. Materials

Zinc acetate dihydrate (≥99%), butan-1-ol (≥99.5%), acetone (≥99.5%), and silicone oil were obtained from Sigma-Aldrich, Darmstadt, Germany. Isopropanol (≥99.5%) was acquired from Acros Organics (Geel, Belgique). Monoethanolamine (100%) was obtained from Emprove (Darmstadt, Germany). Sodium polyacrylate (PAAS) was supplied by *Cosmedia* sp. (Ludwigshafen, Germany). Muller–Hinton broth and Trypto Soybean Casein were purchased from DIFCOTM (Sparks, MD, USA) and BioMerieux (Darmstadt, Germany). Powder paint was supplied by Dolci (Auvergne-Rhône-Alpes, France) and Eugon LT SUP by BioMerieux (Auvergne-Rhône-Alpes, France).

2.2. Synthesis of ZnO Nanoparticles

The protocol applied to obtain ZnO nanopowders of various sizes has been described in detail in a previous article [50]. A zinc precursor, with a concentration of 0.1 M, was dissolved in 100 mL butan-1-ol in the presence of a complexing agent, monoethanolamine (MEA). Water was introduced into the reaction medium to induce the precipitation of the NPs and to obtain nanopowders with a satisfying yield. NP size was mainly controlled by the ratio of zinc ions to complexing agent $[Zn^{2+}]/[MEA]$ and the hydrolysis rate $[Zn^{2+}]/[H_2O]$. The nanopowders were collected via centrifugation, followed by three washes with isopropanol and acetone to remove organic residues. Next, 2 wt% nanopowders were dispersed in Mueller–Hinton (MH) broth, followed by ultrasonic treatment in a J.P. Selecta ultrasonic bath at 150 W and 42 kHz for 1h in the presence of 0.4 wt% PAAS used as a dispersant. The protocol for preparing stable suspensions of NPs was inspired by that of Luo et al. [51].

The synthesis parameters used to prepare ZnO nanopowders are summarized in Table 1.

Table 1. Synthesis parameters of ZnO nanopowders.

Sample Size	$[Zn^{2+}]/[MEA]$	$[Zn^{2+}]/[H_2O]$	Agitation Time	Temperature
22 nm	1	5	22 h	80 °C
35 nm	1	10	2 h	110 °C
66 nm	2	10	22 h	110 °C

2.3. ZnO Nanoparticles' Characterization

The phase identification and microstructural characterization of ZnO nanopowders were carried out using X-ray diffraction (XRD) measurements on an EQUINOX 100 XRG 3000 diffractometer manufactured by INEL (Orléans, France)using a monochromatic cobalt source (λ Kα1 (Co) = 1.788976 Å). Diffraction patterns were processed using the Rietveld method implemented in MAUD (Material Analysis Using Diffraction) software (V2.998). Peaks were fitted according to a standardized procedure. The parameters refined were cell parameters, NP size, and the presence of microstrain. The crystallographic information file for ZnO wurtzite was obtained from the Crystallography Open Database (Ref 2300450). In the final step, an arbitrary texture option was used to optimize the quality of the Rietveld pattern refinement. This characterization was completed using Transmission Electronic Microscopy (TEM) analysis performed on a JEOL 2011(Tokyo, Japan) equipped with a Gatan Imaging Filter (DIF) 200 (Pleasanton, CA, USA). Raman spectroscopy measurements were also carried out on the powder samples using an HORIBA Jobin-Yvon HR800 spectrometer (Palaiseau, France) with an excitation wavelength (λ = 633 nm) to confirm the formation of ZnO NPs.

2.4. Minimal Inhibitory Concentration (MIC)

The MIC is the lowest concentration of NPs that prevents visible bacterial growth during incubation. Different concentrations of NPs were tested against bacteria to determine the MIC. These concentrations were prepared using microdilutions of the ZnO NP stock suspension. In total, 200 µL of each sample were then inoculated on a 96-well microplate in the presence of a final microorganism concentration of 4.67 Log_{10} CFU/mL. Physiological water was added to the empty microplate wells to ensure good humidity. Samples were incubated in a FLUOstar Omega spectrophotometer for 24 h with double orbital shaking at 300 rpm to monitor changes in optical density. Experiments were performed in triplicate. Negative controls included culture medium, NP solution, and PAAS solution. Positive controls consisted of PAAS solution in contact with microorganisms without NPs, as well as microorganisms in MH medium alone, without dispersant or NPs. The MIC was evaluated as the lowest concentration at which the optical density of bacteria remained constant.

The Biological Resource Center of Institut Pasteur (CRBIP) in Paris, France, provided the bacterial strains, which included *Escherichia coli* ATCC 8739 (CIP 53 126), *Pseudomonas aeruginosa* ATCC 9027 (CIP 82118), and *Staphylococcus aureus* ATCC 6538 (CIP 53 156). The bacteria were previously cultivated on MH agar from cryotubes stored at −80 °C. Incubation temperatures were set at 37 °C for *E. coli* and *S. aureus*, and at 30 °C for *P. aeruginosa*.

2.5. Minimal Bactericidal Concentration (MBC)

MBC is the lowest concentration of NPs resulting in at least a 99.9% reduction in cell viability. Various concentrations of NPs were incubated with bacteria in the FLUOstar at the appropriate temperature for 24h. After incubation, samples were diluted, and a volume of 1 µL was inoculated onto MH agar. The MH agar plates were then incubated at appropriate temperatures for colony counting. Percentage cell reduction was calculated according to the following formula:

$$\text{Percentage of reduction} = (1 - (C_f / C_i)) \times 100 \text{ in \%} \quad (1)$$

$$C_{i,f} = \log(n/(V * d)) \quad (2)$$

where

C_i is the initial concentration of microorganisms in contact with NPs before incubation,

C_f is the final concentration of microorganisms in contact with NPs after 24 h of incubation,

n is the number of colonies counted,

V is the inoculated volume,

d is the dilution factor.

2.6. Kinetic Growth of Bacteria

The growth kinetics of bacteria in contact with NPs were monitored by measuring the samples' optical density (OD) over time using the FLUOstar Omega spectrophotometer at a wavelength of 600 nm. OD_{600} measurement was used as a rapid and cost-effective means of monitoring the growth of bacteria throughout their culture in contact with NPs. NP concentrations at which the optical density of bacteria was not constant during MIC determination, as explained above, were used to study the impact of NP size on bacterial growth kinetics. The lag period, the specific growth rate of bacteria, and the percentage inhibition of NPs were evaluated using OD_{600} data. The formulas have been previously cited in reference [50] and are shown below:

$$\mu_x = (\ln(X_2) - \ln(X_1))/(t_2 - t_1) \text{ in } h^{-1} \quad (3)$$

$$G = \ln(2)/\mu_x \text{ in hour} \quad (4)$$

$$\text{Inhibition} = (OD_f^{\text{bacteria}} - \left(OD_f^{\text{NPs+bacteria}} - OD_{\text{control}}^{\text{NPs-bacteria}}\right)/OD_f^{\text{bacteria}}) \times 100 \text{ in \%} \quad (5)$$

where

μ_x is the specific growth rate;

X_2 and X_1 represent biomass at times t_1 and t_2, respectively, during the exponential growth phase in CFU/mL;

$t_2 - t_1$ is the time corresponding to biomass growth from X_1 to X_2 in hours;

G is the generation time in hours;

OD_f^{bacteria} is the final optical density of the positive control with bacteria alone;

$OD_f^{\text{NPs+bacteria}}$ is the final optical density of bacteria in contact with NPs;

$OD_{\text{control}}^{\text{NPs-bacteria}}$ is the optical density of NPs alone without bacteria.

The conversion of OD_{600} to CFU/mL was performed using a calibration equation OD = f(X) established within the laboratory for each bacteria under the operational conditions, where X represents the biomass in CFU/mL.

2.7. Paint Formulation with ZnO Nanoparticles

To obtain a suitable dispersion, a preservative-free Dolci-brand paint powder was dispersed in sterile distilled water at a mass ratio of 1:1 using a EUROSTAR 20 digital stator rotor emulsifier. Next, a 1 wt% solution of 22 nm ZnO NPs was added. The paint was then applied by dip-coating it onto standard glass substrates (VWR) pre-treated with sulfuric acid to ensure better paint adhesion. The paint was then left to dry for 24 h.

2.8. Measurement of the Antibacterial Activity of Paints Containing Nanoparticles

The antibacterial activity of the paints was assessed following ISO 22196:2011 [52] with slight modifications. A total of 0.1 mL bacterial suspension, prepared in 1/500 NB nutrient broth (3.0 g of meat extract, 10.0 g of peptone, and 5.0 g of sodium chloride), at 6 Log CFU/mL was spread onto paint films. Samples were then covered with polypropylene film (2×5 cm^2) to maintain humidity and ensure good contact between samples and bacteria. They were incubated at 35 °C under $\geq$90% relative humidity for 24 h. After incubation, bacterial cells were recovered from the paint films by stirring in 10 mL of Eugon LT broth in the presence of 10 g of 1 mm glass beads for 1 min. The antibacterial activity was evaluated via colony counting on agar plates. Positive controls were conducted using paint without NPs. All tests were performed in triplicate, and the antibacterial activity was calculated using the following formula [52]:

$$R = U_t - A_t \text{ in } \text{Log}_{10} \text{ CFU/cm}^2 \quad (6)$$

R is the antibacterial activity;

U_t is the average of the common logarithm of the number of viable bacteria, in cells/cm^2, recovered from the untreated test specimens after 24 h.

3. Results

3.1. Characterization of ZnO Nanoparticles

All ZnO samples are well crystallized in the wurtzite phase, as confirmed using X-ray diffraction (Figure 1a) and Rietveld refinement (Figure 1b). Rietveld refinement analysis showed the stability of the cell parameters (a, c) and revealed varying sizes—22 nm, 35 nm, and 66 nm (Table 2). In addition, the transmission electron microscopy (TEM) image of 22 nm NPs confirmed the formation of small and well-crystallized ZnO wurtzite NPs (Figure 1c). Raman spectra also confirmed the crystallinity of the samples, showing characteristic Raman modes indicative of the ZnO wurtzite structure (Figure 1d).

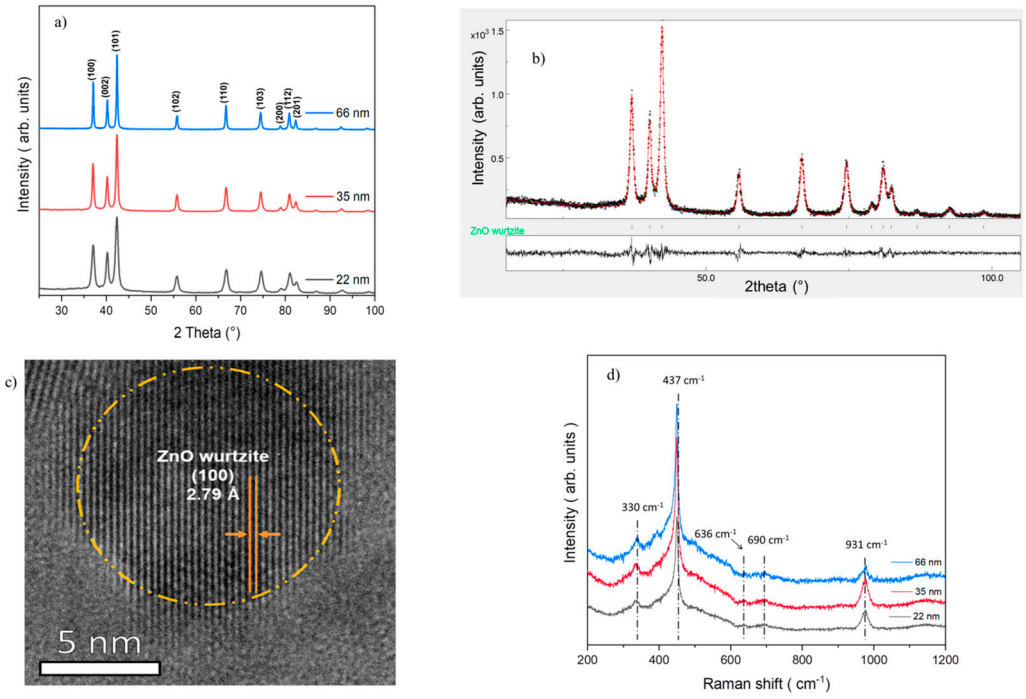

Figure 1. (**a**) XRD patterns of samples; (**b**) Rietveld refinement of 22 nm ZnO; (**c**) TEM of 22 nm ZnO dispersed in MH broth; and (**d**) Raman spectra of samples.

Table 2. Crystallographic parameters of the obtained ZnO nanoparticles.

Crystallite Size (nm)	Lattice Parameters (Å)		Microstrain (%)	Sig = GoF
	a = b	c		
22	3.25	5.20	0.002	1.18
35	3.25	5.21	0.001	1.21
66	3.25	5.21	0.001	1.60

3.2. Correlation between ZnO Nanoparticle Size and Minimal Inhibitory Concentration (MIC)

The MIC represents the lowest concentration of ZnO NPs that inhibits visible bacterial growth after the incubation period. A significant decrease in the MIC of ZnO NPs against *E. coli* was observed as their size decreased, with respective values of 0.45 mg/mL, 0.40 mg/mL, and 0.85 mg/mL for sizes 22 nm, 35 nm, and 66 nm. Similarly, a reduction in MIC was noted for *P. aeruginosa*, with values decreasing from 1.25 mg/mL and 1.60 mg/mL to 1.85 mg/mL for sizes of 22 nm, 35 nm, and 66 nm, respectively. The antibacterial activity of ZnO NPs against *E. coli* and *P. aeruginosa* increased as their size decreased. The MIC of

ZnO NPs against *S. aureus* remained stable at 0.15 mg/mL regardless of their size. These results are presented in Figure 2.

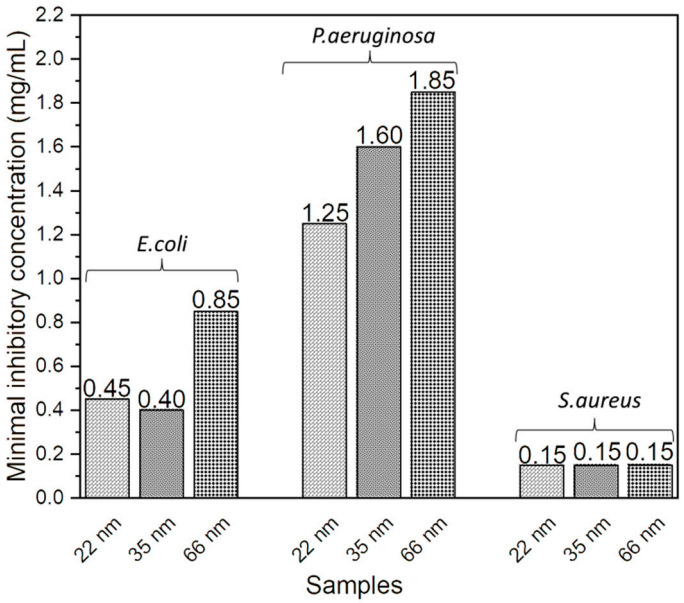

Figure 2. Effect of ZnO nanoparticle size on MIC against *E. coli*; *P. aeruginosa*; and *S. aureus*.

3.3. Correlation between ZnO NP Size and Minimal Bactericidal Concentration (MBC)

The MBC corresponds to the lowest concentration of NPs, resulting in the death of 99.9% of the initial bacterial population. It was observed that the MBC of NPs against the three bacteria decreased as their size decreased, indicating an improvement in the antibacterial activity of the NPs and confirming the results obtained previously (Figure 3). Specifically, its values were 0.5 mg/mL, 0.6 mg/mL, and 1.05 mg/mL for sizes of 22 nm, 35 nm, and 66 nm against *E. coli*, respectively. For *P. aeruginosa*, the values were 11 mg/mL, 13 mg/mL, and 15 mg/mL for sizes of 22 nm, 35 nm, and 66 nm, respectively. And for *S. aureus*, the MBC values were 0.30 mg/mL, 1.55 mg/mL, and 1.70 mg/mL for sizes of 22 nm, 35 nm, and 66 nm, respectively.

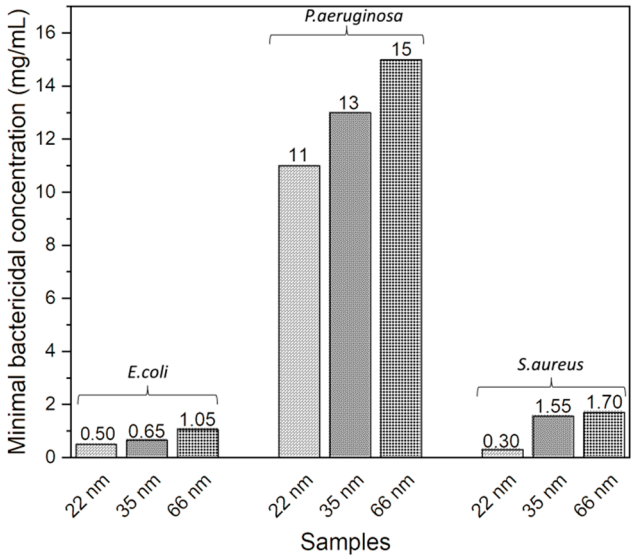

Figure 3. Effect of the size of ZnO NPs on their MBC against *E. coli*, *P. aeruginosa*, and *S. aureus*.

3.4. ZnO NP Size Effect on Bacterial Growth Kinetics

Figure 4 shows the evolution of the optical density of P.aeruginosa bacteria in the presence of different NP sizes—22 nm (Figure 4a), 35 nm (Figure 4b), and 66 nm (Figure 4c)—at various concentrations. Increasing the concentration improved antibacterial activity, as the optical density was lower at higher concentrations. For NP concentrations where optical density did not remain constant over 24 h, the lag phase, during which the optical density remains at 0 before increasing, was longer with smaller NPs, indicating a stronger bacterial growth inhibition. For example, at a concentration of 1.35 mg/mL (in green in Figure 4), the lag phase of the bacteria with 22 nm NPs was longer than that with 35 nm, which was longer than that with 66 nm. Similarly, the growth rate, indicated by the slope, was higher with larger NPs, showing a faster bacterial growth and less inhibition. Additionally, the final bacterial density, related to the percentage inhibition, was higher with larger NPs. These observations enabled the calculation of these parameters and the evaluation of the impact of NP size on them. The effect of ZnO NP size on the lag phase, specific growth rate, and inhibition percentage for different bacteria is detailed in Figure 5.

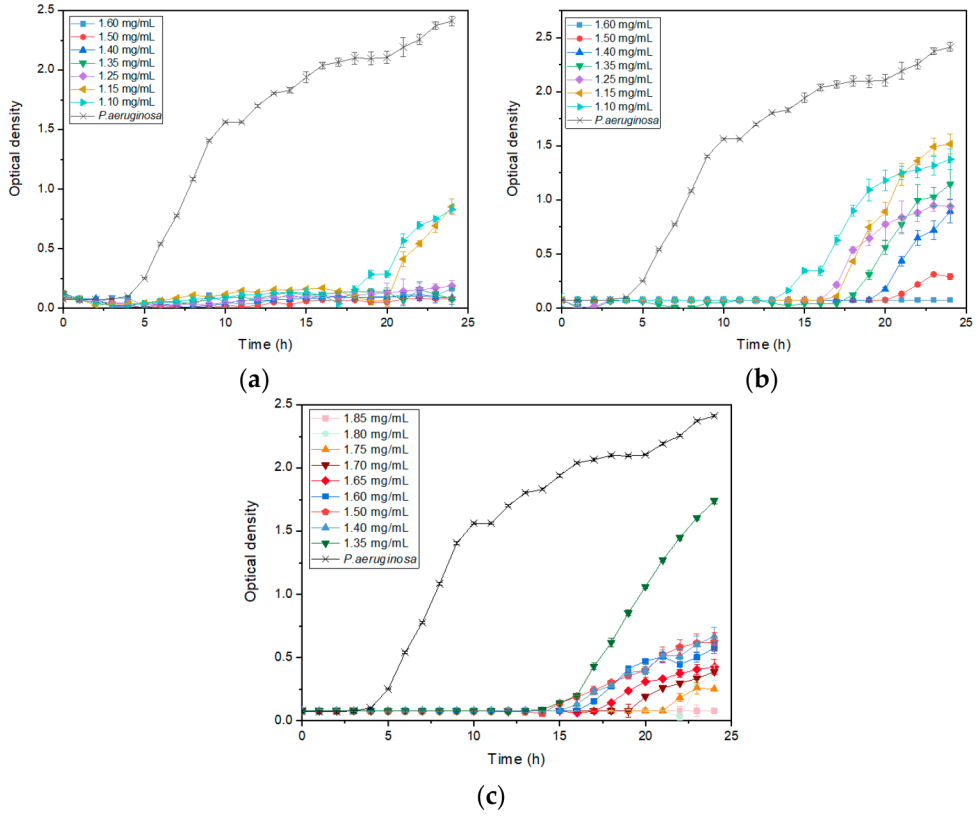

Figure 4. OD_{600} growth of *P. aeruginosa* in contact with (**a**) 22 nm; (**b**) 35 nm; and (**c**) 66 nm ZnO nanoparticles at different concentrations.

The inhibition percentage generally increased with decreasing NP size, independently of bacteria (Figure 5a). While no significant impact is observed with *E. coli* and *S. aureus*, the influence of ZnO NP size is evident with *P. aeruginosa*. The 22 nm and 35 nm ZnO NPs showed similar inhibition levels on *E. coli* growth across tested concentrations except at 0.3 mg/mL, where inhibition percentages were 74.78%, 76.93%, and 65.59% for 22 nm, 35 nm, and 66 nm NPs, respectively.

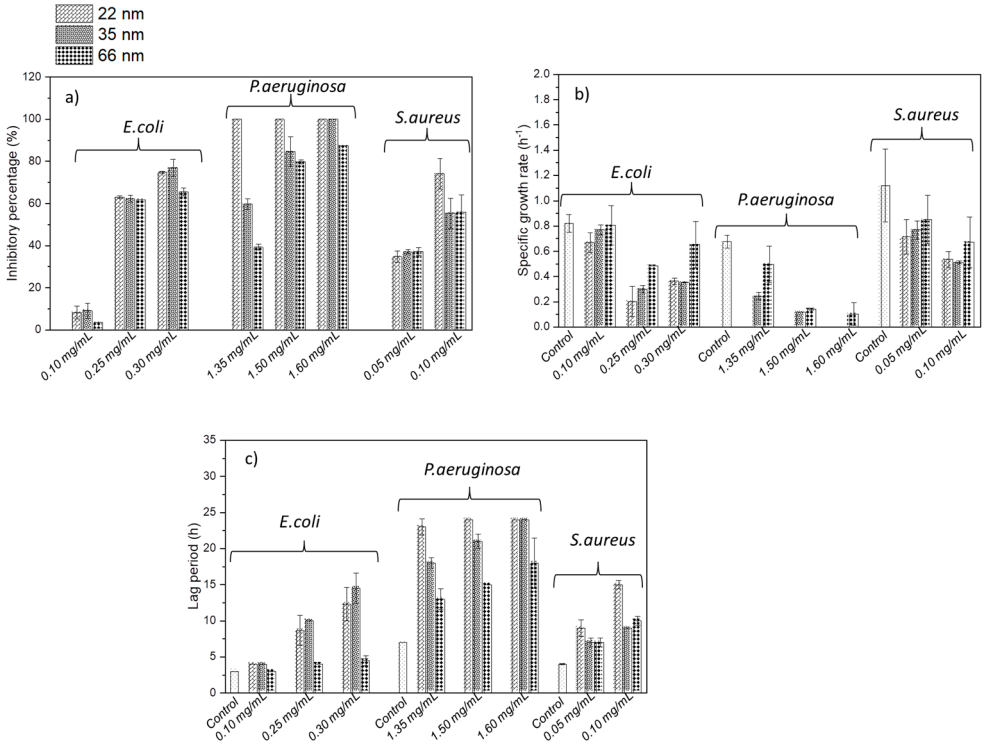

Figure 5. ZnO NP size effect on the growth parameter of *E. coli*; *P. aeruginosa*; and *S. aureus*: (**a**) inhibitory percentage; (**b**) specific growth rate; and (**c**) lag period at different concentrations.

The impact of NP size on inhibition percentage was particularly pronounced in P. aeruginosa across all concentrations tested. At 1.35 mg/mL, inhibition percentages decreased from 100%, 59.70% to 39.33% for 22 nm, 35 nm, and 66 nm NPs, respectively. Similarly, at 1.50 mg/mL, inhibition percentages decreased from 100%, 84.72% to 79.72% for the respective NPs sizes compared to the control. At 1.60 mg/mL, inhibition percentages decreased from 100% for 22 nm and 35 nm NPs to 87.59% for 66 nm NPs.

For *S. aureus*, inhibition percentages were identical for 35 nm and 66 nm NPs across all tested concentrations—37% for 35 nm and 66 nm NPs at 0.05 mg/mL, 34% for 22 nm NPs at 0.1 mg/mL, 56% at 0.1 mg/mL, and 74% for 22 nm NPs at 0.1 mg/mL.

Regarding the specific growth rate, representing bacterial proliferation rate, we observe a general trend across all microorganisms where smaller ZnO NPs decreased the specific growth rate. For *E. coli*, the specific growth rate was 0.67 h^{-1} with 22 nm NPs, compared to 0.8 h^{-1} with 35 nm and 66 nm NPs at 0.1 mg/mL concentration. At 0.25 mg/mL, it decreased to 0.2 h^{-1}, 0.3 h^{-1}, and 0.49 h^{-1} with 22 nm, 35 nm, and 66 nm NPs, respectively. At a 0.3 mg/mL NP concentration, the specific growth rate was 0.35 h^{-1} with 22 nm and 35 nm NPs, and 0.65 h^{-1} with 66 nm NPs.

P. aeruginosa exhibited rates of 0 h^{-1}, 0.25 h^{-1}, and 0.50 h^{-1} with 22 nm, 35 nm, and 66 nm NPs, respectively, at 1.35 mg/mL. At a 1.50 mg/mL concentration, the rates were 0 h^{-1}, 0.12 h^{-1}, and 0.14 h^{-1} with the respective NP sizes. Finally, at a concentration of 1.60 mg/mL, the specific growth rate of P. aeruginosa was 0 h^{-1} for 22 nm and 35 nm NPs, and 0.10 h^{-1} for 66 nm NPs.

For *S. aureus*, at 0.05 mg/mL, the specific growth rate was 0.71 h^{-1}, 0.77 h^{-1}, and 0.85 h^{-1} with 22 nm, 35 nm, and 66 nm NPs, respectively. On average, it was 0.52 h^{-1} with 22 nm and 35 nm NPs, and 0.67 h^{-1} with 66 nm NPs.

Further elucidation of the impact of NP size on bacterial growth kinetics was provided by examining the lag phase (Figure 5c). The lag phase, representing the time for bacteria to initiate growth after inoculation, also exhibits a general trend across all microorganisms, wherein smaller ZnO particles prolong the bacterial latency period. At 0.1 mg/mL, the lag phase remained stable across all sizes for *E. coli*, averaging 4 h. However, notable

reductions were observed at higher concentrations. For instance, at 0.25 mg/mL, the lag phase of *E. coli* decreased from 8.5 h to 10 h to 4 h with 22 nm, 35 nm, and 66 nm NPs, respectively. Similarly, at 0.30 mg/mL, it decreased to 12 h, 14.5 h, and 4.5 h with the respective NPs sizes.

In the case of *P. aeruginosa*, at a concentration of 1.35 mg/mL, the lag phase reduced from 23 h to 13 h with 22 nm, 35 nm, and 66 nm NPs. This reduction was also observed at 1.50 mg/mL, where the lag phase was 24 h, 21 h, and 15 h with 22 nm, 35 nm, and 66 nm NPs, respectively. Similarly, at a 1.60 mg/mL NP concentration, the lag phase remained at 24 h for both 22 nm and 35 nm sizes, and decreased to 18 h for 66 nm NPs.

Similarly, for *S. aureus*, distinct differences in lag phase duration were observed at different concentrations and NPs sizes. At a 0.05 mg/mL concentration, the lag phase persisted for 9 h with 22 nm NPs, while it was reduced to 7 h with 35 nm and 66 nm NPs. Conversely, at a concentration of 0.1 mg/mL, the lag phase extended to 15 h with 22 nm NPs, while it remained at 10 h with 35 nm and 66 nm NPs.

Figure 6 shows an increase in bacterial growth inhibition with decreasing NP size for all microorganisms at different ZnO NP concentrations. For *E. coli*, inhibition was consistent with 22 nm and 35 nm nanoparticles, and was higher than with 66 nm NPs. *P. aeruginosa* inhibition increases with decreasing size. Furthermore, as NP concentration increased, inhibition tended to converge for all three NP sizes. As for *S. aureus*, inhibition is consistent with 66 nm and 35 nm NPs, but weaker than contact with 22 nm NPs. These results confirm those obtained for growth parameters, MIC and MBC.

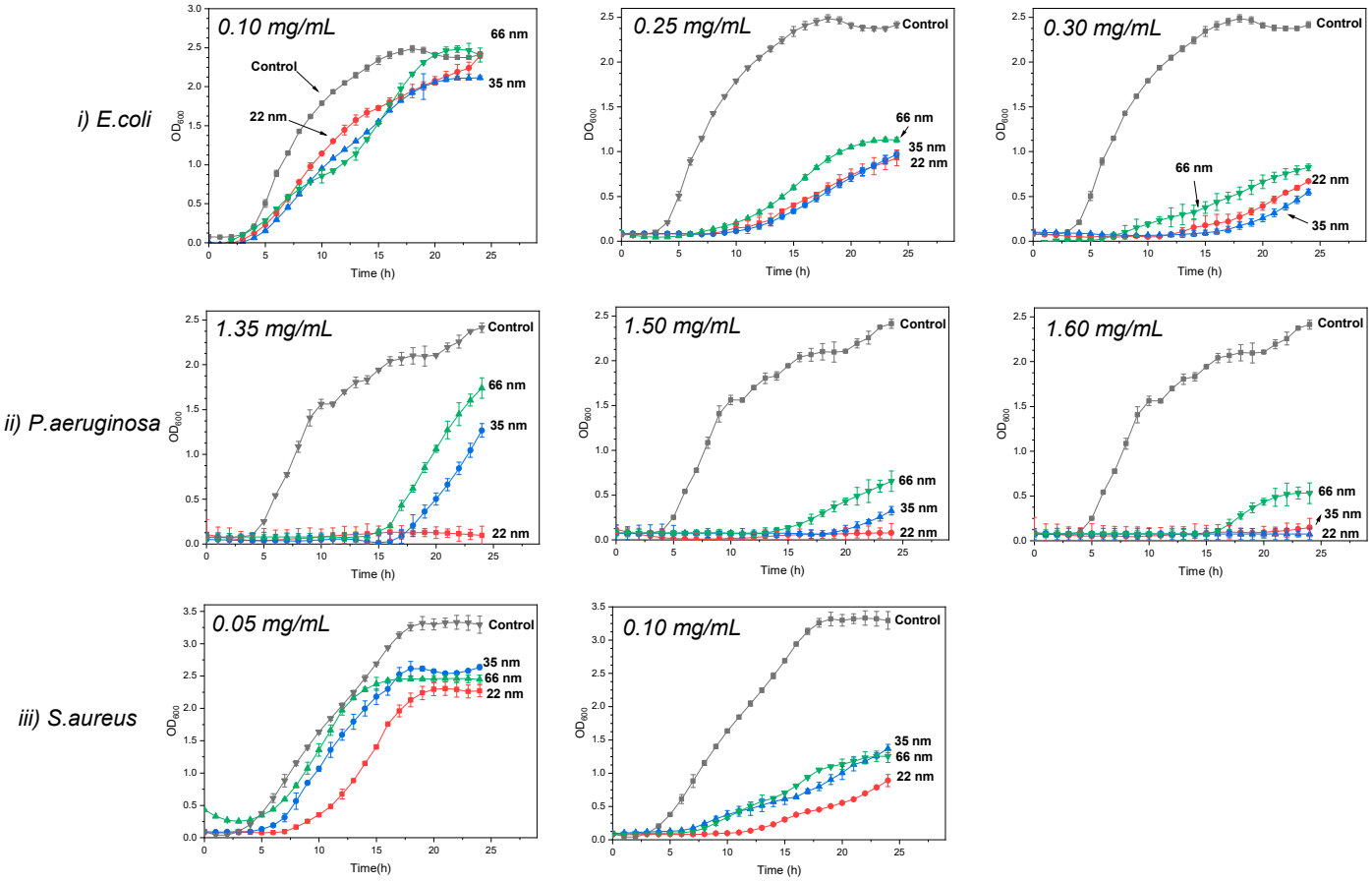

Figure 6. Effect of ZnO NP size on bacterial growth kinetics.

3.5. Antibacterial Activity of ZnO Nanoparticles on Emulsion Waterborne Paint

The paint formulation containing 1wt% 22 nm ZnO NPs demonstrated a high efficacy against *S. aureus* and *E. coli*, while showing no antibacterial activity against *P. aeruginosa*

(Figure 7). This trend was observed when NPs were in suspension, with *P. aeruginosa* exhibiting the lowest sensitivity to NPs. However, NPs in paint films exhibited a better antibacterial activity than in suspension. The number of colonies on agar plates seeded with samples diluted to 10^{-4} was compared to better observe the activity of NPs in paint on *P. aeruginosa*, unlike other bacteria where samples are directly presented on agar plates. The number of residual cells in Table 3 confirmed the inhibitory effect of NPs in the paint against *S. aureus* and *E. coli*, as well as the lack of inhibition against *P. aeruginosa*. Notably, paint's detachment from slides occurred after the vortexing step used to remove bacteria from the glass slide.

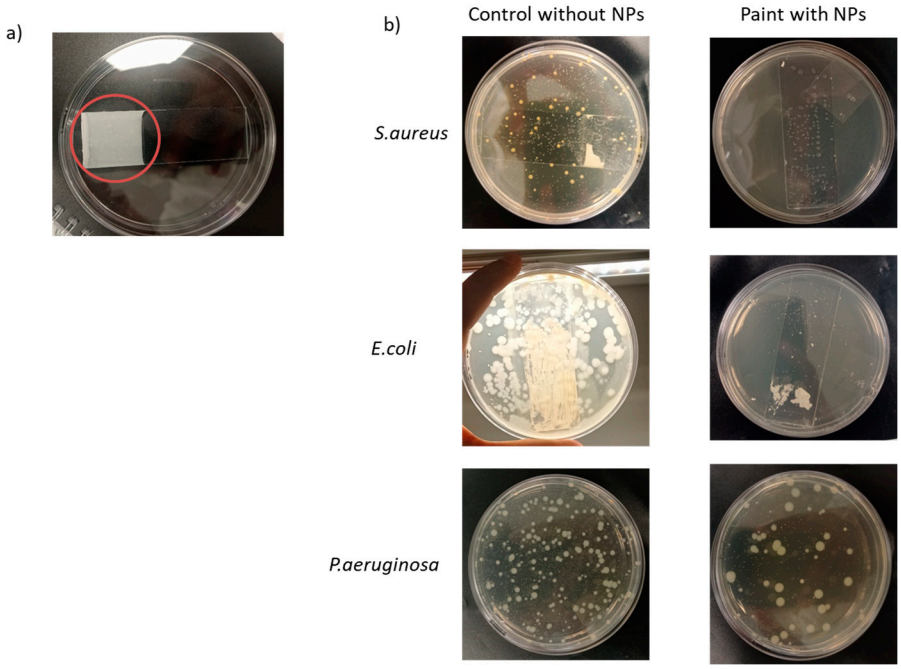

Figure 7. (**a**) A paint film containing 22 nm nanoparticles, onto which 0.1 mL of bacterial suspension is applied without vortexing; (**b**) evaluation of antibacterial properties of paint containing ZnO nanoparticles against *S. aureus*; *E. coli*; and *P. aeruginosa*.

Table 3. Residual survival of bacteria after 24 h of contact with paint.

Bacteria	Control at 24 h	Sample at 24 h
S. aureus	4.55 ± 0.32 Log CFU/cm^2	<1 Log_{10} CFU/cm^2
E. coli	3.90 ± 0.02 Log_{10} CFU/cm^2	<1 Log_{10} CFU/cm^2
P. aeruginosa	6.41 ± 0.11 Log_{10} CFU/cm^2	6.18 ± 0.08 Log_{10} CFU/cm^2

4. Discussion

The most important findings of this study can be summarized as follows: Firstly, decreasing the size of ZnO NPs (22 nm, 35 nm, and 66 nm) enhanced their antibacterial efficacy by lowering their minimum inhibitory concentration (MIC) and minimum bactericidal concentration (MBC). Notably, *P. aeruginosa* exhibited a lower susceptibility to NPs than the other bacterial strains, necessitating higher concentrations for a bactericidal effect. Furthermore, the reduction in MIC and MBC with decreasing NPs size was particularly pronounced when dealing with *P. aeruginosa*.

Several investigations have explored the effects of ZnO NPs on MIC and MBC values [53–58]. Consistent with our findings, most researchers have observed a significant enhancement in antibacterial effectiveness with smaller NPs. For instance, Pasquet et al. [53] reported a superior antimicrobial activity with smaller ZnO crystals against *E. coli* and *P. aeruginosa*, noting a proportional increase in MIC and MBC with larger NPs.

Álvarez-Chimal et al. [59] have observed consistent findings, indicating that ZnO NPs sized at 7 nm, 10 nm, 16 nm, and 30 nm show increased MBC values against both *S. aureus* and *E. coli* as their size increases. Remarkably, the MBC values reported in their study, ranging from 10 to 80 mg/mL, are higher than those observed in the present investigation, likely due to differences in NP composition. However, our results regarding *S. aureus* diverge from those of Lallo Da Silva et al. [38], who have documented elevated MIC values with larger NPs against *S. aureus* strains. Palanikumar et al. [55] reported that ZnO NPs with sizes of 15 nm, 25 nm, and 38 nm exhibited identical MICs against *S. aureus* MRSA, with a value of 0.2 mg/mL, aligning with our findings. Despite *S. aureus* consistently displaying similar MIC values regardless of NP size, we observed a decline in cell viability, as indicated by MBC measurements, with decreasing particle size. The MIC and MBC values obtained in this study are less than or equal to those reported in the literature for ZnO NPs of the same size as those studied here [32,60].

Previous studies have suggested that *E. coli* is more susceptible to ZnO NPs than *P. aeruginosa*, while *S. aureus* is more sensitive than *P. aeruginosa*. The variation in susceptibility among *P. aeruginosa* with other bacteria can be attributed to a complex interplay of factors, including the production of extracellular polymeric substances (EPSs) [61], detoxification systems, and specific metabolic and genetic responses. The extensive coding capacity of the *P. aeruginosa* genome enables remarkable metabolic adaptability and versatility in response to environmental changes [62]. Factors dictating the antibacterial effect can explain the difference in sensitivity of *S. aureus* and *E.coli* towards ZnO, specifically the structural differences between Gram(-) and Gram(+) bacteria. In Gram(+) bacteria, such as *S. aureus*, there is no outer membrane, and the cell wall is thick, consisting of a large amount of mucopeptides as well as surface components of lipoteichoic acids (LTAs). In contrast, Gram(-) bacteria, like *E.coli*, have a relatively thin cell wall but possess an outer membrane. The lack of an outer membrane could explain why *S. aureus* were more sensitive to ZnO NPs than *E. coli*.

Secondly, the study suggested that the diminution in the size of ZnO NPs can slow down bacterial growth. Few studies have delved into the role of ZnO NP size in the kinetic growth of bacteria. Nevertheless, Baek et al. discovered that the growth inhibition rate (%) of *E. coli* increased as the size of ZnO NPs decreased (12.7 nm, 15.7 nm, and 17.2 nm) [63]. These results align with those of Mirhosseini et al. [48] and Raghupathi et al. [49], who have similarly observed increased growth inhibition against *S. aureus* and *E. coli* with smaller ZnO NP sizes.

The antibacterial activity of ZnO NPs is attributed to several mechanisms, including releasing reactive oxygen species (ROS), destroying the cell membrane, and internalizing NPs into bacterial cells. The reduction in NP size can influence these mechanisms and slow bacterial growth in several ways. The heightened reactivity of smaller-sized NPs due to their larger specific surface area can promote increased ROS release upon interaction with bacteria, leading to the greater oxidation and deterioration of essential cellular components, thus slowing bacterial growth. Also, the reduced size of NPs can result in more efficient internalization into bacterial cells. Lastly, the decrease in NP size can also increase the likelihood of direct contact with the cell membrane, potentially causing more significant membrane disruption and the leakage of cellular components, thereby compromising bacterial viability. Furthermore, the similar MIC values of NPs against *S. aureus* may be attributed to the fact that *S. aureus* is a cocci-shaped bacteria that tends to form "grape-like" clusters. The internal cocci in these clusters could explain these observations. There appears to be a maximum size beyond which NPs cannot penetrate between these grape-like clusters, thus maintaining unchanged antibacterial activity. Furthermore, the inhibitory effects of NPs on *P. aeruginosa* growth tend to converge as their concentration increases, probably because the minimum inhibitory concentration (MIC) is close.

Thirdly, ZnO nano-based paints exhibit bactericidal activity against *E. coli* and *S. aureus*. These findings align with the literature, demonstrating the effectiveness of paints containing ZnO nanoparticles against various bacteria, including *E. coli* and *S. aureus* [64–66]. For

example, Fiori et al. [64] found that the most significant antimicrobial effect against *S. aureus*, assessed using an agar diffusion test, was achieved with paint formulated with 1.2% 9 nm ZnO NPs. The antibacterial activity of NPs was higher when incorporated in paint, probably due to the optimization of the NP–cell interaction surface.

5. Conclusions

The reduction in the size of ZnO nanoparticles enhanced their antibacterial activity against *E. coli*, *P. aeruginosa*, and *S. aureus*. Additionally, it decreased the growth kinetics of bacteria by reducing their specific growth rate, prolonging their lag time, and increasing their inhibition percentage. For example, in *P. aeruginosa*, nanoparticle concentrations at 1.35 mg/mL showed inhibition percentages that decreased from 100% for 22 nm NPs, to 59.70% for 35 nm NPs and 39.33% for 66 nm NPs. This study emphasizes the critical importance of ZnO NP size in their ability to inhibit and eradicate pathogenic Gram-negative and Gram-positive bacteria. Furthermore, applying these ZnO nanoparticles in paint formulations presented a promising strategy to combat nosocomial infections. A prospective direction for this study is to investigate the antibacterial activity of their thin films and the safety of ZnO NPs.

Author Contributions: Conceptualization, I.E.-H., M.T., A.L., C.M. and R.A.; methodology, I.E.-H. and C.M.; software, I.E.-H.; validation, I.E.-H.; formal analysis, I.E.-H. and S.D.; investigation, I.E.-H.; data curation, I.E.-H., A.L. and H.M.; writing—original draft preparation, I.E.-H.; review and editing, R.A., A.L. and M.T.; visualization, S.D. and A.R.; supervision, A.L., R.A., C.M. and M.T.; project administration, R.A. and M.T.; funding acquisition, R.A. and M.T. All authors have read and agreed to the published version of the manuscript.

Funding: This research received no external funding.

Data Availability Statement: The corresponding author will make the raw data supporting this article's conclusions available upon request.

Acknowledgments: The authors would like to acknowledge Paule Arielle and Amelia Murray from the School Ecole de Biologie Industrielle (EBI) for their assistance in the determination of MBC by counting colonies, and Maria Konstantakoupoulou and Valérie Bockelé from the Laboratoire des Sciences des Procédés et des Matériaux (LSPM) laboratory for their help in obtaining the MET image and XRD data, respectively. The authors would also like to acknowledge Andrei Kanaev from the Galilée Institute for reviewing this article.

Conflicts of Interest: The authors declare no conflicts of interest.

References

1. Baviskar, A.S.; Khatib, K.I.; Rajpal, D.; Dongare, H.C. Nosocomial Infections in Surgical Intensive Care Unit: A Retrospective Single-Center Study. *Int. J. Crit. Illn. Inj. Sci.* **2019**, *9*, 16–20. [CrossRef] [PubMed]
2. Dadgostar, P. Antimicrobial Resistance: Implications and Costs. *Infect. Drug Resist.* **2019**, *12*, 3903–3910. [CrossRef] [PubMed]
3. Ajulo, S.; Awosile, B. Global Antimicrobial Resistance and Use Surveillance System (GLASS 2022): Investigating the Relationship between Antimicrobial Resistance and Antimicrobial Consumption Data across the Participating Countries. *PLoS ONE* **2024**, *19*, e0297921. [CrossRef] [PubMed]
4. Morrison, L.; Zembower, T.R. Antimicrobial Resistance. *Gastrointest. Endosc. Clin. N. Am.* **2020**, *30*, 619–635. [CrossRef] [PubMed]
5. Strengthening the EU Response to Prevention and Control of Antimicrobial Resistance (AMR): Policy Priorities for Effective Implementation Strengthening the EU Response to Prevention and Control of Antimicrobial Resistance (AMR): Policy Priorities for Effective Implementation. Available online: https://eurohealthobservatory.who.int/publications/i/strengthening-the-eu-response-to-prevention-and-control-of-antimicrobial-resistance-(amr)-policy-priorities-for-effective-implementation (accessed on 1 July 2024).
6. Raghunath, A.; Perumal, E. Metal Oxide Nanoparticles as Antimicrobial Agents: A Promise for the Future. *Int. J. Antimicrob. Agents* **2017**, *49*, 137–152. [CrossRef] [PubMed]
7. Pachaiappan, R.; Rajendran, S.; Show, P.L.; Manavalan, K.; Naushad, M. Metal/Metal Oxide Nanocomposites for Bactericidal Effect: A Review. *Chemosphere* **2021**, *272*, 128607. [CrossRef] [PubMed]
8. Tiwari, V.; Mishra, N.; Gadani, K.; Solanki, P.S.; Shah, N.A.; Tiwari, M. Mechanism of Anti-Bacterial Activity of Zinc Oxide Nanoparticle Against Carbapenem-Resistant *Acinetobacter baumannii*. *Front. Microbiol.* **2018**, *9*, 1218. [CrossRef] [PubMed]

9. Gautam, S.; Das, D.K.; Kaur, J.; Kumar, A.; Ubaidullah, M.; Hasan, M.; Yadav, K.K.; Gupta, R.K. Transition Metal-Based Nanoparticles as Potential Antimicrobial Agents: Recent Advancements, Mechanistic, Challenges, and Future Prospects. *Discov. Nano* **2023**, *18*, 84. [CrossRef] [PubMed]
10. Sukhanova, A.; Bozrova, S.; Sokolov, P.; Berestovoy, M.; Karaulov, A.; Nabiev, I. Dependence of Nanoparticle Toxicity on Their Physical and Chemical Properties. *Nanoscale Res. Lett.* **2018**, *13*, 44. [CrossRef]
11. Raha, S.; Ahmaruzzaman, M. ZnO Nanostructured Materials and Their Potential Applications: Progress, Challenges and Perspectives. *Nanoscale Adv.* **2022**, *4*, 1868–1925. [CrossRef]
12. Sarojini, S.; Jayaram, S. An Impact of Antibacterial Efficacy of Metal Oxide Nanoparticles: A Promise for Future. In *Bio-Manufactured Nanomaterials: Perspectives and Promotion*; Pal, K., Ed.; Springer International Publishing: Cham, Switzerland, 2021; pp. 393–406; ISBN 978-3-030-67223-2.
13. Jiang, S.; Lin, K.; Cai, M. ZnO Nanomaterials: Current Advancements in Antibacterial Mechanisms and Applications. *Front. Chem.* **2020**, *8*, 580. [CrossRef] [PubMed]
14. Izzi, M.; Sportelli, M.C.; Torsi, L.; Picca, R.A.; Cioffi, N. Synthesis and Antimicrobial Applications of ZnO Nanostructures: A Review. *ACS Appl. Nano Mater.* **2023**, *6*, 10881–10902. [CrossRef]
15. Dutta, G.; Sugumaran, A. Bioengineered Zinc Oxide Nanoparticles: Chemical, Green, Biological Fabrication Methods and Its Potential Biomedical Applications. *J. Drug Deliv. Sci. Technol.* **2021**, *66*, 102853. [CrossRef]
16. Mendes, C.R.; Dilarri, G.; Forsan, C.F.; Sapata, V.d.M.R.; Lopes, P.R.M.; de Moraes, P.B.; Montagnolli, R.N.; Ferreira, H.; Bidoia, E.D. Antibacterial Action and Target Mechanisms of Zinc Oxide Nanoparticles against Bacterial Pathogens. *Sci. Rep.* **2022**, *12*, 2658. [CrossRef] [PubMed]
17. Ahmad, I.; Alshahrani, M.Y.; Wahab, S.; Al-Harbi, A.I.; Nisar, N.; Alraey, Y.; Alqahtani, A.; Mir, M.A.; Irfan, S.; Saeed, M. Zinc Oxide Nanoparticle: An Effective Antibacterial Agent against Pathogenic Bacterial Isolates. *J. King Saud. Univ. Sci.* **2022**, *34*, 102110. [CrossRef]
18. Perveen, R.; Shujaat, S.; Qureshi, Z.; Nawaz, S.; Khan, M.I.; Iqbal, M. Green versus Sol-Gel Synthesis of ZnO Nanoparticles and Antimicrobial Activity Evaluation against Panel of Pathogens. *J. Mater. Res. Technol.* **2020**, *9*, 7817–7827. [CrossRef]
19. Abdal Dayem, A.; Hossain, M.K.; Lee, S.B.; Kim, K.; Saha, S.K.; Yang, G.-M.; Choi, H.Y.; Cho, S.-G. The Role of Reactive Oxygen Species (ROS) in the Biological Activities of Metallic Nanoparticles. *Int. J. Mol. Sci.* **2017**, *18*, 120. [CrossRef] [PubMed]
20. Babayevska, N.; Przysiecka, Ł.; Iatsunskyi, I.; Nowaczyk, G.; Jarek, M.; Janiszewska, E.; Jurga, S. ZnO Size and Shape Effect on Antibacterial Activity and Cytotoxicity Profile. *Sci. Rep.* **2022**, *12*, 8148. [CrossRef] [PubMed]
21. Girma, A.; Abera, B.; Mekuye, B.; Mebratie, G. Antibacterial Activity and Mechanisms of Action of Inorganic Nanoparticles against Foodborne Bacterial Pathogens: A Systematic Review. *IET Nanobiotechnol.* **2024**, *2024*, 5417924. [CrossRef]
22. Bhattacharya, P.; Dey, A.; Neogi, S. An Insight into the Mechanism of Antibacterial Activity by Magnesium Oxide Nanoparticles. *J. Mater. Chem. B* **2021**, *9*, 5329–5339. [CrossRef]
23. Kessler, A.; Hedberg, J.; Blomberg, E.; Odnevall, I. Reactive Oxygen Species Formed by Metal and Metal Oxide Nanoparticles in Physiological Media—A Review of Reactions of Importance to Nanotoxicity and Proposal for Categorization. *Nanomaterials* **2022**, *12*, 1922. [CrossRef] [PubMed]
24. Abebe, B.; Zereffa, E.A.; Tadesse, A.; Murthy, H.C.A. A Review on Enhancing the Antibacterial Activity of ZnO: Mechanisms and Microscopic Investigation. *Nanoscale Res. Lett.* **2020**, *15*, 190. [CrossRef] [PubMed]
25. Agarwal, H.; Menon, S.; Venkat Kumar, S.; Rajeshkumar, S. Mechanistic Study on Antibacterial Action of Zinc Oxide Nanoparticles Synthesized Using Green Route. *Chem. Biol. Interact.* **2018**, *286*, 60–70. [CrossRef] [PubMed]
26. Modi, S.K.; Gaur, S.; Sengupta, M.; Singh, M.S. Mechanistic Insights into Nanoparticle Surface-Bacterial Membrane Interactions in Overcoming Antibiotic Resistance. *Front. Microbiol.* **2023**, *14*, 1135579. [CrossRef] [PubMed]
27. Raghav, A.; Kaur, S.; Setia, G.; Kumar, S. Nanomaterials Induced Cell Disruption: An Insight into Mechanism. In *Biogenic Nanomaterials for Environmental Sustainability: Principles, Practices, and Opportunities*; Shah, M.P., Bharadvaja, N., Kumar, L., Eds.; Springer International Publishing: Cham, Switzerland, 2024; pp. 227–249; ISBN 978-3-031-45956-6.
28. Thakur, S.; Neogi, S. Effect of Doped ZnO Nanoparticles on Bacterial Cell Morphology and Biochemical Composition. *Appl. Nanosci.* **2021**, *11*, 159–171. [CrossRef]
29. Xin, Z.; He, Q.; Wang, S.; Han, X.; Fu, Z.; Xu, X.; Zhao, X. Recent Progress in ZnO-Based Nanostructures for Photocatalytic Antimicrobial in Water Treatment: A Review. *Appl. Sci.* **2022**, *12*, 7910. [CrossRef]
30. Kaur, H.; Rauwel, P.; Rauwel, E. Chapter 6—Antimicrobial Nanoparticles: Synthesis, Mechanism of Actions. In *Antimicrobial Activity of Nanoparticles*; Guisbiers, G., Ed.; Advanced Topics in Biomaterials; Elsevier: Amsterdam, The Netherlands, 2023; pp. 155–202; ISBN 978-0-12-821637-8.
31. Ghaffari, S.-B.; Sarrafzadeh, M.-H.; Salami, M.; Alvandi, A. A Comparative Study of the Action Mechanisms and Development Strategies of Different ZnO-Based Nanostructures in Antibacterial and Anticancer Applications. *J. Drug Deliv. Sci. Technol.* **2024**, *91*, 105221. [CrossRef]
32. Sharma, S.; Kumar, K.; Thakur, N.; Chauhan, S.; Chauhan, M.S. The Effect of Shape and Size of ZnO Nanoparticles on Their Antimicrobial and Photocatalytic Activities: A Green Approach. *Bull. Mater. Sci.* **2020**, *43*, 20. [CrossRef]
33. Jaiswal, P.B.; Jejurikar, S.; Mondal, A.; Pushkar, B.; Mazumdar, S. Antibacterial Effects of ZnO Nanodisks: Shape Effect of the Nanostructure on the Lethality in *Escherichia coli*. *Appl. Biochem. Biotechnol.* **2023**, *195*, 3067–3095. [CrossRef]

34. Motelica, L.; Oprea, O.-C.; Vasile, B.-S.; Ficai, A.; Ficai, D.; Andronescu, E.; Holban, A.M. Antibacterial Activity of Solvothermal Obtained ZnO Nanoparticles with Different Morphology and Photocatalytic Activity against a Dye Mixture: Methylene Blue, Rhodamine B and Methyl Orange. *Int. J. Mol. Sci.* **2023**, *24*, 5677. [CrossRef]
35. Zubair, N.; Akhtar, K. Morphology Controlled Synthesis of ZnO Nanoparticles for In-Vitro Evaluation of Antibacterial Activity. *Trans. Nonferrous Met. Soc. China* **2020**, *30*, 1605–1614. [CrossRef]
36. Gharpure, S.; Ankamwar, B. Synthesis and Antimicrobial Properties of Zinc Oxide Nanoparticles. *J. Nanosci. Nanotechnol.* **2020**, *20*, 5977–5996. [CrossRef] [PubMed]
37. Droepenu, E.K.; Amenyogbe, E.; Boatemaa, M.A.; Opoku, E. Study of the Antimicrobial Activity of Zinc Oxide Nanostructures Mediated by Two Morphological Structures of Leaf Extracts of *Eucalyptus robusta* Sm. *Heliyon* **2024**, *10*, e25590. [CrossRef] [PubMed]
38. Lallo da Silva, B.; Caetano, B.L.; Chiari-Andréo, B.G.; Pietro, R.C.L.R.; Chiavacci, L.A. Increased Antibacterial Activity of ZnO Nanoparticles: Influence of Size and Surface Modification. *Colloids Surf. B Biointerfaces* **2019**, *177*, 440–447. [CrossRef] [PubMed]
39. Bouttier-Figueroa, D.C.; Cortez-Valadez, M.; Flores-Acosta, M.; Robles-Zepeda, R.E. Green Synthesis of Zinc Oxide Nanoparticles Using Plant Extracts and Their Antimicrobial Activity. *BioNanoSci* **2024**. [CrossRef]
40. Aldeen, T.S.; Ahmed Mohamed, H.E.; Maaza, M. ZnO Nanoparticles Prepared via a Green Synthesis Approach: Physical Properties, Photocatalytic and Antibacterial Activity. *J. Phys. Chem. Solids* **2022**, *160*, 110313. [CrossRef]
41. Awasthi, A.; Sharma, P.; Jangir, L.; Kamakshi; Awasthi, G.; Awasthi, K.K.; Awasthi, K. Dose Dependent Enhanced Antibacterial Effects and Reduced Biofilm Activity against *Bacillus Subtilis* in Presence of ZnO Nanoparticles. *Mater. Sci. Eng. C* **2020**, *113*, 111021. [CrossRef]
42. Dadi, R.; Kerignard, E.; Traoré, M.; Mielcareck, C.; Kanaev, A.; Azouani, R. Evaluation of Antibacterial Efficiency of Zinc Oxide Thin Films Nanoparticles against Nosocomial Bacterial Strains. *Chem. Eng. Trans.* **2021**, *84*, 13–18. [CrossRef]
43. Wang, F.; Qi, J.; Zhu, L. Ag/MoS_2 Nanozyme-Modified ZnO Nanopillar Surface for Enhanced Synergistic Mechanical and Chemical Antibacterial Activity. *Colloids Surf. A Physicochem. Eng. Asp.* **2024**, *687*, 133494. [CrossRef]
44. Zaman, Y.; Ishaque, M.Z.; Waris, K.; Shahzad, M.; Siddique, A.B.; Arshad, M.I.; Zaman, H.; Ali, H.M.; Kanwal, F.; Aslam, M.; et al. Modified Physical Properties of Ni Doped ZnO NPs as Potential Photocatalyst and Antibacterial Agents. *Arab. J. Chem.* **2023**, *16*, 105230. [CrossRef]
45. Xiang, E.; Moran, C.S.; Ivanovski, S.; Abdal-hay, A. Nanosurface Texturing for Enhancing the Antibacterial Effect of Biodegradable Metal Zinc: Surface Modifications. *Nanomaterials* **2023**, *13*, 2022. [CrossRef] [PubMed]
46. Xu, L.; Liang, H.-W.; Yang, Y.; Yu, S.-H. Stability and Reactivity: Positive and Negative Aspects for Nanoparticle Processing. *Chem. Rev.* **2018**, *118*, 3209–3250. [CrossRef]
47. Amodeo, J.; Pizzagalli, L. Modeling the Mechanical Properties of Nanoparticles: A Review. *C. R. Phys.* **2021**, *22*, 35–66. [CrossRef]
48. Mirhosseini, F.; Amiri, M.; Daneshkazemi, A.; Zandi, H.; Javadi, Z.S. Antimicrobial Effect of Different Sizes of Nano Zinc Oxide on Oral Microorganisms. *Front. Dent.* **2019**, *16*, 105–112. [CrossRef]
49. Raghupathi, K.R.; Koodali, R.T.; Manna, A.C. Size-Dependent Bacterial Growth Inhibition and Mechanism of Antibacterial Activity of Zinc Oxide Nanoparticles. *Langmuir* **2011**, *27*, 4020–4028. [CrossRef]
50. El-Habib, I.; Roynette, A.; Morakchi-Goudjil, H.; Lemarchand, A.; Christine, M.; Azouani, R.; Traore, M. Synthesis by Soft Chemistry of Size-Controlled Zinc Oxide (ZnO) Nanocrystals for Antimicrobial Applications. *MATEC Web Conf.* **2023**, *379*, 06003. [CrossRef]
51. Luo, Z.; Zhu, M.; Guo, M.; Lian, Z.; Tong, W.; Wang, J.; Zhang, B.; Wei, W. Ultrasonic-Assisted Dispersion of ZnO Nanoparticles and Its Inhibition Activity to *Trichoderma viride*. *J. Nanosci. Nanotechnol.* **2018**, *18*, 2352–2360. [CrossRef]
52. *ISO 22196:2011(En)*; Measurement of Antibacterial Activity on Plastics and Other Non-Porous Surfaces. ISO: Geneva, Switzerland, 2011. Available online: https://www.iso.org/obp/ui/#iso:std:iso:22196:ed-2:v1:en (accessed on 18 March 2024).
53. Pasquet, J.; Chevalier, Y.; Couval, E.; Bouvier, D.; Noizet, G.; Morlière, C.; Bolzinger, M.-A. Antimicrobial Activity of Zinc Oxide Particles on Five Micro-Organisms of the Challenge Tests Related to Their Physicochemical Properties. *Int. J. Pharm.* **2014**, *460*, 92–100. [CrossRef] [PubMed]
54. Jones, N.; Ray, B.; Ranjit, K.T.; Manna, A.C. Antibacterial Activity of ZnO Nanoparticle Suspensions on a Broad Spectrum of Microorganisms. *FEMS Microbiol. Lett.* **2008**, *279*, 71–76. [CrossRef]
55. Palanikumar, L.; Ramasamy, S.N.; Balachandran, C. Size-Dependent Antimicrobial Response of Zinc Oxide Nanoparticles. *IET Nanobiotechnol.* **2014**, *8*, 111–117. [CrossRef]
56. Azam, A.; Ahmed, A.S.; Oves, M.; Khan, M.; Memic, A. Size-Dependent Antimicrobial Properties of CuO Nanoparticles against Gram-Positive and -Negative Bacterial Strains. *Int. J. Nanomed.* **2012**, *7*, 3527–3535. [CrossRef] [PubMed]
57. Lallo da Silva, B.; Abuçafy, M.P.; Berbel Manaia, E.; Oshiro Junior, J.A.; Chiari-Andréo, B.G.; Pietro, R.C.R.; Chiavacci, L.A. Relationship Between Structure And Antimicrobial Activity Of Zinc Oxide Nanoparticles: An Overview. *Int. J. Nanomed.* **2019**, *14*, 9395–9410. [CrossRef]
58. Applerot, G.; Lipovsky, A.; Dror, R.; Perkas, N.; Nitzan, Y.; Lubart, R.; Gedanken, A. Enhanced Antibacterial Activity of Nanocrystalline ZnO Due to Increased ROS-Mediated Cell Injury. *Adv. Funct. Mater.* **2009**, *19*, 842–852. [CrossRef]
59. Álvarez-Chimal, R.; García-Pérez, V.I.; Álvarez-Pérez, M.A.; Tavera-Hernández, R.; Reyes-Carmona, L.; Martínez-Hernández, M.; Arenas-Alatorre, J.Á. Influence of the Particle Size on the Antibacterial Activity of Green Synthesized Zinc Oxide Nanoparticles Using *Dysphania Ambrosioides* Extract, Supported by Molecular Docking Analysis. *Arab. J. Chem.* **2022**, *15*, 103804. [CrossRef]

60. Aldin, K.S.; Al-Hariri, S.; Ali-Nizam, A. Effectiveness of ZnO Nano Particles against the Foodborne Microbial Pathogens *E. coli* and *S. aureus*. *Jordan J. Chem. (JJC)* **2020**, *15*, 87–94. [CrossRef]
61. Grossich, R.; Lemos Vilches, M.; Costa, C.S.; Pezzoni, M. Role of Pel and Psl Polysaccharides in the Response of *Pseudomonas aeruginosa* to Environmental Challenges: Oxidative Stress Agents (UVA, H_2O_2, Sodium Hypochlorite) and Its Competitor *Staphylococcus aureus*. *Microbiology* **2023**, *169*, 001301. [CrossRef] [PubMed]
62. Pang, Z.; Raudonis, R.; Glick, B.R.; Lin, T.-J.; Cheng, Z. Antibiotic Resistance in Pseudomonas Aeruginosa: Mechanisms and Alternative Therapeutic Strategies. *Biotechnol. Adv.* **2019**, *37*, 177–192. [CrossRef] [PubMed]
63. Baek, S.; Joo, S.H.; Kumar, N.; Toborek, M. Antibacterial Effect and Toxicity Pathways of Industrial and Sunscreen ZnO Nanoparticles on *Escherichia coli*. *J. Environ. Chem. Eng.* **2017**, *5*, 3024–3032. [CrossRef]
64. Fiori, J.; Silva, L.; Picolli, K.C.; Ternus, R.; Ilha, J.; Decalton, F.; de Mello, J.M.; Riella, H.; Fiori, M. Zinc Oxide Nanoparticles as Antimicrobial Additive for Acrylic Paint. *Mater. Sci. Forum* **2017**, *899*, 248–253. [CrossRef]
65. Agustin, W.; Albari, M.T.; Ghifari, M.A.; Ghifari, M.R.; Purnamasari, D.; Mandeli, R.S. The Antibacterial Properties of Paint with the Addition of ZnO Nanoparticles. *AIP Conf. Proc.* **2024**, *3001*, 030004. [CrossRef]
66. Foudi, H.; Soukeur, A.; Rekhila, G.; Trari, M.; Amara, M. Synthesis and Characterization of ZnO Nanoparticles for Antibacterial Paints. *Chem. Pap.* **2023**, *77*, 1489–1496. [CrossRef]

Journal of
Functional
Biomaterials

MDPI

Systematic Review

Prosthetic Joint Infection Research Models in NZW Rabbits: Opportunities for Standardization—A Systematic Review

Julia L. van Agtmaal [1], Sanne W. G. van Hoogstraten [1] and Jacobus J. C. Arts [1,2,*]

[1] Laboratory for Experimental Orthopaedics, Department of Orthopaedic Surgery, Care and Public Health Research Institute (CAPHRI), Maastricht University Medical Centre, 6229 Maastricht, The Netherlands; julia.vanagtmaal@maastrichtuniversity.nl (J.L.v.A.); s.vanhoogstraten@maastrichtuniversity.nl (S.W.G.v.H.)
[2] Department of Biomedical Engineering, Orthopaedic Biomechanics, Eindhoven University of Technology, 5612 Eindhoven, The Netherlands
* Correspondence: j.arts@mumc.nl

Abstract: Prosthetic joint infection (PJI) is a major complication following total arthroplasty. Rising antimicrobial resistance (AMR) to antibiotics will further increase therapeutic insufficiency. New antibacterial technologies are being developed to prevent PJI. In vivo models are still needed to bridge the translational gap to clinical implementation. Though rabbit models have been used most frequently, there is no consensus about methodology and measured outcomes. The PubMed, Scopus, and EMBASE databases were searched for literature on PJI in rabbit models. Data extraction included bias control, experimental design, and outcome measures of the NZW rabbit models in the articles. A total of 60 articles were included in this systematic literature review. The articles were divided into six groups based on the PJI intervention: no intervention used (21%), revision surgery (14%), prevention with only antibiotics (21%), prevention with surface modifications (7%), prevention with coatings (23%), and others (14%). Despite the current availability of guidelines and recommendations regarding experimental design, bias control, and outcome measures, many articles neglect to report on these matters. Ultimately, this analysis aims to assist researchers in determining suitable clinically relevant methodologies and outcome measures for in vivo PJI models using NZW rabbits to test new antimicrobial technologies.

Keywords: prosthetic joint infection; NZW rabbit; in vivo; antibacterial technologies; ARRIVE guidelines

1. Introduction

Up to 1 million total hip arthroplasties (THAs) and total knee arthroplasties (TKAs) are performed in the United States every year [1]. With an increasingly aging population, and rising risk factors such as malnutrition, obesity, or other co-morbidities such as osteoarthritis, the total number of THAs and TKAs is expected to grow even further [1–3]. Kurtz et al. [4] have stated that by 2030 this number is predicted to increase by 174% for THA and 673% for TKA. Though THA and TKA generally lead to patient satisfaction, prosthetic joint infection (PJI) following primary TKA and THA arises in 1–2% of all surgeries [1,5–8]. Delayed healing, inadequate functional outcome, decreased quality of life, and increased mortality occur as a consequence of PJI [6,9]. PJI increases hospital resources immensely, increasing the economic burden on the healthcare system [10]. PJI is a significant contributor to primary THA and TKA failure and is responsible for 30–40% of all failures in revision THAs and TKAs [1,5,7]. With an increasing number of THAs and TKAs, the incidence of PJI will likely also further increase.

Currently, most PJIs are caused by the Gram-positive bacteria *Staphylococcus aureus* (*S. aureus*) and *Staphylococcus epidermidis* (*S. epidermidis*) [7,9,11]. However, the rate of PJIs caused by Gram-negative bacteria has increased, reaching up to 40% in TKA and total shoulder arthroplasty (TSA) [12].

Currently, the standard of care to treat PJI and biofilms is to start with high-dose antibiotics [13]. If the infection is not cleared by antibiotics alone, the surgical options are debridement with a one- or two-staged revision, or debridement, antibiotics, and implant retention (DAIR) procedures [13,14]. However, bacteria can form biofilms: an accumulation of tightly packed bacteria on the implant, encased by an extracellular matrix that protects the bacteria [15]. Once bacteria have adhered to the surface of the implant, and have won the so-called race for the surface and colonized the implant surface, biofilm formation happens rapidly and hampers host tissue cell function [16].

Biofilm formation is not limited to the implant; it can be dispersed to the bone, bone cement, synovial fluid, and tissue surrounding the bone [7]. This extracellular matrix mainly consists of proteins, polysaccharides, and extracellular DNA [17]. Biofilm formation consists of four stages: bacterial adhesion, biofilm formation, biofilm maturation, and biofilm dispersal. Biofilm dispersal means that not only does the PJI persist, but other body sites can also become infected [15]. The biofilm forms a physical barrier, slowing antibiotic diffusion and hindering the patient's internal immune cells, allowing the PJI to continue [13,15,18,19]. Bacteria within a biofilm are 500–5000 times less susceptible to antibiotics as compared to planktonic bacteria, creating "persister cells" that are dormant, highly tolerant to antibiotics, and reactivated when treatment has stopped [13]. Moreover, due to systemic overuse and misuse of antibiotics, the incidence of antimicrobial resistance (AMR) to antibiotics is growing fast, putting patients with PJIs at risk of therapeutic insufficiency [9,20,21]. PJI and AMR are, therefore, an ever-growing threat, and new technologies are needed to prevent bacterial attachment and biofilm formation on the implant surface.

Research into developing treatment or prevention options for PJI and biofilm formation has become increasingly prevalent, focusing on new antibacterial coatings, surface designs, or other compounds to protect implants, with or without antibiotics. There are three main antimicrobial mechanisms for antibacterial coatings: anti-fouling or non-adhesive, contact-killing, and antimicrobial-releasing [22]. Multiple in vitro test methods are available to test these technologies, where the choice of in vitro test depends on the antimicrobial mechanism [22]. However, studies have shown that in vitro results do not necessarily translate to in vivo results [23,24]. This is due to a lack of standardization in in vitro testing, a lack of clinically relevant test protocols, and the complexity of in vivo systems [23]. Several important in vivo factors cannot be replicated or integrated easily in vitro. First, in vitro tests are often performed under static conditions, whereas fluid flow may influence the in vivo results [25]. Also, the immune response is excluded in in vitro testing, neglecting the effect of the antimicrobial on the immune system and the impact of the immune system on biofilm formation [26]. Furthermore, antimicrobials may bind to blood serum proteins, which can alter their effect [27]. In addition, quorum sensing is a communication system used by bacteria to control biofilm formation, which is often disregarded in vitro [25]. Last, a high hammering force is applied during THA and TKA surgeries, possibly creating microfractures and affecting the implant coating by scratching or damaging them [28]. Testing the mechanical properties of antibacterial coatings is often overlooked. Therefore, preclinical in vivo models are needed to study both the host response and integration of the implant, as well as the interaction with pathogens, to bridge the translational gap to the clinic [24]. Additionally, the Food and Drug Administration (FDA) and the Medical Device Regulation (MDR) emphasize the importance of in vivo experimentation as a critical step before clinical studies. In vivo tests are essential to test the biocompatibility, safety, infection prevention efficacy, and tissue response to the implant and the new antimicrobial compounds.

Rabbits have been used in up to 35% of musculoskeletal in vivo models, and most frequently to study PJI in vivo [29–31]. In particular, New Zealand White (NZW) rabbits are most commonly used [32]. They are docile, non-aggressive, and easy to handle and observe, yet still large enough to implement orthopedic implants [30,33]. The bone and joint biology and the response to infections of rabbits mimic that of human joint infections. This similarity

in infection susceptibility, pathogenesis, and immune response is crucial when evaluating PJI and the effectiveness of antimicrobial treatments for clinical applications [30,34]. In contrast, rats and mice, the most frequently used animals in testing, are less susceptible to infection than rabbits [32,34]. Also, rabbits are relatively low in cost and take up limited space, compared to large animal models [33].

Though rabbit models have been used widely to study PJI and new antimicrobial technologies, there is no consensus about the exact methodology and outcome measures [24,35]. Moriarty et al. [24] state that many common errors are still made in these in vivo studies, such as not quantifying the bacteria. Due to these discrepancies in methodologies and outcomes, antibacterial techniques cannot be compared to one other, and it remains unclear when a technique's antibacterial efficacy is good enough to progress to a larger animal model or clinical studies. Furthermore, papers often fail to document all aspects of their studies according to the ARRIVE guidelines, a checklist of recommendations for the full and transparent reporting of research involving animals [36]. Due to this unclarity, more rabbits are currently being used than necessary. Reporting information is important to avoid the repetition of experiments and unnecessarily using animals in inconclusive research [37]. It is important to use animals responsibly, improve the treatment of the animals, and increase the quality of the studies by implementing Russel and Burch's 3R principles: reduction, refinement, and replacement [38].

A review of NZW rabbit models to study PJI and treatment interventions, and the applied methodologies of these studies, is necessary to increase standardization in these models. Therefore, this systematic review will focus on the methodology and measured outcomes in in vivo models that mimic PJI in NZW rabbits. First, similarities in methodologies and outcome parameters among the included studies will be identified. Second, areas that present opportunities for methodological standardization will be defined and discussed. The bias control, experimental design, and experimental outcomes of all included studies will be assessed to do this. Ultimately, this analysis aims to assist researchers in determining suitable clinically relevant methodologies and outcome assessments in an in vivo PJI model using NZW rabbits to test new antimicrobial technologies. This can result in more standardization and a better assessment of the antibacterial potential of new technologies to prevent or treat PJI using in vivo NZW rabbit models. To conclude, this systematic review will provide a comprehensive analysis of current methodologies and outcomes measured in NZW rabbit PJI models, aiming to enhance standardization and improve the evaluation of antimicrobial interventions.

2. Methods

This literature search was conducted according to the Preferred Reporting Items for Systematic Reviews and Meta-Analysis (PRISMA) guidelines [39], and it was registered in the International Prospective Register of Systematic Reviews (PROSPERO, ID number CRD42024411818, York, UK). The PubMed, Scopus, and EMBASE databases were used to search the literature on 8 May 2024. The English language was used as a selection filter for the database searches. For PubMed, the following search string was used: ((“prosthesis-related infections” [MeSH]) OR “PJI” OR “prosthetic joint infection” OR “joint replacement infection” OR “arthroplasty infection” OR “implant infection” OR ((“osteomyelitis” [MeSH]) AND “implant”) OR (“orthopaedic infection” AND “implant”) OR (“bone infection” AND “implant”) OR “prosthetic infection” OR “peri-prosthetic infection” OR “implant-related infection” OR “DAIR”) AND ((“rabbits” [MeSH]) OR (“lagomorpha” [MeSH])) AND (“experimental model” OR (“models, animal” [MeSH]) OR “preclinical model” OR “in vivo”). This search string was adapted to conform to the Scopus database and can be found in Appendix A. Lastly, the search for EMBASE is shown in Appendix A, Table A1. Osteomyelitis and DAIR were included in the search strings, as certain studies utilize models pertinent to PJI, even though they are not the focus of this research.

Using Covidence™ (Veritas Health Innovation, Melbourne, Australia) [40], an online software platform designed to streamline the process of conducting systematic reviews,

all article abstracts were screened individually and blinded by two reviewers (J.v.A. and S.v.H.). Articles focusing on rabbit models used to study orthopedic implant infections were included for further full-text screening. During the full-text screening, articles were excluded based on multiple criteria. Firstly, the applied exclusion criteria based on publication criteria were used: articles published before 2000, review articles or discussions, conference abstracts, letters to the editor, studies that were not published in peer-reviewed journals, non-English studies, and non-retrievable studies. Secondly, based on study type, the following exclusion criteria were applied: in vitro studies, in vivo studies on animals other than NZW rabbits, and clinical trials. Thirdly, based on the relevance of the articles, the applied exclusion criteria were infections unrelated to bone or orthopedics, studies that investigate interventions that are not relevant to PJI, studies that use implants that are not for joints, studies about FRI or DAIR that did not use models relevant to PJI, studies that do not use a bacterial inoculum or that grow biofilm in vitro before the operation, and studies that do not use an implant. Lastly, based on reporting criteria, the applied exclusion criteria were studies that do not report on outcomes such as infection rates, microbiological findings, histopathological findings, and implant-related complications. Articles that investigated bone cement or bone void-filling biomaterials were only included if their intended use was a two-stage revision as a solution for PJI. If the two independent researchers could not decide on conflicting articles, a third independent reviewer (J.A.) evaluated the article. Finally, after the screening process, data extraction was performed, including bias control, experimental design, and outcome measures. Data extraction was performed by one reviewer, and 33% of the articles were cross-checked by the second reviewer.

3. PRISMA Results and Data Extraction

A total of 575 studies were found on the three databases PubMed, Scopus, and Embase, of which 295 remained after duplicate removal (Figure 1). During the abstract screening, 107 studies were excluded due to their content being unrelated to rabbit models used to study orthopedic implants and infections. Of these 107 studies, a consensus was reached for all but four by the first two researchers. Assessment of these four articles was completed by the third reviewer (J.A.). Of the remaining 188 studies of which the full texts were assessed for eligibility, 128 were excluded (Figure 1). Only four of these studies had to be assessed by the third reviewer (J.A.) due to a lack of consensus among the first two researchers. The main reasons for exclusion were that the articles studied osteomyelitis (n = 32) or FRI models (n = 22). This left 60 studies for extraction. The first researcher (J.v.A.) carried out the extraction of the 60 articles. The second researcher (S.v.H.) cross-checked 20 of these articles. The data extracted by both researchers was highly comparable; therefore, not all articles were extracted by the second researcher.

The data extraction was divided into three parts: bias control, experimental design methodology, and measured outcomes. As is displayed in Table 1, the section on bias control focused on the blinding and randomization of the studies, the rabbit characteristics, humane endpoints, and care of the rabbits. The section on experimental design methodology is described in Tables 2 and 3. This section includes the aim and duration of the study, and information about the inoculum, implant, interventions, and experimental groups, including dropout percentage per group. The measured outcomes of each study are shown in Tables 4 and 5. This table focuses on bacterial culture, health monitoring, hematology, histology, and staining. Based on the interventions against PJI that were found in all included articles, the articles were divided into six groups: no intervention used against PJI, revision surgery, prevention of PJI with only antibiotics, prevention of PJI with surface modifications, prevention of PJI with coatings, and others (Figure 2).

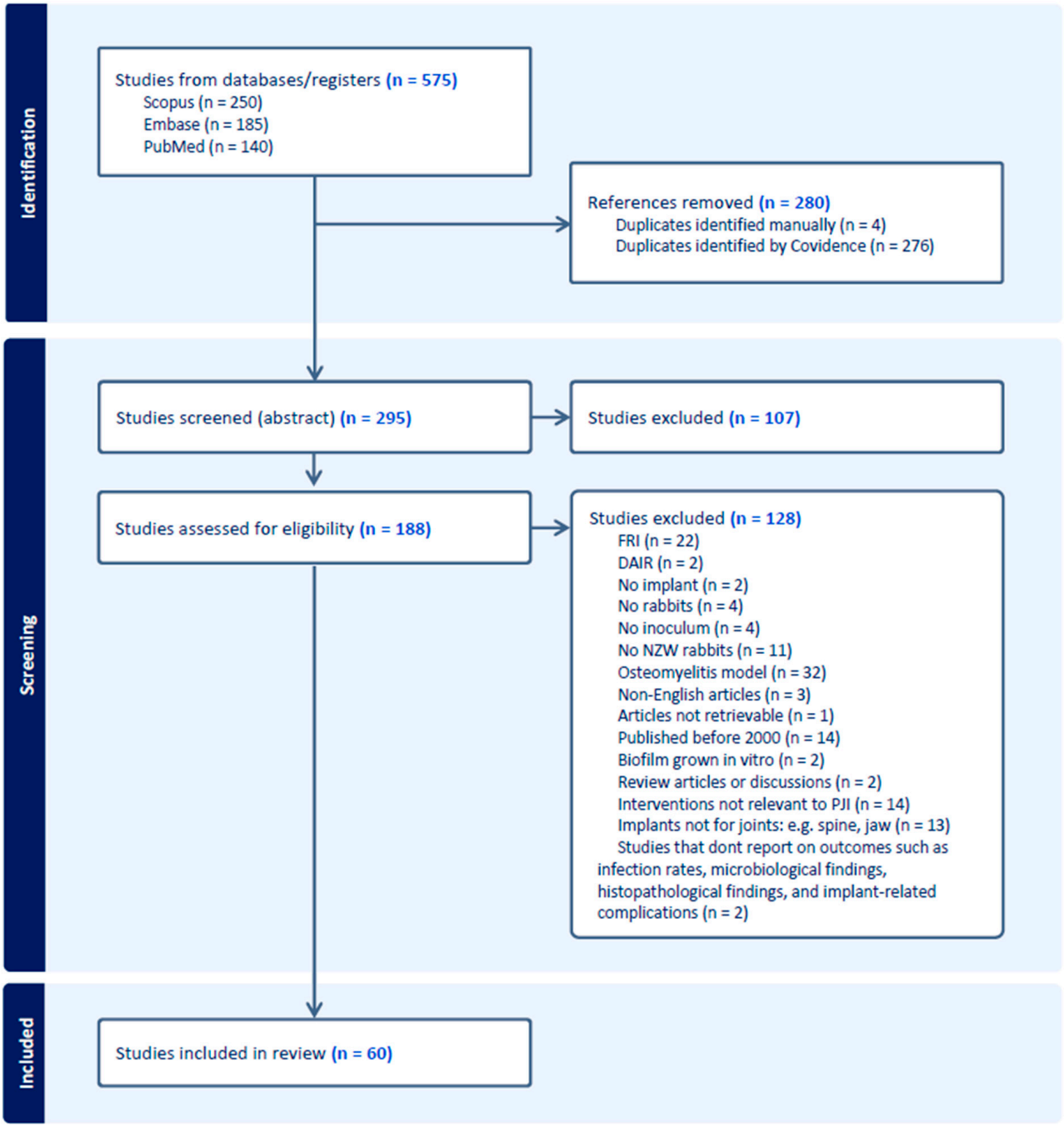

Figure 1. PRISMA flow diagram of article selection. The database search resulted in a total of 575 studies. After duplicate removal and screening, 60 studies were left for data extraction.

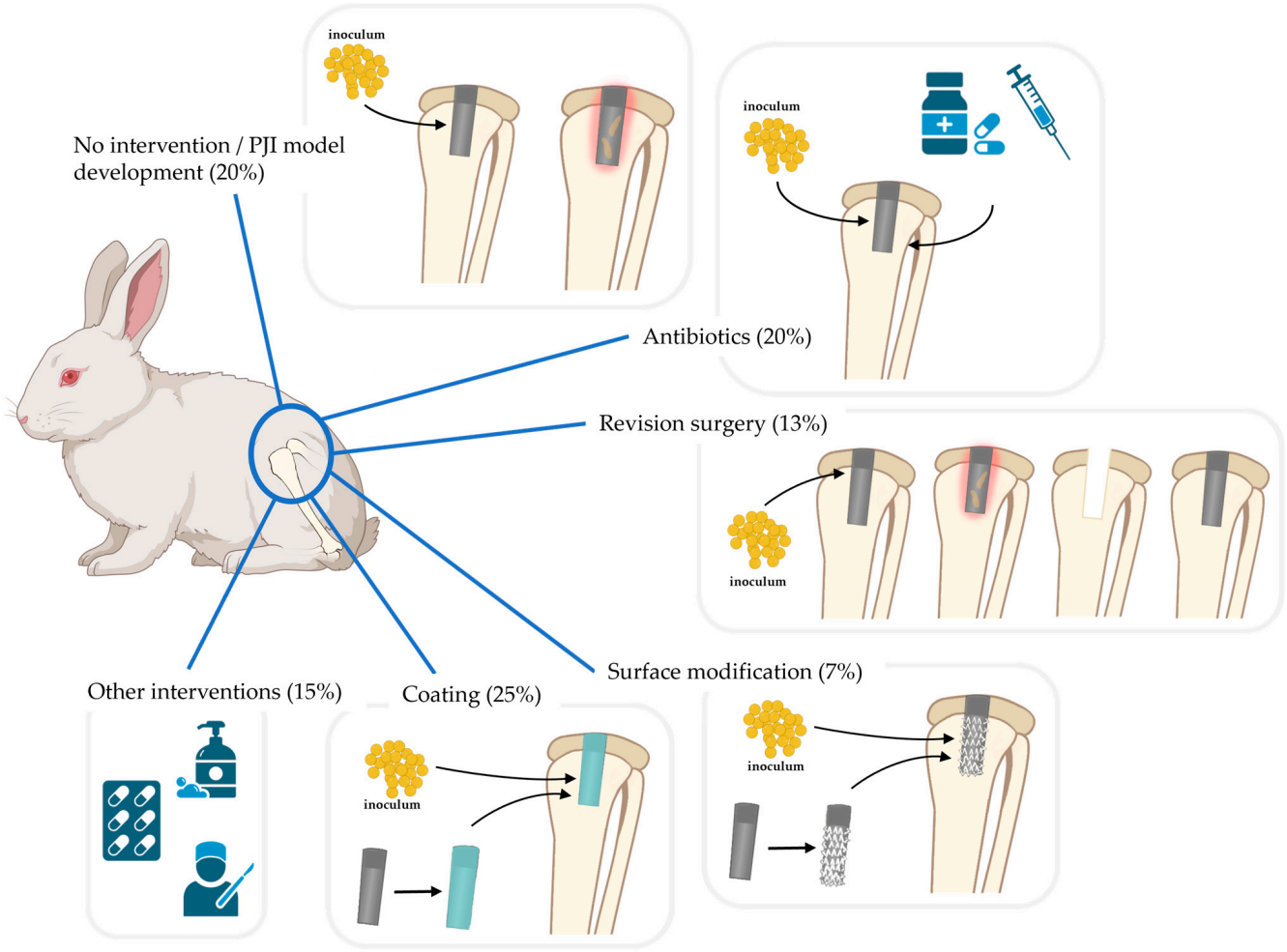

Figure 2. Interventions used in the NZW rabbit PJI models in the articles included in this review. Articles studied no intervention/PJI model development (20%); antibiotics alone as prevention for PJI (20%); revision surgery as treatment for PJI (13%); surface modification of the implant as prevention for PJI (7%); coating on the implant as prevention for PJI (25%); or other interventions (15%). Created with Biorender.com (accessed on 14 May 2024).

4. NZW Rabbit Models to Investigate PJI

This systematic review focused on in vivo models to investigate PJI and antimicrobial technologies in New Zealand White (NZW) rabbits. The 57 included studies were grouped based on the intervention used against PJI. This categorization showed that 20% of the articles used no intervention against PJI in their research (Figure 2), which implies that all these studies were developing or validating a new rabbit PJI model. This number of model development papers emphasizes the need for standardized guidelines to set up a suitable, clinically relevant, in vivo PJI model in NZW rabbits. This need for standardized criteria was previously highlighted during the 2023 international consensus meeting on musculoskeletal infection (MSKI) [41]. Standardization will result in a reduction in animal use. Furthermore, with the rise of antimicrobial resistance (AMR) to antibiotics [9,20,21], it is noteworthy that 20% of all articles investigated existing and on-the-market antibiotics as the only antimicrobial agent. The other studies were categorized as revision surgery (13%), which included one- and two-stage revision; surface modifications of the implant (7%), like polishing; implant coatings (25%); and other interventions that did not fit the different categories (15%). All studies were reviewed on their bias control, experimental design, and reported outcomes.

4.1. Bias Control

Bias should always be avoided in research [24]. Table 1 shows how bias control was handled in all reviewed studies. Bias control in in vivo studies is essential for maintaining research integrity, validity, and ethical conduct. Furthermore, bias control enhances the reliability and reproducibility of research findings. Therefore, translating results from preclinical in vivo animal studies towards clinical studies depends on bias control [23,42]. First, as stated by Moriarty et al. [24], blinding and randomization are the minimal requirements to limit bias. Second, as elucidated by both the ARRIVE guidelines [43,44] and Moriarty et al. [24], reporting the animal characteristics in in vivo experiments is highly recommended to limit the effect of potential bias. Animal characteristics include the species, strain, sex, age or skeletal maturity, and weight of the animal [24,43]. These guidelines also highlight the importance of including the housing and husbandry details of an in vivo experiment [24,43]. Husbandry details also contain welfare-related assessments, including humane endpoints at which point the suffering of the rabbits is no longer justified by the scientific value the experiment provides [43,45].

4.1.1. Blinding and Randomization

The risk of bias is highly dependent on blinding and randomization in studies. As stated by Bespalov et al. [46], blinding and randomization are necessary if the study results have an impact on decision-making and cannot be easily repeated due to ethical or resource-related reasons. Both requirements are present in this review, as rabbit in vivo studies are essential before proceeding to clinical studies, and the number of used animals in research should be reduced as much as possible [46,47]. Two types of blinding should be performed: blinding the researchers performing the surgery, which minimizes the chance of performance bias, and blinding the researchers performing the analysis of the results, minimizing the risk of detection bias [46,48]. Figure 3a illustrates that in 70% of the included studies, it was not stated if the involved researcher performing the surgery was blinded to which implant, treatment, and inoculum they were inserting in the rabbits, or if the results were analyzed blinded. Only 18.3% of the studies stated that the experiments were performed blinded, and in 8.3% of the studies only the results were blinded to the researchers analyzing the data. In 3.3% of the studies, there was only one experimental group, making blinding unnecessary. This lack of blinding of the studies, or the reporting thereof, allows room for conscious or unconscious biases to influence results. Since researchers frequently face a conflict of interest in their eagerness to get their products to market, it is essential to avoid any biases.

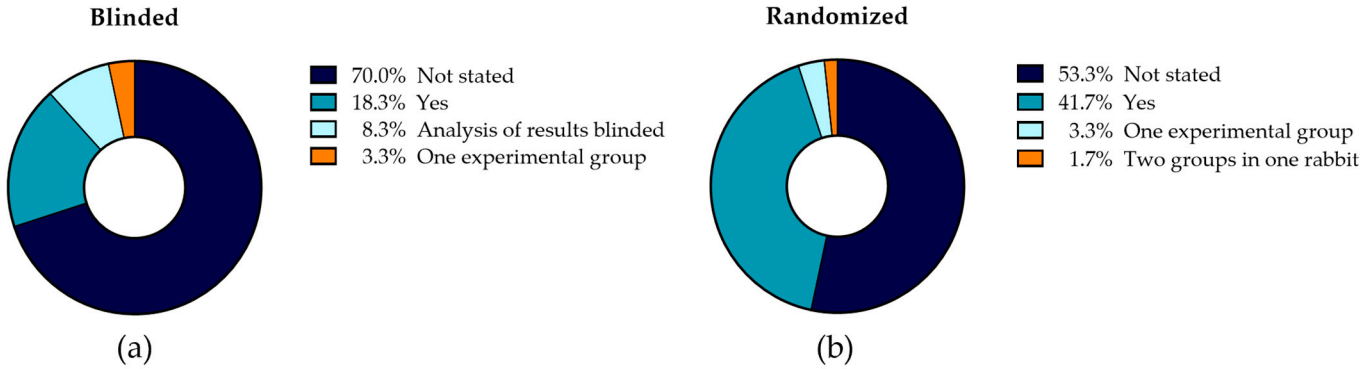

Figure 3. Analysis of bias control Table 1, including: (**a**) blinding of the studies; (**b**) randomization of the studies.

Using randomization to create experimental groups allows researchers to use probability theory to determine if outcome differences are due to chance [46]. Furthermore, randomization minimizes the chance of selection bias, reducing the chance that rabbits with preferable features are grouped. As can be seen in Figure 3b, 53.3% of the studies did

not report on the randomization of their experiment. A form of randomization was used in 41.7% of the studies to assign experimental groups to the rabbits. The remaining 5% consisted of studies in which randomization was no option because there was only one experimental group, or two experimental groups were implemented into one rabbit. The lack of randomization in more than half of the studies diminishes comparability between experimental groups. As stated before, the scarcity of documentation, blinding, and randomization found in the reviewed studies weakens the scientific integrity, reliability, and reproducibility of the studies. Notably, Laajala et al. [42] state that preclinical studies also benefit from implementing the best practices of human clinical trials. These best practices include blinding and randomization, increasing translation from preclinical to clinical studies. Variability and false positives in the intervention effects are reduced when creating randomized, blinded groups that are representative of the population that are handled and treated similarly.

4.1.2. Rabbit Characteristics

Common sources of variation within preclinical models are genetic differences, sex, age range, and weight [42,49]. These can be found in Table 1 ('rabbit characteristics'). As all included studies in this systematic review use NZW rabbits, genetic differences are limited as much as possible. As elucidated in Figure 4a–c, the sex, mean weight, and age of the rabbits are not stated in 33.3%, 18.3%, and 46.7% of the studies, respectively. The ARRIVE guidelines highly recommend including these four characteristics in animal research [43,44]. Variation in study results within experimental groups may be limited by defining which rabbits to include in the experiment and creating balanced experimental groups [42]. Unfortunately, as this information is unknown in the studies where the characteristics are not stated, this creates uncertainty about whether disparities between experimental groups are due to the different treatments or due to differences in animal characteristics.

The sex of the animals is a biological variable in research outcomes, and, as stated by the National Institutes of Health (NIH) and ARRIVE guidelines, should be taken into account and reported in all in vivo and clinical studies [43,44,50]. Males and females may differ in physiology, metabolism, hormonal profiles, and cellular functions, which can impact experimental outcomes [50]. Kunutsor et al. [51] emphasize this in their study, where they determined that males have a higher chance of developing PJI compared to females. Studying only one sex can increase bias, limit the generalizability of the results, and decrease reproducibility [50,52]. Furthermore, excluding males or females may lead to potential harm or suboptimal outcomes for the excluded population and, as follows, impair the translation to the clinic [53]. Multiple studies therefore advise including both sexes in the design of preclinical studies, to account for differences between the sexes [43,44,50,53,54].

However, no study analyzed in this systematic review included both sexes. As shown in Figure 1, most studies (38.3%) used only female rabbits, 28.3% used only male rabbits, and 33.3% did not state the sex of the rabbits. Though using both sexes in animal models is advised, several arguments exist for using only one sex. First, rabbits that are housed in pairs need to establish a hierarchy. Thurston et al. [55] demonstrated that when housed in pairs, 1% of the female pairs and 20% of the male pairs had to be separated due to fighting. Second, although males have a higher chance of developing PJI as compared to females, Mironenko et al. [56] concluded that the incidence of treatment success does not differ between the sexes in humans. Third, the higher percentage of studies that use female rabbits might be explained by their larger size, making handling the rabbits easier [57]. However, no major anatomical differences exist between surgical areas between the sexes [57,58]. Fourth, in some studies, male animals are preferred due to their hormonal stability; however, female rabbits are induced ovulaters, meaning they remain in estrus until copulation, after which ovulation starts [59]. Therefore, their hormonal balance is relatively stable as well. Last, as stated previously, there may be differences in response to PJI treatments between males and females due to, e.g., their hormonal profiles and immune response [50]. Due to this possible difference in response between male and female rabbits,

the number of rabbits per experimental group should also increase, significantly raising the study's costs. Ultimately, researchers should specify which sex they utilize in their research and provide a rationale for their choice, conforming with the ARRIVE guidelines.

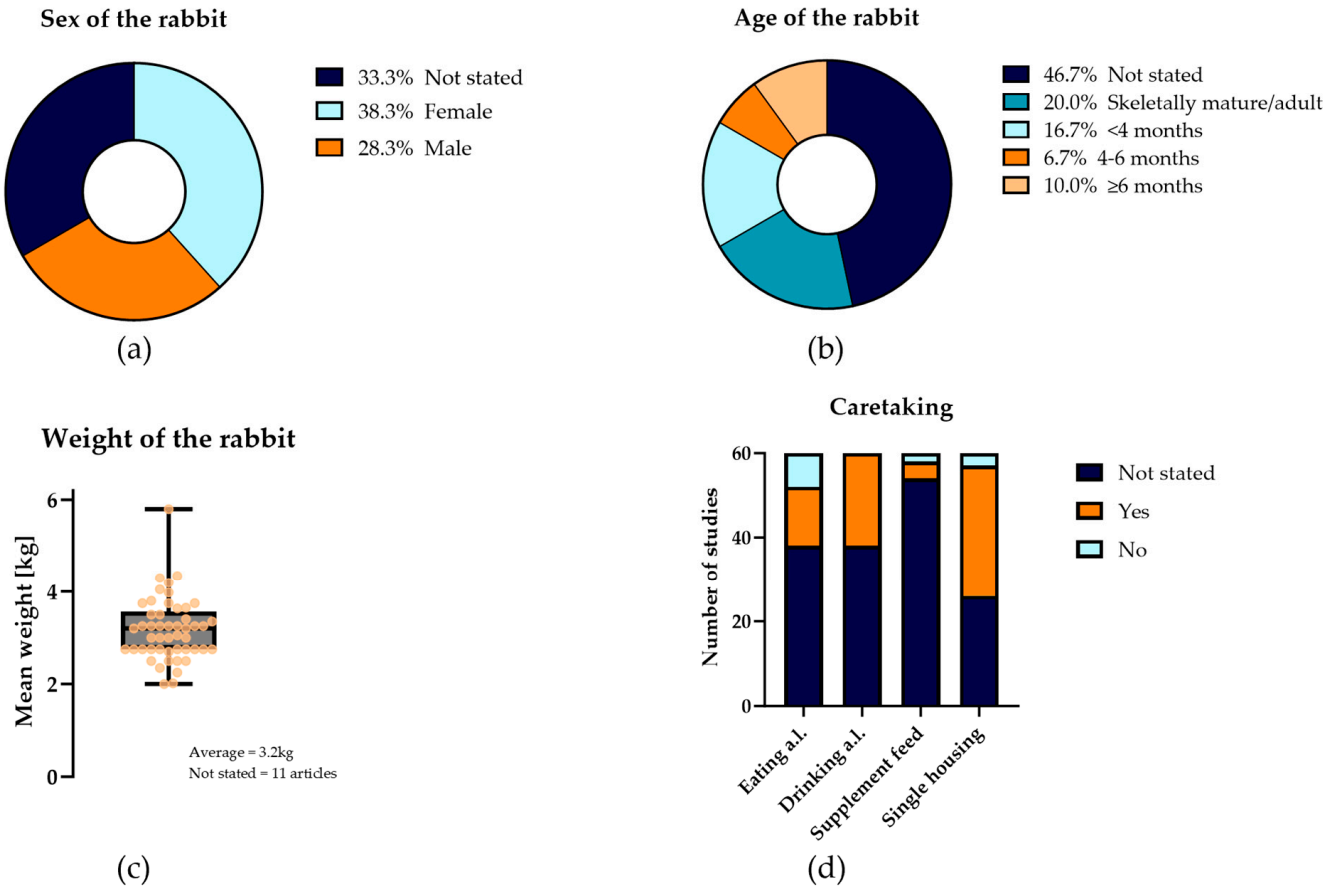

Figure 4. Analysis of bias control Table 1, including (**a**) the sex of the rabbits included in the studies; (**b**) the age of the rabbits included in the studies; (**c**) the weight of the rabbits included in the studies; (**d**) caretaking of the rabbits included in this study, including if they could eat and drink ad libitum (a.l.), if they were provided with supplemental feeding when necessary, and if they were single housed or not.

The age and starting weight of the rabbits are important factors in defining the skeletal maturity of the rabbits. Skeletal maturity is important, as a mature bone structure is essential for proper implant placement and fixation. Skeletal maturity is reached at five to six months of age [35]. Furthermore, young rabbits are less prone to infections, as maternal antibodies still protect them [60,61]. Marchandeau et al. [60] state that these antibodies both prevent infections and allow attenuated infections that activate the immune system of the young rabbit. Differentiating between the effect of these maternal antibodies and the antimicrobial compound that is tested is therefore challenging. Also, as stated by Moriarty et al. [23], PJI is most prevalent in the older human population, resulting in possible co-morbidities and altered immune systems. Using young rabbits complicates clinical translation, as they do not represent the target patient group. Masoud et al. [62] measured the growth, weight, and tibial length over 34 weeks. They concluded that skeletal growth was complete at 28 weeks. At sixteen weeks, the mean body weight was 72%, the mean body length at 91%, and the mean tibial length at 94% of the adult value. Figure 4b shows that 16.7% of the studies used rabbits younger than four months, meaning they had not yet skeletally matured. A total of 35% of the studies used skeletally mature rabbits: they were either four to six months (6.7%), older than six months (10%), or it was stated that they

were skeletally mature (20.0%). However, it would be better for papers claiming skeletal maturity to specify the exact age and starting weight of the rabbits for standardization purposes. To confirm the skeletal maturity of the rabbit, it would be most optimal to perform an X-ray to determine if the growth plates are closed [63]. The weight of adult NZW rabbits may range from 2 to 6 kg [63]. No studies included in this review reported the starting weight to be below this; however, 18% did not report on the rabbits' starting weights at all. As with the other rabbit characteristics, reporting of the age and weight of the rabbits is inadequate, despite their potential influence on the results of the experiments.

4.1.3. Housing and Husbandry

As stated previously, housing and husbandry details are important to include in performing and reporting in vivo experiments, both for the scientific value and the validity, as well as from an ethical perspective [24,43]. Housing and husbandry include the humane endpoints and the caretaking of the rabbits, as found in Table 1. For scientific value and validity, it is important to set the endpoints, as letting rabbits be included in results that are suffering too much or have comorbidities might influence the results [43,45]. Furthermore, the caretaking protocol for the rabbits should be set beforehand and precisely documented. This might otherwise result in preferential treatment of the experimental group receiving the antibacterial technique. Voehringer et al. [56] state that study designs can be more efficient. Research methods can be improved by including sufficient animal care and husbandry, which is linked to reduction and refinement [38]. A gold standard publication checklist, published by Hooijmans et al. [64,65], which integrates the reduction and refinement principle of the 3Rs, also emphasizes the need for animal husbandry and care standardization, including housing, nutrition, and water intake. Figure 4d shows that the studies included in this review often fail to report on caretaking details. It was examined whether studies reported the availability of water and food ad libitum (a.l.), the housing conditions of the rabbits (single or group housing), and whether supplemental feeding was provided when rabbits experienced significant weight loss. The details were not stated in 61% of the studies for water and food a.l., 40% for single housing conditions, and 89% for supplemental feeding.

As stated by the European Parliament in their directive on animal protection [66], death as an endpoint to a procedure should be avoided as far as possible and replaced by earlier, humane endpoints. The severity and duration of pain, distress, and suffering of the animals due to adverse effects of the surgery or treatment should be minimized and should justify the scientific value added by the research, in line with the 3Rs [67,68]. A total of 75% of the included studies in this research did not report on their humane endpoints. Several humane endpoints have been published online for when this pain and suffering no longer justify the scientific value added by the research [68]. Several humane endpoints often found in infection research in rabbits, as shown in this review, are bone fracture, severe weight loss, and infection outside the joint. Ultimately, reporting of the humane endpoints and caretaking is essential to minimize bias.

Table 1. Bias control extraction results. Abbreviations used: ns = not stated.

Reference	Bias Control		Rabbit Characteristics			Humane Endpoints	Caretaking			
	Blinded	**Randomized**	**Sex (m/f/ns)**	**Age Range or Skeletally Mature (s.m.)**	**Weight Range (kg))**	**1. Fracture 2. Weight Loss (%) 3. Infection Outside Joint 4. Persistent Swelling and Discharge 5. Other Signs of Systemic Infection (Fever, Depression)**	**Eating a.l.**	**Drinking a.l.**	**Supplemental Feed**	**Single Housing**
No intervention used										
[69]	Yes	ns	m	ns	Mean 4.2 kg	Dehiscence of surgical wound, screw exposure, MRSA expression	Yes	Yes	ns	Yes
[70]	Histology grading	ns	f	s.m.	Ns	2 (>10% in 2 weeks), 3, 4, 5	ns	ns	ns	Yes
[71]	Only 1 group	Only 1 group	f	8–12 weeks	2–3.5 kg	ns	Yes	Yes	ns	Yes
[29]	Yes	Yes	f	6 months	3.5–4 kg	1, 2 (>20%), 3	Yes	Yes	Yes	No
[72]	ns	Yes	f	ns	3.5–4 kg	1, 2 (>20%), 3	Yes	Yes	Yes	No
[73]	ns	ns	m	4 months	3–3.6 kg	ns	No	Yes	ns	Yes
[74]	ns	ns	f	74–120 days	2.9–3.5 kg	ns	ns	ns	ns	Yes
[75]	ns	Yes	f	74–120 days	1.7–3.0 kg	ns	Yes	Yes	ns	Yes
[76]	Data analysis	Yes	m	ns	3.0–3.5 kg	ns	ns	ns	ns	Yes
[77]	ns	Yes	f	~180 days	2.5–3.0 kg	1, not developing an infection in the infection group	No	Yes	ns	Yes
[78]	PET/CT results	ns	ns	ns	ns	ns	ns	ns	ns	Yes
[30]	X-ray evaluation	ns	f	ns	ns	2 (>20%)	Yes	Yes	Yes	Yes
Revision										
[79]	ns	Yes	ns	6–8 months	5.8 ± 0.24 kg	2 (>20%), 4, complete loss of function of the left limb, rejection of nutriment	ns	ns	ns	Yes
[80]	ns	ns	ns	ns	ns	ns	Yes	Yes	No	Yes
[81]	ns	Yes	f	ns	2.5–3 kg	ns	ns	ns	ns	Yes

Table 1. *Cont.*

Reference	Bias Control		Rabbit Characteristics			Humane Endpoints	Caretaking			
	Blinded	Randomized	Sex (m/f/ns)	Age Range or Skeletally Mature (s.m.)	Weight Range (kg))	1. Fracture 2. Weight Loss (%) 3. Infection Outside Joint 4. Persistent Swelling and Discharge 5. Other Signs of Systemic Infection (Fever, Depression)	Eating a.l.	Drinking a.l.	Supplemental Feed	Single Housing
[82]	ns	Yes	ns	ns	ns	ns	ns	ns	ns	ns
[83]	ns	ns	f	ns	~3 kg	No PJI 1 week after inoculation	Yes	Yes	No	ns
[84]	ns	ns	f	Adult	3000–3500 g	ns	No	Yes	ns	Yes
[85]	Yes	Yes	f	ns	3–4 kg	ns	ns	ns	ns	ns
[86]	ns	ns	f	Adult	2840–3100 g	ns	ns	ns	ns	ns
Prevention: antibiotics only										
[87]	ns	ns	m	Adult	3–4.5 kg	3	ns	ns	ns	ns
[88]	ns	Yes	f	ns	1.22–3.02 kg	ns	ns	ns	ns	ns
[89]	ns	Yes	ns	ns	3–4 kg	ns	ns	ns	ns	ns
[90]	ns	Yes	ns	ns	2.5–3 kg	ns	ns	ns	ns	Yes
[91]	ns	ns	m	Adult	2.7 ± 0.2 kg	ns	ns	Yes	ns	Yes
[92]	Yes	ns	f	7 months	3.0–3.5 kg	3	ns	ns	ns	ns
[93]	ns	Yes	m	ns	1.8–2.2 kg	ns	ns	ns	ns	ns
[94]	Yes	ns	ns	ns	2.2–2.8 kg	ns	ns	ns	ns	Yes
[95]	ns	ns	ns	ns	2.5–3 kg	ns	ns	ns	ns	ns
[96]	ns	ns	ns	ns	ns	ns	ns	ns	ns	ns
[97]	ns	Yes	ns	ns	2.5–3 kg	ns	ns	ns	ns	Yes
[98]	ns	Yes	f	>6 months	3.0–3.5 kg	ns	ns	ns	ns	ns

Table 1. *Cont.*

Reference	Bias Control		Rabbit Characteristics			Humane Endpoints	Caretaking			
	Blinded	Randomized	Sex (m/f/ns)	Age Range or Skeletally Mature (s.m.)	Weight Range (kg))	1. Fracture 2. Weight Loss (%) 3. Infection Outside Joint 4. Persistent Swelling and Discharge 5. Other Signs of Systemic Infection (Fever, Depression)	Eating a.l.	Drinking a.l.	Supplemental Feed	Single Housing
Prevention: surface modification										
[99]	ns	ns	m	ns	ns	ns	ns	ns	Yes	Yes
[100]	ns	ns	f	34 weeks	3.98 ± 0.54 kg	1, 2 (% ns), 3	ns	ns	ns	Yes
[101]	ns	ns	m	26 ± 8 weeks	3.7–3.9 kg	2 (% ns), profoundly decreased general condition	ns	ns	ns	Yes
[102]	ns	Yes	m	s.m.	3.2 ± 0.2 kg	ns	Yes	Yes	ns	Yes
Prevention: coating										
[103]	Only 1 group	Only 1 group	ns	ns	3500–5200 g	Wound dehiscence with implant exposure	ns	ns	ns	Yes
[104]	Yes	ns	f	16 weeks	ns	2 (>15%), 3, Shock	No	Yes	ns	No
[105]	Yes	ns	ns	ns	3.7–4.4 kg	ns	ns	ns	ns	ns
[106]	Histology grading	Yes	ns	Adult	3000–3500 g	ns	Yes	Yes	ns	Yes
[107]	ns	Yes	m	Adult	3000–3500 g	ns	No	Yes	ns	Yes
[108]	ns	ns	f	s.m.	4.3 ± 0.4 kg	1, 2 (>10% in 2 weeks), 3, 4, local infection with severe lameness	ns	ns	ns	ns
[109]	Yes	ns	f	ns	2.6–3.5 kg	ns	No	ns	ns	Yes
[110]	ns	ns	f	ns	ns	ns	ns	ns	ns	ns
[111]	Yes	ns	f	s.m. *1	2900–3600 g	ns	No	Yes	ns	Yes
[112]	ns	ns	m	2 months	~3 kg	ns	Yes	Yes	ns	ns
[113]	ns	Yes	m	8 months	2.5–3 kg	ns	ns	ns	ns	ns
[114]	ns	Yes	m	3 months	~2.5 kg	ns	ns	ns	ns	ns

Table 1. *Cont.*

Reference	Bias Control		Rabbit Characteristics			Humane Endpoints	Caretaking			
	Blinded	Randomized	Sex (m/f/ns)	Age Range or Skeletally Mature (s.m.)	Weight Range (kg))	1. Fracture 2. Weight Loss (%) 3. Infection Outside Joint 4. Persistent Swelling and Discharge 5. Other Signs of Systemic Infection (Fever, Depression)	Eating a.l.	Drinking a.l.	Supplemental Feed	Single Housing
[115]	ns	Yes	m	ns	2.5–3.0 kg	ns	ns	ns	ns	ns
[116]	ns	ns	m	3 months	2–3 kg	ns	Yes	Yes	ns	Yes
[117]	ns	ns	ns	3–4 months	2.5 ± 0.5 kg	ns	ns	ns	ns	ns
Other										
[118]	Yes	Yes *2	ns	ns	3.2–4.1 kg	ns	Yes	Yes	ns	ns
[119]	ns	Yes	ns	ns	ns	ns	ns	ns	ns	ns
[120]	Yes	ns	m	s.m.	3.0–3.5 kg	ns	No	Yes	ns	Yes
[121]	ns	ns	m	Adult	3045–4225 g	ns	ns	ns	ns	ns
[122]	ns	ns	ns	8–12 weeks	ns	ns	ns	ns	ns	ns
[123]	ns	Yes	ns	4–5 months	2.0–2.5 kg	ns	ns	ns	ns	ns
[124]	ns	Yes	ns	ns	2.5–3.5 kg	ns	Yes	Yes	ns	Yes
[125]	ns	ns	f	70–100 days	2.5–3.0 kg	ns	ns	ns	ns	Yes
[126]	ns	Yes	ns	ns	2.5–3.0 kg	ns	ns	ns	ns	ns

*1—The article says 'young adult'; however, the authors have been contacted and have confirmed that the growth plates were closed. *2—Each rabbit has a randomly assigned control and experimental knee.

4.2. Experimental Design

Translating the results from in vivo experiments on antibacterial technologies to the clinic is challenging [23,24]. Currently, in vivo preclinical results do not consistently anticipate clinical outcomes [23]. Choosing the right experimental design and methodology is crucial in bridging this gap as much as feasible. In addition, the research aim is inextricably connected to the experimental design. A first proof-of-concept in vivo experiment might involve different parameters compared to a final preclinical study before human trials. Tables 2 and 3 illustrate the experimental design parameters of the studies analyzed in this review, including the study's duration, inoculum and implant details, and the interventions against PJI tested in the research and in which experimental groups they were tested.

4.2.1. Study Duration

As stated above, the study aim is the leading factor determining the experimental design. This especially applies to the duration of the study. The duration of the study is dependent on the mode of action of the antibacterial technology and on what outcome measures are evaluated. The durations of the experiments in the included studies in this research are illustrated in Figure 5a, and they range from 84 days [79,103] to 2 days [110]. Studies that only look at infection progression, and not osseointegration, most often last 27 days (n = 11), 7 days (n = 8), or 14 days (n = 6). For a first pilot in vivo study for surface modifications, or contact-killing or anti-fouling coating, where the antibacterial substance should be immediately active, and that only investigates the antibacterial activity of the coating, 7 to 14 days might be sufficient. For antibacterial-releasing coatings or revision surgeries, the duration of the experiment is dependent on the time to establish an infection and the activation or release of the antibacterial substance. If the short-term functioning of the antibacterial substance has been established, testing the long-term effect should also be evaluated.

An ideal duration should be found for the antibacterial compound to work, to initiate an infection in the control group, and not prolong unnecessary animal suffering. Remarkably, two studies lasted 84 days. One of these studies was by Brunotte et al. [79], where the study was divided into four parts of 4 weeks each: initial insertion of the implant and inoculum; revision stage 1 with implant removal, debridement, and insertion of a spacer; revision stage two with spacer removal and insertion of a new implant; and euthanasia. Bitika et al. [103] also chose 84 days, as they state that this time is needed for mature osseointegration of titanium implants. However, in their study, the only outcome measures are bacterial culture and health monitoring, with no quantification of osseointegration. For the study of Brunotte et al. [79], a duration of 84 days might be justifiable, as this is needed to test the intended use of their antibacterial compound. However, for Bitika et al. [103], their antibacterial compound and study outcomes do not justify this prolonged animal suffering. In contrast, Neut et al. [110], had a study duration of only two and seven days, although they expected their CFU count for the experimental groups to be <1 log for both time points. The results from day two and day seven were comparable, and the need for the two time points is not elucidated. At two days post-surgery, the rabbits might still be recovering, which could affect some results, such as certain hematology values, making them unreliable.

In addition to the antibacterial compound's impact on infection progression, its effect on bone integration is also important. To investigate bone integration, the study duration should be sufficient for bone to remodel. The studies included in this review that investigated bone growth around the implant most frequently used 42 days (n = 7) (Figure 5a). Several of these studies concluded that six weeks was sufficient for bone apposition on the implant surfaces [72,78,98,115,127]. Efstathopoulos et al. [80] studied bone growth from two to six weeks after implant removal and insertion of enriched acrylic bone cement, and they concluded that bone remodeling was best at six weeks. Several other studies, not included in this review, that investigated bone integration of an implant found that bone formation starts at three weeks, and a rigid bone–implant interface is seen at six

weeks [128–132]. Hermida et al. [133] concluded there was no significant difference in bone-to-implant contact between six and twelve weeks. These studies suggest that six weeks is likely sufficient to assess the osseointegration of the implant and the effect of the antibacterial compound on this integration.

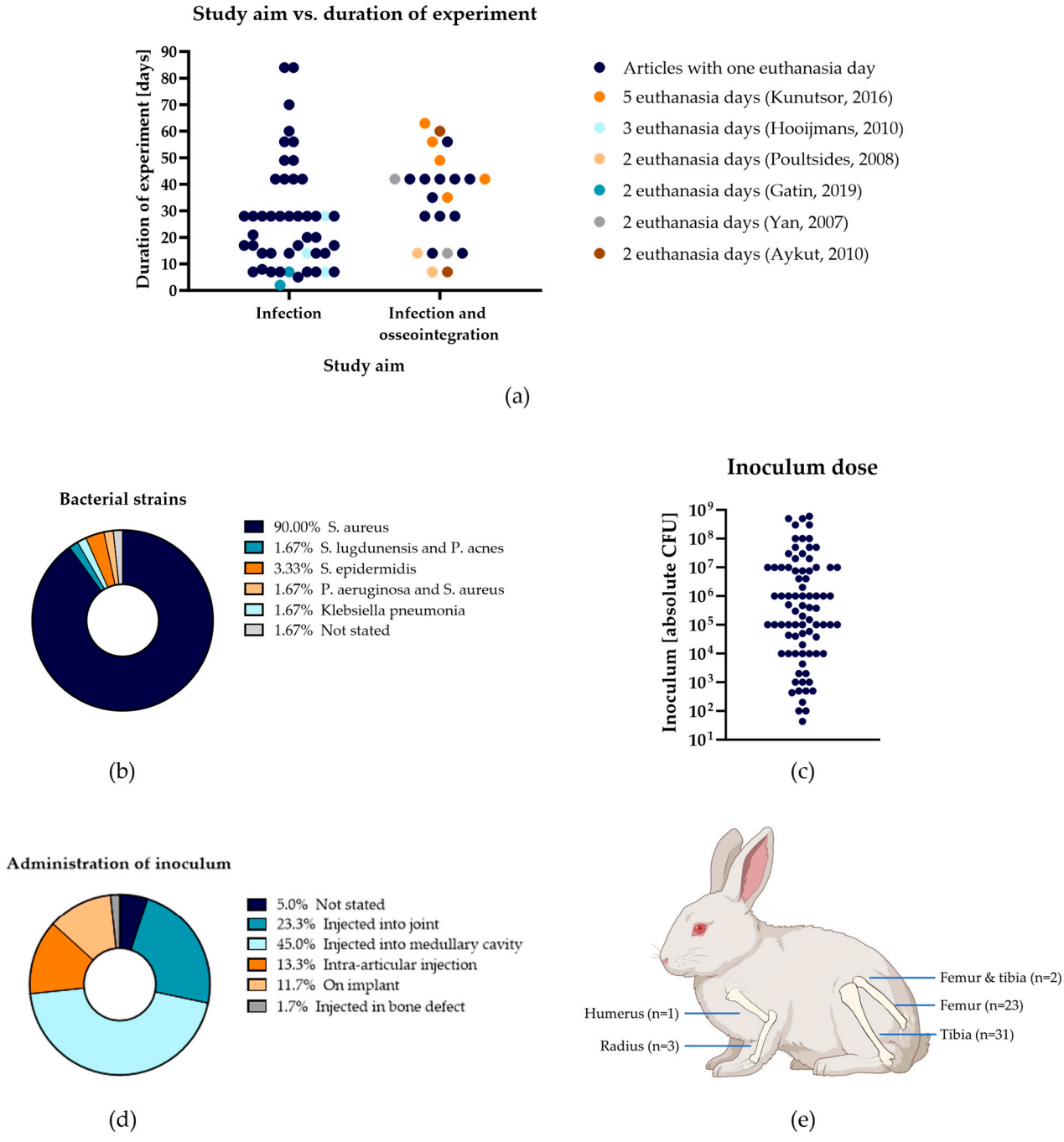

Figure 5. Analysis of the experimental design of the articles included in this review, including: (**a**) the duration of the experiments from inoculation to euthanasia for studies that only investigated infection (**left**) and studies that investigated infection and osseointegration (**right**), and articles that studied multiple study durations were colored separately; (**b**) bacterial strains used in the studies; (**c**) the inoculum dose [absolute CFU] that was used to inoculate the rabbits; (**d**) the bone in which the implant was inserted; and (**e**) the way in which the inoculum was administered to the rabbit ([52,65,74,82,87,89]). Created with Biorender.com (accessed on 20 August 2024).

4.2.2. Inoculum—Bacterial Strain

Of the included studies in this research, 90% used one or multiple strains of *S. aureus* to inoculate the rabbits (Figure 5b). Again, the pathogenic factor needs to be chosen depending on the aim of the study. As previously stated, most PJIs are caused by *S. aureus* and *S. epidermidis* [7,9]. While *S. aureus* is the most common pathogen in Europe and China, *S. epidermidis* is most common in the US [15,134]. Therefore, depending on the location of the study, different pathogens might be chosen. Although *S. aureus* and *S. epidermidis* are the most common pathogens in PJI, Gahukamble et al. [70] focused on *Staphylococcus lugdunensis* and *Propionibacterium acnes*, pathogens that used to be seen as contaminants when culturing clinical isolates. As *S. lugdunensis* and *P. acnes* are increasingly recognized as pathogens causing PJI, they state the importance of observing these bacteria in a rabbit model [135–137]. Few studies focus on Klebsiella pneumonia and *P. aeruginosa*, though PJI involving these pathogens is difficult to treat and requires more research [81,103,138]. As *P. aeruginosa* often shows in polymicrobial infections with *S. aureus*, Bitika et al. [103] inoculated with both bacteria. The World Health Organization has published a list of priority pathogens that require new antibacterial techniques. This list emphasizes the importance of expanding research beyond *S. aureus* alone [139].

Although 90% of all included studies in this review use *S. aureus* to inoculate the rabbits, 29 different strains of *S. aureus* have been used. These 29 strains range from standard cell lines to clinical isolates (33%), and from MRSA (28%) to MSSA (specifically stated for 12%). However, studies often do not state if their strain is a clinical isolate (66%) or if they use MRSA or MSSA (50%). The strain can impact the study outcomes, as each strain can exhibit significantly different characteristics. The strains can differ in toxin production, biofilm formation, gene regulator types, immune evasion mechanisms, and the possibility of creating persister cells or small colony variants [140]. Tuchscherr et al. [141] found a wide range of cytotoxicity and invasiveness between multiple clinical *S. aureus* strains. Interestingly, they also found that the host cleared low-cytotoxicity strains less efficiently compared to the highly cytotoxic strains [141]. Guo et al. [142] investigated 20 cohort studies on PJI and determined that MSSA was responsible for PJI at a rate 2.5 times higher than that caused by MRSA. However, the chance of treatment failure is higher for MRSA compared to MSSA [143,144]. Understanding the characteristics of the bacterial strain is important, as all these factors can influence their susceptibility to the tested antibacterial technologies. Though clinical isolates or resistant strains have greater clinical relevance for research, standard cell lines have the advantage of being better characterized and provide a more standardized result.

4.2.3. Inoculum—Dose

Inoculum sizes in the included studies in this research ranged from 4.3×10^1 CFU [101] to 6×10^8 CFU [94] (Figure 5c). This range of inoculum doses makes it extremely difficult to compare infection clearance rates between experiments and antibacterial technologies. When choosing the inoculum size, it is important to ensure that the CFU concentration in the inoculum is sufficient to establish an infection in the untreated rabbits that their immune systems cannot clear, while avoiding an excessively high and clinically unrealistic CFU concentration. Of the 20% of studies that used no antibacterial intervention, several studies were dose-finding studies for the number of CFUs needed to create a PJI. Craig et al. [69] found that a lower incidence of infection occurred with a low dose of 10^2 CFU compared to higher doses. They also state that inoculums $>10^6$ CFU will probably lead to greater animal morbidity due to sepsis [69]. This was confirmed by Poultsides et al. [73], who found a 100% dropout rate in the group that received 5×10^8 CFU. The appropriate inoculum dose should be selected based on the study aim, the chosen strain, and its virulence.

4.2.4. Inoculum—Administration

Besides differences in bacterial strains and inoculum sizes, the administration method of the inoculum is another variable. There are several administration routes that can take

place prior to or after the insertion of the implant, and they can be contained or not. The influence of these administration methods is often overlooked. PJI can arise in a patient due to several causes, and the main contributor is still under debate. Contamination can arise during surgery; from hematogenous spread from infections elsewhere in the body or intravascular devices; from direct extension from the skin; from a bacterial reservoir in the deeper skin; or from soft tissue close to the implant [145–147]. Zeller et al. [148] classified clinical PJIs as hematogenous (35%), late chronic (30%), early postoperative (19%), or undetermined (16%). The studies included in this review used several methods to create an infection in the rabbits, as can be seen in Figure 5d. Most studies inoculated the subjects by injecting the bacteria into the medullary cavity in which the implant was inserted (45.0%). Others were inoculated by injecting bacteria into the joint (23.3%), via intra-articular injection (13.3%), by incubating the implant in a bacterial inoculum before insertion (11.7%), or by injection in the bone defect (1.7%). A total of 5% of the studies did not state the method of inoculation. Of the included studies, 78.3% did not employ a method to contain the inoculum in the insertion site, 16.7% used bone wax, and 5.0% used other options to contain the inoculum. As there is no one way for patients to contract PJI, there is also no one way to induce it in vivo.

4.2.5. Implant

Whereas the femur is the largest long bone that can be implanted, the tibia is more easily accessible [33]. The most popular choices of bone in the included studies in this research are therefore the tibia (51.7%), the femur (38.3%), or a combination of the two (3.3%) (Figure 5e). Only 1.7% used the humerus, and 5.0% used the radius. This variability is also in alignment with the distribution of arthroplasties in patients. Currently, TKAs and THAs extremely outnumber TSA. However, the incidence of TSA is increasing faster than that of TKAs and THAs, increasing the need for research on the humerus [149]. Most implants are a simplification of implants used in humans; therefore, the intended use is not completely mimicked, and which long bone is used in the rabbits is less critical. Again, it is important to look at what outcome measures are studied. In a study that only looks at antimicrobial activity, the choice of bone is of less importance compared to when osseointegration is also studied, as in these cases the weight-bearing qualities of the limb can affect the results. As rabbits jump off with their hind legs, the femur and tibia experience more force than the radius and humerus. This difference in movement mechanics should also be considered when looking at bone ingrowth.

4.2.6. Experimental Groups and Group Size

The number of experimental groups and group size differ greatly between all studies included in this review. The number of experimental groups ranges from only one group to testing and comparing several antibacterial technologies, testing both infected and uninfected controls, testing several inoculum sizes and time points on one antibacterial technology, and testing several bacterial strains. Especially in the studies that did not test an intervention, but aimed to establish and validate a new model, uninfected rabbits were used as controls. An uncoated implant or the use of the current standard of care with an infection was used as a control in most other studies. López-Torres et al. [71] had only one study group. However, they aimed to set up and validate the PJI rabbit model without the use of any intervention. Three other studies used one limb as the control group and one limb as the experimental group within the same rabbit [87,103,118]. Craig et al. [69] also tested several inoculum sizes or saline as control within the same rabbit. Using one rabbit for the control and experimental group may create experimental inaccuracy, as the infection is not restricted to the limb it is injected into. If systemic infection develops, or a rabbit reaches a humane endpoint, it is unknown to which group this belongs. Brunotte et al. [79] tested four different inoculum sizes in their rabbits but did not have a control group. Having a control group that is either uninfected or has no antibacterial technology is important to set a baseline to which to compare the intervention groups. Furthermore, a

control group validates the model, as it ensures that observed effects in the other groups are due to the intervention. Concerning group sizes, López-Torres et al. [71] use the largest group size, with fifteen rabbits in one experimental group. On the contrary, Moriarty et al. [101] and Horn et al. [100] tested different inoculum sizes per experimental group, resulting in subgroup sizes of only one rabbit. Yang et al. [112] had the smallest (full) group size, with three rabbits per group. Zhao et al. [115] and Zhou et al. [117] did not report on the total number of rabbits used, or the experimental group size, making their results unreliable. To increase the validity, accuracy, and reliability of the experimental results, a power calculation should be conducted to estimate the experimental group size [24,48,150]. Applying this power calculation reduces the unnecessary use of rabbits. As underpowered experiments produce unreliable results and overpowered experiments use more animals than necessary, it is a delicate balance [48]. Predicting the effect size in a power calculation might be challenging because of the lack of correlation between in vitro and in vivo data.

4.2.7. Dropout Number

In 40% of the studies included in this research, the dropout number was not stated, or the total number of rabbits per group that survived could not be found in the results. This does not follow the ARRIVE guidelines, as they state that any adverse outcome should be described [43,44]. For the studies that reported on dropout numbers, seven studies did not specify to which group the dropped-out rabbits belonged [79,83,100,101,111,119,126]. Furthermore, four studies replaced the dropped-out rabbits with new rabbits [94,100,106,111]. Two of these studies, by Horn et al. [100] and Oosterbos et al. [111], did not state which group the replaced animals belonged to. Replacing these animals raises data integrity concerns as data consistency and reliability are compromised. Even if a full study duration is not completed, the data created by this rabbit's response are valuable. Studies are meticulously designed with specific sample sizes and conditions. Introducing new subjects midway can introduce variables that were not accounted for initially, such as differences in age, weight, and health status. Furthermore, blinding and randomization are not possible anymore when rabbits from only specific groups are replaced. Especially in the studies where it is not mentioned which animals are replaced, or where animals from the group with the antibacterial compound are replaced, bias is introduced. This bias and variability can potentially skew the results toward a better outcome for a desired group, creating difficulty in drawing conclusions. Furthermore, replacing these animals raises ethical concerns. It creates a disregard for individual animal welfare and is not in line with Russel and Burch's 3Rs [38]. Replacing dropped-out rabbits often means subjecting additional animals to potential pain, stress, and suffering associated with experimental procedures. Studies should always report on their dropout number, and refrain from replacing rabbits. Instead, they should design their studies with appropriate sample sizes that account for potential dropouts. Furthermore, statistical methods are available to handle missing data.

Table 2. Experimental design extraction results—part 1. Abbreviations used: ns = not stated.

References	Aim of Study	Duration of the Study (Days)	Inoculum			
			Strain (c.i. = Clinical Isolate)	Inoculum Size (Absolute CFU/Used Volume)	Administration Way/Site	Containment Method
No intervention used						
[69]	To design and evaluate a novel small animal model for the investigation of biomaterial centered infection in total joint arthroplasty with future plans to utilize this model for the evaluation of novel anti-infective therapeutics.	7	MRSA ST-021 (c.i.)	100 µL saline, 10^2, 10^3 or 10^4 CFU in 100 µL saline in other knee.	Injected into knee joint	None
[70]	To observe the effects of *P. acnes* and *S. lugdunensis* in an established rabbit model of implant-related osteomyelitis, in the absence of implant material wear debris, and characterize the resultant infections with respect to histological and microbiological outcomes.	2	*P. acnes*, LED2, and *S. lugdunensis* 010729 (all c.i.)	3×10^7 CFU in 50 µL	Injected into the tibial medullary cavity	Water-soluble alkylene copolymer
[71]	To develop an animal model which is clinically representative of PJI and can serve as a foundation for future research to develop new therapeutic and preventative strategies.	7	*S. aureus* ATCC 29213	10^5 CFU in 1 mL	Intra-articular inoculation with 25-G needle	None
[29]	To establish an improved rabbit implant infection model, based on several previously published models resembling clinical orthopaedic implant infections.	42	MSSA UAMS-1 ATCC 49230 (c.i.)	3.8×10^5 CFU in 100 µL saline	Injected intramedullary	Bone wax
[72]	To evaluate 18F-FDG microPET as an implant osteomyelitis imaging tool using a *Staphylococcus aureus*-induced peroperative implant infection in rabbits.	42	*S. aureus* UAMS-1 ATCC 49230	3.8×10^4 CFU in 100 µL saline	Injected into intramedullary cavity	Bone wax
[73]	The aim of this study is to establish a new experimental model of hematogenous implant-related infection (IRI) by a community-acquired methicillin-resistant *S. aureus* (CA-MRSA) strain.	56	MRSA MLST-80 clone	3 or 5×10^8 CFU in 1 mL saline	Injection with 26-G catheter through femoral artery	None

Table 2. *Cont.*

References	Aim of Study	Duration of the Study (Days)	Inoculum			
			Strain (c.i. = Clinical Isolate)	Inoculum Size (Absolute CFU/Used Volume)	Administration Way/Site	Containment Method
[74]	To test the ability of 99mTc-ciprofloxacin imaging to discriminate between infected and uninfected prosthetic joints, using a previously validated rabbit model of prosthetic joint infection.	20	MSSA (c.i.)	10^7 CFU/0.5 mL	Intra-articular injection	None
[75]	To test the ability of 99mTc-UBI 29-41 (UBI) to discriminate between infected and uninfected prosthetic joints using a previously validated rabbit model.	20	MSSA 17548 (c.i.)	10^7 CFU/0.5 mL	Intra-articular injection	None
[76]	To investigate whether 99mTc-annexin V imaging was effective in differentiating early stage PJI from uninfected prosthetic joints in a validated rabbit model.	21	MSSA ATCC29213	10^6 CFU/0.5 mL	Injected with a 1 mL syringe at the level of the lower patellar border	None
[77]	To establish and evaluate a novel PJI animal model with different bacterial concentrations using 18F-fluorodeoxyglucose (FDG) and 68Ga-fibroblast activation protein inhibitor (FAPI) PET/CT.	14	*S. aureus* ATCC29213	10^7 CFU, 10^6 CFU, 10^5 CFU and 10^4 CFU/0.5 mL saline	Injected in canal	None
[78]	To explore the performance characteristics of 18F-FDG and 68Ga-FAPI in PJI and aseptic loosening models.	42	ns	Control group no inoculum, 10^5 CFU *S. aureus*, 10^8 CFU *S. epidermidis*/0.5 mL	Injected into knee joint	None
[30]	The purpose of this study was to develop and characterize a rabbit model of chronic PJI using common radiological and clinical markers.	28	*S. aureus* ATCC 25923	1×10^6 CFU/1 µL	Intraosseous injection into a predrilled bone tunnel	Bone wax
			Revision			
[79]	The aim of this study was to establish a new small animal model for simulating a two-stage-revision procedure by implant-related MRSA infections.	84	MRSA, EDCC 5443, and EDCC 5398, (all c.i.)	10^5 or 10^7 CFU in 20 µL	Intramedullary tibia canal injection	None

Table 2. *Cont.*

References	Aim of Study	Duration of the Study (Days)	Inoculum			
			Strain (c.i. = Clinical Isolate)	Inoculum Size (Absolute CFU/Used Volume)	Administration Way/Site	Containment Method
[80]	To evaluated the efficacy of a system designed to gradually release grepafloxacin from acrylic bone cement (polymethyl methacrylate, PMMA) for the treatment of experimentally chronic osteomyelitis induced in rabbits.	35–63	MRSA (c.i.)	1×10^7 CFU/100 µL	Injection into upper third of the right femur	None
[81]	To evaluate the efficacy of a colistin-impregnated cement spacer, alone or in combination with systemic colistin with or without systemic meropenem, using a rabbit model of PJI caused by carbapenemase-producing Klebsiella pneumoniae (CPKP) that closely mimics human infection, adapted from a previous model.	14	KPC-producing Klebsiella pneumonia KPC99Y (c.i.)	5×10^8 CFU in 0.5 mL	Injected into knee, close to prosthesis	None
[82]	To compared the efficacy of a teicoplanin-impregnated cement spacer alone with that of a teicoplanin-impregnated cement spacer combined with systemic teicoplanin, using a rabbit model of MRSA knee prosthesis infection that closely mimics human infection.	28	MRSA	10^8 CFU in 0.5 mL	Injection into knee, close to prosthesis	None
[83]	To determine the effectiveness of bone cement containing rifampicin microcapsules, to establish the in vivo safety profile of microencapsulated rifampicin and to register the rifampicin intra-articular release profile.	28	MSSA, ATCC29213	10^5 CFU in 1 mL	Intra-articular injection	None
[84]	To compare the efficacy of tobramycin-containing bone cement with that of systemic cefazolin for treatment of infection in a one-stage revision model.	42	*S. aureus* Wood-46, ATCC 10832	10^6 CFU in 0.1 mL or 10^5 CFU in 0.1 mL	Injected into medullary canal	None
[85]	To study the effectiveness of gentamicin-loaded PNDJ (G-PNDJ) hydrogels in treating orthopaedic infections in a rabbit model.	49	*S. aureus* UAMS-1, ATCC 4923	7.5×10^6 CFU in 50 µL TSB	Inoculated after wire implantation, unspecified how	None

Table 2. *Cont.*

References	Aim of Study	Duration of the Study (Days)	Inoculum			
			Strain (c.i. = Clinical Isolate)	Inoculum Size (Absolute CFU/Used Volume)	Administration Way/Site	Containment Method
[86]	To test the effect of continuous wave ultrasound (CWU) on antimicrobial efficacy of antibiotic-loaded bone cement (ALBC) assessed by clinical performance, radiology, bacteriology, and histology in vivo in a rabbit model.	60	*S. aureus* ATCC13565	10^8 CFU in 0.1 mL	Injected into upper femur and joint cavity	Surgical wax
Prevention: antibiotics only						
[87]	To assess the effectiveness of tobramycin-impregnated microspheres in preventing infection, and to analyse if implant integration was affected by the presence of infection or the microspheres themselves.	14	*S. aureus* ATCC 49230	20×10^6 CFU in 10 µL	Pipetted directly onto the implant	None
[88]	This study examined and compared the antimicrobial effectiveness of teicoplanin- and clindamycin-coated titanium wires on an experimental model of *Staphylococcus aureus* infection.	7	*S. aureus* ATCC 29123	500 CFU, volume unknown	21G green needle in intramedullary canal	None
[89]	The objective of this animal study was to examine the efficacy of a coating of minocycline and rifampin to prevent colonization of a grit-blasted titanium-alloy implant, osteomyelitis, and device-related osteomyelitis due to *S. aureus*.	7	*S. aureus* ATCC25923	0.5×10^3 CFU/mL in 25 µL	Injected in intramedullary canal of femur	None
[90]	To compare the efficacies of ceftaroline-fosamil (CPT-F) or vancomycin (VAN) alone or combined with rifampin (RIF) against MRSA in a knee PJI model in rabbits that closely simulates human infection.	17	MRSA ST20121238 (c.i.)	5×10^7 CFU in 0.5 mL	Injected close to prosthesis after closing the skin	None

Table 2. *Cont.*

References	Aim of Study	Duration of the Study (Days)	Inoculum			
			Strain (c.i. = Clinical Isolate)	Inoculum Size (Absolute CFU/Used Volume)	Administration Way/Site	Containment Method
[91]	To test the ability of an antibacterial-loaded bioreabsorbable hydrogel coating (DAC®), obtained by derivatization of low molecular weight hyaluronic acid (HA) with poly-D,L-lactic acid (PDLLA), to reduce bacterial acute colonization in an animal model of intraoperative high-load bacterial contamination of an implant.	7 or 84 *1	MRSA (c.i.)	10^6 or 10^4 CFU in 0.2 mL	Injected into medullary cavity with an 18-gauge needle	Bone wax
[92]	To establish a new MRSA peri-implant osteomyelitis animal model, and to determine clinical parameters to monitor the infection after MRSA inoculation, and under anti-microbiological therapy with vancomycin.	4	MRSA ATCC33591	10^6 CFU in 25 µL	Coated intra-operatively on implant	None
[93]	To evaluate the surface morphologies, hydrogel swelling, drug release kinetics and antibacterial properties of a localized drug delivery system.	7, 14, 28	*S. aureus* ATCC29213	3×10^7 CFU/0.1 mL	Injected into marrow cavity	Bone wax
[94]	To investigate using a coprecipitation drug-loading approach the effects of nanotubular anodized titanium coated with gentamicin (NTATi-G) on infection prevention and bone cell biocompatibility in a rabbit model with *Staphylococcus aureus* inoculation in the tibial metaphysis.	42	*S. aureus* ATCC25923	6×10^8 CFUin 0.2 mL	Injected into intramedullary canal	Bone wax
[95]	To evaluate the efficacy of levofloxacin, alone or in combination with rifampin, for treatment of rabbit experimental prosthetic knee infections due to *S. aureus*	17	*S. aureus* 17848 (c.i)	10^7 CFU/0.5 mL PBS	Injected into closed knee, close to the prosthesis	None
[96]	To compare the efficacies of quinupristin-dalfopristin (Q-D) and vancomycin, alone and in combination with rifampin, using a rabbit model of experimental MRSA knee prosthesis infection that closely mimics MRSA infections in humans.	14	MRSA strain HM 1054 (c.i.)	5×10^7 CFU/0.5 mL	Injection close to prosthesis after surgery	None

Table 2. *Cont.*

References	Aim of Study	Duration of the Study (Days)	Inoculum			
			Strain (c.i. = Clinical Isolate)	Inoculum Size (Absolute CFU/Used Volume)	Administration Way/Site	Containment Method
[97]	To compare the efficacie of of high-dose daptomycin (equivalent to 8 mg/kg/day in humans) or vancomycin, both alone and with adjunctive rifampin, in an experimental MRSA joint prosthesis infection.	17	MRSA S271 (c.i.)	5×10^7 CFU in 0.5 mL PBS	Injected in knee close to prosthesis after surgery	None
[98]	To compare linezolid and vancomycin in the treatment of MRSA infections of orthopedic implants, in a new rabbit model with titanium implants experimentally infected with MRSA.	42	MRSA ATCC33591	10^6 CFU/25 µL	Implants coated before surgery	None
Prevention: surface modification						
[99]	To evaluate the antibiotic release, in vitro cytocompatibility, and in vivo effectiveness in preventing PJI caused by *S. aureus* of the F- and P-doped, bottle-shaped nanotubular oxide layer grown in Ti-6Al-4V alloy loaded with a mixture of gentamicin and vancomycin (GV).	35	*S. aureus* Sa5 (c.i.)	10^6 CFU in 100 µL	Injected into medullary canal through the intertrochanteric crest	None
[100]	The aim of our study was to determine if the local resistance to infection of a cannulated IM nail is less than that of a solid nail and more similar to that of a hollow nail.	28	*S. aureus* V 8189-94 (c.i.)	4×10^4 to 4×10^6 CFU/100 µL	Intravenous catheter into medullary cavity	Hemostatic collagen plug
[101]	The aim of the present study was to determine the effect of polishing TAN IM nails on susceptibility to infection in an animal model.	28	*S. aureus*, JAR 06.01.31 (c.i.)	4.3×10^1 CFU, 4.3×10^2, 4.3×10^3 or 4.3×10^4 CFU in 50 µL	Injected into medullary canal with 14 gauge catheter	Water soluble alkaline co-polymer

Table 2. *Cont.*

References	Aim of Study	Duration of the Study (Days)	Inoculum			
			Strain (c.i. = Clinical Isolate)	Inoculum Size (Absolute CFU/Used Volume)	Administration Way/Site	Containment Method
[102]	To evaluate in an in vivo normal model the osteogenic response and the osteointegration of an anodic spark deposition nanostructured titanium surface doped with gallium (ASD + Ga) in comparison with two other surface treatments of titanium: an anodic spark deposition treatment without gallium (ASD) and an acid etching treatment (CTR). Moreover the study assesses the osteoprotective potential and the antibacterial effect of the previously mentioned surface treatments in an experimentally-induced peri-implantitis model.	7 or 14	*S. aureus* ATCC 25923	10^5 CFU/mL, volume unknown	Implant inoculated for 6 min before placement	None
Prevention: coating						
[103]	To test the antibacterial efficacy of silver coated titanium implants in an in vivo contaminated rabbit knee fixation model before proceeding with clinical studies.	84	*S. aureus*, *P. aeruginosa* (all c.i.)	2×10^3 CFU/0.2 mL for *S. aureus*, 2×10^7 CFU/0.2 mL for *P. aeruginosa*	Injection into the joint capsule using a 30 G needle and 0.5 mL syringe.	None
[104]	To investigate the hyaluronic-acid-based hydrogel DAC® as carrier for local delivery of antimicrobial agents for infection in an in vivo implant-related infection model.	28	*S. aureus* Wood 46 ATCC 10832	10^5 CFU in 50 µL	Injected in medullary canal before placing implant	None
[105]	First, to establish a suitable in vivo osteomyelitis model in rabbits, second to evaluate the antimicrobial activity of a silver multilayer coating (SML) under realistic pre-clinical conditions.	7	MSSE RKI 10-0062 (c.i.)	2×10^4 CFU, volume ns	Wires incubated in a test tube over a length of 9 cm in bacterial solution for 30 to 60 min under dynamic conditions, with an inoculum of ~1×10^6 CFU/mL	None

Table 2. *Cont.*

References	Aim of Study	Duration of the Study (Days)	Inoculum			
			Strain (c.i. = Clinical Isolate)	Inoculum Size (Absolute CFU/Used Volume)	Administration Way/Site	Containment Method
[106]	To test whether silver ion-containing calcium phosphate-based ceramic nanopowder-coated implants prevented implant-related infection by comparing silver-coated, hydroxyapatite (HA)-coated, and uncoated titanium implants in vivo using radiology, histology, and microbiology	42	MRSA ATCC43300	5×10^2 CFU/50 µL	Injected with small pipette into medullary canal	None
[107]	To test if silver ion doped calcium phosphate based ceramic nano-powder coated intramedullary nails prevent bacterial infection as compared with uncoated nails in an in vivo rabbit study.	70	MRSA ATCC 43300	0.5×10^5 CFU in 50 µL	Injected into intramedullary canal	None
[108]	To study the efficacy of a biodegradable Polymer-Lipid Encapsulation MatriX (PLEX) loaded with the antibiotic doxycycline as a local prophylactic strategy against implant-associated osteomyelitis. Activity was tested against both a doxycycline-susceptible (doxyS) methicillin-susceptible *S. aureus* (MSSA) as well as a doxycycline-resistant (doxyR) methicillin-resistant *S. aureus* (MRSA).	28	*S. aureus* JAR060131 (doxyS MSSA) MRSA strain LUH15101 (doxyR MRSA), (all c.i.)	DoxyS: $5.9 \pm 1.3 \times 10^4$ CFU/100 µL; DoxyR: $4.7 \pm 1.2 \times 10^5$ CFU/100 µL	Pipetted into medullary cavity	None
[109]	To investigate in an in vivo contaminated implant bed model, the efficacy of adding tobramycin to a PA-coated titanium foam implant in preventing implant related Staphylococcal infection and study the effects on osseointegration; this in comparison to both PA-coated and uncoated implants.	28	*S. aureus* Wood 46, ATCC10832	None, 10^3, 10^4 or 10^5 CFU/100 µL	Injected with micropipette into medullary canal	None

Table 2. *Cont.*

References	Aim of Study	Duration of the Study (Days)	Inoculum			
			Strain (c.i. = Clinical Isolate)	Inoculum Size (Absolute CFU/Used Volume)	Administration Way/Site	Containment Method
[110]	This study describes the development of a new, robust hydroxyapatite (HA)-coating containing gentamicin on titanium alloy (Ti-6Al-4V) covered with a protective, biodegradable poly (lactic-co-glycolic acid) (PLGA)-overlayer, that prevents colonization of cementless orthopaedic prostheses by perioperatively introduced bacteria. In vivo evaluation of the antibacterial efficacy of the PLGA-gentamicin-HA-coating was carried out in a contaminated prosthesis model in rabbits, while effects of the coating on bone fixation and osseointegration were assessed in a canine condylar defect model, to demonstrate technology potential for clinical translation.	2 or 7	*S. aureus* ATCC 25923	1×10^5 CFU/100 µL	Pipetted into medullary canal	Bone wax
[111]	To investigate histomorphometrically the osseointegration (bone contact and bone area) of hydroxyapatite (HA)-coated and noncoated titanium implants in the presence of local infection compared with the absence of local infection.	28	*S. aureus* Wood 46 ATCC 10832	10^2, 10^3, 10^4, or 10^5 CFU/0.1 mL	Pipetted in medullary canal	None
[112]	In this study, the post porous hydroxyapatite (HA) coated Ti4Al4V is prepared for the subsequent electrolytic deposition of vancomycin–chitosan composite to control the drug release. The aim of this study is to test the antibacterial effect in a rabbit infection animal model.	28	*S. aureus* ATCC 6538P	10^7 CFU/20 µL	Injected with 16G needle before insertion pin	None

Table 2. *Cont.*

References	Aim of Study	Duration of the Study (Days)	Inoculum			
			Strain (c.i. = Clinical Isolate)	Inoculum Size (Absolute CFU/Used Volume)	Administration Way/Site	Containment Method
[113]	In this study, they created Ag-supported/TiO_2 nanotubes (Ag/TNT) by a combination of electrochemical anodization and pulse electrodeposition and prepare a super-hydrophobic coating by modifying the surface of the Ag/TiO_2 nanotubes with 1H, 1H, 2H, 2H-perfluorooctyl-triethoxysilane (PTES). We evaluate the inhibitory effect of the coating on bacterial adhesion and killing adherent bacteria and assess its effect on Ag release.	28	*S. aureus* 8325	2×10^2 CFU/20 µL	Injected into medullary cavity	Bone wax
[114]	The aims of the present study were to: (1) characterize the relation between Cu2+ dose and antibacterial activity and in vitro biocompatibility; (2) test the effect of the coating in a small animal bone fracture model	28	*S. aureus* BNCC186335	10^4 CFU/100 µL	Injected into proximal and distal parts of tibia after transection in the middle	None
[115]	The antibacterial efficacy and osteogenic properties of ZnO and ZnO/$Zn_3(PO_4)_2$ nanostructures on Ti-based implants are systematically evaluated in vitro and in vivo, and the underlying mechanisms are carefully dissected.	14 or 42 *2	*S. aureus*	10^5 CFU/mL, volume unknown	Implants were incubated for 30 min before implantation	None
[116]	In the present study, biomimetic hierarchical micropore/nanorod patterned coatings (MNRs) on Ti were developed, in which the nanorods revealed a fixed interrod spacing of about 70 nm and consisted of fluorine (F) incorporated Ca9Sr1(PO4)6(OH)2 (Sr1−HA, strontium containing hydroxyapatite) with the fixed Sr but different F content. The antibacterial activities were assessed in a bacterial-infected rabbit model.	56	*S. aureus* ATCC43300	2×10^3 CFU/20 µL	Injected into medullary cavity with a microsyringe	None

Table 2. *Cont.*

References	Aim of Study	Duration of the Study (Days)	Inoculum			
			Strain (c.i. = Clinical Isolate)	Inoculum Size (Absolute CFU/Used Volume)	Administration Way/Site	Containment Method
[117]	The aim was to test titanium as implant covalently immobilized with a polyethylene glycol (PEG)-based thermoresponsive polymer (MPEG) and an antimicrobial peptide (AMP) HHC36 onto the implant surface. We demonstrated that the two components endowed the surface with spatiotemporal control over the different biofunctions at the three service stages of the implant. The in vivo behavior in two infection models in New Zealand white rabbits was tested.	7 and 60	*S. aureus* ATCC 6538P	7.5×10^6 CFU/15 µL	ns	None
Other						
[118]	To test if a dilute Betadine lavage of 3.5% would achieve a significant decrease in bacterial counts compared with an isolated saline lavage in an in vivo knee PJI model.	14	*S. aureus* ATCC 25923	10^6 CFU/100 µL	Injected with 22-gauge needle in knee joint	None
[119]	To investigate biodistribution and tolerability of oly(*n*-isopropylacrylamide-co-dimethylbutyrolactone acrylamide-co-Jeffamine M-1000 acrylamide) (PNDJ) hydrogels as sustained release carriers.	49	MSSA ATCC 49230, MRSA ATCC BAA-1556	7.5×10^6 CFU/volume ns	Administered before closing in defect radius	None
[120]	To evaluated the late resistance to hematogenous contamination by microbial pathogens of implants and bone-implant interface and the development of late clinical infection when cementless components with different surface or structural properties are implanted	56	MRSA strainMLST-80 PVL+ clone (c.i.)	3×10^8 CFU/1 mL (group B-E) or 1 mL sterile saline (group A)	Injected with 26-gauge needle in femoral artery 4 weeks after implantation	None

Table 2. *Cont.*

References	Aim of Study	Duration of the Study (Days)	Inoculum			
			Strain (c.i. = Clinical Isolate)	Inoculum Size (Absolute CFU/Used Volume)	Administration Way/Site	Containment Method
[121]	To evaluate the efficacy of a bioabsorbable antibiotic containing bone (Ab-PLGA) screw compared to a stainless steel (SS) screw in the prevention of biomaterial-related infection due to *Staphylococcus aureus*.	42	*S. aureus* 52/52A/80	3×10^4 CFU/mL, volume unknown	6 min incubation of screw before implantation	None
[122]	A rabbit PJI model was used with the highly pathogenic USA300 community-associated methicillin-resistant *S. aureus* (MRSA) strain to further evaluate the protective efficacy of a combination of three previously described monoclonal antibodies (MAbs) targeting alpha-hemolysin (Hla) with MEDI4893 *, clumping factor A with AZD7745 *, and leukocidins (LukSF, LukED, HlgAB, and HlgBC) with AZD8887 (AZD6389 *).	8	MRSA USA300/SF8300	5×10^5 CFU/300 µL	Intra-articular injection	None
[123]	In present study, in order to determine the antibacterial activity of the new Ti–Cu sintered alloy we conducted an in vivo experiment on the basis of previous in vitro research by Zhang et al.	14	*S. aureus* ATCC6538	1.0×10^5 CFU/10 µL	Injected into medullary cavity	Bone wax
[124]	The aim of this study was to investigate the effects of allicin on biofilm formation, and whether allicin could potentiate the bactericidal effect of vancomycin in a rabbit PJI model.	17	*S. epidermidis* RP62A	10^4 CFU in 1 mL	Injected into knee joint	None
[125]	The present study aimed to isolate broad-range bacteriocins from Lactobacillus rhamnosus (ATCC 53103) and investigate their antibacterial effect on *S. aureus* in a rabbit model of knee implant infection.	5	*S. aureus* ATCC29213	1.5×10^5 CFU/0.5 mL	Intra-articular injection	None

Table 2. *Cont.*

References	Aim of Study	Duration of the Study (Days)	Inoculum			
			Strain (c.i. = Clinical Isolate)	Inoculum Size (Absolute CFU/Used Volume)	Administration Way/Site	Containment Method
[126]	The purpose of the experiment is to verify the preventive effect of antibacterial peptide PR39 on periprosthetic infection, which may provide a new solution for the treatment of periprosthetic infection in the future.	14	*S. aureus* ATCC 25923	4×10^6 CFU/100 µL	Injected into knee joint	None

*1 7 days for treatment groups, 84 days for histocompatibility evaluation; *2 14 days for antibacterial properties, 42 days for osseointegration.

Table 3. Experimental design extraction results—part 2. Abbreviations used: Impl. = implant; VAN = vancomicin; s.s. = stainless steel; Ti = titanium; GEN = Gentamicin; RIF = Rifampicin; ns = not stated.

References	Implant				Interventions Used against PJI	Total Number of Rabbits	Experimental Groups and Number of Rabbits per Group (*n*)	Dropout Number	
	Description	Material	Movement Prevention	Location (Specified)				Per Experimental Group [%]	Total [%]
No intervention used									
[69]	Diameter 4.0 mm, length 15 mm	S.S. cannulated screw with sterile UHMWPE washer	PMMA	Femur (lateral femoral condyle)	None	22	100 µL saline in one knee, 10^4 CFU in 100 µL saline in other knee (*n* = 11) 10^2 in 100 µL saline in one knee, 10^3 in 100 µL saline in other knee (*n* = 11)	9 0	5
[70]	Diameter 2.5 mm, length 85 m	S.S.	No	Tibia (medullary cavity)	None	18	Uninoculated (*n* = 6) *P. acnes* (*n* = 6) *S. lugdumensis* (*n* = 6)	0 0 0	0

Table 3. *Cont.*

References	Implant				Interventions Used against PJI	Total Number of Rabbits	Experimental Groups and Number of Rabbits per Group (*n*)	Dropout Number	
	Description	Material	Movement Prevention	Location (Specified)				Per Experimental Group [%]	Total [%]
[71]	Tibial insert, 'rabbit specific' implants made using CT scans and 3D reconstruction, mimicking anatomical irregularities of the tibial plateau	S.S.	Metaphyseal anchoring and bone cement	Tibia (implant replaced the tibial plateau surface)	None	15	Tibial insert (n = 15)	0	0
[29]	Length 20 mm, diameter 4 mm	Grit-blasted Ti (TiAl6V4)	No	Tibia (proximal medullary cavity)	None	22	Contamination group (n = 11) Sterile saline control group (n = 11)	18 36	27
[72]	Length 20 mm, diameter 4 mm	Grit-blasted Ti alloy (TiAl6V4)	No	Tibia (proximal medullary cavity)	None	22	Uncontaminated implant group (n = 11) Contaminated implant group (n = 11)	27 36	32
[73]	Cylinder diameter 3 mm, length 30 mm, cylindrical cup 5 × 5 mm	Porous tantalum, cylindrical silicon cup	No	Tibia (proximal medullary canal)	None	30	Received 1 mL of 5×10^8 CFU/mL at 4 weeks (n = 10) Received 1 mL of 3×10^8 CFU/mL at 4 weeks (n = 10) Received 1 mL saline at 4 weeks (n = 10)	100 0 0	33
[74]	Tibial component (Silastic, great toe implant HP, Swanson Design; Dow Corning, Valbonne, France), implant head 15 × 5 mm, stem length 14 mm	Silicone elastomer	No	Tibia (tibial plateau and medullary cavity of the metaphysis)	None	13	Infected (n = 6) Uninfected (n = 7)	33 14	23

Table 3. *Cont.*

References	Implant				Interventions Used against PJI	Total Number of Rabbits	Experimental Groups and Number of Rabbits per Group (*n*)	Dropout Number	
	Description	Material	Movement Prevention	Location (Specified)				Per Experimental Group [%]	Total [%]
[75]	Tibial component (Silastic, great toe implant HP, Swanson Design; Dow Corning, Valbonne, France), implant head 15 × 5 mm, stem length 14 mm	Silicone elastomer	No	Tibia (tibial plateau and medullary cavity of the metaphysis)	None	20	Infected (*n* = 12) Uninfected, 1 mL saline injected (*n* = 8)		ns
[76]	Tibial component (Silastic, great toe implant HP, Swanson Design; Dow Corning, Valbonne, France), implant head 15 × 5 mm, stem length 14 mm	Silicon elastomer	No	Tibia (tibial plateau and medullary cavity of the metaphysis)	None	24	Infected (*n* = 12) Uninfected, injection of 0.5 mL saline (*n* = 12)		ns
[77]	Screw with diameter 4 mm, length 20 mm	ns	Self-locking	Femur and tibia (in femoral shaft at intercondylar notch and ACL footprint in tibia)	None	40	0.5 mL saline (*n* = 8) 2×10^7 CFU/mL in 0.5 mL saline (*n* = 8) 2×10^6 CFU/mL in 0.5 mL saline (*n* = 8) 2×10^5 CFU/mL in 0.5 mL saline (*n* = 8) 2×10^4 CFU/mL in 0.5 ml saline (*n* = 8)	12 38 13 38 13	23
[78]	Screws, diameter 3 mm, length 20 mm	ns	Self-locking	Femur (intercondylar fossa and anterior cruciate ligament	None	36	Control (*n* = 6) Aseptic loosening (*n* = 10) *S. aureus* (*n* = 10) *S. epidermidis* (*n* = 10)	0 20 30 20	19

Table 3. *Cont.*

References	Implant				Interventions Used against PJI	Total Number of Rabbits	Experimental Groups and Number of Rabbits per Group (*n*)	Dropout Number	
	Description	Material	Movement Prevention	Location (Specified)				Per Experimental Group [%]	Total [%]
[30]	Screw	ns	ns	Femur (distal femur knee joint)	None	13	Infected (n = 5) Non-infected (n = 5) Separate cohort (n = 3) for bacterial viability assays	0 0 0	0
Revision									
[79]	ns	K-wires, S.S.	No	Tibia (medullary canal)	Two-stage revision with debridement + VAN loaded cement spacers. A total of 1.2 g of VAN was used per 40 g of PMMA. The local VAN release rate was 1.569 mg VAN over four days.	12	MRSA EDCC 5443, 10^5 CFUs (n = 3) MRSA EDCC 5443, 10^7 CFUs (n = 3) MRSA EDCC 5398, 10^5 CFUs (n = 3) MRSA EDCC 5398, 10^7 CFUs (n = 3)	ns ns ns ns	8
[80]	ns	Metal needle	No	Femur (upper third of the right femur)	After 3 weeks, needle/implant is removed. Followed by a local injection of a mixture of acrylic bone cement enriched by grepafloxacin 4%. Per time point 1 control animal.	36	Sacrificed at week 2 (n = 6) Sacrificed at week 3 (n = 6) Sacrificed at week 4 (n = 6) Sacrificed at week 5 (n = 6) Sacrificed at week 6 (n = 6)		ns

Table 3. *Cont.*

References	Implant				Interventions Used against PJI	Total Number of Rabbits	Experimental Groups and Number of Rabbits per Group (*n*)	Dropout Number	
	Description	Material	Movement Prevention	Location (Specified)				Per Experimental Group [%]	Total [%]
[81]	Arthroplasty implant of the first metatarsophalangeal joint (Silastic, great toe implant HP; Swanson Design, Dow-Cornin)	Silicone elastomer	No	Tibia (partial knee replacement with tibial component)	Seven days after inoculation the prosthesis was removed and replaced by a cement spacer. Six treatment/control groups: (i) drug-free spacer; (ii) colistin-loaded spacer; (iii) drug-free spacer + colistin intramuscular (i.m.); (iv) colistin i.m. + colistin spacer; (v) drug-free spacer + colistin i.m. + meropenem subcutaneous (s.c.); and (vi) colistin i.m. + meropenem s.c. + colistin spacer.	72	Control, drug-free spacer (n = 12)	8	8
							Colistin-loaded spacer (Coli-Ce) (n = 13)	8	
							Drug-free spacer + colistin intramuscular (i.m.) (Coli S) (n = 11)	9	
							Coli-Ce + Coli S (n = 12)	25	
							Coli S + meropenem subcutaneous (s.c.) (Mero S) (n = 12)	0	
							Coli-Ce + Coli S + Mero S (n = 12)	0	

Table 3. *Cont.*

References	Implant				Interventions Used against PJI	Total Number of Rabbits	Experimental Groups and Number of Rabbits per Group (*n*)	Dropout Number	
	Description	Material	Movement Prevention	Location (Specified)				Per Experimental Group [%]	Total [%]
[82]	Tibial component, antibiotic-loaded spacer	ns	No	Tibia (partial knee replacement, tibial component)	Prosthesis replacement by a cement spacer with or without teicoplanin, and with or without systemic antibiotic treatment, or injections of teicoplanin.	56	Untreated controls (*n* = 11) Impl. replacement by drug-free cement spacer (*n* = 10) Impl. replacement by teicoplanin-loaded cement spacer (1.2 g of teicoplanin/40 g of cement) (*n* = 12) i.m. injections of teicoplanin (20 mg/kg of body weight, twice a day for 7 days) (*n* = 11) Systemic antibiotic treatment combined with teicoplanin-loaded spacers (*n* = 12)		ns
[83]	ns	S.S.	No	Tibia (proximal metaphysis)	First revision 1 week after inoculation: group R received a spacer containing GEN and RIF microcapsules, group C received a spacer containing GEN.	15	Group C (*n* = 7) Group R (*n* = 8)	ns ns	7

Table 3. *Cont.*

References	Implant				Interventions Used against PJI	Total Number of Rabbits	Experimental Groups and Number of Rabbits per Group (*n*)	Dropout Number	
	Description	Material	Movement Prevention	Location (Specified)				Per Experimental Group [%]	Total [%]
[84]	Length 25 mm, diameter 3.9 mm	Preformed cement on a central metal wire	No	Tibia (medullary canal)	One-stage revision: medullary canal was debrided and washed, after which tobramycin-containing bone cement was inserted.	30	Tobramycin-containing bone cement (*n* = 10) Plain Simplex-P bone cement, no antibiotics (*n* = 10) Plain Simplex-P bone cement, with systemic antibiotics (cefazolin) injected every 8 h from day 28 to 42 (*n* = 10)	10 20 0	10
[85]	Kirschner wire, length 1 cm	S.S.	No	Radius (medullary canal)	Debridement with higher-dose G-PND (3.14 wt%).	16	Debridement, new wire with higher-dose G-PND (3.14 wt%) (*n* = 8) Debridement, new wire without hydrogel (*n* = 8)		ns
[86]	Length 30 mm, diameter 3 mm	Metal	No	Femur (upper 1/3rd)	Two-stage revision with CWU on ALBC.	16	Revision with CWU on ALBC (*n* = 8) Control group with ALBC but without insonation (*n* = 8)		ns
Prevention: antibiotics only									
[87]	Diameter 5 mm, length 10 mm	Tantalum	No	Radius (midshaft periosteum, with cortical damage)	Antibiotic-impregnated microspheres.	14	Infection + control limb in each rabbit (*n* = 14)		27
[88]	Diameter 2 mm, length 35 mm	Ti	No	Tibia (medullary canal)	Teicoplanin and Clindamycin coating.	30	Teicoplanin coating (*n* = 10) Clindamycin coating (*n* = 10) Uncoated coating (*n* = 10)		ns

Table 3. *Cont.*

References	Implant				Interventions Used against PJI	Total Number of Rabbits	Experimental Groups and Number of Rabbits per Group (*n*)	Dropout Number	
	Description	Material	Movement Prevention	Location (Specified)				Per Experimental Group [%]	Total [%]
[89]	Length 15 mm, diameter 2.8 mm	Ti-alloy pin	No	Femur (medullary canal)	Minocycline coating, RIF coating.	28	Minocycline and RIF coated (n = 14) Uncoated (n = 14)	7 14	11
[90]	Arthroplasty implant of the first metatarsophalangeal joint (Silastic, great toe implant HP; Swanson Design, Dow-Cornin). Nail length 14 mm, implant head diameter 15 mm, height 5 mm	Silicone elastomer	No	Tibia (nail in medullary canal, head replaced tibial plateau)	At 7 days postinfection, rabbits began treatment with CPT-F (60 mg/kg of body weight i.m. b.i.d.) or VAN (60 mg/kg i.m. b.i.d.) alone or combined with RIF (10 mg/kg i.m. b.i.d.).	66	No treatment control (n = 14) CPT-F (n = 12) VAN (n = 12) CPT-F plus RIF (n = 14) VAN plus RIF (n = 14)		ns
[91]	Diameter 3 mm, length 40 mm, surface roughness of 7 μm	Sandblasted Ti	No	Femur (medullary cavity, intercondylar region of right femur)	DAC®hydrogel loaded with 0%, 2%, or 5% (w/v) VAN.	40	Histocompatibility study (n = 10) High load (10^6 CFU), 0 % VAN-loaded DAC (n = 5) High load (10^6 CFU), 2%VAN-loaded DAC (n = 5) High load (10^6 CFU), 5% VAN-loaded DAC (n = 5) Low load (10^4 CFU), 0 % VAN-loaded DAC (n = 5) Low load (10^4 CFU), 2 % VAN-loaded DAC (n = 5) Low load (10^4 CFU), 5% VAN-loaded DAC (n = 5)		ns

Table 3. *Cont.*

References	Implant				Interventions Used against PJI	Total Number of Rabbits	Experimental Groups and Number of Rabbits per Group (*n*)	Dropout Number	
	Description	Material	Movement Prevention	Location (Specified)				Per Experimental Group [%]	Total [%]
[92]	Diameter 4.1 mm, length 5 mm	Ti, coated with pure Ti powder at 0.35 mm thickness (Plasmapore)	No	Femur (in cancellous bone via lateral femoral condyle)	VAN treatment at 25 mg/kg subcutaneous neck soft tissue, twice daily for ten days.	18	MRSA, no treatment (n = 6) MRSA + treatment with VAN (n = 6) MRSA, no treatment (n = 6)	17 17 0	11
[93]	Area 20 × 5 mm^2, thickness 0.1 mm	Ti foils	Sutured to the bone	Tibia (2 mm hole drilled in external tibial epicondyle)	VAN encapsulated in a poly(ethylene glycol) (PEG)-based hydrogel film that was covalently bound to Ti implants and subsequently covered by a PEG-poly(lactic-co-caprolactone) (PEG-PLC) membrane. Additionally, crosslinked starch (CSt) was mixed with the hydrogel.	36	2 mg VAN (n = 12) 4 mg VAN (n = 12) No VAN (n = 12)		ns
[94]	Ti 0.25 × 0.25 cm, NTATi length of 1.05 µm, an inner diameter of 125 nm, and an outside diameter of 170 nm	Pure Ti and nanotubular anodized Ti uncoated (NTATi)	No	Tibia (proximal medullary cavity)	NTATi with GEN (NTATi-G), Ti coated with GEN (Ti-G), NTATi, Ti.	36	NTATi with GEN (NTATi-G) (n = 8) Ti coated with GEN (Ti-G) (n = 8) NTATi (n = 8) Ti (n = 8)	0 0 0 25	11 *1

Table 3. *Cont.*

References	Implant				Interventions Used against PJI	Total Number of Rabbits	Experimental Groups and Number of Rabbits per Group (*n*)	Dropout Number	
	Description	Material	Movement Prevention	Location (Specified)				Per Experimental Group [%]	Total [%]
[95]	Arthroplasty implant of the first metatarsophalangeal joint (Silastic HP great toe implant; Swanson Design, Dow-Corning)	Silicone elastomer	No	Tibia (tibial plateau and metaphysis)	Levofloxacin and/or RIF from day 7 to day 14.	45	Untreated control (*n* = 10) Levofloxacin alone (*n* = 12) RIF alone (*n* = 11) Levofloxacin and RIF (*n* = 12)		0
[96]	A tibial component (Silastic great toe implant HP; Swanson Design; Dow-Corning France, S.A.)	ns	No	Tibia (tibial plateau and medullary cavity of metaphysis)	Intramuscular injections of Q-D or VAN, with or without RIF, from days 4 to 11.	52	Q-D (*n* = 12) Q-D + RIF (*n* = 10) VAN (*n* = 10) VAN + RIF (*n* = 11) Untreated control (*n* = 9)		ns
[97]	Arthroplasty implant of the first metatarsophalangeal joint (Silastic HP great toe implant; Swanson Design, Dow-Corning) used as tibial component, stem 14 mm	Silicone elastomer	No	Tibia (tibial plateau and medullary cavity of metaphysis)	Starting 7 days postinfection, rabbits were treated with daptomycin (22 mg/kg of body weight i.v. o.d.) or VAN (60 mg/kg i.m. twice daily [b.i.d.]), alone or combined with RIF (10 mg/kg i.m. b.i.d.).	60	Untreated group (*n* = 12)	25	12
							Daptomycin (*n* = 12)	0	
							Vancoymycin (*n* = 12)	33	
							Daptomycin + RIF (*n* = 12)	0	
							VAN + RIFg (*n* = 12)	0	

Table 3. *Cont.*

References	Implant				Interventions Used against PJI	Total Number of Rabbits	Experimental Groups and Number of Rabbits per Group (*n*)	Dropout Number	
	Description	Material	Movement Prevention	Location (Specified)				Per Experimental Group [%]	Total [%]
[98]	Diameter 4.1 mm, length 5 mm	Ti alloy, coated with pure Ti powder at 0.35 mm thickness (plasmapore)	Polyethylene cap	Femur (through lateral condyle medullary canal)	Antibiotics received twice daily for 10 days. Linezolid orally, VAN subcutaneous injection.	36	Uninfected, no antibiotics (*n* = 6) Uninfected, VAN (*n* = 6) Uninfected, Linezolid (*n* = 6) Infected, no antibiotics (*n* = 6) Infected, VAN (*n* = 6) Infected, Linezolid (*n* = 6)	17 17 0 0 0 0	6
Prevention: surface modification									
[99]	Diameter 3 mm, length 20 mm	Kirschner wires, Ti–6Al–4V	No	Femur (intertrochanteric crest)	Bottle-shaped TiO_2 nanotubes (bNT).	20	Chemically polished without infection (*n* = 5) Chemically polished with infection (*n* = 5) bNT without infection (*n* = 5) bNT with infection (*n* = 5)		ns

Table 3. *Cont.*

References	Implant				Interventions Used against PJI	Total Number of Rabbits	Experimental Groups and Number of Rabbits per Group (*n*)	Dropout Number	
	Description	Material	Movement Prevention	Location (Specified)				Per Experimental Group [%]	Total [%]
[100]	Length 80 mm, diameter 2.5 mm, inner drill hole 2.0 mm in slotted and 1.6 mm in cannulated nail. Slotted nail had additionally a posterior longitudinal slit of 0.4 mm	Ti–niobium–aluminum alloy (TiA16Nb7)	None	Tibia (medullary cavity)	Cannulated (CN) vs. solid (SN) and hollow slotted nail (HN).	69	Solid (SN) implant: inoculum of 4×10^4 CFU ($n = 1$), 2×10^5 CFU ($n = 4$), 3×10^5 CFU ($n = 6$), 4×10^5 CFU ($n = 8$), 2×10^6 CFU ($n = 2$), 4×10^6 CFU ($n = 1$) Hollow slotted (HS) implant: inoculum of 4×10^4 CFU ($n = 1$), 2×10^5 CFU ($n = 4$), 3×10^5 CFU ($n = 6$), 4×10^5 CFU ($n = 6$), 2×10^6 CFU ($n = 2$), 4×10^6 CFU ($n = 1$) Cannulated (CN) implant: inoculum of 4×10^4 CFU ($n = 1$), 2×10^5 CFU ($n = 4$), 3×10^5 CFU ($n = 6$), 4×10^5 CFU ($n = 9$), 2×10^6 CFU ($n = 2$), 4×10^6 CFU ($n = 1$)	ns ns ns	6 *1

Table 3. *Cont.*

References	Implant				Interventions Used against PJI	Total Number of Rabbits	Experimental Groups and Number of Rabbits per Group (*n*)	Dropout Number	
	Description	Material	Movement Prevention	Location (Specified)				Per Experimental Group [%]	Total [%]
[101]	Diameter 2.5 mm, length 85 mm	Ti–aluminum–niobium (TAN) or electropolished S.S. (EPSS)	No	Tibia (medullary canal, cranial to the joint)	Polished vs. non-polished nail.	72	EPSS (n = 19: n = 4 for 10^1 CFU, n = 8 for 10^2 CFU, n = 6 for 10^3 CFU, n = 1 for 10^4 CFU) Standard TAN (n = 20: n = 4 for 10^1 CFU, n = 8 for 10^2 CFU, n = 6 for 10^3 CFU, n = 2 for 10^4 CFU) Polished TAN (n = 20: n = 4 for 10^1 CFU, n = 7 for 10^2 CFU, n = 7 for 10^3 CFU, n = 2 for 10^4 CFU)	ns Ns Ns	18
[102]	Diameter 3 mm, length 13 mm	Grade 2 biomedical Ti	No	Femur (distal epiphysis)	Acid-etched Ti, anodic spark deposition nanostructured Ti surface, anodic spark deposition nanostructured Ti surface doped with gallium. A total of 24 implants (8 per surface) were inserted into the left and right femoral epiphysis.	12	1 week, inoculated (n = 2 per modification) 1 week, not inoculated (n = 2 per modification) 2 weeks, inoculated (n = 2 per modification) 2 weeks, not inoculated (n = 2 per modification)		ns

Table 3. *Cont.*

References	Implant				Interventions Used against PJI	Total Number of Rabbits	Experimental Groups and Number of Rabbits per Group (*n*)	Dropout Number	
	Description	Material	Movement Prevention	Location (Specified)				Per Experimental Group [%]	Total [%]
Prevention: coating									
[103]	Knee implant with tibial (on a screw of 20 mm long and 3.5 mm diameter) and femoral component (on a screw 15 mm long, 3–2 mm diameter)	Ti4Al6V	Screws locked	Tibia and femur (total knee implant)	Sol-gel silver coated Ti (right knee as control, left knee experimental).	26	Pilot studies (*n* = 2) Experimental rabbits (*n* = 24)	0 21	19
[104]	Diameter 4 mm, length 25 mm, roughness 5.6 µm	Sand-blasted Ti	No	Tibia (medullary canal)	The rods were coated with unloaded hydrogel (Gel), hydrogel loaded with 2 % (Van2) or 5 % VAN (Van5), bioactive glass (BAG) or *n*-acetyl-L-cysteine (NAC).	42	Gel (*n* = 12) Van2 (*n* = 6) Van5 (*n* = 6) BAG (*n* = 6) NAC (*n* = 6) No gel (*n* = 6)	8 0 0 17 0 0	5
[105]	Diameter 2.0 mm, length 150 mm	Ti K-wires	Advanced Surface® ceramic multilayer coating	Tibia (medullary channel)	Silver multilayer coating (SML).	27	SML coated (*n* = 12) Uncoated (*n* = 12) SML coated without microbial load (*n* = 3)		ns
[106]	Length 25 mm, diameter 2.5 mm, lower ends bent to mimic knee prostheses	Ti alloy (Ti6Al4V)	No	Femur (medullary canal)	Implants were uncoated, hydroxyapatite-coated, or silver-coated.	27	Uncoated (*n* = 9) Hydroxyapatite-coated (*n* = 9) Silver-coated (*n* = 9)	22 11 11	15 *1

Table 3. *Cont.*

References	Implant				Interventions Used against PJI	Total Number of Rabbits	Experimental Groups and Number of Rabbits per Group (*n*)	Dropout Number	
	Description	Material	Movement Prevention	Location (Specified)				Per Experimental Group [%]	Total [%]
[107]	Length 25 mm, diameter 2 mm	Ti-alloy (Ti6Al4V)	No	Femur (medullary canal)	Hydroxyapatite coated or silver doped hydroxyapatite-coated implant.	33	Uncoated (*n* = 11)	18	6
							Hydroxyapatite coated (*n* = 11)	0	
							Silver doped hydroxyapatite coated (*n* = 11)	0	
[108]	Length 55 mm, diameter 3 mm	Medical grade Ti-6% aluminum-7% niobium TAN	No	Humerus (medullary cavity, entry point between greater tuberosity and deltoid ridge)	A PLEX coating containing polylactic-co-glycolic acid (PLGA); dipalmitoyl phosphatidyl choline (DPPC) and distearoyl phosphatidyl choline (DSPC); and cholesterol with doxycycline hyclate was used.	28	DoxyS + uncoated implant (*n* = 6)	17	8
							DoxyS + coated implant (*n* = 6)	0	
							DoxyR + uncoated implant (*n* = 6)	0	
							DoxyR + coated implant (*n* = 6)	17	

Table 3. *Cont.*

References	Implant				Interventions Used against PJI	Total Number of Rabbits	Experimental Groups and Number of Rabbits per Group (*n*)	Dropout Number	
	Description	Material	Movement Prevention	Location (Specified)				Per Experimental Group [%]	Total [%]
[109]	Total diameter 4.5 mm, length 12 mm, coating 1.5 mm thick	Solid Ti6Al4V core, coated with Ti foam	No	Tibia (proximal medullary canal)	Implants were uncoated (Ti), PeriApatite-coated, or Tobramycin–PeriApatite-coated (PA-tobra). Prior to insertion, the implant bed was contaminated with none, 10^3, 10^4, or 10^5 CFU.	72	Ti (n = 24, ns how many per inoculum size)	0	1.4
							PA (n = 24, ns how many per inoculum size)	17	
							PA-tobra (n = 24, ns how many per inoculum size)	0	
[110]	Diameter 2.5 cm, height 0.4 cm, surface area 4.9 cm^2	Ti-6Al-4V, grit-blasted with alumina grit	None	Femur (medullary canal, from the piriformis fossa)	HA-coated and PLGA-GEN-HA-coated pins.	14	HA-coated pins, sacrificed day 2 (n = 3) PLGA-GEN-HA-coated pins, sacrificed day 2 (n = 3) HA-coated pins, sacrificed day 7 (n = 4) PLGA-GEN-HA-coated pins, sacrificed day 7 (n = 4)		ns
[111]	Diameter 3.9 mm, length 20 mm	Grit-blasted Ti alloy (Ti6Al4V)	No	Tibia (anterior to the insertion of the ACL, medullary canal)	Two cylinders of the same type were put in the left and right tibia. of one rabbit. Either HA-coated cylinders or uncoated cylinders (Ti).	32	HA-coated cylinders (n = 4 per inoculum size)	ns	6 *1
							Uncoated cylinders (Ti) (n = 4 per inoculum size)	ns	

Table 3. *Cont.*

References	Implant				Interventions Used against PJI	Total Number of Rabbits	Experimental Groups and Number of Rabbits per Group (*n*)	Dropout Number	
	Description	Material	Movement Prevention	Location (Specified)				Per Experimental Group [%]	Total [%]
[112]	Diameter 2 mm, length 50 mm	Ti6Al4V alloy	No	Tibia (into the medullary cavity)	HA-coated Ti6Al4V alloy with VAN-chitosan composite coating.	6	VAN-chitosan/HA composite coated (n = 3) Uncoated (n = 3)		ns
[113]	Length 3 mm, diameter 2.5 mm	Ti	No	Femur (at the lower end of femur and lateral knee joint)	Both hind legs were used for implantation with Ti rods with TNT, Ag/TNT, or S-Ag/TNT structured surfaces.	15	Ti rods of TNT structured surfaces (TNT group, n = 10) Ti rods of Ag/TNT structured surfaces (Ag/TNT group, n = 10) Ti rods of S-Ag/TNT structured surfaces (S-Ag/TNT group, n = 10)		0
[114]	Diameter 2 mm, length 90 mm	Ti6Al4V Kirschner wires	No	Tibia (medullary canal 0.5 cm below the right tibial plateau and advanced to the distal end)	K-wires were coated with (1) PDLLA coating with no $CuCl_2$ and (2) PDLLA coating with $CuCl_2$.	24	PDLLA coating, no Cu, with saline (n = 6) PDLLA coating, with 1.0 mg/mL $CuCl_2$, with saline (n = 6) PDLLA coating, no Cu, with bacteria (n = 6) PDLLA coating, with 1.0 mg/mL $CuCl_2$ with bacteria (n = 6)	17	4

Table 3. *Cont.*

References	Implant				Interventions Used against PJI	Total Number of Rabbits	Experimental Groups and Number of Rabbits per Group (*n*)	Dropout Number	
	Description	Material	Movement Prevention	Location (Specified)				Per Experimental Group [%]	Total [%]
[115]	Diameter 3 mm, length 5 mm	Ti medical grade	No	Femur (transverse defect at distal side)	ZnO nanorods are first synthesized on the Ti substrate and then partially converted into $Zn_3(PO_4)_2$.	ns	Ti (*n* = ns) Ti-ZnO (*n* = ns) Ti-ZnP2 (*n* = ns)		ns
[116]	Diameter 2 mm, length 10 mm	Ti	No	Femur (medullary cavity)	MNRs on Ti were developed, with fixed interrod spacing of about 70 nm, and fluorine (F) incorporated $Ca_9Sr_1(PO_4)_6(OH)_2$ (Sr_1−HA, strontium containing hydroxyapatite) with the fixed Sr but different F content.	24	Ti (*n* = 4) MNR-F0 (*n* = 4) MNR-F1 (*n* = 4) MNR-F2 (*n* = 4) MNR-F5 (*n* = 4) MNR-F7 (*n* = 4) Ti + PBS (*n* = 4)		ns
[117]	Diameter 2 mm, length 6 mm	Ti	No	Femur (two holes (φ 2 mm) were drilled on each leg)	Implant coated with polyethylene glycol (PEG)-based thermoresponsive polymer (MPEG) and an antimicrobial peptide (AMP) HHC36.	ns	Ti (*n* = ns) Ti-M2 (Ti treated with MPEG2 solution) (*n* = ns) Ti-A (Ti treated with HHC36 peptide solution) (*n* = ns) Ti-M2-A (Ti-M2 treated with HHC36 peptide solution) (*n* = ns)		ns

Table 3. *Cont.*

References	Implant				Interventions Used against PJI	Total Number of Rabbits	Experimental Groups and Number of Rabbits per Group (*n*)	Dropout Number	
	Description	Material	Movement Prevention	Location (Specified)				Per Experimental Group [%]	Total [%]
Other									
[118]	Screw 4 × 14 mm, with U-shaped washer	S.S. screw, UHMWPE washer	No	Femur (lateral femoral condyle)	Seven days after inoculation each knee was lavaged twice. Each rabbit had one experimental knee with 3.5% dilute Betadine solution, and one control knee with normal saline.	8	*n* = 8	0	0
[119]	Kirshner wire, length 1 cm	Stainless steel	No	Radius (1 cm defect was created)	PNDJ1.51 with tobramycin, low-dose antimicrobial loaded bone cement (ALBC) with tobramycin, systemic tobramycin.	30	PNDJ1.51 with tobramycin (*n* = 6 MSSA) PNDJ1.51 with tobramycin (*n* = 6 MRSA) Low-dose antimicrobial-loaded bone cement (ALBC) with tobramycin (*n* = 7 MSSA) Systemic tobramycin (*n* = 7 MSSA)	ns ns ns ns	13
[120]	Length 40 mm, diameter 3.5 mm	Ti	No	Tibia (proximal metaphysis and diaphysis)	Smooth Ti, grit-blasted Ti, HA-coated Ti, trabecular metal, cancellous Ti rods.	50	Smooth Ti (*n* = 10) Grit-blasted Ti (*n* = 10) HA-coated Ti (*n* = 10) Trabecular metal (*n* = 10) Cancellous Ti rods (*n* = 10)		0

Table 3. *Cont.*

References	Implant				Interventions Used against PJI	Total Number of Rabbits	Experimental Groups and Number of Rabbits per Group (*n*)	Dropout Number	
	Description	Material	Movement Prevention	Location (Specified)				Per Experimental Group [%]	Total [%]
[121]	Ab-PLGA screw: outer diameter 2.7 mm, length 24 mm, pitch 0.0 mm. (Group I and III). Control screw: diameter 2.7 mm, length 14 mm, pitch 1.0 mm (Group II and IV)	Ab-PLGA: self-reinforced ciprofloxacin containing poly(lactide-co-glycolide) 80:20. Control: standard S.S.	Screwed into bone	Tibia (proximal metaphysis)	Ab-PLGA screw with ciprofloxacin or a S.S. screw. The surgical field was lavaged with 100 mL of sterile saline in the inoculated groups. In negative control animals (no inoculum), a similar lavage of the wound space was performed, but with 150 mg of cefuroxime sodium.	24	Ab-PLGA screw + *S. aureus* (*n* = 8) SS screw + *S. aureus* (*n* = 8) Ab-PLGA (*n* = 4) SS screw (*n* = 4)		ns
[122]	Screw and washer	s.s. screw, UHMWPE washer	Cement	Femur (tunnel was created through condyle)	Administration of AZD6389 * or IgG1, as control, 12 h before inoculation.	26	AZD6389 * (*n* = 13) Control (*n* = 13)		ns
[123]	Length 2 cm, diameter 0.2 cm	Ti–CU sintered alloy, pure Ti as control	No	Femur (medullary cavity)	Ti–Cu nail (Cu–Ti/Ba) or pure Ti nail with infection sacrificed either at day 1, 7, 14, or 28.	24	Cu–Ti/Ba (*n* = 3 per day of sacrifice) Ti/Ba (*n* = 3 per day of sacrifice)		ns

Table 3. *Cont.*

References	Implant				Interventions Used against PJI	Total Number of Rabbits	Experimental Groups and Number of Rabbits per Group (*n*)	Dropout Number	
	Description	Material	Movement Prevention	Location (Specified)				Per Experimental Group [%]	Total [%]
[124]	Screw diameter 3.5 mm, length 15 mm. Washer inner diameter 3.5 mm, external diameter 8 mm, thickness 1.5 mm	s.s. screw and UHMWPE washer	No	Femur (lateral femoral condyle)	Lavage with allicin, with or without VAN (14 days after inoculation).	32	Normal saline (n = 8) VAN (n = 8) Allicin (n = 8) Allicin with VAN (n = 8)		ns
[125]	Silastic implant (Dow Corning, Midland, MI, USA), length 14 mm, implant head 15 × 5 mm	Silicone	No	Tibia (medullary cavity, replacing tibia plateau)	Injected with 1 mL of bacteriocin suspension or saline.	12	Bacteriocin (n = 6) Control, saline (n = 6)		ns
[126]	2 mm diameter, 15 mm long	Kirschner wires	No	Femur (medullary canal, through intercondylar notch)	Bone marrow stem cells (BMSCs) infected with the recombinant PR-39 lentiviruses (pLV/PR-39).	24	BMSCs infected with pLV/PR-39 (n = 12) Control, BMSCs infected with pLV/EGFP (n = 12)	ns ns	4

*[1] Rabbits were replaced in these studies.

4.3. Outcome Measures

What outcome measures are relevant for an experiment depends on the research goal. Bacterial culture and health monitoring are standard when investigating new antibacterial technologies against PJI in a rabbit. Hematology, histology, and imaging can study infection and bone growth more extensively. Tables 4 and 5 show all outcome measures implemented by the studies included in this review and are discussed below. The range of possible outcome measures is extensive. Nevertheless, it is essential to adhere to the 3Rs principle [38]. Increasing the number of outcome measures often necessitates including additional rabbits in the experimental groups. Therefore, the scientific value gained from including additional outcome measures must justify the increased burden on the animals or a larger group size.

4.3.1. Bacterial Culture

In a PJI rabbit model, bacterial culture is the most important outcome measure when studying bacterial adhesion and biofilm formation and its prevention. Bacterial culture can confirm or negate and quantify an infection and assess the antimicrobial efficacy of the novel antibacterial compound. Moreover, culturing is still the gold standard in diagnosing PJI in the clinic, and implant sonication is the most likely diagnostic test to confirm PJI [151]. Remarkably, three studies included in this review did not report on any bacterial culture. A significant amount of variation between the cultured tissue, the culturing method, and the unit of measurement was observed among the studies included in this review.

The cultured tissue in the studies included in this review ranges from one swab to culturing multiple tissues. The most cultured tissues are the implant, bone tissue, soft tissue, synovial fluid, and periprosthetic tissue. A blood sample may also be cultured to detect systemic infection. The samples used for the culture depend on the working mechanisms of the antibacterial technology and the study's objective. One article included in this review did not specify what material they cultured [119]. The cultured tissues vary the most for the studies included in this review that did not use an intervention against PJI. Craig et al. [69] cultured samples from the arterial blood; joint capsule; synovial scar surrounding the screw, surrounding bone, liver, and kidney samples; and the UHMPHE washer, screw, and affixed bone cement complex. However, this was their only outcome measure other than basic health monitoring. Other studies only cultured the exudate around the implant (Sarda et al. [74], Sarda-Mantel et al. [75], Tang et al. [76]); however, they tried to visualize the infection using 99mTc scintigraphy and used the culture as a control. This demonstrates that the selection and number of cultures to perform depend on the study's objective and the other employed outcome measures. For the studies included in this review that used revision, antibiotics, surface modifications, coatings, or other antibacterial techniques, the antibacterial working mechanism is leading for the cultures. Brunotte et al. [79] studied a spacer during two-stage revision; therefore, they cultured both implants and the spacer to track bacterial growth over time. For antibacterial technologies that depend on surface modifications or a contact-killing or anti-fouling coating, the most important outcome is if bacteria are still growing on the implant. However, it is still interesting if bacteria survive in the tissue around the implant, even though they cannot survive on the implant itself. Interpretation of this data might be difficult, as a negative culture of the implant, combined with a positive culture of tissue surrounding the implant, does not mean the bacterial technology does not sufficiently work. All studies included in this review that researched surface modifications cultured the implant and the bone or interfacial tissue surrounding the implant. For coatings or techniques that leach the antibacterial compound into the tissue surrounding the implant, both the implant and surrounding tissue should be cultured. Unfortunately, the rabbits used for tissue culturing cannot be used for histology or imaging for which the implant must be taken out or slices of the limb must be made. Therefore, it is inefficient and wasteful to use a rabbit for a single tissue culture when multiple cultures could provide more information. The suffering of the animals should

yield as much quantifiable data as possible. Conducting multiple cultures can aid in quantifying the bacteria and determining their distribution.

The culturing method, and the unit of measurement this results in, vary greatly too. Several studies use a swab method, from which it can be concluded if a site was infected or not. Overstreet et al. [85] and Zhang et al. [114] used swabs as their sole bacterial culture method. However, relying solely on swabs can overlook deeper-seated bacteria, result in false negatives when bacterial counts are low, and the results are dependent on the technique and the specific location swabbed. Most studies included in this review that used a swab also plated out samples, generating quantifiable data. In these instances, swabs can offer additional information on less critical sites. Plating out the sonicate of the implant or homogenized soft tissue or bone is commonly performed. The culturing of these fluids differs per study and laboratory. However, the plating of serial dilutions is the most common and results in the exact CFU per sample. There are exceptions, like Brunotte et al. [79], who rolled the implants over an agar plate, or Yu et al. [123], who counted until a maximum of 1000 CFU. Serial dilution of samples should be performed in all studies, as it provides clear, quantifiable data and aids in distinguishing between experimental groups. Of the studies included in this review, 10% did not report the used culturing method [80,87,89,98,104,119], and 10% did not report the unit of their outcome measure [73,81,83,85,90,127].

4.3.2. Health Monitoring

Health monitoring, including measuring the weight and temperature of the rabbits and checking for clinical signs of infection, is important for maintaining and assessing animal welfare (refinement) [64]. Animal welfare monitoring is important in deciding whether a humane endpoint has been met [45]. Among the studies included in this review, 28% did not report any health monitoring. Of the 60 studies, only 26 reported the rabbits' weights, 25 reported the rabbits' temperatures, and 28 reported clinical signs of infection. Whereas temperature and weight are standard physiological markers of illness, there is a wide range of clinical signs of infection that researchers can look for, as presented in Tables 4 and 5. As stated by Mapara et al. [33], health monitoring should include assessing if the rabbit is bright, alert, active, inquisitive, has a smooth coat, and a good body condition. Pain or infection may be shown as a change in gait, abnormal weight distribution, retraction of injuries, changed postures, swelling, inflammation, decreased activity, bad wound healing, or decreased food and water intake. Exorbitant pain may lead to shock or abstinence from eating, which may lead to death [33]. Monitoring the rabbits' health may lead to preventative care to maintain the welfare of the rabbits, like administering extra analgesia or force-feeding. A well-designed score sheet may help the caretakers of the rabbits to assess their health objectively and should be used in all animal studies [24,152]. Multiple score sheets already exist, like the Bristol Rabbit Pain Scale [153] and the Rabbit Grimace Scale [154]. The ARRIVE guidelines also state that welfare-related assessments and health status should be documented [43,44].

Table 4. Outcome measures extraction results—part 1. Abbreviations used: ns = not stated.

Reference	Bacterial Culture			Health Monitoring (1 = Measured Daily, 2 = Measured Weekly, 3 = Post-Mortem, 4 = Not Stated When)			Hematology (1 = Measured Daily, 2 = Measured Weekly)			
	Tissue Cultured	CULTURE Method (1= Homogenized (For Bone) or Vortexed (For Implant), Sonicated, Serial Diluted, and Plated)	Outcome Unit	Weight	Temperature	Clinical Signs of Infection a. Swelling b. Inflammation c. Activity d. Food Intake e. Wound Healing f. Pus g. Clinical Signs of Infection	C-reactive Protein (CRP)	Erythrocyte Sedimentation Rate (ESR)	Leucocyte WBC/ Differentiation	Interleukin-6 (IL-6)
No intervention used										
[69]	Arterial blood, joint capsule, synovial scar surrounding the screw, UHMPHE washer, screw with bone cement complex, surrounding bone, liver and kidney samples	Biopsies, sonicated and plated	CFU/g of tissue, CFU/mL joint fluid, CFU/unit for the screw–washer complex		1	Inside joint and fluid were graded on a three-point scale of infection				
[70]	Tibial plateau at point of insertion and nail and bone surrounding the nail	Swabs and sonication	CFU	2	2	4, c, d, g			2	
[71]	Intra-articular samples, and sample from bone (tibial canal), soft tissue (synovial and capsule), and implant	Sonicated, seeded on agar plates	CFU	At time of inoculation and 7 days thereafter	At time of inoculation and 7 days thereafter	4, f, macroscopic appearance of the joint, fistula, or other wound complications. Knee bending and weight-bearing		Yes	Yes	
[29]	Knee joint cavity and tibial plateau and tuberositas tibiae	Swabs and tissue removal, homogenized, cultured		2, and on the day of surgery	2, and on the day of surgery	4, b, e, a, use of hindlegs	Yes	Yes	Yes	

Table 4. *Cont.*

Reference	Bacterial Culture			Health Monitoring (1 = Measured Daily, 2 = Measured Weekly, 3 = Post-Mortem, 4 = Not Stated When)			Hematology (1 = Measured Daily, 2 = Measured Weekly)			
	Tissue Cultured	CULTURE Method (1= Homogenized (For Bone) or Vortexed (For Implant), Sonicated, Serial Diluted, and Plated)	Outcome Unit	Weight	Temperature	Clinical Signs of Infection a. Swelling b. Inflammation c. Activity d. Food Intake e. Wound Healing f. Pus g. Clinical Signs of Infection	C-reactive Protein (CRP)	Erythrocyte Sedimentation Rate (ESR)	Leucocyte WBC/ Differentiation	Interleukin-6 (IL-6)
[72]	Bone	Cultured	Bacterial growth yes/no	4		4, weight bearing on the operated leg	Yes	Yes		
[73]	Bone with marrow	Homogenized		Before implantation, inoculation, and sacrifice	Before implantation, inoculation, and sacrifice	1, c, d, e, g		Before implantation, inoculation, and sacrifice	Before implantation, inoculation, and sacrifice	
[74]	Exudate around prosthesis	Spread onto blood-agar	Infection yes/no			3 arthritis, osteitis, and tibial myelitis analysis				
[75]	Exudate around prosthesis	Spread onto blood-agar	Infection yes/no							
[76]	Exudate around prosthesis	Cultivated on blood agar for 72 h	CFU yes/no			3, b, f, joint effusion, abscess formation, cortical lysis				
[77]	Implant and knee joint	1	log10 CFU/joint or implant	2	2		2			
[78]	Soft tissue	72 h growth	Bacterial growth yes/no				Biweekly			Biweekly
[30]	Implant	Sonicated and cultured	CFU	Every 48 h	Every 48 h		Day 3/5/7/ 14/21/28	Day 3/5/7/ 14/21/28	Day 3/5/7/ 14/21/28	

Table 4. *Cont.*

Reference	Bacterial Culture			Health Monitoring (1 = Measured Daily, 2 = Measured Weekly, 3 = Post-Mortem, 4 = Not Stated When)			Hematology (1 = Measured Daily, 2 = Measured Weekly)			
	Tissue Cultured	CULTURE Method (1= Homogenized (For Bone) or Vortexed (For Implant), Sonicated, Serial Diluted, and Plated)	Outcome Unit	Weight	Temperature	Clinical Signs of Infection a. Swelling b. Inflammation c. Activity d. Food Intake e. Wound Healing f. Pus g. Clinical Signs of Infection	C-reactive Protein (CRP)	Erythrocyte Sedimentation Rate (ESR)	Leucocyte WBC/ Differentiation	Interleukin-6 (IL-6)
Revision										
[79]	Removed K-wires (day 28 and day 84) and spacers (day 56)	Rolled on agar plate and sonication with plating	CFU/mL	1		a				
[80]	Implant		Positive yes/no			4, c, d, g, local pain. formation of fistulae				
[81]	Upper third of tibia	Crushed, pulverized				Skin aspect was noted 14 days after inoculation				
[82]	Bone	Homogenized, plated	CFU/g of bone							
[83]	Intra-articular culture and Bone, soft tissue, and spacers	ns and sonicated		Day 0, 8, 11, 15, 22, 29, 36	Day 0, 8, 11, 15, 22, 29, 36	Checked for fistulas in contact with articulation		Day 0, 8, 11, 22, 29, 36	Day 0, 8, 11, 22, 29, 36	
[84]	Bone	1	CFU/g of bone	Regularly	Regularly			2	2, WBC	
[85]	Wire and biopsy of adjacent tissue	Swab cultures				a				
[86]	Cortical bone, bone marrow, muscle tissue, bone, and synovial fluid	Homogenized and cultured	Scored 0–10	Day 1, 30, 60	Day 1, 30, 60	3, g, pain on palpation, abscess	Day 1, 30, 60	Day 1, 30, 60		

Table 4. *Cont.*

Reference	Bacterial Culture			Health Monitoring (1 = Measured Daily, 2 = Measured Weekly, 3 = Post-Mortem, 4 = Not Stated When)			Hematology (1 = Measured Daily, 2 = Measured Weekly)			
	Tissue Cultured	CULTURE Method (1= Homogenized (For Bone) or Vortexed (For Implant), Sonicated, Serial Diluted, and Plated)	Outcome Unit	Weight	Temperature	Clinical Signs of Infection a. Swelling b. Inflammation c. Activity d. Food Intake e. Wound Healing f. Pus g. Clinical Signs of Infection	C-reactive Protein (CRP)	Erythrocyte Sedimentation Rate (ESR)	Leucocyte WBC/ Differentiation	Interleukin-6 (IL-6)
Prevention: antibiotics only										
[87]	Tissue and pus or hematoma present adjacent to the implant		Positive of negative culture	Before euthaniza-tion	1	4, a, redness, ambulatory status, favoring limb				
[88]	Swabs of entrance of implant and intramedullary canal. Bone, implant	Swabs cultured. Bone: 1	Bacterial growth yes/no	1						
[89]	The implanted femoral bone swabs, blood sample	Swabs	CFU			4, e, g, mobility, ability to thrive				
[90]	Prosthesis and bone	Smear and crushed, pulverized								
[91]	Intra-medullary femur, blood sample	Swab, culture	CFU/mL							
[92]				Day 0, 7, 14, 21, 42	Day 0, 7, 14, 21, 42				Pre-op and 6 weeks post-op	
[93]					2, minus week 3				WBC, 1, 2, 4 weeks	

Table 4. *Cont.*

Reference	Bacterial Culture			Health Monitoring (1 = Measured Daily, 2 = Measured Weekly, 3 = Post-Mortem, 4 = Not Stated When)			Hematology (1 = Measured Daily, 2 = Measured Weekly)			
	Tissue Cultured	CULTURE Method (1= Homogenized (For Bone) or Vortexed (For Implant), Sonicated, Serial Diluted, and Plated)	Outcome Unit	Weight	Temperature	Clinical Signs of Infection a. Swelling b. Inflammation c. Activity d. Food Intake e. Wound Healing f. Pus g. Clinical Signs of Infection	C-reactive Protein (CRP)	Erythrocyte Sedimentation Rate (ESR)	Leucocyte WBC/ Differentiation	Interleukin-6 (IL-6)
[94]	Tibia and bone tissue	Rolled in agar and cultured in broth	CFU on agar/cloudiness of broth	Days 0, 3, 7, 14, 21, 28, 35, 42	Day 0, 3, 7, 14, 21, 28, 35, 42	4, clinical signs of infection				
[95]	Tibia	1	CFU/g bone							
[96]	Upper 1/3rd of Tibia	1	CFU/g of bone							
[97]	Implant, Tibia	Implant smear. Bone: 1	Sterile yes/no, log10 CFU/g of bone							
[98]	Bone and tissue		Infection yes/no							
Prevention: surface modification										
[99]	Implant and bone	Sonication, plated	CFU/g bone, CFU/cm^2 implant	1	1	Pain and stress of the rabbits were observed				
[100]	Bone and implant	Bone crushed and spread on agar plate; implant rolled on agar plate	Qualitative	1	1					
[101]	Nail and proximal tibial bone that surrounded the nail	Vortexed, sonicated, plated	CFU/nail or CFU/bone fragment	First 3 days, and on days of blood sampling	First 3 days, and on days of blood sampling				Day 0 and 72, weekly until the end of the study	

Table 4. *Cont.*

Reference	Bacterial Culture			Health Monitoring (1 = Measured Daily, 2 = Measured Weekly, 3 = Post-Mortem, 4 = Not Stated When)			Hematology (1 = Measured Daily, 2 = Measured Weekly)			
	Tissue Cultured	CULTURE Method (1= Homogenized (For Bone) or Vortexed (For Implant), Sonicated, Serial Diluted, and Plated)	Outcome Unit	Weight	Temperature	Clinical Signs of Infection a. Swelling b. Inflammation c. Activity d. Food Intake e. Wound Healing f. Pus g. Clinical Signs of Infection	C-reactive Protein (CRP)	Erythrocyte Sedimentation Rate (ESR)	Leucocyte WBC/ Differentiation	Interleukin-6 (IL-6)
[102]	Implant surface and interfacial tissue exposed along the implant	Swabs and tissue samples plated	CFU							
Prevention: coating										
[103]	Implant + swab and irrigation from knee	Cultured	Infection yes/no	2	2	4, general well-being, posture				
[104]	Anterior bone fragments		CFU/g of bone					Week 1, 2, 3, and 4 post-op		
[105]	Implant and bone marrow	Sonicated/ vortexed and plated	CFU/g of bone/marrow			3, a, b, f, edema, bone marrow quality				
[106]	Medullary canal, implant	Swab from canal, implant: 1	Positive culture yes/no, CFU/mL		2	1, c, d, e				
[107]	Intramedullary canal and rods	Swab culture and sonication and plating	CFU/cm^2			4, c, d, e	Before surgery, week 2, 6, 10			
[108]	Implant and humerus	1	CFU/bone fragment or implant	2, and day 3			2, and day 3		2, and day 3, WBC	
[109]	Tibia	1	CFU/g of bone	1	1	1, c, d, e		2	2	

Table 4. *Cont.*

Reference	Bacterial Culture			Health Monitoring (1 = Measured Daily, 2 = Measured Weekly, 3 = Post-Mortem, 4 = Not Stated When)			Hematology (1 = Measured Daily, 2 = Measured Weekly)			
	Tissue Cultured	CULTURE Method (1= Homogenized (For Bone) or Vortexed (For Implant), Sonicated, Serial Diluted, and Plated)	Outcome Unit	Weight	Temperature	Clinical Signs of Infection a. Swelling b. Inflammation c. Activity d. Food Intake e. Wound Healing f. Pus g. Clinical Signs of Infection	C-reactive Protein (CRP)	Erythrocyte Sedimentation Rate (ESR)	Leucocyte WBC/ Differentiation	Interleukin-6 (IL-6)
[110]	Bone, implant	1	CFU/g of bone, CFU/implant	4	4	1, g, abscess formation, cortical lysis			Midway, end of study, WBC and differentiation	
[111]	Tibia	1	CFU/g of bone	4	4	4, c, d, e		Yes	WBC	
[112]	Blood, knee joint, and tibia marrow	Cultivated on blood agar	Bacterial growth yes/no							
[113]	Implant	Sonicated and plated	Bacterial growth yes/no							
[114]	Implant	Swab culture	Qualitative assessment		Regularly		2		2, WBC	
[115]	Implant	Sonicated and plated, and turbidity measured	CFU							
[116]	Implant and femur	1	CFU							
[117]	Implant and marrow	4 h culture in broth then plated	CFU							

Table 4. *Cont.*

Reference	Bacterial Culture			Health Monitoring (1 = Measured Daily, 2 = Measured Weekly, 3 = Post-Mortem, 4 = Not Stated When)			Hematology (1 = Measured Daily, 2 = Measured Weekly)			
	Tissue Cultured	CULTURE Method (1= Homogenized (For Bone) or Vortexed (For Implant), Sonicated, Serial Diluted, and Plated)	Outcome Unit	Weight	Temperature	Clinical Signs of Infection a. Swelling b. Inflammation c. Activity d. Food Intake e. Wound Healing f. Pus g. Clinical Signs of Infection	C-reactive Protein (CRP)	Erythrocyte Sedimentation Rate (ESR)	Leucocyte WBC/ Differentiation	Interleukin-6 (IL-6)
Other										
[118]	Blood, implant, bone, joint capsule	1	CFU/g of biopsied tissue	1		1, e, distress				
[119]			Sterile yes/no			4, a, f				
[120]	Implant, bone–implant interface, metaphyseal bone	Conventional cultures and PCR	CFU			1, d, e, g, physical condition				
[121]	Subfascial soft tissues, screw heads, screw tract, and removed screws	Swab cultures and incubation in broth	CFU/g of bone	Yes, in week 3 and 6		4, a, and erythema				
[122]	Implant, joint capsule, all infected synovial tissue	Sonicated and cultured	log10 CFU			3, a, f, erythema,				
[123]	Implant and surrounding tissue swabs	Cultured in medium	CFU, max of 1000		1	1, incision redness, swollen, exudate		Day 1/4/7/14	WBC day 1/4/7/14	Day 1/4/7/14
[124]	Screws	Washed, sonicated, plated	CFU/mL	4	4					
[125]							1			1
[126]	Bone	1	CFU				Day 1, 3, 7, 14	Day 1, 3, 7, 14		

Table 5. Outcome measures extraction results—part 2.

Reference	Histology (Stained Area Specified)				Imaging				Other
					X-ray		Other		
	H&E Staining	Other	Infection Scoring (1 = Qualitative, 2 = Semi-Quantitative Ordinal scoring)	Bone Apposition Scoring	Pre-Mortem	Post-Mortem	Pre-Mortem	Post-Mortem	
No intervention used									
[69]									
[70]	Yes	Brown and Brenn stain	1		Post-operative to assess placement of implant	To assess migration of implant and signs of osteomyelitis			
[71]									
[29]		Masson–Goldner or Gram staining	2		After 6 weeks, osteomyelitis scoring system			µCT with osteomyelitis scoring system	Fluorescence microscopy, 3 different calcium-binding fluorophores were administered at week 2 (calcein green), 4 (xylenol orange), and the day before sacrifice (calcein blue)
[72]		Masson–Goldner or Gram			Weekly, periosteal elevation, cortical thickening, and osteolysis		18F-FDG uptake PET before and at week 1, 3, and 6, infection	µCT, ex vivo, infection yes/no	
[73]		Gram staining	2			Yes			PCR to reveal the presence of *S. aureus* DNA. RT-PCR to confirm viability of microorganisms

Table 5. *Cont.*

Reference	Histology (Stained Area Specified)				Imaging				Other
					X-ray		Other		
	H&E Staining	Other	Infection Scoring (1 = Qualitative, 2 = Semi-Quantitative Ordinal scoring)	Bone Apposition Scoring	Pre-Mortem	Post-Mortem	Pre-Mortem	Post-Mortem	
[74]							99mTc-Ciprofloxacin Imaging, 5/12/19 days after surgery		
[75]							99mTc-UBI 29-41 scintigraphy day 9 and 20		
[76]	Yes		1				MRI day 7 and 21, biodistribution of 99mTc-annexin V		
[77]							Weekly 18F-FDG and 68Ga-FAPI PET/CT, SUVmax, SUVmean, MTV, and total lesion glycolysis/total lesion fibrosis		Change in knee width pre- and post-operatively
[78]	Yes	IHC for CD45 and FAP	1				Biweekly 18F-FDG and 68Ga-FAPI PET/CT [SUVmax, SUVmean, MTV]	μCT for BS/BV, BS/TV, BV/TV	Pullout strength, FAP
[30]	Yes	Modified Gram's	1		Weekly for Friedman assessing				

Table 5. *Cont.*

Reference	Histology (Stained Area Specified)				Imaging				Other
					X-ray		Other		
	H&E Staining	Other	Infection Scoring (1 = Qualitative, 2 = Semi-Quantitative Ordinal scoring)	Bone Apposition Scoring	Pre-Mortem	Post-Mortem	Pre-Mortem	Post-Mortem	
Revision									
[79]	Yes	Toluidine-blue, Gram staining	1						
[80]	Yes		1			Yes, bone thickness, sclerosis, cysts, diaphysitis			
[81]									
[82]									
[83]									
[84]					After first operation, and before and after revision surgery on day 28, reactive bone tissue and infection				PCR for bacterial DNA in tibial cortex
[85]	Yes								
[86]	Yes	Gram	2						
Prevention: antibiotics only									
[87]		Methylene blue		Tissue ingrowth [%]		Yes, radiographs of both forelimbs			
[88]									

Table 5. *Cont.*

Reference	Histology (Stained Area Specified)				Imaging				Other
					X-ray		Other		
	H&E Staining	Other	Infection Scoring (1 = Qualitative, 2 = Semi-Quantitative Ordinal scoring)	Bone Apposition Scoring	Pre-Mortem	Post-Mortem	Pre-Mortem	Post-Mortem	
[89]									
[90]									
[91]									Toluidine blue, acid fuchsin, and fast green used for histocompatibility study only, not infection model
[92]	Yes	Masson-Goldner trichrome	2						
[93]	Yes		1		1 and 2 weeks, inflammatory response				
[94]	Yes	Toluidine-blue	2		X-rays taken on days 0, 7, 14, 21, 28, 35 and 42. Seven inflammatory criteria were scored, maximum score of 17				
[95]									
[96]									

Table 5. *Cont.*

Reference	Histology (Stained Area Specified)				Imaging				Other
					X-ray		Other		
	H&E Staining	Other	Infection Scoring (1 = Qualitative, 2 = Semi-Quantitative Ordinal scoring)	Bone Apposition Scoring	Pre-Mortem	Post-Mortem	Pre-Mortem	Post-Mortem	
[97]									Mutant-resistant MRSA sought in positive cultures (defined as having 3-fold-increased MICs)
[98]		Masson–Goldner trichrome		Calcified and non-calcified tissue around implant [%]					Mechanical testing of implant stability
Prevention: surface modification									
[99]	Yes			Osseointegration, bone–implant membrane interface, polymorphonuclear cellularity per high-power field. Complete, partial, non-existent osseointegration					
[100]		Gram	1		After operation and 28 days, for osteomyelitis				

Table 5. *Cont.*

Reference	Histology (Stained Area Specified)				Imaging				Other
					X-ray		Other		
	H&E Staining	Other	Infection Scoring (1 = Qualitative, 2 = Semi-Quantitative Ordinal scoring)	Bone Apposition Scoring	Pre-Mortem	Post-Mortem	Pre-Mortem	Post-Mortem	
[101]									
[102]	Yes	Masson's trichrome and Gram staining.		Bone to implant contact (BIC) (%), Bone volume (BV) (%), Mineralizing volume (MV) (%)	Immediately after surgery to verify implant location	After sacrifice to evaluate bony tissue adjacent to implant			Fluorescence microscopy: calcein green on 5th and 6th day to all animals, xylenol orange on 12th and 13th day only to 2 week animals
Prevention: coating									
[103]									
[104]		Fuchsin and methylene blue	2					μCT, analysis of bone apposition on the implant surface (% of bone–implant contact)	Injections of fluorochromes (xylenol orange and calcein green) were used to visualize dynamic bone formation. At day 3 and 10 or day 7 and 21
[105]	Yes	Gram	2						
[106]	Yes		1			Osteolysis around implant scored			
[107]	Yes	Masson's trichrome	1						

Table 5. *Cont.*

Reference	Histology (Stained Area Specified)				Imaging				Other
					X-ray		Other		
	H&E Staining	Other	Infection Scoring (1 = Qualitative, 2 = Semi-Quantitative Ordinal scoring)	Bone Apposition Scoring	Pre-Mortem	Post-Mortem	Pre-Mortem	Post-Mortem	
[108]	Yes	Brown–Brenn	1		Day 1 and 7, for infection signs			Head of nail used for SEM	
[109]		Fuchsine and methylene blue	2	Bone–implant contact, bone area	Check implant position				
[110]									
[111]		Basic fuchsin and methylene blue	1	Bone–implant contact, bone area [%]					
[112]	Yes		1						
[113]	Yes	Masson trichrome	1		Week 2 and 4 for infection signs		Week 1 and 2 radionuclide bone scanning for inflammation signs		
[114]	Yes		2			Yes, for fracture healing and callus index			
[115]	Yes	Giemsa staining for bacteria.						µCT [BV/TV, BS/BV, tTb.Th, Tb.*n*, and Tb.Sp] and FE-SEM of implant	Fluorochromes staining with alazarin red and calcein for bone formation and methylene blue acid magenta

Table 5. *Cont.*

Reference	Histology (Stained Area Specified)				Imaging				Other
					X-ray		Other		
	H&E Staining	Other	Infection Scoring (1 = Qualitative, 2 = Semi-Quantitative Ordinal scoring)	Bone Apposition Scoring	Pre-Mortem	Post-Mortem	Pre-Mortem	Post-Mortem	
[116]		Van Gieson's picrofuchsin		Bone-to-implant contact					Pullout strength
[117]	Yes	Methylene blue and basic fuchsin		Area of fibrous connective tissue at bone–implant interface				μCT [BV/TV, tTb.Th, Tb.*n*, and Tb.Sp]	
Other									
[118]									
[119]									
[120]						Ex-vivo fluoroscopy for infection/osteolysis			
[121]	Yes					Sequestral bone formation, periosteal new bone formation, destruction of bone, screw loosening, peri-implant reaction, soft-tissue calcification, and swelling evaluated, numerical score was assigned for each variable	18F-FDG-PET imaging, for imaging of biomaterial-related infection		

Table 5. *Cont.*

Reference	Histology (Stained Area Specified)				Imaging				Other
					X-ray		Other		
	H&E Staining	Other	Infection Scoring (1 = Qualitative, 2 = Semi-Quantitative Ordinal scoring)	Bone Apposition Scoring	Pre-Mortem	Post-Mortem	Pre-Mortem	Post-Mortem	
[122]								SEM of implant	Total weight of infected synovial tissue
[123]	Yes		1		Day 1/7/14/28 for evaluation of periosteal reaction, osteolysis, or abscess formation				
[124]								SEM of washer surface biofilm formation	
[125]		0.01% acridine orange							
[126]	Yes				Day 14, to check bone density				

4.3.3. Hematology

As rabbits are prey animals, they hide or show few clinical signs of illness [33,155]. Hematology might provide extra information about infection progression and the health of the rabbit, without sacrifice. The most common hematology parameters to test in PJI research are C-reactive protein (CRP), erythrocyte sedimentation rate (ESR), and white blood cell count (WBC), optionally including leukocyte differentiation [156,157]. Only 38% of the studies included in this review used hematology. Twelve studies measured CRP, thirteen measured ESR, sixteen measured WBC, and three measured IL-6.

Both CRP and ESR are non-specific markers for PJI, and could also be elevated from post-operative inflammation [156]. Several studies included in this research that compared uncontaminated and contaminated implants have also shown that, in rabbits, a rise in CRP, ESR, and WBC correlates with PJI [30,72,73,127]. As leukopenia can also be a stress response, changes in leukocyte differentiation are a better indication of infection than WBC alone, e.g., a deviation from the 1:1 ratio between neutrophils and lymphocytes [155,158]. Furthermore, monocytosis may indicate chronic inflammation, although, from a normal monocyte count, it cannot be concluded that inflammation is not present [155]. Odekerken et al. [127] compared an uncontaminated and contaminated implant in NZW rabbits, and found a lower lymphocyte count, a higher neutrophils count, and monocytosis in the contaminated group. Interleukin-6 (IL-6) is potentially a more accurate parameter; however, clinical studies that report on this marker in PJI are limited [157]. Wang et al. [78] studied PJI in NZW rabbits, and found higher IL-6 values for the contaminated group compared to the uncontaminated group. Interpretation of hematological parameters in rabbits might be difficult, as prolonged stress might influence these parameters [155]. CRP, ESR, WBC, and IL-6 are not accurate enough to conclude that an infection is present or not, but they indicate there might be an infection and should be used as supplements to other outcome measurements [159].

4.3.4. Histology

Different stainings can aid in scoring areas surrounding the implant for infection or bone apposition. The choice of staining depends on the goal of the study. More than half (60%) of the studies included in this research used histology as an outcome parameter, of which Hematoxylin and Eosin (H&E) was the most popular. Due to the wide variety of staining techniques available, the study's objective should guide the selection of the appropriate staining method. Table 6 presents an overview of all stainings used in the articles included in this review, and what tissues are colored. As preparing and analyzing the histological samples is technically difficult, the expertise available can also guide in selecting the appropriate method. Unfortunately, histology cannot be performed in the same rabbits used for bacterial culture, and longitudinal studies are not possible in the same animal, increasing the sample size. The variability and reliability of the results can be impacted by variations in staining techniques and the quality of the tissue samples. However, including histology in a study allows for a detailed examination of tissue and cellular composition, adding an understanding of the working mechanism of the antibacterial technologies compared to untreated groups. Histology can indicate the extent of infection, inflammation, and tissue damage, providing a comprehensive understanding of the pathological changes associated with PJI.

Table 6. Overview of various staining techniques and their application used in the articles included in this review.

Staining	Tissue Stained (Color)	References
Hematoxylin and Eosin (H&E)	Nuclei (blue) Cytoplasm and extracellular matrix (pink) Condensation of hematoxylin in nuclei is cell-specific Differentiates between osteocytes, osteoblasts, chondrocytes, and fibroblasts	[30,70,76,78–80,85,86,92–94,99,102,105–108,112–115,117,121,123,126]
(Modified) Gram	Gram-positive bacteria (purple-brown) Gram-negative bacteria (red) Eukaryotic cells do not stain	[29,30,72,73,79,86,100,102,105]
Brown Brenn	Gram-positive bacteria (blue) Gram-negative bacteria (red) Nuclei (red) Background tissue (yellow)	[70,108]
(Modified) Masson–Goldener trichrome	Collagen fibers (green/blue) Muscle fibers (red) Cytoplasm (red/pink) Nuclei (dark brown/black) Differentiates between calcified and non-calcified tissue	[29,72,92,98,102,107,113]
Fuchsin and methylene blue	Nuclei (blue) Cytoplasm (red/pink) Cartilage (blue to purple)	[87,104,109,111,117]
Toluidine-blue	Stains specific structures in tissues differently Used to visualize pathological and cortical bone formation, muscle, and bone sequesters	[79,94]
0.01% acridine orange	Visualize biofilm	[125]
Van Gieson's picrofuchsin	Bone tissue (red) Fibrous tissue (yellow)	[116]
Giemsa	Eukaryotic cells (purple) Bacterial cells (pink)	[115]

4.3.5. Imaging

Contrary to histology, for which the group size must increase, imaging is a non-invasive method to provide extra information without sacrificing the rabbits (Table 7). Furthermore, new technologies are being developed to track infection or bone growth over time. Half of the studies included in this review did not incorporate any imaging techniques. As radiography is a standard diagnostic procedure, it is the most used imaging technique in the studies included in this review. X-ray is a widely available and relatively inexpensive imaging option. Fourteen studies used X-ray pre-mortem, and nine studies used it post-mortem. X-ray is used to study placement and migration of the implant; signs of osteomyelitis; periosteal elevation; osteolysis; bone thickness; sclerosis; cysts; diaphysitis; soft tissue swelling and calcification; deformity; sequestrum formation; spontaneous fracture; callus index; and abscess formation. Several studies have used imaging techniques pre-mortem. PET scanning was used independently for 18F-fluorodeoxyglucose (18F-FDG) (Mäkinen et al. [121]), including CT and 68 Ga-fibroblast activation protein inhibitor (68Ga-FAPI) (Wang et al. [77,78]), or including μCT (Odekerken et al. [72]). 18F-FDG is a glucose analog and radioactive tracer, and it is taken up by cells with high glucose demand, such as inflammatory cells [160]. All four studies showed a higher 18F-FDG uptake in the infected groups. Both studies by Wang et al. [77,78] showed greater sensitivity to 68Ga-FAPI in detecting infection compared to 18F-FDG. Unfortunately, PET scans are significantly more

expensive than X-rays for rabbits, reflecting the specialized equipment required, compared to the more routine and widely available X-ray procedures. Technetium-99m (99mTc) has been used to detect infection by labeling it to annexin V, which binds to apoptotic cells (by Tang et al. [76]); ciprofloxacin, which targets living bacteria by binding to DNA gyrase (by Sarda et al. [74]); and ubiquicidin (UBI) 29-41, an antimicrobial peptide that binds to bacterial cell membranes (by Sarda-Mantel et al. [75]). 99mTc-ciprofloxacin accumulation was found in both infected and uninfected joints in the rabbits; however, 99mTc-annexin V and UBI29-41 could differentiate between infected and uninfected joints. Both the study by Tang et al. [76] and the study by Sarda-Mantel et al. [75] state that more research is needed before 99mTc labeling can be used as a diagnostic tool. Zhang et al. [113] used 99Tc-MDP, the stable end product of the decay of 99mTc, for bone scanning and visualization of areas with increased bone turnover. Tang et al. [76] also used MRI to visualize tissue changes around the prosthesis.

In addition to X-rays, μCT and SEM were used as post-mortem imaging techniques. After excision of the extremity including the implant, μCT can be implemented for both infection and bone apposition scoring. Bone apposition on the implant surface can be measured using the bone and tissue volume, and bone histomorphometry can be analyzed using the trabecular thickness, number, and separation [78,104,115,117]. μCT can give detailed insights into the bone (micro)structure and provide quantitative data. As the extremity needs to be excised and can be fixed, μCT is widely available, as samples can be sent to different laboratories. Several studies used SEM imaging to visualize the formed biofilm on the implant [108,115,122,124]. SEM can provide good visualization of the disposition of bacteria on the implant and the formed biofilm. However, bacterial adhesion cannot be quantified. SEM imaging is performed after explanting and fixating the implant, making the implant unusable for further bacterial cultures.

Table 7. Overview of imaging methods used by the articles included in this review. The outcome measures, including what is exactly visualized, are specified.

Imaging Method	Use	Pre- or Post-Mortem	References
X-ray	Placement and migration of the implant; signs of osteomyelitis; periosteal elevation; osteolysis; bone thickness; sclerosis; cysts; diaphysitis; soft tissue swelling and calcification; deformity; sequestrum formation; spontaneous fracture; callus index; and abscess formation	Both	[29,30,70,72,80,84,87,93,94,100, 102,106,108,109,113,114,120,121, 123,126]
PET (18F-FDG)	18F-FDG is a glucose analog and radioactive tracer and is taken up by cells with high glucose demand, visualizing inflammatory cells. PET 18F-FDG can be combined with, (μ)CT or 68Ga-FAPI	Pre-mortem	[72,77,78,121]
Scintigraphy with Technetium-99m labelling	Bone scanning, detects infection when labeled to Annexin V (binds to apoptotic cells); Ciprofloxacin (targets living bacteria); Ubiquicidin (binds to bacterial cell membrane)	Pre-mortem	[74–76]
Scintigraphy with 99Tc-MDP labeling	Bone scanning and visualization of areas with increased bone turnover.	Pre-mortem	[113]
μCT	Infection and bone apposition scoring. Can give detailed insights into the bone (micro)structure (bone and tissue volume, and bone histomorphometry can be analyzed using the trabecular thickness/number/separation). Provides quantitative data	Both	[78,104,115,117]
SEM	Visualize formed biofilm on implant	Post-mortem	[108,115,122,124]

Choosing an imaging technique is again dependent on the research goal of a study. However, it is also dependent on the availability of the imaging apparatus. Pre-mortem imaging techniques add valuable information, and animals can be followed over time as they do not need to be sacrificed. X-rays are available at most animal research institutes and may provide valuable information at a relatively low cost. Other pre-mortem techniques might provide more information about bone growth or infection; however, they are not available at all institutes and come with higher costs. SEM is more easily available; however, it requires sacrificing the rabbits.

4.3.6. Other Outcome Measures

The studies included in this review have measured several other outcomes that are less standard for a PJI rabbit model. Latex agglutination tests are commonly used to detect if *S. aureus* is present; however, they cannot differentiate between strains and sometimes give false negatives for MRSA [161]. Poultsides et al. [73] and Nijhof et al. [84] used PCR to check if the bacteria present in their bacterial cultures was the same strain as they injected at the start of the experiment or if the rabbit was infected with another strain. However, PCR cannot differentiate between living and dead bacteria. Furthermore, RT-PCR can be used to confirm the viability of the microorganisms [73]. Another study, by Saleh Mghir et al. [97], sought the development of mutant strains in their positive cultures, defined as having a three-fold-increased MIC. Infection was further analyzed by Wang et al. [78] by measuring a type II transmembrane protein FAP. FAP is involved in infection response and inflammation and is expressed when cells are under pressure [7]. Mao et al. [122] used the total weight of the infected synovial tissue (pus) as a measurement of infection. Fluorochrome staining was used to evaluate bone growth over time without sacrificing the rabbits. Several calcium-binding fluorophores can be injected at different time points. Four studies included in this review used two time points [102,104] or three time points [115,127]. Fluorescence microscopy is used after sacrificing the rabbits for visualizing dynamic bone growth. Mechanical testing of the excised limb was performed to evaluate the bone–implant integration and stability of the implant in several studies included in this review. Wang et al. [78] and Zhou et al. [116] tested the pull-out strength of the implant, and Schroeder et al. [98] measured the displacement of the implant after loading. Additional outcome measures may provide relevant information and aid the translation of PJI interventions to the clinic. Especially in longer studies, more information about bone ingrowth of the implant provides relevant information on how the implant might function in the clinic.

4.4. Limitations

Systematic reviews are valuable tools to evaluate and summarize multiple articles; however, they are not without their limitations. Every systematic review has the limitation of publication bias. Positive results are more likely to be published compared to studies without statistical significance, skewing the overall findings [162]. Positive studies may even result in multiple publications, as also seen in this review by multiple publications by the same author. As in most systematic reviews, language bias was also apparent in this review, as only English articles were included. Furthermore, comparing articles is difficult, as multiple articles have omitted information. This is shown by the number of cells that are empty in Tables 1–5 and the percentages of 'not stated' in Figures 3–5. If articles had followed the ARRIVE guidelines, comparisons would have been more straightforward [43,44]. The overall quality of a systematic review is influenced by the quality of the studies included. Despite incomplete reporting, an overview of the available evidence is still valuable, though combining results and drawing strong conclusions may be challenging. Among the articles that information could be extracted from, heterogeneity was high. The methodology of a study was often adapted to the tested antibacterial technology. Differences in study populations, interventions, outcomes, and methodologies can make it difficult to combine and interpret results. These limitations show the importance of following guidelines set for in vivo experiments.

4.5. Animal-Free Science

Implementation of Russel and Burch's 3R principles of reduction, refinement, and replacement should be used in all studies [38]. Optimization of bias control, the experimental design, and choosing the right outcome measures result in reduction and refinement. However, replacement is not discussed yet. Good in vitro data for antimicrobial activity and biocompatibility are needed to move on to in vivo or clinical experiments. Several reviews give an overview of the current availability of in vitro experiments to test the antimicrobial properties of new technologies. Methods range from simple static disc diffusion tests to more complex systems that take flow displacement into account [22,163,164]. All reviews conclude there is no one golden standard to use, especially since the working mechanisms of all antimicrobial compounds differ. As stated previously, several important in vivo factors cannot be replicated or integrated easily in vitro, which makes the translation from in vitro to in vivo challenging [23]. The lab-on-a-chip (LOC) technique has become more popular in the medical sector, aiming to bridge the gap between in vitro and in vivo systems. To simulate bone remodeling, cells are combined with mechanical, electrophysical, and biological stimuli, recreating cellular-, tissue-, and organ-level processes [165,166]. Currently, LOC has been used to simulate bone remodeling; however, to simulate PJI, bacteria would also have to be considered in the system. Although LOC is a promising technique for the future, currently, in vivo experiments are still needed before clinical studies. All antimicrobial compounds should be tested thoroughly in vitro to minimize the use of animals as much as possible. Unfortunately, complete replacement of animals is not possible yet.

4.6. Checklist for the Assessment of PJI in an In Vivo NZW Rabbit Model

To improve reproducibility and be able to compare studies to each other better, compliance with certain standards is necessary. During the 2023 international consensus meeting on musculoskeletal infection (MSKI), the need for unified and standardized criteria for animal testing in the treatment of MSKI was expressed [41].

Several guidelines already exist, like the ARRIVE guidelines [44], a checklist for publishing in vivo studies for orthopedic device-related infections by Moriarty et al. [24], and the Gold Standard Publication Checklist [64]. These lists have been adapted in Table 8, including the main points of this systematic review. Adhering to this checklist will potentially result in reproducible studies with limited bias, improving the overall quality of research. Furthermore, this checklist takes the 3Rs into account, resulting in less animal suffering.

Table 8. Checklist for setting up an in vivo NZW rabbit model for the assessment of PJI.

Aspect	Includes
Bias control	
Bias control	Blinding
	Randomization
	Humane endpoints (scoring sheets should be used to check if humane endpoints are met)
Rabbit characteristics	Sex (justification if not mixed male/female)
	Age (rabbits should be skeletally mature)
	Weight (rabbits should be skeletally mature)
Caretaking	Eating and supplemental feed
	Drinking
	Housing conditions

Table 8. *Cont.*

Aspect	Includes
Experimental design	
General	Aim of study
	Antimicrobial technology tested
	Duration of study (based on study aim and working mechanism intervention)
	Total number of rabbits used
	Experimental groups and size (based on power calculations. Control group must always be included)
	Dropout number
	Acclimatization period
	Use of prophylactic antibiotics
Inoculum	Strain (explain why this species and strain)
	Inoculum size (explain size, report both CFU/mL and total volume used)
	Administration method (should mimic clinical situation)
	Containment method used or not
Implant	Description (size)
	Material
	Movement prevention
	Location
Outcomes	
Bacterial culture	Tissue cultured (specify what and how much tissue was used)
	Culture method
	Outcome unit
Health monitoring	Weight
	Temperature
	Clinical signs of infection
Hematology	CRP
	ESR
	WBC/leukocyte differentiation
	IL-6
Histology	Staining and tissues colored
Imaging	Method and outcome parameters
	Pre- or post-mortem
Other	Specify what/how outcome is measured, and what the link is to the study aim

5. Conclusions

In vivo NZW rabbit models can aid in studying new antibacterial technologies and PJI prevention. However, consensus in bias control, experimental design, outcome measures, and documentation thereof is missing. Regarding bias control and complying with the 3Rs, standardized guidelines are necessary. Blinding and randomization are essential to minimize bias and should consistently be implemented in the rabbit models. Further-

more, documentation of rabbit characteristics and animal caretaking is necessary to ensure scientific integrity, reliability, and reproducibility. The exact methodology and outcome parameters to be studied depend on the working mechanism and intended use of the antibacterial technique. Therefore, there is no gold standard in setting up these experiments. *S. aureus* might be the most logical option to inoculate due to its high prevalence in PJI; however, researchers should consider their research aim when choosing the pathogen, especially with regard to clinical or resistant strains. Determining the experimental design is crucial to better bridge the gap from in vivo experiments to the clinic. Given the wide range of potential outcome measures, the scientific value gained from including additional outcome measures must justify the increased burden on the animals or a larger group size. At a minimum, studies investigating new antibacterial technologies against PJI in a rabbit model should include bacterial culture, including documentation of the tissue cultured, the culture method, the outcome unit, and health monitoring. This review provides an overview of experimental requirements and outlines what should be documented and published for all NZW rabbit PJI models, based on and modified from existing guidelines, like the ARRIVE guidelines. Ultimately, this analysis aims to assist researchers in determining suitable clinically relevant methodologies and outcome measures for in vivo PJI models using NZW rabbits to test new antimicrobial technologies.

Author Contributions: Conceptualization, J.L.v.A., S.W.G.v.H. and J.J.C.A.; methodology, J.L.v.A., S.W.G.v.H. and J.J.C.A.; investigation, J.L.v.A. and S.W.G.v.H.; data curation, J.L.v.A. and S.W.G.v.H.; writing—original draft preparation, J.L.v.A.; writing—review and editing, S.W.G.v.H. and J.J.C.A.; visualization, J.L.v.A. and S.W.G.v.H.; supervision, J.J.C.A.; project administration, J.L.v.A.; funding acquisition, J.J.C.A. All authors have read and agreed to the published version of the manuscript.

Funding: This publication is part of the EMILIO project (with project number LSHM21057), co-funded by the PPP Allowance made available by Health-Holland, Top Sector Life Sciences & Health. This publication is also part of the DARTBAC project (with project number NWA.1292.19.354) of the research program NWA-ORC, which is (partly) financed by the Dutch Research Council (NWO).

Institutional Review Board Statement: Not applicable.

Informed Consent Statement: Not applicable.

Data Availability Statement: The original contributions presented in this study are included in the article; further inquiries can be directed to the corresponding author.

Acknowledgments: The authors would like to thank Thomay-Claire Hoelen for helping with defining the search strings and the use of Covidence.

Conflicts of Interest: The authors declare no conflicts of interest. The funding agencies had no role in the design of the study.

Appendix A

Appendix A.1. Scopus Search String

TITLE-ABS-KEY({prosthesis-related infections } OR {PJI} OR {prosthetic joint infection} OR {joint replacement infection} OR {arthroplasty infection} OR {implant infection} OR ({osteomyelitis} AND {implant}) OR ({orthopaedic infection} AND {implant}) OR ({bone infection} AND {implant}) OR {prosthetic infection} OR {peri-prosthetic infection} OR {implant-related infection} OR {DAIR}) AND TITLE-ABS-KEY (rabbit* OR {lagomorpha} OR {new zealand white} OR rodent*) AND TITLE-ABS-KEY ({experimental model} OR {animal model} OR {preclinical model} OR {in vivo}) AND (LIMIT-TO (DOCTYPE,"ar")) AND (LIMIT-TO (LANGUAGE,"English")).

Appendix A.2. EMBASE Search String

Table A1. EMBASE database search string.

Number	Search Term
N1	"prosthesis-related infections" OR "PJI" OR "prosthetic joint infection" OR "joint replacement infection" OR "arthroplasty infection" OR "implant infection" OR ("osteomyelitis" AND "implant") OR ("orthopaedic infection" AND "implant") OR ("bone infection" AND "implant") OR "prosthetic infection" OR "peri-prosthetic infection" OR "implant-related infection" OR "DAIR"
N2	"rabbit*" OR "lagomorpha" OR "new zealand white" OR "rodent*"
N3	"model" OR "experimental model" OR "animal model" OR "preclinical model" OR "in vivo"
N4	N1 AND N2 AND N3

References

1. Parvizi, J.; Fassihi, S.C.; Enayatollahi, M.A. Diagnosis of Periprosthetic Joint Infection Following Hip and Knee Arthroplasty. *Orthop. Clin. N. Am.* **2016**, *47*, 505–515. [CrossRef] [PubMed]
2. Sabah, S.A.; Alvand, A.; Price, A.J. Revision knee replacement for prosthetic joint infection: Epidemiology, clinical outcomes and health-economic considerations. *Knee* **2021**, *28*, 417–421. [CrossRef] [PubMed]
3. Klug, A.; Gramlich, Y.; Rudert, M.; Drees, P.; Hoffmann, R.; Weissenberger, M.; Kutzner, K.P. The projected volume of primary and revision total knee arthroplasty will place an immense burden on future health care systems over the next 30 years. *Knee Surg. Sports Traumatol. Arthrosc.* **2021**, *29*, 3287–3298. [CrossRef] [PubMed]
4. Kurtz, S.; Ong, K.; Lau, E.; Mowat, F.; Halpern, M. Projections of primary and revision hip and knee arthroplasty in the United States from 2005 to 2030. *J. Bone Jt. Surg.* **2007**, *89*, 780–785. [CrossRef]
5. Corvec, S.; Portillo, M.E.; Pasticci, B.M.; Borens, O.; Trampuz, A. Epidemiology and new developments in the diagnosis of prosthetic joint infection. *Int. J. Artif. Organs* **2012**, *35*, 923–934. [CrossRef] [PubMed]
6. Del Pozo, J.L.; Patel, R. Infection associated with prosthetic joints. *N. Engl. J. Med.* **2009**, *361*, 787–794. [CrossRef] [PubMed]
7. Davidson, D.J.; Spratt, D.; Liddle, A.D. Implant materials and prosthetic joint infection: The battle with the biofilm. *EFORT Open Rev.* **2019**, *4*, 633–639. [CrossRef] [PubMed]
8. Aggarwal, V.K.; Rasouli, M.R.; Parvizi, J. Periprosthetic joint infection: Current concept. *Indian J. Orthop.* **2013**, *47*, 10–17. [CrossRef] [PubMed]
9. Wei, H.; Song, X.; Liu, P.; Liu, X.; Yan, X.; Yu, L. Antimicrobial coating strategy to prevent orthopaedic device-related infections: Recent advances and future perspectives. *Biomater. Adv.* **2022**, *135*, 212739. [CrossRef]
10. Xu, Y.; Huang, T.B.; Schuetz, M.A.; Choong, P.F. Mortality, patient-reported outcome measures, and the health economic burden of prosthetic joint infection. *EFORT Open Rev.* **2023**, *8*, 690–697. [CrossRef]
11. Arciola, C.R.; An, Y.; Campoccia, D.; Donati, M.; Montanaro, L. Etiology of implant orthopedic infections: A survey on 1027 clinical isolates. *Int. J. Artif. Organs* **2005**, *28*, 1091–1100. [CrossRef]
12. Da Silva, R.B.; Salles, M.J. Outcomes and risk factors in prosthetic joint infections by multidrug-resistant gram-negative bacteria: A retrospective cohort study. *Antibiotics* **2021**, *10*, 340. [CrossRef]
13. Khatoon, Z.; McTiernan, C.D.; Suuronen, E.J.; Mah, T.-F.; Alarcon, E.I. Bacterial biofilm formation on implantable devices and approaches to its treatment and prevention. *Heliyon* **2018**, *4*, e01067. [CrossRef] [PubMed]
14. Lazic, I.; Scheele, C.; Pohlig, F.; von Eisenhart-Rothe, R.; Suren, C. Treatment options in PJI–is two-stage still gold standard? *J. Orthop.* **2021**, *23*, 180–184. [CrossRef] [PubMed]
15. Arciola, C.R.; Campoccia, D.; Montanaro, L. Implant infections: Adhesion, biofilm formation and immune evasion. *Nat. Rev. Microbiol.* **2018**, *16*, 397–409. [CrossRef] [PubMed]
16. Subbiahdoss, G.; Kuijer, R.; Grijpma, D.W.; van der Mei, H.C.; Busscher, H.J. Microbial biofilm growth vs. tissue integration: "the race for the surface" experimentally studied. *Acta Biomater.* **2009**, *5*, 1399–1404. [CrossRef] [PubMed]
17. Bhattacharya, M.; Wozniak, D.J.; Stoodley, P.; Hall-Stoodley, L. Prevention and treatment of *Staphylococcus aureus* biofilms. *Expert Rev. Anti-Infect. Ther.* **2015**, *13*, 1499–1516. [CrossRef] [PubMed]
18. Paharik, A.E.; Horswill, A.R. The staphylococcal biofilm: Adhesins, regulation, and host response. *Virulence Mech. Bact. Pathog.* **2016**, 529–566. [CrossRef]
19. Yang, S.; Li, X.; Cang, W.; Mu, D.; Ji, S.; An, Y.; Wu, R.; Wu, J. Biofilm tolerance, resistance and infections increasing threat of public health. *Microb. Cell* **2023**, *10*, 233. [CrossRef]
20. Salam, M.A.; Al-Amin, M.Y.; Salam, M.T.; Pawar, J.S.; Akhter, N.; Rabaan, A.A.; Alqumber, M.A.A. Antimicrobial Resistance: A Growing Serious Threat for Global Public Health. *Healthcare* **2023**, *11*, 1946. [CrossRef]
21. Amann, S.; Neef, K.; Kohl, S. Antimicrobial resistance (AMR). *Eur. J. Hosp. Pharm.* **2019**, *26*, 175–177. [CrossRef] [PubMed]

22. Sjollema, J.; Zaat, S.A.J.; Fontaine, V.; Ramstedt, M.; Luginbuehl, R.; Thevissen, K.; Li, J.; van der Mei, H.C.; Busscher, H.J. In vitro methods for the evaluation of antimicrobial surface designs. *Acta Biomater.* **2018**, *70*, 12–24. [CrossRef] [PubMed]
23. Moriarty, T.F.; Grainger, D.W.; Richards, R.G. Challenges in linking preclinical anti-microbial research strategies with clinical outcomes for device-associated infections. *Eur. Cell Mater.* **2014**, *28*, 112–128. [CrossRef] [PubMed]
24. Moriarty, T.F.; Harris, L.G.; Mooney, R.A.; Wenke, J.C.; Riool, M.; Zaat, S.A.J.; Moter, A.; Schaer, T.P.; Khanna, N.; Kuehl, R.; et al. Recommendations for design and conduct of preclinical in vivo studies of orthopedic device-related infection. *J. Orthop. Res.* **2019**, *37*, 271–287. [CrossRef]
25. Bevers, R.T.; van de Voort, M.H.; van Loo, I.H.; Geurts, J.; Arts, J.J. The role of material technologies targeting *P. aeruginosa* and *S. aureus* quorum sensing in biofilm formation. *Med. Res. Arch.* **2022**, *10*. [CrossRef]
26. Berti, A.; Rose, W.; Nizet, V.; Sakoulas, G. Antibiotics and innate immunity: A cooperative effort toward the successful treatment of infections. In *Open Forum Infectious Diseases*; Oxford University Press: Oxford, NY, USA, 2020; p. ofaa302.
27. Beer, J.; Wagner, C.C.; Zeitlinger, M. Protein binding of antimicrobials: Methods for quantification and for investigation of its impact on bacterial killing. *AAPS J.* **2009**, *11*, 1–12. [CrossRef] [PubMed]
28. Sakai, R.; Takahashi, A.; Takahira, N.; Uchiyama, K.; Yamamoto, T.; Uchida, K.; Fukushima, K.; Moriya, M.; Takaso, M.; Itoman, M. Hammering force during cementless total hip arthroplasty and risk of microfracture. *Hip Int.* **2011**, *21*, 330–335. [CrossRef]
29. Odekerken, J.C.E. Modern Orthopaedic Implant Coatings—Their Pro's, Con's and Evaluation Methods. *Mod. Surf. Eng. Treat.* **2013**, 45–73.
30. Yagi, H.; Kihara, S.; Mittwede, P.N.; Maher, P.L.; Rothenberg, A.C.; Falcione, A.D.C.M.; Chen, A.; Urish, K.L.; Tuan, R.S.; Alexander, P.G. Development of a large animal rabbit model for chronic periprosthetic joint infection. *Bone Jt. Res.* **2021**, *10*, 156–165. [CrossRef]
31. Pearce, A.; Richards, R.; Milz, S.; Schneider, E.; Pearce, S. Animal models for implant biomaterial research in bone: A review. *Eur. Cell Mater.* **2007**, *13*, 1–10. [CrossRef]
32. Hickman, D.; Johnson, J.; Vemulapalli, T.H.; Crisler, J.; Shepherd, R. Commonly used animal models. *Princ. Anim. Res. Grad. Undergrad. Stud.* **2017**, 117–175. [CrossRef]
33. Mapara, M.; Thomas, B.S.; Bhat, K. Rabbit as an animal model for experimental research. *Dent. Res. J.* **2012**, *9*, 111.
34. Gatin, L.; Saleh-Mghir, A.; Massin, P.; Crémieux, A.-C. Critical analysis of experimental models of periprosthetic joint infection. *Orthop. Traumatol. Surg. Res.* **2015**, *101*, 851–855. [CrossRef] [PubMed]
35. Bottagisio, M.; Coman, C.; Lovati, A.B. Animal models of orthopaedic infections. A review of rabbit models used to induce long bone bacterial infections. *J. Med. Microbiol.* **2019**, *68*, 506–537. [CrossRef]
36. ARRIVE Guidelines. Available online: https://arriveguidelines.org/ (accessed on 1 August 2024).
37. Voehringer, P.; Nicholson, J.R. Minimum information in In Vivo research. *Handb. Exp. Pharmacol.* **2019**, *257*, 197–222.
38. Tannenbaum, J.; Bennett, B.T. Russell and Burch's 3Rs then and now: The need for clarity in definition and purpose. *J. Am. Assoc. Lab. Anim. Sci.* **2015**, *54*, 120–132. [PubMed]
39. Page, M.J.; McKenzie, J.E.; Bossuyt, P.M.; Boutron, I.; Hoffmann, T.C.; Mulrow, C.D.; Shamseer, L.; Tetzlaff, J.M.; Akl, E.A.; Brennan, S.E.; et al. The PRISMA 2020 statement: An updated guideline for reporting systematic reviews. *BMJ* **2021**, *372*, n71. [CrossRef] [PubMed]
40. Covidence Systematic Review Software. Available online: www.covidence.org (accessed on 1 July 2024).
41. Jennings, J.A.; Arts, J.J.; Abuhussein, E.; Alt, V.; Ashton, N.; Baertl, S.; Bhattacharyya, S.; Cain, J.D.; Dintakurthi, Y.; Ducheyne, P. 2023 International Consensus Meeting on musculoskeletal infection: Summary from the treatment workgroup and consensus on treatment in preclinical models. *J. Orthop. Res.* **2024**, *42*, 500–511. [CrossRef] [PubMed]
42. Laajala, T.D.; Jumppanen, M.; Huhtaniemi, R.; Fey, V.; Kaur, A.; Knuuttila, M.; Aho, E.; Oksala, R.; Westermarck, J.; Mäkelä, S. Optimized design and analysis of preclinical intervention studies in vivo. *Sci. Rep.* **2016**, *6*, 1–13. [CrossRef]
43. Kilkenny, C.; Browne, W.; Cuthill, I.C.; Emerson, M.; Altman, D.G. *Animal Research: Reporting In Vivo Experiments—The ARRIVE Guidelines*; Sage: London, UK, 2011; Volume 31, pp. 991–993.
44. Kilkenny, C.; Browne, W.J.; Cuthill, I.C.; Emerson, M.; Altman, D.G. Improving bioscience research reporting: The arrive guidelines for reporting animal research. *Animals* **2014**, *4*, 35–44. [CrossRef]
45. Auer, J.A.; Goodship, A.; Arnoczky, S.; Pearce, S.; Price, J.; Claes, L.; Von Rechenberg, B.; Hofmann-Amtenbrinck, M.; Schneider, E.; Müller-Terpitz, R. Refining animal models in fracture research: Seeking consensus in optimising both animal welfare and scientific validity for appropriate biomedical use. *BMC Musculoskelet. Disord.* **2007**, *8*, 72. [CrossRef]
46. Bespalov, A.; Wicke, K.; Castagné, V. Blinding and randomization. In *Good Research Practice in Non-Clinical Pharmacology and Biomedicine*; Springer: Berlin, Germany, 2019; p. 81.
47. Fenwick, N.; Griffin, G.; Gauthier, C. The welfare of animals used in science: How the "Three Rs" ethic guides improvements. *Can. Vet. J.* **2009**, *50*, 523. [PubMed]
48. Huang, W.; Percie du Sert, N.; Vollert, J.; Rice, A.S. General principles of preclinical study design. In *Good Research Practice in Non-Clinical Pharmacology and Biomedicine*; Springer: Berlin, Germany, 2020; pp. 55–69.
49. Kilkenny, C.; Parsons, N.; Kadyszewski, E.; Festing, M.F.; Cuthill, I.C.; Fry, D.; Hutton, J.; Altman, D.G. Survey of the quality of experimental design, statistical analysis and reporting of research using animals. *PLoS ONE* **2009**, *4*, e7824. [CrossRef] [PubMed]
50. Miller, L.R.; Marks, C.; Becker, J.B.; Hurn, P.D.; Chen, W.J.; Woodruff, T.; McCarthy, M.M.; Sohrabji, F.; Schiebinger, L.; Wetherington, C.L.; et al. Considering sex as a biological variable in preclinical research. *FASEB J.* **2017**, *31*, 29–34. [CrossRef] [PubMed]

51. Kunutsor, S.K.; Whitehouse, M.R.; Blom, A.W.; Beswick, A.D.; Team, I. Patient-related risk factors for periprosthetic joint infection after total joint arthroplasty: A systematic review and meta-analysis. *PLoS ONE* **2016**, *11*, e0150866. [CrossRef] [PubMed]
52. Sukoff Rizzo, S.J.; McTighe, S.; McKinzie, D.L. Genetic background and sex: Impact on generalizability of research findings in pharmacology studies. In *Good Research Practice in Non-Clinical Pharmacology and Biomedicine*; Springer: Berlin, Germany, 2020; pp. 147–162.
53. Tannenbaum, C.; Ellis, R.P.; Eyssel, F.; Zou, J.; Schiebinger, L. Sex and gender analysis improves science and engineering. *Nature* **2019**, *575*, 137–146. [CrossRef] [PubMed]
54. Clayton, J.A. Studying both sexes: A guiding principle for biomedicine. *FASEB J.* **2016**, *30*, 519. [CrossRef] [PubMed]
55. Thurston, S.; Burlingame, L.; Lester, P.A.; Lofgren, J. Methods of pairing and pair maintenance of New Zealand White rabbits (*Oryctolagus cuniculus*) via behavioral ethogram, monitoring, and interventions. *JoVE (J. Vis. Exp.)* **2018**, *16*, e57267.
56. Mironenko, C.M.; Kapadia, M.; Donlin, L.; Figgie, M.; Carli, A.V.; Henry, M.; Goodman, S.M.; Miller, A.O. 239. Sex Differences in Prosthetic Joint Infection. In *Open Forum Infectious Diseases*; Oxford University Press: Oxford, UK, 2021.
57. Higuera-Rueda, C.A.; Piuzzi, N.S.; Milbrandt, N.B.; Tsai, Y.H.; Klika, A.K.; Samia, A.C.S.; Visperas, A. The Mark Coventry Award: PhotothermAA Gel Combined with Debridement, Antibiotics, and Implant Retention (DAIR) Significantly Decreases Implant Biofilm Burden and Soft-Tissue Infection in a Rabbit Model of Knee Periprosthetic Joint Infection. *J. Arthroplast.* **2024**, *39*, S2–S8. [CrossRef]
58. Visperas, A.; Santana, D.; Ju, M.; Milbrandt, N.B.; Tsai, Y.H.; Wickramasinghe, S.; Klika, A.K.; Piuzzi, N.S.; Samia, A.C.S.; Higuera-Rueda, C.A. Standardized quantification of biofilm in a novel rabbit model of periprosthetic joint infection. *J. Bone Jt. Infect.* **2022**, *7*, 91–99. [CrossRef]
59. Weisbroth, S.H.; Flatt, R.E.; Kraus, A.L. *The Biology of the Laboratory Rabbit*; Academic Press: New York, NY, USA, 2013.
60. Marchandeau, S.; Pontier, D.; Guitton, J.-S.; Letty, J.; Fouchet, D.; Aubineau, J.; Berger, F.; Léonard, Y.; Roobrouck, A.; Gelfi, J. Early infections by myxoma virus of young rabbits (*Oryctolagus cuniculus*) protected by maternal antibodies activate their immune system and enhance herd immunity in wild populations. *Vet. Res.* **2014**, *45*, 26. [CrossRef] [PubMed]
61. Attili, A.-R.; Nebbia, P.; Bellato, A.; Galosi, L.; Papeschi, C.; Rossi, G.; Linardi, M.; Fileni, E.; Cuteri, V.; Chiesa, F. The effect of age and sampling site on the outcome of *Staphylococcus aureus* infection in a rabbit (*Oryctolagus cuniculus*) farm in Italy. *Animals* **2020**, *10*, 774. [CrossRef] [PubMed]
62. Masoud, I.; Shapiro, F.; Kent, R.; Moses, A. A longitudinal study of the growth of the New Zealand white rabbit: Cumulative and biweekly incremental growth rates for body length, body weight, femoral length, and tibial length. *J. Orthop. Res.* **1986**, *4*, 221–231. [CrossRef]
63. Dutta, S.; Sengupta, P. Rabbits and men: Relating their ages. *J. Basic Clin. Physiol. Pharmacol.* **2018**, *29*, 427–435. [CrossRef]
64. Hooijmans, C.R.; Leenaars, M.; Ritskes-Hoitinga, M. A gold standard publication checklist to improve the quality of animal studies, to fully integrate the Three Rs, and to make systematic reviews more feasible. *Altern. Lab. Anim.* **2010**, *38*, 167–182. [CrossRef]
65. Hooijmans, C.R.; de Vries, R.; Leenaars, M.; Curfs, J.; Ritskes-Hoitinga, M. Improving planning, design, reporting and scientific quality of animal experiments by using the Gold Standard Publication Checklist, in addition to the ARRIVE guidelines. *Br. J. Pharmacol.* **2011**, *162*, 1259–1260. [CrossRef] [PubMed]
66. European Parliament; European Council. 63/EU of the European Parliament and of the Council of 22 September 2010 on the protection of animals used for scientific purposes. *Off. J. Eur. Union* **2010**, *276*, 33–79.
67. Stokes, W.S. Humane endpoints for laboratory animals used in regulatory testing. *ILAR J.* **2002**, *43*, S31–S38.
68. Department of Animals in Science and Society, Faculty of Veterinary Medicine Utrecht University. Humane Endpoints in Laboratory Animal Experimentation. Available online: https://www.humane-endpoints.info/en (accessed on 29 May 2024).
69. Craig, M.R.; Poelstra, K.A.; Sherrell, J.C.; Kwon, M.S.; Belzile, E.L.; Brown, T.E. A novel total knee arthroplasty infection model in rabbits. *J. Orthop. Res.* **2005**, *23*, 1100–1104. [CrossRef]
70. Gahukamble, A.D.; McDowell, A.; Post, V.; Salavarrieta Varela, J.; Rochford, E.T.; Richards, R.G.; Patrick, S.; Moriarty, T.F. *Propionibacterium acnes* and *Staphylococcus lugdunensis* cause pyogenic osteomyelitis in an intramedullary nail model in rabbits. *J. Clin. Microbiol.* **2014**, *52*, 1595–1606. [CrossRef] [PubMed]
71. López, T., II; Sanz-Ruíz, P.; Navarro-García, F.; León-Román, V.E.; Vaquero-Martín, J. Experimental reproduction of periprosthetic joint infection: Developing a representative animal model. *Knee* **2020**, *27*, 1106–1112. [CrossRef]
72. Odekerken, J.C.; Brans, B.T.; Welting, T.J.; Walenkamp, G.H. (18)F-FDG microPET imaging differentiates between septic and aseptic wound healing after orthopedic implant placement: A longitudinal study of an implant osteomyelitis in the rabbit tibia. *Acta Orthop.* **2014**, *85*, 305–313. [CrossRef] [PubMed]
73. Poultsides, L.A.; Papatheodorou, L.K.; Karachalios, T.S.; Khaldi, L.; Maniatis, A.; Petinaki, E.; Malizos, K.N. Novel model for studying hematogenous infection in an experimental setting of implant-related infection by a community-acquired methicillin-resistant *S. aureus* strain. *J. Orthop. Res.* **2008**, *26*, 1355–1362. [CrossRef] [PubMed]
74. Sarda, L.; Saleh-Mghir, A.; Peker, C.; Meulemans, A.; Cremieux, A.C.; Le Guludec, D. Evaluation of 99mTc-ciprofloxacin scintigraphy in a rabbit model of *Staphylococcus aureus* prosthetic joint infection. *J. Nucl. Med.* **2002**, *43*, 239–245. [PubMed]
75. Sarda-Mantel, L.; Saleh-Mghir, A.; Welling, M.M.; Meulemans, A.; Vrigneaud, J.M.; Raguin, O.; Hervatin, F.; Martet, G.; Chau, F.; Lebtahi, R.; et al. Evaluation of 99mTc-UBI 29-41 scintigraphy for specific detection of experimental *Staphylococcus aureus* prosthetic joint infections. *Eur. J. Nucl. Med. Mol. Imaging* **2007**, *34*, 1302–1309. [CrossRef]

76. Tang, C.; Wang, F.; Hou, Y.; Lu, S.; Tian, W.; Xu, Y.; Jin, C.; Wang, L. Technetium-99m-labeled annexin V imaging for detecting prosthetic joint infection in a rabbit model. *J. Biomed. Res.* **2015**, *29*, 224–231. [CrossRef]
77. Wang, Y.; Liu, H.; Yao, S.; Guan, Z.; Li, Q.; Qi, E.; Li, X.; Zhang, J.; Tian, J. Using18F-flurodeoxyglucose and68Ga-fibroblast activation protein inhibitor PET/CT to evaluate a new periprosthetic joint infection model of rabbit due to *Staphylococcus aureus*. *Nucl. Med. Commun.* **2022**, *43*, 232–241. [CrossRef] [PubMed]
78. Wang, Y.; Li, Y.; Han, L.; Wang, J.; Zhang, C.; Qi, E.; Zhang, D.; Zhang, X.; Huan, Y.; Tian, J. 18F-FDG and 68 Ga-FAPI PET/CT for the evaluation of periprosthetic joint infection and aseptic loosening in rabbit models. *BMC Musculoskelet. Disord.* **2022**, *23*, 592. [CrossRef] [PubMed]
79. Brunotte, M.; Rupp, M.; Stötzel, S.; Sommer, U.; Mohammed, W.; Thormann, U.; Heiss, C.; Lips, K.S.; Domann, E.; Alt, V. A new small animal model for simulating a two-stage-revision procedure in implant-related methicillin-resistant *Staphylococcus aureus* bone infection. *Injury* **2019**, *50*, 1921–1928. [CrossRef]
80. Efstathopoulos, N.; Giamarellos-Bourboulis, E.; Kanellakopoulou, K.; Lazarettos, I.; Giannoudis, P.; Frangia, K.; Magnissalis, E.; Papadaki, M.; Nikolaou, V.S. Treatment of experimental osteomyelitis by Methicillin Resistant *Staphylococcus aureus* with bone cement system releasing grepafloxacin. *Injury* **2008**, *39*, 1384–1390. [CrossRef] [PubMed]
81. Gatin, L.; Mghir, A.S.; Mouton, W.; Laurent, F.; Ghout, I.; Rioux-Leclercq, N.; Tattevin, P.; Verdier, M.C.; Cremieux, A.C. Colistin-containing cement spacer for treatment of experimental carbapenemase-producing *Klebsiella pneumoniae* prosthetic joint infection. *Int. J. Antimicrob. Agents* **2019**, *54*, 456–462. [CrossRef]
82. Ismael, F.; Bléton, R.; Saleh-Mghir, A.; Dautrey, S.; Massias, L.; Crémieux, A.C. Teicoplanin-containing cement spacers for treatment of experimental *Staphylococcus aureus* joint prosthesis infection. *Antimicrob. Agents Chemother.* **2003**, *47*, 3365–3367. [CrossRef] [PubMed]
83. López, T., II; Vaquero-Martín, J.; Torres-Suárez, A.I.; Navarro-García, F.; Fraguas-Sánchez, A.I.; León-Román, V.E.; Sanz-Ruíz, P. The tale of microencapsulated rifampicin: Is it useful for the treatment of periprosthetic joint infection? *Int. Orthop.* **2022**, *46*, 677–685. [CrossRef] [PubMed]
84. Nijhof, M.W.; Fleer, A.; Hardus, K.; Vogely, H.C.; Schouls, L.M.; Verbout, A.J.; Dhert, W.J. Tobramycin-containing bone cement and systemic cefazolin in a one-stage revision. Treatment of infection in a rabbit model. *J. Biomed. Mater. Res.* **2001**, *58*, 747–753. [CrossRef] [PubMed]
85. Overstreet, D.; McLaren, A.; Calara, F.; Vernon, B.; McLemore, R. Local gentamicin delivery from resorbable viscous hydrogels is therapeutically effective. *Clin. Orthop. Relat. Res.* **2015**, *473*, 337–347. [CrossRef]
86. Yan, S.; Cai, X.; Yan, W.; Dai, X.; Wu, H. Continuous wave ultrasound enhances vancomycin release and antimicrobial efficacy of antibiotic-loaded acrylic bone cement in vitro and in vivo. *J. Biomed. Mater. Res. B Appl. Biomater.* **2007**, *82*, 57–64. [CrossRef]
87. Ambrose, C.G.; Clyburn, T.A.; Mika, J.; Gogola, G.R.; Kaplan, H.B.; Wanger, A.; Mikos, A.G. Evaluation of antibiotic-impregnated microspheres for the prevention of implant-associated orthopaedic infections. *J. Bone Jt. Surg. Am.* **2014**, *96*, 128–134. [CrossRef] [PubMed]
88. Aykut, S.; Oztürk, A.; Ozkan, Y.; Yanik, K.; Ilman, A.A.; Ozdemir, R.M. Evaluation and comparison of the antimicrobial efficacy of teicoplanin- and clindamycin-coated titanium implants: An experimental study. *J. Bone Jt. Surg. Br.* **2010**, *92*, 159–163. [CrossRef]
89. Darouiche, R.O.; Mansouri, M.D.; Zakarevicz, D.; Alsharif, A.; Landon, G.C. In vivo efficacy of antimicrobial-coated devices. *J. Bone Jt. Surg. Am.* **2007**, *89*, 792–797. [CrossRef]
90. Gatin, L.; Saleh-Mghir, A.; Tasse, J.; Ghout, I.; Laurent, F.; Crémieux, A.C. Ceftaroline-Fosamil efficacy against methicillin-resistant *Staphylococcus aureus* in a rabbit prosthetic joint infection model. *Antimicrob. Agents Chemother.* **2014**, *58*, 6496–6500. [CrossRef]
91. Giavaresi, G.; Meani, E.; Sartori, M.; Ferrari, A.; Bellini, D.; Sacchetta, A.C.; Meraner, J.; Sambri, A.; Vocale, C.; Sambri, V.; et al. Efficacy of antibacterial-loaded coating in an in vivo model of acutely highly contaminated implant. *Int. Orthop.* **2014**, *38*, 1505–1512. [CrossRef] [PubMed]
92. Helbig, L.; Simank, H.G.; Lorenz, H.; Putz, C.; Wölfl, C.; Suda, A.J.; Moghaddam, A.; Schmidmaier, G.; Guehring, T. Establishment of a new methicillin resistant *Staphylococcus aureus* animal model of osteomyelitis. *Int. Orthop.* **2014**, *38*, 891–897. [CrossRef] [PubMed]
93. Li, D.; Lv, P.; Fan, L.; Huang, Y.; Yang, F.; Mei, X.; Wu, D. The immobilization of antibiotic-loaded polymeric coatings on osteoarticular Ti implants for the prevention of bone infections. *Biomater. Sci.* **2017**, *5*, 2337–2346. [CrossRef]
94. Liu, D.; He, C.; Liu, Z.; Xu, W. Gentamicin coating of nanotubular anodized titanium implant reduces implant-related osteomyelitis and enhances bone biocompatibility in rabbits. *Int. J. Nanomed.* **2017**, *12*, 5461–5471. [CrossRef] [PubMed]
95. Muller-Serieys, C.; Saleh Mghir, A.; Massias, L.; Fantin, B. Bactericidal activity of the combination of levofloxacin with rifampin in experimental prosthetic knee infection in rabbits due to methicillin-susceptible *Staphylococcus aureus*. *Antimicrob. Agents Chemother.* **2009**, *53*, 2145–2148. [CrossRef]
96. Saleh-Mghir, A.; Ameur, N.; Muller-Serieys, C.; Ismael, F.; Lemaitre, F.; Massias, L.; Feger, C.; Bléton, R.; Crémieux, A.C. Combination of quinupristin-dalfopristin (synercid) and rifampin is highly synergistic in experimental *Staphylococcus aureus* joint prosthesis infection. *Antimicrob. Agents Chemother.* **2002**, *46*, 1122–1124. [CrossRef]
97. Saleh-Mghir, A.; Muller-Serieys, C.; Dinh, A.; Massias, L.; Crémieux, A.C. Adjunctive rifampin is crucial to optimizing daptomycin efficacy against rabbit prosthetic joint infection due to methicillin-resistant *Staphylococcus aureus*. *Antimicrob. Agents Chemother.* **2011**, *55*, 4589–4593. [CrossRef]

98. Schroeder, K.; Simank, H.G.; Lorenz, H.; Swoboda, S.; Geiss, H.K.; Helbig, L. Implant stability in the treatment of MRSA bone implant infections with linezolid versus vancomycin in a rabbit model. *J. Orthop. Res.* **2012**, *30*, 190–195. [CrossRef]
99. Auñón, Á.; Esteban, J.; Doadrio, A.L.; Boiza-Sánchez, M.; Mediero, A.; Eguibar-Blázquez, D.; Cordero-Ampuero, J.; Conde, A.; Arenas, M.; de-Damborenea, J.J.; et al. *Staphylococcus aureus* Prosthetic Joint Infection Is Prevented by a Fluorine- and Phosphorus-Doped Nanostructured Ti-6Al-4V Alloy Loaded With Gentamicin and Vancomycin. *J. Orthop. Res.* **2020**, *38*, 588–597. [CrossRef]
100. Horn, J.; Schlegel, U.; Krettek, C.; Ito, K. Infection resistance of unreamed solid, hollow slotted and cannulated intramedullary nails: An in-vivo experimental comparison. *J. Orthop. Res.* **2005**, *23*, 810–815. [CrossRef] [PubMed]
101. Moriarty, T.F.; Campoccia, D.; Nees, S.K.; Boure, L.P.; Richards, R.G. In vivo evaluation of the effect of intramedullary nail microtopography on the development of local infection in rabbits. *Int. J. Artif. Organs* **2010**, *33*, 667–675. [CrossRef]
102. Ravanetti, F.; Chiesa, R.; Ossiprandi, M.C.; Gazza, F.; Farina, V.; Martini, F.M.; Di Lecce, R.; Gnudi, G.; Della Valle, C.; Gavini, J.; et al. Osteogenic response and osteoprotective effects in vivo of a nanostructured titanium surface with antibacterial properties. *J. Mater. Sci. Mater. Med.* **2016**, *27*, 52. [CrossRef] [PubMed]
103. Bitika, O.; Uzuna, H.; Kecika, A. In-vivo analysis of antibacterial silver coated titanium implants in a contaminated rabbit knee model. *Turk. Klin. J. Med. Sci.* **2013**, *33*, 1462–1472. [CrossRef]
104. Boot, W.; Vogely, H.C.; Jiao, C.; Nikkels, P.G.; Pouran, B.; van Rijen, M.H.; Ekkelenkamp, M.B.; Hänsch, G.M.; Dhert, W.J.; Gawlitta, D. Prophylaxis of implant-related infections by local release of vancomycin from a hydrogel in rabbits. *Eur. Cell Mater.* **2020**, *39*, 108–120. [CrossRef]
105. Fabritius, M.; Al-Munajjed, A.A.; Freytag, C.; Jülke, H.; Zehe, M.; Lemarchand, T.; Arts, J.J.; Schumann, D.; Alt, V.; Sternberg, K. Antimicrobial silver multilayer coating for prevention of bacterial colonization of orthopedic implants. *Materials* **2020**, *13*, 1415. [CrossRef]
106. Kose, N.; Otuzbir, A.; Pekşen, C.; Kiremitçi, A.; Doğan, A. A silver ion-doped calcium phosphate-based ceramic nanopowder-coated prosthesis increased infection resistance. *Clin. Orthop. Relat. Res.* **2013**, *471*, 2532–2539. [CrossRef] [PubMed]
107. Kose, N.; Çaylak, R.; Pekşen, C.; Kiremitçi, A.; Burukoglu, D.; Koparal, S.; Doğan, A. Silver ion doped ceramic nano-powder coated nails prevent infection in open fractures: In vivo study. *Injury* **2016**, *47*, 320–324. [CrossRef] [PubMed]
108. Metsemakers, W.J.; Emanuel, N.; Cohen, O.; Reichart, M.; Potapova, I.; Schmid, T.; Segal, D.; Riool, M.; Kwakman, P.H.S.; De Boer, L.; et al. A doxycycline-loaded polymer-lipid encapsulation matrix coating for the prevention of implant-related osteomyelitis due to doxycycline-resistant methicillin-resistant *Staphylococcus aureus*. *J. Control Release* **2015**, *209*, 47–56. [CrossRef] [PubMed]
109. Moojen, D.J.F.; Vogely, H.C.; Fleer, A.; Nikkels, P.G.J.; Higham, P.A.; Verbout, A.J.; Castelein, R.M.; Dhert, W.J.A. Prophylaxis of infection and effects on osseointegration using a tobramycin-periapatite coating on titanium implants—An experimental study in the rabbit. *J. Orthop. Res.* **2009**, *27*, 710–716. [CrossRef] [PubMed]
110. Neut, D.; Dijkstra, R.J.B.; Thompson, J.I.; Kavanagh, C.; van der Mei, H.C.; Busscher, H.J. A biodegradable gentamicin-hydroxyapatite-coating for infection prophylaxis in cementless hip prostheses. *Eur. Cells Mater.* **2015**, *29*, 42–56. [CrossRef]
111. Oosterbos, C.J.M.; Ch Vogely, H.; Nijhof, M.W.; Fleer, A.; Verbout, A.J.; Tonino, A.J.; Dhert, W.J.A. Osseointegration of hydroxyapatite-coated and noncoated Ti6Al4V implants in the presence of local infection: A comparative histomorphometrical study in rabbits. *J. Biomed. Mater. Res.* **2002**, *60*, 339–347. [CrossRef]
112. Yang, C.C.; Lin, C.C.; Liao, J.W.; Yen, S.K. Vancomycin-chitosan composite deposited on post porous hydroxyapatite coated Ti6Al4V implant for drug controlled release. *Mater. Sci. Eng. C Mater. Biol. Appl.* **2013**, *33*, 2203–2212. [CrossRef] [PubMed]
113. Zhang, L.; Yang, Y.; Zhang, W.; Lv, H.; Yang, F.; Lin, C.; Tang, P. Inhibitory effect of super-hydrophobicity on silver release and antibacterial properties of super-hydrophobic Ag/TiO2 nanotubes. *J. Biomed. Mater. Res.—Part B Appl. Biomater.* **2016**, *104*, 1004–1012. [CrossRef] [PubMed]
114. Zhang, C.; Li, X.; Xiao, D.; Zhao, Q.; Chen, S.; Yang, F.; Liu, J.; Duan, K. Cu^{2+} Release from Polylactic Acid Coating on Titanium Reduces Bone Implant-Related Infection. *J. Funct. Biomater.* **2022**, *13*, 78. [CrossRef] [PubMed]
115. Zhao, F.; Gao, A.; Liao, Q.; Li, Y.; Ullah, I.; Zhao, Y.; Ren, X.; Tong, L.; Li, X.; Zheng, Y.; et al. Balancing the Anti-Bacterial and Pro-Osteogenic Properties of Ti-Based Implants by Partial Conversion of ZnO Nanorods into Hybrid Zinc Phosphate Nanostructures. *Adv. Funct. Mater.* **2024**, *34*, 2311812. [CrossRef]
116. Zhou, J.; Li, B.; Zhao, L.; Zhang, L.; Han, Y. F-Doped Micropore/Nanorod Hierarchically Patterned Coatings for Improving Antibacterial and Osteogenic Activities of Bone Implants in Bacteria-Infected Cases. *ACS Biomater. Sci. Eng.* **2017**, *3*, 1437–1450. [CrossRef]
117. Zhou, H.; Ye, S.; Xu, M.; Hao, L.; Chen, J.; Fang, Z.; Guo, K.; Chen, Y.; Wang, L. Dynamic surface adapts to multiple service stages by orchestrating responsive polymers and functional peptides. *Biomaterials* **2023**, *301*, 122200. [CrossRef]
118. Gilotra, M.; Nguyen, T.; Jaffe, D.; Sterling, R. Dilute betadine lavage reduces implant-related bacterial burden in a rabbit knee prosthetic infection model. *Am. J. Orthop.* **2015**, *44*, E38–E41. [PubMed]
119. Heffernan, J.M.; Overstreet, D.J.; Vernon, B.L.; McLemore, R.Y.; Nagy, T.; Moore, R.C.; Badha, V.S.; Childers, E.P.; Nguyen, M.B.; Gentry, D.D.; et al. In vivo evaluation of temperature-responsive antimicrobial-loaded PNIPAAm hydrogels for prevention of surgical site infection. *J. Biomed. Mater. Res.—Part B Appl. Biomater.* **2022**, *110*, 103–114. [CrossRef]
120. Komnos, G.; Banios, K.; Kolonia, K.; Poultsides, L.A.; Petinaki, E.; Sarrou, S.; Zintzaras, E.; Karachalios, T. Do trabecular metal and cancellous titanium implants reduce the risk of late haematogenous infection? An experimental study in rabbits. *HIP Int.* **2021**, *31*, 766–773. [CrossRef]

121. Mäkinen, T.J.; Veiranto, M.; Knuuti, J.; Jalava, J.; Törmälä, P.; Aro, H.T. Efficacy of bioabsorbable antibiotic containing bone screw in the prevention of biomaterial-related infection due to *Staphylococcus aureus*. *Bone* **2005**, *36*, 292–299. [CrossRef]
122. Mao, Y.; Valour, F.; Nguyen, N.T.Q.; Doan, T.M.N.; Koelkebeck, H.; Richardson, C.; Cheng, L.I.; Sellman, B.R.; Tkaczyk, C.; Diep, B.A. Multi-mechanistic Monoclonal Antibody Combination Targeting Key *Staphylococcus aureus* Virulence Determinants in a Rabbit Model of Prosthetic Joint Infection. *Antimicrob. Agents Chemother.* **2021**, *65*, 10–1128. [CrossRef]
123. Yu, B.; Wen, J.Q.; Jiang, Y.; Chen, Y.; Yu, G.N.; Ren, H.F.; Ge, D.Z.; Wang, Z.Y. Antibacterial activity of a novel titanium-copper (Ti-Cu) sintered alloy in preventing periprosthetic joint infection in rabbit model. *J. Biomater. Tissue Eng.* **2019**, *9*, 607–614. [CrossRef]
124. Zhai, H.; Pan, J.; Pang, E.; Bai, B. Lavage with allicin in combination with vancomycin inhibits biofilm formation by *Staphylococcus epidermidis* in a rabbit model of prosthetic joint infection. *PLoS ONE* **2014**, *9*, e102760. [CrossRef] [PubMed]
125. Zhou, B.; Zhang, D. Antibacterial effects of bacteriocins isolated from lactobacillus rhamnosus (ATCC 53103) in a rabbit model of knee implant infection. *Exp. Ther. Med.* **2018**, *15*, 2985–2989. [CrossRef] [PubMed]
126. Zhu, Y.; Weng, X.; Zhang, J.; Mao, J. Protective effect of additional cathelicidin antimicrobial peptide PR-39 on prosthetic-joint infections. *J. Orthop. Surg.* **2023**, *31*, 10225536231175237. [CrossRef]
127. Odekerken, J.C.; Arts, J.J.; Surtel, D.A.; Walenkamp, G.H.; Welting, T.J. A rabbit osteomyelitis model for the longitudinal assessment of early post-operative implant infections. *J. Orthop. Surg. Res.* **2013**, *8*, 38. [CrossRef]
128. Hayakawa, T.; Yoshinari, M.; Kiba, H.; Yamamoto, H.; Nemoto, K.; Jansen, J.A. Trabecular bone response to surface roughened and calcium phosphate (Ca-P) coated titanium implants. *Biomaterials* **2002**, *23*, 1025–1031. [CrossRef]
129. Sul, Y.T.; Byon, E.S.E.S.; Jeong, Y.Y. Biomechanical measurements of calcium-incorporated oxidized implants in rabbit bone: Effect of calcium surface chemistry of a novel implant. *Clin. Implant Dent. Relat. Res.* **2004**, *6*, 101–110. [CrossRef]
130. Breding, K.; Jimbo, R.; Hayashi, M.; Xue, Y.; Mustafa, K.; Andersson, M. The effect of hydroxyapatite nanocrystals on osseointegration of titanium implants: An in vivo rabbit study. *Int. J. Dent.* **2014**, *2014*, 171305. [CrossRef] [PubMed]
131. Roberts, W.E.; Smith, R.K.; Zilberman, Y.; Mozsary, P.G.; Smith, R.S. Osseous adaptation to continuous loading of rigid endosseous implants. *Am. J. Orthod.* **1984**, *86*, 95–111. [CrossRef] [PubMed]
132. Slaets, E.; Carmeliet, G.; Naert, I.; Duyck, J. Early cellular responses in cortical bone healing around unloaded titanium implants: An animal study. *J. Periodontol.* **2006**, *77*, 1015–1024. [CrossRef] [PubMed]
133. Hermida, J.C.; Bergula, A.; Dimaano, F.; Hawkins, M.; Colwell, C.W.; D'Lima, D.D. An in vivo evaluation of bone response to three implant surfaces using a rabbit intramedullary rod model. *J. Orthop. Surg. Res.* **2010**, *5*, 57. [CrossRef]
134. Peng, H.-M.; Zhou, Z.-K.; Wang, F.; Yan, S.-G.; Xu, P.; Shang, X.-F.; Zheng, J.; Zhu, Q.-S.; Cao, L.; Weng, X.-S. Microbiology of periprosthetic hip and knee infections in surgically revised cases from 34 centers in mainland China. *Infect. Drug Resist.* **2021**, *25*, 2411–2418. [CrossRef] [PubMed]
135. Levy, P.Y.; Fenollar, F.; Stein, A.; Borrione, F.; Cohen, E.; Lebail, B.; Raoult, D. *Propionibacterium acnes* postoperative shoulder arthritis: An emerging clinical entity. *Clin. Infect. Dis.* **2008**, *46*, 1884–1886. [CrossRef] [PubMed]
136. Sampathkumar, P.; Osmon, D.R.; Cockerill, F.R., III. Prosthetic joint infection due to *Staphylococcus lugdunensis*. *Mayo Clin. Proc.* **2000**, *75*, 511–512. [CrossRef] [PubMed]
137. Shah, N.B.; Osmon, D.R.; Fadel, H.; Patel, R.; Kohner, P.C.; Steckelberg, J.M.; Mabry, T.; Berbari, E.F. Laboratory and clinical characteristics of *Staphylococcus lugdunensis* prosthetic joint infections. *J. Clin. Microbiol.* **2010**, *48*, 1600–1603. [CrossRef] [PubMed]
138. Tsai, Y.; Chang, C.-H.; Lin, Y.-C.; Lee, S.-H.; Hsieh, P.-H.; Chang, Y. Different microbiological profiles between hip and knee prosthetic joint infections. *J. Orthop. Surg.* **2019**, *27*, 2309499019847768. [CrossRef]
139. WHO Publishes List of Bacteria for Which New Antibiotics Are Urgently Needed. Available online: https://www.who.int/news/item/27-02-2017-who-publishes-list-of-bacteria-for-which-new-antibiotics-are-urgently-needed (accessed on 1 August 2024).
140. Eiselt, V.A.; Bereswill, S.; Heimesaat, M.M. Phage therapy in prosthetic joint infections caused by *Staphylococcus aureus*—A literature review. *Eur. J. Microbiol. Immunol.* **2024**, *14*, 75–85. [CrossRef]
141. Tuchscherr, L.; Pöllath, C.; Siegmund, A.; Deinhardt-Emmer, S.; Hoerr, V.; Svensson, C.-M.; Thilo Figge, M.; Monecke, S.; Löffler, B. Clinical *S. aureus* isolates vary in their virulence to promote adaptation to the host. *Toxins* **2019**, *11*, 135. [CrossRef] [PubMed]
142. Guo, G.; Wang, J.; You, Y.; Tan, J.; Shen, H. Distribution characteristics of *Staphylococcus* spp. in different phases of periprosthetic joint infection: A review. *Exp. Ther. Med.* **2017**, *13*, 2599–2608. [CrossRef] [PubMed]
143. Hischebeth, G.; Randau, T.; Ploeger, M.; Friedrich, M.; Kaup, E.; Jacobs, C.; Molitor, E.; Hoerauf, A.; Gravius, S.; Wimmer, M. *Staphylococcus aureus* versus *Staphylococcus epidermidis* in periprosthetic joint infection—Outcome analysis of methicillin-resistant versus methicillin-susceptible strains. *Diagn. Microbiol. Infect. Dis.* **2019**, *93*, 125–130. [CrossRef]
144. Lora-Tamayo, J.; Murillo, O.; Iribarren, J.A.; Soriano, A.; Sánchez-Somolinos, M.; Baraia-Etxaburu, J.M.; Rico, A.; Palomino, J.; Rodríguez-Pardo, D.; Horcajada, J.P. A large multicenter study of methicillin–susceptible and methicillin–resistant *Staphylococcus aureus* prosthetic joint infections managed with implant retention. *Clin. Infect. Dis.* **2013**, *56*, 182–194. [CrossRef] [PubMed]
145. Dreikausen, L.; Blender, B.; Trifunovic-Koenig, M.; Salm, F.; Bushuven, S.; Gerber, B.; Henke, M. Analysis of microbial contamination during use and reprocessing of surgical instruments and sterile packaging systems. *PLoS ONE* **2023**, *18*, e0280595. [CrossRef] [PubMed]
146. Guarch-Pérez, C.; Riool, M.; de Boer, L.; Kloen, P.; Zaat, S. Bacterial reservoir in deeper skin is a potential source for surgical site and biomaterial-associated infections. *J. Hosp. Infect.* **2023**, *140*, 62–71. [CrossRef] [PubMed]

147. Rakow, A.; Perka, C.; Trampuz, A.; Renz, N. Origin and characteristics of haematogenous periprosthetic joint infection. *Clin. Microbiol. Infect.* **2019**, *25*, 845–850. [CrossRef] [PubMed]
148. Zeller, V.; Kerroumi, Y.; Meyssonnier, V.; Heym, B.; Metten, M.-A.; Desplaces, N.; Marmor, S. Analysis of postoperative and hematogenous prosthetic joint-infection microbiological patterns in a large cohort. *J. Infect.* **2018**, *76*, 328–334. [CrossRef] [PubMed]
149. Wagner, E.R.; Farley, K.X.; Higgins, I.; Wilson, J.M.; Daly, C.A.; Gottschalk, M.B. The incidence of shoulder arthroplasty: Rise and future projections compared with hip and knee arthroplasty. *J. Shoulder Elb. Surg.* **2020**, *29*, 2601–2609. [CrossRef]
150. Ko, M.J.; Lim, C.-Y. General considerations for sample size estimation in animal study. *Korean J. Anesthesiol.* **2021**, *74*, 23–29. [CrossRef] [PubMed]
151. Ahmad, S.S.; Shaker, A.; Saffarini, M.; Chen, A.F.; Hirschmann, M.T.; Kohl, S. Accuracy of diagnostic tests for prosthetic joint infection: A systematic review. *Knee Surg. Sports Traumatol. Arthrosc.* **2016**, *24*, 3064–3074. [CrossRef] [PubMed]
152. Bugnon, P.; Heimann, M.; Thallmair, M. What the literature tells us about score sheet design. *Lab. Anim.* **2016**, *50*, 414–417. [CrossRef] [PubMed]
153. Benato, L.; Murrell, J.; Rooney, N. Bristol Rabbit Pain Scale (BRPS): Clinical utility, validity and reliability. *BMC Vet. Res.* **2022**, *18*, 341. [CrossRef] [PubMed]
154. Miller, A.L.; Leach, M.C. Pain recognition in rabbits. *Vet. Clin. Exot. Anim. Pract.* **2023**, *26*, 187–199. [CrossRef] [PubMed]
155. Melillo, A. Rabbit clinical pathology. *J. Exot. Pet Med.* **2007**, *16*, 135–145. [CrossRef] [PubMed]
156. Vaishya, R.; Sardana, R.; Butta, H.; Mendiratta, L. Laboratory diagnosis of prosthetic joint infections: Current concepts and present status. *J. Clin. Orthop. Trauma* **2019**, *10*, 560–565. [CrossRef] [PubMed]
157. Berbari, E.; Mabry, T.; Tsaras, G.; Spangehl, M.; Erwin, P.J.; Murad, M.H.; Steckelberg, J.; Osmon, D. Inflammatory blood laboratory levels as markers of prosthetic joint infection: A systematic review and meta-analysis. *JBJS* **2010**, *92*, 2102–2109. [CrossRef] [PubMed]
158. Brewer, N.R. Biology of the rabbit. *J. Am. Assoc. Lab. Anim. Sci.* **2006**, *45*, 8–24.
159. Van den Kieboom, J.; Bosch, P.; Plate, J.; IJpma, F.; Kuehl, R.; McNally, M.; Metsemakers, W.; Govaert, G. Diagnostic accuracy of serum inflammatory markers in late fracture-related infection: A systematic review and meta-analysis. *Bone Jt. J.* **2018**, *100*, 1542–1550. [CrossRef] [PubMed]
160. Ashraf, M.A.; Goyal, A. Fludeoxyglucose (18F). In *StatPearls [Internet]*; StatPearls Publishing: Treasure Island, FL, USA, 2023.
161. Andriesse, G.; Elberts, S.; Vrolijk, A.; Verhulst, C.; Kluytmans, J. Evaluation of a fourth-generation latex agglutination test for the identification of *Staphylococcus aureus*. *Eur. J. Clin. Microbiol. Infect. Dis.* **2011**, *30*, 259–264. [CrossRef]
162. Yuan, Y.; Hunt, R.H. Systematic reviews: The good, the bad, and the ugly. *Off. J. Am. Coll. Gastroenterol. ACG* **2009**, *104*, 1086–1092. [CrossRef]
163. Schumacher, A.; Vranken, T.; Malhotra, A.; Arts, J.; Habibovic, P. In vitro antimicrobial susceptibility testing methods: Agar dilution to 3D tissue-engineered models. *Eur. J. Clin. Microbiol. Infect. Dis.* **2018**, *37*, 187–208. [CrossRef] [PubMed]
164. Coenye, T.; Nelis, H.J. In vitro and in vivo model systems to study microbial biofilm formation. *J. Microbiol. Methods* **2010**, *83*, 89–105. [CrossRef] [PubMed]
165. George, E.L.; Truesdell, S.L.; York, S.L.; Saunders, M.M. Lab-on-a-chip platforms for quantification of multicellular interactions in bone remodeling. *Exp. Cell Res.* **2018**, *365*, 106–118. [CrossRef] [PubMed]
166. Kim, S.; Rajendran, A.K.; Amirthalingam, S.; Kim, J.H.; So, K.-H.; Hwang, N.S. Recent technological advances in lab-on-a-chip for bone remodeling. *Biosens. Bioelectron. X* **2023**, *14*, 100360. [CrossRef]

Journal of
Functional Biomaterials

MDPI

Article

Electrodepositing Ag on Anodized Stainless Steel for Enhanced Antibacterial Properties and Corrosion Resistance

Yi Shao [1,2], Yue Jiang [1,2], Yongfeng Wang [2], Qiangsheng Dong [3], Cheng Wang [1], Yan Wang [2], Feng Xue [1,2], Chenglin Chu [1,2,*] and Jing Bai [1,2,*]

[1] Jiangsu Key Laboratory for Advanced Metallic Materials, School of Materials Science and Engineering, Southeast University, Nanjing 211189, China; sy@i-bmd.org (Y.S.); sadhu_jiang@126.com (Y.J.); cheng.wang@seu.edu.cn (C.W.); xuefeng@seu.edu.cn (F.X.)
[2] Institute of Biomedical Devices (Suzhou), Southeast University, Suzhou 215163, China; yfwang0319@163.com (Y.W.); wangyan@i-bmd.org (Y.W.)
[3] Jiangsu Key Laboratory of Advanced Structural Materials and Application Technology, School of Materials Science and Engineering, Nanjing Institute of Technology, Nanjing 211167, China; qsdong@njit.edu.cn
* Correspondence: clchu@seu.edu.cn (C.C.); baijing@seu.edu.cn (J.B.)

Abstract: Antibacterial stainless steels have been widely used in biomedicine, food, and water treatment. However, the current antibacterial stainless steels face challenges in balancing corrosion resistance and antibacterial effectiveness, limiting their application range and lifespan. In this study, an oxide layer sealed with antibacterial Ag particles was constructed on the surface of 304 stainless steel through anodizing and electrodeposition, and the process parameters were optimized for achieving long-term antibacterial properties. The electrochemical tests demonstrated that the composite coating effectively enhanced the corrosion resistance of 304 stainless steel. The X-ray photoelectron spectroscopy analysis revealed the close binding mechanism between the Ag particles and the micropores in the oxide layer. Furthermore, the antibacterial stainless steel has an antibacterial rate of 99% against *Escherichia coli* (*E. coli*) and good biocompatibility. This study provides an effective approach for designing efficient, stable, and safe antibacterial stainless steel.

Keywords: stainless steel; anodization; corrosion resistance; antibacterial property

1. Introduction

Stainless steel is one of the most widely used metal materials due to its outstanding corrosion resistance, mechanical properties, and machinability, making it favored in various fields [1,2]. However, in specific areas such as medical devices and kitchenware, bacterial contamination occurs on conventional stainless steels, causing cross-infection risk and posing a serious threat to human health. Therefore, antibacterial stainless steels have garnered widespread attention and become a crucial topic of current research.

Various types of antibacterial stainless steels have been developed, such as surface-treated antibacterial stainless steel, alloy-based antibacterial stainless steel, etc. [2–4]. The methods for preparing surface-treated antibacterial stainless steel mainly include surface coating [5,6], ion implantation [7,8], magnetron sputtering [9,10], and electrodeposition [11–13]. Although these antibacterial stainless steels have achieved certain success in antibacterial effects, there are many disadvantages such as high cost and poor corrosion resistance. Due to the frequent exposure to corrosive environments, antibacterial stainless steel with poor corrosion resistance cannot be used in serious corrosion situations. In addition, antibacterial agents are introduced into stainless steel for enhanced antibacterial properties, but alter material structures, thereby affecting its corrosion resistance and other

aspects of performance. Currently, the process costs for most antibacterial stainless steels are relatively high, such as alloy-based stainless steel requiring a large number of antibacterial elements, while surface-treated types equipment is complex and costly, making it difficult to achieve large-scale production. Therefore, it is particularly important to develop a low-cost antibacterial stainless steel with good antibacterial properties and excellent corrosion resistance.

Anodizing is a well-established technique for preparing porous oxide films on metal surfaces [11,14,15]. The parameters such as pore size, depth, and porosity can be finely controlled by adjusting the electrolyte composition and relevant oxidation processes. Consequently, a uniformly ordered nanoporous film structure can be formed on metal surfaces, significantly enhancing the corrosion resistance and wear resistance of metal materials [16]. More importantly, the unique potential of the nanoporous film structure provides a carrier for antibacterial elements filling, successfully creating metal materials with antibacterial properties. In comparison to ion implantation surface modification, anodizing provides a deeper depth for the deposition of antibacterial elements [17], revealing its enormous potential for application in the preparation of special performance stainless steels.

In this study, the 304 stainless steels were selected as the substrate, one of the most widely used stainless steel brands in the medical device and food industry, and antibacterial stainless steel was successfully prepared using the anodizing and electrodeposition methods. By optimizing the processing technology, we obtained a novel antibacterial stainless steel with excellent antibacterial and corrosion resistance based on low production costs. Therefore, this study provides a new perspective for the preparation of novel antibacterial stainless steel.

2. Material and Methods

2.1. Materials Preparation

Commercial 304 austenitic stainless steel (0.04% C, 1.02% Mn, 0.03% P, 0.01% S, 0.44% Si, 18.4% Cr, 7.93% Ni) (2 cm × 2 cm × 1 mm) (Zhejiang Qingshan Iron and Steel Co. Ltd, Lishui, China) was used as the substrate. The stainless steel samples were mechanically polished then cleaned in an ultrasonic cleaner (PS-120A, JieKang Ultrasonic Equipment Co., Ltd, Dongguan, China.) after the degreasing treatment (50 g/L NaOH, 40 g/L Na_2CO_3, 30 g/L Na_2PO_4, 5 g/L Na_2SiO_3) to ensure a clean surface. An electropolishing was performed for samples in the electrolyte (600 mL/L H_3PO_4, 300 mL/L H_2SO_4, 50 mL/L glycerol, 5 mL/L saccharin) at 50 °C. The stainless steel sheet was used as the anode, and the graphite sheet as the cathode, with a cathode-to-anode area ratio of 1.5:1 and an anode–cathode distance of 5 cm. The electrolyte was stirred using a magnetic stirrer (RCT basic, IKA, Staufen, Germany) at a stirring rate of 20 rpm. The electropolishing was carried out for 5 min using a fully controlled DC stabilized power supply (MS1003D, MaiSheng Power Technology Co., Ltd, Shenzhen, China) at a current density of 30 A/dm^2.

2.2. Antibacterial Surface Modification

A mixed solution of phosphoric acid (H_3PO_4) and ethylene glycol (EG) was used as the electrolyte for anodization. Pre-treated stainless steel samples were placed in the electrolytic cell, with the samples serving as the anode, and graphite serving as the cathode. The cathode-to-anode area ratio was maintained at 1.5:1, and the cathode–anode distance was set as 5 cm. Anodization was conducted at 0 °C, with an applied voltage of 15 V for 1 h. The antibacterial film containing silver was further prepared by electrochemical deposition using anodic oxidation film of stainless steel as carrier. The alternating current deposition was conducted using a voltage-controlled mode, with the addition of $MgSO_4$ as an auxiliary during the deposition process [18]. The process parameters for the electrolyte

are as follows: the electrolyte consisted of 2 g/L of silver nitrate, 20 g/L of sulfuric acid, and 12 g/L of magnesium sulfate, with the temperature controlled at 25 °C.

2.3. Surface Microstructure Characterization

The surface microstructure of the stainless steel samples with the anodized oxide film and antibacterial layer were observed by field emission scanning electron microscope (SEM) (Sirion200, FEI, Hillsboro, OR, USA). The X-ray photoelectron spectroscopy (XPS) (K-Alpha+, Thermo Fisher Scientific, Waltham, MA, USA) was used to determine the elemental composition and chemical states of surface films on the stainless steel. During XPS analysis, the surface of the antibacterial film was etched at 0.25 nm/s by argon ion sputtering, and the elements in different positions in the film were quantitatively and chemically analyzed by the atomic sensitivity factor method.

2.4. Wear Resistance Tests

The wear resistance of the antibacterial layer on the stainless steel surface was assessed using the rubber eraser abrasion tester (DDC-NM290, Dongguan Zhongyi Chuangtian Instrument Equipment Co., Ltd, Dongguan, China.), with untreated stainless steel samples as the control. The rubber wheel used in this study has a shore hardness of 60 degrees (60 HA) and the test stroke is 10 mm, and one round trip is one cycle. The tester was set at a speed of 50 rpm, and the surfaces were worn with a rubber eraser under a load of 4.9 N for 1000 reciprocating abrasions. The weight loss was measured by a precision analytical balance to calculate wear resistance.

2.5. Corrosion Resistance Evaluation

The ParStat4000 electrochemical workstation (Ametek, Inc, Berwyn, PA, USA) was used to evaluate the corrosion resistance of the uncoated and coated stainless steel at room temperature. A 3.5 wt% NaCl solution was utilized as the corrosive medium, and a three-electrode cell was employed in which the stainless steel sample was the working electrode, a platinum sheet electrode was the auxiliary electrode, and a saturated calomel electrode (SCE) was the reference electrode. The coated samples with an exposed area of 1 cm^2 were immersed in the corrosive medium for 30 min to stabilize the open-circuit potential. Electrochemical impedance spectroscopy (EIS) plots were collected at a frequency range of 10 mHz to 100 kHz. Potential polarization curves were obtained at a potential range of −0.5 V to 0.5 V and a scanning rate of 1 mV/s to fully capture the electrochemical behavior of the tested samples and maintain the validity of the Tafel region for accurate corrosion parameter determination.

2.6. Antibacterial Performance Tests

Escherichia coli (*E. coli*) and *Staphylococcus aureus* (*S. aureus*) were selected as the test bacterial strains to evaluate the antibacterial effect of the stainless steel surface according to ISO 22196-2011 standard [19]. *E. coli* (CICC 10899) and *S. aureus* (CICC 10384) were purchased from the China Center of Industrial Culture Collection (CICC). Untreated stainless steel was used as the control group. A droplet of 0.4 mL bacterial solution with a concentration of 2.5×10^5~10×10^5 CFU/mL was placed on the surface of a 50 mm × 50 mm × 1 mm test piece and covered with polyethylene (PE) film. The samples were incubated at 37 °C for 48 h, followed by colony counting. Each group was performed in triplicate for statistical reliability.

2.7. Cell Activity Assay

Live/Dead Cell Staining: Normal Human Dermal Fibroblasts (NHDFs) were cultured in a complete culture medium containing 10% fetal bovine serum and antibiotics (100 U/mL

penicillin, 100 μg/mL streptomycin) at 37 °C in a 5% CO_2 humidified incubator. The experimental group was treated with 100 μL of different concentrations of a new type of antibacterial stainless steel (NASS) extract in the culture medium, whereas the positive control group was treated with 100 μL culture medium containing DMSO. The cells were cultured for 24 h. Subsequently, following the instructions of the Live/Dead Cell Imaging Kit (C2015M, Beyotime, Shanghai, China), the culture medium was removed, and the cells were washed once with PBS. Then, 100 μL of Calcein AM/PI detection working solution was added to the cells, and they were incubated in the dark at 37 °C for 30 min. Subsequently, images were captured using an inverted fluorescence microscope (IX83, Olympus, Tokyo, Japan). Live cells emitted green fluorescence, while dead cells emitted red fluorescence. Each group was performed in triplicate for statistical reliability.

MTT assay: After culturing NHDF cells in a 37 °C, 5% CO_2 humidified incubator for 24 h, different concentrations of a new antibacterial stainless steel (NASS) extract were added to the experimental group. Subsequently, 100 μL of 0.5 mg/mL MTT solution (CT0025, Leagene, Beijing, China) was added to each well after another 24 h of incubation. The cells were further incubated at 37 °C in the dark for 4 h, following which the absorbance at 490 nm (A490nm) was measured. Each group was conducted with 5 replicates to ensure statistical reliability.

2.8. Statistical Analysis

Statistical data were analyzed using GraphPad Prism 8 software (v8.4.2), and the significance was analyzed using the ordinary one-way ANOVA method. Significance was denoted by letters, where the same letter indicates no significance, while different letters indicate significant differences. All data were presented as mean ± SD ($n \geq 3$).

3. Results and Discussion

3.1. Preparation and Characterization of Anodic Oxidation Layer on Stainless Steel

In order to obtain a uniformly ordered nanoporous oxide film, pre-treated stainless steel samples were conducted using anodic oxidation. The research indicated that anodic oxidation using phosphoric acid (H_3PO_4) as an electrolyte can form dense and stable oxide films on stainless steel, thereby improving its corrosion resistance. Additionally, ethylene glycol (EG) as a solvent can protect the stainless steel surface to retard serious anodic oxidation effects for enhanced corrosion resistance [15]. Therefore, a H_3PO_4-EG electrolyte was used for anodic oxidation and the optimal conditions for anodic oxidation were studied by adjusting the ratio of H_3PO_4 and EG.

The results indicated that the ratio of H_3PO_4 and EG affected anodic oxidation effects on the surface of stainless steel (Figure 1). When the ratio of H_3PO_4:EG was 5:5, the stainless steel surface formed closely packed small pores with an average pore diameter of 118 nm, exhibiting relatively regular polygonal shapes, poor orderliness, and continuous pore phenomena. The average thickness of the membrane reached 2.5 μm (Figure 1a,d,g). At the ratio of H_3PO_4:EG was 3:7, the average pore diameter decreased to 105 nm, with pores appearing as regular hexagons, demonstrating good orderliness and a more uniform distribution. The membrane also exhibited the highest density, and the average thickness of the membrane reached 2.5 μm (Figure 1b,e,h). When the ratio of H_3PO_4 decreased to 1:9 of H_3PO_4:EG, the surface did not form a micro-nanopore structure but appeared as irregular striped patterns, with an average membrane thickness of only 0.6 μm (Figure 1c,i).

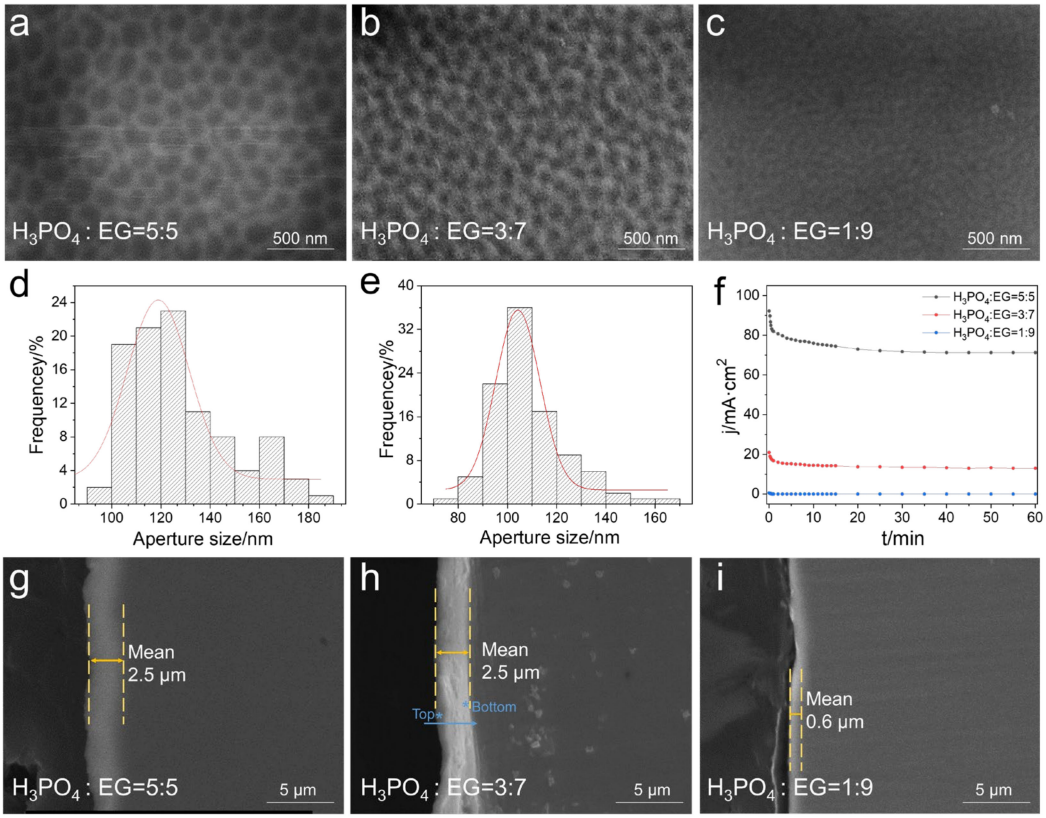

Figure 1. The effects of electrolyte with different phosphoric acid contents on the anodization of stainless steel. (**a**–**c**) Surface morphology of stainless steel after anodization; (**d**–**f**) Relationship curve between anodization current density and time. The red line in (**d**,**e**) represents the fitted curve. (**g**–**i**) Cross-sectional morphology of stainless steel after anodization. * in (**h**) represents the top and bottom positions used to measure the EDS spectrum of the anodized stainless steel film.

When the ratio of H_3PO_4 to EG is 5:5 and 3:7, the current density versus time curve shows a significant inflection point, initially decreasing linearly due to the formation of a barrier layer. As the reaction progresses, the barrier layer gradually dissolves, leading to the formation of a porous film structure on the stainless steel surface. At this point, the current density stabilizes or tends to slowly increase. Since the current density is higher at a ratio of 5:5, the reaction is more intense, resulting in nanopore structures with slightly larger pore sizes compared to a ratio of 3:7, with a more disordered pore distribution. Additionally, due to the higher current density, more heat is released during the reaction, intensifying the dissolution process and resulting in shallower pores. When the ratio is 1:9, it is speculated that the current density is too low to enable the formation of nanopore structures on the surface (Figure 1f). Therefore, in order to achieve the optimal effect of anodized porous membrane-loaded antibacterial agents, an electrolyte with a ratio of H_3PO_4:EG of 3:7 was used.

Surface analysis was performed using an energy-dispersive spectrometer (EDS) attached to Sirion200 SEM to investigate the chemical composition of the stainless steel anodic oxidation film (Figure 2). EDS line scan spectra revealed that the oxygen content at the top of the oxide film was significantly higher than in the base material, while the content of metal elements such as Fe, Cr, and Ni was noticeably lower in the oxide film. Particularly, the Fe content exhibited the most significant decrease (Figure 2a–c and Table S1). These results indicated that the nanoporous anodic oxidation film formed by anodic oxidation on the stainless steel surface was mainly composed of oxides of Fe, Cr, and Ni, in which oxides of Fe were dominated. These findings aligned with the mechanism of stainless steel surface anodic oxidation [20].

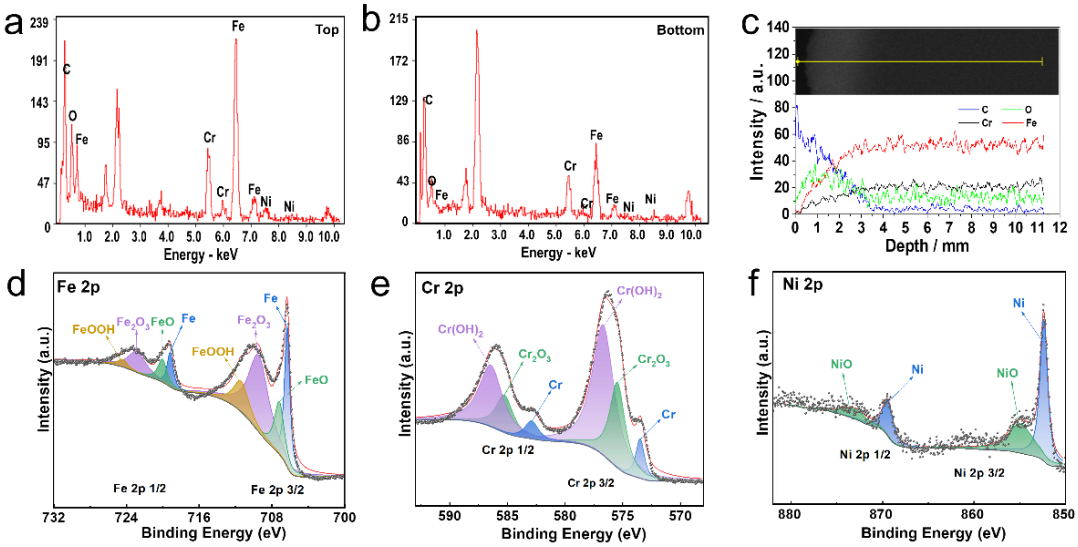

Figure 2. EDS spectrum and XPS spectrum of stainless steel anodized film. EDS spectra of the top (**a**), bottom (**b**), and section line scan (**c**) of the anodic oxide film. The yellow line in (**c**) represents the scanning line for EDS monitoring. (**d**–**f**) XPS spectrum of anodized stainless steel film. The black points represent raw data from XPS measurement, and the red lines represent the fitting data for XPS analysis.

XPS was performed to clarify the chemical states of O, Fe, Cr, and Ni in the oxide film, as shown in Figure 2d–f. Fe 2p 3/2 can be distinguished to four peaks at 706.7 eV, 707.10 eV, 709.60 eV, and 711.50 eV, which, respectively, represent combined states of Fe in FeO, metallic Fe, Fe_2O_3, and FeOOH after deconvolution (Figure 2d) [21,22]. In addition, four deconvoluted peaks are also dissociated in the Fe 2p 1/2 peak. Relatively, Cr 2p 3/2 can be divided into peaks at 573.4 eV, 575.5 eV, and 576.7 eV, which relate to Cr, Cr_2O_3, and $Cr(OH)_2$ (Figure 2e). According to Ni 2p, Ni 2p predominantly existed in the forms of metallic Ni and NiO (Figure 2f) [23,24]. These findings suggested that the porous film formed on the surface after the anodic oxidation of stainless steel was primarily composed of hydroxides.

While anodic oxide films of stainless steel have been prepared by different techniques, many researchers have also studied the formation mechanism of the nanoporous film structure during the anodic oxidation process [11,25,26]. In this study, it was found that in the anodizing process of stainless steel, the curve of current density with time decreased rapidly at the initial stage of the reaction, and then gradually stabilized after falling to the minimum value, and only fluctuated in a small range (Figure 3).

The surface anodic oxide film of stainless steel was formed at the interface between the electrolyte and the stainless steel substrate, where O^{2-} and OH^- migrated from the electrolyte to the interface, while metal ions such as Fe^{2+}/Fe^{3+}, Cr^{3+}/Cr^{6+}, and Ni^{2+} migrated from the substrate to the interface. The porous film formed on the surface of stainless steel after anodizing is mainly composed of hydroxides such as FeOOH, $Cr(OH)_3$, NiOOH, and metal oxides such as Fe_2O_3, Cr_2O_3, and NiO. It can be inferred that the following reactions occurred at the anode:

$$2H_2O \rightarrow O_2 + 4H^+ + 4e^-$$

$$Cr^{3+} + 3OH^- = Cr(OH)_3$$

$$xM\ (Fe, Cr, Ni) + O_2 \rightarrow M_xO_y(Fe_2O_3, Fe_3O_4, Cr_2O_3, CrO_3, NiO)$$

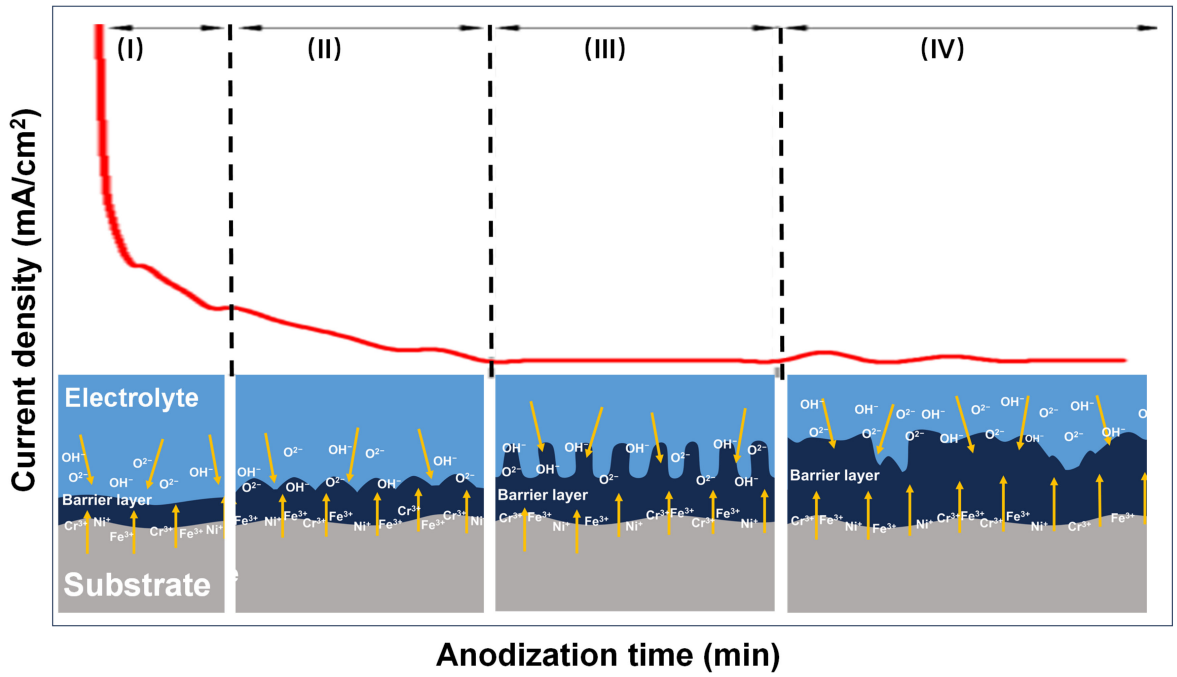

Figure 3. Schematic illustration of the structural changes in the porous film on the surface of stainless steel. The yellow arrows represent the ion migration tracks, and the red curve represents the variation of current density as a function of anodization time. I, II, III and IV represent the anodization stage, respectively.

As shown in Figure 3, the formation mechanism of the porous film on the surface of stainless steel can be roughly divided into four stages.

(I) During the anodizing process under constant voltage, a dense and uniform oxide film, also known as the barrier layer, was rapidly formed on the surface of the stainless steel. At this stage, the current density rapidly decreased.

(II) The uneven oxide film on stainless steel caused the change in surface roughness, and the electric field distribution became extremely disordered. Local electric field concentration occurred at the depressions in the oxide layer, resulting in accelerated dissolution of the oxide film and the formation of a large number of nanoscale micropores.

(III) When the formation rate at the film bottom was balanced with the dissolution rate at the film top, the growth of the porous layer entered a stable stage. At this stage, the porous layer exhibited a uniformly distributed pore structure, and the current density stabilized.

(IV) With further extension of time, the balance between the dissolution and the formation of the oxide layer was disrupted. At this stage, the dissolution rate at the edge of the pores increased, exceeding the rate of formation of the bottom oxide layer. The nanoporous structure began to dissolve, resulting in a reduction in depth. At the same time, pore edge collapse occurred in some areas, and the nanostructures began to be destroyed.

Nanoporous structures were prepared on the surface of stainless steel by anodizing, and the pore size and depth could be controlled by the process parameters, thus providing a carrier and space for the filling antibacterial elements, which was a novel method for preparing surface-modified antibacterial stainless steel [17]. Although nanoporous oxide films with ideal thickness and excellent properties have been prepared through anodic oxidation, the commonly used oxidation processes were sulfuric acid–chromic acid or phosphoric acid–chromic acid systems [11]. This type of electrolyte system largely produced hexavalent chromium ions, posing severe risks to human health and causing persistent

environmental pollution [27–30]. Studies have shown that an appropriate amount of trivalent chromium not only is not harmful to human health but also has immune-enhancing functions, and is therefore present in many food and supplement products [31–33].

This study innovatively selected an H_3PO_4-EG electrolyte system to prepare an anodic oxide film on stainless steel, which mainly consisted of hydroxides such as FeOOH and $Cr(OH)_3$, and oxides such as Fe_2O_3 and Cr_2O_3, with chromium existing in the form of trivalent chromium ions (Figure 2d–f). Therefore, the electrolyte system in this study was more environmentally friendly compared to conventional electrolyte systems.

3.2. Preparation and Characterization of Ag Antibacterial Layer on Stainless Steel

In order to enhance the adhesion of the metal coating, an Ag-containing antibacterial layer was prepared on the surface of anodized stainless steel using the alternating current deposition method. In comparison to direct current deposition, the pulse interval during alternating current deposition constrained the extent of crystal growth, thereby reducing the possibility of forming large coarse crystals. It is important to note that the deposition time should not be too short or too long, as either scenario may result in antibacterial particles not being fully embedded within the porous film or give rise to severe corrosion on the surface of the stainless steel (Figure 4a–d).

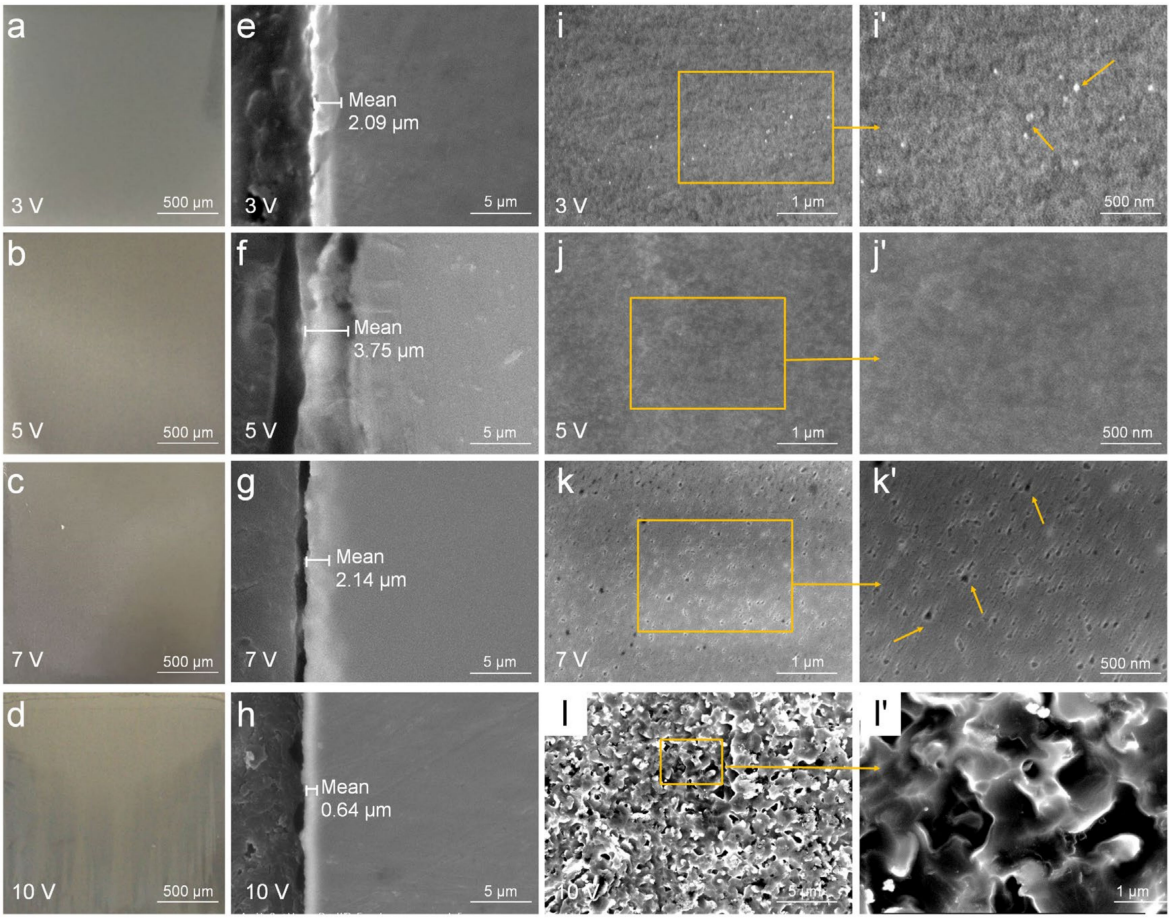

Figure 4. The morphologies of Ag-containing antibacterial layer on stainless steel surface. (**a**–**d**) Appearance of stainless steel samples after electrodeposition at different voltages. (**e**–**h**) The cross-section morphologies and (**i**–**l′**) the surface morphologies were observed by SEM. (**i′**–**l′**) is the magnification of the yellow box in (**i**–**l**), respectively. The deposition time was 2 min and the deposition voltages were 3 V, 5 V, 7 V, and 10 V, respectively.

The effect of different deposition voltages on the microstructure of the antibacterial layer was studied under the deposition time of 2 min (Figure 4e–l′). The results indicated that under an alternating current voltage of 3 V, the porous layer was covered with a uniformly thick deposition layer of approximately 2.09 μm (Figure 4e). However, the filling degree within the porous layer varied, and local areas exhibited particle aggregation, as indicated by the arrows (Figure 4i,i′). The thickness of the deposited layer on the stainless steel surface exhibited a certain degree of thinning relative to the thickness of the porous film after anodic oxidation. This is because during the initial stage of AC electric deposition, the reduction reaction of hydrogen ions caused a certain degree damage to the barrier layer of the oxide film, resulting in a thinner barrier layer of the oxide film. When the voltage was increased to 5 V, the density and uniformity of the deposition layer improved along with the deposited material filling the porous structure, resulting in a thickness increase to approximately 3.75 μm, and the microporous structure on the stainless steel anodized film nearly disappeared (Figure 4f,j,j′). Although the barrier layer initially experienced a certain degree of thinning, following the decrease in thickness of the barrier layer, the deposition reaction of Ag accelerated. Under higher voltage, it continuously reduced and deposited onto the stainless steel surface, resulting in a uniformly increasing thickness of the deposited layer. When the voltage was 7 V, the surface of the deposition layer displayed noticeable unevenness and defects, with numerous irregular small micropores, as indicated by the arrows, and the thickness decreased to 2.14 μm (Figure 4g,k,k′). Under a voltage of 10 V, severe corrosion occurred on the antibacterial stainless steel surface, with large areas of the antibacterial layer peeling off, rendering it difficult to obtain a smooth surface, and the antibacterial layer essentially disappeared (Figure 4h,l,l′). These results indicated that excessively high voltage caused the antibacterial ions to be reduced too quickly on the stainless steel surface, leading to local peeling or breakdown of the deposition layer, thus affecting the integrity and stability of the antibacterial layer.

The elemental composition and chemical state of the antibacterial film on the stainless steel surface were further analyzed (Figure 5). The XRD spectra showed that in addition to the basic elements O, Cr, Fe, and Ni of the stainless steel porous oxide film, the antibacterial film also contained a certain amount of Ag (Figure 5a,b). EDS spectra of cross-sectional line scanning revealed a substantial increase in oxygen content relative to the matrix (Figure 5c), which was consistent with the change in elemental content of the porous film carrier on the surface of stainless steel, proving that the carrier was a porous film with metal oxides as its main component. The content of the Ag element also increased to a certain extent compared to the substrate (Figure 5d). Additionally, the XRD phase analysis of the antibacterial layer indicated the presence of diffraction peaks with a relatively high content of Ag.

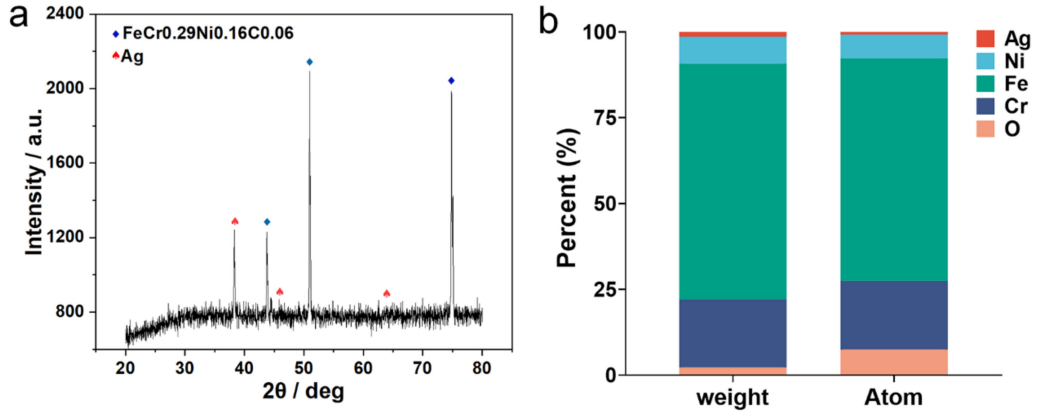

Figure 5. *Cont.*

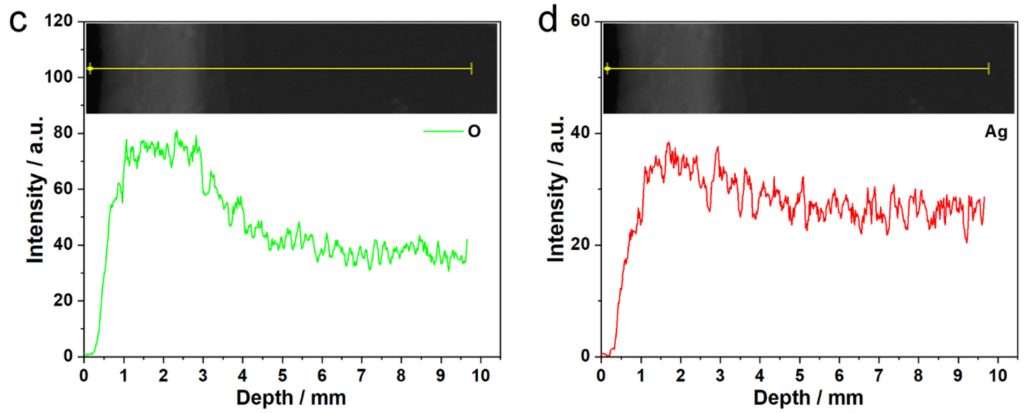

Figure 5. Composition analysis of antibacterial film on stainless steel surface. (**a**) XRD spectrum of antibacterial film surface; (**b**) Distribution of surface elements on antibacterial film; (**c**,**d**) EDS spectrum of cross-sectional line scan of antibacterial film. The yellow lines represent the scanning lines for EDS monitoring, the green line displays the distribution of O element, and the red line in (**d**) displays the distribution of Ag element.

Figure 6 displayed the XPS results of Ag-containing antibacterial film on the stainless steel surface. The Fe 2p spectrum is composed of Fe_2O_3 peaks and Fe-related satellite peaks (Figure 6a). After 30 s of etching, the Fe-related satellite peaks disappear. The Fe 2p 3/2 spectrum can be dissociated into two peaks of Fe (713.9 eV) and Fe_2O_3 (709.6 eV). Whether or not it has been etched, the Cr 2p 3/2 spectrum displays two peaks at 576.80 eV and 578.10 eV, representing Cr_2O_3 and $Cr(OH)_3$ (Figure 6b). The Ag 3d spectrum showed that the photoelectron peaks of 368.4 eV and 374.27 eV corresponded to Ag and Ag_2O, and the Ag content at the bottom of the deposition layer was higher than that at the top (Figure 6c), indicating that Ag existed in the form of elemental Ag and its oxide states, and was deposited within the pores of the porous oxide film.

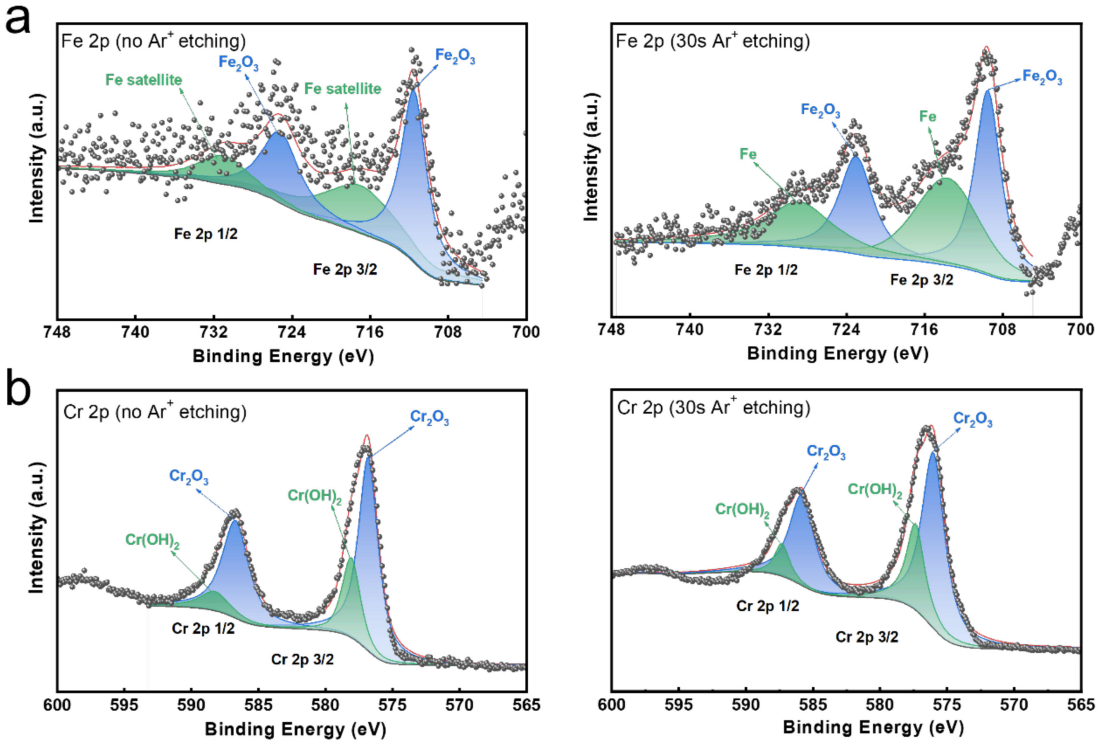

Figure 6. *Cont.*

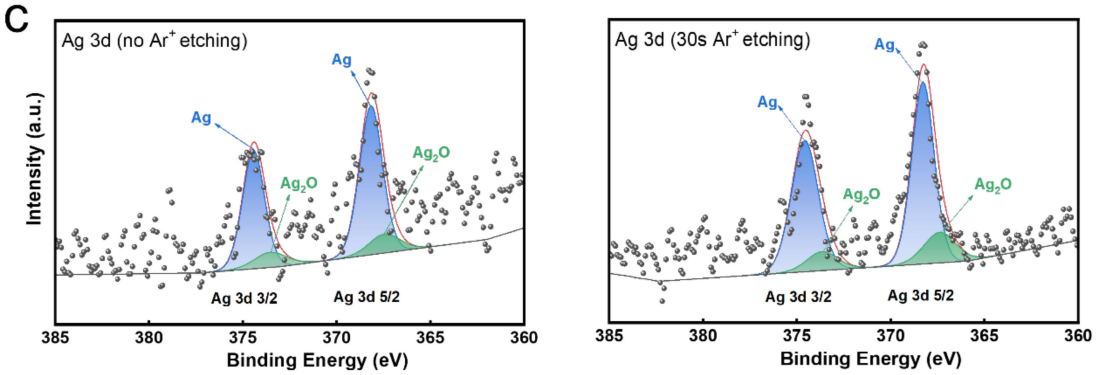

Figure 6. XPS spectrum of Ag-containing antibacterial film on stainless steel surface. (**a**) Fe 2p3; (**b**) Cr 2p3; (**c**) Ag 3d. The black points represent raw data from XPS measurement, and the red lines represent the fitting data for XPS analysis.

3.3. Corrosion Resistance of the Stainless Steel

To assess the practical value of the stainless steel, the wear resistance and corrosion resistance were tested. The results showed that no obvious scratches or spalling occurred in all samples after 1000 reciprocating times, with minimal changes in both mass and color (Table S2). It is proved that the stainless steel surfaces with Ag-containing films exhibit excellent wear resistance.

Then, the corrosion resistance of the Ag-containing films stainless steel was studied by electrochemical impedance spectroscopy (Figure 7). The Nyquist plot clearly showed that the stainless steel with Ag-containing films had the largest impedance arc radius, indicating the best corrosion protection of the film, while the anodized film exhibited the worst corrosion resistance (Figure 7a). From a quantitative perspective, the Bode plot (Figure 7b) showed that the impedance modulus of the stainless steel with Ag-containing films in the low-frequency region (0.1–10 Hz) was significantly higher than the other two samples. Furthermore, the introduction of Ag caused changes in the properties of the anodized film, as compared to the anodized film without Ag (Figure 7c). As indicated by the arrow in Figure 7c, the phase angle for Ag 5V 2min sample approaching 90° reflects enhanced capacitive behavior, which suggests the formation of a dense and stable passive film, effectively insulating the surface and providing strong protection against corrosion.

The potentiodynamic polarization curves of the stainless steel with Ag-containing films in the corrosive medium are shown in Figure 7d. The ordinate of the intersection points of the anodic and cathodic branches was the corrosion potential (E_{corr}), reflecting the ease of corrosion reactions in the samples. A higher E_{corr} indicates lower susceptibility to corrosion [34]. The stainless steel sample deposited for 2 min had the highest self-corrosion potential E_{corr} (−0.051 V vs. SCE) in the corrosive medium, while the E_{corr} of untreated and solely anodized stainless steel was −0.101 V and −0.169 V, respectively. This indicates that the stainless steel samples deposited for 2 min through electrochemical deposition had the lowest propensity for spontaneous corrosion reactions, thus demonstrating superior corrosion resistance.

To comprehensively evaluate its corrosion resistance, the self-corrosion current density (I_{corr}) was determined by fitting Tafel plots (Table S4). A lower I_{corr} indicates greater stability of the sample in the corrosive environment. After anodizing, the I_{corr} value for stainless steel increased, whereas deposition of Ag resulted in a significant decrease in I_{corr}, indicating that Ag deposition enhanced the corrosion resistance of the anodized stainless steel surface. These results collectively suggested that anodization reduced the corrosion resistance of stainless steel, while electrochemical deposition of Ag significantly enhanced its corrosion resistance.

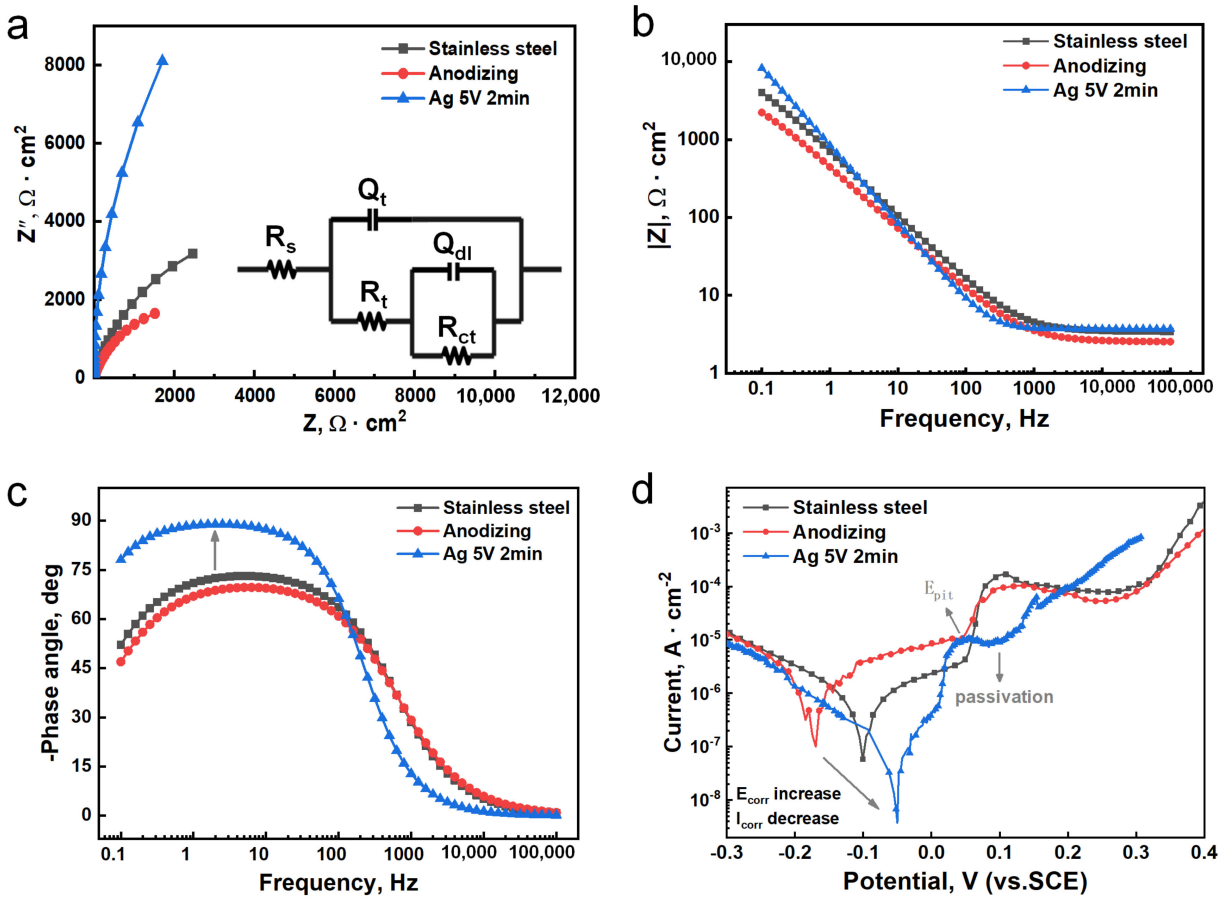

Figure 7. AC impedance spectrum of antibacterial stainless steel at different deposition times. (**a**) Nyquist; (**b**) Bode |Z|; (**c**) Bode-Phase; (**d**) polarization curves.

3.4. Antibacterial Properties and Biocompatibility of the Stainless Steel

The antibacterial properties of the new stainless steel were further studied. The results showed that the stainless steel with the Ag-containing antibacterial layer exhibited excellent antibacterial effects (Figure 8). In comparison with the specimens prepared at 3 V-2 min, 7 V-2 min, and 10 V-2 min, the stainless steel with the Ag-containing antibacterial film prepared at 5 V-2 min demonstrated the best antibacterial performance, with an antibacterial rate exceeding 99.9% against *E. coli* and 99.8% against *S. aureus* (Figure 8b,c). This aligns with the observed surface microstructure of the Ag-containing antibacterial film, which displayed corrosion.

The previous results showed that the Ag element in the antibacterial film existed in the form of metallic Ag and AgO after deposition (Figure 6), with AgO having a strong reduction potential. Based on the current antibacterial mechanisms of catalytic reaction, it was speculated that silver oxide (AgO) can activate oxygen in air and water, generating reactive oxygen species (O^{2-}) and hydroxyl radicals (-OH). O^{2-} exhibited strong oxidation-reduction capability, while -OH was more chemically reactive (Figure 8d). After being entered into bacterial cells, it can combine with the thiol groups in dehydrogenases, hindering bacterial energy metabolism and placing them in a suppressed state, thereby impeding bacterial proliferation and leading to bacterial death.

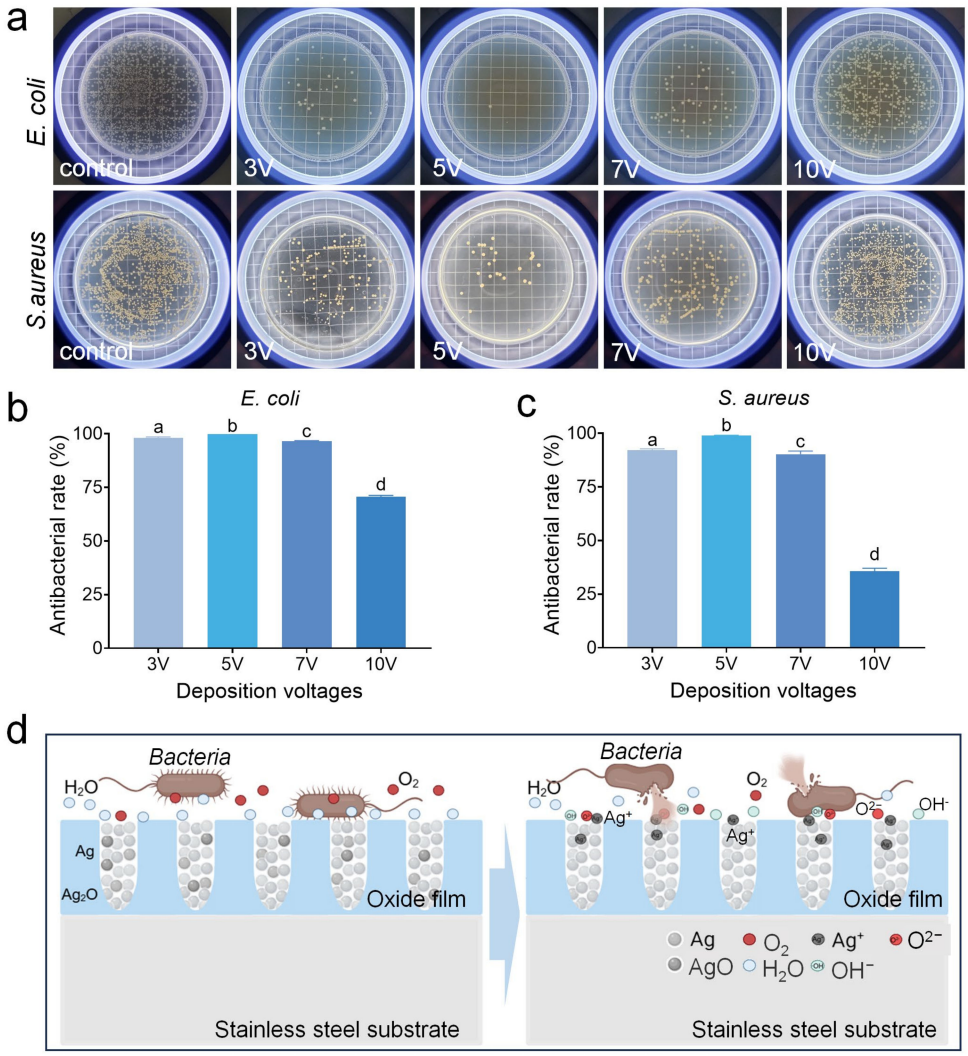

Figure 8. The antibacterial properties of antibacterial stainless steel under different processes. (**a**) Typical colony counting pictures against *E. coli* and *S. aureus*. (**b**) Antibacterial rate against *E. coli*. (**c**) Antibacterial rate against *S. aureus*. Different letters indicate significant differences between groups. (**d**) Schematic diagram of antibacterial film killing bacteria on the surface of stainless steel.

The staining of live and dead cells of the new antibacterial stainless steel (NASS) showed that the control group exhibited normal cell development, whereas the positive control DMSO group showed extensive cell death with only a few cells surviving (Figure 9). Interestingly, the new antibacterial stainless steel extracts prepared at 5 V-2 min were co-cultured with NADH cells, the new antibacterial stainless steel extracts prepared at 5 V-2 min were co-cultured with NHDF cells, and the cells not only developed normally, but also showed a significant decrease in dead cells, with a noticeable increase in cell density compared to the control group (Figure 9a). It is noteworthy that the performance of the 100% NASS group exceeded that of the 50% NASS group. Furthermore, MTT assay results further confirmed that both the 50% NASS and 100% NASS groups exhibited higher cell viability than the control group, with the cell viability even surpassing 100% (Figure 9b). These results collectively demonstrated the excellent biocompatibility of the new antibacterial stainless steel, suggesting promising applications in the medical device field.

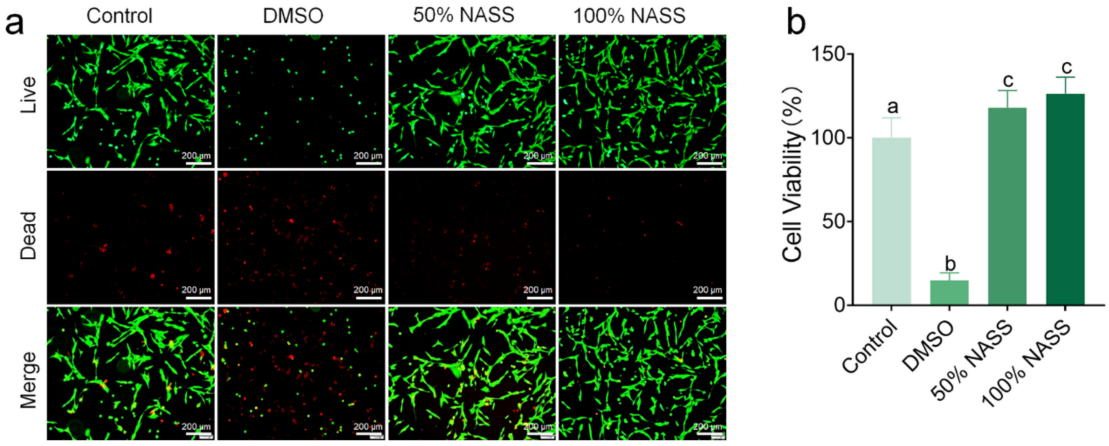

Figure 9. The new antibacterial stainless steel exhibited excellent biocompatibility. (**a**) Live/dead staining of cell morphology after co-culture with the stainless steel extract for 24 h. Live cells were stained as green, and dead cells were stained as red. (**b**) MTT assay used to measure the growth rate of NHDF cells. Control: negative control; DMSO: positive control; NASS: New Antibacterial Stainless Steel. n = 5, different letters denote significant differences between the groups.

4. Conclusions

In conclusion, this study utilized 304 stainless steels as the substrate and selected a more environmentally friendly system of phosphoric acid-ethylene glycol electrolytes. Through optimized processing techniques of anodization and electrodeposition, a low-cost antibacterial stainless steel with significantly improved antibacterial and corrosion-resistant properties was prepared. Ag-containing film improved the E_{corr} and decreased the I_{corr} of the stainless steel substrate, and exhibited a higher impedance modulus, revealing enhanced corrosion resistance. Future work will include experiments in different media with varying bacterial concentrations to further evaluate the long-term corrosion resistance and antibacterial properties of the materials. Additionally, it demonstrated excellent biocompatibility, making it a potential candidate for medical applications in the future.

Supplementary Materials: The following supporting information can be downloaded at: https://www.mdpi.com/article/10.3390/jfb16010019/s1. Table S1: Element content of different oxide layers on stainless steel anodized film. Table S2: Weight of stainless steel before and after rubbing. Table S3: Equivalent circuit component parameters of AC impedance spectrum. Table S4: Fitting results of antibacterial stainless steel polarization curves under different deposition times.

Author Contributions: Conceptualization, Y.S., C.C. and J.B.; Data curation, Y.S., Y.J. and Y.W. (Yongfeng Wang); Formal analysis, Y.S., Y.J., Y.W. (Yongfeng Wang), Q.D. and F.X.; Funding acquisition, F.X. and J.B.; Investigation, Y.S. and Y.J.; Validation Y.W. (Yan Wang); Methodology, Y.S.; Project administration, J.B.; Resources, C.C.; Supervision, C.C. and J.B.; Writing—original draft, Y.S., Y.J. and Y.W. (Yongfeng Wang); Writing—review and editing, Y.S., Y.W. (Yongfeng Wang), Q.D., C.W., Y.W. (Yan Wang), C.C. and J.B. All authors have read and agreed to the published version of the manuscript.

Funding: This research was funded by the Science and Technology Project of Jiangsu Province (BE2023671), Suzhou Science and Technology Project (SJC2023005), Nanjing Science and Technology Project (202309015).

Institutional Review Board Statement: Not applicable.

Informed Consent Statement: Not applicable.

Data Availability Statement: Dataset available on request from the authors.

Acknowledgments: We are very grateful for the help provided by Guanzhen Li, Dongfang Chen, Kun Qian, and Jiaqi Zhao in writing the manuscript.

Conflicts of Interest: The authors declare no conflicts interests.

References

1. Erfani, A.; Pirouzifard, M.K.; Pirsa, S. Photochromic biodegradable film based on polyvinyl alcohol modified with silver chloride nanoparticles and spirulina; investigation of physicochemical, antimicrobial and optical properties. *Food Chem.* **2023**, *411*, 135459. [CrossRef]
2. Kaplan, M.A.; Gorbenko, A.D.; Ivannikov, A.Y.; Kartabaeva, B.B.; Konushkin, S.V.; Demin, K.Y.; Baikin, A.S.; Sergienko, K.V.; Nasakina, E.O.; Bannykh, I.O.; et al. Investigation of Antibacterial Properties of Corrosion-Resistant 316L Steel Alloyed with 0.2 wt.% and 0.5 wt.% Ag. *Materials* **2022**, *16*, 319. [CrossRef] [PubMed]
3. Li, J.; Guo, S.; Zhao, G.; Li, H.; Ma, L.; Li, Y. Research on Stamping Formability and Microstructure of Copper-Containing Antibacterial Stainless Steel. *J. Mater. Eng. Perform.* **2023**, *32*, 10265–10274. [CrossRef]
4. Zhang, Y.M.; Qin, K.; Du, Q.P.; Huang, J.Q.; Shuai, G.G.; Jie, X.H. Study on Antibacterial Properties of SUSXM7 Cu- Bearing Austenitic Stainless Steel. *Adv. Mater. Res.* **2013**, *652–654*, 997–1001. [CrossRef]
5. Di Cerbo, A.; Mescola, A.; Rosace, G.; Stocchi, R.; Rossi, G.; Alessandrini, A.; Preziuso, S.; Scarano, A.; Rea, S.; Loschi, A.R.; et al. Antibacterial Effect of Stainless Steel Surfaces Treated with a Nanotechnological Coating Approved for Food Contact. *Microorganisms* **2021**, *9*, 248. [CrossRef]
6. Qing, Y.; Li, K.; Li, D.; Qin, Y. Antibacterial effects of silver incorporated zeolite coatings on 3D printed porous stainless steels. *Mater. Sci. Eng. C* **2020**, *108*, 110430. [CrossRef]
7. Qin, H.; Cao, H.; Zhao, Y.; Jin, G.; Cheng, M.; Wang, J.; Jiang, Y.; An, Z.; Zhang, X.; Liu, X. Antimicrobial and Osteogenic Properties of Silver-Ion-Implanted Stainless Steel. *ACS Appl. Mater. Interfaces* **2015**, *7*, 10785–10794. [CrossRef]
8. Ni, H.-W.; Zhang, H.-S.; Chen, R.-S.; Zhan, W.-T.; Huo, K.-F.; Zuo, Z.-Y. Antibacterial properties and corrosion resistance of AISI 420 stainless steels implanted by silver and copper ions. *Int. J. Miner. Met. Mater.* **2012**, *19*, 322–327. [CrossRef]
9. Elangovan, T.; Balasankar, A.; Arokiyaraj, S.; Rajagopalan, R.; George, R.P.; Oh, T.H.; Kuppusami, P.; Ramasundaram, S. Highly Durable Antimicrobial Tantalum Nitride/Copper Coatings on Stainless Steel Deposited by Pulsed Magnetron Sputtering. *Micromachines* **2022**, *13*, 1411. [CrossRef] [PubMed]
10. Wang, L.; Zhang, F.; Fong, A.; Lai, K.; Shum, P.; Zhou, Z.; Gao, Z.; Fu, T. Effects of silver segregation on sputter deposited antibacterial silver-containing diamond-like carbon films. *Thin Solid Film.* **2018**, *650*, 58–64. [CrossRef]
11. Asoh, H.; Nakatani, M.; Ono, S. Fabrication of thick nanoporous oxide films on stainless steel via DC anodization and subsequent biofunctionalization. *Surf. Coat. Technol.* **2016**, *307*, 441–451. [CrossRef]
12. Isa, N.N.C.; Mohd, Y.; Mohamad, S.A.S.; Zaki, M.H.M. Antibacterial activity of copper coating electrodeposited on 304 stainless steel substrate. In Proceedings of the Advanced Materials for Sustainability and Growth: Proceedings of The 3rd Advanced Materials Conference 2016 (3rd AMC 2016), Langkawi, Malaysia, 28–29 November 2016; Volume 1901, p. 020009.
13. Zanca, C.; Carbone, S.; Patella, B.; Lopresti, F.; Aiello, G.; Brucato, V.; Pavia, F.C.; La Carrubba, V.; Inguanta, R. Composite Coatings of Chitosan and Silver Nanoparticles Obtained by Galvanic Deposition for Orthopedic Implants. *Polymers* **2022**, *14*, 3915. [CrossRef] [PubMed]
14. Liu, S.; Tian, J.; Zhang, W. Fabrication and application of nanoporous anodic aluminum oxide: A review. *Nanotechnology* **2021**, *32*, 222001. [CrossRef]
15. Hassan, A.; Ali, G.; Park, Y.J.; Hussain, A.; Cho, S.O. Formation of a self-organized nanoporous structure with open-top morphology on 304L austenitic stainless steel. *Nanotechnology* **2020**, *31*, 315603. [CrossRef] [PubMed]
16. Lee, J.; Wooh, S.; Choi, C.-H. Fluorocarbon lubricant impregnated nanoporous oxide for omnicorrosion-resistant stainless steel. *J. Colloid Interface Sci.* **2020**, *558*, 301–309. [CrossRef] [PubMed]
17. Lilja, M.; Sörensen, J.H.; Brohede, U.; Åstrand, M.; Procter, P.; Arnoldi, J.; Steckel, H.; Strømme, M. Drug loading and release of Tobramycin from hydroxyapatite coated fixation pins. *J. Mater. Sci. Mater. Med.* **2013**, *24*, 2265–2274. [CrossRef] [PubMed]
18. Mohanty, U.S.; Tripathy, B.C.; Singh, P.; Keshavarz, A.; Iglauer, S. Roles of organic and inorganic additives on the surface quality, morphology, and polarization behavior during nickel electrodeposition from various baths: A review. *J. Appl. Electrochem.* **2019**, *49*, 847–870. [CrossRef]
19. *ISO 22196-2011*; Measurement of Antibacterial Activity on Plastics and Other Non-Porous Surfaces. International Organization for Standardization (ISO): Geneva, Switzerland, 2011; ISO/TC 61/SC 6.
20. Kuzin, A.V.; Gorichev, I.G.; Lainer, Y.A. Stimulating effect of phosphate ions on the dissolution kinetics of iron oxides in an acidic medium. *Russ. Metall.* **2013**, *2013*, 652–657. [CrossRef]
21. Erdogan, Y.K.; Ercan, B. Anodized Nanostructured 316L Stainless Steel Enhances Osteoblast Functions and Exhibits Anti-Fouling Properties. *ACS Biomater. Sci. Eng.* **2023**, *9*, 693–704. [CrossRef] [PubMed]

22. Zhao, J.; Zhai, Z.; Sun, D.; Yang, C.; Zhang, X.; Huang, N.; Jiang, X.; Yang, K. Antibacterial durability and biocompatibility of antibacterial-passivated 316L stainless steel in simulated physiological environment. *Mater. Sci. Eng. C* **2019**, *100*, 396–410. [CrossRef]
23. Mazinanian, N.; Hedberg, Y.S. Metal Release Mechanisms for Passive Stainless Steel in Citric Acid at Weakly Acidic pH. *J. Electrochem. Soc.* **2016**, *163*, C686–C693. [CrossRef]
24. Schnippering, M.; Carrara, M.; Foelske, A.; Kötz, R.; Fermín, D.J. Electronic properties of Ag nanoparticle arrays. A Kelvin probe and high resolution XPS study. *Phys. Chem. Chem. Phys.* **2007**, *9*, 725–730. [CrossRef]
25. Zhang, B.; Ni, H.; Chen, R.; Zhan, W.; Zhang, C.; Lei, R.; Zha, Y. A two-step anodic method to fabricate self-organised nanopore arrays on stainless steel. *Appl. Surf. Sci.* **2015**, *351*, 1161–1168. [CrossRef]
26. Hakiki, N.E. Influence of surface roughness on the semiconducting properties of oxide films formed on 304 stainless steel. *J. Appl. Electrochem.* **2008**, *38*, 679–687. [CrossRef]
27. Sharma, P.; Singh, S.P.; Parakh, S.K.; Tong, Y.W. Health hazards of hexavalent chromium (Cr (VI)) and its microbial reduction. *Bioengineered* **2022**, *13*, 4923–4938. [CrossRef] [PubMed]
28. Liang, J.; Huang, X.; Yan, J.; Li, Y.; Zhao, Z.; Liu, Y.; Ye, J.; Wei, Y. A review of the formation of Cr(VI) via Cr(III) oxidation in soils and groundwater. *Sci. Total. Environ.* **2021**, *774*, 145762. [CrossRef]
29. Moffat, I.; Martinova, N.; Seidel, C.; Thompson, C.M. Hexavalent chromium in drinking water. *J. Am. Water Works Assoc.* **2018**, *110*, E22–E35. [CrossRef]
30. Sivapirakasam, S.P.; Mohan, S.; Kumar, M.C.S.; Paul, A.T.; Surianarayanan, M. Control of exposure to hexavalent chromium concentration in shielded metal arc welding fumes by nano-coating of electrodes. *Int. J. Occup. Environ. Health* **2017**, *23*, 128–142. [CrossRef] [PubMed]
31. Henriksen, C.; Bügel, S. Chromium—A scoping review for Nordic Nutrition Recommendations 2023. *Food Nutr. Res.* **2023**, *67*, 10325. [CrossRef]
32. Hassouna, S.S.; Sheta, E.; Zaki, I.; Harby, S.A.; Allam, E.A. Trivalent chromium supplementation ameliorates adjuvant induced rheumatoid arthritis through up-regulation of FOXP3 and decrease in synovial Cathepsin G expression. *Inflammopharmacology* **2022**, *30*, 2181–2195. [CrossRef] [PubMed]
33. DesMarias, T.L.; Costa, M. Mechanisms of Chromium-Induced Toxicity. *Curr. Opin. Toxicol* **2019**, *14*, 1–7. [CrossRef]
34. Fabbricino, M.; Korshin, G.V. Changes of the corrosion potential of iron in stagnation and flow conditions and their relationship with metal release. *Water Res.* **2014**, *62*, 136–146. [CrossRef]

Journal of
Functional Biomaterials

MDPI

Article

In Vitro Bacterial Growth on Titanium Surfaces Treated with Nanosized Hydroxyapatite

Maria Holmström [1,*], Sonia Esko [2], Karin Danielsson [1] and Per Kjellin [1]

[1] Promimic AB, Entreprenörsstråket 10, 431 53 Mölndal, Sweden; per.kjellin@promimic.com (P.K.)
[2] Department of Applied Chemistry, Chalmers University of Technology, 412 96 Göteborg, Sweden
* Correspondence: maria.holmstrom@promimic.com

Abstract: Bacterial growth on implant surfaces poses a significant obstacle to the long-term success of dental and orthopedic implants. There is a need for implants that promote osseointegration while at the same time decreasing or preventing bacterial growth. In this study, the existing methods for the measurement of bacterial biofilms were adapted so that they were suitable for measuring the bacterial growth on implant surfaces. Two different strains of bacteria, *Pseudomonas aeruginosa* and *Staphylococcus epidermidis*, were used, and the in vitro effect of bacterial growth on titanium surfaces coated with an ultrathin (20–40 nm thick) layer of nanosized hydroxyapatite (nHA) was investigated. After 2 h of biofilm growth, there was a 33% reduction in both *S. epidermidis* and *P. aeruginosa* bacteria on nHA compared to Ti. For a more mature 24 h biofilm, there was a 46% reduction in *S. epidermidis* and a 43% reduction in *P. aeruginosa* on nHA compared to Ti. This shows that coating nHA onto implants could be of benefit in reducing implant-related infections.

Keywords: nanosized hydroxyapatite; implant; surface coating; antibacterial; biofilm; *S. epidermidis*; *P. aeruginosa*

1. Introduction

The use of dental and orthopedic implants is steadily increasing. A highly undesirable phenomenon in implant surgery is infection at the implantation site. Surgical site infections are troublesome, with increased patient morbidity and mortality, longer hospital stays and increased healthcare costs. The treatment is even more demanding in relation to implants and can, in the worst case, lead to implant rejection. Infections may be classified as either early-onset or late-onset, but the border between these phases varies in the literature, with anywhere from 30 days to 2 years post-surgery being classified as a late infection [1–7].

Bacterial strains that are known to cause infections in orthopedic implant surgery include coagulase-negative staphylococci such as *S. epidermidis*, *S. aureus*, streptococci, *P. aeruginosa*, *E. coli*, enterococci, *Cutibacterium* species and *Enterobacter* species [4–6,8,9]. Early infections often arise due to direct inoculation during surgery, whereas late-onset infections occur via hematogenous spread [6,8]. Generally, early infections are caused by more virulent bacterial strains, whereas late infections are due to less virulent strains [7,8].

The risk of human staphylococcal infection has been shown to be more than 10,000-fold increased in the presence of a foreign body [10], and in a guinea pig infection model, an inoculum of *S. aureus* of as little as 100 Colony Forming Units (CFUs) in the presence of subcutaneous implants was found to cause an infection, whereas 10^8 CFUs could be cleared by the immune system without signs of infection in the absence of a foreign body [11]. A lowered bacterial number causing infections in the presence of implants has also been

observed in other animal infection models, as well as in patients [12–15]. This may be due to several factors, in addition to the immune response and frustrated phagocytosis associated with implants. Biofilm bacteria can alter the immune response to evade elimination using quorum-sensing molecules [16]. Staphylococcal biofilms have been shown to drive the immune response into an anti-inflammatory and fibrotic response and alter both neutrophil and macrophage function [16–19]. The immune response also alters depending on the implant topography and the bacterial species present [20].

Infection rates depend on patient factors, surgery procedures and hygiene routines [21], as well as the implant design [22]. Antibiotic treatment, both systemic and local, is one strategy for reducing infection rates. Another approach is to modify the implant's surface. One can distinguish between two different types of methods for combatting bacterial growth on an implant surface: bacteriostatic and bactericidal. Both approaches are commonly used together. In the bacteriostatic approach, the surface prevents the growth of bacteria. This can be achieved by creating superhydrophilicity [23] through surface topographical changes and by applying antifouling coatings, such as polymer brushes [24]. A smoother surface lowers the surface area and thereby decreases the amount of attachment points for the bacteria [25]. This method is used for external fixation pins [26] and dental abutments [22]. However, in patients, many factors influence the risk of implant infections, and significant differences between smooth, moderately rough and rough surfaces when it comes to biofilm formation and peri-implantitis are not always observed [27,28].

The bactericidal approach involves modifying the implant's surface to kill bacteria. Noble metal coatings [29,30], coatings containing antibiotics [31] and hydrogels [32] have been successfully used to induce a bactericidal effect, as has the use of quaternary ammonium compounds [33] and nanopatterning of surfaces, such as creating nano-pillars and nano-pores [34].

Apart from infection, insufficient bone-to-implant integration is another factor that increases the failure rate of dental and orthopedic implants, and to improve the integration, the properties of the implant surface are of vital importance. Factors such as micro-roughness, nano-roughness, chemical composition and physical and mechanical factors all affect osseointegration [35]. However, the factors that are known to affect osseointegration are often similar to the properties that affect bacterial growth, especially regarding surface texturing techniques. Making an implant surface rougher through blasting and/or acid etching is known to promote osseointegration, but it also provides a great substrate for bacterial growth. Conversely, a polished smooth surface that displays a low bacterial growth rate often has poor osseointegration. Ideally, an implant surface should display fast osseointegration and also have antibacterial properties, and the challenge is naturally to combine these properties.

Hydroxyapatite (HA) coatings are well known to improve implant osseointegration [36,37]. Thick (>50 μm) plasma-sprayed HA was introduced on orthopedic implants in the 1980s, with a significant effect on implant integration. In later years, some concerns were raised about the clinical problems with thick HA coatings, such as delamination and wear [38,39], and it was suggested that thinner coatings may be better in stimulating osseointegration without these risks. Implant treatment using ultrathin coatings of nHA is known to have a significant effect on osseointegration [40–42], even in compromised bone [43,44]. However, the effect of bacterial growth on nHA is not well studied.

There are many different ways to study bacterial biofilm growth, including static and flow cell models, culturing and microscopy studies. For the sake of simplicity, surface-coated discs are often coated on one side and placed in well plates or flasks for biofilm growth; then, biofilm removal is performed using ultrasound treatment. However, for this

procedure, the question arises of what is growing on the non-coated part of the disc. This may pose a problem, and coating both sides of the discs is not always a viable option.

The aim of the current study was, therefore, to refine the existing methods to investigate bacterial growth on surfaces and to use this method to investigate the bacterial growth on Ti substrates, with or without a coating of ultrathin (20–40 nm) nHA. The null hypothesis was that there was no difference between Ti and nHA-coated Ti. For this purpose, a drop method was used, placing a liquid drop containing bacteria onto discs for growth. In addition, a well plate was created to press onto the Ti and nHA-modified Ti disc, only to expose the top surfaces to bacteria. A bottom plate was placed below the Ti discs, and everything was held together by screws. A bacterial count of 1×10^6 or 50,000 CFU/mL of *S. epidermidis* or *P. aeruginosa* was used and allowed to form 2 or 24 h biofilms before biofilm removal and culturing.

2. Materials and Methods

2.1. Surface Preparation

Two types of Ti discs were used in this study: 1 cm Ø discs of Ti grade 4 and 2 cm Ø discs of Ti grade 2 (Kullbergs Mikroteknik AB, Lycke, Sweden). The larger diameter was chosen to improve the statistics for the 24 h experiments; Ti grade 2 and grade 4 both consist of Ti, with no difference in biological response, but grade 4 has a higher mechanical strength. Both grades are frequently used for implants. All discs were ground using P400 grit sandpaper (Biltema, Partille, Sweden), ultrasonically cleaned for 10 min per step using isopropanol (Fisher Scientific, Hampton, NH, USA, 99%), 1 M HNO_3 (Scharlau, Barcelona, Spain, 65%), H_2O type 1 and isopropanol. The 2 cm discs were also thermally cleaned for 5 min at 450 °C (Nabertherm, Lilienthal, Germany) to obtain a more homogenous nHA layer. This procedure was performed for both the control discs and the discs to be coated with nHA. Then, the discs were either used as Ti controls or surface treated with nHA. In short, the nHA layer was applied through spin coating; an in-house synthesized coating liquid containing nHA (40–80 µL) was applied to the surfaces, which were then placed on a spin coater using a spin speed of 2500 rpm for 3 s and finally thermally treated at 450 °C. A more thorough description of the coating procedure and coating liquid is provided in reference [42].

2.2. Surface Characterization

Scanning electron microscopy (SEM) and energy dispersive X-ray analysis (EDX) were performed using a Zeiss FEG-SEM Sigma (Oberkochen, Germany) with Gemini optics and equipped with EDX. Three discs were studied, and 3 EDX spectra were obtained for each disc, giving a total of 9 spectra for each type of disc.

As presented below, 24 h bacterial biofilms were also studied using SEM. Before SEM analysis, the biofilms were left overnight in 4% buffered paraformaldehyde (VWR, Radnor, PA, USA) and then rinsed 3 times in phosphate-buffered saline (PBS) (Sigma Aldrich, St. Louis, MO, USA, 0.01 M) before being subjected to a drying gradient of 50, 60, 70, 80, 90 and 100% ethanol (Fisher Scientific, Hampton, NH, USA, $\geq$99%) for 10 min per step. The samples were then left in 50% hexamethyldisilazane (Thermo Fisher, Waltham, MA, USA, 98%) in ethanol for 20 min and finally left in 98% hexamethyldisilazane and allowed to dry in ambient air. Before SEM analysis, the samples were gold-sputtered for 60 s, 10 mA (Emitech K550X, Quorum, Laughton, UK), yielding a gold layer of 3 nm according to the manufacturer.

To investigate the nHA layer thickness, an extremely smooth titanium-deposited (PVD method) silicon wafer was coated with the nHA surface and studied in a transmission electron microscope (TEM, FEI Tecnai T20, FEI, Hillsboro, OR, USA) in bright field mode at

200 kV acceleration voltage. For the nHA sample to be analyzed using TEM, an electron-transparent thin foil from the sample was prepared using a combined focused ion beam and scanning electron microscope workstation (FEI Versa 3D). Over the region of interest, a 3 × 12 µm Platinum layer of 2 µm thickness was deposited first by using electron beam deposition (2 kV) and then ion (Ga^+) beam deposition (50 pA, 30 kV). Platinum deposition occurred by scanning the electron or ion beam over the area of interest so that secondary electrons interacted with and decomposed an organometallic precursor gas that was injected into the chamber. Two trenches were subsequently milled out (5 nA, 30 kV) on both sides of the Pt layer. The sample was then tilted, and the foil was milled loose on three sides (3 nA, 30 kV). A sharp (radius < 2 µm) tungsten micromanipulator needle (Omniprobe, Oxford Instruments, Abingdon, UK) was inserted into the chamber and attached to the sample foil. The remaining side connecting the foil with the substrate was milled off. The foil was then attached to a copper TEM half-grid by means of Platinum deposition. The foil was then thinned to a thickness of less than 100 nm using decreasing ion currents and acceleration voltages (from 0.5 nA, 30 kV down to 7.7 pA, 5 kV).

To evaluate the surface roughness, white light coherence scanning interferometry was performed according to ISO 25178-604 [45] using a MicroXAM (ADE Phase Shift Technology, Tuscon, AZ, USA) with a magnification of 50×. Two discs from each substrate were used, and for each disc, three areas were measured.

Static contact angle measurements were performed to investigate the wettability of the samples. First, 5 µL drops of type 1 water [46] (Elga LabWater, High Wycombe, UK, 18.2 MΩ-cm) were dropped onto the surfaces, either the Ti controls or nHA-coated Ti. Photographs were obtained, and contact angles were determined manually using software (ImageJ, version 1.54 g Java 1.8.0_345 (64 bit)). Three drops were tested for each substrate, with one drop per disc.

2.3. X-Ray Diffraction Analysis

A powder produced directly from the coating liquid was analyzed using powder XRD. A Bruker D8 Discover was used (Billerica, MA, USA). The XRD analysis was performed using Cu-K_α radiation (λ = 1.5418 Å) with a 2θ between 20° and 60° (step size 0.020°) for a total analysis time of 28 min. As a hydroxyapatite reference pattern, COD 96-900-2214 of the Crystallographic Open Database was used.

2.4. Calcium Assay

A colorimetric calcium assay was performed to investigate the amount of calcium ions on the nHA-coated surfaces, which, in turn, can be used to calculate the approximate thickness of the nHA coating. First, 12 mm nHA-coated discs were dipped in 5 mL 0.01 M HNO_3 (Scharlau, Barcelona, Spain, 65%) for 5 min; this procedure dissolved all nHA that was present on the disc. Then, 5 mL of a solution consisting of 60 µM ArsenazoIII (Sigma Aldrich, St. Louis, MO, USA) in 0.1 M Tris solution (Fisher Scientific, Hampton, NH, USA) was added; this step increased the pH of the solution. The calcium–dye complex turned purple-red, and its absorbance was immediately measured at 650 nm (Jenway 7315 Spectrophotometer, Cole-Parmer, Vernon Hills, IL, USA) and compared to a standard curve.

2.5. Bacterial Strains and Culture

S. epidermidis CCUG 39,508 and *P. aeruginosa* CCUG 56,489 were grown on Brain heart infusion (BHI) agar (Fisher Scientific, Hampton, NH, USA) at 37 °C and then stored in a fridge at 4 °C. These species were chosen as they are common Gram-positive and Gram-negative species causing implant-associated infections. Colonies were then transferred to BHI medium, cultured overnight at 37 °C to stationary phase, and used for 2 h biofilm

experiments. For 24 h biofilms, overnight samples were immediately used if in mid-logarithmic phase; otherwise, they were transferred to fresh BHI and re-cultured into mid-exponential growth phase, corresponding to Abs_{600nm} between 0.5 and 0.7 (Jenway 7315 Spectrophotometer). The time points 2 and 24 h were chosen in order to obtain one early and one mature biofilm.

2.6. Biofilm Assay

The samples for 2 h biofilms were diluted to 1 $\times 10^6$ bacteria/mL in BHI, and 80 µL (80,000 bacteria) was added as a drop onto the top of 1 cm Ø discs and cultured for 2 h at 37 °C in air before biofilm removal. The drop method enabled biofilm growth on only the coated surface, but it had limitations on how long culturing was possible due to drying effects.

For the 24 h biofilms, 9-well metal plates were created to culture biofilms on one side of the discs only. The well plates consisted of a top part with holes to create the wells, into which 2 cm Ti discs were fitted with a silicone O-ring. Below the discs, a silicone sheet was fitted to maintain the liquid inside the wells, supported by a Teflon plate and a solid metal bottom plate, all of which were held together by screws; see Figure 1. For these tests, 2 cm discs were used instead of 1 cm to increase biofilm surface areas and statistical accuracy.

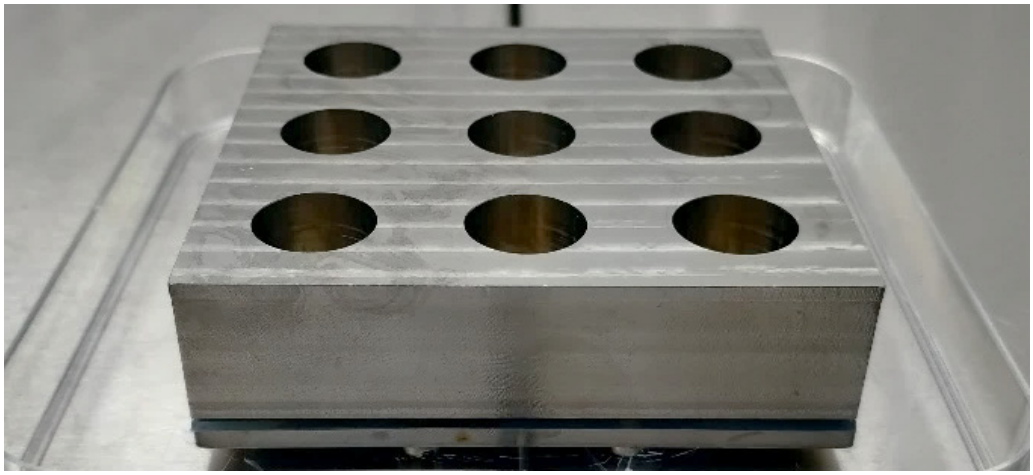

Figure 1. Assembled 9-well plate.

Log phase bacteria for 24 h studies were ultrasonically homogenized for 10 s at 20% power (Bandelin Sonopuls, Probe MS72, Bandelin electronic GmBH & Co., Berlin, Germany) and diluted to 50,000 bacteria/mL in BHI using a Bürker Türk counting chamber (Brand GmbH, Wertheim, Germany) and an optical microscope (Zeiss Axioskop 40, Oberkochen, Germany). A total of 1 mL bacterial solution was added to each disc and cultured for 24 h at 37 °C in air.

After growth, the discs were rinsed in 1 mL PBS (0.01 M, Sigma Aldrich, St. Louis, MO, USA). The 1 cm discs were transferred to 1 mL fresh PBS, and the 2 cm discs were transferred to 2 mL PBS. For 24 h *P. aeruginosa*, the discs were pipetted 5 times to remove visible biofilm from the discs. Then, all the discs were ultrasonicated for 5 min (Elmasonic S 80 H, 37 kHz, Elma Schmidbauer GmbH, Singen, Germany) for biofilm removal. Due to the presence of visible bacterial aggregates, 24 h *P. aeruginosa* solutions were then ultrasonically homogenized for 10 s at 20% power (Bandelin Sonopuls, Probe MS72, Bandelin electronic GmBH & Co., Berlin, Germany) to dislodge the agglomerates. The bacterial solutions were then serially diluted in PBS, and 7 $\times$ 10 µL drops per dilution were cultured on BHI agar plates at 37 °C in air overnight, according to the drop plate method. Seventeen different 2 h triplicate biofilm experiments were performed, yielding an *n*-value of 51. For the 24 h

biofilms, 8 experiments were performed in triplicates or quadruplicates, yielding an *n*-value of 30.

2.7. Confocal Microscopy

The confocal microscope used was a ZEISS LSM 980 with Airyscan 2 (Oberkochen, Germany). Samples were stained using LIVE/DEAD *Bac*Light, kit L13152 (Invitrogen, Waltham, MA, USA), with propidium iodide and Syto 9, prepared according to the manufacturer. A total of 10 µL was added to each disc and incubated in the dark at room temperature for 15 min before observation.

2.8. Statistical Analysis

A two-sided student's *t*-test for unpaired samples of unequal variance was utilized for statistical analysis. Any *p*-value below 0.05 was considered statistically significant.

3. Results

3.1. Surface Characterization

SEM images of the 1 and 2 cm discs of pure Ti and nHA-coated Ti are shown in Figures 2 and 3. At 500× magnification, both surfaces looked smooth, whereas at 40,000× magnification, the nHA-treated Ti was shown to be covered by a homogeneous layer of HA crystals. The average crystal size was estimated from SEM imaging to be 100 ± 20 nm in length and 6 ± 2 nm wide.

This crystal size was in a similar range as previous studies [42,47]. A 12 mm nHA-coated disc used for the calcium assay is seen in Figure 4, which shows the same nHA crystals and similar coverage as the other discs.

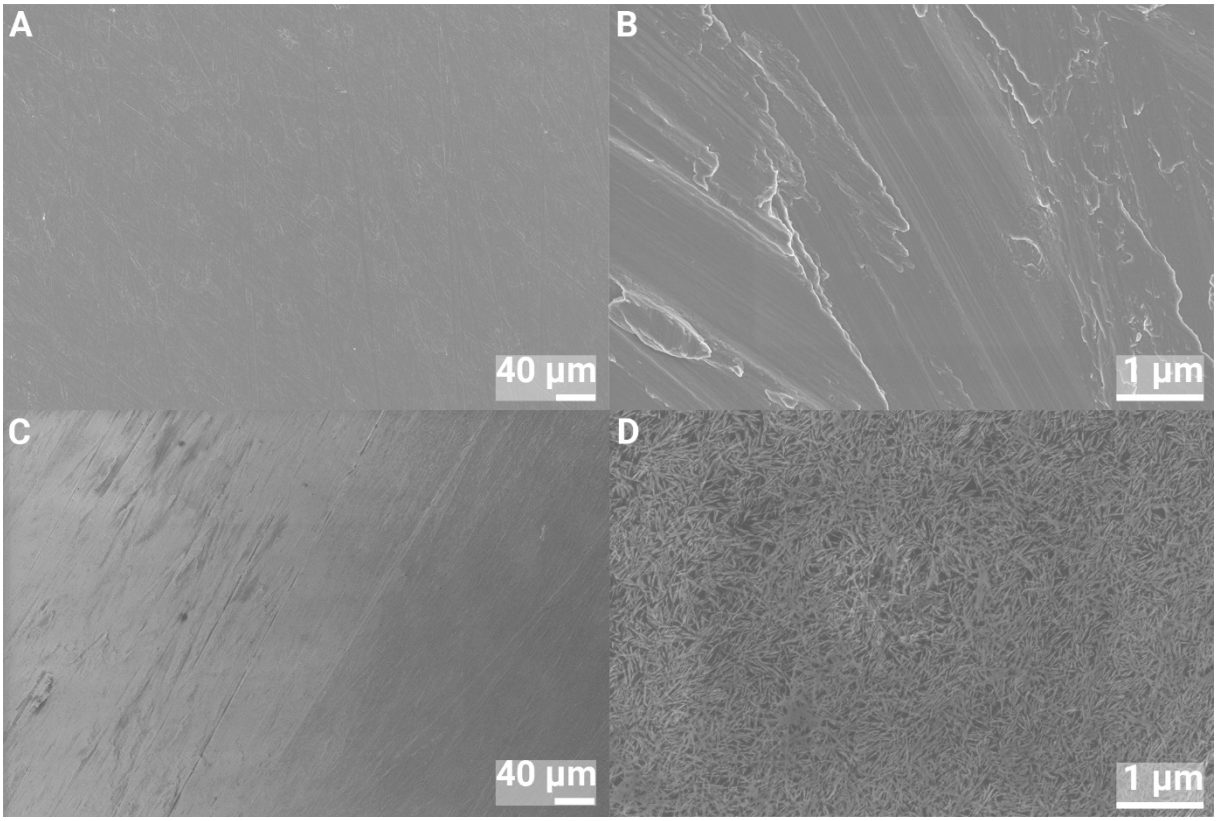

Figure 2. SEM images of 1 cm Ti discs at 500× (**left**) and 40,000× (**right**) magnification. (**A**,**B**) Ti and (**C**,**D**) nHA-coated Ti.

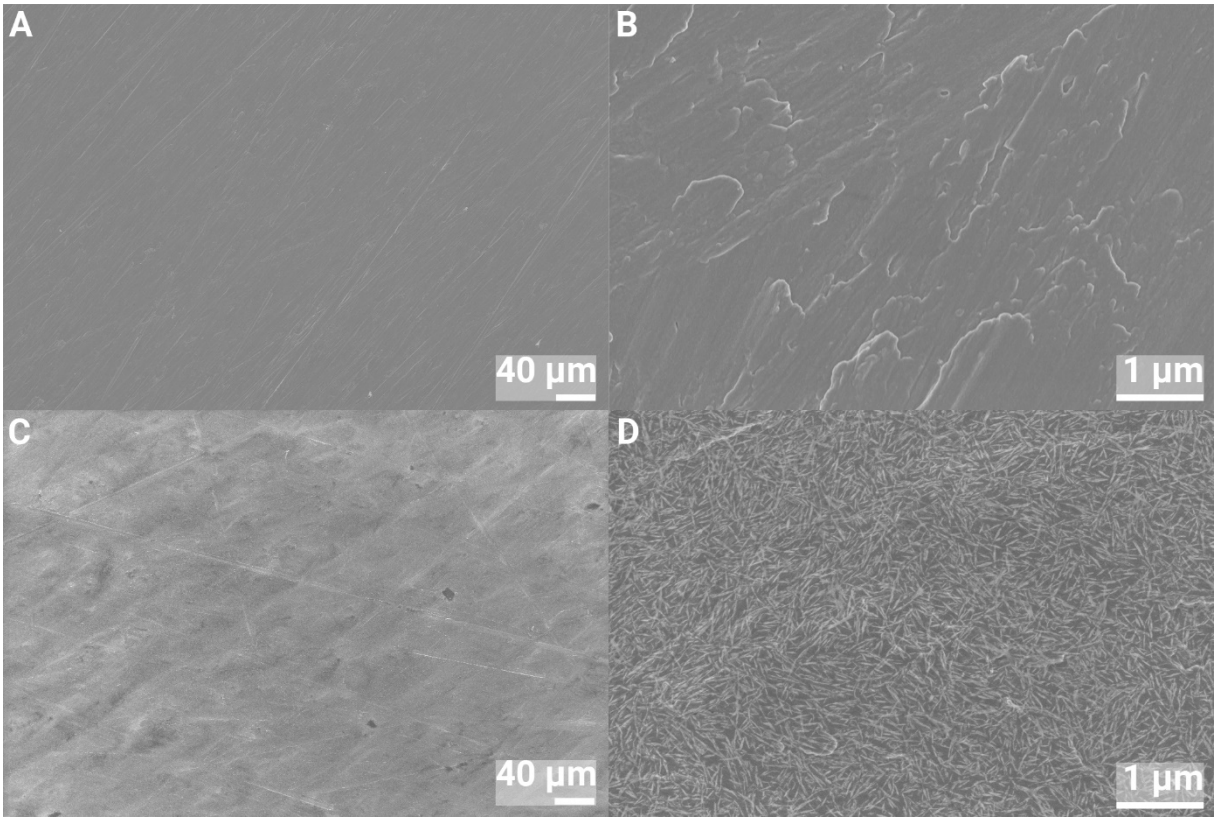

Figure 3. SEM images of 2 cm Ti discs at 500× (**left**) and 40,000× (**right**) magnification. (**A**,**B**) Ti and (**C**,**D**) nHA-coated Ti.

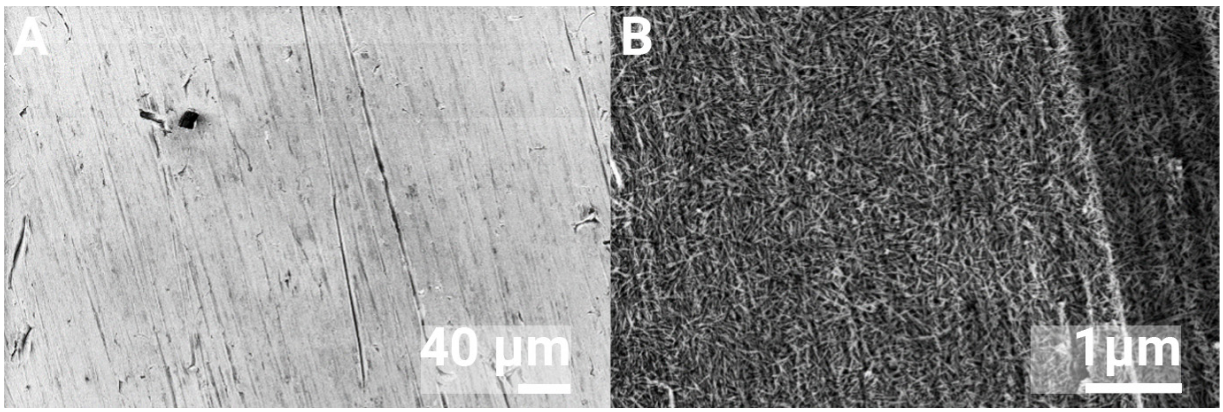

Figure 4. SEM images of the nHA coating on discs used for the Ca assay, at 500× (**A**) and 40,000× (**B**) magnification.

The EDX data in Table 1 show that the elemental composition of nHA-treated Ti grade 4 contains 0.42% calcium and 0.32% phosphorus, in addition to titanium, oxygen and carbon, whereas the grade 2 discs contained 0.25% calcium and 0.19% phosphorus. An increase in oxygen content for the heat-treated discs was also observed; this effect is most likely due to an increase in the TiO_2 layer thickness.

To confirm the presence of hydroxyapatite, an XRD analysis was performed, and the resulting diffractogram was identified as hydroxyapatite (COD 96-900-2214). The broad peaks in the diffractogram were a result of the small crystal size, as shown in Figure 5.

Table 1. EDX analysis of Ti and nHA-coated Ti of grades 2 and 4 (atomic percent).

Element	C	O	Ti	Ca	P
Ti grade 4	3.13 ± 0.23	12.90 ± 0.45	83.97 ± 0.61	-	-
nHA, Ti grade 4	2.06 ± 0.25	28.09 ± 1.09	69.11 ± 1.58	0.42 ± 0.15	0.32 ± 0.13
Ti grade 2	2.65 ± 0.13	25.61 ± 1.41	71.74 ± 1.46	-	-
nHA, Ti grade 2	1.75 ± 0.19	30.09 ± 1.25	67.72 ± 1.28	0.25 ± 0.04	0.19 ± 0.05

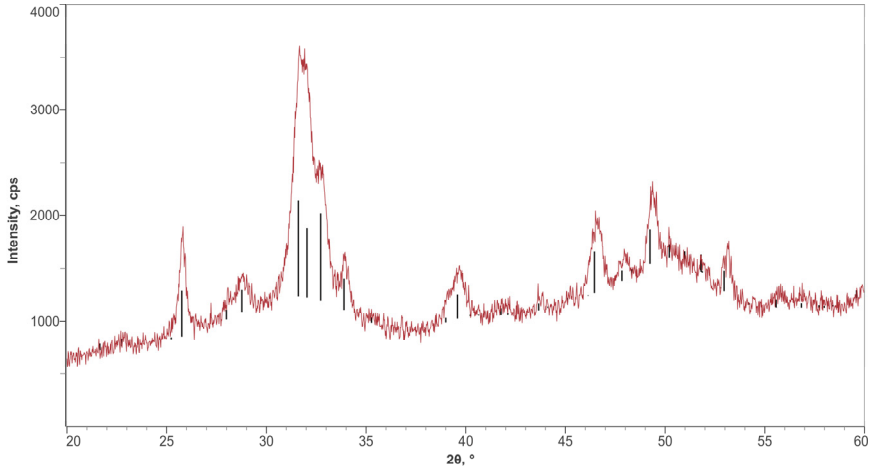

Figure 5. XRD diffractogram confirming HA in the nHA coating. Red represents the tested nHA, and black represents the reference peaks for HA.

The calcium assay was performed on eight discs, which gave an average calcium ion content of 3.2 μg/cm^2. With an HA molecular weight of 502.31 g/mol, this corresponds to 8 μg HA/cm^2. Assuming a solid layer and a density for HA of 3.15 g/cm^3, a rough estimate of the layer thickness can be calculated. An HA content of 8 μg/cm^2 then yields a thickness of 25 nm.

The Ca assay-calculated value was further investigated using TEM analysis of a cross-section of the nHA layer. From this analysis, the nHA layer was determined to be 10–20 nm, as shown in Figure 6.

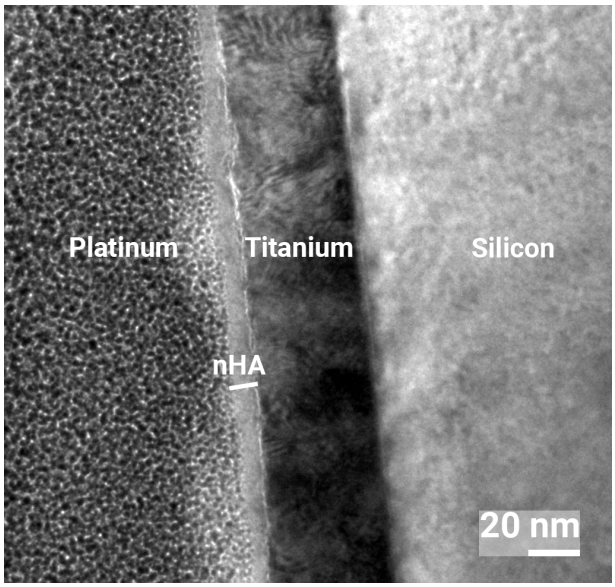

Figure 6. TEM cross-sectional image of nHA coating at 800,000× magnification showing a 10–20 nm thick nHA layer.

The values of the surface roughness measured using interferometry can be found in Table 2. All surfaces had Sa values of 0.21–0.27, which are considered as smooth implant surfaces, but Ti grade 2 was somewhat rougher than Ti grade 4 [48]. Sdr values for Ti grade 2 were slightly higher than for Ti grade 4, indicating it contained finer features. The summit density (Sds) was low for all surfaces, but nHA had marginally higher Sds for both titanium grades, indicating the presence of somewhat more peaks per surface area.

Table 2. Surface roughness values of Ti and nHA-coated Ti of grades 2 and 4.

Substrate	Sa (μm)	Sdr (%)	Sds (1/μm^2)
Ti grade 4	0.23 ± 0.04	6.20 ± 1.96	0.20 ± 0.02
nHA, Ti grade 4	0.21 ± 0.05	5.29 ± 1.06	0.26 ± 0.03
Ti grade 2	0.25 ± 0.04	7.51 ± 1.14	0.22 ± 0.01
nHA, Ti grade 2	0.27 ± 0.05	7.10 ± 0.38	0.24 ± 0.03

The contact angle measurements showed the nHA-coated Ti to be superhydrophilic (contact angle < 10°), whereas the Ti controls were hydrophilic with a contact angle of 39 ± 0.5° for the 1 cm Ti discs (grade 4) and 53 ± 5.5° for the 2 cm Ti discs (grade 2); see Figure 7.

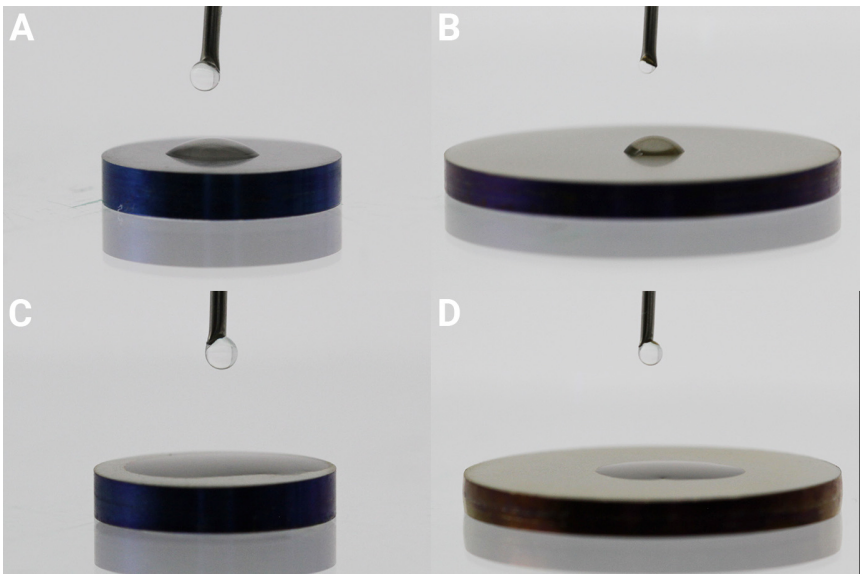

Figure 7. Water contact angle of 1 cm Ø (**A**,**C**) and 2 cm Ø (**B**,**D**) discs, control Ti (**A**,**B**) and nHA-coated Ti (**C**,**D**) showing the superhydrophilicity of the nHA coating.

3.2. Confocal Laser Scanning Microscopy

Ultrasonic removal of bacteria from surfaces has shown superior results for biofilm removal [49,50]; however, one concern in the present study was that bacterial removal was insufficient, which would lead to measurement errors. If bacteria stick harder to the nHA-treated surfaces compared to the Ti surfaces, fewer bacteria would then be cultured, and hence, an erroneous, lower number of bacteria would be the result. Therefore, Confocal Laser Scanning microscopy (CLSM) was performed to investigate the efficiency of the ultrasonic removal of biofilms from the control Ti and nHA-coated Ti. Images were obtained before and after ultrasound treatment for 5 min at 37 kHz. The control samples that were not ultrasound-treated showed 24 h biofilms of *S. epidermidis* or *P. aeruginosa* covering the substrates, as shown in Figures 8 and 9, where green bacteria were alive and red bacteria were considered dead or membrane compromised. After the ultrasound treatment, most bacteria were removed from both Ti and nHA. However, it was observed

that slightly more bacteria were present on the ultrasound-treated nHA compared to Ti, but most of the retained bacteria were dead and would thus not affect the culturing results. Dead or compromised bacteria may have attached and deformed on the surface, and thus, they were stuck harder to it.

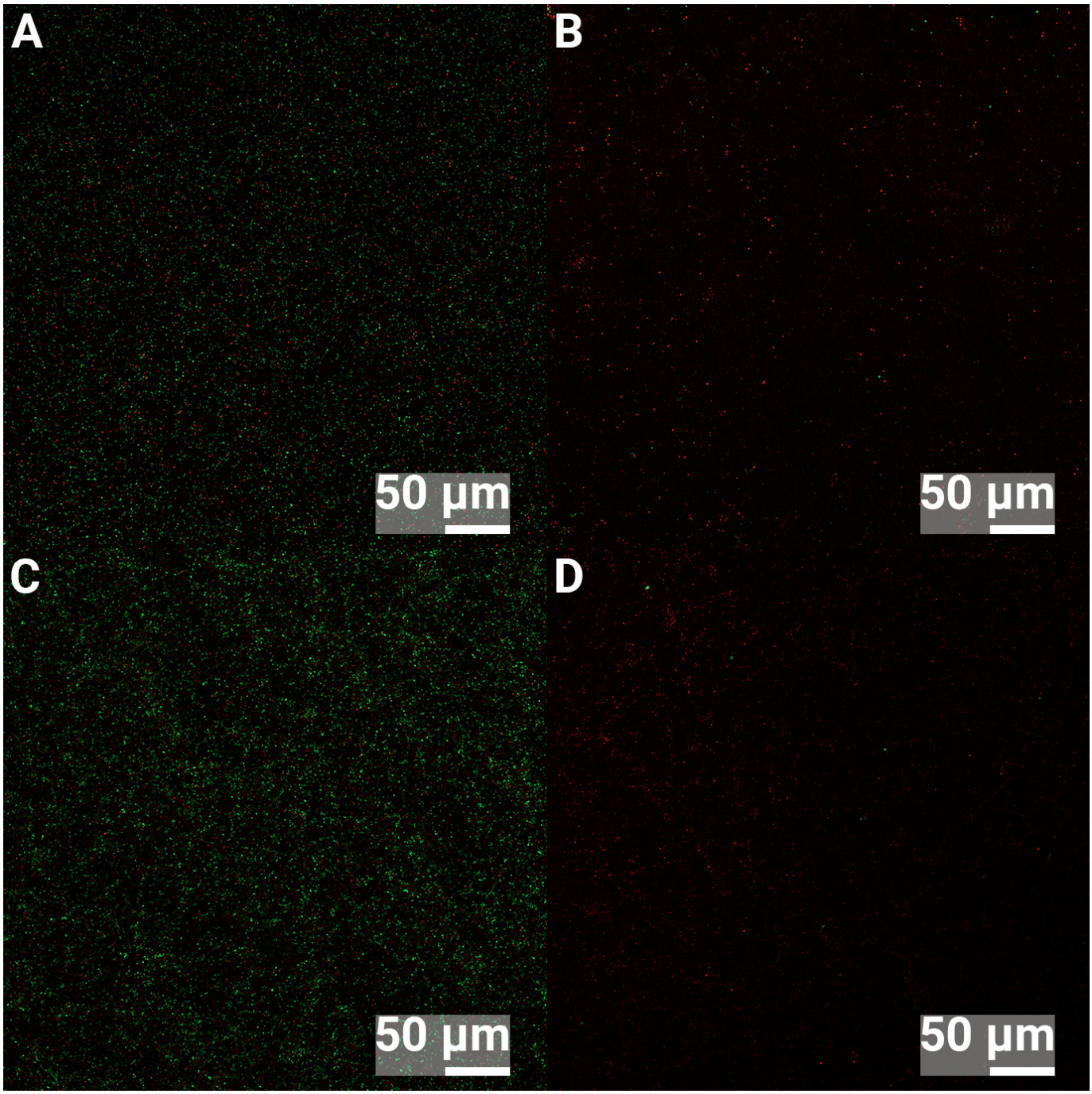

Figure 8. CLSM images of 24 h biofilms of *S. epidermidis*. (**A**) shows Ti and no ultrasound treatment, (**B**) shows Ti and 5 min ultrasound treatment, (**C**) shows nHA and no ultrasound treatment and (**D**) shows nHA with 5 min ultrasound treatment. Green bacteria are alive, and red bacteria are dead.

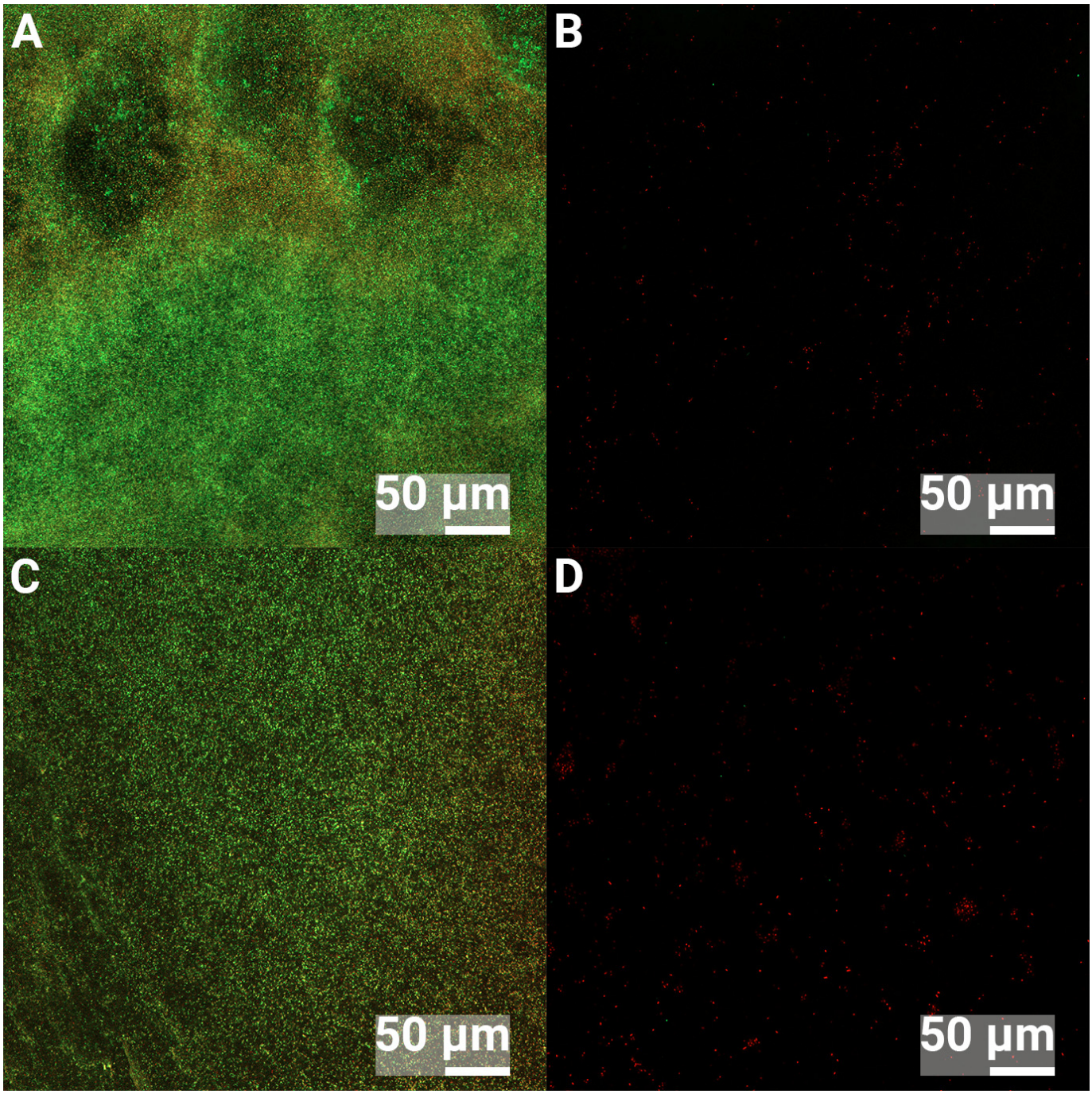

Figure 9. CLSM images of 24 h biofilms of *P. aeruginosa*. (**A**) shows Ti and no ultrasound treatment, (**B**) shows Ti and 5 min ultrasound treatment, (**C**) shows nHA and no ultrasound treatment and (**D**) shows nHA with 5 min ultrasound treatment. Green bacteria are alive, and red bacteria are dead.

3.3. Biofilm Assay

To investigate the potential action of nHA, both early and more mature biofilms were studied using a biofilm assay. For the 2 h biofilms, a drop of bacteria was added to the top surface of the Ti disc. This setup was performed to prevent any misleading results from bacteria adhering to the sides and bottom of the discs that had no nHA treatment, as is the case when placing discs in well plates and adding bacteria in the well.

As can be seen in Figure 10, for both *S. epidermidis* and *P. aeruginosa*, there was a 33% reduction in bacteria on the nHA-treated Ti compared to pure Ti ($p = 0.007$ for *S. epidermidis* and $p = 0.033$ for *P. aeruginosa*).

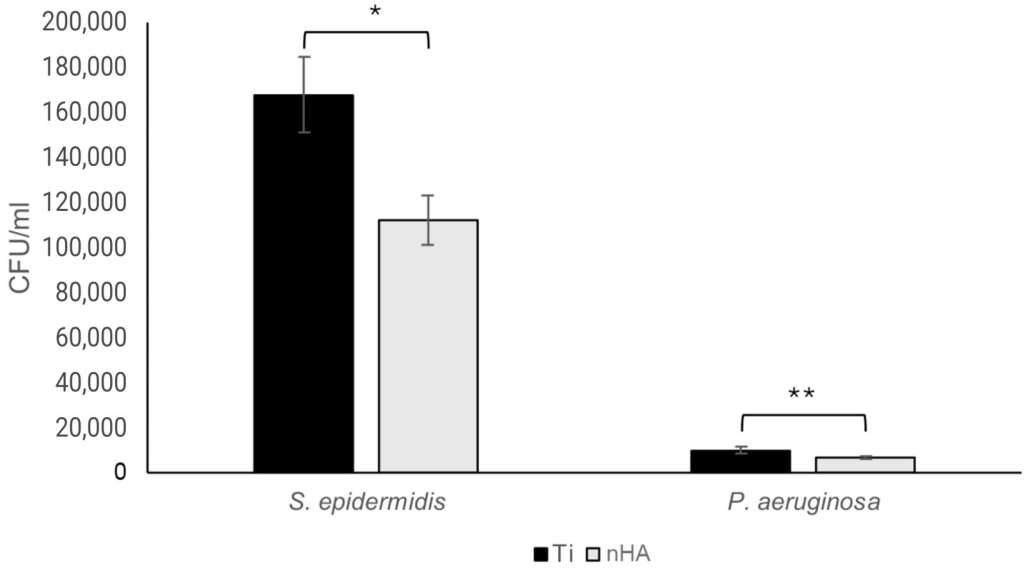

Figure 10. For 2 h *S. epidermidis* biofilms, there was a statistically significant 33.1% reduction (* $p = 0.007$) in bacterial growth on nHA compared to Ti, whereas there was a 33.0% reduction (** $p = 0.033$) for *P. aeruginosa*. Bars show the mean ± the standard error of the mean.

Interestingly, *S. epidermidis* grew faster during the two hours than *P. aeruginosa*, resulting in a rather large discrepancy in the final bacterial content, even though the same number of bacteria was added at the start. After 24 h, the results were reversed, with more *P. aeruginosa* than *S. epidermidis* biofilm bacteria. Studying the 24 h biofilms, there was a statistically significant 45.5% reduction in *S. epidermidis* ($p = 0.025$), as shown in Figure 11, and a 43.0% reduction in *P. aeruginosa* ($p = 0.013$), as shown in Figure 12.

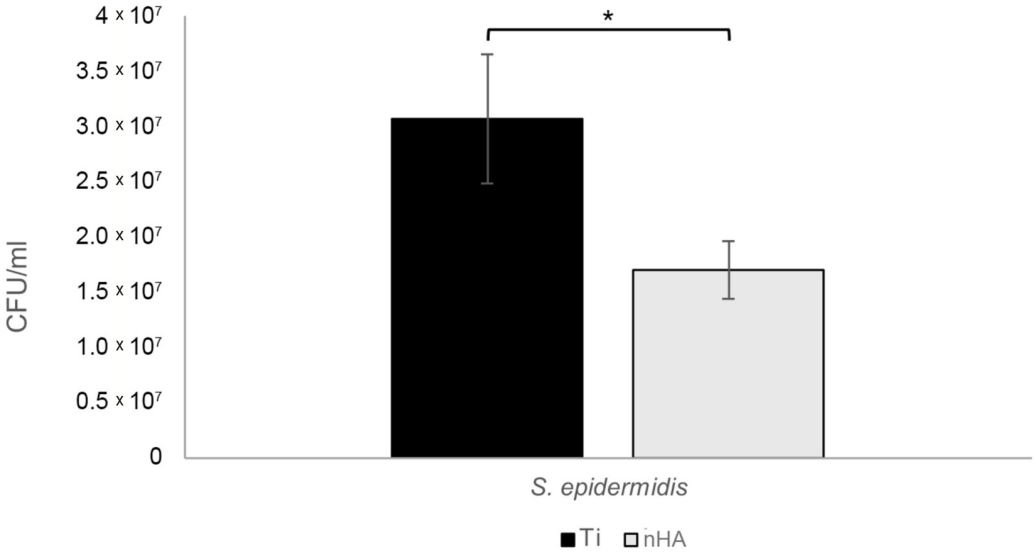

Figure 11. For 24 h *S. epidermidis* biofilms, there was a statistically significant 44.5% reduction (* $p = 0.025$) of bacterial growth on nHA compared to Ti. Bars show the mean ± the standard error of the mean.

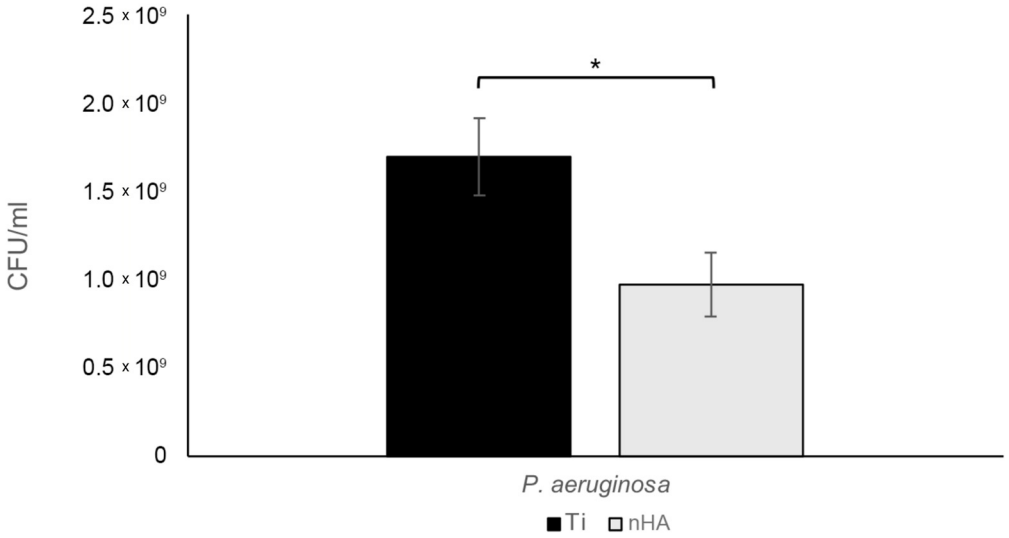

Figure 12. For 24 h *P. aeruginosa* biofilms, there was a statistically significant 43.0% reduction (* $p = 0.013$) in bacterial growth on nHA compared to Ti. Bars show the mean ± the standard error of the mean.

3.4. SEM of Biofilms

SEM analysis was performed on 24 h biofilms. There were no visible differences in the appearance of individual bacteria on pure Ti compared to nHA-treated Ti, and cell division was observed for both *S. epidermidis* and *P. aeruginosa*; see Figures 13 and 14. A few lysed bacteria were observed on the surfaces, although somewhat more lysed *P. aeruginosa* than *S. epidermidis* were found. This could be due to their thinner cell wall being more affected by the drying steps and the vacuum of the SEM. Since the bacteria, in general, did not appear compromised, the nHA seemed to be bacteriostatic rather than bactericidal.

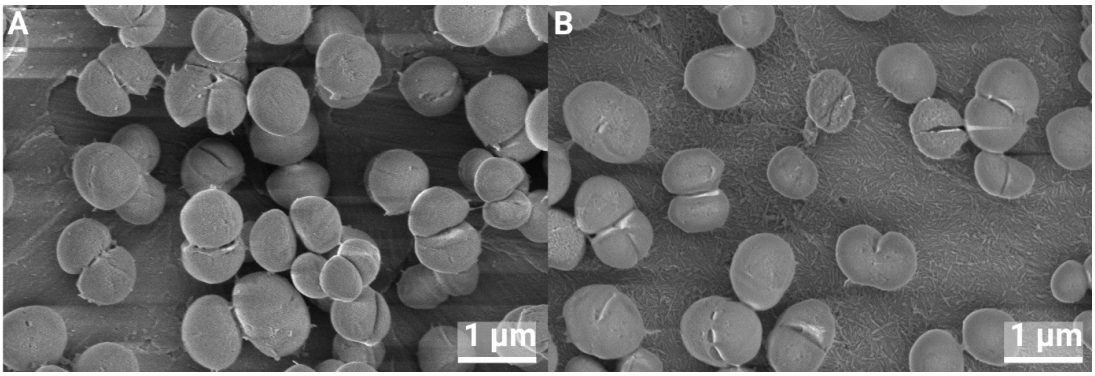

Figure 13. *S. epidermidis* growth on Ti (**A**) and nHA-treated Ti (**B**) for 24 h, at 40,000× magnification.

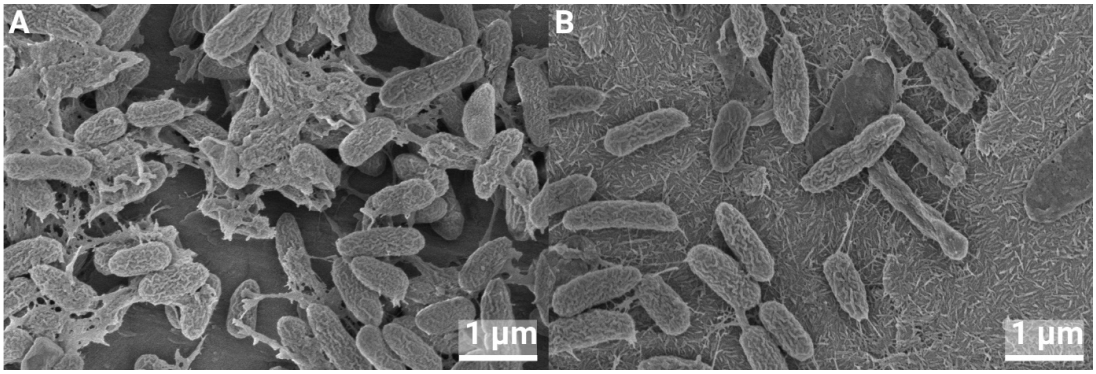

Figure 14. *P. aeruginosa* growth on Ti (**A**) and nHA-treated Ti (**B**) for 24 h, at 40,000× magnification.

4. Discussion

The surface characterization with SEM revealed nHA crystals to be homogeneously distributed all over the Ti substrate. The cross-sectional analysis performed with TEM showed an nHA layer thickness of 10–20 nm. However, as the TEM analysis was performed on an extremely smooth Si wafer, the nHA layer was expected to be thicker on rougher substrates, such as the ground Ti discs. The calculated value from the Ca assay on the discs was 25 nm, and it could be estimated to be up to 40 nm depending on substrate roughness and geometry. Two titanium grades were used in this study: Ti grade 2 and 4. Ti grade 2 was slightly rougher than Ti grade 1, and when coated with nHA, the summit density was a bit higher, indicating the presence of slightly more peaks. As Ti grade 2 is softer than grade 4, the results can be due to the grinding process using P400 paper. The nHA was superhydrophilic, which has been shown to increase interactions with biological tissue and subsequent osseointegration [51]; this would be of importance in a clinical setting.

In general, bulk HA is not regarded as an antibacterial material, but as the size of the HA is decreased to the nano-region, properties change. Studies using HA nanoparticles in the range of 19–200 nm demonstrated antibacterial effects against several bacterial species in the planktonic phase or on agar plates, such as *E. faecalis*, *E. coli*, *S. aureus*, *Bacillus* sp. and *S. mutans* [52–55]. Nanosized HA pressed into cylindrical samples and then sintered showed antibacterial effects against *S. epidermidis*, *S. aureus* and *P. aeruginosa,* depending on the sintering temperature [56]. Biofilm bacteria from pooled salivary samples showed reduced growth in the presence of nHA rods coated on Ti [57]. These studies showed a partial eradication of bacteria using nHA, with a bacterial elimination varying from 33 to 46%, depending on time and species. Interestingly, in this study the antibacterial effect was similar for both Gram-positive and Gram-negative bacteria, which is essential in a clinical setting where bacterial contamination may vary. As with all in vitro tests, the limitation is whether this effect is also visible in vivo; however, using this nHA coating on implants has the potential to reduce the number of infections related to implants.

In the literature, a vast array of different kinds of nHA is described, and some studies also report an increase in bacterial growth. Although antimicrobial against planktonic *C. albicans* after 24 h growth, an initial load of 1.5×10^8 CFU/mL of *S. mutans* and *L. rhamnosus* increased in growth when HA nanoparticles were present [58]. It was hypothesized that a large bacterial load crowded the surface and created a monolayer biofilm, to which new bacteria that did not sense the surface effect could attach. It is, therefore, reasonable to believe that a high bacterial load makes it difficult to distinguish the growth of bacteria in the bulk from the growth on the surface of a substrate; therefore, the bacterial load was set to a lower amount in the present study.

For in vitro studies, this lower bacterial load is more clinically relevant, as the potential number of contaminating bacteria during implantation surgery is often low. Implant surgery should take place in ORs with ultraclean air, where there are $\leq$10 CFU/m^3 [59]; 270 CFUs attached to airborne particles have been estimated to fall onto a 250 cm^2 wound area during hip replacement [60]. Another study investigating airborne particulate contaminations during 13 hip arthroplasties showed a total CFU count of 1786, with higher numbers for longer surgery durations and higher staff counts [61]. In patients undergoing orthopedic trauma surgery, cutting the skin after disinfection and swabbing the cut yielded 4–9000 CFUs, with a median of 8 [62]; in total knee arthroplasties, the mean bacterial contamination level was 10.6 CFU/g [15]. A low initial bacterial load is also applied in many animal infection models. A rabbit spinal implant infection model using MRSA showed consistent local infection from 10^3 CFUs and higher. In a similar setup, *E. coli* consistently produced infection using 10^5 CFUs. In rats, 10^6 *S. aureus* showed consistent infections in a spinal model, whereas for dogs, it was 10^2 CFUs *S. aureus* [14].

Intraoperative contamination during implant surgery is common, and the main sources are the skin of patients and airborne particles from personnel. Even a low number of bacteria adhering early to the implant may interfere with the bone healing process. Both the antibacterial effect shown here and the ability of nHA to osseointegrate, even in metabolically challenged patients [63], improve the odds for the immune system and antibacterial therapy to eradicate potential bacteria and prevent infections.

Attempts to find out the antibacterial mechanism of hydroxyapatite have been made for nanoparticles in solution. The most common proposed mechanism is the uptake of particles by bacteria with subsequent disruption of DNA replication, formation of reactive oxygen species and direct damage to cell membranes [64]. Another possible mechanism is dissolved calcium and phosphate ions exerting an antibacterial effect [53,64], which causes damage to the cell wall and altered permeability [65,66].

The dissolution of the nHA coating may be one explanation for the observed bacteriostatic effect, but the SEM analysis after 24 h showed no effect on the appearance of the crystalline nHA layer. Even if the crystals were still visible, some dissolution on the surface of the crystals could occur. However, given that the total amount of nHA was measured to be around 8 $\mu g/cm^2$, and TEM analysis showed the nHA layer to be 10–20 nm thick, the amount of Ca and P from the surface dissolution of the crystals would be extremely small. Therefore, a bacteriostatic effect resulting from Ca and P release is a less plausible explanation. Superhydrophilicity may be another explanation, which is well known to inhibit bacterial attachment [67], although a complete eradication of bacteria is not always obtained [23]. Yet another factor is the surface charge. In physiological pH, HA is negatively charged [68], and a possible mechanism would be that negatively charged bacteria are repelled by the negatively charged HA surface. The mechanism of the antibacterial effect of the nHA used in this study may depend on several factors and needs further investigation.

5. Conclusions

The coating used in this study showed nanosized HA crystals homogeneously spread over a Ti substrate in a 20–40 nm thick layer, which was superhydrophilic. The nHA layer showed a significant antibacterial effect, varying from 33% to 44.5% reduction, for 2 and 24 h biofilms, respectively, using *S. epidermidis* and *P. aeruginosa*, and was similar for both the Gram-positive and Gram-negative strains. The antibacterial effect seemed to be physicochemical rather than biological, which reduces the risk of bacterial resistance. This can be of benefit on implants in a clinical setting. Future research may investigate the antibacterial mechanism responsible for the results of this study. In addition, an in vivo study can be performed to investigate the antibacterial effects in an animal model.

Author Contributions: Conceptualization, M.H. and P.K.; methodology, M.H. and P.K.; validation, M.H.; formal analysis, M.H. and S.E.; investigation, M.H., S.E. and K.D.; writing—original draft preparation, M.H.; writing—review and editing, P.K.; visualization, M.H. and S.E.; supervision, M.H. and P.K. All authors have read and agreed to the published version of the manuscript.

Funding: This research received no external funding.

Institutional Review Board Statement: Not applicable.

Informed Consent Statement: Not applicable.

Data Availability Statement: The original contributions presented in this study are included in this article; further inquiries can be directed to the corresponding author. The data are available on request from the authors.

Acknowledgments: We acknowledge the Center for Cellular Imaging at the University of Gothenburg and the National Microscopy Infrastructure, NMI (VR-RFI 2019-00022), for providing microscope accessibility and training. Kalle Martinsson at Promimic is acknowledged for valuable help with the graphics and layout of this manuscript. Edmund Hansla at Promimic is acknowledged for valuable help with surface coating and general laboratory tasks.

Conflicts of Interest: Authors Maria Holmström, Karin Danielsson and Per Kjellin are employed by Promimic AB and own stocks in the company. Author Sonia Esko declares no conflicts of interest.

References

1. Aggarwal, V.K.; Rasouli, M.R.; Parvizi, J. Periprosthetic joint infection: Current concept. *Indian J. Orthop.* **2013**, *47*, 10–17. [CrossRef]
2. Choi, S.W.; Lee, J.C.; Lee, W.S.; Hwang, J.Y.; Baek, M.J.; Choi, Y.S.; Jang, H.D.; Shin, B.J. Clinical differences between delayed and acute onset postoperative spinal infection. *Medicine* **2022**, *101*, e29366. [CrossRef] [PubMed]
3. Clark, C.E.; Shufflebarger, H.L. Late-developing infection in instrumented idiopathic scoliosis. *Spine* **1999**, *24*, 1909–1912. [CrossRef] [PubMed]
4. Parchi, P.D.; Evangelisti, G.; Andreani, L.; Girardi, F.; Darren, L.; Sama, A.; Lisanti, M. Postoperative Spine Infections. *Orthop. Rev.* **2015**, *7*, 5900. [CrossRef]
5. Köder, K.; Hardt, S.; Gellert, M.S.; Haupenthal, J.; Renz, N.; Putzier, M.; Perka, C.; Trampuz, A. Outcome of spinal implant-associated infections treated with or without biofilm-active antibiotics: Results from a 10-year cohort study. *Infection* **2020**, *48*, 559–568. [CrossRef] [PubMed]
6. Dapunt, U.; Bürkle, C.; Günther, F.; Pepke, W.; Hemmer, S.; Akbar, M. Surgical site infections following instrumented stabilization of the spine. *Ther. Clin. Risk Manag.* **2017**, *13*, 1239–1245. [CrossRef]
7. Guo, G.; Wang, J.; You, Y.; Tan, J.; Shen, H. Distribution characteristics of Staphylococcus spp. in different phases of periprosthetic joint infection: A review. *Exp. Ther. Med.* **2017**, *13*, 2599–2608. [CrossRef] [PubMed]
8. Arciola, C.R.; Campoccia, D.; Montanaro, L. Implant infections: Adhesion, biofilm formation and immune evasion. *Nat. Rev. Microbiol.* **2018**, *16*, 397–409. [CrossRef] [PubMed]
9. Sampedro, M.F.; Huddleston, P.M.; Piper, K.E.; Karau, M.J.; Dekutoski, M.B.; Yaszemski, M.J.; Currier, B.L.; Mandrekar, J.N.; Osmon, D.R.; McDowell, A.; et al. A biofilm approach to detect bacteria on removed spinal implants. *Spine* **2010**, *35*, 1218–1224. [CrossRef] [PubMed]
10. Elek, S.D.; Conen, P.E. The virulence of Staphylococcus pyogenes for man; a study of the problems of wound infection. *Br. J. Exp. Pathol.* **1957**, *38*, 573–586.
11. Zimmerli, W.; Waldvogel, F.A.; Vaudaux, P.; Nydegger, U.E. Pathogenesis of foreign body infection: Description and characteristics of an animal model. *J. Infect. Dis.* **1982**, *146*, 487–497. [CrossRef] [PubMed]
12. Poelstra, K.A.; Barekzi, N.A.; Grainger, D.W.; Gristina, A.G.; Schuler, T.C. A novel spinal implant infection model in rabbits. *Spine* **2000**, *25*, 406–410. [CrossRef]
13. Laratta, J.L.; Shillingford, J.N.; Hardy, N.; Lehman, R.A.; Lenke, L.G.; Riew, K.D. A Dose-Response Curve for a Gram-Negative Spinal Implant Infection Model in Rabbits. *Spine* **2017**, *42*, E1225–E1230. [CrossRef] [PubMed]
14. Wang, Y.; Che, M.; Zheng, Z.; Liu, J.; Ji, X.; Sun, Y.; Xin, J.; Gong, W.; Na, S.; Jin, Y.; et al. Animal Models for Postoperative Implant-Related Spinal Infection. *Orthop. Surg.* **2022**, *14*, 1049–1058. [CrossRef]
15. Alomar, A.Z.; Alfayez, S.M.; Binnasser, A.; Aljassir, F.F. Intraoperative evaluation and level of contamination during total knee arthroplasty. *Acta Ortop. Bras.* **2022**, *30*, e243232. [CrossRef]
16. Khajanchi, B.K.; Kirtley, M.L.; Brackman, S.M.; Chopra, A.K. Immunomodulatory and protective roles of quorum-sensing signaling molecules N-acyl homoserine lactones during infection of mice with Aeromonas hydrophila. *Infect. Immun.* **2011**, *79*, 2646–2657. [CrossRef]
17. Thurlow, L.R.; Hanke, M.L.; Fritz, T.; Angle, A.; Aldrich, A.; Williams, S.H.; Engebretsen, I.L.; Bayles, K.W.; Horswill, A.R.; Kielian, T. Staphylococcus aureus biofilms prevent macrophage phagocytosis and attenuate inflammation in vivo. *J. Immunol.* **2011**, *186*, 6585–6596. [CrossRef] [PubMed]
18. Hanke, M.L.; Angle, A.; Kielian, T. MyD88-dependent signaling influences fibrosis and alternative macrophage activation during Staphylococcus aureus biofilm infection. *PLoS ONE* **2012**, *7*, e42476. [CrossRef] [PubMed]
19. Kristian, S.A.; Birkenstock, T.A.; Sauder, U.; Mack, D.; Götz, F.; Landmann, R. Biofilm formation induces C_3a release and protects *Staphylococcus epidermidis* from IgG and complement deposition and from neutrophil-dependent killing. *J. Infect. Dis.* **2008**, *197*, 1028–1035. [CrossRef] [PubMed]

20. Belgiovine, C.; Pellegrino, L.; Bulgarelli, A.; Lauta, F.C.; Di Claudio, A.; Ciceri, R.; Cancellara, A.; Calcaterra, F.; Mavilio, D.; Grappiolo, G.; et al. Interaction of Bacteria, Immune Cells, and Surface Topography in Periprosthetic Joint Infections. *Int. J. Mol. Sci.* **2023**, *24*, 9028. [CrossRef] [PubMed]
21. Tucci, G.; Romanini, E.; Zanoli, G.; Pavan, L.; Fantoni, M.; Venditti, M. Prevention of surgical site infections in orthopaedic surgery: A synthesis of current recommendations. *Eur. Rev. Med. Pharmacol. Sci.* **2019**, *23*, 224–239. [CrossRef]
22. Milleret, V.; Lienemann, P.S.; Gasser, A.; Bauer, S.; Ehrbar, M.; Wennerberg, A. Rational design and in vitro characterization of novel dental implant and abutment surfaces for balancing clinical and biological needs. *Clin. Implant. Dent. Relat. Res.* **2019**, *21* (Suppl. S1), 15–24. [CrossRef]
23. Jeong, W.S.; Kwon, J.S.; Lee, J.H.; Uhm, S.H.; Ha Choi, E.; Kim, K.M. Bacterial attachment on titanium surfaces is dependent on topography and chemical changes induced by nonthermal atmospheric pressure plasma. *Biomed. Mater.* **2017**, *12*, 045015. [CrossRef]
24. Skovdal, S.M.; Jørgensen, N.P.; Petersen, E.; Jensen-Fangel, S.; Ogaki, R.; Zeng, G.; Johansen, M.I.; Wang, M.; Rohde, H.; Meyer, R.L. Ultra-dense polymer brush coating reduces Staphylococcus epidermidis biofilms on medical implants and improves antibiotic treatment outcome. *Acta Biomater.* **2018**, *76*, 46–55. [CrossRef]
25. Subramani, K.; Jung, R.E.; Molenberg, A.; Hammerle, C.H. Biofilm on dental implants: A review of the literature. *Int. J. Oral Maxillofac. Implant.* **2009**, *24*, 616–626.
26. Savarino, L.; Fini, M.; Ciapetti, G.; Cenni, E.; Granchi, D.; Baldini, N.; Greco, M.; Rizzi, G.; Giardino, R.; Giunti, A. Biologic effects of surface roughness and fluorhydroxyapatite coating on osteointegration in external fixation systems: An in vivo experimental study. *J. Biomed. Mater. Res. A* **2003**, *66A*, 652–661. [CrossRef]
27. Scheeren Brum, R.; Apaza-Bedoya, K.; Labes, L.G.; Volpato, C.Â.M.; Pimenta, A.L.; Benfatti, C.A.M. Early Biofilm Formation on Rough and Smooth Titanium Specimens: A Systematic Review of Clinical Studies. *J. Oral Maxillofac. Res.* **2021**, *12*, e1. [CrossRef] [PubMed]
28. Saulacic, N.; Schaller, B. Prevalence of Peri-Implantitis in Implants with Turned and Rough Surfaces: A Systematic Review. *J. Oral Maxillofac. Res.* **2019**, *10*, e1. [CrossRef] [PubMed]
29. Zeller, B.; Stöckli, S.; Zaugg, L.K.; Astasov-Frauenhoffer, M.; Hauser-Gerspach, I.; Waltimo, T.; Zitzmann, N.U. Biofilm formation on metal alloys, zirconia and polyetherketoneketone as implant materials in vivo. *Clin. Oral Implant. Res.* **2020**, *31*, 1078–1086. [CrossRef]
30. Meier, D.; Astasov-Frauenhoffer, M.; Waltimo, T.; Zaugg, L.K.; Rohr, N.; Zitzmann, N.U. Biofilm formation on metal alloys and coatings, zirconia, and hydroxyapatite as implant materials in vivo. *Clin. Oral Implant. Res.* **2023**, *34*, 1118–1126. [CrossRef] [PubMed]
31. Hegde, V.; Park, H.Y.; Dworsky, E.; Zoller, S.D.; Xi, W.; Johansen, D.O.; Loftin, A.H.; Hamad, C.D.; Segura, T.; Bernthal, N.M. The Use of a Novel Antimicrobial Implant Coating In Vivo to Prevent Spinal Implant Infection. *Spine* **2020**, *45*, E305–E311. [CrossRef] [PubMed]
32. D'Almeida, M.; Attik, N.; Amalric, J.; Brunon, C.; Renaud, F.; Abouelleil, H.; Toury, B.; Grosgogeat, B. Chitosan coating as an antibacterial surface for biomedical applications. *PLoS ONE* **2017**, *12*, e0189537. [CrossRef]
33. Asri, L.A.T.W.; Crismaru, M.; Roest, S.; Chen, Y.; Ivashenko, O.; Rudolf, P.; Tiller, J.C.; van der Mei, H.C.; Loontjens, T.J.A.; Busscher, H.J. A Shape-Adaptive, Antibacterial-Coating of Immobilized Quaternary-Ammonium Compounds Tethered on Hyperbranched Polyurea and its Mechanism of Action. *Adv. Funct. Mater.* **2014**, *24*, 346–355. [CrossRef]
34. Cao, Y.; Su, B.; Chinnaraj, S.; Jana, S.; Bowen, L.; Charlton, S.; Duan, P.; Jakubovics, N.S.; Chen, J. Nanostructured titanium surfaces exhibit recalcitrance towards Staphylococcus epidermidis biofilm formation. *Sci. Rep.* **2018**, *8*, 1071. [CrossRef] [PubMed]
35. Albrektsson, T.; Wennerberg, A. On osseointegration in relation to implant surfaces. *Clin. Implant. Dent. Relat. Res.* **2019**, *21* (Suppl. S1), 4–7. [CrossRef]
36. Voigt, J.D.; Mosier, M. Hydroxyapatite (HA) coating appears to be of benefit for implant durability of tibial components in primary total knee arthroplasty. *Acta Orthop.* **2011**, *82*, 448–459. [CrossRef] [PubMed]
37. Vidalain, J.P. Twenty-year results of the cementless Corail stem. *Int. Orthop.* **2011**, *35*, 189–194. [CrossRef] [PubMed]
38. Røkkum, M.; Reigstad, A.; Johansson, C.B. HA particles can be released from well-fixed HA-coated stems: Histopathology of biopsies from 20 hips 2–8 years after implantation. *Acta Orthop.* **2002**, *73*, 298–306. [CrossRef] [PubMed]
39. Overgaard, S.; Lind, M.; Rahbek, O.; Bünger, C.; Søballe, K. Improved fixation of porous-coated versus grit-blasted surface texture of hydroxyapatite-coated implants in dogs. *Acta Orthop.* **1997**, *68*, 337–343. [CrossRef] [PubMed]
40. Nunes, F.; Oliveira, P.; Bergamo, E.; Kjellin, P.; Novaes, A., Jr.; Ghiraldini, B.; Bezerra, F.; Scombatti de Souza, S. Effect of Smoke Exposure on Gene Expression in Bone Healing around Implants Coated with Nanohydroxyapatite. *Nanomaterials* **2022**, *12*, 3737. [CrossRef]
41. Adam, M.; Ganz, C.; Xu, W.; Sarajian, H.R.; Götz, W.; Gerber, T. In vivo and in vitro investigations of a nanostructured coating material—A preclinical study. *Int. J. Nanomed.* **2014**, *9*, 975–984. [CrossRef] [PubMed]

42. Johansson, P.; Jimbo, R.; Kozai, Y.; Sakurai, T.; Kjellin, P.; Currie, F.; Wennerberg, A. Nanosized Hydroxyapatite Coating on PEEK Implants Enhances Early Bone Formation: A Histological and Three-Dimensional Investigation in Rabbit Bone. *Materials* **2015**, *8*, 3815–3830. [CrossRef]
43. Almeida, D.; Sartoretto, S.C.; Calasans-Maia, J.A.; Ghiraldini, B.; Bezerra, F.J.B.; Granjeiro, J.M.; Calasans-Maia, M.D. In vivo osseointegration evaluation of implants coated with nanostructured hydroxyapatite in low density bone. *PLoS ONE* **2023**, *18*, e0282067. [CrossRef] [PubMed]
44. Bergamo, E.T.P.; de Oliveira, P.; Campos, T.M.B.; Bonfante, E.A.; Tovar, N.; Boczar, D.; Nayak, V.V.; Coelho, P.G.; Witek, L. Osseointegration of implant surfaces in metabolic syndrome and type-2 diabetes mellitus. *J. Biomed. Mater. Res. B Appl. Biomater.* **2024**, *112*, e35382. [CrossRef]
45. *ISO 25178-604:2025*; Geometrical Product Specifications (GPS)—Surface Texture: Areal. Part 604: Nominal Characteristics of Non-Contact (Coherence Scanning Interferometry) Instruments. ISO: Geneva, Switzerland, 2025.
46. *ASTM D1193-99e1*; Standard Specification for Reagent Water. ASTM: West Conshohocken, PA, USA, 2017.
47. Johansson, P.; Jimbo, R.; Naito, Y.; Kjellin, P.; Currie, F.; Wennerberg, A. Polyether ether ketone implants achieve increased bone fusion when coated with nano-sized hydroxyapatite: A histomorphometric study in rabbit bone. *Int. J. Nanomed.* **2016**, *11*, 1435–1442. [CrossRef] [PubMed]
48. Wennerberg, A.; Albrektsson, T. Effects of titanium surface topography on bone integration: A systematic review. *Clin. Oral Implant. Res.* **2009**, *20* (Suppl. S4), 172–184. [CrossRef] [PubMed]
49. Moris, V.; Lam, M.; Amoureux, L.; Magallon, A.; Guilloteau, A.; Maldiney, T.; Zwetyenga, N.; Falentin-Daudre, C.; Neuwirth, C. What is the best technic to dislodge Staphylococcus epidermidis biofilm on medical implants? *BMC Microbiol.* **2022**, *22*, 192. [CrossRef]
50. Karbysheva, S.; Di Luca, M.; Butini, M.E.; Winkler, T.; Schütz, M.; Trampuz, A. Comparison of sonication with chemical biofilm dislodgement methods using chelating and reducing agents: Implications for the microbiological diagnosis of implant associated infection. *PLoS ONE* **2020**, *15*, e0231389. [CrossRef]
51. Sartoretto, S.C.; Alves, A.T.; Resende, R.F.; Calasans-Maia, J.; Granjeiro, J.M.; Calasans-Maia, M.D. Early osseointegration driven by the surface chemistry and wettability of dental implants. *J. Appl. Oral Sci.* **2015**, *23*, 279–287. [CrossRef]
52. Guerreiro-Tanomaru, J.M.; Vázquez-García, F.A.; Bosso-Martelo, R.; Bernardi, M.I.; Faria, G.; Tanomaru, M.F. Effect of addition of nano-hydroxyapatite on physico-chemical and antibiofilm properties of calcium silicate cements. *J. Appl. Oral Sci.* **2016**, *24*, 204–210. [CrossRef]
53. Lamkhao, S.; Phaya, M.; Jansakun, C.; Chandet, N.; Thongkorn, K.; Rujijanagul, G.; Bangrak, P.; Randorn, C. Synthesis of Hydroxyapatite with Antibacterial Properties Using a Microwave-Assisted Combustion Method. *Sci. Rep.* **2019**, *9*, 4015. [CrossRef]
54. Ragab, H.; Ibrahim, F.; Abdallah, F.; Al-Ghamdi, A.; El-Tantawy, P.F.; Yakuphanoglu, F. Synthesis and In Vitro Antibacterial Properties of Hydroxyapatite Nanoparticles. *IOSR J. Pharm. Biol. Sci.* **2014**, *9*, 77–85. [CrossRef]
55. Park, M.; Sutherland, J.B.; Rafii, F. Effects of nano-hydroxyapatite on the formation of biofilms by Streptococcus mutans in two different media. *Arch. Oral Biol.* **2019**, *107*, 104484. [CrossRef]
56. Grenho, L.; Manso, M.C.; Monteiro, F.J.; Ferraz, M.P. Adhesion of Staphylococcus aureus, Staphylococcus epidermidis, and Pseudomonas aeruginosa onto nanohydroxyapatite as a bone regeneration material. *J. Biomed. Mater. Res. A* **2012**, *100*, 1823–1830. [CrossRef]
57. Abdulkareem, E.H.; Memarzadeh, K.; Allaker, R.P.; Huang, J.; Pratten, J.; Spratt, D. Anti-biofilm activity of zinc oxide and hydroxyapatite nanoparticles as dental implant coating materials. *J. Dent.* **2015**, *43*, 1462–1469. [CrossRef]
58. Zakrzewski, W.; Rybak, Z.; Pajączkowska, M.; Nowicka, J.; Szymonowicz, M.; Rusak, A.; Wiglusz, R.J.; Szyszka, K.; Chmielowiec, J.; Chodaczek, G.; et al. Antimicrobial Properties and Cytotoxic Effect Evaluation of Nanosized Hydroxyapatite and Fluorapatite Dedicated for Alveolar Bone Regeneration. *Appl. Sci.* **2024**, *14*, 7845. [CrossRef]
59. Whyte, W.; Lidwell, O.M.; Lowbury, E.J.L.; Blowers, R. Suggested bacteriological standards for air in ultraclean operating rooms. *J. Hosp. Infect.* **1983**, *4*, 133–139. [CrossRef]
60. Lidwell, O.M. Airborne bacteria and surgical infection. *Am. J. Med.* **1981**, *70*, 693–697. [CrossRef] [PubMed]
61. Stocks, G.W.; Self, S.D.; Thompson, B.; Adame, X.A.; O'Connor, D.P. Predicting bacterial populations based on airborne particulates: A study performed in nonlaminar flow operating rooms during joint arthroplasty surgery. *Am. J. Infect. Control* **2010**, *38*, 199–204. [CrossRef] [PubMed]
62. Guarch-Pérez, C.; Riool, M.; de Boer, L.; Kloen, P.; Zaat, S.A.J. Bacterial reservoir in deeper skin is a potential source for surgical site and biomaterial-associated infections. *J. Hosp. Infect.* **2023**, *140*, 62–71. [CrossRef] [PubMed]
63. Granato, R.; Bergamo, E.T.P.; Witek, L.; Bonfante, E.A.; Marin, C.; Greenberg, M.; Kurgansky, G.; Coelho, P.G. Clinical, histological, and nanomechanical parameters of implants placed in healthy and metabolically compromised patients. *J. Dent.* **2020**, *100*, 103436. [CrossRef]

64. Baskar, K.; Anusuya, T.; Devanand Venkatasubbu, G. Mechanistic investigation on microbial toxicity of nano hydroxyapatite on implant associated pathogens. *Mat. Sci. Eng. C* **2017**, *73*, 8–14. [CrossRef] [PubMed]
65. Knabel, S.J.; Walker, H.W.; Hartman, P.A. Inhibition of Aspergillus flavus and Selected Gram-positive Bacteria by Chelation of Essential Metal Cations by Polyphosphates. *J. Food Prot.* **1991**, *54*, 360–365. [CrossRef]
66. Xie, Y.; Yang, L. Calcium and Magnesium Ions Are Membrane-Active against Stationary-Phase Staphylococcus aureus with High Specificity. *Sci. Rep.* **2016**, *6*, 20628. [CrossRef]
67. Shao, H.; Ma, M.; Wang, Q.; Yan, T.; Zhao, B.; Guo, S.; Tong, S. Advances in the superhydrophilicity-modified titanium surfaces with antibacterial and pro-osteogenesis properties: A review. *Front. Bioeng. Biotechnol.* **2022**, *10*, 1000401. [CrossRef] [PubMed]
68. Kinnari, T.J.; Esteban, J.; Martin-de-Hijas, N.Z.; Sánchez-Muñoz, O.; Sánchez-Salcedo, S.; Colilla, M.; Vallet-Regí, M.; Gomez-Barrena, E. Influence of surface porosity and pH on bacterial adherence to hydroxyapatite and biphasic calcium phosphate bioceramics. *J. Med. Microbiol.* **2009**, *58 Pt 1*, 132–137. [CrossRef]

MDPI AG
Grosspeteranlage 5
4052 Basel
Switzerland
Tel.: +41 61 683 77 34

Journal of Functional Biomaterials Editorial Office
E-mail: jfb@mdpi.com
www.mdpi.com/journal/jfb

Academic Open
Access Publishing

mdpi.com

ISBN 978-3-7258-4178-3